NUREG/CR-3110
PNL-4584
Vol. 2

Reliability of Nondestructive Examination

Chapters 7 - 11

Prepared by S. H. Bush

Pacific Northwest Laboratory
Operated by
Battelle Memorial Institute

Prepared for
U.S. Nuclear Regulatory Commission

GPO Printed copy price: $13.00

NUREG/CR-3110
PNL-4584
Vol. 2
R5

Reliability of Nondestructive Examination

Chapters 7 - 11

Manuscript Completed: August 1983
Date Published: October 1983

Prepared by
S. H. Bush

Pacific Northwest Laboratory
Richland, WA 99352

Prepared for
Division of Engineering Technology
Office of Nuclear Regulatory Research
U.S. Nuclear Regulatory Commission
Washington, D.C. 20555
NRC FIN B2289

ABSTRACT

This eighteen-chapter, three-volume study evaluates the various nondestructive examination (NDE) techniques now used to detect flaws in components of nuclear systems so that the reliability of the techniques may be increased. The significance of flaws at various locations in pressure boundary components are assessed along with ways to optimize the NDE procedures needed to detect, locate and size them. Emphasis is placed on an integrated program which also considers design, fabrication procedures, and materials. The data available on the reliability of detecting, locating and sizing flaws by NDE are used to construct a probabilistic fracture mechanics model. The model highlights the significance of the failure to detect flaws, and to accurately locate or size them in the context of component failure probability.

This study was conducted under the U.S. Nuclear Regulatory Commission program on the "Integration of NDE Reliability and Fracture Mechanics." Its objectives include 1) improving examination procedures for incorporation into the American Society for Mechanical Engineers (ASME), Boiler and Pressure Vessel Codes, Section III, V, XI; and 2) gaining a better insight into the influence of improved reliability of NDE in detecting, locating and sizing flaws on component failure probabilities.

CONTENTS BY VOLUMES

ACRONYMS

ACRS	Advisory Committee on Reactor Safeguards
AD	Arbeitsgemeinschaft Druckbehälter
AD-RHP	Arbeitsgemeinschaft Druckbehälter-Reactor HP
AE	Acoustic Emission
AEC	Atomic Energy Commission
AEC/NRC	Atomic Energy Commission/Nuclear Regulatory Commission
AFML	Air Force Materials Lab
AH	Acoustic Holography
ALN	Adaptive Learning Network
ANL	Argonne National Laboratory
ARPA	Advanced Research Projects Agency
ASME	American Society for Mechanical Engineers
AVG	Abstand-Verstärker-Grosse
AVS	Distance Amplification Size
BNA	Barkhausen Noise Analysis
BWR	Boiling Water Reactor
CAP	Correct Acceptance Probability
CEGB	Central Electricity Generating Board
CRP	Correct Rejection Probability
DAC	Distance Amplitude Correction
DDP	Defect Detection Probability
DGS	Distance-Gain-Size
DG(z)	German Association for NDE Methods
DWR	Druckwasser Reaktor (German PWR)

EBS	Electronic Block Simulator
EDM	Electric Discharge Machining
EMA	Electromagnetic-Acoustic
EMAT	Electromagnetic Acoustic Transducers
EL	Error in Location
EPFM	Elastic-Plastic Fracture Mechanics
EPRI	Electric Power Research Institute
ES	Error in Sizing
ET	Engineering Testing
FRG	Federal Republic of Germany
GYFM	General Yield Fracture Mechanics
HAZ	Heat Affected Zone
HP	German Pressure Code Series
HSST	Heavy-Section Steel Technology
IAEA	International Atomic Energy Agency
ICP	Industry Cooperative Program
IGSCC	Intergranular Stress Corrosion Cracking
ISI	Inservice Inspection
ITV	Intermediate Test Vessel
IWG-RRPC	International Working Group on Reliability of Reactor Pressure Components
JAEC	Japan Atomic Energy Commission
LEFM	Linear Elastic Fracture Mechanics
LMFBR	Liquid Metal Fast Breeder Reactor
MPT	Magnetic Particle Testing
MMA	Manual Metal Arc (welding)

MIG	Metal Inert Gas (welding)
MITI	Ministry of Technology and Industry (Japan)
NASA	National Aeronautics and Space Administration
NBS	National Bureau of Standards
NDE	Nondestructive Examination
NRC-Res	Nuclear Regulatory Commission—Office of Research
PISC	Plate Inspection Steering Committee
PSI	Preservice Inspection
PT	Penetrant Testing
PVRC	Pressure Vessel Research Committee
PWHT	Post Weld Heat Treatments
PWR	Pressurized Water Reactor
PZT	Lead Zirconate Titanate (transducer)
QA	Quality of Acceptance
RF	Radio Frequency
RPV	Reactor Pressure Vessel
RSK	Reaktor-Sicherheit (German Reactor Safety Commission)
RT	Radiographic Testing
RTD-BAM	Röntgen-Technische-Dienst (RT)-Bundesanstalt für Materialprüfung (German Federal Institute for Material Testing)
SAFT-UT	Synthetic Aperture Focusing Technique for Ultrasonic Testing
SAR	Safety Analysis Report
SCC	Stress Corrosion Cracking
SET	Stress Exposure Technique
SMIRT	Structural Materials in Reactor Technology
SWP	Special Work Permit

USNRC	United States Nuclear Regulatory Commission
UT	Ultrasonic Testing
UT/ADP	Ultrasonic Automatic Data Processing System
WRC	Welding Research Council

ACKNOWLEDGMENTS

The support and assistance of the following members of the staff of Pacific Northwest Laboratory in preparing this document is greatly appreciated: Kay Drake, who assisted in all phases of its preparation; Pat Randklev, who coordinated and assisted in administering its production; Mary Sheeley, Kelly Feuerbacher, and Kay Chase, who prepared the camera-ready copy; and John Nageley, who edited it. The work of the PNL Graphics group, under Gene Wattenburger, is apparent on many pages of this report. Dr. Joseph Muscara was the USNRC Project Manager.

I wish to thank the following organizations and companies for granting permission to quote and cite, and include illustrative material, from the books, journals, reports and conference, seminar and symposium proceedings that they have published:

- Academic Press, Inc., New York, New York.
- Academic Press, Inc. Ltd., London, England.
- American Institute of Physics, New York, New York: Journal of Acoustical Society of America, Journal of Applied Physics, and Applied Physics Letters.
- American Nuclear Society, La Grange Park, Illinois: Nuclear Technology.
- American Physical Society, New York, New York: A Physical Review.
- American Society for Metals, Metals Park, Ohio.
- American Society for Nondestructive Testing, Inc., Columbus, Ohio: Materials Evaluation, Paper Summaries, and Conference Proceedings.
- American Society for Quality Control, Technometric Management Committee, Milwaukee, Wisconsin: Journal of Quality Technology and Technometrics.
- American Society for Testing and Materials, Philadelphia, Pennsylvania.
- American Society of Mechanical Engineers, New York, New York: Journal of Applied Mechanics, Journal of Engineering for Industry, and The Boiler Pressure Vessel Codes.

- American Statistical Association, Washington, D.C: Technometrics.
- American Welding Society, Miami, Florida: Welding Journal.
- Applied Science Publishers, Ltd., Essex, England: International Journal of Pressure Vessels and Piping, and Reliability Engineering.
- Architectural Institute of Japan, Tokyo, Japan.
- Argonne National Laboratory, Chicago, Illinois.
- Babcock and Wilcox, New Orleans, Louisiana.
- Battelle, Pacific Northwest Laboratories, Richland, Washington.
- Battelle's Columbus Laboratories, Columbus, Ohio.
- British Engine Insurance, Ltd., Manchester, England: Technical Report.
- British Institute of Nondestructive Testing, Northampton, England: British Journal of NDT.
- Bundesanstalt für Materialprüfung, Berlin, Germany.
- Butterworth Scientific, Ltd., (formerly IPC Science and Technology Press, Ltd.) London, England: Ultrasonics Journal, Ultrasonics International, Non-Destructive Testing, and NDT International.
- Central Electricity Generating Board, London, England.
- Combustion Engineering, Inc., Windsor, Connecticut.
- Comite Franscaise d'Etude des Essais Non Destructifs, Laboratoire Nacional D'Essai, Paris, France.
- Commissariat a L'Énergie Atomique, Saclay, France.
- Commission of the European Communities, Brussels, Belgium.
- Committee on the Safety of Nuclear Installations of OECD Nuclear Energy Agency, Paris, France.
- Council of the Institution of Mechanical Engineers, London, England.
- Danish Welding Institute, Copenhagen, Denmark.
- Det Norske Veritas, Oslo, Norway.
- Deutsche Gesellschaft für Zerstörungsfreie Prüfung e.V., Berlin, Germany.

- Deutscher Verbad für Materialprüfung, Duesseldorf, Germany: Materialprüfung.
- Electric Power Research Institute, Palo Alto, California.
- Elsevier North-Holland, Inc., New York, New York.
- Fachinformationszentrum Energie, Physik, Mathematik, Lindau, Germany: 4th International Conference on NDE.
- General Electric Corporation, Fairfield, Connecticut.
- Hanford Engineering Development Laboratory, Richland, Washington.
- Holosonics, Inc., Richland, Washington.
- Institute of Electrical and Electronic Engineers, Inc., New York, New York: IEEE Transactions on Sonics and Ultrasonics, IEEE Proceedings.
- Institution of Civil Engineers, London, England: Journal of British Nuclear Energy Society.
- Institution of Nuclear Engineers, London, England.
- International Atomic Energy Agency, Vienna, Austria.
- International Institute of Welding, London, England: Welding in the World.
- Ishikawajima-Harima Heavy Industries Co., Ltd., Tokyo, Japan: IHI Engineering Review.
- Kobe Technical Institute, Kobe, Japan.
- Los Alamos National Laboratory, Los Alamos, New Mexico.
- Lund Institute of Technology, Lund, Sweden.
- M.A.N. Maschenenfabrik, Nurnberg, Germany.
- McGraw-Hill Book Company, New York, New York.
- National Aeronautics and Space Administration, Washington, D.C.
- National Bureau of Standards, Gaithersberg, Maryland.
- National Research Institute for Metals, Tokyo, Japan: Transactions of the National Research Institute for Metals.

- New England Institute, Ridgefield, Connecticut.
- North-Holland Publishing Company, Amsterdam, Holland: Nuclear Engineering and Design.
- Nuclear Engineering International, Surrey, England: Nuclear Engineering International.
- Oak Ridge National Laboratory, Oak Ridge, Tennessee: Nuclear Safety.
- Plenum Publishing Corporation, New York, New York: Soviet Journal of Nondestructive Testing.
- Pressure Vessel Research Committee, Welding Research Council, New York, New York: Welding Research Abroad.
- Rockwell International Corporation, Pittsburgh, Pennsylvania.
- Röntgen Technische Dienst. bv, Rotterdam, The Netherlands.
- The Royal Society, London, England: Proceedings.
- Scientific Applications, Inc., Palo Alto, California.
- Society for Experimental Stress Analysis, Brookfield Center, Connecticut: Experimental Mechanics.
- Southwest Research Institute, San Antonio, Texas.
- Studsvik Energiteknik AB (formerly Atomenergi AB), Nykoping, Sweden.
- Technischen Überwachungs Verein e.V., Rheinland Westphalia, Essen, Germany.
- United Kingdom Atomic Energy Authority, Harwell, England.
- U.S. Air Force, Wright Patterson Air Force Base, Ohio: USAF Technical Report.
- University of Tokyo Press, Tokyo, Japan.
- Welding Institute, Abington Hall, Cambridge, England: Welding Institute, Automatic Welding.
- Westinghouse Electric Corporation, Pittsburgh, Pennsylvania.
- John Wiley and Sons, New York, New York.

CHAPTER 7

ULTRASONIC EQUIPMENT--CHARACTERISTICS AND LIMITATIONS

CONTENTS

FIGURES

TABLES

CHAPTER 7

ULTRASONIC EQUIPMENT--CHARACTERISTICS AND LIMITATIONS

7.1 INTRODUCTION

In this chapter, both theoretical upper-bound limits and variability typical of electronic circuitry and transducers will be considered. Existing limitations and the possibilities of improvement will be covered.

In order to fulfill this scope, and to place the status of UT equipment in the proper perspective, the review is in the context of piping and vessel underclad cracking as specific systems to be examined. Three categories were selected:

- Conventional fine-grained materials containing weldments with minimal geometric reflectors. Large diameter thick-walled ferritic piping uniformly bored and then butt welded would be an example.
- Fine-grained ferritic alloys in thick (>6 in. or >15 cm) sections containing weldments plus some form of overlay cladding of a coarse-grained austenitic alloy. The examination is presumed to be through the cladding and the cladding may or may not be finished to provide a relatively smooth surface for UT. Concern will be detection of defects in or directly beneath the cladding.
- Austenitic alloys either wrought (fine-grained) or cast (coarse-grained) containing dendritic weldments. Wall thickness may be less than a centimeter to 8 to 10 cm (3 to 4 in.). Diameters will range from 4 in. (10 cm) to greater than 30 in. (75 cm). The piping will contain counterbores as geometric reflectors. Emphasis will be on detection of cracks originating at the inner bore.

A fourth category not related to examination of systems will be reproducibility of specific components making up a UT system both separately and when evaluated as a system. An attempt will be made to establish the inherent variability of systems as fabricated and as a function of time. In essence, this will consider each component as a "black box" with an assessment of "black box" variability.

Since conventional systems are covered in the available tests dealing with ultrasonics, discussion of such systems will be limited to establishing them as a baseline with regard to their meeting or failing to meet reasonable values of detection reliability plus acceptable levels for sizing and location of defects. Emphasis will be given to discussion of newer techniques now becoming state of the art. Their strengths and weaknesses will be reviewed, including whether sufficient information exists to permit a meaningful assessment.

The next section will attempt to set the stage for discussion of specific systems by reviewing those equipment factors that it is necessary to control to optimize the detection of defects in systems.

Several chapters, specifically 4, 5, 6 and 13, have touched on equipment and equipment limitations under specific conditions. Those deemed relevant are rereviewed in this chapter. An obvious factor influencing reliability of detection is the relevant code such as ASME V or XI setting forth the conditions of acceptable equipment calibration, etc. This specific aspect is covered in Chapter 14 and to a degree in Chapter 2; one such case is 20% DAC versus 100% DAC.

The approach in this and other chapters has been one of critically reviewing a large number of articles and selecting those believed to be relevant to the scope of the given chapter; thereafter, the effort was to correctly interpret the authors' coverage. Obviously, there is a finite possibility of incorrect interpretation and presentation. If this occurs, we apologize to the authors for any incorrect interpretation of their results.

7.2 EQUIPMENT PARAMETERS AFFECTING DEFECT DETECTION RELIABILITY

Emphasis in this section is on angle-beam contact techniques typically used in UT of piping. A broad overview of those critical equipment parameters influencing defect detection was given in a paper by Mundry and Wüstenberg.[7.2.1] They discuss signal significance which is defined as "the capability to discern between actual flaw echoes and all irrelevant indications such as grain noise, electronic interference, etc." This definition is an excellent one to use in measuring equipment performance.

Specific optimization criteria were developed to evaluate defect detection methods; namely,

- sufficient defect detection capability of the inspection system itself
- sufficient defect detection probability if a test object is actually inspected by the system
- sufficient signal significance of the test method.

The authors[7.2.1] considered the case of flaw sizing and location and suggested optimization criteria for defect evaluation:

- sufficient travel time resolution of the test method
- sufficiently narrow beam and precise knowledge of the beam-axis direction
- sufficient lateral resolution.

The first two items deal with flaw location and indirectly with sizing. The third item on lateral resolution is essential in accurately sizing flaws, particularly those normal to the surface. While the first two apply to pulse-echo, all three are relevant to imaging systems.

Specific factors influencing defect detection such as beam spread, frequency, bandwidth, wave mode and beam direction were discussed and are cited in modified form here:[7.2.1]

- Beam Spread. Figure 7.2.1 illustrates the options. A very wide beam should detect almost everything and locate nothing. Furthermore, a wide beam covers a large volume, and this may cause scattering and spurious echoes from surface areas of the test piece, leading to a reduction in detection probability. For conventional planar probes the best compromise is the medium width beam. An alternate is focused probes which scan limited volumes, but have good potential for sizing and locating defects in the volumes scanned. An economic penalty may exist with their use because of time required for a complete scan. Phased arrays discussed later pro- vide a future option.
- Frequency needs to be considered in terms of the operational frequency, the central value of the spectrum used, and the bandwidth. The operational frequency will be determined by the interaction between probe, cable and equipment. Bandwidth will vary with equipment and probe. Increasing the bandwidth may improve signal-to-noise (S/N) ratio in the material. Figure 7.2.2 illustrates how the detection probability increases with a decrease in frequency. The upper

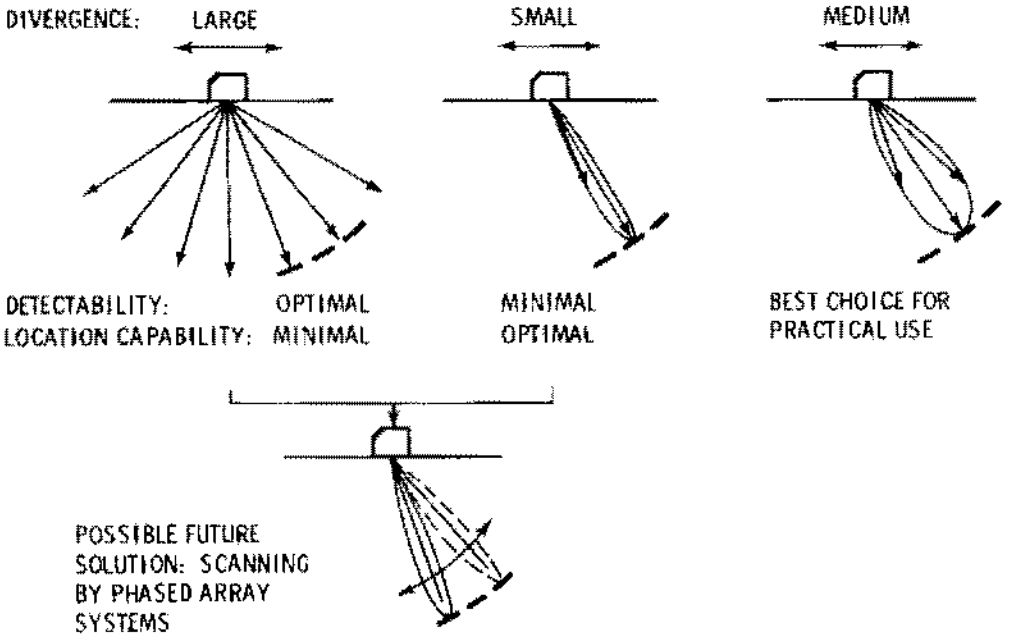

FIGURE 7.2.1. Influence of Divergency on Detection Probability and Defect Location

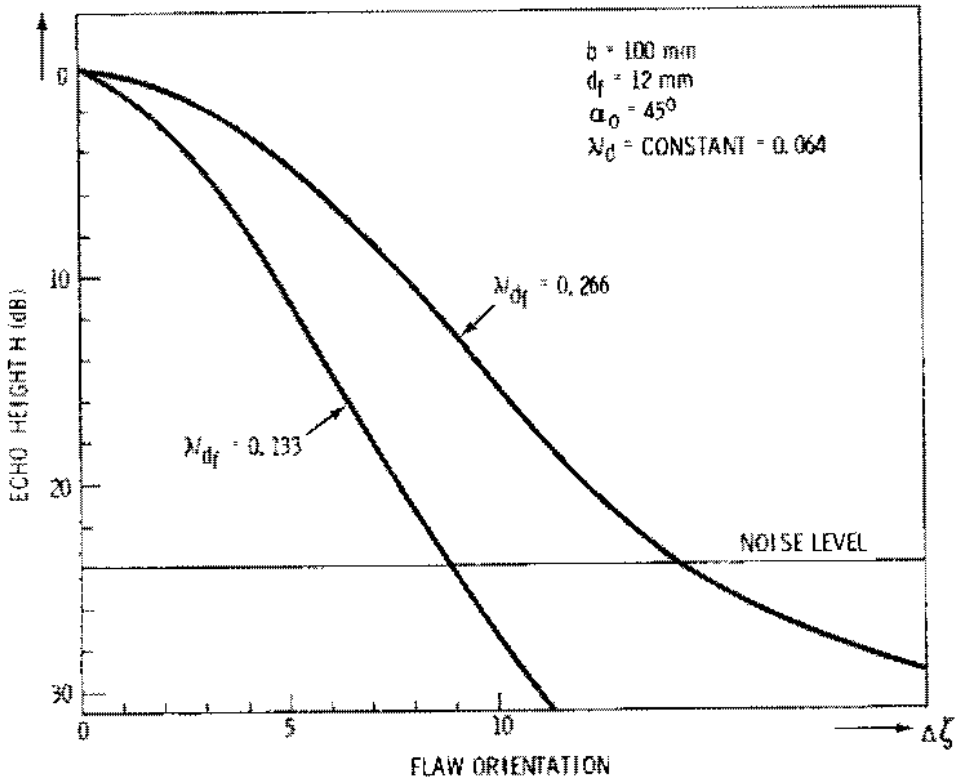

FIGURE 7.2.2. Orientation Dependency and Frequency

curve is one half the lower. As the frequency decreases, the S/N ratio should increase because reflection echoes from defects comparable in size to the wave lengths increase as a function of frequency squared while grain noise increases with the third to fourth power of frequency. While lower frequencies are preferred, particularly for coarse-grained material, a lower limit is set by probe ringing. This ringing interferes in particular with the detection of near-surface defects. Therefore, 1 to 2 MHz represents a good compromise.

- Wave mode represents an option. Generally, oblique incidence shear waves are preferred to avoid mode conversion from various surfaces which occurs when longitudinal waves are used over a range of incident angles. In some instances longitudinal waves are the preferred choice particularly for coarse-grained materials such as cast austenitic alloys where shear waves suffer scattering, attenuation

and skewing. This is particularly true for examination of near-surface areas where high-angle shear-wave echoes suffer interference from surface waves.

- Beam direction selection depends on the system being examined and the presumed flaws. Typically 45° or 60° probes are used, or sometimes 70° probes. The tandem technique is another option, particularly applicable to detecting flaws oriented normal to the surface. Figure 7.2.3 illustrates how no single angle is sufficient to detect flaws with a spectrum of orientations.

7.2.1 Defect Evaluation

The conclusions of the authors[7.2.1] relevant to sizing and location of flaws are particularly interesting. They relegate some well-known techniques to a figurative trash bin. This confirms their often expressed opinions that techniques optimized for detection aren't necessarily the best for sizing.

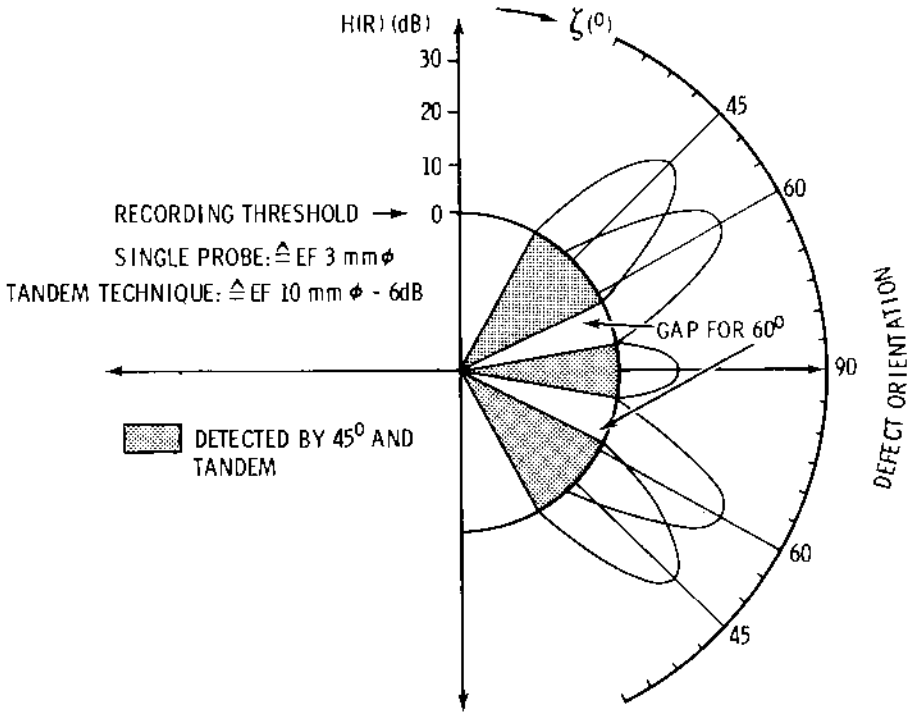

FIGURE 7.2.3. Detectability of Inclined Flaws with Tandem and Single-Probe Techniques

As indicated in the following conclusions, they feel acoustic holography, focused probes and possibly phased arrays present the best options:

1. A conclusive determination of defect size by use of the 6- to 20-dB drop method is impossible if the lateral dimensions of the defects are smaller than the sound-field diameter.

2. B- or C-scan presentation surely may be useful to improve the estimation about defect positions and orientations, but not for defect sizing if the defects are small relative to the sound-field diameter.

3. It is well known that the DGS method (reflectivity diagram) provides sizes of virtually circular reflectors, but not of actual flaws.

4. The applicability of ultrasonic pulse spectrometry in practical operation has not yet been proved finally. This method may perhaps be promising, especially if in addition to the amplitude spectrum also the phase spectrum is taken into account.

5. The suitability of echodynamics is limited and it may be replaced perhaps by the more modern linear holography.

6. Phased array systems may be very helpful in the future. But they are still in an early stage of development.

7. Today acoustic holography and focusing probes seem to offer the best possibilities for sizing of actual flaws.

7.2.2 Conventional Fine-Grained Alloys

An optimum system to be examined with UT would be a simple geometry such as a flat plate, no system-related geometric discontinuities, no cladding, and a homogeneous fine-grained structure. With such a component one would not anticipate beam skewing, attenuation, excessive grain-related noise, etc. Even in such systems where flaws should yield large S/N ratios the success record has not been outstanding with conventional pulse-echo equipment. Chapter 3 confirms this is both PVRC and PISC programs. Some of the problem is in operator interpretation which is not covered here. Another problem is that equipment was not optimum for some of the flaws. This aspect will be treated in section 7.3 dealing with inherent component variability.

7.2.3 Austenitic Clad Components

A reactor pressure vessel represents an excellent example of a clad, thick-walled component. A typical pressurized water reactor (PWR) will have a wall about 10-in. (25-cm) thick. Such a vessel will be clad with an austenitic alloy. Depending on manufacturer, year of fabrication, nuclear steam supplier, etc., the cladding could be single-wire, multi-wire or strip-clad process. The specific combination of austenitic alloys used in the weld wires could vary also. These same variables will determine whether the surface was ground after cladding or not. This means a simple statement that the vessel is clad does not provide much information to the NDE team.

In the United States PWR design essentially limits UT to the inside of the reactor pressure vessel (RPV). Access is not provided in the RPV cavity for NDE from the outer surface such as is required in Germany.

The postulated pressurized thermal shock accident, where a severe cooling transient occurs with the systems at operating pressure, places a premium on UT establishing whether there are flaws in or immediately under the cladding in the region subjected to high neutron fluxes. Since UT in the near-surface region currently represents a major thrust, we will examine the role of cladding in the detection of near-surface flaws as they influence selection of UT-equipment systems.

An irregular surface can introduce major variability in a contact UT examination. For this analysis such behavior is recognized; however, a uniform surface will be assumed to focus on direct cladding effects.

Typically a weld-applied austenitic cladding will have a coarse-grained highly oriented dendritic structure. This structure and the austenite-ferrite interface will represent a large number of geometric reflectors contributing to the system noise level. The dendrites will lead to some beam skewing. These problems compound the difficulties of near-surface examination under the best of conditions; however, they are of lesser importance with high-angle longitudinal waves.

Mundry and Wüstenberg[7.2.1] cite the problems of shear-wave UT through cladding. Figure 7.2.4 represents a case of a 45° 1-MHz shear wave probe used

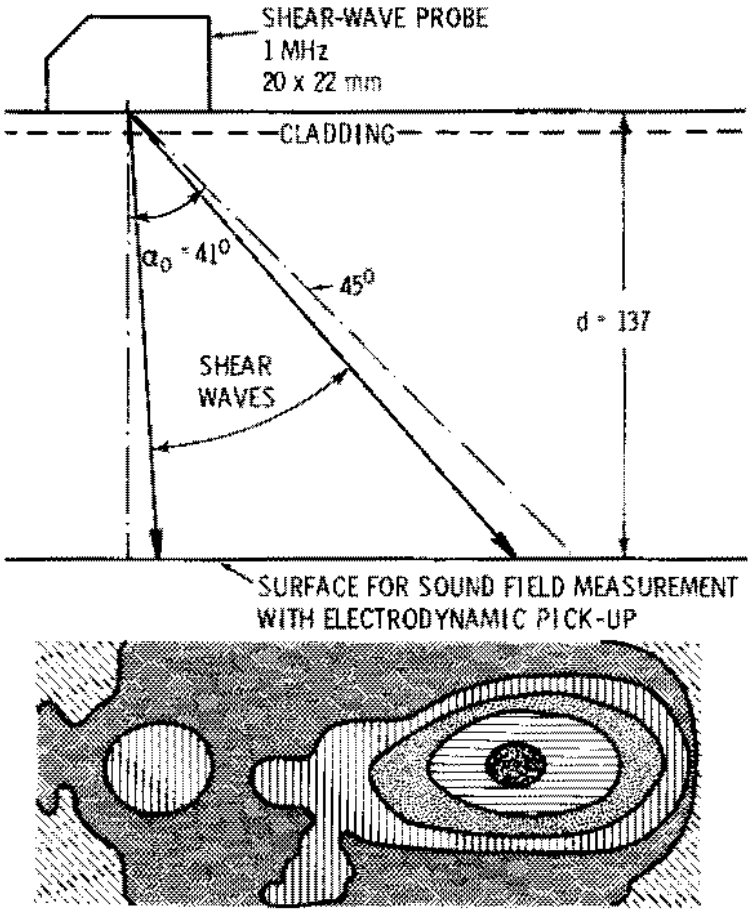

FIGURE 7.2.4. Secondary Waves from Shear-Wave UT Produced by a Cladding Surface

on a clad surface. The cladding shifts the beam from 45° to 41°. Concurrently a spurious shear wave is generated essentially normal to the surface. The 90° wave echo may lead to prediction of non-existent flaws. The sensitivity of incident angle is illustrated by experiments where a change of 4° completely suppressed the normal shear wave. Presumably, scanning will have been parallel to welding direction of the cladding.

Another study[7.2.2] cites equipment measures to improve S/N ratio when examining through cladding:

- Short pulses are preferred.
- Lower frequencies should be used.

Several UT techniques were suggested to examine through cladding:

- focused probes
- transmitter-receiver technique
- tandem
- longitudinal creeping wave
- high-angle longitudinal probes
- signal averaging
- spatial averaging.

Factors other than those listed, such as transducer size and immersion or contact, are known to influence S/N behavior. The pros and cons of these and other techniques will be considered more extensively in a later section. Only a few of the problems will be reviewed here. One case is that of the tandem-probe technique. By the time the tandem probe has been adjusted on the calibration block followed by corrections due to transfer behavior, fluctuations in transfer behavior and inhomogeneous sensitivity distribution in the inspected zones the total adds up to 12 to 18 dB which increase the number of indications requiring analysis and to a reduction in signal significance. There can be a substantial difference in near-surface response of tandem probes. Figure 7.2.5 illustrates the response of an unoptimized and an optimized set of tandem probes used through cladding.

7.2.4 Coarse-Grained Austenitic Structures

The problems of beam attenuation and skewing cited in 7.2.3 are more pronounced in coarse-grained austenitic alloy castings and weldments. This favors lower frequencies and longitudinal waves. Since the greater portion of Chapter 13 deals with this phenomenon, the details will not be repeated here. With regard to equipment optimized for use with austenitic alloys, those details will be addressed in a later section of this chapter.

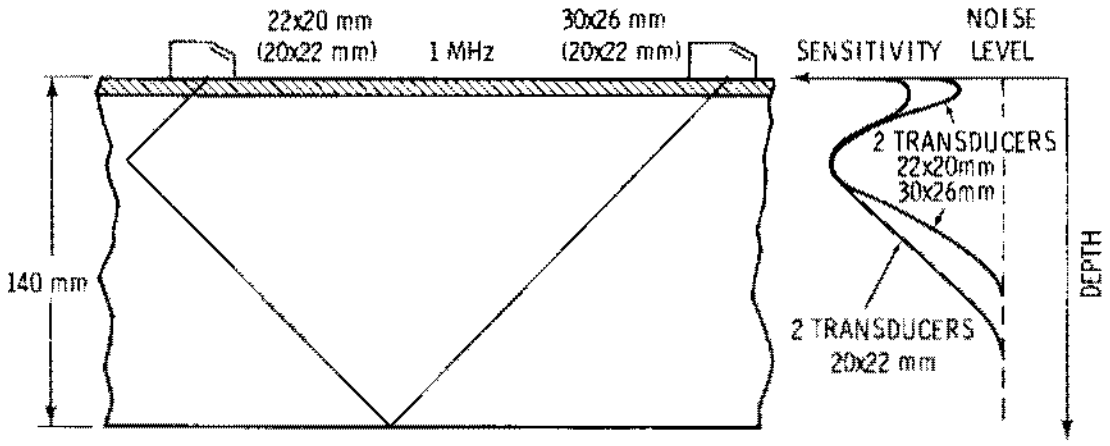

FIGURE 7.2.5. Reduction of the Noise from the Cladding for a Tandem Technique

7.3 EQUIPMENT VARIABILITY OR LIMITATIONS

The thrust of this section will be to examine information pertaining to basic limitations in components, or unit-to-unit variability requiring particular attention. A general overview will be given first followed by defects specific to a given class of components.

PVRC studies[4.5.5] indicate that the two most important parameters are system operating frequency spectrum and the beam profile or radiation pattern of the transducer in the material under consideration. Both were discussed in section 7.2 and Figures 7.2.1 and 7.2.2 relate to these parameters.

The variability of transducers is another factor. Radiation patterns, intensity and frequency response, usually are not reproducible to within 20% even from the same manufacturer.[4.5.1] Furthermore, transducer characteristics decay with usage, with a mean useful life of about six months. A later section will examine transducer problems more extensively.

A definitive paper on equipment variability was authored by Caussin and Verspeelt.[7.3.1] The authors cite only two reports (as of 1981) in the open literature pertaining to the influence of UT equipment variability on test results. The work of Chalaye et al. was reported where 60 pairs of equipment and probes, purportedly identical, were tested. Some 2000 records of echo amplitudes were obtained from artificial reflectors, and the amplitudes were calibrated against the reflection obtained from 2ø-mm side-drilled holes positioned at the depths of the reflectors. Results of a statistical analyses indicated a spread of 12 dB at 2 sigma. Unfortunately, the transducers in these studies had not been precalibrated rendering the data suspect.

Similar results were observed in the PISC data. Teams using the same calibration/test procedure reported data from actual weld flaws. When analyzed, the spread was 18 dB with only two teams reporting amplitudes differing by less than 2 dB. Incidentally, these two teams were the only ones who characterized and selected their equipment against a common standard.

The authors[7.3.1] considered the three equipment factors required to be measured in ASME XI or V:

- the linearity of the amplifier
- the accuracy of the gain control
- the measurement of the ultrasonic beam.

The following equipment-related factors are not required to be determined by ASME XI and often are not:

- the amplitude and shape of the excitation pulse
- the generator output impedance
- the amplifier input impedance
- the amplifier frequency response
- the characteristic impedance of cables
- the probe frequency distribution
- the ultrasonic beam generated by the probes.

A program was developed to quantify the influence of some of the preceding parameters in such a way as to modify one parameter without affecting the others. Table 7.3.1 lists those parameters varied or controlled. The combinations of parameters cited permitted 36 configurations.

Three sets of measurements were taken to determine the following factors:

1. frequency response of the probes
2. equipment sensitivity both
   A) absolute
   and
   B) relative.

Frequency response was measured in the configurations cited in Table 7.3.2 by obtaining the echo on the bottom wall of a fine-grain carbon steel block. The signal was taken at the apparatus input. The parameters cited in Table 7.3.2 were measured with a frequency spectrum analyzer; namely,

- frequency at maximum power: f_m
- cutoff frequencies at -3 dB: f_+ and f_- (ASTM uses -6 dB)
- central frequency: $f_0 = \frac{f_+ + f_-}{2}$
- bandwidth: $B = f_+ - f_-$
- quality factor: $Q = f_0/B$

TABLE 7.3.1. Ultrasonic Equipment Factors Examined

	Values
Independently Controllable Characteristics	
Generator-Output Impedance (Z_o)	12.5, 25, 50 ohm
Amplifier-Input Impedance (Z_{in})	50-ohm resistive (2 MHz) 800-ohm capacitive
Frequency Response (three settable bands)	Low-Pass (LP) 0.65 - 2.25 MHz High-Pass (HP) 1.25 - 4.45 MHz Wide-Band (WB) 0.29 - 9.76 MHz
Characteristics Held Constant	
Generator-Pulse Amplitude	-100 V on 50-ohm load
Generator-Pulse Rise Time	22 ns on 50-ohm load
Generator-Pulse Repetition Frequencies	--
Amplifier Linearity	Better than 5%
Amplifier-Gain Accuracy	Better than 0.5 dB
Probe Characteristics	
P1: Low Damping; Impedance	4 MHz, 10ø mm, $\pm$2 μH in Parallel on $\pm$ 1 nF
P2: High Damping; Impedance	1 MHz; 25.4ø mm; $\pm$2 nF
Cable	50 ohm or 1/2 length 25 ohm

Equipment sensitivity was obtained by successively coupling the probes to a standard calibration block and measuring the echoes to obtain absolute sensitivity. For relative sensitivity the probes were coupled successively to a standard calibration block, to two fine-grained carbon steel blocks, and to an austenitic steel block. Measurements in all cases were done in such a way as to avoid coupling variability. The probes were fixed in place with selector switches or cables being varied. All echoes were obtained on the bottom surface of each block with corresponding wave paths in the range 1.3 to 2.5 μm near-field length. When using the calibration block, a thickness within 5 mm

TABLE 7.3.2. Probe Frequency Response

Configuration		Cable	P1: 4 MHz, 10-mm Dia, Low Damping						P2: 1 MHz, 25.4 mm Dia, High Damping					
			f_m (MHz)	f_+ (MHz)	f_- (MHz)	f_o (MHz)	$B_{-3\ dB}$ (MHz)	Q	f_m (MHz)	f_+ (MHz)	f_- (MHz)	f_o (MHz)	$B_{-3\ dB}$ (MHz)	Q
12.5	R	1/2	4.37	4.7	4.16	4.45	0.54	8.2	0.90	1.25	0.74	0.99	0.51	1.9
12.5	C	1/2	4.37	4.54	4.18	4.36	0.36	12.2	0.97	1.10	0.36	0.77	0.83	0.9
25	R	1/2	4.37	4.71	4.13	4.42	0.58	7.6	0.92	1.25	0.76	1	0.49	2.0
25	C	1/2	4.35	4.5	4.23	4.36	0.27	16	0.97	1.21	0.35	0.76	0.26	0.9
50	R	1/2	4.36	4.7	4.16	4.43	0.54	8.2	0.94	1.23	0.78	1	0.45	2.2
50	C	1/2	4.33	4.47	4.21	4.34	0.26	16.7	1	1.25	0.35	0.8	0.90	0.9
12.5	R	1/1	4.41	4.7	4.1	4.45	0.5	8.9	0.91	1.30	0.73	1.02	0.59	1.7
12.5	C	1/1	4.34	4.42	4.14	4.28	0.28	15.3	0.99	1.31	0.42	0.87	0.19	1
25	R	1/1	4.38	4.7	4.18	4.44	0.52	8.5	0.93	1.26	0.78	1.02	0.18	2.1
25	C	1/1	4.33	4.45	4.14	4.3	0.31	13.6	0.99	1.28	0.42	0.84	0.84	1
50	R	1/1	4.37	4.7	4.17	4.43	0.53	8.4	0.90	1.28	0.74	1.01	0.54	1.87
50	C	1/1	4.23	4.42	4.14	4.28	0.28	15.3	0.96	1.26	0.42	0.84	0.84	1
$\mu \pm \sigma$			4.35 ± 0.04	4.59 ± 0.14	4.16 ± 0.04	4.38 ± 0.07	0.41 ± 0.13	11.6 ± 3.8	0.96 ± 0.06	1.26 ± 0.03	0.57 ± 0.19	0.91 ± 0.10	0.65 ± 0.19	1.46 ± 0.54

of the thickness of the test piece was used. Gain settings necessary to hold echoes consistent were recorded with an accuracy of ±0.5 dB.

Results in Table 7.3.2 on frequency response of the probes can be summarized as follows:

- Probes P1: 4 MHz, 10-mm dia, low damping:
  - The dispersions of f_m, f_+, f_- and f_0 were limited to a few percent of the mean values.
  - The dispersion of B and Q reached about 30% of the mean values.
  - Compared with the frequency responses of the apparatus, the LP band was totally unmatched and the HP band most of the time did not go up to f_+.
  - The quality factor (Q) was almost constant on a resistive load (Z_{in}:R), the highest on capacitive load (Z_{in}:C), and only slightly influenced by the cable length.
  - On capacitive load, Q was sensitive to both cable length and z_0.
- Probes P2: 1 MHz, 25.4-mm dia, high damping:
  - The dispersions of f_m, f_+, and f_0 were restricted to a few percent of the mean values.
  - The dispersions of f_-, B, and Q reached about 30% of the mean values.
  - Compared with the frequency response of the apparatus, only the WB band matched the probe response. In half of the cases the LP band did not go low enough in frequency.
  - The quality factor (Q) was almost constant on a capacitive load, the highest on a resistive one, and only slightly influenced by the cable length.
  - On a resistive load, Q was sensitive to both cable length and z_0.

Table 7.3.3a contains the equipment absolute sensitivity data and Table 7.3.3b contains similar data for relative sensitivity. Figures 7.3.1a

TABLE 7.3.3a. Mean Values and Standard Deviations of Absolute Sensitivity Readings

Wave Path (mm)	LP μ ± σ (dB)	LP d (%)	HP μ ± σ (dB)	HP d (%)	WB μ ± σ (dB)	WB d (%)
			Probe P1			
15	54.3 ± 4.0	7	50.5 ± 3.65	7	60.3 ± 4.0	7
30	55.9 ± 4.5	8	52.3 ± 4.68	9	62.0 ± 4.2	7
45	57.8 ± 4.7	8	54.0 ± 4.9	9	63.7 ± 4.6	7
			Probe P2			
15	68.8 ± 0.8	1	72.7 ± 1.2	2	80.8 ± 0.8	1
30	65.0 ± 1.1	2	69.7 ± 0.8	1	78.0 ± 0.0	0
45	65.7 ± 0.52	1	71.3 ± 1.0	1	78.5 ± 0.6	1

TABLE 7.3.3b. Mean Values and Standard Deviations of Relative Sensitivity

Wave Path (mm)	LP μ ± σ (dB)	LP d (%)	HP μ ± σ (dB)	HP d (%)	WB μ ± σ (dB)	WB d (%)
			Probe P1			
15	2.1 ± 0.8	38	2.3 ± 1.3	57	2.2 ± 0.9	41
30	5.0 ± 1.0	20	4.8 ± 0.8	17	5.1 ± 1.0	20
45	3.3 ± 1.0	30	3.3 ± 1.3	39	3.4 ± 0.9	26
			Probe P2			
15	4.33 ± 0.82	19	6.5 ± 1.22	19	4 ± 0.00	0
30	11.67 ± 1.52	4	13.67 ± 0.52	4	10.17 ± 0.41	4
45	10.1 ± 0.41	4	12.33 ± 0.82	7	8.5 ± 0.84	10

and 7.3.1b contain the data on the 15-mm condition cited in Table 7.3.3a. The variables are those cited in Table 7.3.1. As can be seen, there are definite differences in response for a given instrument; namely,

- Probes P1: 4 MHz, 10-mm dia, low damping:
  - The dispersion reached 20 dB maximum.
  - The best sensitivity appeared with a capacitive load.

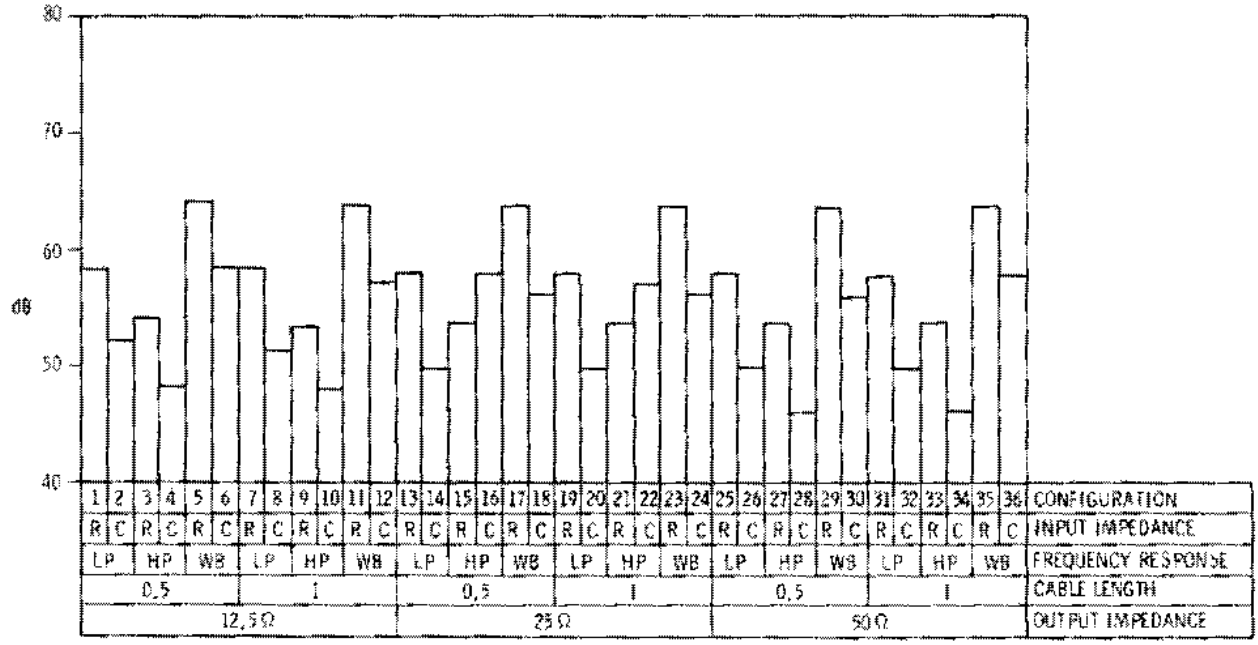

(a) Straight Beam Probe: 4 MHz, 10-mm Dia, Low Damping

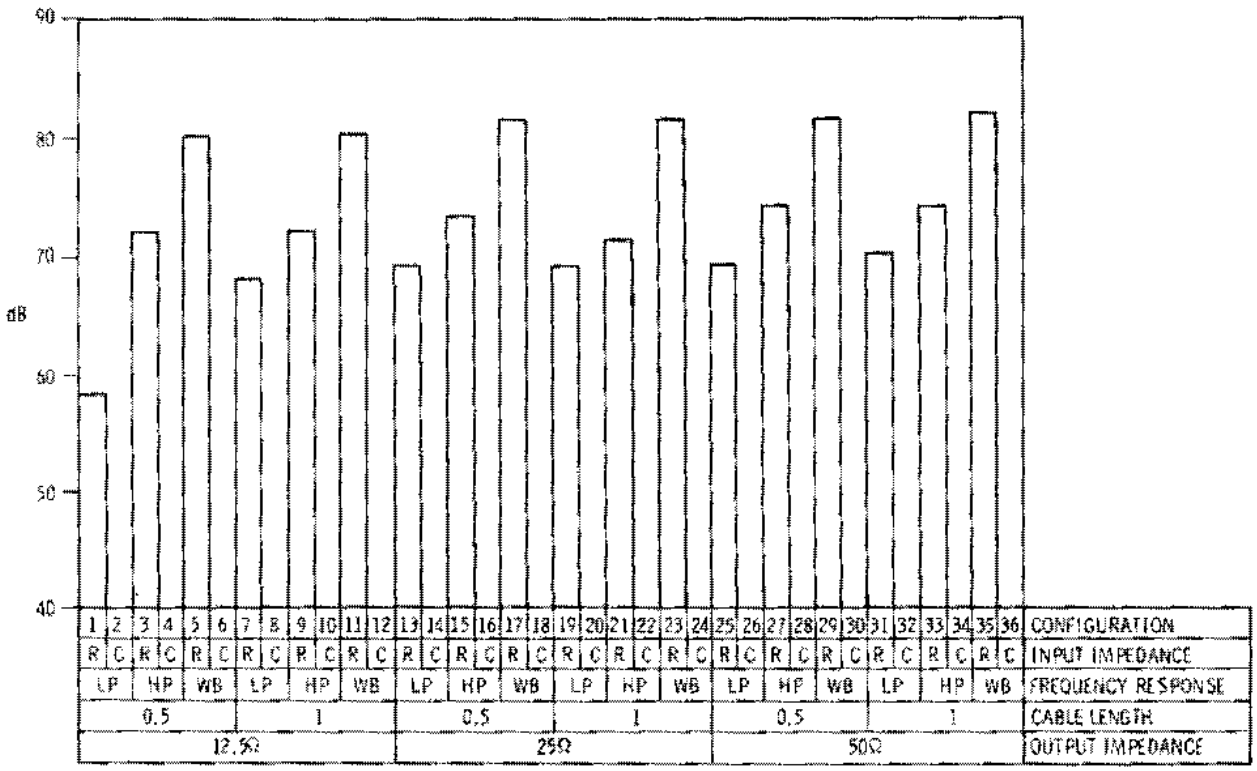

(b) Straight Beam Probe: 1 MHz, 25.4-mm Dia, High Damping

FIGURE 7.3.1. Influence of Characteristics on System Sensitivity

- For a given load, the best sensitivity was obtained for the best matching of the apparatus frequency response (HP).
- With a capacitive load and the proper frequency matching, the sensitivity increased with the output impedance and the cable length had no influence.

- Probes P2: 1 MHz, 25.4-mm dia, high damping:
  - The capacitive load represented by the probe was too high for the generator and no discernable echo was obtained in such a configuration.
  - With the resistive load a dispersion of 14-dB maximum was reached.
  - The best sensitivity was obtained with the LP band which matched the probe frequency response at best.
  - The other parameters had a small influence but it appeared that a low output impedance should be preferred.

In similar fashion, the relative sensitivity data were obtained. In principle, the calibration with three test pieces against a common calibration block should eliminate instrumentation effects. Differences should be due to differences in attenuation and coupling, and should be constant for all configurations. As can be seen in Table 7.3.3b and Figures 7.3.2a and 7.3.2b, this was not the case. Probe differences were as follows:

- Probes P1: 4 MHz, 10-mm dia, low damping
  - In this case the dispersion reached a maximum of 4 dB.
  - At low-output impedance, the variations were irregular.
  - At 50-ohm output impedance, only the input impedance played a role.

- Probes P2: 1 MHz, 25.4-mm dia, high damping:
  - With that probe the dispersion reached a maximum of 7 dB.

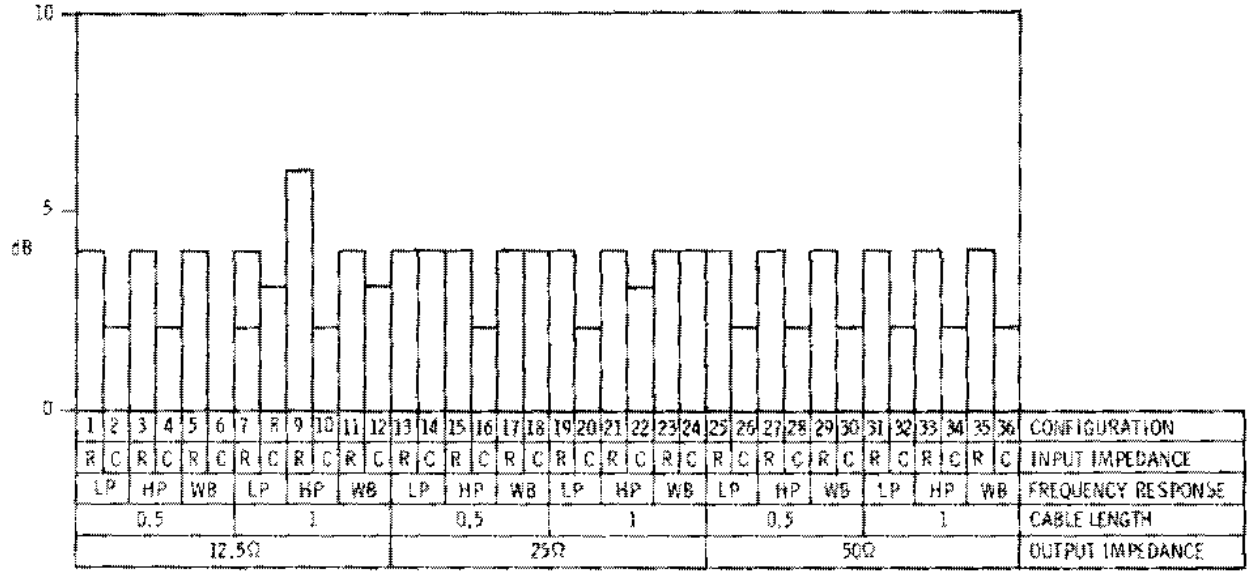

(a) Straight Beam Probe, 4 MHz, 10 mm Dia, Low Damping

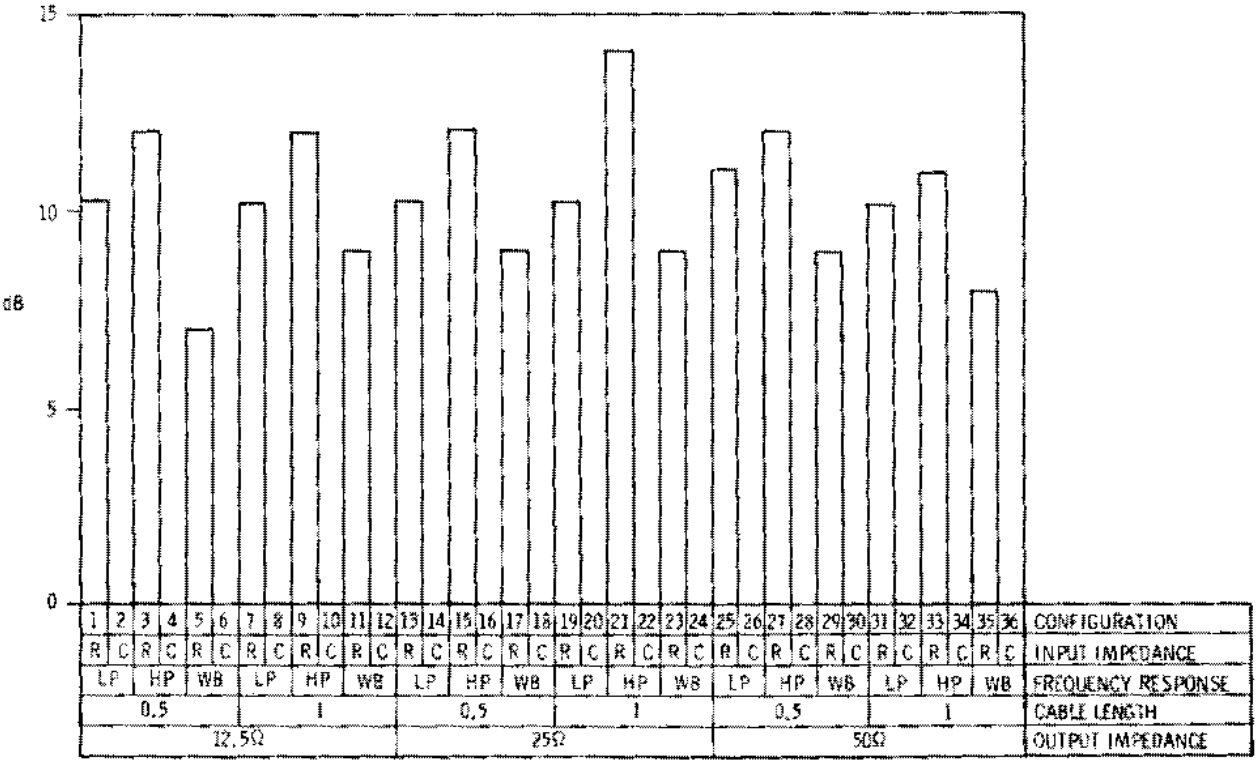

(b) Straight Beam Probe: 1 MHz, 25.4-mm Dia, High Damping

FIGURE 7.3.2. Influence of Characteristics on Transfer Measurement

- It seemed that all parameters affected the dispersion; however, the best suited band (LP) and the lowest output impedance seemed more appropriate.

An overall examination of the authors'[7.3.1] data reveals that equipment can meet ASME XI Code requirements yet have characteristics unknown to the operator. These variables will influence the performance of the inspection:

- The frequency response of the probes was affected.
- An absolute sensitivity dispersion of 20 dB occurred.
- After calibration a range of 7 dB in echo amplitude existed.

Even with properly matched probes, cables and equipment, careless use can generate major non-reproducibility.

7.3.1 Transducers

Transducer variability has been studied for several years. An obvious problem is what constitutes a significant variable, and this needs to be tied to the use of the system. Bredael[7.3.2] states this quite well:

> It is hard to make a definitive classification as regards probe quality, since the selection of a probe is so dependent on the problem involved. In some cases the frequency is critical (echo encephalography, thickness monitoring using the resonance method, etc.), but in other cases the damping is critical (phase measurements, microporosity analysis, bubble noise monitoring, etc.). In the same way, focal length or focal point diameter may be critical. For weld inspection the beam angle is often highly critical, etc. So the best way seems to check if the data supplied by the manufacturers correspond to those measured by the user on receipt and after aging or use.

The author[7.3.2] cites general agreement of measurements on receipt of probes with those cited by the manufacturer (82% confidence). During operation, 5-MHz probes generally work at 6.2 MHz (63%). As frequency increases, the probes usually operate below the cited level. The author considers frequency error to be directly proportional to the mechanical damping or inversely proportional to the quality factor Q. The focal length is generally shorter than indicated (81% shorter in 91% of probes analyzed). The manufacturer usually does not give the dimensions of the focal point or the angle between the mechanical axis (reference plane) and the acoustic beam. Bredael[7.3.2]

reported a mean asymmetry of 15% in 30% of units analyzed, and a mean eccentricity of 0.07 cm based on statistical analysis of the data.

Sachse and Hsu[7.3.3] describe the characteristics of a "good" transducer contrasted to an "ideal" transducer. With the "ideal" transducer the exact relationship between input and output is known absolutely. This is not true for a "good" transducer whose response characteristics should meet the requirements of any materials testing condition. The characteristics defining a "good" transducer include

- high sensitivity as a receiver (S/N ratio)
- controlled geometric radiation field effects
- controlled frequency response
- absence of "ill" characteristics
- high power as source
- wide dynamic range
- linear electro-mechanical-acoustic response.

Generally, the first two are considered to be the most significant.

The authors[7.3.3] cite the following characteristics they consider to be most sought in transducer response: a broad-band device having a uniform response in the frequency domain and a delta transfer function in the time domain. A device with these characteristics when operated in the pulse-echo mode would have high resolution and would faithfully transduct any incident UT signal into an electrical signal in the receiver mode. Unfortunately, real transducers usually have low sensitivity. If high sensitivity is desired, a narrow-band unit is the answer.

A transducer possessing all of the features cited for a "good" transducer is not available. Most transducers emphasize one or two characteristics at the expense of the others. Furthermore, the situation is further complicated by variability. A transducer might be found meeting a specified series of requirements for a given measurement; however, the likelihood that a second "identical" transducer will, in fact, have an identical response is very slim.

Dijkstra[7.3.4] cites the T.U.V. requirement for the use of a real scale test and reference blocks for probe parameter determination and for calibration

of multiple probe systems. The blocks must be fabricated of representative materials. For example, in nuclear components the original clad layer and surface conditions have to be used, and they should contain the prescribed calibration reflector for optimum reflection by a completely mounted probe system. The preceding is a requirement on site. In addition, the following transducer properties are to be measured in the laboratory:

- sensitivity in finding test reflectors and sensitivity reserve
- beam widths, both in impulse echo and in tandem, and pitch-and-catch technique, both longitudinal and transverse directions
- S/N ratio at all distances used during examination and also on original clad if available.

The emphasis in final checkout on calibration blocks is on partial recognition that so-called calibrated probes can yield invalid results.

Birks and Lawrie[7.3.5] attempted to relate probe parameters to their significance with regard to the detection of flaws in components. They used different probes with the same equipment to measure the percentage of DAC from a series of defects in a weld mockup simulating a pressure vessel. DAC values varied markedly from probe to probe, and probe responses from the various flaws were not consistent. An extension of this work used probes meeting the criteria in Table 7.3.4. Of 18 probes tested, seven were rejected because they were outside tolerance. Five did not meet frequency; two had low gain and one of these had an asymmetric beam.

The authors[7.3.5] schematically illustrate the implications of varying probe parameters in calibration blocks and with planar flaws. Figure 7.3.3a,b,c illustrates the effects due to frequency changes. It is essential to remember that only the frequencies selected from the search unit spectrum and reaching the detector are important. The purpose of tolerances is to obtain reproducible signals under the same conditions; unfortunately, this is not that common an occurrence.

Figure 7.3.3a represents the case of a transducer beam reflecting from a side-drilled reference hole. In this case, the axis of the radiation pattern

TABLE 7.3.4. Tentative Probe Specifications and Tolerances

Probe Parameters	Specified Tolerance[a]	Possible Significance
Center frequency (f_o)	$\pm$10% f_N	A decrease in frequency increases width of beam profile, increasing signal from a reflector.
Frequency bandwidth (6 dB)	$\pm$25% f_o	As bandwidth increases reflector response increases.
Beam exit point	$\pm$0.025 in.	Incorrect exit point introduces errors in flaw location.
Refracted angle	$\pm 2^\circ$	Relatively minor deviations can have substantial effect on reflector signal
Lateral-beam symmetry	$\pm$0.125 in. at Y_o^+	Similar to refracted angle in being strongly related to reflector.
Y_o^+ position	$\pm$10% calculated	Function of effective frequency and transducer dimensions.
Sensitivity	30-dB reserve	Not a major factor--usually there is a reserve in dB.

(a) No scientific basis for tolerances; they may be excessive or inadequate.

approaches the reference hole at normal incidence and is reflected back along this same axis. This means a reference hole provides an adjustment in sensitivity limited to one direction along the beam axis. With defects, particularly planar defects, whose orientation may have angles away from that normal to the beam such as in Figure 7.3.3b, the maximum response is off-axis on both the search unit and the defect radiation patterns. The illustrated pattern is relevant to both longitudinal and shear waves. Figure 7.3.3c illustrates how changes in probe frequency can influence both beam profile and radiation pattern. A decrease in frequency broadens the beam profile and increases the radiation pattern response. Obviously changes in frequency will adversely affect reproducibility. A further effect at higher frequencies is the behavior of a tilted defect which acts like a low pass filter cutting out the higher

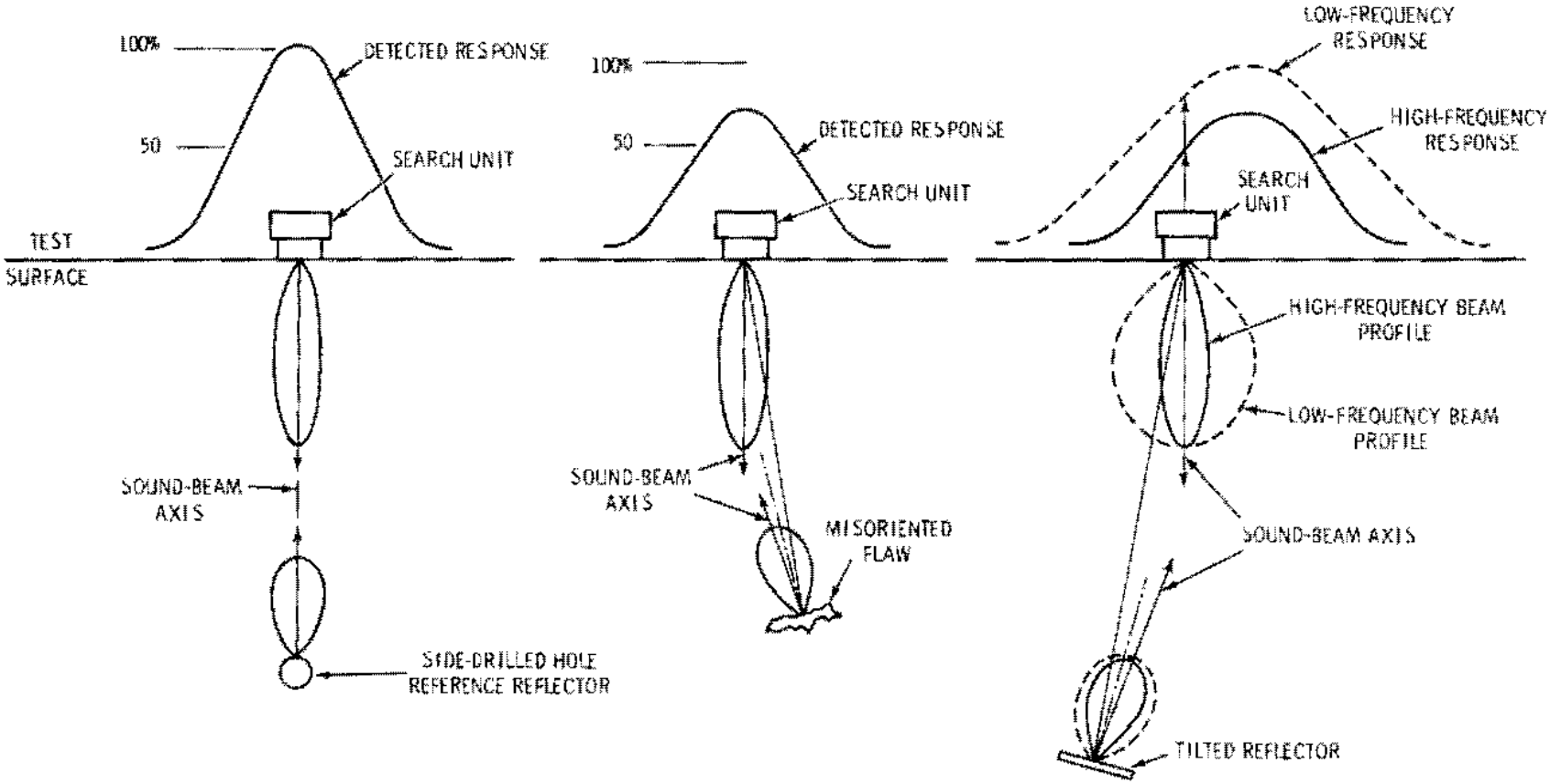

(a) Sound-Beam Configurations During Calibration

(b) Interaction of Sound Beams for Misoriented Flaws

(c) Comparison of High-and Low-Frequency Response

FIGURE 7.3.3.

frequency signals. This means a broad bandwidth probe will give a higher response than will a narrow bandwidth probe.

Another parameter examined[7.3.6] was refracted angle. Figure 7.3.4 reveals how rotation into the normal to the defect will enhance signal while rotation away will decrease signal.

Other factors cited in Table 7.3.4 can affect radiated amplitude.

The preceding comments have attempted to establish the significance of variation in some transducer parameters. The following will attempt to determine how variable probes are or have been. In Chapter 4 comments were made relevant to probe variability. For example, Yee and Couchman[4.5.1] cite significant variability within a given class of transducers and Bastien[4.5.7] found the situation even worse between classes of transducers.

Posakony[7.3.6] tested one class of transducers (quartz) in accordance with ASTM E-127-75. He found that the design of the probe, particularly as it applied to the relationship between the size of ground and positive electrodes, could have a substantial effect on the sound beam. For example, a positive

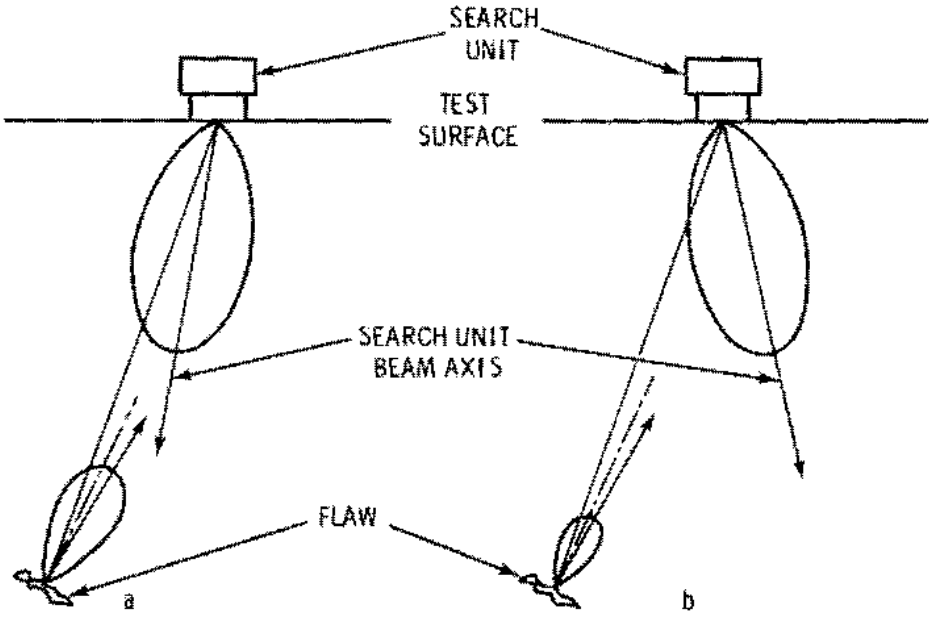

FIGURE 7.3.4. Effect of Rotating Out-of-Tolerance Sound Beam

electrode smaller than the ground electrode will develop electric and acoustic field fringing resulting in an increase in apparent size of aperture.

Variations in the far-field pressure profile were reported which dramatically influenced the amplitude of the echo response from a test block leading to incorrect adjustment of sensitivities or DAC electronics which can result in establishing inaccurate accept/reject criteria.

The preceding was due to the limited scope in ASTM E127 other than the on-axis and cross-axis profiles. Manufacturers may provide a variety of probes utilizing different designs which "apparently" satisfy the ASTM requirements.

The largest and most significant studies located were those of Lidington and Silk[7.3.7,7.3.8] who tested 228 probes in the first[7.3.7] and 148 in the second study.[7.3.8] Since an immersion technique was used, the relevance to shear- or longitudinal-wave contact probes can be inferred only. The following parameters were examined:

- natural frequency of probes
- variations in pulse shape
- non-exponential pulse decay
- presence of other frequencies
- beam misalignment
- secondary beams
- beam quality.

In the frequency range of interest for piping and pressure vessels -- namely, below 5 MHz--probes have a mean somewhat biased to the high side of the nominal frequency with relative narrow variance (σ^2). The authors[7.3.7] consider frequencies more than 25% away from the nominal value as adversely influencing examinations.

Pulse shape was measured in terms of both pulse length and number of cycles. The significance of this parameter for contact probes is not known.

Some probes exhibited non-exponential signal decay which did not seem to correlate with the other parameters.

A factor probably related to a definite malfunction of the transducer is the presence of frequencies other than the primary. Both harmonic and unrelated frequencies were observed.

Beam misalignment represents a potentially more severe fault. Frequencies below 6 MHz appear more susceptible than those above 6 MHz. Contact probes were less susceptible than immersion probes. Misalignments exceed 2.5° in nearly 10% of the probes.

Secondary beams occasionally occur leading to a serious error unless detected.

Probe sensitivity was not a critical factor for the great majority of probes; however, beam quality as exemplified by angular misalignment, poor beam profile, insensitive areas on the probe face, hollow beam, etc., was important in that a substantial percentage of probes suffered from these quality defects.

Table 7.3.5 incorporates the probabilities of the preceding defects in both studies.[7.3.7, 7.3.8] Beam misalignment, other frequencies and poor beam quality are significant factors.

A limited program sponsored by the Air Force[7.3.9] characterized 23 UT transducers using 17 parameters including ability to detect and size four sample

TABLE 7.3.5. Probabilities of Malfunction (Only "Other Frequency in Response" is likely to give serious effect on measurements. The last two malfunctions have been correlated to some extent.)

Possible Malfunction	Earlier Estimate of Probability, %	Latest Estimate of Probability, %
Frequency deviation (<25%)		
(a) Probes >6.5 MHz	3	5
(b) Probes <6.5 MHz	66	53
Non-exponential decay	10	20
Other Frequencies in response	18	18
Beam Misalignment (>2.5°)	9	9.5
Secondary beams	4.5	5.5
Low sensitivity	6.5	8
Poor beam quality	12	11

flaws (flat-bottom hole, Elox notch low-cycle fatigue crack, high-cycle fatigue crack). Statistical correlation techniques were used to establish those parameters with high correlation values. Of the 17 parameters (six pertained to RF power spectrum and wave form, five to beam characteristics, one to conversion efficiency, one to electric noise, and the flaw-response ratio related to the four sample flaws), only four pairs among the parameters related to electrical and beam characteristics showed correlations greater than 50%:

- the spectrum-symmetry ratio (SSR) and spectrum-inflection ratio (SIR)--59%
- the bandwidth ratio (BWR) and the far-field ratio (FFR)--67%
- the beam-width error (BWE) and the effective-diameter ratio (EDR)--68%
- the beam-symmetry ratio (BSR) and the beam-inflection ratio (BIR)--86%.

Flaw-response ratio (FRR) of the various flaws were checked for correlation with spectral and beam parameters. Correlations existed with center frequency. Beam parameters such as effective radiation area, beam-width error, and in particular loop sensitivity had strong correlations.

Based on a performance rating only two of the 23 transducers rated good, 11 fair and 10 poor. The significance of poor was apparent when examining the fatigue cracks. Some transducers had high S/N ratios permitting easy detection; others had no signal. There was a factor of 40 variation in response.

Of interest was the poor record of 2.25-MHz transducers.

Since tests were limited to longitudinal wave, the implication of shear-wave behavior and of beam misalignment were not examined.

The very strong correlation of flaws and the transducer-loop sensitivity ratio (LSR) make this parameter worthy of further application:

$$LSR = -20 \log_{10} V_T/V_E$$

where V_T is the initial pulse applied at transducer and V_E is the return echo from a parallel flat surface.

The correlation with FRR isn't surprising since

$$FRR = -20 \log_{10} V_T/V_{e\ (flaw)}$$

where V_e is the flaw-echo amplitude.

An examination of the parameters investigated by Lidington and Silk[7.3.7, 7.3.8] and Smith et al.[7.3.9] reveals a surprising lack of overlap in parameters: frequency deviation and low sensitivity were comparable, poor beam quality overlapped partially, and non-exponential decay corresponds somewhat to damping. Checking other frequencies was limited and secondary beams and beam misalignment were nonexistent in the Air Force study[7.3.9].

Farley[7.3.10] discussed a Babcock and Wilcox, Ltd. program where probe standards such as BS 4331, parts 2 and 3, and a CEGB draft standard were used to characterize 30 flaw detectors (mainly used ones of five types) and 70 probes (all new "miniature" type of two makes). Results relevant to the flaw detectors will be discussed in section 7.3.2.

Table 7.3.6 covers the variety of measurements taken on the probes. An interesting conclusion based on the results was that the specialized probe assessment techniques were valuable for probes used in a developmental laboratory for the complete characterization of individual probes; however, none is absolutely necessary for routine checks where "test-block" methods are deemed sufficient. These methods generated a wealth of data. The summarized results follow:

Results of Tests on Probes

Probe Index: Many probes had emission points more than 1 mm from the index mark, some were more than 3 mm away.

It would be better if there were no marks at all, or else just a scale referenced to one end of the probe.

Beam Angle: Most probes had angles within 2° of the nominal but a small number were 3 or 4° away. Again this indicates the need for the measurement of the angle of each probe by the operator.

TABLE 7.3.6. Summary of Tests of Probes Under B&W Program(7.3.10)

Meeting BS-4331[a]	CEGB Standard[b]	Additional Tests at CEGB NDT Center
Probe Index	Pulse Characteristics	At CEGB NDT Center
Beam Angle	Pulse Shape	Frequency Spectrum Analyses
Beam Squint (skew)	Pulse Length	Photoelastic Visualization
Beam Profile	Spacing of Cycles	Immersion Tank Plotting
Sensitivity and S/N Ratio	Operating Frequency	Impedance Meter Measurement
Dead Zone		
Resolution	Beam Characteristics	At B&W
Dominant Frequency	Index Point	Electrodynamic Beam Plotting
Pulse Length	Beam Angle	
	Squint	
	Side Lobes	
	Longitudinal Waves	
	Surface Waves	
	Backwards Shear Waves	
	Subsidiary Maxima	
	Sensitivity	
	Gain Reserve	
	S/N Ratio	
	Internal Echoes	
	Internal Echo Amplitude	

(a) Require Flaw Detector and Calibration Block only.
(b) Medium Frequency, Miniature, Shear Wave, Angle Probes.

Beam Squint (skew): Only one of the 70 probes had a squint greater than 2° and this was 2.5°.

Beam Profile: The profiles of probes of the same type were reasonably consistent but this is a probe feature which should be measured by the operator when the profile is required. The lateral beam spread of one make of miniature angle probe was nearly twice that of another make despite their similarity of crystal size and frequency.

Sensitivity and Signal-to-Noise Ratio: At ranges between 10 and 120 mm for the single-crystal probes (20 and 50 mm for twin-crystal probes) the ratio between the signal from a 1.5-mm side-drilled hole target

and the overall system noise exceeded 20 dB for almost all the probes. This test is important because the results at shorter ranges demonstrate a feature of twin-crystal probes that must be recognized: below the surface there is a blind zone (of 10 to 15 mm) where the sensitivity is much reduced compared with that of single-crystal probes. The precise length of the blind-zone depends on the probe geometry and whether or not the crystals are "toed-in."

Dead Zone: All the probes tested (single and twin) were able to detect a 1.5-mm hole at a depth of 1 mm from the testing surface.

Resolution: All the probes tested appeared capable of resolving the 2-mm step in the resolution block. However, the test is not reproducible and not a true measure of resolution. The ability of a probe to resolve defects closely spaced in range is better quantified by a pulse length measurement.

Dominant Frequency: This is checked by measuring cycle-to-cycle spacing on an unrectified display of the pulse. Spectrum analysis does give a more accurate result but for most purposes the test-block method would be adequate. The results indicate that the mean frequency of each group of probes lies below their nominal frequency -- by 0.25 to 0.50 MHz -- and that probes within a group generally have frequencies within $\pm$10% of the mean and $\pm$20% of the nominal.

Pulse Length: This is measured between the 10% points in the pulse envelope. A significant difference was found between the two types of probes checked. One make of probe had pulse lengths between 1.5 and 3.5 μS, the other had shorter pulses, 0.5 to 2.0 μS. Only 9 of 36 of the first make of probe met the CEGB 2.5 μS or 3 μS limits while all 18 of the second make met the requirement.

The role of components, other than the transducer, making up a probe can be significant. Posakony[7.3.6] cited the leads as a factor. Bainton and Silk[7.3.11] investigated influence of backing material and bonded region on the overall performance of a probe. The acoustic impedance of a material such as tungsten/Araldite often will be substantially lower than a transducer such as lead zirconate titanate (PZT). Unless packing densities are controlled, the acoustic impedance may drop below 80%. The boundary layer should be no more than a few microns in thickness. This again requires careful control.

An example of the type of problem that can affect an array of transducers is given by Bruneel et al.[7.3.12] The authors found that electrical coupling often occurs between nearby transducers, especially for very narrow transducers leading to a narrowing of the radiation (or reception) pattern of individual transducers.

7.3.1.1 Transducer variability represents a major problem. Until the variability is resolved the option will be to calibrate and certify prior to use. An approach combining tests in the laboratory and in the field is considered the correct approach.

7.3.2 Generators and Amplifiers

Two critical items of equipment in a UT system are signal generators and output signal amplifiers. Tests have been made with various off-the-shelf units combined with a series of probes to examine relative behavior; however, no detailed experiment aimed at definitive measurements of variability of these components is known in the open literature. The work of Caussin and Verspelt[7.3.1] comes closest to such a study and clearly indicates the significance of some variables taken for granted in such equipment. The same is believed true with regard to exploring the overall system behavior where the individual components all exhibit acceptable behavior, but the system is less than optimum.

Farley[7.3.10] discussed flaw detector variability where flaw detector covers the pulse generator, etc. Table 7.3.7 lists the tests conducted and their source; e.g., BS-4331 or ASME XI. Again, the results are given:

TABLE 7.3.7. Suggested Tests on Flaw Detectors by Standards and for Purchase and Periodic Checking

By Standards	ASME XI	BS 4331	Purchase and Periodic Checking
(a) Tests Involving Only a Probe and Calibration Blocks			
* Resolution of probe/flaw detector		X	
* Timebase linearity		X	Timebase linearity
* Attenuator accuracy	X	X	Attenuator accuracy
* Amplifier linearity	X	X	Amplifier linearity
* Echo-pulse duration		X	
(b) Tests Requiring the Use of an Oscilloscope			
** Transmission pulse parameters		X	Transmitter pulse parameters:
** Transmitter output impedance		X	pulse amplitude
** Stability of pulse repetition frequency		X	pulse shape
			rise time
			decay time
			pulse duration
			repetition frequency
(c) Tests Requiring Additional Electronic Equipment			
** Measure pulse repetition frequency		X	
** Amplifier frequency response		X	Amplifier frequency response
** Equivalent input noise		X	Equivalent input noise
** Amplifier dead time		X	Amplifier dead time

NB: The following equipment is required: three calibration blocks, oscilloscope, frequency counter, function generator, trigger unit and attenuator. Methods are defined in BS 4331: Pt. 2.

Results of Tests on Flaw Detectors

Resolution:	Results using 2-mm step on the resolution block were not reproducible.
Timebase Linearity:	27 sets were better 1.5% and within their manufacturers' specifications; others were 2%, 3% and 2%.
Attenuator Accuracy:	Almost all sets checked had attenuators accurate to ± 1 dB in 20 dB. Two new sets initially gave poor results until the attenuators were "run-in."
Amplifier Linearity:	The vertical linearity of all sets tested was very good, between 90% and 10% of full-screen height.
Echo Pulse Duration:	Generally, the duration of the rectified and detected echo-pulse was shorter than the length of the unrectified pulse for the same probe. The echo-pulse duration was influenced far more by the choice of flaw detector than by the frequency band setting used.
Transmitter Pulse Parameters:	Amplitude varied between 90 and 310 V (with one faulty set giving only 11 V); rise times fell between 26 and 200 nS, decay times between 62 and 310 nS. Output impedances were between 10 and 50% and were consistent for particular types of flaw detectors. Pulse repetition frequencies varied greatly from set to set, typically by a factor of two and in some cases differed from the manufacturers' specification by the same amount.
Amplifier Frequency Response:	There is a wide variation in frequency bandwidth between nominally identical flaw detectors; e.g., for one type bandwidths ranged from 0.88 to 3.18 MHz, for another type bandwidths were from 0.88 to 4.59 MHz on a particular band setting. Center frequencies showed similar variations between flaw detectors of the same type.

Equivalent Input Noise: This ranged from a best value of 5 μV on the best flaw detector tested to an upper limit of 400 mV and an extreme case of 900 mV on the faulty set.

Amplifier Dead Time: This parameter showed large variations between sets of the same type (e.g., 0.8 to 3.5 μS on one flaw detector type) and very large values on one particular type of set. On these tests, the worst values obtained were 18 to 25 μS, which could give a dead range of 20 mm of steel when testing with a miniature angle probe, 37.5 mm when testing with a compression probe.

Pade and Enrietto[7.3.13] as a part of their study of UT detection of cracks in cast stainless steel[13.5.1] examined UT systems variability. Five test instruments were used in conjunction with five different probes. The following cast test specimens were used in the evaluation:

- Specimen V-3 contained an outside diameter fatigue crack which was visibly discernible to a depth of 26% through-wall (0.55 in.) on one side and 24% through-wall (0.5 in.) on the other side of the specimen.
- Specimen OV-2 contained an inside diameter fatigue crack 14% through-wall (0.3 in.) deep on both sides of the specimen.
- Specimen DW-2 contained an inside diameter fatigue crack 5% through-wall (0.1 in.) on both sides of the specimen.
- Specimen DW-1 was the calibration standard which contained 3/16 in. diameter side-drilled holes at 1/4T, 1/2T, and 3/4T depths (T equals specimen thickness). The standard also contained a 2-in. long, 1/16-in. deep V-notch on the inside diameter.

Transducer effectiveiness was evaluated through measurement of the following test parameters:

- the ability to calibrate the test system
- the ability to detect the cracks in the test specimens
- the recorded length of the crack based on 50% DAC sizing level
- the average S/N ratio in the vicinity of the crack indication.

The probe characteristics were as follows:

- Krautkramer, 0.5-MHz, 36.5-mm diameter transducer mounted on a 63-mm by 52-mm by 110-mm wedge machined to produce a 45° refracted longitudinal wave in carbon steel.
- Vincotte, 1.0-MHz, 15-mm by 20-mm dual pitch-catch transducers with a crossover focal point of 50 mm in steel. The crystals were mounted in a 52-mm by 40-mm by 46-mm case. The crystals were designed to produce a 60° refracted longitudinal wave in steel.
- Vincotte, 1.0-MHz, 15-mm by 20-mm dual pitch-catch transducers with a crossover focal point of 85 mm in steel. The crystals were mounted in a 52-mm by 40-mm by 46-mm case. The transducers were designed to produce a 45° refracted longitudinal wave in steel.
- Vincotte, 2.0-MHz, 10-mm by 10-mm dual pitch-catch transducers with a crossover focal point of 25 mm in steel. The crystals were mounted in a 40-mm by 20-mm by 46-mm case. The transducers were designed to produce a 45° refracted longitudinal wave in steel.
- Automation Industries, Inc., 10-MHz, 1.5-in. diameter search unit mounted in an 87-mm by 75-mm by 72-mm water box with a flexible membrane at the contact area. The fixture was designed to produce a 40° refracted longitudinal wave in steel.

Results of the evaluations are given in Table 7.3.8. An assessment of its contents indicates the following:

- All transducers except the Vincotte 60° search unit were capable of being calibrated in accordance with the procedure.
- The Krautkramer 0.5-MHz search unit, when used with the Sonics Mark I, Krautkramer USIP 11, or Sperry UM 721 test instrument, consistently detected all three cracks. The Vincotte, 2.0-MHz, 45°, 10-mm by 10-mm probe detected the 15% through-wall crack with all test instruments, the 25% through-wall crack with the UJ Reflectoscope and UM 721 Reflectoscope test instruments, and the 5% through-wall crack with the UJ Reflectoscope and Krautkramer USIP 11. The

TABLE 7.3.8. An Evaluation of Combinations of Test Instruments and Special Transducers

Test Instrument	Krautkramer 0.5 MHz, 45° L-wave	Vincotte[a] 2.0 MHz, 45° L-wave	Vincotte[a,d] 1.0 MHz, 45° L-wave	Automation Industries 1.0 MHz, 40° L-wave
Sonics Mark I	Y | Y 3.5 | Y 2.25 — 4:1 Y 2.6 | Y 2.8 — 3:1 ; N — | Y 1.25 — 3:1	Y | N — | N — N — | Y 0.75 — 2:1 ; N — | N —	Y | Y 3.5 | N — N — | Y 3.5 — 9:1 ; N — | N —	Y | Y 2.6 | N — Y 2.46 | Y 36 — 6:1 ; N — | Y 0.55 — 6:1
Krautkramer USIP 11	Y | Y 1.7 | Y 1.8 — 2:1 Y 2.9 | Y 2.8 — 2:1 ; N — | Y 2.0 — 2:1	Y | N — | N — N — | Y 1.4 — 3:1 ; Y 0.3 | N — — 2:1	Y | Y 3.5 | N — N — | Y 3.5 — 3:1 ; N — | N —	Y | Y 3.5 | N — N — | Y 3.5 — 2:1 ; N — | N —
Krautkramer USM-2	N (b) — — — ; — — — —	Y | N — | N — N — | Y 2.1 — 2:1 ; N — | N —	Y | Y 3.5 | N — N — | Y 3.5 — 3:1 ; N — | N —	N (b) — — — ; — — — —
Automation Industries U.S. Reflectoscope	(c) — — — ; — — — —	Y | N — | Y 0.4 N — | Y 0.56 — 3:1 ; N 0.4 | N — — 2:1	Y | Y 0.5 | N — N — | Y 1.4 — 4:1 ; Y 0.25 | N — — 2:1	Y | Y 1.6 | N — N — | Y 1.8 — 6:1 ; Y 0.5 | N — — 5:1
Sperry UM 721 Reflectoscope	Y | Y 1.9 | Y 0.6 — 5:1 Y 1.5 | Y 2.06 — 5:1 ; N — | Y 0 — 2:1	Y | N — | Y 0.55 N — | Y 3.5 — 3:1 ; N — | N —	Y | Y 3.5 | N — N — | Y 3.5 — 4:1 ; N — | N —	(c) — — — ; — — — —

KEY

Ability to Calibrate Test System	Specimen V-3 Surface 3	Specimen V-3 Surface 4	
Yes or No	Yes or No 0.00	Yes or No 0.00	Detectable Flaw Length, in.
	2:1		Signal-to-Noise Ratio
Yes or No 0.00 / Yes or No 0.00 — 3:1	Yes or No 0.00 / Yes or No 0.00 — 4:1		Detectable Flaw Length, in. / Signal-to-Noise Ratio

Surface 1 Specimen DW-2 | Surface 2 Specimen DW-2 | Surface 1 Specimen DW-2 | Surface 2 Specimen DW-2

NOTES

(a) KK Type WL 3BI impedance matching device used with all Vincotte probes.
(b) Screen presentation poor; gain-level setting maximum.
(c) Faulty instrument.
(d) A Vincotte 1.0-MHz 60° L-wave probe was used with all instruments; however, it could not be calibrated.

Vincotte, 1.0-MHz, 60°, 15-mm by 20-mm search unit could not be used to examine the test specimens because it was not possible to calibrate the test system when using this probe. The Vincotte, 1.0-MHz, 45°, 15-mm by 20-mm search unit detected the 25% and 15% through-wall cracks with all test instruments but detected 5% through-wall cracks only when used with the UJ Reflectoscope. The Westinghouse-Automation Industries 40° refracted longitudinal wave fixture was evaluated using the Sonics Mark I, Krautkramer USIP 11, and UJ Reflectoscope. All cracks were detected except the 5% through-wall crack when using the Krautkramer USIP 11.

- The recorded crack length should theoretically have been the full 3.5-in. width of the specimen. However, the crack orientation and through-wall depth could vary across the width of the specimen. None of the search unit-test instrument combinations evaluated detected the crack at or above 50% DAC across the full width of the cracked samples. The Vincotte, 1.0-MHz, 15- by 20-mm, 45° unit did detect the 15% and 25% through-wall cracks in all cases except when the probe was used with the UJ Reflectoscope. The 1.0-MHz Westinghouse-Automation Industries probe recorded an average of 64% of the crack length from at least one surface while the Krautkramer search unit recorded an average of 55% of the crack length, usually from both sides of the weld.

- In all the tests where a crack was detected, the crack S/N ratio was 2:1 or greater with the exception of the Vincotte, 2.0-MHz, 45°, 10-mm by 10-mm probe when using the UJ Reflectoscope. The better overall S/N ratios were obtained with the Westinghouse-Automation Industries fixture where the ratios were between 6:1 and 7:1 using the Sonics Mark I instrument and between 5:1 and 7:1 when using the UJ Reflectoscope. The Vincotte search unit had a S/N ratio of 9:1 on the 15% through-wall crack when using the Sonics Mark I test instrument.

- Prior to using the special acoustic impedance matching devices with the Vincotte probes, the screen presentations for the Vincotte probe

were difficult to interpret due to crosstalk between the transmitter and receiver crystals and noise levels up to 10% full screen height in the areas of interest. When using the impedance matching devices, the crosstalk was eliminated and the noise level dropped to less than 5% full screen height. However, the ability to detect cracks was not significantly improved.

- When using the Vincotte probes, the maximum sensitivity should be at the crossover points. Theoretically, when using a 45° refracted sound beam to examine centrifugally cast stainless steel specimens, a focus point of approximately 76 mm would provide the maximum sensitivity at the opposite surface of the specimens where cracks would be expected to start. When using a 60° probe, a crossover point of approximately 108 mm would provide the optimum sensitivity in the area of interest. Because of the need to match the crossover point with the area of interest, the lack of satisfactory test results from the Vincotte 45° probe with a crossover point of 25 mm and the 60° search unit with a crossover point of 55 mm was expected. As excepted, the best test results from the Vincotte probes were obtained from the 45° probe with an 85-mm focal crossover point.

The following conclusions were reached based on the evaluation of special search unit:

- Of all the special transducers evaluated, the Krautkramer 45°, 0.5-MHz search unit appeared to provide the most satisfactory overall test results. A very significant problem with the Krautkramer probe was that it was too large (63 mm by 52 mm by 110 mm) for use in field testing primary piping welds. Although the Westinghouse-Automation 40° refracted longitudinal wave fixture used in the reliability study is also too large for field testing, a new miniaturized design using a 1.0-in. diameter search unit in a tapered water tube has been evaluated and provides similar results on test specimens.
- There was a very significant variation in test results when the only test parameter varied was the test instrument. This effect has been noted in other programs.

- Couplant was another variable that affected test results. Pure glycerine provided more accurate test data than did Exosen 30.
- Of the three Vincotte probes evaluated, the 1.0-MHz, 45° search unit with an 85-mm crossover point provided the most accurate test results. However, the unit did not consistently detect the 5% through-wall crack. The other two Vincotte probes were not considered adequate primarily due to a mismatch of the crossover points and the location of the cracks.
- The Westinghouse-Automation Industries 40° refracted longitudinal-wave fixture is equal to or better than the special search units evaluated in the study.
- During the program, several combinations of test instruments and search units were evaluated on the same test samples. There was a wide variation noted in test results from combination to combination. The same phenomena have been observed in several other programs. It appears that it is extremely important that the test instrument and search unit be matched for the test to be conducted.

The authors[7.3.13] in their final conclusion remark on the importance of matching test instrument and search unit for a given test. We concur completely with this statement. In fact it is surprising that the KK USM-2 and Automation Industries UJ Reflectoscope were used with the 0.5-MHz probe. There is ample experience confirming their inapplicability for this frequency range.

In a paper by Bayre and McCormack[7.3.14] the results of a cooperative program aimed at greater reliability of bearings are discussed. High-frequency UT using a surface or near-surface wave was the technique. Of interest were the following results pertinent to equipment variability:

- Transducers with a different emitted frequency spectrum yield dissimilar inspection results.
- A major source of transducer error is the lack of coincidence of focal point and Fraunhofer point.

- The slope linearity and amplitude of the analog output of different ultrasonic instruments vary much more than the oscilloscope presentation. Using beam reflected signal for establishing counting levels results in a much smaller error than using voltage analog output.
- The impedance between transducers and instruments has a significant effect on both frequency of beam and focal length of transducers. For example, with some tuned pulsed instruments changing input cable from 8 to 15 ft changed output frequency from 10 to 5 MHz.

With regard to the above item, particularly the second, there is disagreement with the conclusion by other researchers.

7.3.3 Signal Processing

There undoubtedly is a potential for error and variability in the various systems used to modify or to interpret the output signals; however, no studies are known related to such a source of variability. Whether the contribution is limited or substantial is not known.

7.4 ULTRASONIC EQUIPMENT FOR EXAMINATION OF CONVENTIONAL FINE-GRAINED (WELDMENTS) SYSTEMS

The pulse-echo UT system will be emphasized in this section to serve as a basis for comparison to the other sections on UT through cladding or in coarse-grained austenitic structures.

A fine-grained material containing a minimum of surface geometric reflectors represents a potentially ideal system from the point of view of UT. An obvious example would be a thick-rolled ferritic plate with a butt weld and both surfaces finish ground to an acceptable smoothness. Some of the PVRC and PISC blocks discussed in Chapter 3 approximated this description. Others, because of the "dirty" steel, contained many internal geometric reflectors posing problems.

A pulse-echo UT system will consist of a signal generator (transmitter), a transducer, an amplifier, and a unit such as a CRT to observe the signal. The pulse-echo UT system represents one link in the detection chain. As discussed in sections 7.2. and 7.3, the signal response is highly sensitive to the response characteristics of the individual components with no assurance that a given combination of "good" components will yield a "good" system. Other links in the detection chain include the type of calibration blocks and calibration procedure; types of flaws, their orientation tightness, location, etc.; and the reaction of the operator to signals observed during an examination. All links in the detection chain are important.

The PVRC and PISC data illustrate how inattention to calibration procedures can invalidate results on the specimens. This was discovered after the first PVRC round robin so rigorous calibration procedures were initiated. In PISC the same situation occurred. A few teams were careful in calibration and did well on the plates. Others paid lip-service to calibration and did poorly on the plates, which they expected to be the case because they distrusted the technique, and cited the gross limitations of pulse-echo.

The operator is an important link. Two teams with very similar equipment will see signals in a given location. One will call it a flaw, the other a

geometric reflector. A basic problem with the pulse-echo technique, where decisions are limited to interpretation of signal amplitude alone, is the high degree of subjectivity. One operator can examine the shape of a signal with relatively low S/N ratio and call it a flaw; others will depend on amplitude alone and completely miss the flaw. Obviously, the first is depending on more than signal amplitude so he has moved outside the bounds of a decision based on amplitude alone.

Several techniques exist for the better display of the signals related to the component being examined; for example;

- A-scan - Ultrasonic amplitude versus time. The base line indicates elapsed time superposed on the through-thickness section.
- B-scan - A distance-time UT plot showing thickness of component and flaws in the thickness in profile.
- C-scan - An amplitude-area UT plot displaying defects on the scanning surface of the component.
- P-scan - A projection image scanning showing flaw projections on both scanning surface and through-thickness surface.

All of the preceding depend on pulse-echo amplitude signals which are analyzed. In P-scan a microprocessor in the circuit measures, analyzes and records all signals, removing some degree of subjectivity from the examination.

7.4.1 Conclusions

Pulse-echo examination results can vary widely because of the degree of subjectivity in the evaluations. In some instances, excellent results are obtained; in others, results are very poor. If decisions are based on an amplitude signal alone, great care must be exercised to ensure that the optimum signal is developed, and operators with the appropriate field experience are a critical link. It is recognized that other techniques such as tandem provide an alternate. They will be discussed in a later section to examine the effect of other parameters on signal.

7.5 EQUIPMENT FOR EXAMINING COARSE-GRAINED AUSTENITICS

A great deal of the material on equipment for examining course-grained auctenitics discussed in this section is applicable to Section 7.6 pertaining to examination of clad ferritic alloys. Factors affecting scattering apply and attenuation is a function of thickness so it applies in principle. Since much of the information is covered extensively in Chapter 13, the reader is referred there for detailed coverage. Significant aspects will be introduced here but not elaborated on.

7.5.1 Significance of Cracking

Austenitic alloys represent a special case in fracture mechanics. Because of their toughness over a wide spectrum of temperature, linear-elastic fracture mechanics is not appropriate. Options are elastic-plastic fracture mechanics or general-yield fracture mechanics. They will withstand relatively large flaws without failure and leak-before-break is the anticipated failure mechanism.

In wrought austenitic alloys, intergranular stress corrosion cracking (IGSCC) has been the predominant failure mechanism. Such cracking occurs most often in the weld heat-affected zones, sometimes in regions of cold work, rarely in the weld. It is much more common in BWRs than PWRs. Cast austenitics are essentially immune to IGSCC for the same reason that welds rarely crack. The delta ferrite present in both cast and weld material minimized IGSCC. Residual stress, sensitization and oxygen in the coolant promote IGSCC. Initiation periods may be short or long depending on these parameters. Propagation may be very rapid or quite slow. A rule of thumb is that larger piping (>16 in.) have long initiation and propagation times; smaller piping may have rapid rates in both initiation and propagation. In fact, UT of 4- to 8-in. lines may reveal no evidence of IGSCC and the lines may have leaking cracks within a year.

Because of the toughness of the austenitic alloys, the decision as to what represents an acceptable flaw in the context of ASME XI Standards needs reconsideration. The rules applied to ferritic are very conservative. ASME XI is

reconsidering standards for austenitics in the context of their toughness to see whether or not larger values are permissible. An obvious advantage of larger values would be in enhanced reliability of detection, particularly in coarse-grained materials where smaller flaws have signals buried in the background noise.

7.5.2 Mechanisms Affecting UT-Beam and Equipment Selection

Chapter 13 devotes substantial coverage to UT beam behavior in austenitic weldments and coarse-grained structures. The following are of particular concern:

- beam skewing
- beam bending and direction along dendrites
- beam scattering
- beam attenuation.

The latter two are interrelated and particularly important with regard to frequencies in the equipment of interest; therefore, they will be reexamined in this chapter.

In a statistical mechanics context, several mechanisms contribute to Type II errors (missing the defect) and to Type I errors (false alarming). Sources of Type II errors include beam refraction, reflection and scattering beam absorption, beam curvature or skewing (beam redirection is a special case), beam defocusing, mode conversion and attenuation. Sources of Type I error include back-scatter and focusing, pulse spreading, mode conversion and amplitude fluctuations.

The two major attenuation mechanisms are interface and grain-boundary scattering. In weldments and cladding the major contributors are the large grains and rough interfaces where "large" indicates sizes comparable to or greater than the wavelength. A portion of the beam energy will be intercepted and reradiated or scattered with the net effect being increased attenuation and greater signal noise. The two-dimensional inhomogeneities located at or near interfaces such as fusion lines or rough surfaces (cracks, etc.) lead to surface scattering. Grain size is the other major contributor where these grains lead to three-dimensional or volume scattering.

The sum of backscattering contributions from all inhomogeneities distributed along or near the interfaces is termed surface reverberation while the grain contribution is defined as volume reverberation.

A somewhat simplified presentation of formulas used in defining scatter and attenuation follows for the simple homogeneous materials case:

$A(x)$ = sound amplitude
$A_s(x)$ = mean backscattering amplitude
x = sound path
A_o = amplitude excited in material under test
α = attenuation coefficient
$\alpha = \alpha_s + \alpha_n$
α_s = scattering coefficient
α_n = absorption coefficient
Δ = pulse length
SNR = acoustic signal-to-noise ratio

The amplitude of the signal reflected from the back wall will be

$$A(x) = A_o \exp(-\alpha x) \tag{7.5.1}$$

The mean backscattering amplitude will be

$$A_s(x) = A_o (\alpha_s \Delta)^{1/2} \exp(-\alpha x) \tag{7.5.2}$$

The SNR will be

$$SNR \sim \frac{A(x)}{A_s(x)} \sim (\alpha_s \Delta)^{-1/2} \sim \Delta^{-1/2} \tag{7.5.3a}$$

or, in terms of dB,

$$SNR\ (dB) = 20 \log \frac{A(x)}{A_s(x)} = -10 \log (\alpha_s \Delta) \tag{7.5.3b}$$

Another key factor will be the type of wave used, longitudinal versus shear wave.

The scattering coefficients α_s will consist of two parts where the first contains the scattered ultrasonic wave of the incident wave type and the second part corresponds to the mode conversion process such as excitation of shear waves (T) or by incident longitudinal wave (L) or vice versa.[7.5.1]

For the incident longitudinal wave

$$\alpha_s^L = \alpha_s^{LL} + \alpha_s^{LT} \tag{7.5.4}$$

and the incident shear wave

$$\alpha_s^T = \alpha_s^{TT} + \alpha_s^{TL}$$

The Rayleigh or volume scattering is

$$\alpha_s^L = \frac{8\pi^3}{375} \cdot \frac{Vf^4A^2}{\rho_o^2 V_L^8} \left| 2 + 3\left(\frac{V_L}{V_T}\right)^5 \right| \text{ mm}^{-1} \tag{7.5.5}$$

$$\alpha_s^T = \frac{6\pi^3}{375} \cdot \frac{Vf^4A^2}{\rho_o^2 V_T^8} \left| 3 + 2\left(\frac{V_T}{V_L}\right)^5 \right| \text{ mm}^{-1} \tag{7.5.6}$$

where $V \equiv d^3$

A^2 = elastic anisotropy of a single crystal

ρ_o = density

V_L = wave velocity for longitudinal waves

V_T = wave velocity for shear waves

f = frequency

An example for steel is

$$f = \text{constant} \quad \alpha_S^T = 4.6 \cdot \alpha_S^L$$

$$\lambda = \text{constant} \quad \alpha_S^T = 0.4 \cdot \alpha_S^L$$

The scattered shear wave is a factor $3/2\ (V_L/V_T)^5$ greater than that of longitudinal waves. In steel, this corresponds to a factor of 31.

A more accurate formula than 7.5.2 will be

$$L: \quad A_S^L(x) = A_0 \left(\alpha_S^{LL}\ \Delta\right)^{1/2} \exp\left(-\left|\alpha_A + \alpha_S^{LL} + \alpha_S^{LT}\right| X\right) \qquad (7.5.7)$$

$$T: \quad A_S^T(x) = A_0 \left(\alpha_S^{TT}\ \Delta\right)^{1/2} \exp\left(-\left|\alpha_A + \alpha_S^{TT} + \alpha_S^{TL}\right| X\right) \qquad (7.5.8)$$

Again, in steel

$$\frac{A_S^T(x)}{A_S^L(x)} = \left(\frac{\alpha_S^{TT}}{\alpha_S^{LL}}\right)^{1/2} = (0.4 \cdot 31)^{1/2} = 3.6 \qquad (7.5.9)$$

which corresponds to an amplitude ratio of 11 dB so the S/N ratio is better for L-waves than for T-waves in the Rayleigh region by this amount.

An analysis of the preceding indicates that UT systems emphasizing control of the following parameters enhance the possibility of detection and aid in minimizing the levels of background noise:

- Longitudinal waves are preferred.
- Very short pulses are needed to establish the desired axial profile of the beam.

- Lateral control of the beam can be achieved by pitch-catch, transmitter-receiver or focused probes.
- Control of frequency spectrum is vital.

With regard to frequency, the scattering coefficient a_s will vary as the fourth power in the Rayleigh (volume) region when the grain size is large with respect to the wave length. In the stochastic region, where the grain diameter and wave length are essentially equal, a_s will vary as the square of the frequency. Since control of frequency spectrum is critical, a transmitter capable of modulating the pulse amplitude by controlled signals will yield shorter pulses, more rapid pulse decay and suppression of higher frequencies. In contrast, more conventional transmitters do the opposite. At least 10-dB gain is possible with such a transmitter.(7.5.1)

Table 7.5.1 lists the parameters necessary to consider in a piping system as they affect NDE with UT.

7.5.3 UT Equipment Options

There is general agreement concerning various factors requiring control if a reasonable S/N ratio is to be achieved concommitant with an acceptable reliability of flaw detection in austenitic weldments. Previously, the formulas depicting wave behavior were presented and conclusions drawn concerning pulse length, beam width, etc. A similar list was presented in 13.4.3 of Chapter 13 and is repeated here for comparison:

- Select the form of UT waves that interact minimally if at all with the grain structure.(13.2.5, 13.2.6, 13.4.7) Preferred choice is longitudinal waves with optimally polarized shear-waves a possibility. The L-waves also will have less skewing and scattering.
- Optimize frequency (wavelength) to yield acceptable S/N ratio together with good flaw resolution.(13.4.7, 13.4.8) Higher frequencies increase noise and decrease S/N; lower frequencies (<1 MHz) decrease resolution. Optimum ranges 1 to 2.25 MHz.

TABLE 7.5.1. Influence of Various Parameters in Piping Systems on UT Detection Reliability

Weld Joint Combinations			Access: Single Side		Access: Both Sides	Assumed Flaw Location: HAZ			Section		Prognosis	Basis of Prognosis
A	B	C	A	C		A	B	C	Thin	Thick		
Ferritic	Weld	Wrought SS	X			X	X			X	Good	Full UT of weld difficult
				X				X		X	Good	Full UT of weld difficult
					X	X	X	X		X	Good	Full UT of weld difficult
Ferritic	Weld	Cast SS	X			X	X			X	Good	Full UT of weld difficult
				X			X	X		X	Fair-Poor	Full UT of weld difficult, attenuation in casting
					X	X	X	X		X	Good-Fair	Full UT of weld difficult, attenuation in casting
Wrought SS	Weld	Wrought SS	X			X	X			X	Good	Full UT of weld difficult
				X			X	X		X	Good	Full UT of weld difficult
					X	X	X	X		X	Good	Full UT of weld difficult
Wrought SS	Weld	Cast SS	X			X	X			X	Good	Full UT of weld difficult
				X			X	X		X	Fair-Poor	Full UT of weld difficult, attenuation in casting
					X	X	X	X		X	Good-Poor	Full UT of weld difficult, attenuation in casting
Cast SS	Weld	Cast SS	X			X	X			X	Fair-Poor	Full UT of weld difficult, attenuation in casting
			X				X	X		X	Poor to nonexistent	Weld difficult, far side HAZ almost impossible
				X			X	X		X	Fair-Poor	Full UT weld difficult, attenuation in casting
					X	X	X	X		X	Fair-Poor	Full UT weld difficult, attenuation in casting

N.B.--As thickness decreases, attenuation problems decrease.

- Use short broad-band pulses to reduce scattering, improve S/N, reduce false signals.[13.2.6, 13.4.7, 13.4.8] Low-pulse lengths reduce scattering thereby improving S/N; e.g., a tenfold reduction in pulse length improves S/N about 10 dB. Increased bandwidth reduces false signals because of shorter signal times; this approach also reduces signal amplitude.

- Use controlled shaping of the transducer acoustic field to reduce grain scattering (beam focussing).[13.2.6, 13.4.7, 13.4.8]

- Obtain acoustic and electrical matching of transducers and flaw detector (dual probe).[13.4.7]

- Utilize signal processing to increase S/N ratio.[13.4.7] Use variable frequency and bandwidth transmitter pulses. Use signal averaging as an inverse filter.

- Utilize adequate numbers and types of reference blocks to provide meaningful calibration.

In Chapter 6, an extensive program was discussed where six different equipment systems were used on samples with small difficult-to-detect flaws.[7.5.2,7.5.3] Since there was extensive coverage in Chapter 6, only those factors pertaining to the equipment will be addressed here.

A rank ordering of the various types of UT equipment, together with their percentage of success in detecting the defects, is shown in Table 7.5.2.

TABLE 7.5.2. Relative Reliability of Detection of Systems

1a	Multiple beams - shear and longitudinal waves	82%
1b	Multiple beams - shear waves	76%
2a	Short pulses - shear waves	73%
2b	Short pulses - longitudinal waves	39%
3a	Restricted beams - focused probes	58%
3b	Restricted beams - pitch-catch probes	58%
4	Phased arrays	53%
5	Controlled signals	39%
6	Spatial averaging	--

The percentage values in that table are based on tests on several stainless clad stainless plates that were relatively thin so they do not represent the situation in thick-cast stainless sections; however, they permit a rank ordering for purposes of discussion.

7.5.3.1 The Multiple-Beams Technique

The multiple-beams technique has been discussed by Gruber.[7.5.2] It was developed especially for the detection of IGSCC in piping and for welds and heat-affected zones in cladded piping. The MBT approach was aimed at solution of the low S/N ratio typical of clad-base metal interfaces in austenitic piping. Two areas were attacked as noted in Table 7.5.3. The actions cited in Table 7.5.3 are in their suggested order of implementation. Mode II is used to keep false alarming to acceptable levels. In essence, a suspicious indication in Mode I is considered unconfirmed until checked in Mode II. Figures 7.5.1a and b illustrate the two modes of operation with the multiple-beam technique. In Mode I a parallel combination of tests using either S_a or S_b are designed to increase defect detection reliability. In Mode II a series combination of tests using S_a (or S_b) and L_a is designed to increase the probability of correct rejection.

The probes shown in Figure 7.5.1 are inclined to one another by less than 10°. They are highly damped pulse-echo types. Probe B's angle is larger than the critical angle for longitudinal waves in austenitic materials (~29°) so it transmits only a standard 45° shear wave. Probe A has an angle <29° so it transmits both a shear and a longitudinal wave. The inclination (<10°) permits an overlap of the two probes at a selected depth such as the inner bore cladding of large diameter piping.

The size of lucite wedge and probe characteristics were optimized to optimize real-time waveform processing both directional averaging and spatial filtering. No single frequency was considered optimum for spectral averaging so a split-spectrum processing approach was used.

The MBT was optimized for detection of flaws at a clad-base metal interface where the cladding was on the far surface. Some examinations through cladding indicate that MBT is applicable to thick sections typical of reactor

TABLE 7.5.3. Modes of Operation and Salient Features of the Multiple-Beam-Angle (MBA) Crack Detector ("Multiple-Beams Technique," MBT)

Inspection Mode	Operation		Feature/Process to Achieve Purpose	Purpose
	When	Action		
I*	Prior to Pulse Transmission	Pulseshaping and Beamforming	1. Short Pulses	Minimize volume and surface reverberation
			2. Multiple Beams(a)	
	Following Waveform Reception	Waveform Processing	3. Multiple Bands(a)/ Spectral Averaging	Control frequency
			4. Directional Averaging(b)	Control time
			5. Spatial Filtering(b)	Control space
II**		Pattern Recognition	6. Multiple Pulses(a,c)	

(a) Multiple means two or three
(b) Used only in the automatic inspection mode (mode I - inspection)
(c) Used only in the manual reinspection mode (mode II - confirmation)
* Automatic Inspection Mode
** Manual Reinspection (Confirmation) Mode

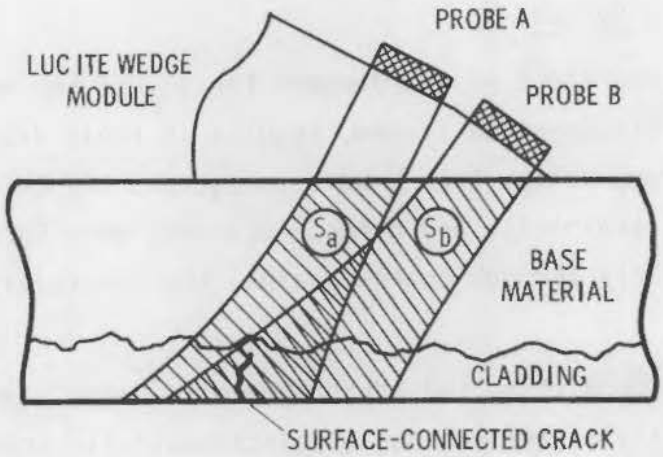

FIGURE 7.5.1a. Multiple Beams Used in the Inspection Mode of Operation (Mode I) of the MBA Crack Detector

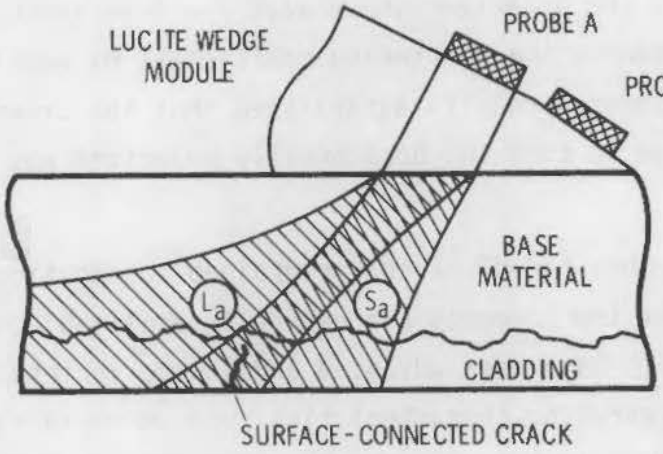

FIGURE 7.5.1b. Multiple Beams Used in the Confirmation Mode of Operation (Mode II) of the MBA Crack Detector

pressure vessels indicating it may be applicable to the detection of cracks under the cladding. Therefore, MBT needs to be considered as an option for section 7.6. While the MBT system has been used to a limited degree on thick sections of cast or wrought austenitics, it should be capable of optimization to be equal to or better than simpler systems. The ability to resolve the attenuation problem depends on probe and equipment optimization rather than technique.

7.5.3.2 Short Pulses

Short pulses represent an improvement for any of the equipment. In the simple pulse-echo single-probe system, results in Table 7.5.2 indicate that shear waves performed better than L-waves; however, the thin section, preponderance of wrought stainless, and defect locations were factors. In thicker sections, particularly through coarse grains, the longitudinal beam would be preferable.

A possibility permitting the advantages of L-waves higher velocity and S-waves detectability is through use of electromagnetic acoustic transducers (EMATS) to generate horizontally polarized shear waves. As noted in Chapter 13, shear waves polarized in this plane are comparable to L-waves. The velocity is nearly double and the wave length halved for the same frequency. For example, at 1 MHz the polarized shear wave $\lambda = 4$ mm versus $\lambda = 2$ mm. This longer wave length reduces the scattering coefficient by nearly a factor of 16. Unfortunately, experimental results established that the oriented austenitic alloy rotated the beam so that the horizontally polarized was shifted to vertically polarized.

The status of probes for UT of coarse-grained austenitics is included here, recognizing that the comments are generally applicable to all pulse-echo equipment. Many claims have been advanced and a wide variety of probes have been developed, incorporating characteristics such as rapid ring down, narrow lateral beam, etc. Even so the current situation is exemplified in one study.

A limited study using 1- to 2-MHz refracted L-waves was conducted on five different probes:

1.	K.B. Aerotech	45°	f ~ 50	SEL
2.	Vincotte	45°	f ~ 85	SEL
3.	SRI	45°		SEL
4.	RTD	45°	f ~ 25	SEL (broad band)
5.	RTD	SEK-2	f ~ 12	for surface defects

A section of cast austenitic ~60-mm thick with a weld in the center was used. This material was known to have poor acoustic properties. Side-drilled

holes were located at 1/4 t, 1/2 t, 3/4 t in HAZ plus notches. None of the probes was considered to be adequate. None could detect the rear corner of the block.

The preceding is typical of other studies. In the thicker sections of coarse-grained castings attenuation is very severe even with optimized probes.

A study by Kupperman et al.[7.5.5] concentrated on conventional pulse-echo equipment. Samples were 4-, 10- and 26-in. (102-, 254-, 660-mm) 304 SS schedule 80 piping containing a variety of artificial defects such as EDM notches, saw cuts, and drilled holes. The notches were transverse and longitudinal as well as being slanted and skewed. These defects were in both welds and wrought material. Also there were intergranular stress corrosion cracks in some HAZs.

A large test matrix was utilized including pulse-echo with focused and planar probes and pitch-catch. It included three frequencies (1, 2.25, 5 MHz), two angles (45°, 60°), two transducer sizes (6, 13 mm), and both flat and curved shoes. A KK Branson Sonoray 303B was used primarily with aerotech probes. With regard to the equipment parameters the following represent conclusions:

- Focusing is advantageous for small reflectors plus being less sensitive to variations in flaw slant angle; there was no advantage with large defects.
- Curved wedges have a slight advantage for small reflectors, none for large reflectors, and are disadvantageous for skewed defects.
- The larger probe is best for a general scan with the smaller good for confirmation, provided weld crown does not force use of the smaller.
- 45° beam angle is best if there is no weld crown; otherwise 60° is the choice.
- 2.25 MHz was best with 5 MHz having high attenuation and 1 MHz a low S/N ratio.
- Dual beam was best for skewed reflectors; otherwise they were disadvantageous.

The operator proved to be a significant variable. With either 45° or 60° shear waves, the signals could not be definitely and unambiguously differentialed between cracks and geometrical discontinuities. An operator familiar with piping could differentiate because of pattern recognition. While the preceding was an extensive study and provided insights into the effects of some parameters, its overall scope was too limited to permit broad inferences concerning equipment capability.

7.5.3.3 Focused Probes

Focused probes, either contact or immersion, have been successful in retaining satisfactory S/N ratios with good flaw detection and sizing. A problem with the more sophisticated systems is detection to very low levels. A "dirty" steel presents difficulties in both examination and evaluation because of computer costs and time. Substantial coverage is given in Chapter 6 to focused probes. Focusing improves the ratio of reflector to beam diameter. Since this is a squared relationship because the areal relationship is the important one, major gains in S/N ratios accrue. For example, reducing beam diameter by a factor of 2 changes S/N ratio 12 dB. A further gain is the enhanced sound pressure per unit area in the focus region leading to increases in gain and in sensitivity.(7.5.1) While the preceding represent obvious gains, it must be recognized that focused probes must be carefully engineered for a specific operation and yield data for a given depth only. A one hundred percent depth examination in a thick section will require a series of probes each covering an increment of thickness. If the examination coverage is reduced (e.g., concentrating on the region near to the inner bore of a pipe) the complexity will be reduced.

Yamazaki and Fuji(7.5.6) examined factors influencing angle-beam focused probes. While such probes have excellent sensitivity, there is no sound theoretical bases for handling curved surface aberation and real-versus-apparent transducer locations. For example, wedge shape is a significant factor in controlling and reducing the spread of the reflection signal. In particular, studies are required to better predict behavior of 70° probes. These most definitely are not off-the-shelf items.

7.5.3.4 Pitch-Catch Probes

Pitch-catch probes usually are considered in the context of separate transmitter and receiver probes; however, a special case is the signal component transmitter-receiver representing a special subset of conventional pitch-catch. Wüstenberg et al.[7.5.7] discuss pitch-catch, tandem, transceiver angle and inclined longitudinal waves transmitter-receiver approaches. Figure 7.5.2 permits a comparison of these various techniques.

Basically T-R probes examine a region where the beams cross, which can be quite small so the S/N ratio is not adversely affected. Since there are both axial and transverse decreases in "grass" there will not be an overall improvement in S/N ratio. T-R probes have a further advantage for coarse-grained materials. While multiple scattering and reflection at big grains near the transmitter are detected and measured with the usual pulse-echo equipment, T-R probes do not pick up these grains. Figure 7.5.3 compares T-R probe, focused beam and pulse-echo in an austenitic weldment illustrating the decrease in background noise.

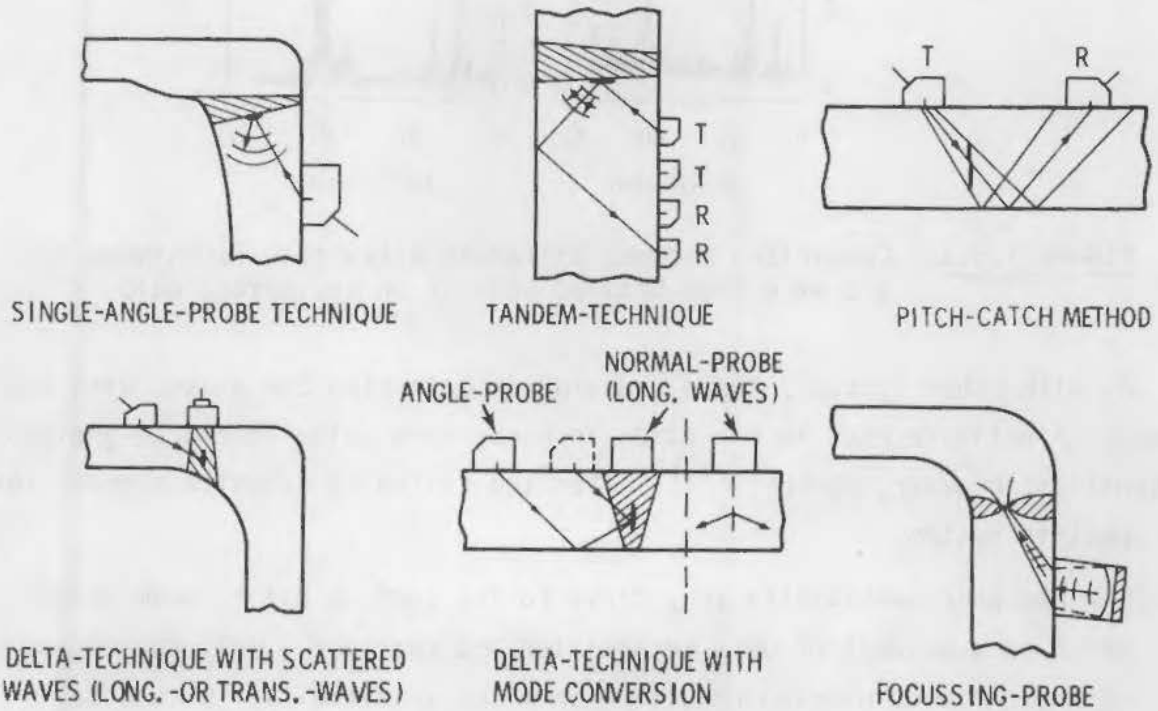

FIGURE 7.5.2. Methods of Ultrasonic Testing for Internal Defects

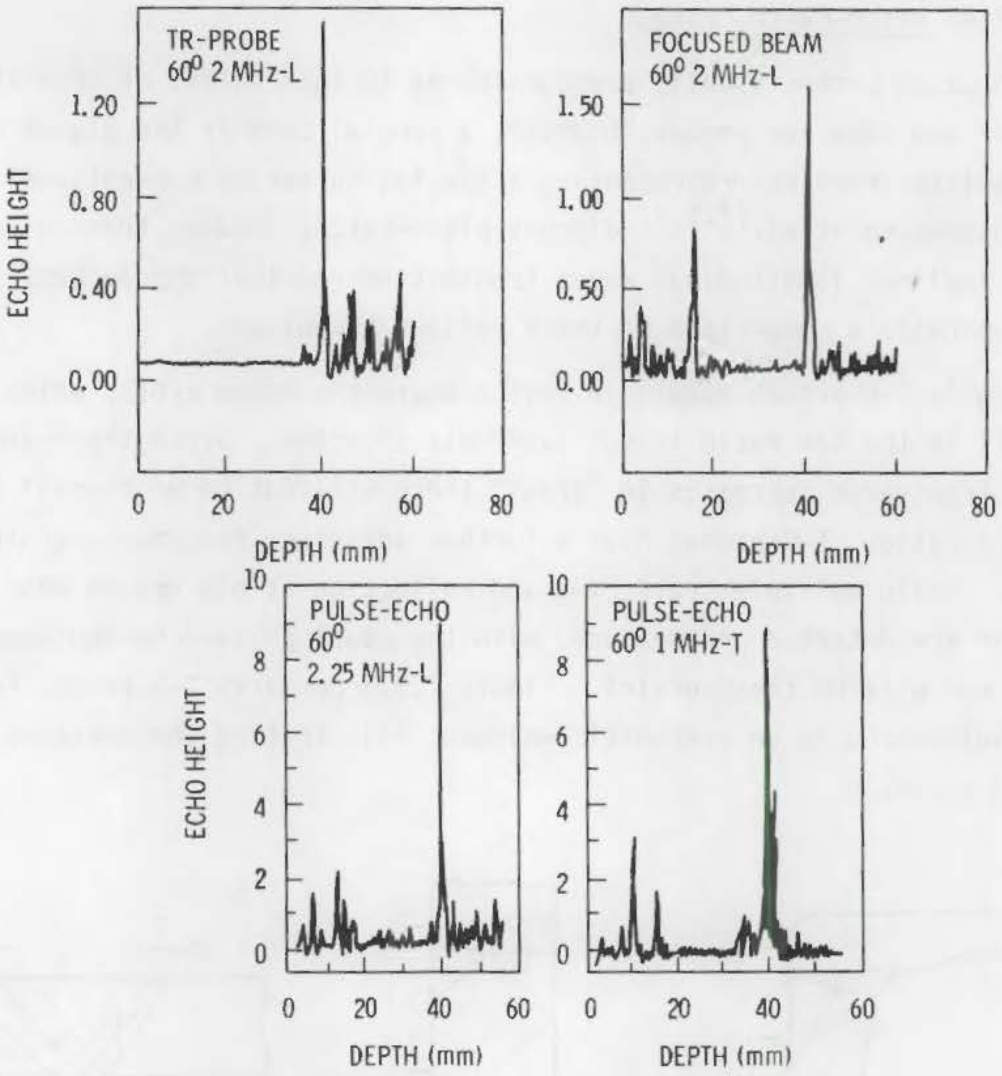

FIGURE 7.5.3. Comparison Between Different Ultrasonic Techniques for a 3-mm ϕ Side-Drilled Hole in an Austenitic Weld

As with other systems, there are minuses balancing the pluses with T-R probes. A definite plus is reduction in background noise in coarse-grained austenitics; however, Bowker(7.5.8) cites the following definite minuses for the specific system:

- T-R has poor sensitivity very close to the surface due to beam shape which is a product of both transmitter and receiver. Only the edges of their fields overlap resulting in a low sensitivity. Of course, single-probes are poor in this region too.

- T-R probes are poorer than single-probes at longer ranges; one reason is that in T-R probes pulse length increases away from the beam axis which is exaggerated in T-R probes.
- At all ranges, single-probes are more sensitive than T-R probes. While toe-in improves T-R probe sensitivity, it leads to higher side lobes yielding forked beams at the longer ranges.
- T-R probes usually are better on rough surfaces because the plastic mount has lower acoustic impedance and accommodates itself to the surface. Single-probes typically are hard-faced so coupling is poor.
- With curved pieces (e.g., piping) where the probe must be contoured to the surface, internal echoes improve single-probe short range performance.
- Flaw orientation is a factor; for example, with T-R probes defects parallel to the beam are more detectable than those normal to the beam.

Licht and Hallett[7.5.9] discuss the pitch-catch technique generally. Figure 7.5.4 illustrates the shadow techniques to assist in locating a flaw. The authors have used this technique to monitor fatigue crack growth. The tandem technique represents a special case of pitch-catch. Tandem is required for reactor pressure vessel examinations in Germany on the basis of its greater reliability in detecting flaws normal to the surface.

7.5.3.5 Phased Arrays

Phased arrays represent a special case, covering pitch-catch, focused, etc. Discussion will be deferred to 7.6 where the application is more obvious.

7.5.3.6 Controlled Signals

Controlled signals (CS) incorporate the short-pulse characteristics, and have been recommended for use in austenitics as noted in Table 7.5.2. They performed relatively poorly on small defects. This was attributed to the manner of producing the CS which resulted in an increase in pulse duration concommitant with the generation of a narrow-band pulse. Another factor is that

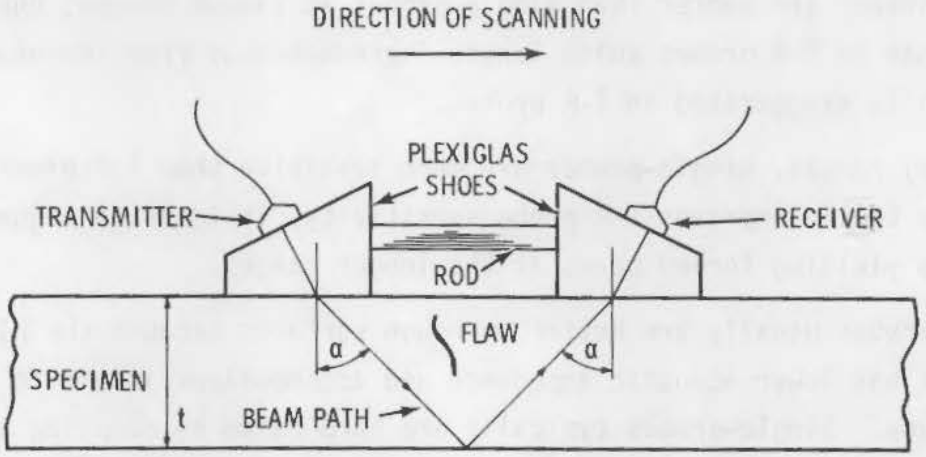

A TYPICAL ARRANGEMENT FOR OBTAINING THE SHADOW PROFILE OF A FLAW IN A PLATE

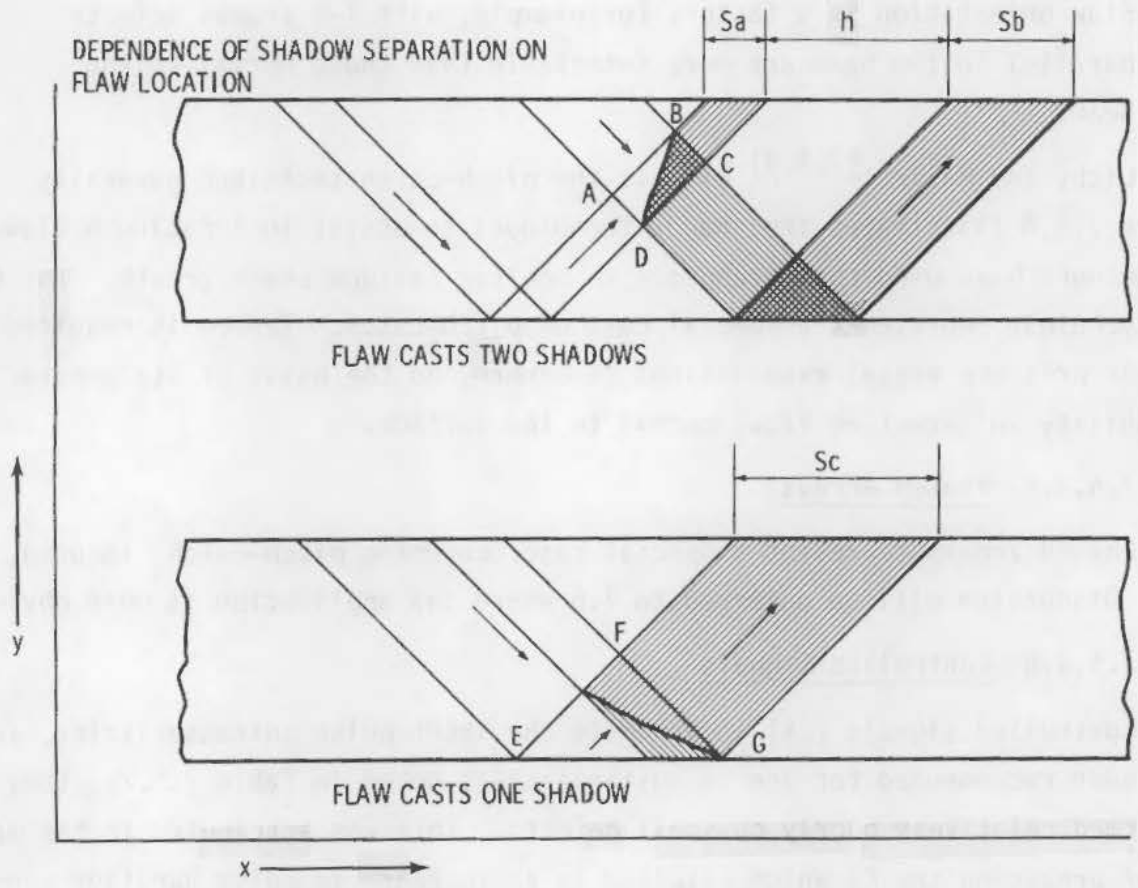

FIGURE 7.5.4. Pitch-Catch Shadow Technique

coarse-grained materials act as a "stop-band" filter essentially removing some frequencies. The optimum frequency for detection of one flaw could be substantially different for another.

7.5.3.7 Spatial Averaging

Signal and spatial averaging have not been successful for flaws comparable in size to grain diameter since the signal is buried in the noise. However, signal averaging, of which spatial averaging is one form, has been quite successful for other cases; e.g., $d_R > d_G$. A paper by Kraus and Goebbels[7.5.10] describes the various signal averaging techniques. In essence, averaging attempts to vary the interference resulting from grains and grain boundaries while keeping the flaw signal constant as a first approximation. The pros and cons of the averaging techniques follow:

- Spatial averaging is based on limited probe movement ($\leq$0.3 mm $\cong$ ASTM G.S. 1) which changes the scattering signal without changing the reflector signal providing $d_R >> d_G$.
- Directional averaging occurs when the angle of incidence is changed slightly (~1°), leading to a change in scattering volume and improved SNR.
- Frequency averaging results when the pulse frequency is changed electronically for fixed probe and angle positions. This can be done with broad-based transducers excited with short pulses. Change of ~0.1 MHz will change the signal drastically.
- Analog and digital averaging are the two processes for signal handling. While digital requires more sophisticated electronics, it is preferred to analog because of the sensitivity of analog to coupling variability which biases the signals. Digital sums effects in the scans and coupling so that coupling will have a general not a local effect.
- High-frequency signals may be used or they can be rectified. With rectified signals, all those above zero are averaged while both positive and negative signals are averaged in the high frequency

case yielding a signal going to zero on averaging. While the high frequency case yields a better SNR, it only applies at limited phase shifts of the reflector signal (~0.1 λ). For greater shifts reflector amplitudes also go to zero. Therefore, taking this factor plus the affects of specimen surfaces into account, rectified signals are preferred.

- Linear or exponential averaging are options. With slower averaging processes, exponential averaging may be the choice; each A-scan is given a varying weighting factor which is an advantage with linear movement. With fast equipment a straightforward averaging of all data occurs which is the preferable approach.

7.6 EQUIPMENT FOR DETECTING AND SIZING UNDERCLAD CRACKS

Pressurized water reactors (PWRs) in most countries are nondestructively examined inservice from the inside because of lack of access to the outer surface. This discussion will assume single-sided access which represents a more limiting case than examination from both surfaces. Factors adversely influencing detection of cracks immediately below the cladding include the following:

- surface roughness or waviness of cladding, particularly with contact probes.
- coarse-grained dendritic structure of cladding causing beam attenuation, skewing or bending.
- relatively rough austenitic clad-ferritic vessel interface increasing the background noise.
- location of hypothetical (or real) cracks immediately below or even slightly in the cladding; this near-surface region is a "dead zone" for many UT techniques.
- choice of technique.

7.6.1 Rayleigh Waves

The pros and cons of using Rayleigh waves to detect and size cracks below cladding was discussed in Chapter 5. Hudgell[5.5.5] discussed three approaches: 1) transmission around a defect; 2) mode conversion at the defect; and 3) acoustic spectroscopy. All are sensitive to surface finish, something that will vary widely from PWR to PWR, particularly in older plants. The fact that the cracks are not surface-breaking and are expected to be quite tight virtually eliminate a traditional Rayleigh approach. Changes in frequency might be beneficial; however, surface and interface roughness represent limitations. Since other techniques discussed in this section are state of the art without suffering from these limitations, Rayleigh waves will be designated as not practical at this time.

7.6.2 Focused Probes

The use of focused probes has been discussed in sections 6.2.3 and 7.5.3.3. The technique has been used extensively in France on PWRs including specific applications to the detection of underclad cracks. Optimizing probe design for the region immediately below the cladding is state of the art; a combination of probe angles would be preferable to enhance the probability of detection of cracks in the clad zone.

Computer storage of the examination data probably would be necessary to permit completion of the examination in a reasonable time with analyses deferred. Typically, everything above background is analyzed, which means that a "dirty" steel could pose substantial problems. This occurred in the PISC-I exercise where the sheer number of signal emitters tended to overwhelm the electronics.

Immersion probes are less sensitive to surface variability than contact probes so they may be the preferred choice in some PWR vessels. Immersion focused probes are considered to be an excellent option for detection and sizing of underclad cracks.

7.6.3 Inclined Longitudinal- or Shear-Wave Probes

Underclad cracks have been detected successfully using 70° longitudinal-wave transmitter-receiver (T-R) probes.[7.6.1] While the technique was used manually, it could be modified for automatic application. This technique as well as immersion focused probes, was used in France to detect the cold cracks occurring in steam generator tube sheets or PWR nozzles. These clad cracks usually were oriented normal to the clad/base-metal interface.

Two T-R probes were selected:

- BAM SE 70 L2 150
- Sonatest SE 2.25 MHz T-R; 26° in a shoe.

Both were optimized for a depth of 8 to 10 mm. A two-stage process was used consisting of using these probes to detect anything at or less than the cladding thickness, and then using a KK 0° SEB 4 KF 8 probe set at 50% reference level to confirm the indications, including those at d > cladding thickness.

Detection from a smooth surface was very good--defects 0.7-mm deep by 5-mm long were detectable. Supposedly, extensive statistics exist confirming the detection reliability; however, these statistics are not in the public domain at this time (early 1982).

Discussions in section 7.5 relevant to short-pulse shear waves[7.5.3] would indicate that they might be a viable option to 70° longitudinal waves; however, there appear to be no conclusive experiments establishing the reliability of high-angle shear waves for the detection of underclad cracks.

A special class of T-R's is the multiple-beam technique discussed by Gruber.[7.5.2] This technique has been applied to the specific case of underclad cracks in thick steel sections and was successful in a limited test. Since the technique can be optimized for angle, frequency, and wave form, its success isn't too surprising.

Another approach that is not state of the art appears to have potential both for detecting underclad cracks and for examining cast austenitic sections. Horizontal shear waves were discussed at some length in Chapter 13 where their advantages over both vertically polarized shear waves and longitudinal waves were cited. The problem has been in their generation. Recently, electromagnetic acoustic transducers (EMATS) have been developed to the point that their general applicability can be examined. A study by Fortunko and Lawrence[7.6.2] cited some pluses for their use:

- specular reflection from planes containing the direction of particle displacement
- generation in any direction lying in the suggested plane with equal efficiency
- inherent discrimination against Rayleigh, longitudinal and shear waves
- absence of mode conversion.

Since they are a noncontact system, surface roughness is less significant; they can be used either in the pitch-catch or pulse-echo mode and both frequency and beam angle are variable over a substantial range.

The direct application of EMATS to the underclad cracking problem has not been reported; at least no source is known; therefore, its potential awaits future studies.

7.6.4 Crack-Tip Diffraction Techniques

The crack-tip diffraction technique has been discussed in Chapter 6.[6.2.13, 6.2.14, 6.3.1] Golan's[6.2.13] paper cites some inherent problems with crack-tip diffraction that are particularly applicable to examination through cladding for cracks at the interface. Factors influencing S/N ratio adversely, include crack closure, grain boundaries, grain size, macro inclusions, etc. One directly relevant is the problem of front surface resolution. The resolution is limited by the index of the transducer defined as the distance between the exit point of the central beam and the edge of the transducer. The smaller the index, the smaller is the undetectable depth or "dead zone"; however, below a certain index size, a strong surface beam will be scattered from the edge of the wedge, leading to a deterioration of front surface resolution. For a layer of 5 to 10 mm the wedge angle should be selected to avoid propagation of surface longitudinal waves which mask the diffracted signal. Resolution in this zone can be improved by using shear-shear waves rather than longitudinal-longitudinal waves. For example, 2.5-mm deep slits were sized to an accuracy of 15% with S-S waves.

The preceding comments relate to the zone immediately below the surface; however, the effects of cladding on the reliability of this technique is not known. While it may have potential, the creeping wave procedure discussed next has been applied to detection of underclad cracks with considerable success making further evaluations of crack-tip diffraction somewhat marginal.

7.6.5 Creeping Longitudinal Waves

Wüstenberg et al.[7.6.3] reviewed the various UT techniques available to detect defects in the near-surface region. These techniques are contained in Table 7.6.1. Most of the techniques cited have been discussed in sections 7.5 and 7.6 or will be discussed in 7.7. Emphasis is given to longitudinal creeping waves for the detection of cracks. Other techniques discussed in section 7.7 could be used for sizing. Unlike Rayleigh waves, creeping longitudinal

TABLE 7.6.1. Near-Surface Inspection by Ultrasound

	Detection	Analysis (e.g., crack depth)
Physical Phenomenon	Bulkwaves (corner effect, crack-tip diffraction)	Spectrum of delaytime
		Crack-tip diffraction
	Guided waves (Rayleigh, creeping L-waves, S.H.)	Shadowing by cracks
		Imaging
Special Techniques	Focused sound fields	Frequency Analysis
	TR-probes	Holography
		Focused fields
Practical Limitations	Surface conditions	
	Waviness, Roughness, Cladding, Access	
	Coarse grained materials	
	Geometry	

waves (and shear horizontal waves) only excite tangential movement at the surface rendering them less susceptible to surface roughness.

Detection of cracks either in the cladding or in the clad/base metal interfacial region are influenced by interface noise and dendritic structure. The creeping wave can examine the surface region and be optimized for the interface region according to the authors.[7.6.3] Unfortunately, no definitive data appear to exist on the reliability of detection of underclad cracks with creeping waves. They have been validated on slits, etc.

Figure 7.6.1 illustrates the near-field and far-field patterns for creeping waves. A definite limitation is the relatively short distance between probe and crack permissible for detection because of the rapid decay of signal noted in Figure 7.6.1. An unknown is the effect of cladding thickness on detectability of underclad cracks.

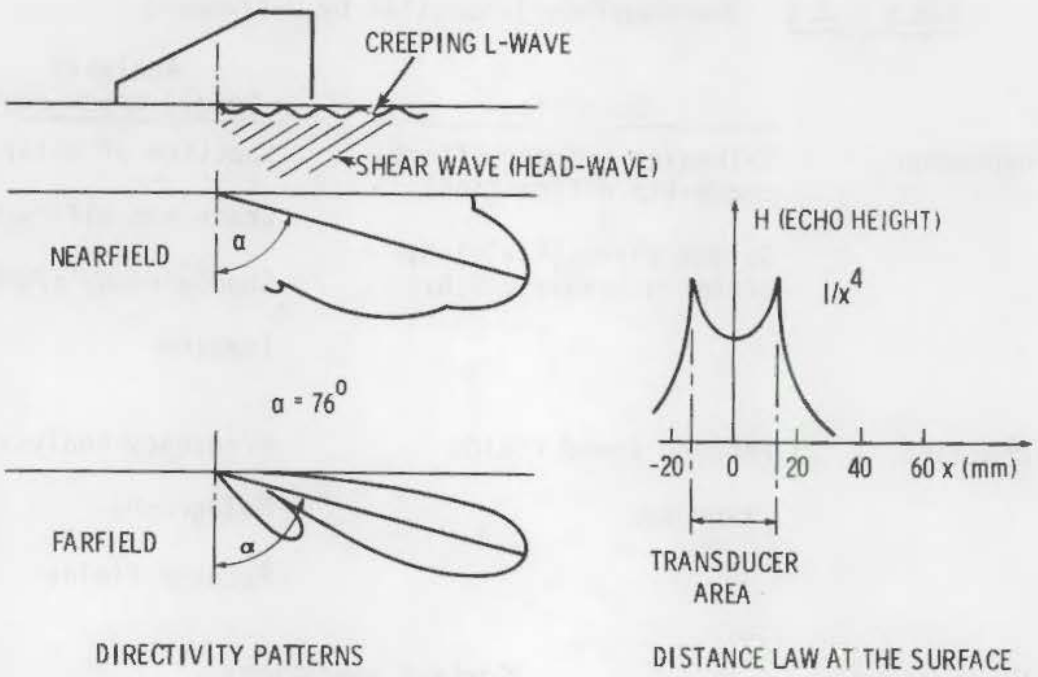

FIGURE 7.6.1. Directivity Pattern and Distance Law for Creeping-Wave Probes

Both wedge angle and transducer size are parameters influencing creeping-wave signal amplitude. For example, Figure 7.6.2 covers two cases. An increase in transducer diameter increases creeping-wave amplitude. The wedge angle is optimized for total reflection of the longitudinal wave.

Some idea of the ability of creeping waves to detect inclined surface defects is given in Figure 7.6.3 for 1.5- and 2.5-mm deep cracks. As noted, the 1.5-mm crack at angles as great as ±20° is still detectable at S/N ratios near 20 dB.

While creeping waves appear to be a powerful tool for underclad cracks, experiments specific to the problem are needed to confirm their use.

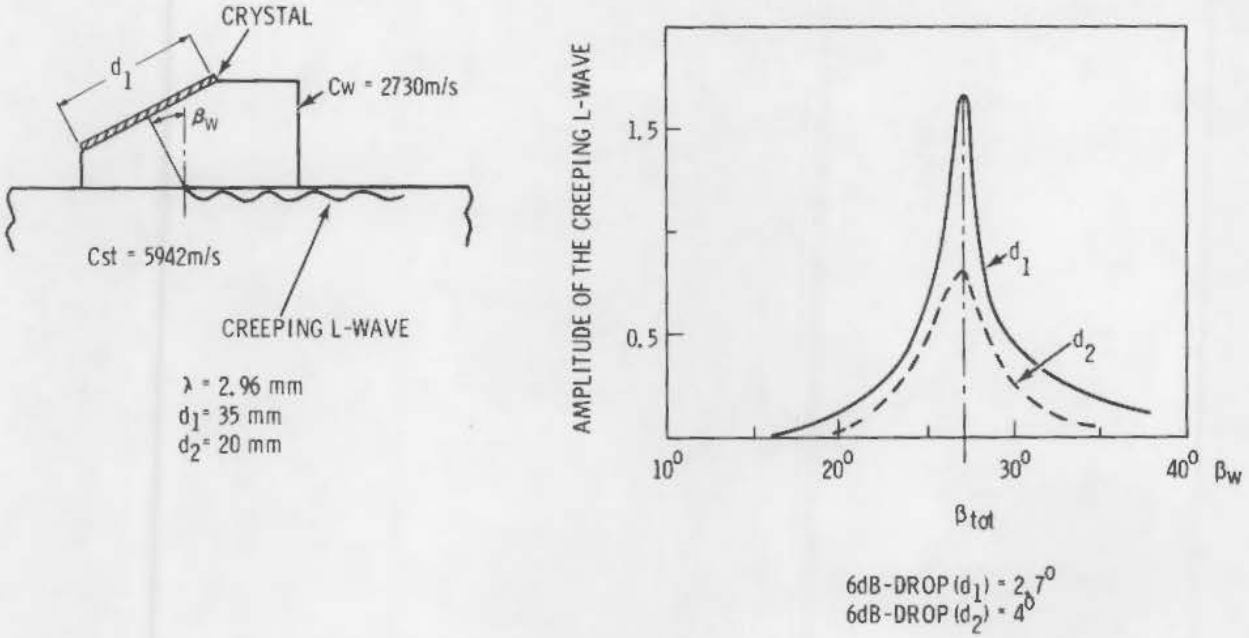

FIGURE 7.6.2. Influence of Wedge Angle and Transducer Size of the Creeping-Wave Amplitude

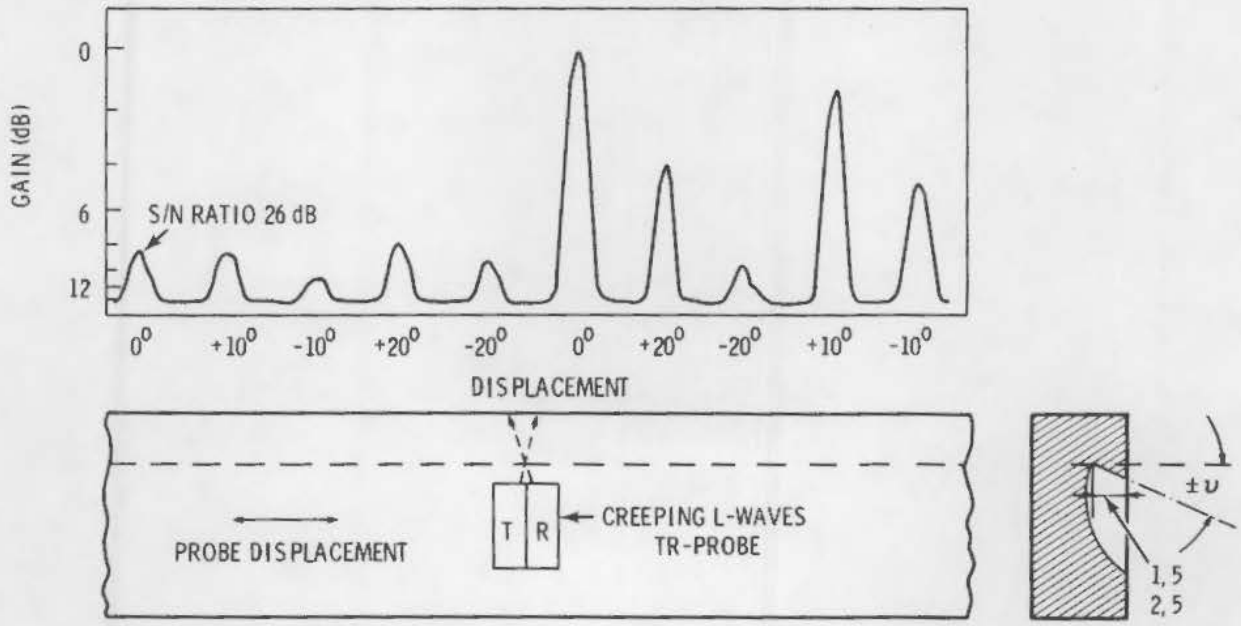

FIGURE 7.6.3. Echodynamic of Inclined Surface Defects

7.7 EQUIPMENT FOR SIZING AND LOCATING DEFECTS

While some systems are equally capable of detecting, sizing and locating defects, only a very few can be applied to a variety of materials to detect flaws in the near-, far- and mid-surface ranges. If the economics of large-scale examination are considered, the options are further limited. Probably, only focused probes meet these criteria for reactor vessels and no system is believed to meet all requirements for austenitic piping.

Possible choices include acoustic holography, SAFT-UT, focused probes, shadow techniques utilizing pitch-catch probes, and crack-tip scattering or diffraction as a special case of pitch-catch.

Wüstenberg et al.[7.6.3] discusses the accuracy of various sizing techniques. Figure 7.7.1 illustrates the relative accuracy over a range of thickness for holographic single and tandem probes and focused tandem probes.

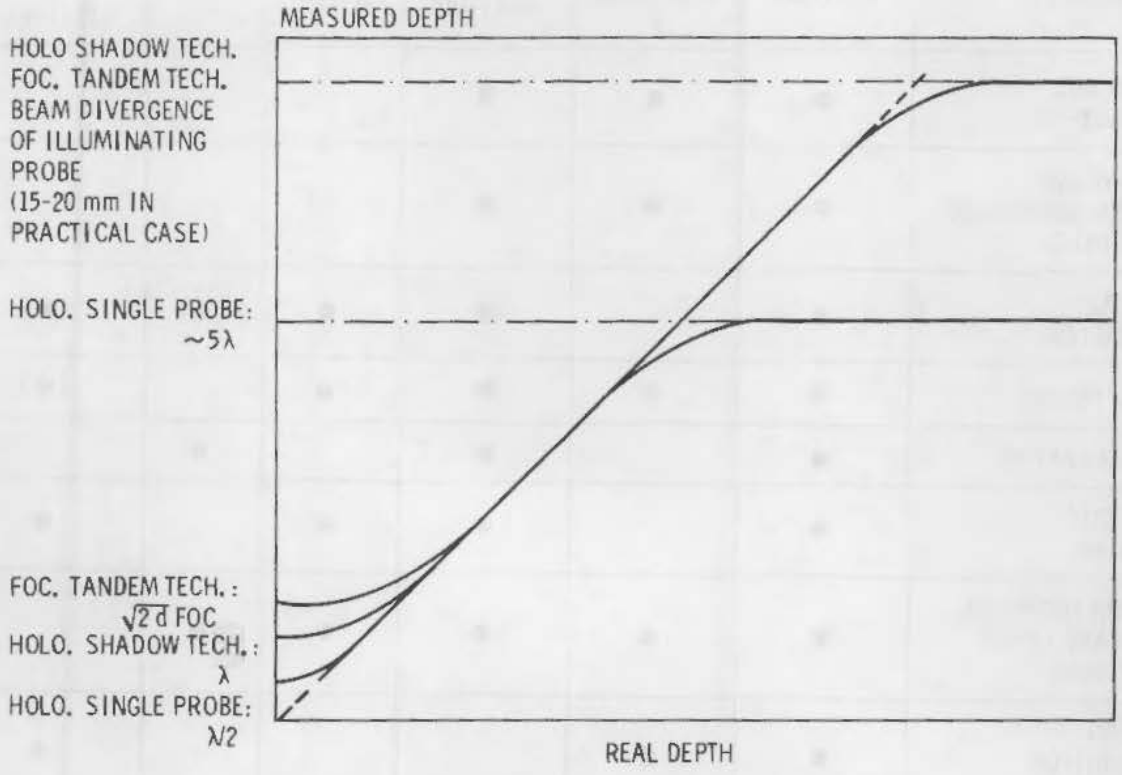

FIGURE 7.7.1. Accuracy of Imaging Techniques

Figure 7.7.1 is valid for cracks with different orientations providing shadow techniques are applied. Otherwise, there is a definite loss in accuracy of sizing.

Wüstenberg and Erhard[7.7.1] provided an excellent overview of various techniques used in detection and sizing. Table 7.7.1 provides a comparison of the various parameters determined by each UT technique. Included are such parameters as probe position, beam direction, echo amplitude, time-of-flight, phase and pulse shape or spectrum.

Figure 7.7.2 complements Figure 7.7.1 by illustrating the range over which imaging techniques are valuable. Very small defects may be sized using DAC or DGS; large defects can be handled by procedures based on dB drop when sizing

TABLE 7.7.1. Sources of Information for Evaluating UT Indications

TECHNIQUES	PROBE POSITION	BEAM DIRECTION z	ECHO AMPLITUDE	TIME OF FLIGHT	PHASE	PULSE SHAPE OF SPECIMEN
DAC OR DGS (AVG) METHOD	●	●	●			
ECHODYNAMIC PATTERN (HALF VALUE AND OTHERS)	●	●	●			
COMBINED EVALUATION	●		●	●	(●)	(●)
FOCUS-PROBES	●	●	●	(●)		(●)
AC HOLOGRAPHY	●		●		●	
SYNTHETIC APERTURE	●		●	●		●
SHADOW TECHNIQUE PITCH AND CATCH SCATTERING	●	●	●	●	●	
PATTERN RECOGNITION (ALN etc.)	●	●				●

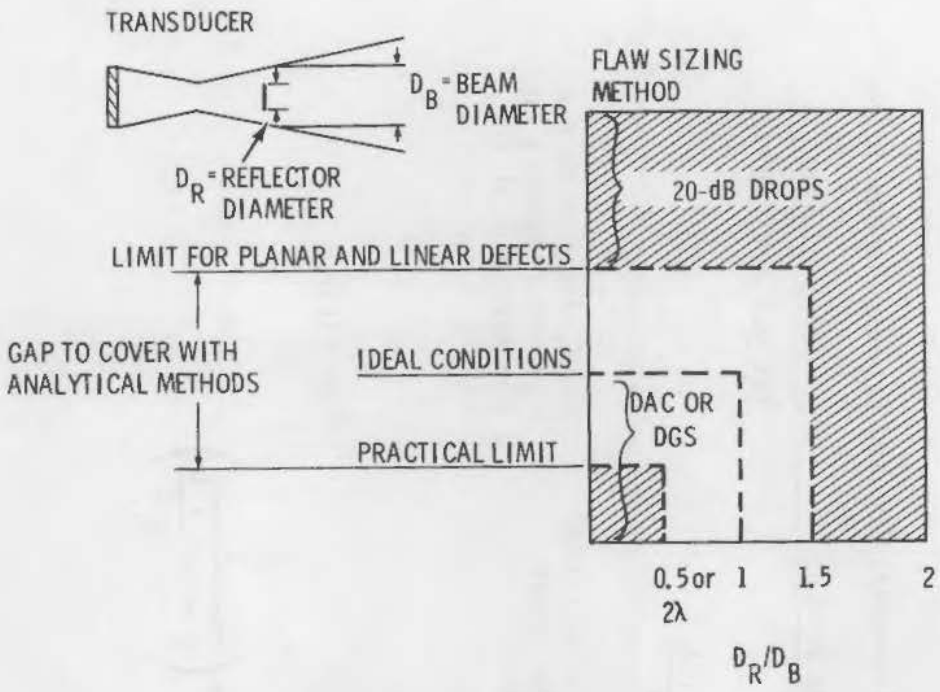

FIGURE 7.7.2. Range of Applicability for Conventional Ultrasonic Flaw Sizing Methods

errors represent a small fraction of the overall size. In the fracture mechanics context the unhatched zone of Figure 7.7.2 represents the region of major concern.

Mundry et al.[7.7.2] critically compared ultrasonic pulse spectroscopy, acoustic holography and focused probes. Deconvolution techniques for NDE such as applied to phase spectrum data derived from acoustic spectroscopy and holography were in their infancy at the time of the paper. Table 7.7.2 presents the inherent limitations of the three techniques in terms of lateral and longitudinal resolution and usable depth range.

7.7.1 Acoustic Holography

Depending on the smoothness or roughness of flaw surfaces, the UT signal may be more specular than diffuse so resolution will be fair. A basis of comparison would be UT C-scan, with holography having better resolution. Longitudinal resolution is very poor; however, some improvement is possible with shorter pulses. Lateral resolution is about 2.5 mm. These latter characteristics are defined more quantitatively in Table 7.7.2. As noted in Figure 7.7.1,

TABLE 7.7.2. Comparison of Analyzing Performances: Holography, Focused Probes, Deconvolution

Parameter	Holography	Focusing Probes	Deconvolution
Lateral Resolution:			Not yet defined
$\Delta L_{x_{min}}$	$\frac{\lambda \cdot b}{L}$	$\frac{\lambda \cdot b}{D_o}$	
Longitudinal Resolution:		If required, travel time can be used for depth discrimination	Good, depends on the maximum frequency in the spectrum of the signal
I_z	$>8\,\lambda \cdot \left(\frac{b}{L}\right)^2 \cdot \left(\frac{1}{1 + 2\,\frac{\lambda \cdot b}{L^2}}\right)$		
Usuable depth range			Far field
	Not yet defined	$<8\,\lambda \cdot \left(\frac{b}{D_o}\right)^2 \cdot \left(\frac{1}{1 + 2\,\frac{\lambda \cdot b}{D_o^2}}\right)$	

single-probe holography has inherent limitations in resolution of defects at ~5 λ. Figure 7.7.2 compares holography in the single-scanning probe with both scanning and illuminating probes in the shadow technique. In addition, the tandem focused-probe technique is illustrated.

Acoustic holography offers a promising approach for flaw sizing. The poor resolution along the beam represents a limitation since that is a critical dimension in flaw sizing for fracture mechanics. There is a more extensive discussion of acoustic holography in Chapter 6.

7.7.2 Focused Probes

Focused probes have been discussed extensively in Chapter 6 and elsewhere in Chapter 7. They represent a complex system requiring computer storage. They have been used extensively in the laboratory and in the field in France with considerable success. A decision to use focused probes for inservice inspections of pressure vessels would be a substantial one for an organization unfamiliar with their use. They can yield excellent results for fully automated examinations; however, the implications of access, cleanliness or dirtiness of the steel, etc., all would require consideration.

The systems can be considered to be state of the art, albeit quite sophisticated. Attention is necessary to establish a family of the ranges of focused probes to ensure coverage through the wall. An alternate approach might be to optimize focused probes for the near- and far-surface regions and depend on conventional probes to cover the central 50 to 70% of the wall.

7.7.3 Synthetic Aperture Focusing Technique (SAFT-UT)

SAFT-UT requires a very sophisticated computer system to analyze the flaw data. To date this has meant the procedure was quite slow. The procedure is discussed in more detail in Section 6.6.3. Current efforts are to increase scanning speed, hopefully by at least an order of magnitude. In contrast to acoustic holography, SAFT-UT has simultaneous high lateral and longitudinal resolution (~1 λ). The following are other characteristics:

- high signal-to-noise ratio
- wide beam-width insonification (multi-angle)

- wide bandwidth insonification (multi-frequency)
- inherently quantitative and volumetric.

While SAFT-UT has obvious advantages, it requires further field development. It is not the type of a unit one would take into a nuclear reactor; at least in the current form.

7.7.4 The Amplitude-Locus-Time (ALOK) Technique

ALOK is derived from Amplituden und Laufzeit Ortskurven. It was developed for use in the NDE of reactor pressure vessels. The principles of ALOK are given in Figure 7.7.3. Data are collected from pulse-echo, or tandem, at various angles (0, 45, 60, etc.) and transit-time locus or amplitude locus curves are generated. The basic aim is to minimize noise, thus enhancing the S/N ratio, plus reconstructing and characterizing flaws through analyses of the transit-time data. In essence, ALOK does the following:

- eliminates noise by forming transit-time locus curves
- permits reconstruction of flaw position and boundary
- classifies flaws as planar or volumetric.

While the ALOK is appealing, it would be desirable to see more quantitative data. Basically, one is analyzing amplitude data and this leads one to question the absolute accuracy of sizing planar flaws at various orientations. In essence the jury is still out.

7.7.5 Phased Arrays

Phased arrays represent an option providing more flexibility than simple pulse-echo techniques. Basically, phased arrays provide three basic functions:

- electronic beam steering
- variable focusing
- side-lobe suppression.

Table 7.7.3 permits a comparison of some of the characteristics of linear, annular and planar arrays. In essence, they can act as conventional pulse-echo or as focused probes. In some cases, they can combine the advantages of opposing techniques without their disadvantages. For example, Gebhardt et al.[7.7.6a, 7.7.6b] discuss sector scans where the high detectability of a broad beam can be combined with the high resolution of a narrow or focused beam

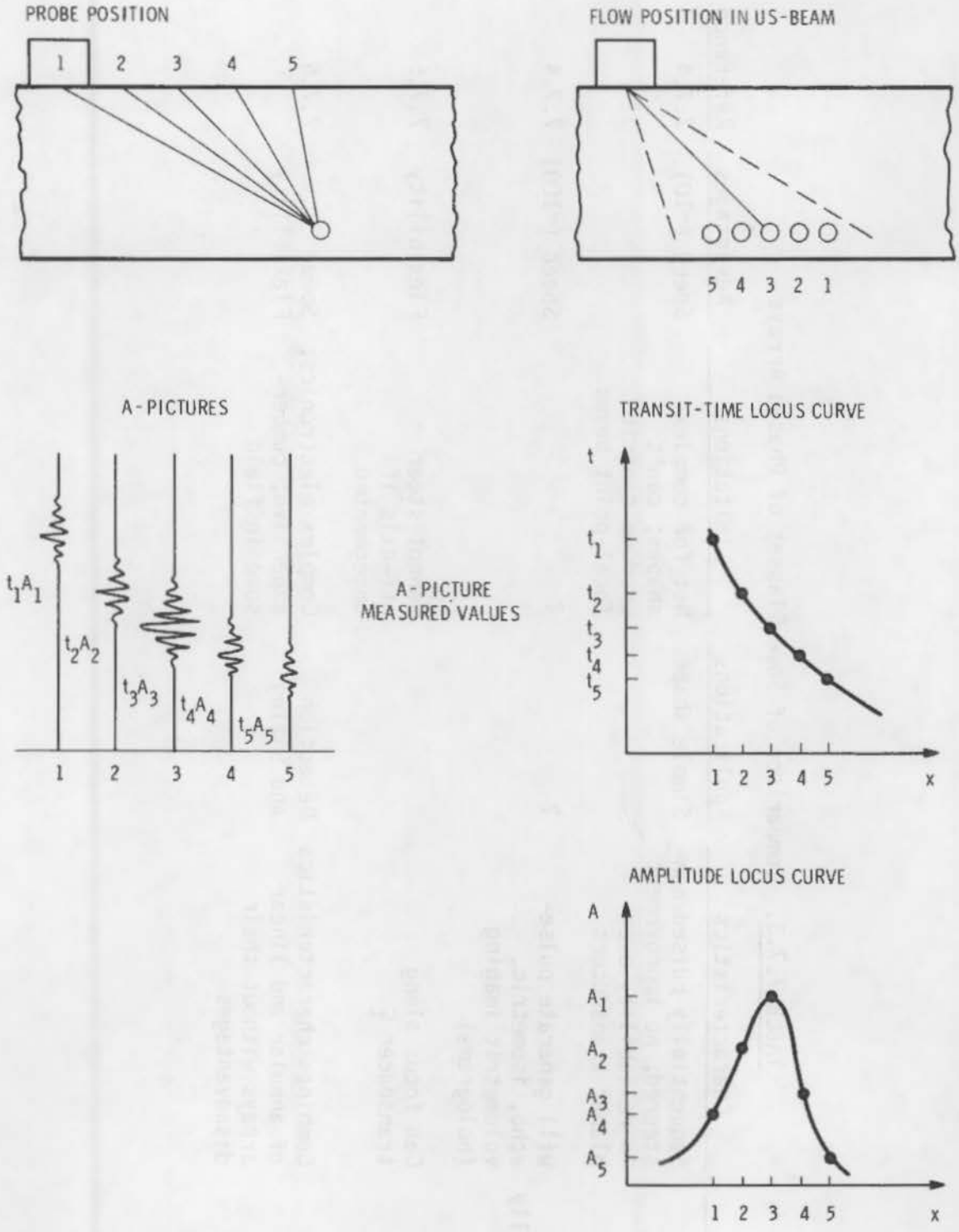

FIGURE 7.7.3. Principles of ALOK--Data Acquisition and Signal Locus Curves (Amplitudenund Laufzeit-Ortskurven).

TABLE 7.7.3. Comparison of Some Classes of Phased Arrays

Class	Characteristics	Applications	Limitations	Advantages	Reference
Linear	Sequentially pulsed non-steered; no improvement in reliability over planar transducers	Simple shapes	Not for complex shapes; can't produce dynamic focal-point beams	Speed (~10)	7.7.4
Linear (Sequentially Pulsed)	Will generate pulse-echo, isometric, volumetric imaging (holograms)	?	?	Speed (~100)	7.7.4
Annular	Can focus along transducer ℄		Cannot steer off-axis if unsegmented	Flexibility	7.7.5
Planar	Combines characteristics of annular and linear arrays without their disadvantages	Detection and Sizing	Complex electronics; expensive; cumber-some in field	Speed Flexibility	7.7.5

without the disadvantages inherent in each; namely, low resolution in broad beams and low detectability in narrow beams. Sector beams can sweep across a region while retaining the characteristics of a narrow beam.

Another option[7.7.6b] is the compound scan where linear probe movement plus sector scanning yields three options:

- sector display which has the possibility of distinguishing between volumetric and planar defects on the basis of amplitude and angle
- compound scan amplitude curves (VAOK) which relate maximum amplitude to probe position, thus eliminating probe characteristics and defining flaw orientation
- superposition of sector display on a storage display (VSB), permitting a comparison of data at several locations and angles to allow an integrated evaluation of defects.

A combination of array, together with the manipulation of the data through sector display or compound scanning, should lead to increased detection with the possibility of determining flaw size and orientation. In the more sophisticated arrays most other UT techniques can be duplicated.

7.7.6 Crack-Tip Diffraction

Crack-tip diffraction has been discussed by Silk[6.12.14] and by Golan.[6.2.13] Chapter 6 has a discussion relevant to the applications, and Chapter 7 discusses pros and cons of the technique. Gruber[6.3.1] in Chapter 6 discusses the Satellite Pulse Technique which represents a special case of crack-tip diffraction. Since time delay can be measured with a high degree of accuracy, it represents a fairly accurate method of crack sizing, providing the signal is detectable. In certain applications, crack-tip diffraction represents a viable option being simple and reproducible. However, it has limitations if there is a residual compressive stress field in the region of the crack.

7.7.7 A Combined Imaging System

Schmitz et al.[7.7.7] reviewed the requirements with regard to flaw detection, sizing, location and orientation in the context of a fracture

mechanics analysis of a structure. They reviewed various sizing techniques. In essence they are divided into two phases for NDE. Phase one relates to the detection of flaws with some form of conventional UT, possibly supplemented with techniques such as ALOK. Phase two consists of sizing by the most appropriate imaging technique.

Their approach was the development of a very flexible system permitting the use of T-R probes, either planar or focused, or linear array operating in a rectangular coordinate system. Once a defect is detected it can be evaluated holographically or signals can be processed to generate amplitude-locus curves. Another option is to conduct acoustic spectroscopy, permitting analyses in both the time and frequency domains.

As a concept the approach is attractive. It appears to have sufficient flexibility to permit selection of the optimum technique for sizing once a flaw is detected. However, more work is required to establish whether there are inherent limitations in the technique.

7.8 CONCLUSIONS AND RECOMMENDATIONS

Several of the techniques described in this chapter appear to have the capability of detecting flaws with acceptable reliability under general or specific situations, such as in a given geometry and material, or in a specific location such as under a cladding. Once detected there appear to be options for sizing and locating flaws either generally or specifically. Unfortunately, no single technique appears to provide all the answers. Perhaps the closest for the reactor pressure vessel case is a focused probe system optimized for the specific geometry.

Table 7.8.1 is an attempt to provide a comparison of the strengths and weaknesses of the various sizing techniques. Most of the parameters were taken from the paper by Schmitz et al.[7.7.7] Unfortunately, many of the answers are highly subjective and subject to disagreement. If considered in a comparative sense, the table permits an assessment of the stong and weak points of the various techniques. In that context it may prove valuable. At this time focused probes and acoustic holography are viable options. Phased arrays in time should be able to duplicate both and take less time. Deconvolution of phase and spectral data has the potential for providing the most accurate information; however, it requires more development, as does SAFT-UT.

Both ALOK and pattern recognition techniques are sensitive to signals and signal recognition. Both use amplitude as a major parameter.

TABLE 7.8.1. Comparison of the Ability of Various Sizing Techniques to Accurately Size Defects, Based on Meeting Certain Parameters

Parameter	Acoustic Holography		Focused Probe			Phased Arrays			Pattern Recognition	Crazy Tip Diffraction	Acoustic Spectroscopy
	Single Probe	Dual Probe	Dual	ALOK	SAFT-UT	Linear	Circular	3-D		e.g., Satellite Pulse	Deconvolution
Reliability of Method	Fair	Fair	Fair-Good	?	Fair-Good	Fair-Poor	Fair-Poor	Good	Fair	Fair-Good	Fair
Ability to Recognize Form Echoes	Poor	Fair	Good	Good	Good	Poor	Poor	Good	Fair-Good	No	?
Lateral Resolution	Good (~2.5 mm)	Good	Good	?	Good	Fair	Fair	Good	Fair	Good	Good
Axial Resolution	Poor	Poor	Good	?	Good	Poor	Good	Good	Poor	Good	Good
Classification Volumetric Versus Planar Defects	Poor	Fair	Good	Fair-Good	Good	Fair	Good	Good	Fair-Good	No	Good
Correct Sizing	Fair-Poor	Fair-Good	~1 λ	?	Good	Poor	Good	Good	Poor	Good to ~1 mm*	Good
Correct Orientation	Poor	Fair	Fair-Good	Fair	Good	Poor	Fair	Good	Poor	Fair	?
Comments	Inherent Limitations in Wave Length re Sizing	Provides Viable Approaches to Sizing	Accurate Sizing Requires Correcting for Beam Diameter	?	Requires Very Sophisti-cated Computer Setup	Essentially Pulse-Echo	Similar to Focused Probe	Very Flexible	Good for Repetitive Defects, Uncertain for Non-Reproducible Defects	Stress Field Can Adversely Affect Reliability and Sizing	Assumes Accurate Handling of Deconvolution to Achieve Answers
Application Through Cladding for Near-Surface Cracks	?	?	Good	?	?	Poor	Good	Good	Poor	?	?
Application to Cast Stainless Steel and SS Weldments	?	?	Fair-Good	Poor	?	Poor	Fair	Good	Poor	Poor	?

7.9 REFERENCES

7.2.1 Mundry, E. and Wüstenberg, H., "Criteria for Optimization of Ultrasonic Inspection Systems for Defect Detection and Defect Evaluation." Specialists Meeting on the Ultrasonic Inspection of Reactor Components, Committee on the Safety of Nuclear Installations of OECD Nuclear Energy Agency, Risley, England, September 27-29, 1976.

7.2.2 Wüstenberg, H, Erhard, A. and Engl, G., "Improved Ultrasonic Flaw Detection and Analyses Techniques for Inservice Inspections of Pressure Vessels." Paper C 33/79, Conference on Periodic Inspection for Pressurized Components, Institute of Mechanical Engineers, London, England, pp. 99-104, May 8-10, 1979.

7.3.1 Caussin, P. and Verspeelt, D., "Influence of the Characteristics of the Equipment on the Efficiency and the Reproducibility of the Ultrasonic Testing Technique." Proceedings of 4th International Conference on NDE in the Nuclear Industry, Fachinformationszentrum Energie, Physik, Mathematik, Lindau, Germany, pp. 399-408, May 1981.

7.3.2 Bredael, I., "Characterization of Ultrasonic Transducers," Chapter 5 of Research Techniques in Non-Destructive Testing, Vol. III. R. S. Sharpe, ed., Academic Press, London, England, 1977.

7.3.3 Sachse, W. and Hsu, H. H., "Ultrasonic Transducers for Materials Testing and Their Characterization." Presented at the 1st International Symposium on Ultrasonic Materials Characterization, June 7-9, 1978.

7.3.4 Dijkstra, F. H., "Characterization of Probes Used for Periodic Inspection," Ultrasonic Materials Characterization. NBS SP-596, H. Berger and M. Linzer, eds., Proceedings of 1st International Symposium on Ultrasonic Materials Characterization, National Bureau of Standards, U.S. Government Printing Office, Washington, D.C., pp. 605-615, November 1980.

7.3.5 Birks, A. S. and Lawrie, W. E., "Search Unit Specifications for Improved Repeatability of Ultrasonic Examinations," Nondestructive Evaluation in the Nuclear Industry. R. Natesh, ed., American Society for Metals, Metals Park, Ohio, pp. 355-368, 1978.

7.3.6 Posakony, G. J., "Performance Differences in Quartz Ultrasonic Search Units," Ultrasonic Materials Characterization. NBS SP-596, H. Berger and M. Linzer, eds., Proceedings of 1st International Symposium on Ultrasonic Materials Characterization, National Bureau of Standards, U.S. Government Printing Office, Washington, D.C., pp. 595-603, November 1980.

7.3.7 Lidington, B. H. and Silk, M. G., "The Variability of Ultrasonic Transducers." Br. J. Nondestr. Test. 14(6):173-184, November 1972.

7.3.8 Lidington, B. H. and Silk, M. G., "A Reappraisal of the Variability of Ultrasonic Transducers." Nondestructive Testing 7(4):204-208, August 1974.

7.3.9 Smith, V. D., Teller, C. M. and Swanson, R. K., "Engineering Services to Determine Acceptance of Ultrasonic Transducers for Nondestructive Inspection." Project 15-5D24, Southwest Research Institute, San Antonio, Texas, 1978.

7.3.10 Farley, J. M., "Specifications for Ultrasonic Probes and Flaw Detectors," Improving The Reliability of Ultrasonic Inspection. British Institute of Nondestructive Testing Symposium, Northampton, England, November 13, 1978.

7.3.11 Bainton, K. F. and Silk, M. G., "Some Factors Which Affect the Performances of Ultrasonic Transducers." Br. J. Nondestr. Test. 22(1):15-20, January 1980.

7.3.12 Bruneel, C., et al., "Electrical Coupling Effects in an Ultrasonic Transducer Array." Ultrasonics 17(6):255-260, November 1979.

7.3.13 Pade, E. R. and Enrietto, J. F., "Reliability of Ultrasonic Test Method for Detecting Natural Fatigue Cracks in Centrifugally Cast Stainless Steel Pipe." WCAP-9894, W Class 3, Westinghouse Electric Corp., Pittsburgh, Pennsylvania, June 1981.

7.3.14 Bayre, W. W. and McCormack, D. D., "Ultrasonic Detection of Inclusions in Steel." Mater. Eval. 28(2):25-31, February 1970.

7.5.1 Goebbels, K., Römer, M. and Crostack, H. A., "On the State-of-the-Art and Advanced Techniques to Improve the Signal-to-Noise Ratio for Ultrasonic Testing of Coarse-Grained Materials," Nondestructive Evaluation in the Nuclear Industry. American Society for Metals, Metals Park, Ohio, pp. 75-99, 1980.

7.5.2 Gruber, G. J., "Detection of Cracks in Bimetallic Structures by the Ultrasonic Multiple-Beams Technique." Southwest Research Institute Seminar, San Antonio, Texas, 1981.

7.5.3 Gruber, G. J. and Kapitza, H., "Reliability Evaluation of Six Ultrasonic Techniques for Cladded Pipe Examination." Southwest Research Institute Seminar, San Antonio, Texas, 1981.

7.5.4 de Raad, J. A., "Comparison of Various SEL Probes for the Inspection of Cast Stainless Steel." Report X1837/1981, Prepared for Sweden by Röntgen Technische Dienst. bv, Rotterdam, The Netherlands, April 1981.

7.5.5 Kupperman, D. S., Reiman, K. J. and Ellingson, W. A., "Evaluation of Ultrasonic Techniques for Detection of Stress-Corrosion Cracks in Stainless Steel Piping." EPRI NP-761, Electric Power Research Institute, Palo Alto, California, June 1978.

7.5.6 Yamazaki, T. and Fuji, T., "Development and Application of Focused Probes for Ultrasonic Angle Beam Testing," Ultrasonic Materials Characterization. NBS SP-596, H. Berger and M. Linzer, eds., Proceedings of 1st International Symposium on Ultrasonic Materials Characterization, National Bureau of Standards, U.S. Government Printing Office, Washington, D.C., pp. 263-270, November 1980.

7.5.7 Wüstenberg, H., et al., "In-Service Inspection of Nuclear Power Plant Components," Reliability of Nuclear Power Plants. International Atomic Energy Agency, Vienna, Austria, pp. 603-614, 1975.

7.5.8 Bowker, K. J., "The Relative Merits of Twin and Single Crystal Probes." Proceedings of Symposium on Improving the Reliability of Ultrasonic Inspection, British Institute of Nondestructive Testing, Northampton, England, November 1978.

7.5.9 Licht, H. and Hallett, J. B., "Mapping the Ultrasonic Defect Shadow in a Pitch-Catch Mode." Proceedings of 4th International Conference on NDE in the Nuclear Industry, Fachinformationszentrum Energie, Physik, Mathematik, Lindau, Germany, pp. 427-434, May 1981.

7.5.10 Kraus, S. and Goebbels, K., "Improvement of Signal-to-Noise Ratio for the Ultrasonic Testing of Coarse-Grained Materials by Signal Averaging Techniques," Ultrasonic Materials Characterization. NBS SP-596, H. Berger and M. Linzer, eds., Proceedings of 1st International Symposium on Ultrasonic Materials Characterization, National Bureau of Standards, U.S. Government Printing Office, Washington, D.C., pp. 551-559, November 1980.

7.6.1 Launay, J. P., et al., "Non-Destructive Evaluation of Underclad Defects." Proceedings of 4th International Conference on NDE in the Nuclear Industry, Fachinformationszentrum Energie, Physik, Mathematik, Lindau, Germany, pp. 417-425, May 1981.

7.6.2 Fortunko, C. M. and Lawrence, W. E., "Weld Inspection with Shear Horizontal Acoustic Waves Generated by EMATS." Proceedings of DARDA/AFML Review of Progress on Quantitative NDE, AFWAL-TR-80-4078, D. O. Thompson and R. B. Thompson, eds., USAF Technical Report, 1980.

7.6.3 Wüstenberg, H., Erhard, A. and Kutzner, J., "Detection and Analysis of Near-Surface Cracks by Ultrasound," Ultrasonic Materials Characterization. NBS SP-596, H. Berger and M. Linzer, eds., Proceedings of 1st International Symposium on Ultrasonic Materials Characterization, National Bureau of Standards, U.S. Government Printing Office, Washington, D.C., pp. 3-10, November 1980.

7.7.1 Wüstenberg, H. and Erhard, A., "Development of Ultrasonic Techniques for Sizing Defects." 1st International Seminar NDE in Relation to Structural Integrity and 5th International Conference on Structural Mechanics in Reactor Technology, T. Jaeger, ed., Commission of the European Communities, Brussels, Belgium, 1979.

7.7.2 Mundry, E., et al., "Flaw Size Determination by Ultrasonic Pulse Spectroscopy, Acoustical Holography, and Focusing Probes--A Critical Comparison." IIW-IIS Colloquium, Commission V, Copenhagen, Denmark, July 1977.

7.7.3a Barbian, O. A., et al., "Reconstruction of Defect Geometry from Sampled Ultrasonic Transit Time and Amplitude Locus-Curves," Nondestructive Evaluation in the Nuclear Industry. American Society for Metals, Metals Park, Ohio, pp. 559-575, 1980.

7.7.3b Grohs, B., et al., "Characterization of Flaw Location, Shape, and Dimensions with the ALOK Systems." Mater. Eval. 40:84-89, January 1982.

7.7.4 Posakony, G. J., "Acoustic Imaging--A Review of Current Techniques for Utilizing Ultrasonic Linear Arrays for Producing Images of Flaws in Solids." Symposium on Elastic Waves and NDT of Materials, American Society of Mechanical Engineers, New York, New York, December 1978.

7.7.5 Light, G. M., "Phased Arrays and Special Transducers." 11th Nuclear Power Education Seminar, Southwest Research Institute, San Antonio, Texas, 1981.

7.7.6a Gebhardt, W., Bonitz, F. and Woll, H., "Defect Reconstruction and Classification by Phased Arrays." Mater. Eval. 40:90-95, January 1982.

7.7.6b Gebhardt, W., et al., "Determination of Crack Characteristics, Size, and Orientation of Defects by Phased Array Technique in NDT," Nondestructive Evaluation in the Nuclear Industry. American Society for Metals, Metals Park, Ohio, pp. 541-557, 1980.

7.7.7 Schmitz, V., Müller, W. and Schäfer, G., "A New Ultrasonic Imaging System." Mater. Eval. 40:101-108, January 1982.

CHAPTER 8

FLAW DETECTION AND SIZING -- THEORETICAL BACKGROUND

CONTENTS

FIGURES

TABLES

CHAPTER 8

FLAW DETECTION AND SIZING -- THEORETICAL BACKGROUND

8.1 INTROOUCTION

It is not the intent in this chapter to review the broad field of nondestructive theory; there are several texts providing such coverage. The following boundary conditions have been established to make the problem more tractable:

- Ultrasonics will be the only nondestructive examination technique reviewed.
- Geometric effects will be limited to those pertinent to reactor pressure vessels and piping.
- Material effects will consider fine-grained ferritics, clad or unclad, and coarse-grained austenitics either isotropic or anisotropic.
- The spectrum of flaw characteristics will be examined, particularly as they interact with various ultrasonic parameters.

Haines and Langston[8.1.1] did an excellent job of defining what they hoped to accomplish with theoretical studies; since a similar goal exists for this chapter, their objective is repeated here:

> The view is taken that "big block" exercises of the PISC type will never provide sufficient data on which a statistical assessment of crack detection reliability may be based. The alternative approach proposed in is that the ultrasonic crack detection process can be sufficiently accurately modelled that the theoretical predictions may be made of detection reliability and sizing accuracy. The models must, however, be experimentally verified by both laboratory tests and by comparison with the detailed results of PISC type exercises.

This represents a laudable goal worth striving for. My subjective judgment is that, given a correctly designed experiment, a statistical assessment is feasible. Also, I agree with the theoretical approach as it applies to detection and am sceptical as it applies to sizing.

Several of the chapters contain comments derived from various theoretical studies; notably Chapters 4, 5, 6, 9, and 13. Some of the more relevant aspects of these studies will be repeated here to provide a more detailed presentation.

To reiterate, the scope of this chapter will be sharply focused on aspects relevant to the optimized UT of piping and pressure vessels to see what theory offers in new approaches or confirms in current approaches.

One additional caveat exists insofar as chapter coverage is concerned. In addition to the four boundary conditions given in the first paragraph, the further limitation is applied of interpreting the information contained in those available references. If I have misinterpreted the author's meaning, I apologize. My intent was to serve as a one-way screen removing information irrelevant to the boundary conditions and presenting the author's meaning as clearly as possible in the relevant areas.

8.2 SURFACE EFFECTS

Extensive experimental evidence confirms the substantial role surface finish plays in UT examinations. For the purpose of this chapter we shall consider three cases where smooth, rough and uneven surfaces may influence UT signals:

- the near surface under coupling and immersion conditions
- interfaces such as clad/base metal
- the far surface where geometrical discontinuities can be important.

A fourth case, that of the weld/base metal interface will be considered under section 8.3 on bulk metal.

Chapter 4 reviews the implications of both surface and component geometry. Haines[4.5.3] in recognition of surface effects assumed an ideal surface. Silk and Lidington[4.5.9] have related surface finish to the relative efficiency of coupling. As the surface degrades due to roughness, scale, pitting, etc., the efficiency of coupling may be reduced from 100% to less than 50%. Another aspect in contact probes is gross surface irregularity such as weld crown. As a transducer rides up on the crown the signal may be lost due to changes in couplant layer. Neither of the above lend themselves to definitive theoretical studies.

The couplant itself can play a substantial role in the response of the signal regardless of the surface finish. While there are many experimental studies where coupling played a role, there are relatively few theoretical studies. Erhard et al.[8.2.1] reported on a joint theoretical-experimental study. The model of the wave front can be seen in Figure 8.2.1.

The theoretical model used to calculate the permeability factor is defined as

$$C = K\left[\frac{1-g^N}{1-g} + \frac{1-h^N}{1-h}\right]$$

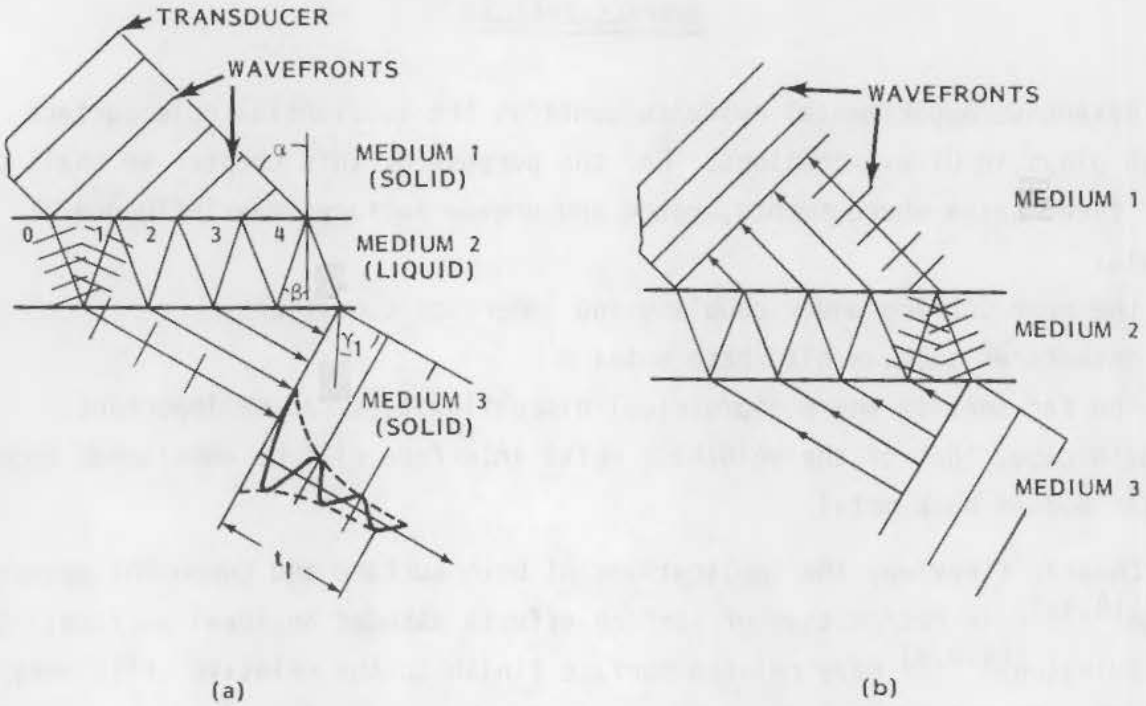

FIGURE 8.2.1. Sound Transmission Through a Coupling Layer Either (a) by Short-Pulse Transmissions or (b) Pulse-echo

where $K = 1/2\ D_{12}D_{23} \exp(i\epsilon) \exp(-al/2)$

$g = R_{21}R_{23} \exp(-al) \exp(i\phi) [\exp(i\omega\Delta t) \exp -x\nu\Delta t]$

$h = R_{21}R_{23} \exp(-al) \exp(i\phi) [\exp(-i\omega\Delta t) \exp(-x\nu\Delta t)]$

$$N = \frac{t_1 \cos\beta\ C_{L2}}{2d} \frac{T}{T_o}$$

where D_{12} = permeability factor from medium 1 to 2

D_{23} = permeability factor from medium 2 to 3

R_{21} = reflectivity factor at interface 2, 1

R_{23} = reflectivity factor at interface 2, 3

ϵ = phase angle of permeability factor D_{23}

ϕ = phase angle of reflectivity factor R_{23}

ω = angular frequency

ν = frequency

l = path of oscillatory reflection

C_{L2} = acoustic velocity of couplant medium

a = absorption coefficient of couplant medium

t_1 = pulse length

d = couplant thickness

Δt = time interval.

It is important to realize that permeability is not being used in the conventional sense. Basically, it is used in the sense of the ability of an acoustic wave to pass through a membrane such as a coupling layer.

A comparison of transmission and pulse-echo in plexiglass-water-steel using short pulses is made with the same combination of plexiglass-glycerine-steel at 0.99 MHz in short and long pulses in Figure 8.2.2. Figure 8.2.3 compares frequencies of 2.0 MHz and 3.58 MHz as well as a general comparison of frequency.

The immersion case is less affected by surface finish than the coupling case; however, in a certain range of roughness for a given wavelength there can be major wave scattering where a water/metal interface exists. This situation occurs for rough flaws and will be discussed in section 8.5 recognizing that much that is said there is applicable here. This is particularly relevant to the rough interface situation.

The third condition often seen in weld counterbore design relates to the axial position of the counterbore, the angle of taper of the counterbore, and the weld root condition. The major problem is mode conversion. This can be established theoretically given the probe parameters and the weld root conditions. Figure 8.2.4 illustrates such mode conversion relationships. While it is possible to predict that a given geometry will lead to mode conversion, conditions near the weld root are usually poorly known so mode conversion may occur when it is not predicted.

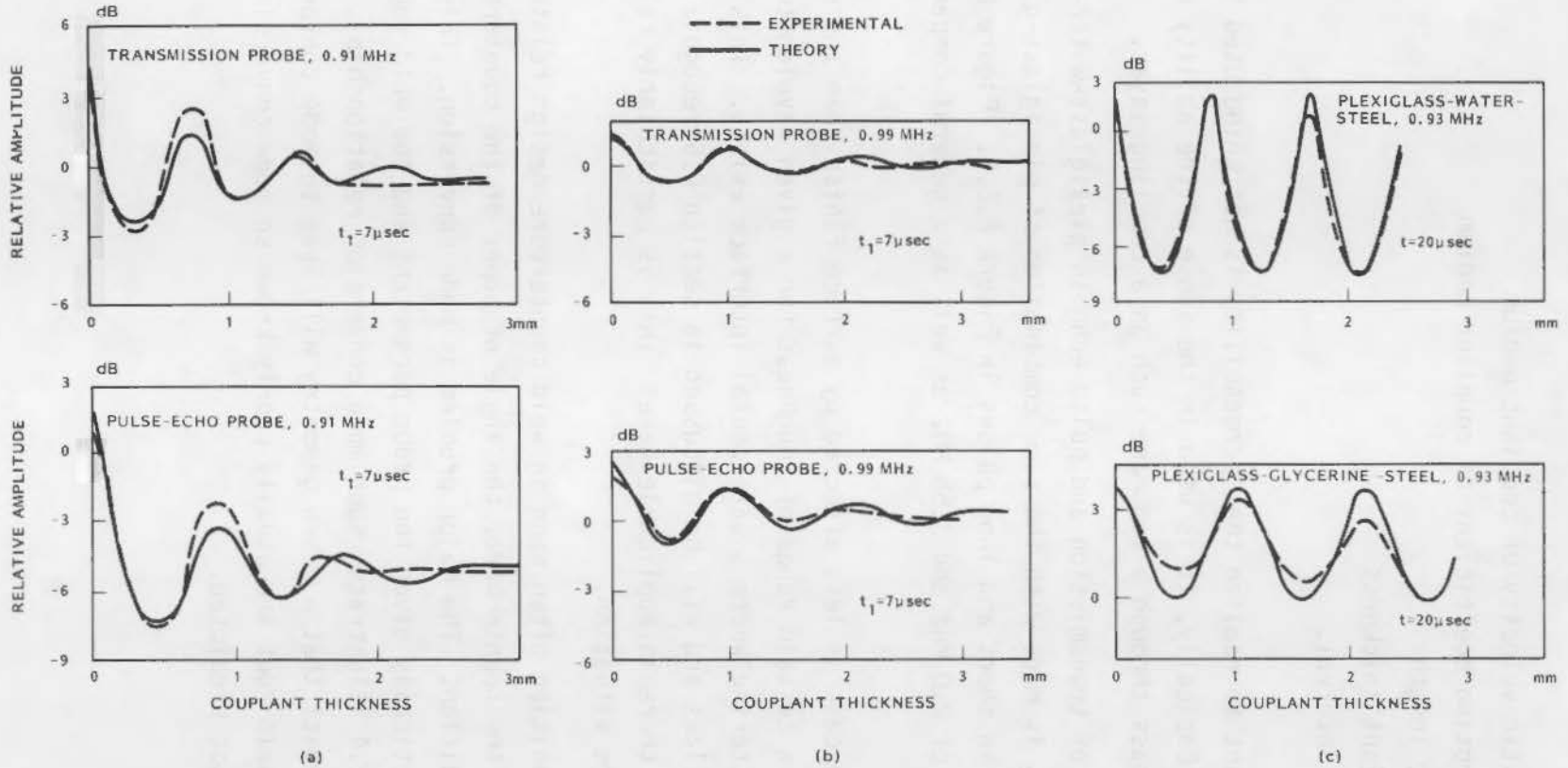

FIGURE 8.2.2. Influence of Couplant Thickness on Sound Transmission with Short Pulses for (a) Plexiglass-Water-Steel; (b) Plexiglass-Glycerine-Steel; and (c) Pulse-Echo Long Pulses. All above using WB 45-N1 probe at 0.91-0.99 MHz.

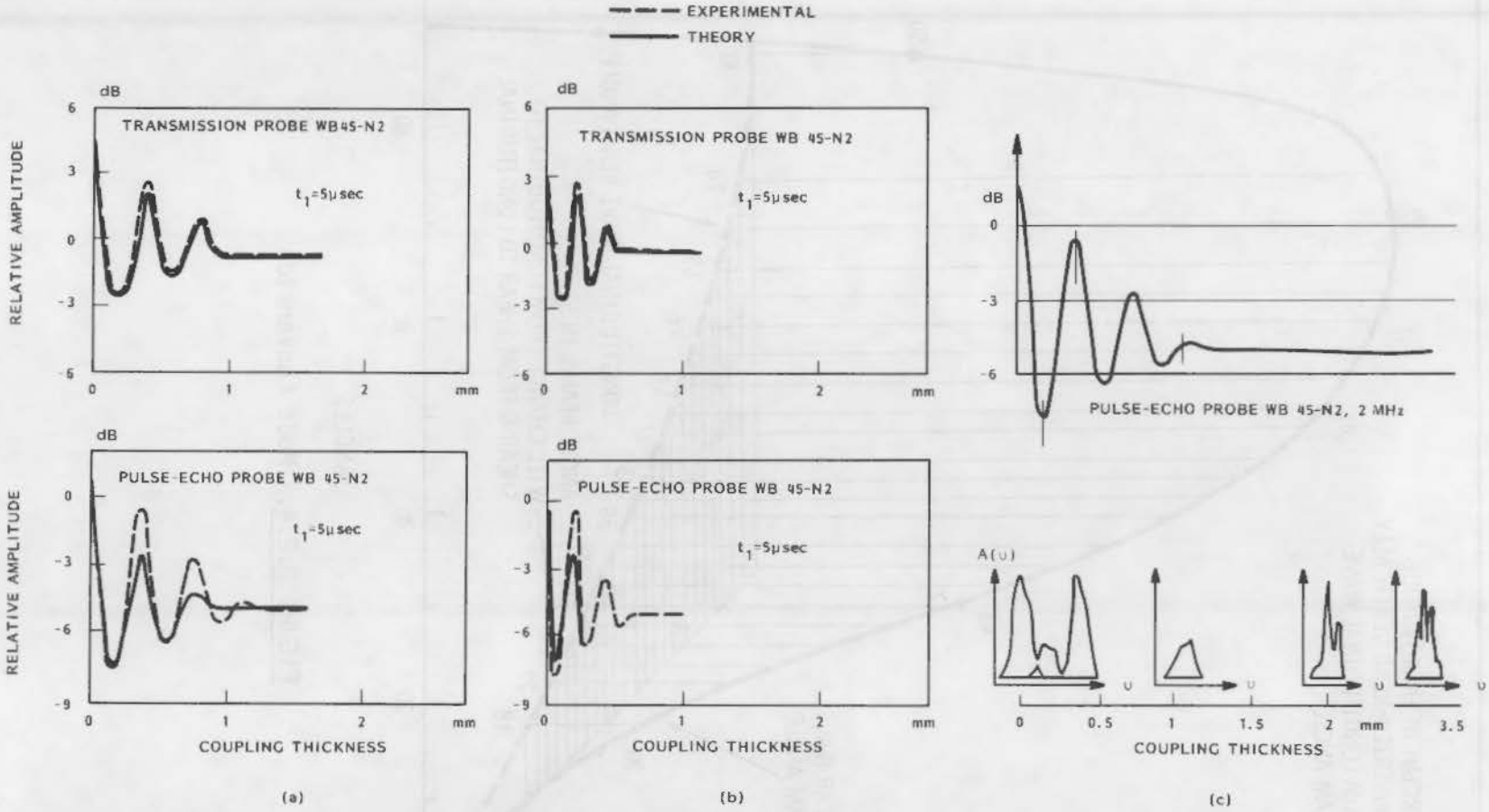

FIGURE 8.2.3. Effect of Frequency on Sound Transmission as a Function of Thickness of Couplant for (a) 2.0 MHz; (b) 3.58-MHz, 45° Angle; and (c) Amplitude-Frequency Response at Given Coupling Thickness. All cases plexiglass-water-steel.

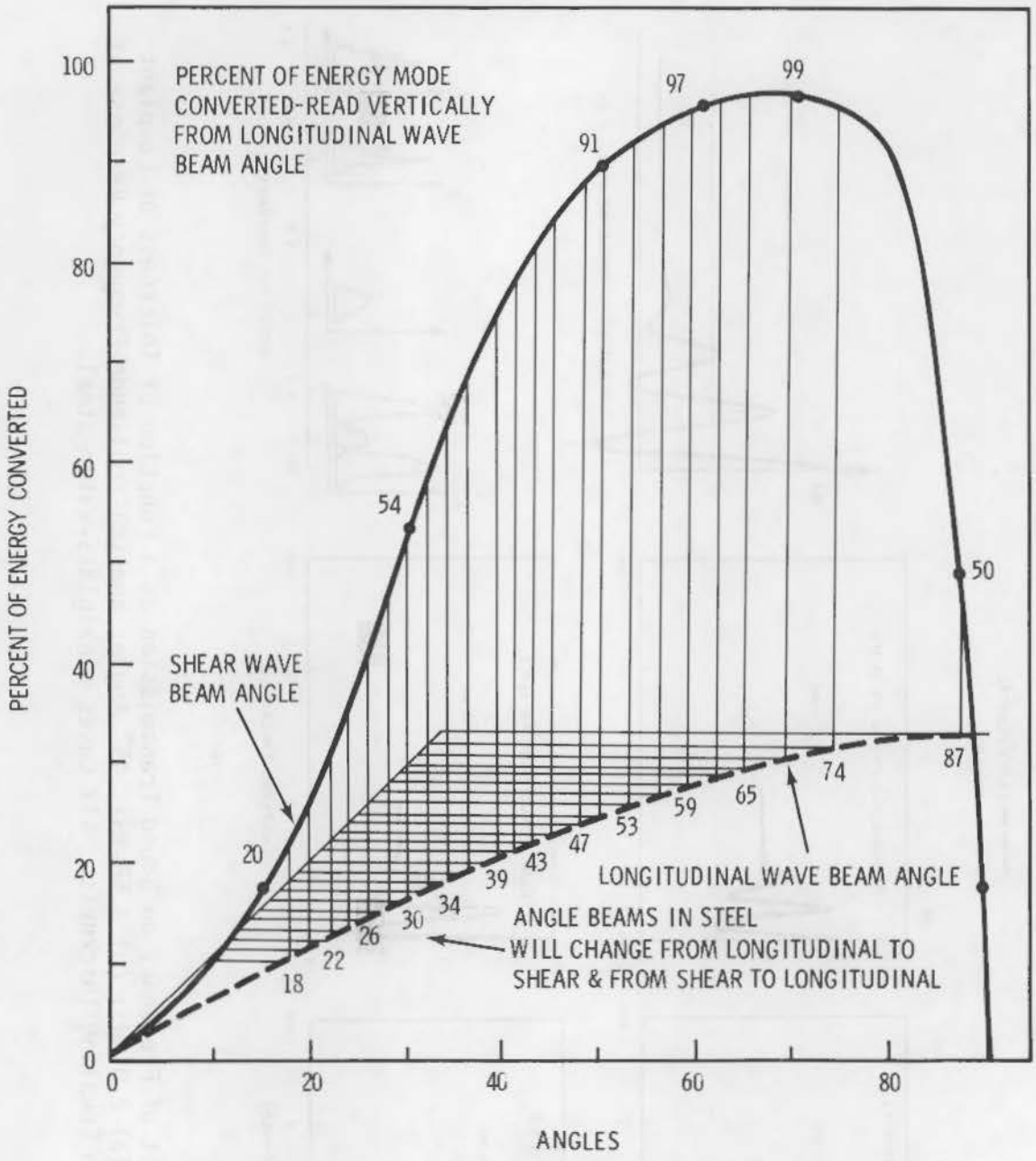

FIGURE 8.2.4. Mode Conversion

8.3 BULK METAL

In bulk metal it is necessary to consider the implications of the following cases:

- austenitic cladding on ferritic base metal
- wrought austenitic containing austenitic welds
- cast austenitic containing austenitic welds.

In these combinations the factors of significance are attenuation due to grain size plus skewing and channeling because of severe anisotropy.

8.3.1 Cladding

No definitive theoretical studies are known relating directly to cladding. By inference one can apply the commentary pertinent to attenuation and skewing in bulk material, recognizing that the cladding represents a relatively thin layer. The implications of attenuation with and without cladding were cited in Chapter 4 and are repeated here. Figure 8.3.1 (also Figure 4.5.3) indicates there can be a 25-dB drop through 5 mm of cladding when using a 70° probe at 2 MHz.[4.5.19] Any theoretical study needs to consider the welding direction of cladding. The change in attenuation and skewing are greater normal to the direction of welding than they are parallel to it. This could be a problem around nozzles. It is particularly true for 45° probes.

8.3.2 Coarse-Grained Nominally Isotropic Alloys

Attenuation tends to be a more significant factor than skewing or channeling in nominally isotropic alloys. A theoretical study by Atthey[8.3.1] builds on earlier work of Lipschitz and Parkhomovski (1950), extending their work into textured or anisotropic materials. He tied his study fairly specifically to austenitic stainless steel considering both the longitudinal and both vertical and horizontally polarized shear waves.

One limitation concerns the range of application. The cases

$$q\bar{a} > 1 \text{ or } >>1 \text{ and } q\bar{a} < 1 \text{ or } << 1$$

where q is wave number and $\bar{a}$ is average grain radius.

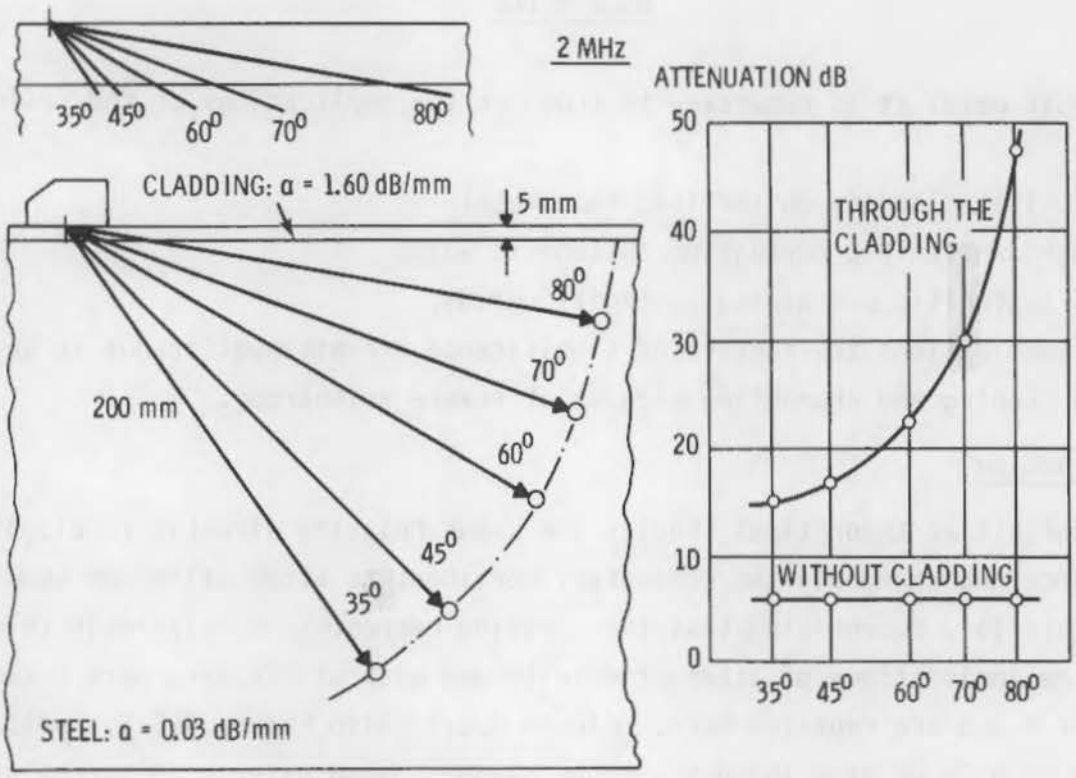

FIGURE 8.3.1. Influence of Cladding on Angle-Beam Penetration

The case $q\bar{a} \cong 1$ is definitely doubtful.

The original assumptions of Lipschitz and Parkhomovski were that

- linear elasticity holds
- within any grain anisotropy is small
- grains are equiaxial
- no preferred orientation
- single phase without voids or inclusions.

Attkey's model modified these assumptions to consider some anisotropy within the grains. His other assumptions were that

- An infinite medium (to simplify math) exists.
- Orientations of adjacent grains are independent.
- $\bar{a}q$ is very small or very large.

The latter assumption divides the analysis into very short or very long wavelengths.

Equations in tensor notation are developed in a general form for any grain distribution and grain shape. He applies them to the case of cubic symmetry using the elastic constants λ and μ with values specific to austenitic stainless steel.

The case of interest was the propagation of a plane wave through an austenitic weldment. This introduced further assumptions, namely, that

- Propagation occurs in the (012) plane.
- Since the composite structure is anisotropic, pure waves either longitudinal or shear cannot be assumed; therefore, quasi-longitudinal ($q^{(1)}$), quasi-shear ($q^{(2)}$ and pure shear ($q^{(3)}$) are substituted.
- The orientation of weld metal (θ_o) about the fiber axis is assumed small ($<20^\circ$).

Using these assumptions, equations consisting of a real part representing wave speed and an imaginary part representing both velocity and attenuation were developed for the three forms of waves in both the short- and long-wavelength cases. The following are these final equations:

$$\gamma^{(1)} = \nu^2\omega^4\bar{V}\left(2/c_L^5+3/c_T^5\right)\left[\theta_o^2\cos^4\Psi + \left(\frac{1}{8}+\frac{1}{4}\theta_o^2\right)\sin^4\Psi\right]/120\pi\rho^2c_L^3 \qquad (8.3.1)$$

$$\gamma^{(2)} = \nu^2\omega^4\bar{V}\left(2/c_L^5+3/c_T^5\right)\left[\frac{1}{2}\theta_o^2 + \left(\frac{1}{8}+5\theta_o^2/4\right)\cos^2\Psi\sin^2\Psi\right]/120\pi\rho^2c_T^3 \qquad (8.3.2)$$

$$\gamma^{(3)} = \nu^2\omega^4\bar{V}\left(2/c_L^5+3/c_T^5\right)\left(\frac{1}{8}\sin^2\Psi + \frac{1}{2}\theta_o^2\cos^2\Psi\right)/120\pi\rho^2c_T^3 \qquad (8.3.3)$$

$$c^{(1)} \simeq [(\lambda+2\mu)/\rho]^{1/2}\left\{1 + \frac{1}{8}\nu\left[4\left(1-\theta_o^2\right)\cos^4\Psi + 12\theta_o^2\sin^2\Psi\cos^2\Psi + 3\left(1-\theta_o^2\right)\sin^4\Psi\right]/(\lambda+2\mu)\right\} \qquad (8.3.4)$$

$$c^{(2)} \simeq [\mu/\rho]^{1/2}\left\{1 + \nu/16\left[4\theta_o^2\cos^4 + \left(14-27\theta_o^2\right)\sin^2\Psi\cos^2\Psi + 4\theta_o^2\sin^4\Psi\right]/\mu\right\} \qquad (8.3.5)$$

$$c^{(3)} \simeq [\mu/\rho]^{1/2} \left\{1 + \nu/16 \left[4\theta_o^2 \cos^2\Psi + \left(2-\theta_o^2\right) \sin^2\Psi\right]/\mu\right\} \qquad (8.3.6)$$

where ν = anisotropy
ω = wave frequency
$\bar{V}$ = average grain volume
c_i = velocity
θ = angle of orientation of weld metal
ρ = density
μ, λ = Lame' constants
Ψ = angle related to (012) plane.

The author[8.3.1] states that there is no suitable experimental evidence to check the values contained within the braces of equations 8.3.1, 8.3.2, 8.3.3. He cites work of Tomlinson et al.[4.5.32] who examined cylinders of austenitic weld metal and cylinders of single-crystal, Nimonic 80 A to establish the quasi-longitudinal attenuation coefficient. In such measurements the amplitude of the transmitted wave depends on both the attenuation in the metal and the coupling between the cylinder and water. Since the Nimonic 80 A specimen was a single crystal, there should be no attenuation due to grain scattering and very little from other mechanisms. However, the signal had the same form and magnitude as with the weld metal, leading to the conclusion that a significant portion of the signal was due to effects other than attenuation; e.g., skewing being a possibility where angular dependence would be important.

Table 8.3.1 contains values of attenuation coefficients for the short and long wavelength cases. Figure 8.3.2 illustrates the variation in wave velocity with angle. Both sets of data are in qualitative agreement with Figure 13.4.12 of Chapter 13 which is reproduced here as Figure 8.3.3.

8.3.3 Anisotropy Effects in Austenitic Alloys

Beam skewing and channeling because of anisotropy is treated extensively in Chapter 13 and 13B. Specifically, section 13.4 deals with the spectrum of attenuation, skewing and channeling as they pertain to austenitic stainless steel and Chapter 13B considers wave propagation and velocity in terms of

TABLE 8.3.1. Some Values of the Attenuation Coefficient Determined from a Theoretical Model

Long Wavelength Attenuation Coefficients (m^{-1})
$\omega = 4\pi \times 10^6\ s^{-1}$, $\bar{V}$ = average grain volume, 20° grain scatter

	Quasi-Longitudinal Wave	Quasi-Shear Wave	Shear Wave
0°	$1.4 \times 10^{11}\bar{V}$	$4.1 \times 10^{11}\bar{V}$	$4.1 \times 10^{11}\bar{V}$
45°	$7.6 \times 10^{10}\bar{V}$	$8.8 \times 10^{11}\bar{V}$	$6.3 \times 10^{11}\bar{V}$
90°	$1.8 \times 10^{11}\bar{V}$	$4.1 \times 10^{11}\bar{V}$	$8.4 \times 10^{11}\bar{V}$

Short Wavelength Attenuation Coefficients (m^{-1})
$\bar{a}_o$ = average grain radius perpendicular to mean fibre axis

	Quasi-Longitudinal Wave	Quasi-Shear Wave	Shear Wave
20°	$3.4 \times 10^{4}\bar{a}_o$	$1.3 \times 10^{6}\bar{a}_o$	$3.1 \times 10^{6}\bar{a}_o$
45°	$2.8 \times 10^{3}\bar{a}_o$	$2.2 \times 10^{5}\bar{a}_o$	$4.2 \times 10^{6}\bar{a}_o$
90°	$1.5 \times 10^{4}\bar{a}_o$	$4.4 \times 10^{5}\bar{a}_o$	$4.6 \times 10^{6}\bar{a}_o$

slowness and wave surfaces. With regard to skewing, theory and experiment are in excellent agreement. Figure 8.3.4 (also Figure 13.4.9) covers the L-wave case illustrating the agreement between theory and experiment.

With regard to channeling, Kupperman and Reimann[4.5.27] cite the guiding of beams from their wave normal typical of the channeling observed by Yoneyama[4.5.24] and others.

Rose et al.[8.3.2] discuss attenuation and skewing behavior in coarse-grained cast-austenitic alloys that would cast doubt on most theoretical models insofar as accurate modeling is concerned. They reported local variations in attenuation with low values 0.4 to 1.0 dB/cm at 5 MHz to high values of 6.2 to 6.5 dB/cm. Often the lows and highs were only inches apart in the material.

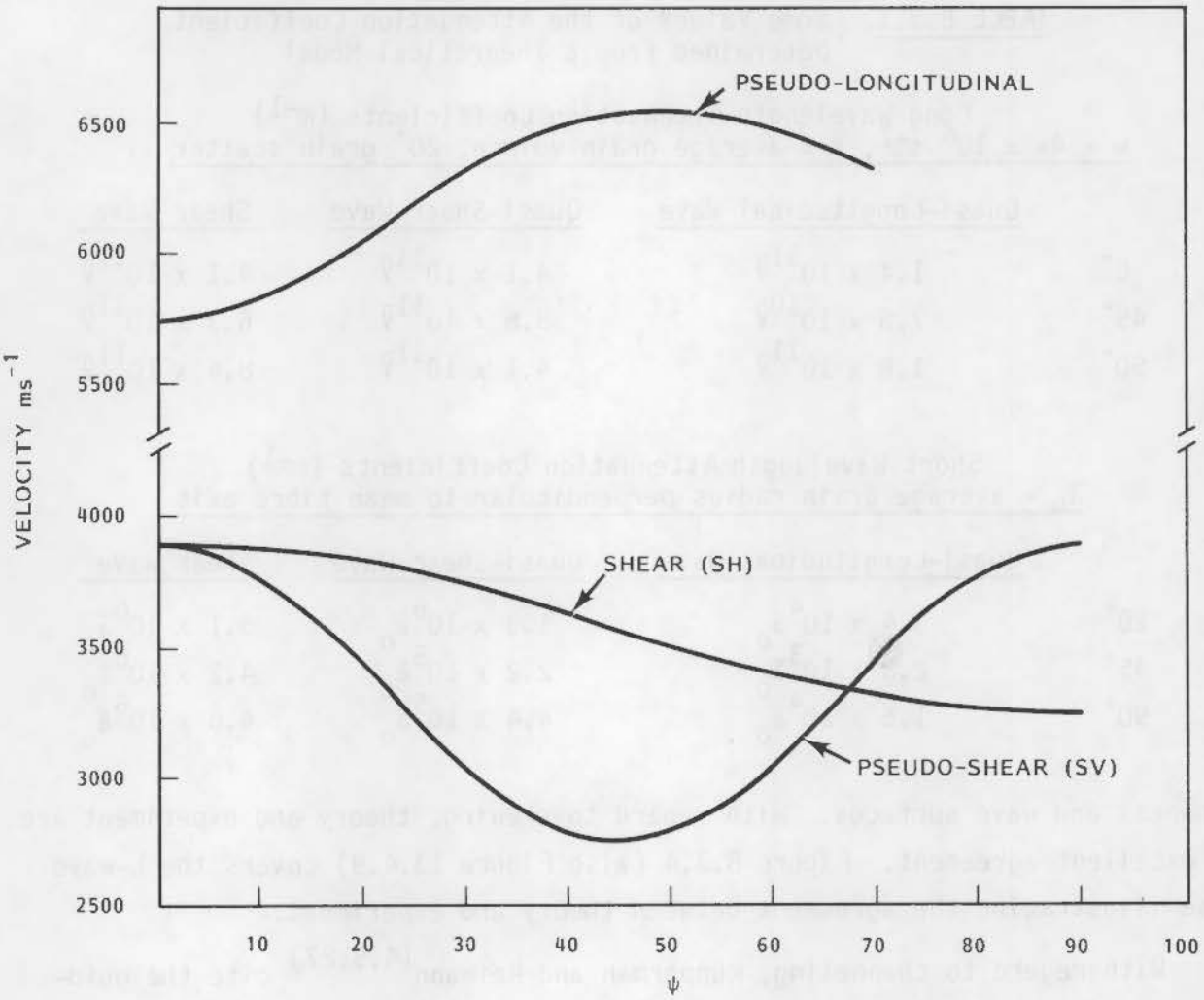

FIGURE 8.3.2. Theoretical Determination of Variation of Wave Velocities with Angle

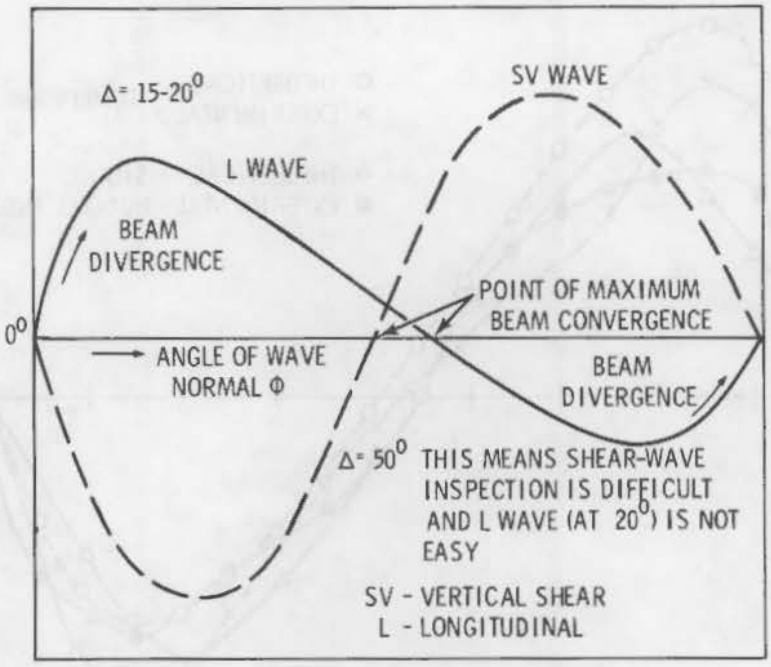

VELOCITY

MAXIMA - L WAVE 45-50°; S WAVE 0°, 90° POLARIZATION //
MINIMA - S WAVES 45° (POLARIZED // x (110)); 90° (POLARIZATION //)

ATTENUATION

MINIMUM - S WAVE Φ = 90° (POLARIZED //); 0° ATTENUATION HIGHER THAN 90°, POSSIBLY DUE TO MODE CONVERSION, GRAIN BOUNDARY SCATTERING, AND ACOUSTIC MISMATCH WHICH IS GREATER ACROSS DENDRITES

FIGURE 8.3.3. Examples of Effects of Beam Skewing in a Weldment with Respect to Velocity, Attenuation, and Beam Spread

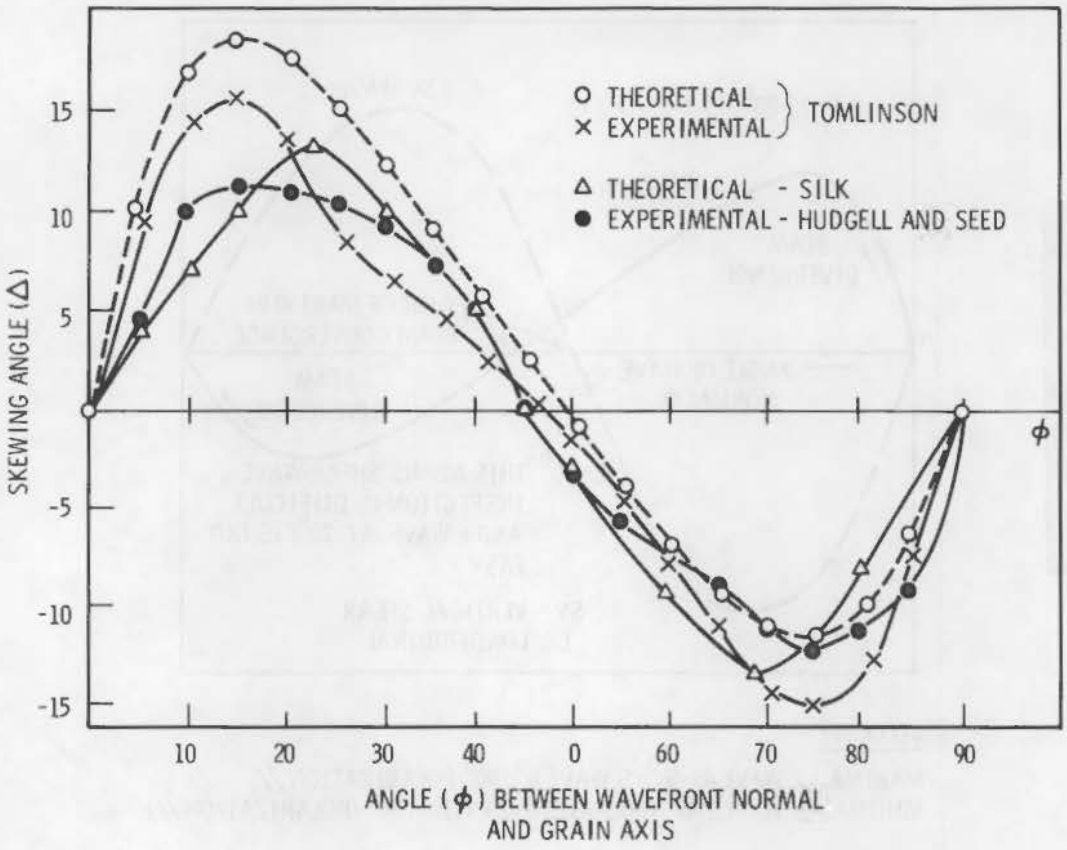

FIGURE 8.3.4. Skewing Angle Δ is a Function of the Angle ϕ Between the Normal to the Wavefront and the Columnar Grain Axis

8.4 TRANSDUCER BEHAVIOR

The following is a quasi-theoretical discussion of some factors influencing beam geometry when decoupled from surface and bulk media effects. Transducer theory as such is not discussed; only beam behavior as it is affected by some parameters.

Legge[8.4.1] touched on several characteristics of ultrasonic pulser, some of which are relatively obvious. These factors are presented in Table 8.4.1.

Wüstenberg et al.[8.4.2] considered the influence of sound-field geometry as it influences defect detection. Probes will vary markedly in divergence ranging from those with large divergence, such as those used for acoustic

TABLE 8.4.1. Factors Influencing Ultrasonic Beam Behavior and Flaw Detection

- A pulse behaves as if it consists of a continuous spectrum of sinusoidal waves; as the pulse is reduced in duration the bandwidth increases.
- Increases in frequency are accompanied by decreases in beam spread.
- A beam will be rich in higher frequencies in the center and high in lower frequencies at the periphery. Higher frequencies tend to be preferentially attenuated.
- Far-field beam spread is due to diffraction and will depend upon the size and shape of transducers and wavelength. Transducer size and pulse shape can be optimized so that axial pulse shape will not vary greatly with distance of propagation.
- The signal-to-noise ratio is proportional to the square root of the bandwidth; therefore, a large bandwidth (short pulse) gives better results than a narrow bandwidth (long pulse).
- The maximum and minimum in the near field of a long-pulse probe are greatly reduced in the near-field of a short-pulse probe.
- A disadvantage of short pulses is the reduction in sensitivity accompanying damping of the transducer.
- The wider the frequency band the greater the information from a reflection because such information is the vector sum of all contributions.

holography, through medium divergence typical of most commercial probes where aperture angles are 2° to 10° and, finally, to probes with small divergences, such as those used in focused sound fields. The following compares divergence as a factor influencing detection:

Type of Probe System	Divergence	Probability of Detection	Signal/Noise Ratio	Interpretation	Costs
Acoustic Holography	Large	++	--	+	-
Most Commercial Probes	Medium	+	+	0	++
Focused Probes	Small	-	++	++	-

+ Favorable; - unfavorable; 0 neither + or -

Another study by Wüstenberg et al.[8.4.3a,8.4.3b] investigated the effect of transducer size and shape on the sound field of angle probes. A relatively simple theory permits calculation of the sound-field distribution in a beam cross section, taking into account such factors as mode conversion at the coupling surface and corresponding point-by-point intensities. Calculated and measured sound intensity patterns agree semi-quantitatively.

It is possible to use the theory to predict the effective transducer size of a angled probe as noted in Figure 8.4.1. Figure 8.4.1a presents the model schematically and Figure 8.4.1b appends the equations used to calculate the characteristics of the sound field. The suggested approach can be used for a variety of probes. Reference 8.4.3a (in German) develops the mathematics of the theory more completely than does 8.4.3b.

Schlengermenn[8.4.4] discussed the factors leading to optimization of probes, specifically focused probes. In essence by following his rules it is possible to develop an optimized focused probe for any application. While his comments apply specifically to a transducer with a circular piston oscillator and a spherical lens, they may be extended to various other methods of forming focused sound fields as well as to other types of oscillators. Figure 8.4.2

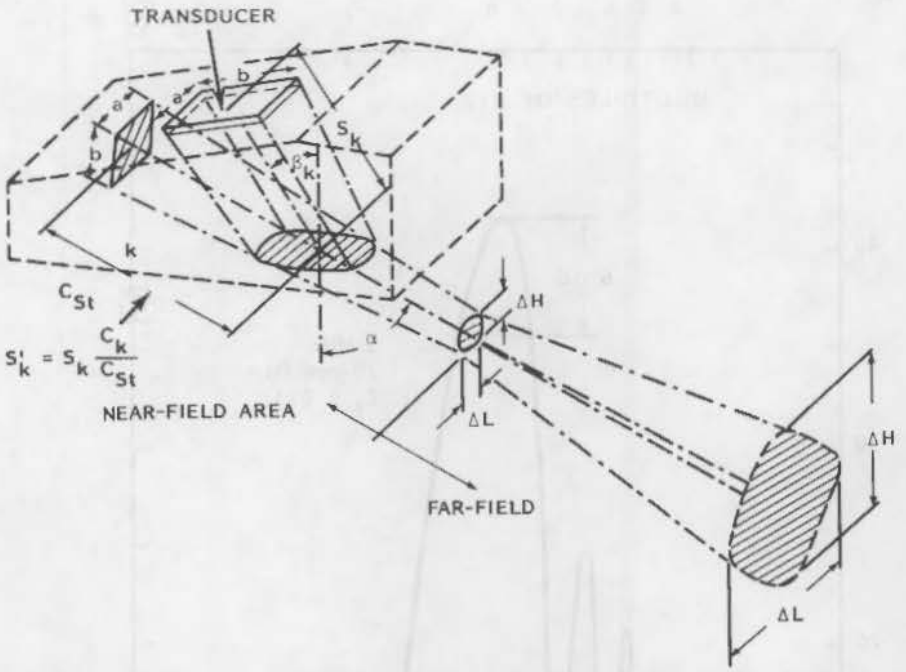

FIGURE 8.4.1a. Simplified Model for the Sound Beam of an Angle Probe

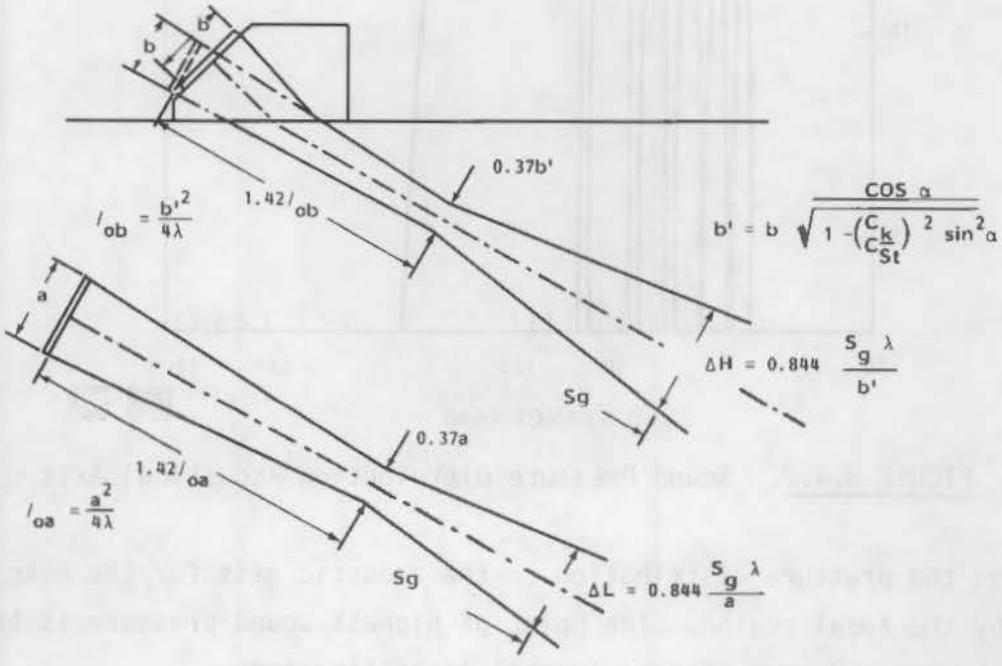

FIGURE 8.4.1b. Characteristics of the Sound Field

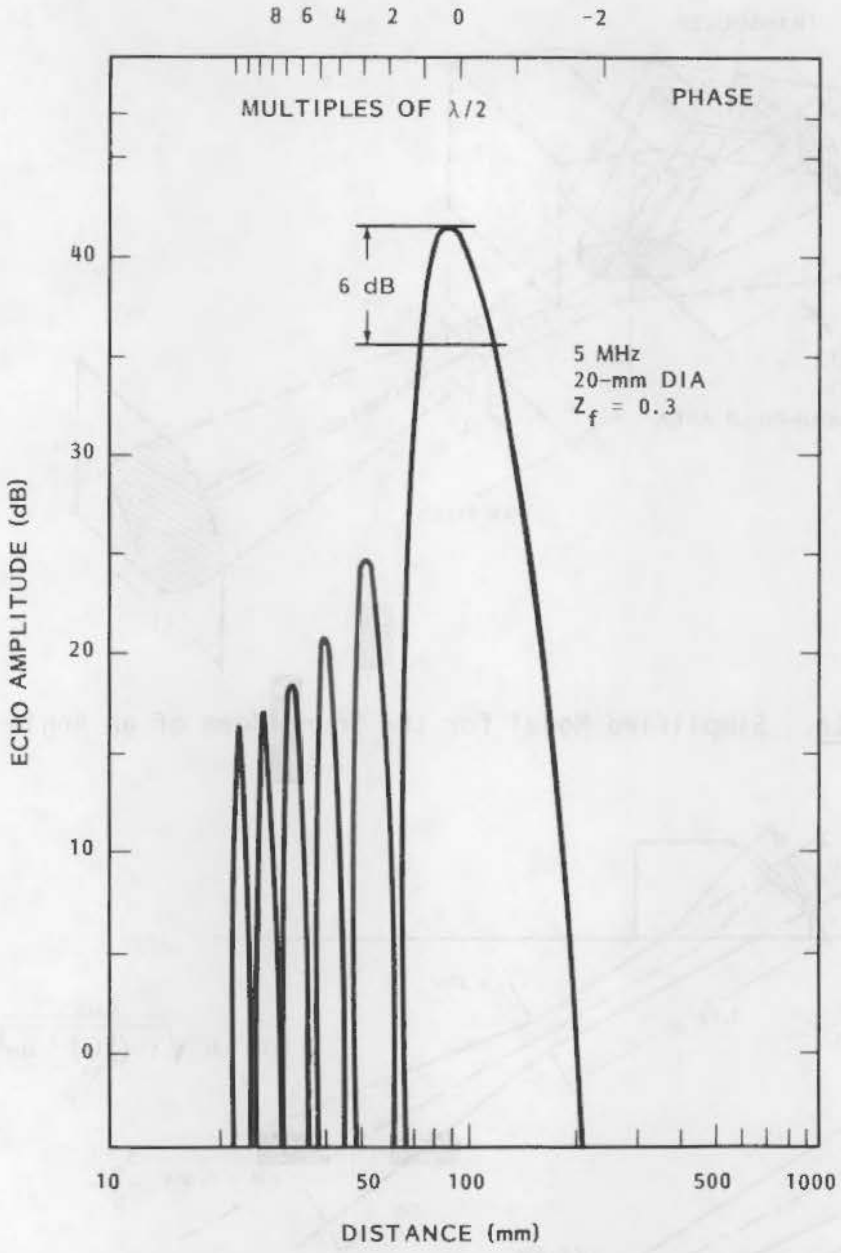

FIGURE 8.4.2. Sound Pressure Distribution Acoustical Axis

illustrates the pressure distribution on the acoustic axis for the near field followed by the focal region. The point of highest sound pressure is taken as the focus because of ease of experimental identification.

The echo amplitude geometry portrayed in Figure 8.4.2 as a series of discrete peaks in the near field would lead to the conclusion that the near-field

regions would be unusable. The actual near field varies substantially from the theoretical. A study by Pasakony,[8.4.5] portrayed schematically in Figure 8.4.3, indicates that the near field remains fairly constant. Even the center dead zone of the transducer is limited to a 1- to 2-dB drop. While Figure 8.4.3 is representative of excitation by a shock pulse, it is considered generally applicable. The scale on Figure 8.4.2 tends to be distorted in that the near-field echo amplitude will be closer to those in Figure 8.4.3 rather than the 20 to 30 dB noted.

The focal distance (z_f) in terms of wavelength and transducer radius defines the focusing factor Z_f which is used to optimize transducer design for various applications. Figures 8.4.4a and b quantify such factors as focal range and radius of curvature in terms of the focusing factor. Using the criteria developed in this paper,[8.4.4] Schlengermann indicated how optimized transducers are designed for various applications.

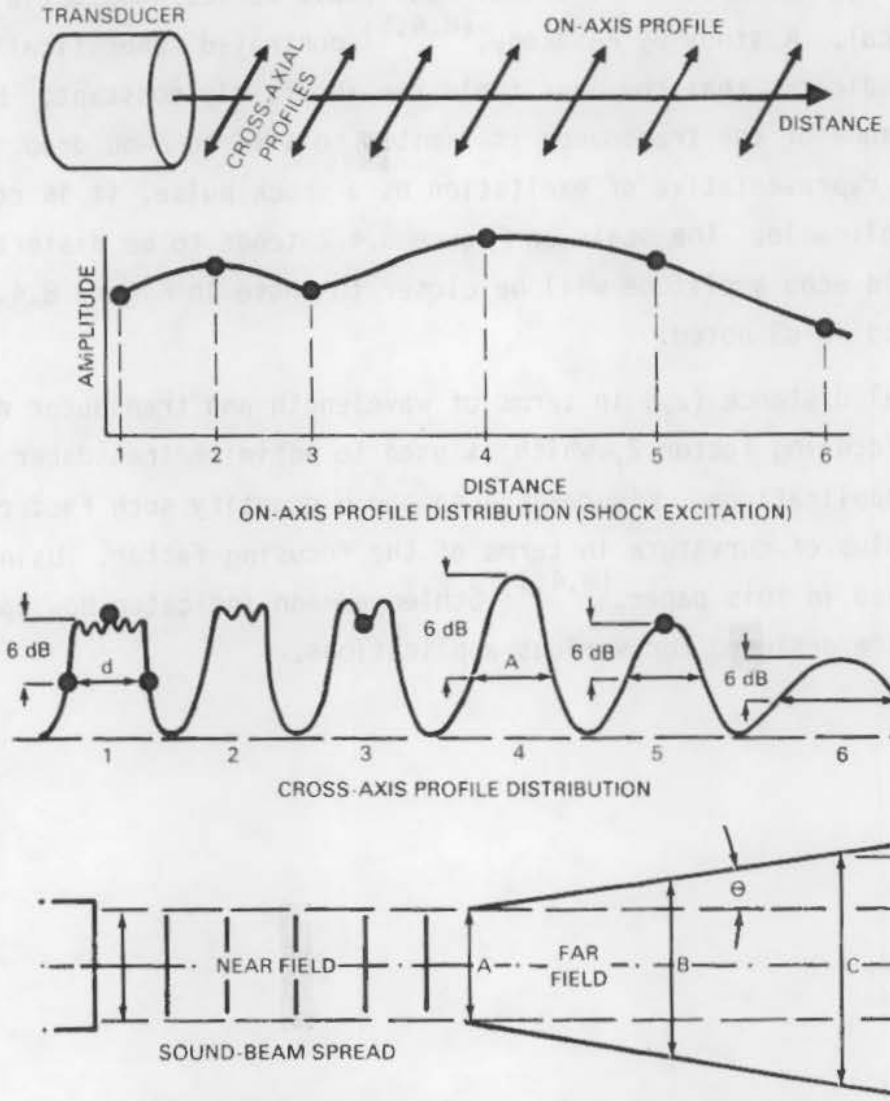

FIGURE 8.4.3. Transducer Sound-Field Patterns

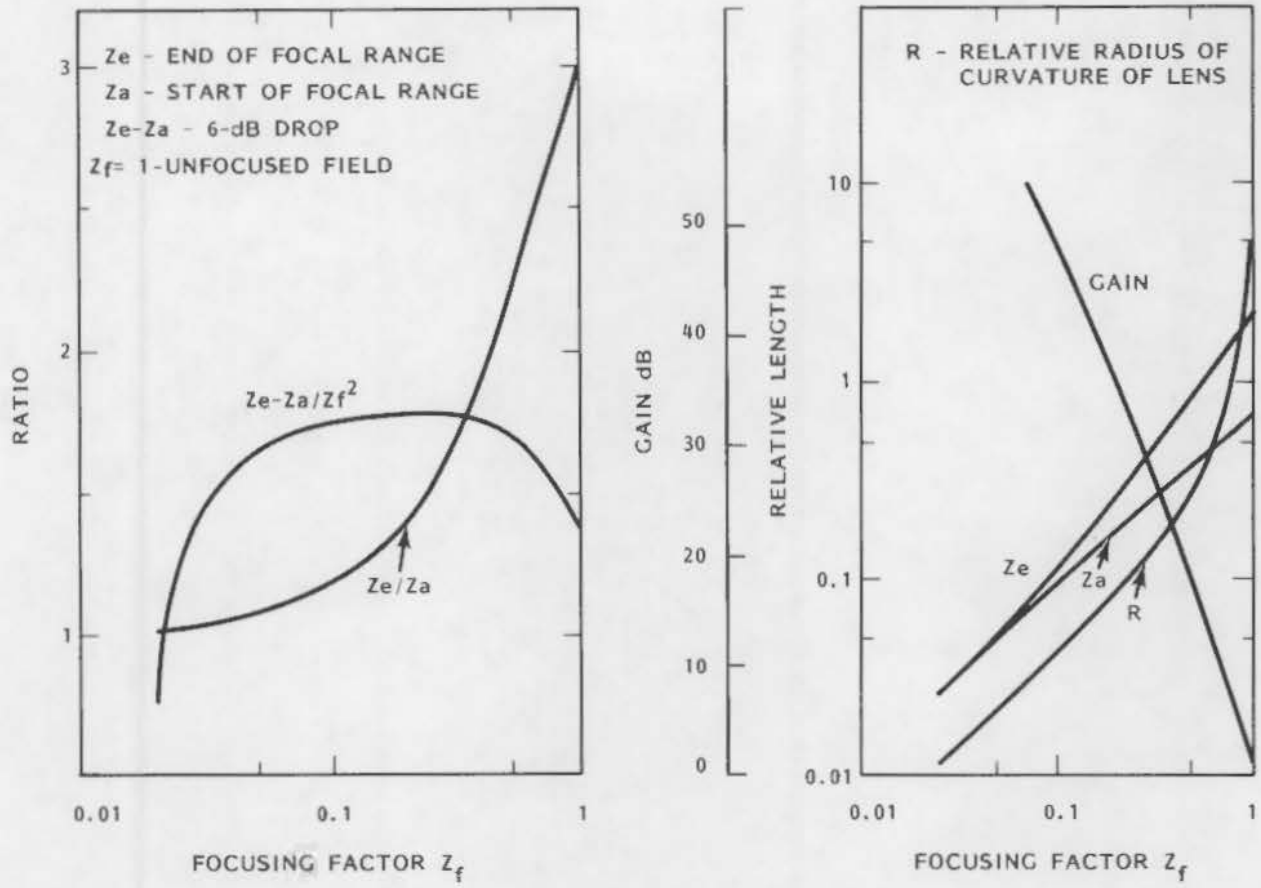

FIGURE 8.4.4. Functions of Focusing Factor

8.5 STUDY OF FLAWS

The ideal situation would be a theoretical approach generally applicable to real solids that rigorously or exactly modeled the behavior of a defect and the interaction of ultrasonic waves with the defect. An exact model would serve as a benchmark for experimental results as well as providing a basis for comparison of simpler approximate models that are less exact but much less time consuming.

As will be seen in the following discussion, most exact models suffer from one or more limitations and the approximate models are even less exact.

It is not the intent in this chapter to present the mathematical derivations relevant to theoretical studies of flaws in ultrasonic fields. Rather, the effort will be in examining the strengths and weaknesses of the various theoretical developments. The remainder of this section is divided between models of spherical defects and various planar defects.

8.5.1 Spherical Defects

Truell and coworkers[8.5.1,8.5.2,8.5.3] explored the behavior of longitudinal- and shear-waves incident on spherical defects. These defects were assumed to be cavities, rigid, liquid-filled or elastic. Table 8.5.1 summarizes some of the parameters. A spherical geometry was selected because it permitted an exact solution using spherical coordinates and partial differential equations. Outputs were scattering cross sections for the various matrix-sphere combinations. Specific combinations[8.5.3] included

A spherical cavity in matrices of Al, Be, Au, polyethylene
Al sphere in Ge
Be sphere in polyethylene
Mg sphere in stainless steel
SS sphere in magnesium.

Solutions for cross sections were based on the Rayleigh approximation for long wavelengths where $\lambda >> r$. This approximation neglects all terms higher than second order in ka in series expansions of Bessel and Hankel functions.

TABLE 8.5.1. Volumetric Defects Analyzed Theoretically

Defect	Analysis (exact or approximate)	Method	Assumptions/Comments	References
Sphere – cavity – rigid – fluid filled – elastic	Exact Also Rayleigh Long λ approximation	Spherical coordinates Partial Diff. Eq. Bessel functions	Infinite Isotropic Linear Elastic medium Long. and Shear wave Both high- and low-Frequency cases Diff. Cross Sections Calculated	8.5.1 8.5.2 8.5.3
Sphere – cavity in Ti – cavity in Al – cavity in SS – Al sphere in Ti – SS sphere in Ti	Exact and approximate (Born)	Cartesian Coor. Integral Eq. plus Born approximation	Isotropic, homogeneous elastic medium Volume of flaw bounded Incident wave is a monochromatic planar wave of given frequency and direction ($\lambda > r$) defined cross sections of spheres	8.5.4 8.5.5
Curved Interface Between Two Media	Approximate	Reciprocity Theorem; Electromagnetic theory Born approximation	Isotropic and Homogeneous Low and High Frequency ($\lambda \gtrless a$)	8.5.6
Right-cylinder Sphere	Approximate	Modified Diffraction Model; Kirchoff's Theory	Rigid Reflector Immersed in fluid medium; reflection Coefficient for particle velocity, $R = -1$	8.5.7

Gubernatis et al.[8.5.4,8.5.5] used an integral equation approach to derive exact solutions of a sphere in a matrix. Both exact solutions and solutions based on the Born approximation were obtained for the combinations cited in Table 8.5.1.

In reference 8.5.5, the authors rederived the equations of Truell and coworkers[8.5.1,8.5.2,8.5.3] and cite specific errors in some equations. See Appendices A and B of reference 8.5.5.

The work of Gubernatis et al.[8.5.4,8.5.5] is of particular interest because the authors apply both an exact and an approximate solution to the various cases of spheres in a homogeneous linearly elastic matrix. Longitudinal plane waves, shear waves polarized in the $\bar{x}$ direction, and a right circularly polarized shear wave were considered. Scattering depends on both the elastic constants and density of the flaws as well as the shape of the flaw. These parameters can be separated permitting solutions in terms of the scattering of various spherical voids as inclusions for the different waves.

The Born approximation has the advantage of simplicity; however, agreement with the various cases was poor compared to the exact solutions, primarily because the approximation does not handle strong scattering in the forward direction for large values of the wave number times the radius of the sphere. The relative agreement (or disagreement) of exact and approximate models varied with similarity of matrix-sphere properties and type of wave.

A more refined approximation is required to handle forward scattering than the Born approximation; however, this approach handles back scattering well for complex defects typical of NDE.

While the spherical inclusion does not have much fracture mechanics significance, the accurate theoretical benchmarking permits an excellent assessment of experimental errors. Work of Kino[8.5.6] using the generalized reciprocity theorem and scattering theory is another approximate method to analyze incident wave behavior when impinging on a defect. Formulas for focused and unfocused transducers generating incident beams were derived in

terms of a scattering matrix. No direct comparisons were given in terms of specific flaws. Both high and low frequencies and the near and far field were examined.

Haines and Langston[8.5.7] used a simplified model based on a modification of Kirchoff's diffraction theory to derive spherical and cylindrical geometry cases for flaws in a medium. An approximate and a simplified approximate approach were used to examine amplitude responses as a function of frequency. The limitation of the Kirchoff approach will be considered later when discussing planar flaws.

8.5.2 Planar Defects--Smooth

Planar defects represent geometries of significance from the point of view of fracture mechanics. Factors determining the relative importance of planar defects include location with respect to the surface, orientation, defect dimension, and stress field.

Most theoretical models attempting to quantify the preceding factors suffer from a variety of problems. The following discussion will attempt to place some of these factors in the proper perspective. An obvious problem for theoretical models compared to field situations is the marked difference between idealized and actual values of parameters. Table 8.5.2 is an attempt to compare differences in these parameters.

A variety of exact and approximate models have been advanced to characterize ultrasonic beam behavior with respect to planar defects. Most suffer from various limitations ranging from relatively trivial to significant. An attempt will be made to limn the strengths and weaknesses of the various models.

Table 8.5.3 presents a cross section of the theoretical models used in defining planar flaws. The contents are representative, not a complete listing. Presumably, all exact and approximate models are covered in the listing. With regard to approximate theories it is believed to cover the spectrum of approaches.

The complexity of the modeling to cover the various behaviors of ultrasonic beams can be seen in Figure 8.5.1. A relatively simple case of a

TABLE 8.5.2. A Comparison of Conditions Assumed in Most Theoretical Calculations with Worst-Case Actual Conditions

Theory-Ideal	Real-Worst Case
Smooth surface	Rough, uneven surfaces
Ideal coupling	Variable coupling
Homogeneous, Isotropic	Variable grain size; may be mixed isotropic and anisotropic in weldment
Usually stress-free	Residual stresses
Simple defect geometry	Irregular, rough
Semi-infinite volume	Variable surfaces promoting geometric reflection
Applies to wavelengths greater or lesser than flaw size	UT testing usually $\lambda \cong$ crack dimension

longitudinal-wave incident on a semi-infinite crack in an isotropic homogeneous elastic solid illustrates reflection, diffraction and mode conversion at the crack tip. Normally, the theoretical models do not handle all of these aspects, particularly if the beam is incident at an angle other than the normal.

8.5.2.1 Exact Models

Numerical solutions of exact models pose major problems because of their complexity. Integral or differential equations, when used for solution, usually require simplification such as modifying the problem to make it axisymmetric and expressing it in cylindrical coordinates. Essentially all exact solutions of planar flaws have used this approach. Wickham[8.5.9] has developed a rigorous approach using crack-type Green functions that he developed. While he[8.5.9] has developed the proof that his solution is exact, there have been no exact numerical solutions published as of early 1982. This applies to Martin[8.5.11] who used Wickham's[8.5.9] approach for a penny-shaped crack.

TABLE 8.5.3. Smooth Planar Defects Analyzed Theoretically (not complete listing)

Defect	Analysis (Exact or Approximate)	Method	Assumptions/Comments	Reference
Generic Plane-Finite	Exact	Crack Green Function	Two-dimensional line source	8.5.9
Semi-Infinite	Exact		Weak or rigid cracks	8.5.8, 8.5.15
Stri-Line	Exact		Short wavelength	8.5.15
Right Angle Surface-Breaking	Exact		Rayleigh wave assumption	8.5.15
Semi-Infinite Undulating Edge	Exact	Perturbation Theory		8.5.15
Penny-Shaped	Exact	Crack Green Functions	Point source	8.5.11, 8.5.15
Penny-Shaped	Approximate	Semi-Rigorous Electromagnetic Theory	Checked exp. $ka > 1$	8.5.12
Penny-Shaped	Approximate	Echo-dynamic model	Far field	8.5.16
Penny-Shaped	Approximate	Kirchoff	Far field	8.5.8
Flat-Bottomed Hole	Approximate	Kirchoff	Far field	8.5.7
Elliptical	Approximate	Electromagnetic Theory	Born app.	8.5.6
Elliptical	Approximate	Electromagnetic Theory Semi-Rigorous	$ka > 1$ Far field	8.5.13
Elliptical	Approximate	Echo-dynamic model	Far field	8.5.13
Half-Plane	Approximate	Optical Diffraction Theory	Focused probes	8.5.16
Fatigue Crack	Approximate	Kirchoff	Beam axis aligned with probe	8.5.15
Surface Crack	Approximate	Optical Diffraction Theory		8.5.14

Exact models and most approximate models use the same series of simplifying assumptions such as

- the solid is homogeneous, isotropic and elastic
- the ultrasonic beam is monochromatic
- the wavelength is much larger or much smaller than the flaw size
- cracks are considered to be rigid or weak to model stress-displacement relationships.

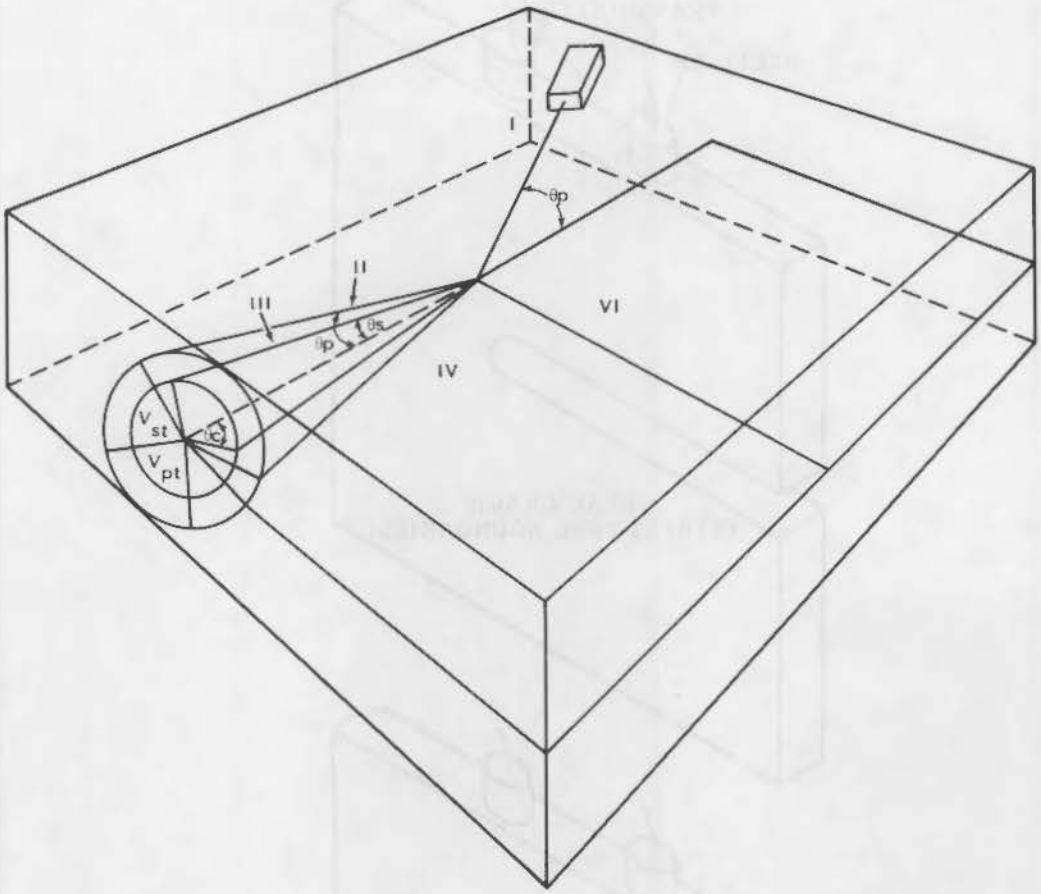

I = INCIDENT COMPRESSIONAL WAVE

II = REFLECTED COMPRESSIONAL WAVE

III = REFLECTED SHEAR WAVE

IV = DIFFRACTED COMPRESSIONAL WAVE

V = DIFFRACTED SHEAR WAVE

VI = DIFFRACTED CONICAL WAVE

VI = RAYLEIGH WAVE

θ_p = COMPRESSIONAL WAVE ANGLE OF INCIDENCE

θ_s = SHEAR WAVE ANGLE OF REFLECTION

θ_c = CRITICAL ANGLE ARCSIN (v_s/v_p)

v_p, v_s = COMPRESSIONAL AND SHEAR-WAVE SPEEDS

OX_1 = CRACK EDGE (CRACK PLANE X_1X_2)

FIGURE 8.5.1. Diffracted and Reflected Wavefronts Produced by an Incident Compressional Wave on a Half-Plane Crack. (Does not consider Lamb waves, wave guiding, multiple scattering.)

Figure 8.5.2 from Kraut[8.5.8] illustrates the rigid versus weak crack models. The rigid crack assumes zero displacement on the boundary and the weak crack assumes a stress-free boundary. Both apply to a half-plane because it is sufficiently simple to permit an exact solution. The half-plane leads to a

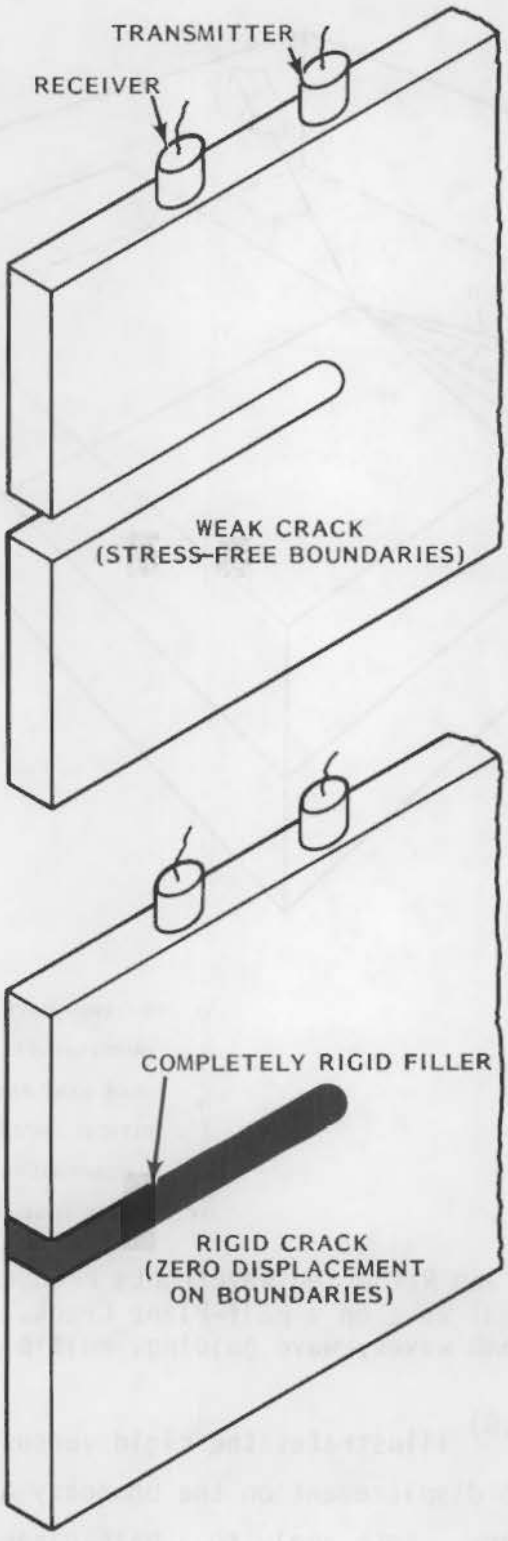

FIGURE 8.5.2. Experimental Models for Scattering and Diffraction from Stress-Free and Rigid Half-plane Cracks

decoupling of displacements parallel to the edge making the remaining problem two dimensional. More general cracks cannot be decoupled and in most instances are limited to an approximate solution.

The half-plane crack is modeled as having finite extent and vanishing thickness. In an elastic solid this simplifies to a two-dimensional region across which displacement and stress may be discontinuous. The model must handle displacements in terms of jumps across the planar crack for both displacement and stress. The end product will be an equation relating the scattered ultrasonic field to terms which define a displacement across the crack plus a stress across the crack. A numerical solution requires an assumption that either stress or displacement is fixed; hence, the rigid or weak models.

Wickham[8.5.9] discusses some of the problems inherent in exact solutions of electrodynamic scattering problems. Both longitudinal- and shear-wave motions are coupled through the boundary conditions. Sometimes an integral transform pair may be chosen that uncouples, thereby reducing the problem to one or more scalar equations; unfortunately, such simplifications often do not occur. Basically, integral transform techniques are limited to problems where the geometry can be simplified to permit a relationship to level surfaces of some curvilinear coordinate systems permitting separated solutions.

Wickham[8.5.9] argues that the need is for a technique for solving diffraction problems essentially independent of crack geometry or theory of special function. Presumably his model supplies this need.

8.5.2.2 Approximate Models

Approximate models have the advantage that numerical solutions can be obtained. Concommitant with their solution will be limitations arising from the simplifying assumptions. An attempt will be made in this section to define the pros and cons of the various approximate models. Generally, the limitations are established through a comparison with exact models.

Figure 8.5.3 attempts to compare the ranges of validity of the various models essentially all of which are approximate. As can be seen they tend to be either long or short wavelength models. The 1- to 10-MHz frequency range

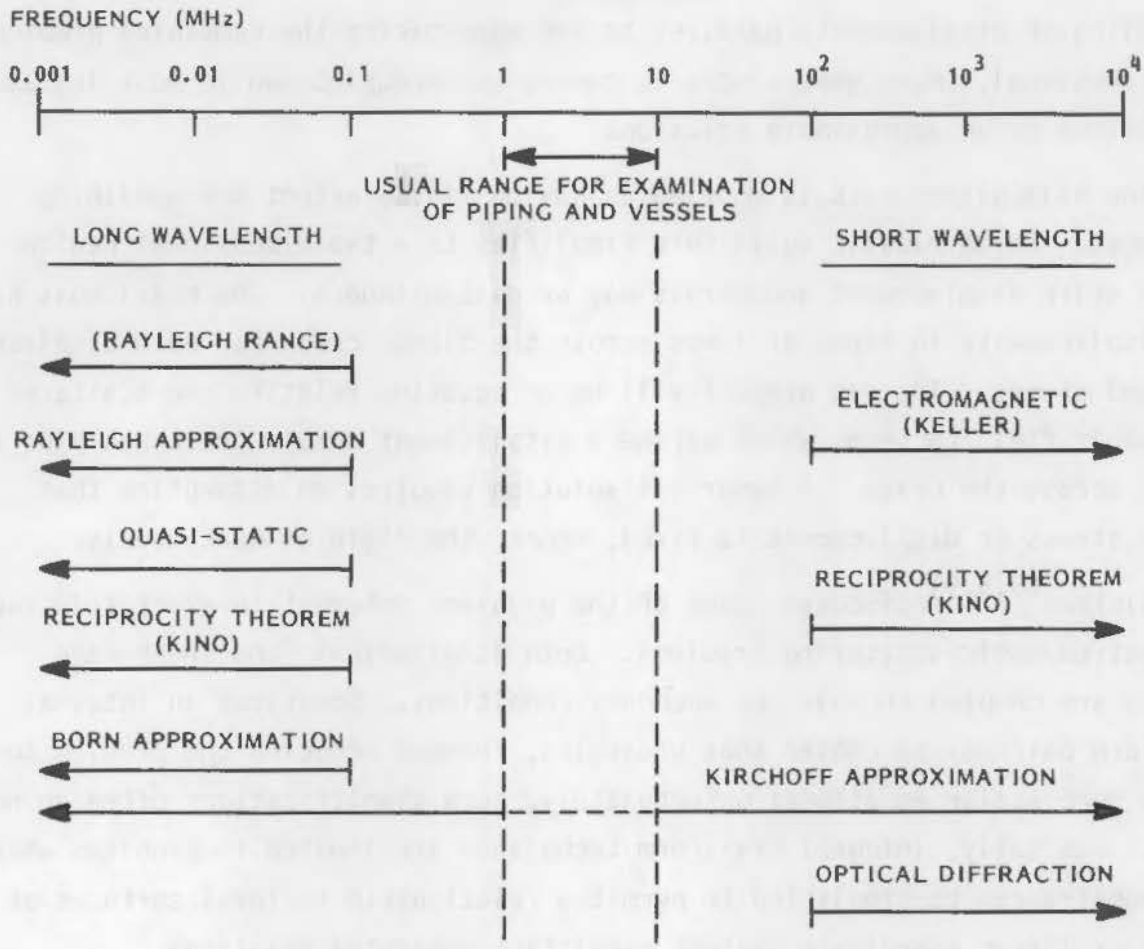

FIGURE 8.5.3. Comparison of Ranges of Validity of Various Theoretical Models in Terms of Wavelength (λ) [Frequency (ν)]

where wavelength approximates in size the flaws of interest either cannot be handled or is handled through further modifications of the various models.

Wickham[8.5.9] stresses the point that neither exact nor approximate models cover the range of major applications of ultrasonics between 1 and 10 MHz.

In the long wavelength range, most approximations are based on some aspect of the Rayleigh approximation which leads to a relatively simple relationship between frequency and defect size. Scattering will vary as the fourth power of the frequency and as the sixth power of the defect diameter. While the above represents a substantial simplification, experimental evidence conforms closely to theory.

Usually, simplifying assumptions are made for the long wavelength case such as the following for a disc-shaped crack:[8.5.8]

- The harmonic normal stress will exist only at the disc surface; displacements will be zero elsewhere on the boundary.
- Displacements are prescribed at the disc surface; stresses are zero elsewhere on the boundary.

The preceding infers that stresses are prescribed over one portion of the boundary and displacements over the remaining portions (or vice versa). This assumption leads to integral equations that can be solved.

In the short wavelength range some modifications of Keller's electromagnetic theory is used. Although theory and experiment check reasonably well, Wickham[8.5.9] argues that the electromagnetic theory suffers from a variety of limitations such as being limited to the leading order terms in a high frequency asymptotic expansion of the field or the lack of validity of the theory over all angles of observations. While various modifications have been made to Keller's theory, proof does not exist concerning its validity for various boundary-value problems.

The original geometrical electrodynamic model was known to yield physically unrealistic boundary values. A modification to a model known as the geometrical theory of diffraction corrected some of the factors; however, the refined model suffers from the problems cited by Wickham.[8.5.9]

Achenbach et al.[8.5.10,8.5.12,8.5.13] have developed the geometrical diffraction theory for scattering by cracks in elastic solids. Three-dimensional diffraction by cracks such as is illustrated in Figure 8.5.1 is applied with wave motions governed by a scalar and a vector wave equation. The modified geometrical theory of diffraction, considered valid in the high-frequency regions, uses canonical solutions for the diffraction of a plane wave by a semi-infinite crack. The model is amenable to accounting for curvature of incident wave fronts, curvature of crack edges, and finite dimensions of a crack. In this approach the diffracted field is comprised of contributions

corresponding to the primary diffracted body wave directly generated by the incident body wave and secondary diffracted body waves generated by waves travelling along the crack face.

Achenbach et al.[8.5.12] and Adler et al.[8.5.13] compared theoretical results based on the GDT theory by Achenbach et al. to experimental values. Figure 8.5.4 compares theoretical and experimental results for scattering of longitudinal waves from penny-shaped and elliptical cracks. The fit is quite good in the 1- to 5-MHz frequency range.

The third approximation model used extensively is based on modifications of Kirchoff's theory. Specific assumptions have been made concerning jumps in stress and displacement across cracks to permit direct evaluations without a rigorous solution of integral equations. Obviously such simplifications may perturb the results to a major degree. Since the Kirchoff approximation has been used extensively, an analysis of the assumptions used as well as the limitations inherent in the model was considered to be worthwhile. The following assumptions and limitations touch on some aspects of it:

- Wave function and its normal are determined entirely by the incident wave on the geometrically illuminated part of the scatterer (crack).
- Wave function and its normal derivative vanish on the dark part of scatterer.
- Scattering of elastic waves is determined by amounts by which displacement jump across a crack which is numerically equal to the corresponding values of the incident wave at the illuminated surface of the crack.
- Kraut argues the Kirchoff approximation is a poor substitute for rigorous diffraction theory because it does not correctly describe the field in the vicinity of the scatterer and in the long wavelength limit.
- The Kirchoff approximation is poor in the Rayleigh range.
- It usually assumes rigid reflectors in fluid medium. The reflection coefficient $R = -1$.

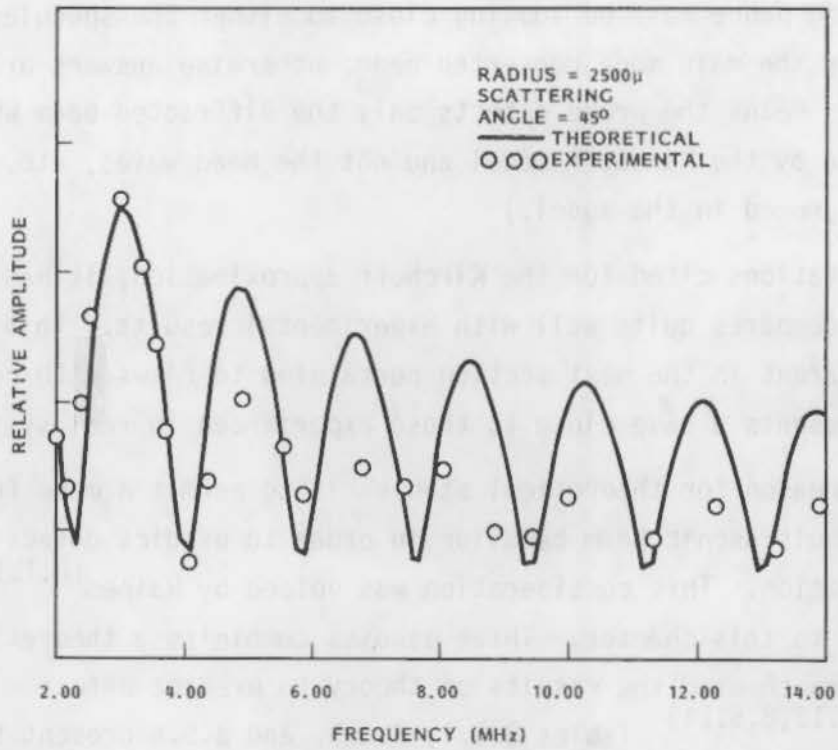

FIGURE 8.5.4a. Amplitude Spectrum of Diffracted Longitudional Wave

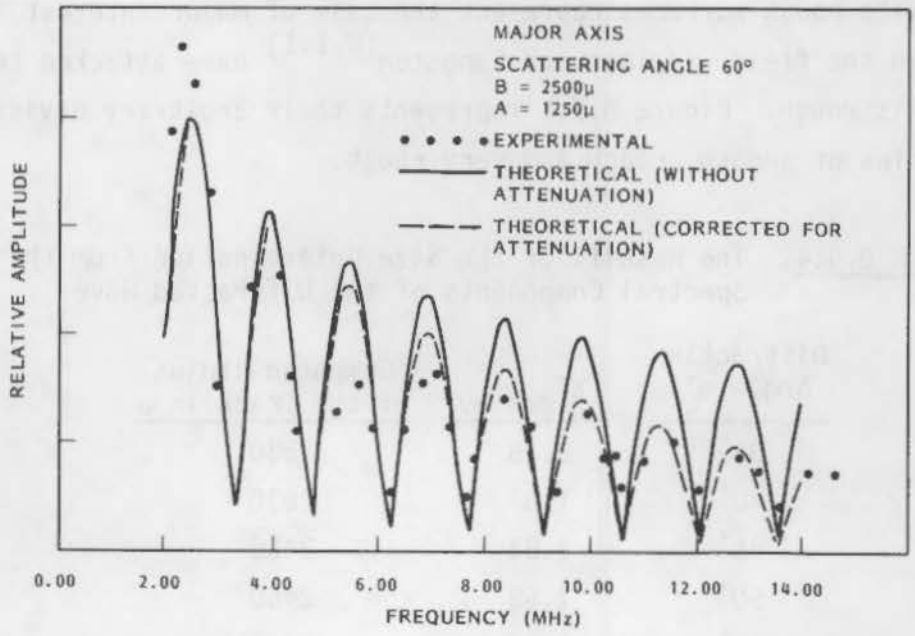

FIGURE 8.5.4b. Longitudional Wave Scattering from an Elliptical Crack with Attenuation Correction

- The receiving probe must be looking close to either the specularly reflected or the main mode converted beam; otherwise answers are poor. (This means the probe detects only the diffracted beam which is predicted by the Kirchoff model and not the head waves, etc., which are ignored in the model.)

Despite the limitations cited for the Kirchoff approximation, it has been used extensively and compares quite well with experimental results. This will become quite apparent in the next section pertaining to flaws with rough surfaces which represents a case close to those experienced in real systems.

An obvious reason for theoretical studies is to permit a more fundamental understanding of ultrasonic beam behavior in order to predict defect size, shape and orientation. This consideration was voiced by Haines[8.1.1] in the introduction to this chapter. Three studies combining a theoretical and experimental approach used the results of theory to predict defect size.[8.5.12,8.5.13,8.5.14] Tables 8.5.4, 8.5.5, and 8.5.6 present these data.

8.5.3 Planar Flaws--Rough Surfaces

Cracks with rough surfaces represent the case of major interest in comparing systems in the field. Haines and Langston[8.1.1] have attacked the problem of how rough is rough. Figure 8.5.5 represents their arbitrary division into three categories of smooth, rough and very rough.

TABLE 8.5.4. The Results of the Size Determination from the Spectral Components of the Diffracted Wave

Diffraction Angle θ_L'	$(\Delta f_{max})_{av}$	Computed Radius of the Crack in μ
35°	2.18	2530
40°	1.87	2630
45°	1.83	2450
50°	1.68	2460
55°	1.60	2410
60°	1.47	2500
65°	1.39	2510

TABLE 8.5.5. Determination of Major (b) and Minor Axis (a) of Elliptical Cracks in Titanium from Scattered Amplitude

	Spectra			
Aspect Ratio	(b) Major axis (μ) Actual	Measured	(a) Minor Axis (μ) Actual	Measured
1	2500	2498	2500	2498
2	2500	2587	1250	1291
4	2500	2358	625	830
8	2500	--	312	285

TABLE 8.5.6. Comparison of Estimated and "Actual" Crack Radius, a

Experimental Conditions	Diffraction Order	Angular Positions of Nulls (degrees) Obs.	Theor.	Estimate of a (μm)	Mean Estimate of a (μm)	"Actual" Size of a (μm)[a] (1 mil = 25.4 μm)
100-MHz Silicon nitride with indentation crack	n = 1	9	8	87		
	n = 2	17	16	92	93 ± 4	100 ± 3
	n = 3	25	24	96		
	n = 4	34	33	97		
2.2-MHz Commercial rolled aluminum with spark erosion slot	n = 1	16	16	1170		
	n = 2	35	33	1130	1160 ± 20	1190 ± 20
	n = 3	55	54	1180		
5.0-MHz Duraluminum with indentation slot	n = 1	10	9	866		
	n = 2	19	18	897	880 ± 16	900 ± 25
	n = 3	30	28	877		

(a) Determined by micrographical examination of crack outline on sample surface.

All studies have been based on some approximation of one or more theories. The paper by deBilly et al.[8.5.17] used electromagnetic scattering theory discussed in the planar cracks section. Haines,[8.5.18] Haines and Langston,[8.1.1,8.5.7] and Coffey[8.5.15] used the Kirchoff approximation.

$\bar{\sigma}$ = rms SURFACE ROUGHNESS PERPENDICULAR TO SURFACE OF DEFECT

TYPE 1. SMOOTH DEFECT $\sigma < \frac{\lambda}{20}$ (80 μm FOR 2-MHz SHEAR)

TREAT AS SMOOTH DEFECT AND APPLY ATTENUATION FACTOR DEPENDENT ON $(\frac{\sigma}{\lambda})$

TYPE 2. ROUGH DEFECT $\frac{\lambda}{20} < \sigma < \frac{\lambda}{5}$ (80 → 320 μm FOR 2-MHz SHEAR)

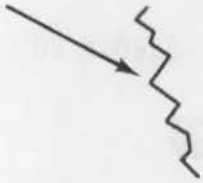

TREAT AS SYSTEM OF INDIVIDUAL REFLECTING FACETS

TYPE 3. VERY ROUGH DEFECT $\sigma > \frac{\lambda}{5}$ (>320 μm FOR 2-MHz SHEAR)

FIGURE 8.5.5. Categories of Defects According to Surface Roughness

By using electromagnetic diffraction theory applied to both smooth and rough surfaces, deBilly et al.[8.5.17] were able to separate the roughness effect. Figure 8.5.6 presents the difference in pulse-echo spectrum for smooth and rough cracks.

A problem with reference 8.5.17 is that it developed the theoretical basis; however, no direct comparison is made between theory and experiment.

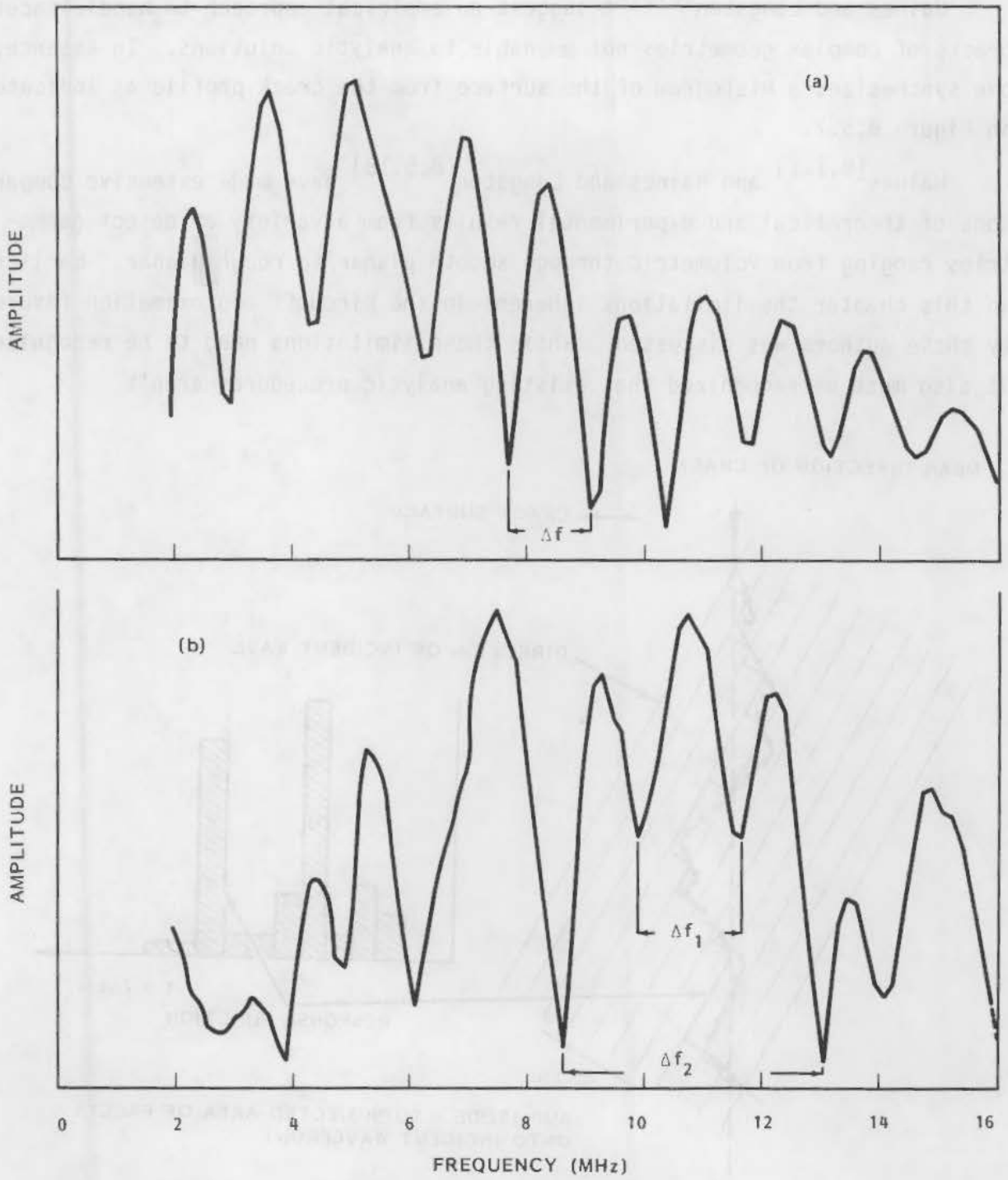

FIGURE 8.5.6. Difference in Pulse-Echo Spectrum: (a) 45° Pulse-echo Spectrum From a Smooth Crack; (b) 55° Pulse-echo Spectrum From a Rough Crack

Haines and Langston[8.5.7] suggest an empirical approach to handle faceted cracks of complex geometries not amenable to analytic solutions. In essence, one synthesizes a histogram of the surface from the crack profile as indicated in Figure 8.5.7.

Haines[8.1.1] and Haines and Langston[8.5.18] have made extensive comparisons of theoretical and experimental results from a variety of defect geometries ranging from volumetric through smooth planar to rough planar. Earlier in this chapter the limitations inherent in the Kirchoff approximation favored by these authors was discussed. While these limitations need to be recognized it also must be recognized that existing analytic procedures aren't

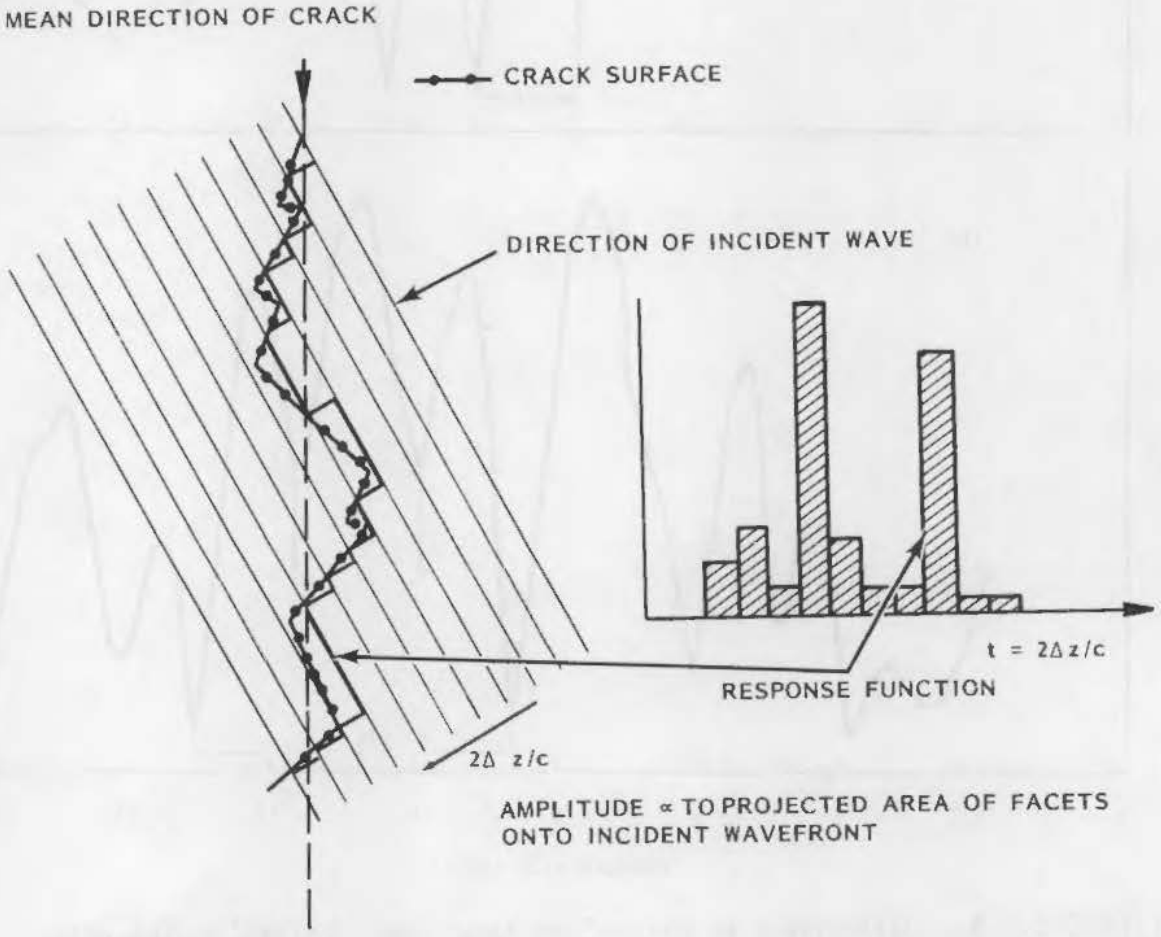

FIGURE 8.5.7. Schematic Geometry Construction of Response Function for a Faceted Crack Surface. An approach to handling geometries having no analytic solution.

particularly amenable to handling irregular cracks. The following will discuss work of the authors[8.1.1,8.5.18] relevant to predicting tilt and skew of planar surfaces. Figure 8.5.8 defines tilt and skew related to UT-beam angle on the flaw surface. As noted, Figure 8.5.8a pertains to pulse echo and Figure 8.5.8b to a technique such as tandem. The separate effects of tilt angle and skew angle can be seen in Figure 8.5.9. Frequency and transducer size can play a role as seen in Figure 8.5.10 where 2 MHz and 4 MHz are compared for two transducer sizes. The preceding curves were derived from theoretical and experimental measurements using flat-bottom holes or discs as the bases for analysis.

Figure 8.5.11 compares theoretically predicted curves for 2.25-MHz longitudinal (a) and shear waves (b) for a spectrum of roughnesses ranging from <5 to 500 μm as functions of angle of tilt. Figure 8.5.12 permits a direct comparison of theoretically derived curves for two levels of roughness (<5-μm and 41-μm RMS) with experimentally measured amplitudes as functions of tile angle. Correlations appear to be good over the range measured.

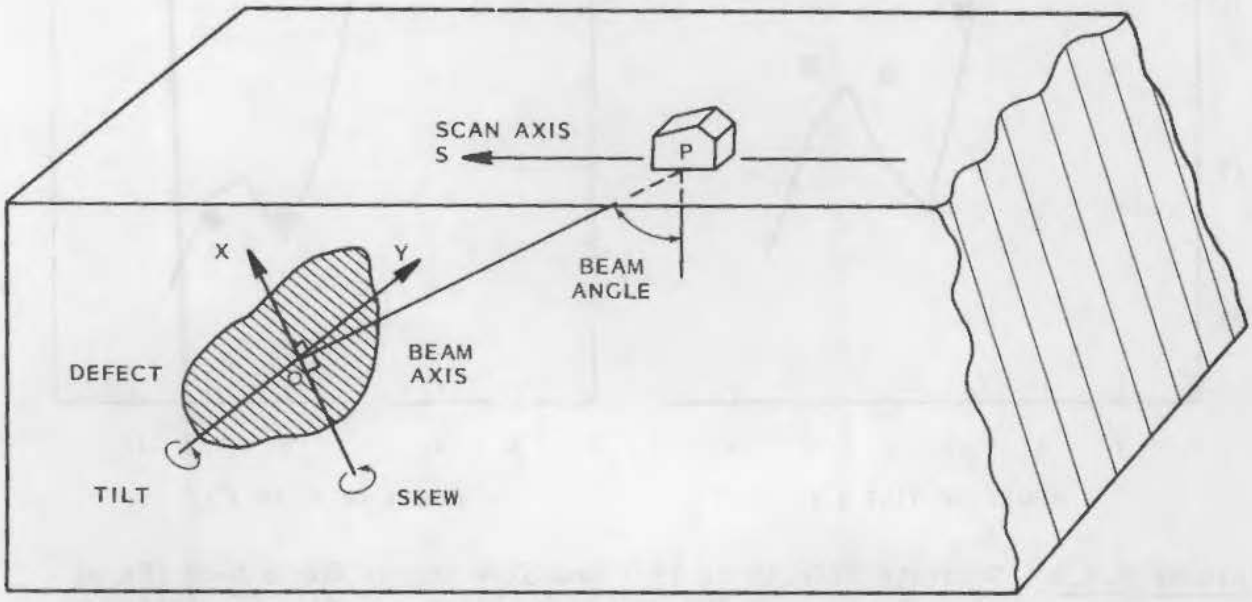

PULSE-ECHO CASE OX, OY, AND OP. THE BEAM AXIS ARE MUTUALLY ORTHOGONAL WITH OY PARALLEL TO THE TEST SURFACE

FIGURE 8.5.8. Definition of Angles of Tilt and Skew

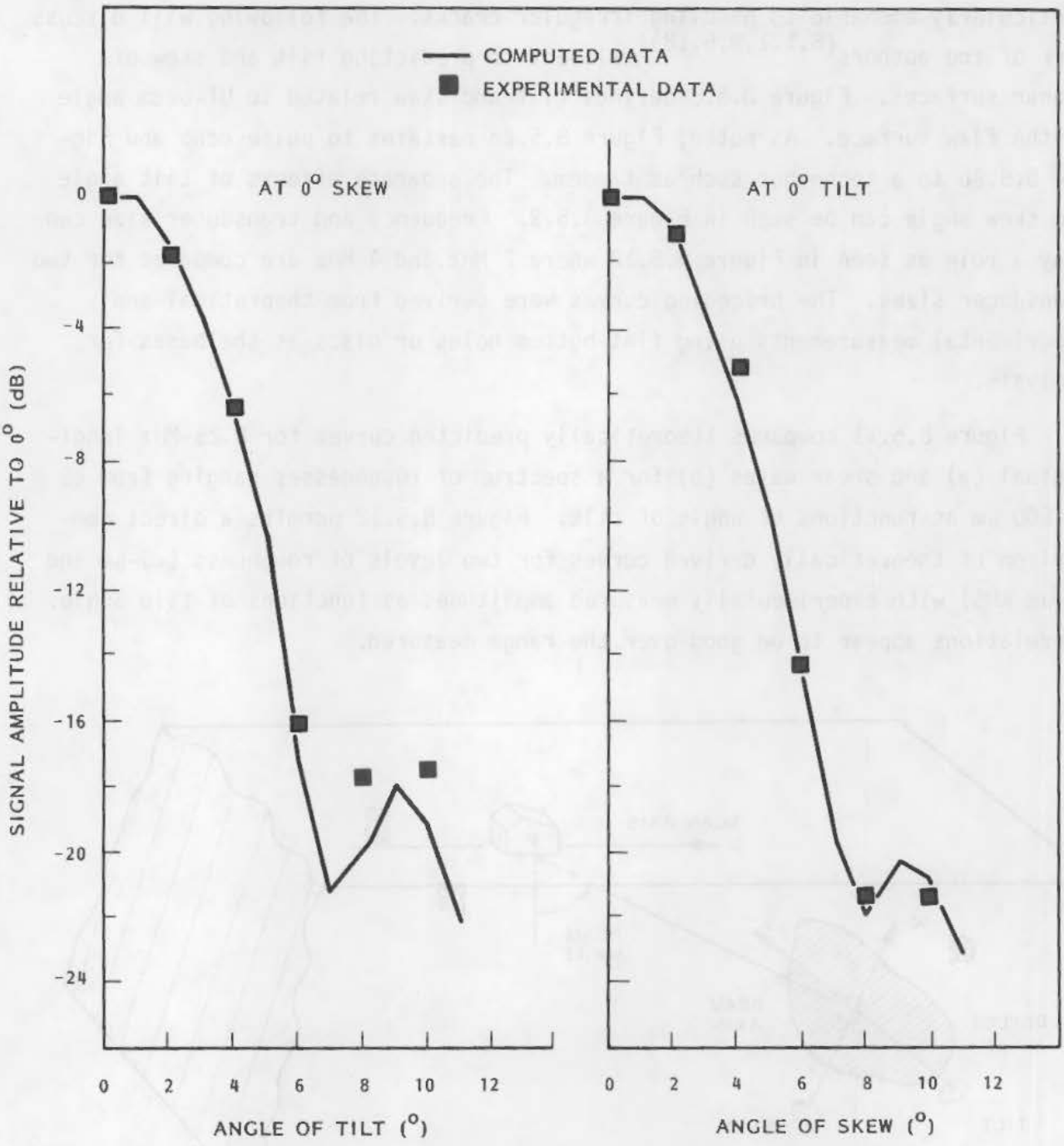

FIGURE 8.5.9. Separate Effects of Tilt and Skew Angles for a 6-mm FBH at 65-mm Depth in a 100-mm Block, Using a 4-MHz, 45° Tandem System

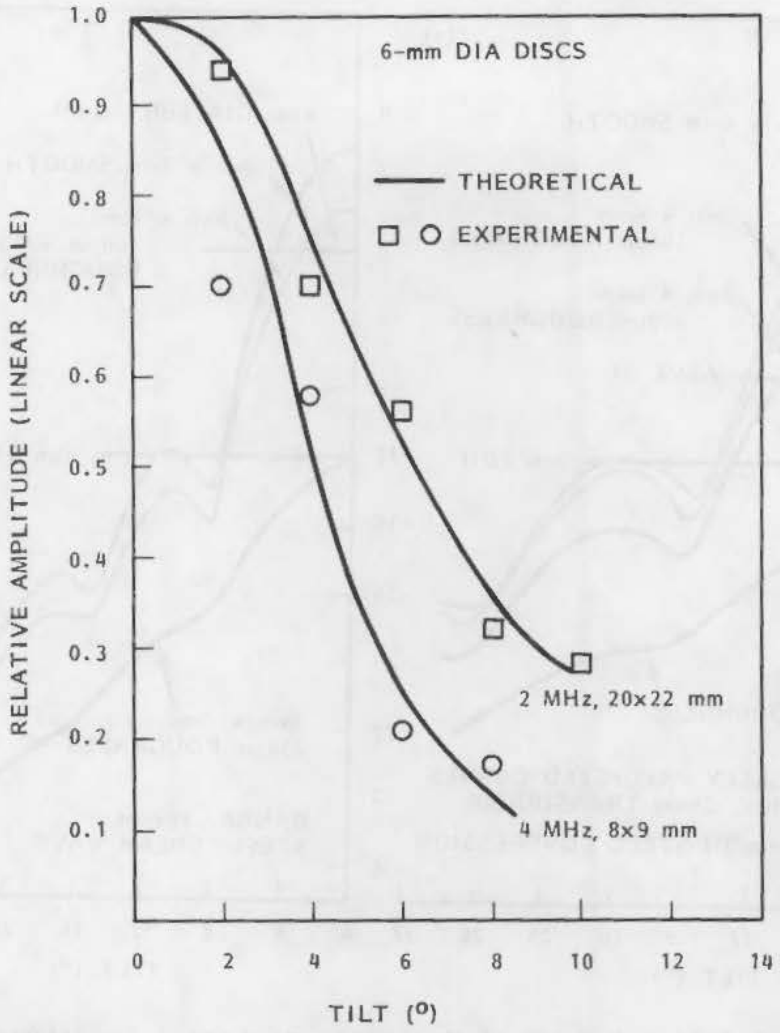

FIGURE 8.5.10. Effect of Tilt on Signal Amplitude

It would be interesting to have the rigorous approach developed by Wickham[8.5.9] or the same approach applied to the penny-shaped crack[8.5.3] directly compared to the theoretical and experimental results of Haines[8.1.1] for discs or flat-bottom holes to establish the level of a difference of the exact compared to the approximate approach. Presumably a later paper by Martin[8.5.11] may provide such values.

Coffey[8.5.15] discusses some aspects of Kirchoff theory as it might be applied to rough cracks. He modified early work using Kirchoff theories as applied to radar and sonar, where a vast literature exists, to the case of a UT beam impinging on a rough crack. His modifications consisted of

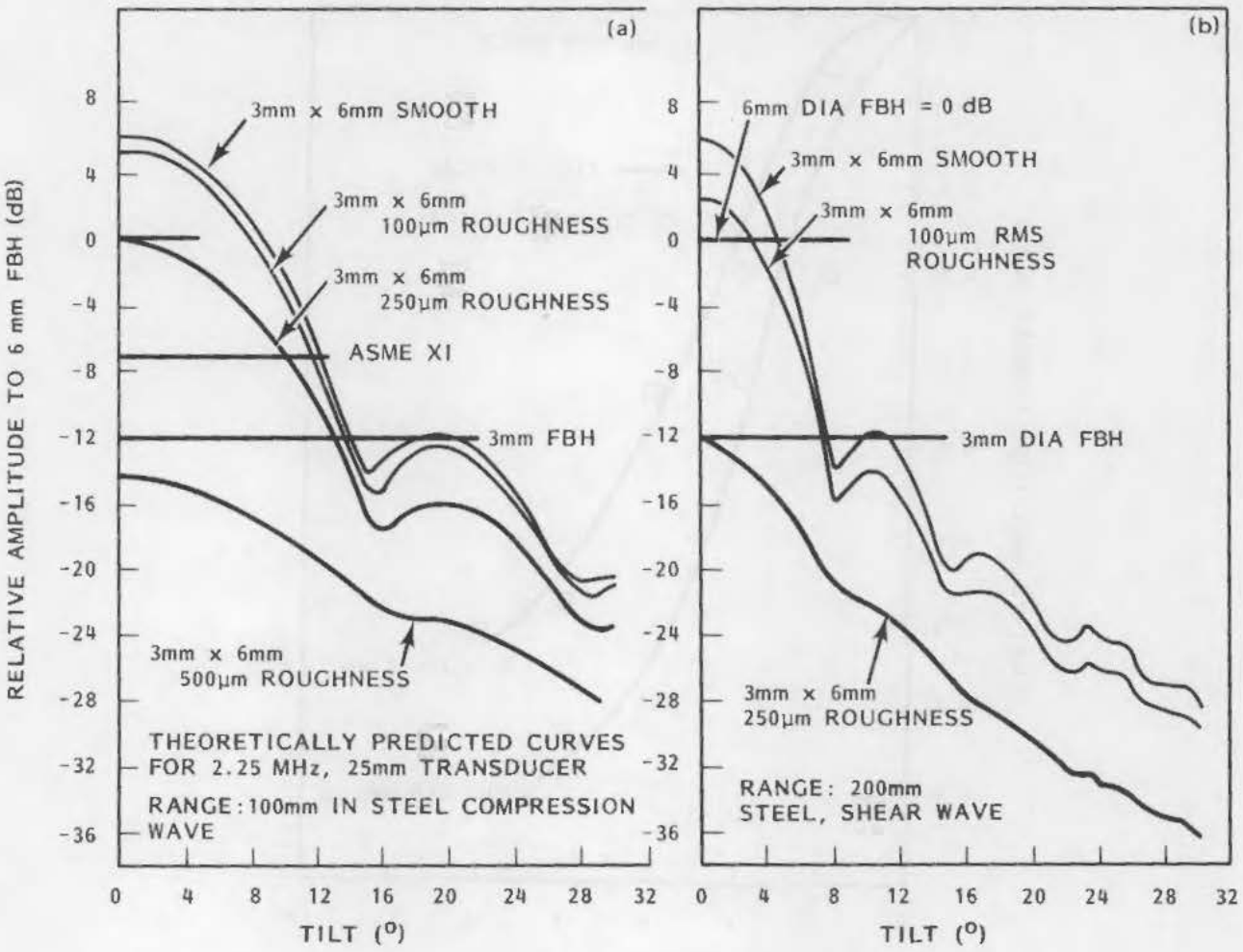

FIGURE 8.5.11. Effect of Roughness of Signal Amplitude: (a) compression wave, (b) Shear Wave

- introducing a finite beam at some arbitrary angle of incidence rather than a very wide beam at normal incidence
- allowing the reflecting surface to be finite rather than infinite.

The following are assumptions inherent in his model:

- The surface is sufficiently rough to have sufficient independent reflecting facets in the beam for the Control Limit Theorem to hold. Therefore, the scattered field will have a Gaussian two-position distribution function.

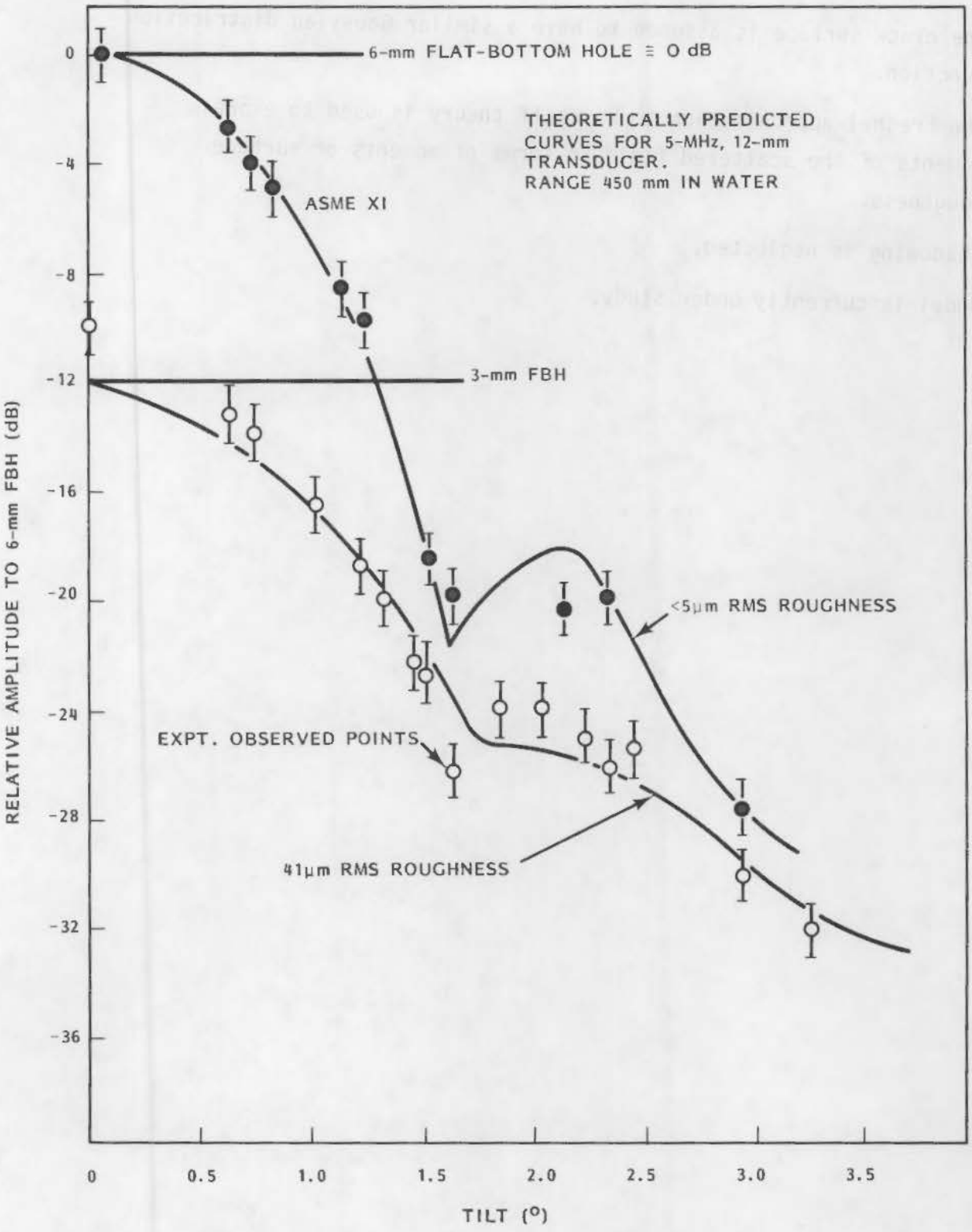

FIGURE 8.5.12. Experimental Compared to Theoretical Results on Rough and Smooth 6-mm Dia Discs

- The crack surface is assumed to have a similar Gaussian distribution function.
- The Fresnel approximation to Kirchoff theory is used to express moments of the scattered field in terms of moments of surface roughness.
- Shadowing is neglected.

This model is currently under study.

8.6 REFERENCES

8.1.1 Haines, N. F. and Langston, D. B., "Progress Report on BNL PWR Inspection Work." BM/AP/189/81, CEGB-BNL, Central Electricity Generating Board, London, England, April 1981.

8.2.1 Erhard, A., et al., "The Influence of the Coupling Layer on the Sound Transmission in Ultrasonic Testing with Inclined Beam." Materialprüf 18(9):312-316, 1976 (in German).

8.3.1 Atthey, D. R., "The Propagation of Elastic Waves Through a Textured Granular Material." RD/M/N1102, Central Electricity Generating Board, London, England, November 1980.

8.3.2 Rose, J. L., Rogovsky, A. J. and Wieser, P., "Austenitic Stainless Steel Casting Inspection Potential," Ultrasonic Materials Characterization. NBS SP-596, H. Berger and M. Linzer, eds., Proceedings of 1st International Symposium on Ultrasonic Materials Characterization, National Bureau of Standards, U.S. Government Printing Office, Washington, D.C., pp. 541-550, November 1980.

8.4.1 Legge, R. D., "Frequency Characteristics of Ultrasonic Pulses Used for Flaw Detection." Proceedings of Conference on Ultrasonics for Industry, pp. 31-36, 1970.

8.4.2 Wüstenberg, H, Kutzner, J. and Engl, G., "Dependence of Echo Amplitude on Defect Orientation in Ultrasonic Examinations." Paper 3H-4, 8th World Conference on Nondestructive Testing, Butterworth Scientific Ltd., Surrey, England, 1976.

8.4.3a Wüstenberg, H. and Schulz, E., "Influence of the Membrane Size and Form on the Sound Field of Angle Probes." BAM 6.21, Bundesanstalt für Materialprüfung, Berlin, Germany, May 1977.

8.4.3b Wüstenberg, H., et al., "The Choice of Transducer Forms of Angle Probes for Ultrasonic Inspection." Materialprüf 18(7):223-230, 1976 (in German).

8.4.4 Schlengermann, U., "The Focused Sound Field--A Versatile Tool for Ultrasonic Evaluation of Materials," Ultrasonic Materials Characterization. NBS SP-596, H. Berger and M. Linzer, eds., Proceedings of 1st International Symposium on Ultrasonic Materials Characterization, National Bureau of Standards, U.S. Government Printing Office, Washington, D.C., pp. 271-283, November 1980.

8.4.5 Posakony, G. J., "Summary Paper - Measurement of Operating Parameters of Ultrasonic Transducers." unpublished, 1982.

8.5.1 Ying, C. F. and Truell, R., "Scattering of a Plane Longitudinal Wave by a Spherical Obstacle in an Isotropically Elastic Solid." J. Appl. Phys. 27(9):1086-1097, September 1956.

8.5.2 Einspruch, N. G., Witterholt, E. J. and Truell, R., "Scattering of a Plane Transverse Wave by a Spherical Obstacle in an Elastic Medium." J. Appl. Phys. 31(5):806-818, May 1960.

8.5.3 Johnson, G. and Truell, R., "Numerical Computations of Elastic Scattering Cross Sections." J. Appl. Phys. 36(11):3466-3475, November 1965.

8.5.4 Gubernakis, J. E., Domany, E. and Krumhansl, J. A., "Formal Aspects of the Theory of the Scattering of Ultrasound by Flaws in Elastic Materials." J. Appl. Phys. 48(7):2804-2811, July 1977.

8.5.5 Gubernatis, J. E., et al., "The Born Approximation in the Theory of the Scattering of Elastic Waves by Flaws." J. Appl. Phys. 48(7):2812-2819, July 1977.

8.5.6 Kino, G. S., "The Application of Reciprocity Theory to Scattering of Acoustic Waves by Flaws." J. Appl. Phys. 49(6):3190-3199, June 1978.

8.5.7 Haines, N. F. and Langston, D. B., "The Reflection of Ultrasonic Pulses from Surfaces." J. Acoust. Soc. Am. 67(5):1443-1454, May 1980.

8.5.8 Kraut, E. A., "Review of Theories of Scattering of Elastic Waves by Cracks." IEEE Trans. Sonics Ultrason. SW-23(3):162-167, May 1976.

8.5.9 Wickham, G. R., "The Diffraction of Stress Waves by a Plane Finite Crack in Two Dimensions: Uniqueness and Existence." Proc. R. Soc. London A378, pp. 241-261, 1981.

8.5.10 Achenbach, J. D. and Gautesen, A. K., "Geometrical Theory of Diffraction for Three-D Elastodynamics." J. Acoust. Soc. Am. 61(2):413-421, February 1977.

8.5.11 Martin, P. A., "Diffraction of Elastic Waves by a Penny-Shaped Crack." Proc. R. Soc. London A378, pp. 241-261, 1981.

8.5.12 Achenbach, J. D., et al., "Diffraction of Ultrasonic Waves by Penny-Shaped Cracks in Metals: Theory and Experiment." J. Acoust. Soc. Am. 66(6):1848-1856, December 1979.

8.5.13 Adler, L and Achenbach, J. D., "Elastic Wave Diffraction by Elliptical Cracks: Theory and Experiment." J. Non-Dest. Eval. 1(2):87-99, 1980.

8.5.14 Tittman, B. R., et al., "A Simple Approach to Estimate the Size of Small Surface Cracks with the Use of Acoustic Surface Waves." Appl. Phys. Lett. 33(1):6-8, January 7, 1978.

8.5.15 Coffey, J. M. and Chapman, R. K., "Some Technical Aspects of NDTAC Research Jobs, ZE 133, ZE 300, ZE 301." Internal report, Central Electricity Generating Board, London, England, April 1981.

8.5.16 Certo, M., "Results of a Literature Survey on the Problem of the Influence of Defect Position and Geomtry on the Ultrasonic Echo Signals." CISE-NT 81.111, Commission of the European Communities, Brussels, Belgium, 1981.

8.5.17 deBilly, M., et al., "Ultrasonic Evaluation of Geometrical and Surface Parameters of Rough Defects in Solids." J. Non-Dest. Eval. 1(4):249-261, 1980.

8.5.18 Haines, N. F., "The Reliability of Ultrasonic Inspection." International Symposium on Applications of Reliability Technology to Nuclear Power Plants, Vol. II, International Atomic Energy Agency, Vienna, Austria, pp. 341-357, October 10-13, 1977.

CHAPTER 9

NDE—FOR MEASUREMENT OF PHYSICAL AND MECHANICAL PROPERTIES

CONTENTS

FIGURES

TABLES

CHAPTER 9

NDE--FOR MEASUREMENT OF PHYSICAL AND MECHANICAL PROPERTIES

9.1 INTRODUCTION

This chapter will concentrate on measurement of material properties and characteristics, other than flaws. Techniques based on magnetic properties, such as Barkhausen Noise Analysis (BNA), Mossbauer Effect, ultrasonics, X-ray, etc., are used to determine residual stress, grain size, surface hardness, bulk tensile properties, cold work, radiation damage, fatigue damage, values of elastic and compliance constants (both second- and third-order), etc. Chapter 9A presents mathematical derivations relevant to property measurement.

Where possible the reliabilities and limitations of the various techniques, as well as their current status, are assessed. Table 9.1.1 is an attempt to place the various techniques into perspective insofar as the status of development at this time is concerned.

Vary[9.1.1] reviewed the literature pertinent to mechanical and physical properties where ultrasonics have been used or have the potential of being used to measure these properties. Table 9.1.2 contains examples of material properties and characteristics that according to Vary[9.1.1] can be nondestructively evaluated. Table 9.1.3 expands on the properties cited in Table 9.1.2 by indicating the ultrasonic property measured and applications by type and class of material. In some instances, the literature is fairly extensive; in others, there are virtually no data. Not included on Vary's[9.1.1] lists are elastic constants, and this is the area where most of the NDE work covered in this chapter has been done.

TABLE 9.1.1. Capabilities and Limitations Inherent in Techniques Used to Measure Residual Stresses

Technique	Requirements: Surface	Requirements: Embedded Radioactive Sources	Limitations: Materials	Limitations: Geometry	Residual Stress: Absolute	Residual Stress: Relative	Residual Stress: Surface Only 1 to 2 Mils	Residual Stress: Various Depths	Status	Accuracy	Precision	Remarks
X-ray Diffraction	Smooth and Clean	No	No	Limited to relatively simple geometries	X		X		U	±10 KSI	High	Preferred orientation causes difficulties; interpretation problems.
Ultrasound												
Dispersion	Smooth	No				X		X	P	~5% Y.S.	?	Basis--anharmonic properties; changes of velocity with frequency.
Shear-Wave Birefringence				Thickness ~0.25-3.0 in.		X		X	P	~5% Y.S.	?	Uses velocity measurements.
Harmonic Generation Tomography						X			L	~10% Y.S.	?	
Electromagnetic												
Barkhausen Noise Analysis	Not critical	No	Only ferromagnetic	Not limiting		X	X		P→U	?	?	Requires calibration.
Variable Frequency Permeability Measurement Method			Only ferromagnetic					X	L			
Real-Time Analysis of Magnetic Material Parameters (RAMMP)			Only ferro magnetic					X	B			
UT Generation Efficiency Method						X	X		L	?	?	Changing frequency will increase depth.
Magnetic Retentivity			Only ferromagnetic						L	?	?	
Direct AC Measurement of Magnetostriction	Not Critical	No	Only ferromagnetic	Can handle by calculation		X		X	C			
Magnetoabsorption						X			B			Stress to ±50 KSI.
Nuclear Hyperfine												
Nuclear Magnetic Resonance		No	Non-magnetic or strong magnetic				X		L	?	1 to 2 KSI	Requires homogeneous magnetic field.
Acoustic NMR (NAR)									L	?	1 to 2 KSI	High magnetic field.
Nuclear Quadrupole Resonance (NQR)							X		L	?	1 to 2 KSI	Need sufficient number of quadruple nuclei.
Acoustic NQR (AQR)									C	?	1 - ±2 KSI	
Nuclear Magnetic Resonance in Ferromagnetics (FNR)			Ferromagnetic						C→I	?	?	
NMR-Diffraction (zeugmatography)							X		C→L	?	1 to 2 KSI	As NMR
Mossbauer Effect	Not critical	Yes				X	X					Sensitive to vibration.
Scattering			Steel (Ferromagnetic)						P-U	±5 KSI	±5 KSI	Requires specially shaped probes; also cannot be used in Ti, Al, etc.
Source									L	?		
Perturbed Angular		Yes	No limitation			X		X	C→L	?		
Conventional												
Strain Gages									U			Standard to compare to
Overlay Grids									U			
Other												
Positron Annihilation												
Laser Speckle?									L			

Status: C - Conceptual L - Lab Confirmation B - Breadboard P - Prototype U - Used in Production

TABLE 9.1.2. Examples of Material Properties and Characteristics That Can Be Nondestructively Evaluated

Mechanical Properties
Tensile Modulus
Shear Modulus
Tensile Strength
Yield Strength
Shear Strength
Fracture Toughness
Hardness

Metallurgical Factors
Microstructure
Grain Size
Phase Composition
Porosity
Inclusions
Hardening Depth
Residual Stress
Heat Treatment
Anisotropy

TABLE 9.1.3. Capabilities of Ultrasonics for Nondestructive Evaluations of Material Properties

Material Property	Ultrasonic Measurement	Applicable Materials
Longitudinal Modulus	Longitudinal velocity	Most engineering solids
Shear Modulus	Transverse velocity	Most engineering solids
Grain Size, Microstructure	Attenuation, acoustic microscopy	Polycrystalline metals, ceramics
Porosity, Void Content	Velocity, attenuation	Fiber composites, ceramics
Hardness or Hardness gradient	Velocity, velocity dispersion	Polycrystalline metals
Tensile Strength	Velocity, stress-wave attenuation	Brittle metals, ceramics, fiber composites
Yield Strength	Frequency-Dependent attenuation	Polycrystalline metals
Fracture Toughness	Frequency-Dependent attenuation	Polycrystalline metals
Bond Shear Strength	Resonance, spectrum analysis	Metal-Metal adhesive bonds
Interlaminar Shear Strength	Attenuation, stress-wave attenuation	Fiber composites

9.2 RESIDUAL STRESSES

The determination of residual stresses, either analytically or experimentally, needs to be related to a given set of parameters such as materials used, geometries of concern, critical location of stresses (inner surface, outer surface, etc.), absolute versus relative stresses, etc. Otherwise, one begins to wade into the problem of measuring stresses and strains and soon is embedded in a morass of techniques with conflicting claims concerning applicability, accuracy, precision, limitations, etc.

The needs for residual stress measurements in the nuclear reactor field are more than sufficient to exceed the capabilities of any single system, and probably, any combination of systems. In this respect the following listing of parameters covers some, but not all, of the factors one should consider:

- Materials--ferritic steels, austenitic steels, nickel alloys, martensitic stainless steels--fortunately, these are all face-centered on body-centered cubics which helps considerably as noted later.
- Geometries--cylindrical such as piping and pressure vessel shell regions as well as complex such as nozzle regions.
- Residual Stress Generators--the source of primary interest is the weldment; others such as forming operations tend to be of secondary interest in a generic sense; however, uncontrolled forming can be a very real problem on an individual plant basis.
- Location of Critical Residual Stresses--primarily on the inner surfaces of austenitic piping where stress contributes to intergranular stress corrosion cracking; may be important in pressure vessel welds on either surface.
- Need for Absolute versus Relative Stresses--while absolute stresses would be desirable, relative stresses in the context of percentage increases tied to the material tensile properties probably are sufficient.

Examples of the above requirements applied to specific systems that are relevant to nuclear plants follow:

- Butt-Welded Stainless Steel Piping--needs three-dimensional plots through the depth of wall as functions of distance from the weld in axial, transverse and circumferential directions. The existing technique is X-ray which yields surface values only. No technique exists for absolute values greater than five mils below the surface. Strain gages give average stress values to greater depths; however, the two techniques are not comparable. X-ray will pinpoint and localize the stress measurement. It will not give the stress gradient which often is wanted.

- Welded Ferritic Steel Plates and Cylinderical Forgings in Pressure Vessels with Wall Thickness of >2 to 12 Inches--stress profiles through the wall thickness adjacent to the welds is desired, particularly with regard to weld repairs made in the field. X-ray will yield surface values, as will rosettes of strain gages applied before welding, or hole drilling after welding. Ultrasonic tomography and other time-of-flight techniques are being investigated for through-thickness stress.

- Large Inset Ferritic Steel Nozzles With Stainless Steel Clad--such as those used in reactor pressure vessels have stress problems at the welds and thermally induced stress cracking in the nozzle itself. No reliable techniques exist for determining these stresses.

The point must be made that residual stresses due to welding and fitup may be extremely difficult to measure precisely due to the rapid shift in stress over a relatively short distance; e.g., in longitudinal direction the surface stress may vary from 50 to 70 ksi tensile ~0.1 in. from weld to ~50 ksi compression 0.3 to 0.4 in. away. This means an accurate measurement and an inaccurate positioning will yield highly ambiguous results.

Another perturbation that has not been examined very extensively is the possibility that the circumferential patterns may vary due to differences in

the welding--downhand, vertical up, vertical down, uphand, etc. Any azimuthal changes in circumferential stress will probably change the longitudinal stress pattern of that azimuth.

The above will affect any of the techniques used to measure residual stress.

The original concerns with residual stresses pertained to their beneficial effects such as surface compressive stresses introduced by shot peening to prevent or delay fatigue crack initiation, or deleterious effects such as extremely high levels of bulk stress introduced by quenching. Of more interest in the nuclear field is the problem of high residual stresses developed during welding of components such as piping. Another situation of concern exists with weld repair of vessels where postweld heat treatment is not feasible. The latter is a potential problem while residual stresses in austenitic weldments are a real problem in BWR piping where the residual stresses have been a major contributor to intergranular stress corrosion cracking. The remainder of this section addresses the state of the art in measurement of residual stresses in ferritic and austenitic materials.

9.2.1 Ferritic Materials

Principal work to date has related to the reactor pressure vessel; however, the data should be pertinent to the large diameter thick-walled piping used in some LWR primary systems. Techniques used include strain gaging, magnetic property measurements, BNA, hole drilling, Mossbauer Effect, X-ray diffraction and ultrasonics.

9.2.1.1 Strain Gaging

Strain gaging has been used extensively for the measurement of surface residual stresses. Smith and Holz[9.2.1] made measurements on two HSST Intermediate Test Vessels. Both preand post-weld strain gage measurements and hole drilling were used to determine the level and distribution of the weld-induced residual stresses in A-533 Grade B Class 1 plate material. Stresses near the weld approached yield and tended to maximize 25 to 50 mm outside the heat-affected zone (HAZ). Rybicki[9.2.2] argues that this technique is subject to several sources of error such as 1) gage drift over several days; 2) the

conversion of strains to residual stress which is complicated by the possibility that the material under the gage may have yielded so that a linear relationship is not applicable; 3) since gages are attached prior to welding, the base state is at that time and any residual stresses existing previously will not be measured; and 4) only surface measurement of stresses is possible (which applies to most other techniques). While Rybicki's[9.2.2] comments were directed to the work of Smith and Holz,[9.2.1] they are equally applicable to most residual stress work based on strain gage measurements.

9.2.1.2 Hole Drilling

Hole drilling was mentioned in the previous section as applied to HSST-ITVs (intermediate test vessel). Smith and Holz[9.2.1] conducted hole drilling to establish the residual stress patterns adjacent to the repair welds. Basically, the procedure is quite simple: 1) apply strain gages, 2) then drill holes adjacent to the gages, and 3) observe changes in strain resulting from the hole drilling. While the procedure is conceptually simple, it is difficult technically and the results can be perturbed due to variations in technique. Rybicki[9.2.2] criticizes this technique as being subject to errors. Examples of such errors are 1) the drilling operation may cause changes in the gage of about 10 ksi; 2) for certain residual stress fields, the drilled hole may act as a stress concentrator so that plasticity occurs around the hole; this can be a very significant error; and 3) such measurements only reflect the state of stress near the surface. Since machining and grinding can cause significant surface stress, these stresses can obliterate those due to welding. Usually, surface preparation is required prior to mounting the strain gages, affecting the welding stresses.

It is interesting to note that Rybicki[9.2.2] argues that neither strain gaging nor hole drilling can be trusted to yield accurate results, yet they compare reasonably well to his calculated surface stresses as can be seen in Figure 9.2.1.

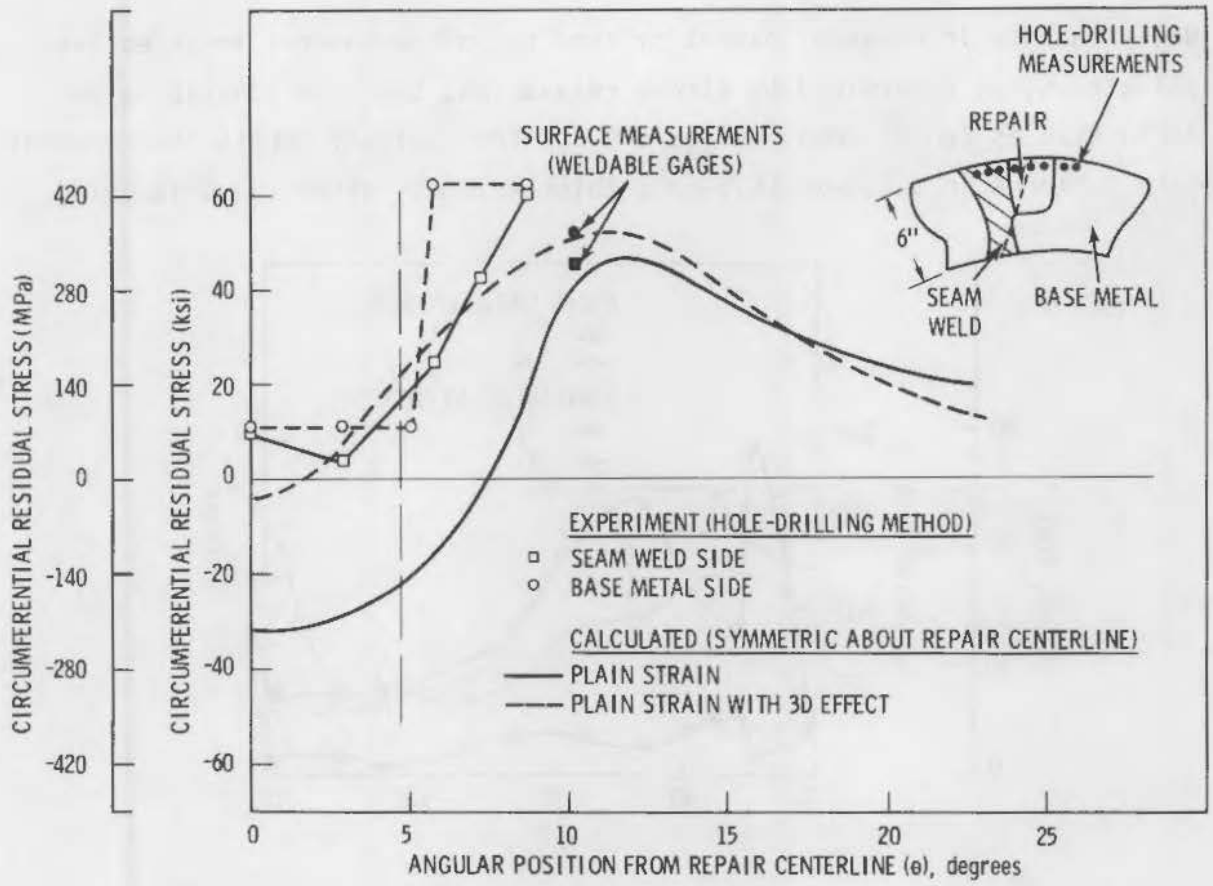

FIGURE 9.2.1. Comparison of Calculated Surface Stresses and Experimental Measurements

9.2.1.3 Magnetic Measurements

Magnetic measurements have been used to determine residual stresses in ferritic alloys.[9.2.3,9.2.4] What appears to be a new technique utilizes remanent magnetization[9.2.3] to determine residual stresses after various post-weld stress relief treatments; however, it would appear that the technique should be equally applicable to measurement of residual stresses under a variety of conditions in ferritic materials. A stress relaxation method was used to determine the macroscopic residual stress which was compared to the remanent magnetism values. The authors attempt to determine fracture mechanics parameters such as maximum allowable crack size in terms of residual stress using a relationship between remanent magnetism and a fracture toughness parameter, K_r.

While changes in remanent magnetism tend to follow changes in effective residual stress, as determined by stress relaxation, the relationship is not that definitive as can be seen in Figure 9.2.2 for residual stress and remanent magnetism patterns in a 165-mm (6.5-in.) thick weldment after two post weld

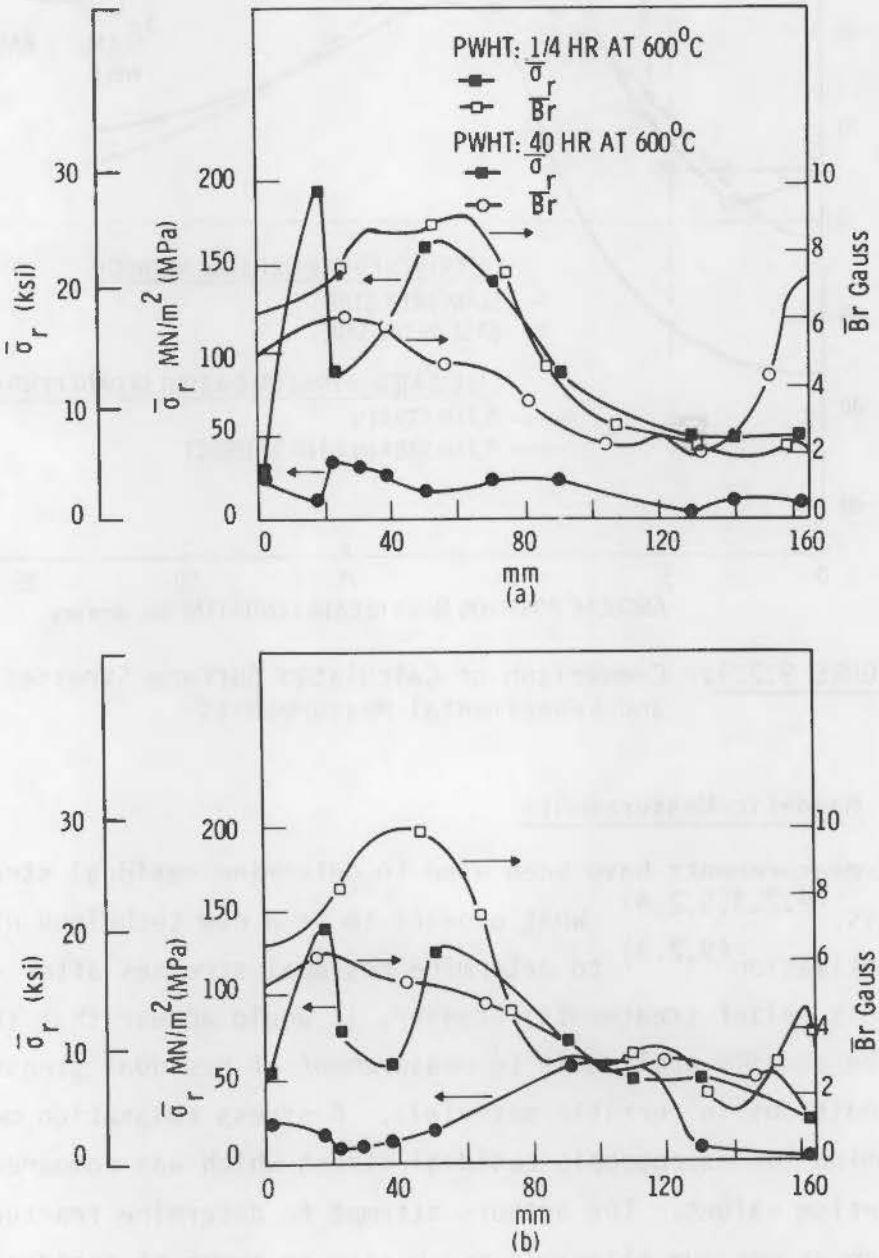

FIGURE 9.2.2. Comparison Between Remanent Magnetization and Effective Residual Stress Along (a) Center of Weldment, (b) Fusion Boundary

heat treatments (PWHT). Figure 9.2.3 presents an even less definitive picture as to the validity of the correlation. While there are definite trends in the remanent magnetization, it appears difficult to quantify the changes.

The work of Iwayanagi et al.[9.2.4] using magnetostriction as a measurement of residual stress highlights the problems in such measurements. While magnetic properties do change markedly with stress, magnetic field strength, chemical composition, cold work, and thermal treatment, all influence the magnetic field, reducing the correlation with regard to residual stress.

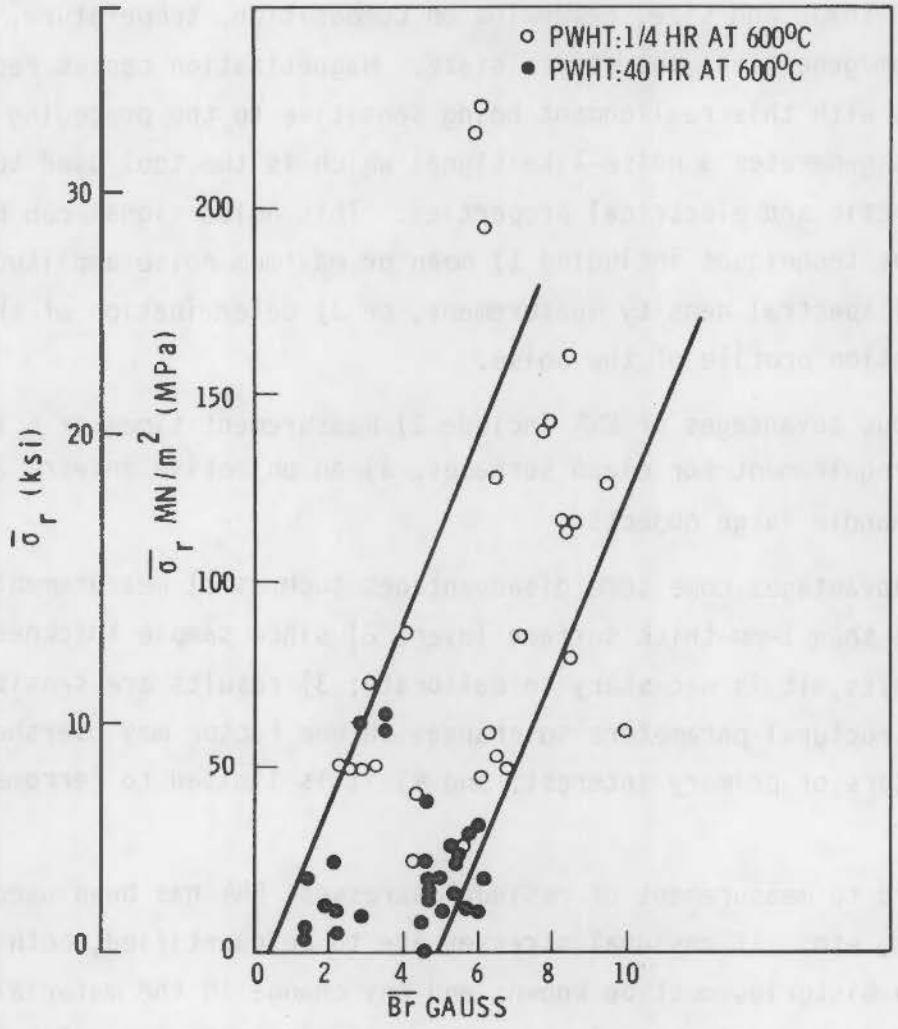

FIGURE 9.2.3. Relationship Between Remanent Magnetization and Effective Weld Residual Stress

9.2.1.4 Barkhausen Noise Analysis (BNA)

BNA is another technique that has been used to detect stresses in ferritic materials. Several authors have discussed the use of BNA; however, the following comments are derived from only one source deemed to be the most relevant.[9.2.5] The authors cite several real or potential applications of BNA such as grain size determination, texture (anisotropy), precipitation and/or aging which includes microstructural changes, deformation, and stress measurement.

BNA is based on orientation of atoms within magnetic domains. These domains vary in shape and size, depending on composition, temperature, microstructure, inhomogeneities, and stress state. Magnetization causes realignment of domains with this realignment being sensitive to the preceding factors. The realignment generates a noise-like signal which is the tool used to detect changes in magnetic and electrical properties. This noise signal can be analyzed by various techniques including 1) mean or maximum noise amplitude measurement, 2) spectral density measurement, or 3) determination of the pulse-height distribution profile of the noise.

Some obvious advantages of BNA include 1) measurement times of 5 to 15 sec, 2) no requirement for clean surfaces, 3) an objective answer, and 4) ability to handle large objects.

With the advantages come some disadvantages such as 1) measurements are limited to less than 1-mm-thick surface layer; 2) since sample thickness may affect the results, it is necessary to calibrate; 3) results are sensitive to several microstructural parameters so changes in one factor may overshadow changes in factors of primary interest; and 4) it is limited to ferromagnetic materials.

With regard to measurement of residual stresses, BNA has been used in gun tubes, bearings, etc. If residual stresses are to be quantified, both material and fabrication histories must be known; and any change in the material parameters either before or during service must be accompanied by a recalibration. Application relevant to stresses include 1) clarification of need for stress relieving, 2) measurement of compressive stresses by shot peening,

3) evaluation of remaining service life (fatigue), 4) monitoring of components operating at high temperatures for creep. Figure 9.2.4 presents a generic type curve typical of many ferritic materials with regard to changes in BNA due to tensile and compressive stresses.

It would appear that BNA has application as a qualitative tool to detect changes and may have application as a quantitative tool where measurements are repetitive and the number of components merits careful calibration.

9.2.1.5 The Mossbauer Effect

The Mossbauer effect has been explored as a tool for measuring residual stressed with limited success.[9.2.6] Residual surface stresses at the yield strength level will produce a maximum shift of ~1% of a typical resonance peak height and width. By heating or cooling the gamma ray energy may be changed sufficiently to enhance the changes and to permit monitoring. Another

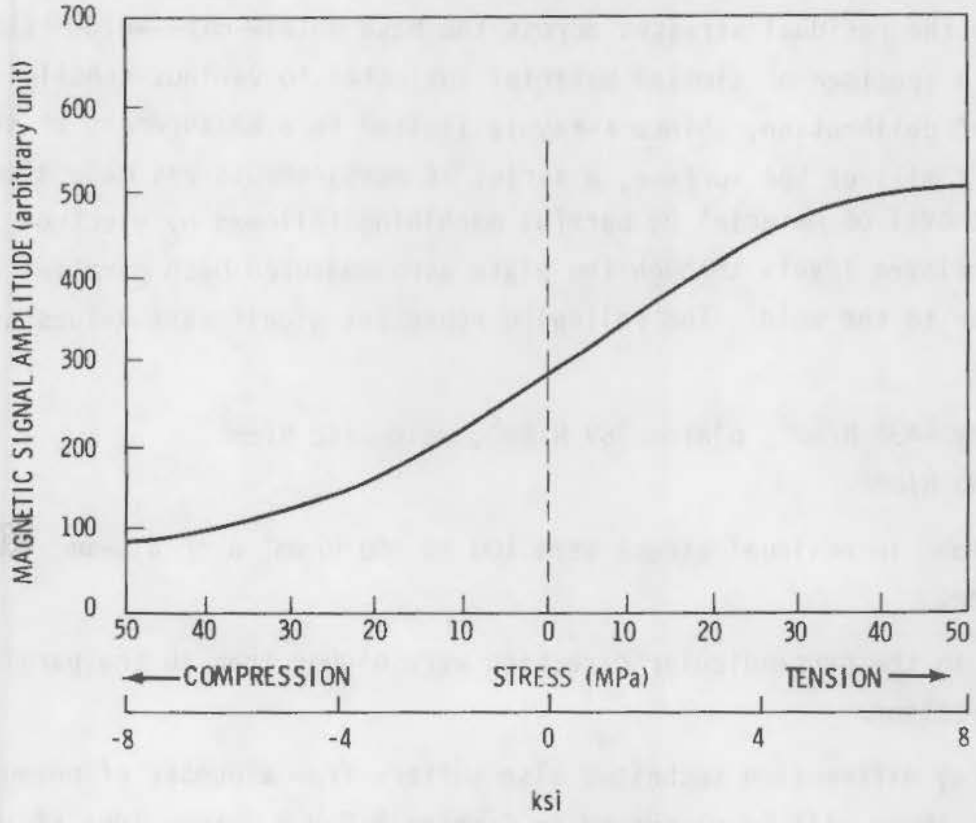

FIGURE 9.2.4. The Dependence of BNA Results on the Stress Level in an AISI 4340 Steel

limitation with large bulk samples such as weldments, where measurements generally are limited to one surface, is that a backscatter technique must be used.

In essence, the Mossbauer effect is a recoilless gamma-ray nuclear-resonance phenomenon where 14.4 keV gamma rays are emitted by a ^{57}Co nucleus upon decaying to ^{57}Fe. Stresses affect the Mossbauer spectra in two ways: 1) the entire absorption pattern shifts, or 2) the pattern collapses (or expands) slightly.

9.2.1.6 X-Ray Diffraction

X-ray diffraction is a long established technique for the measurement of surface residual stresses. A majority of the X-ray data will be presented in the section relevant to austenitic stainless steels; however, one study is of interest with regard to thick sections of ferritic steel.(9.2.7) A submerged arc weldment in an A-533 Grade B Class 1 steel plate about 7.5-in. thick was examined after a 620°C (1150°F) 5-hr stress relief. X-ray diffraction was used to determine the residual stresses across the base metal--HAZ--weld-HAZ-base metal using a specimen of similar material subjected to various tensile loads as a means of calibration. Since X-ray is limited to a measurement of stresses within 1 to 2 mils of the surface, a series of measurements was made after selective removal of material by careful machining followed by electro-polishing. Eleven levels through the plate were measured both parallel and perpendicular to the weld. The following represent significant values and conclusions:

- Accuracy--±39 N/mm^2, plate--369 N/mm^2, weld--448 N/mm^2, HAZ--483 N/mm^2.
- Variations in residual stress were 100 to 350 N/mm^2 over a 5-mm distance.
- Values in the perpendicular direction were higher than in the parallel direction.

The X-ray diffraction technique also suffers from a number of potential limitations; these will be discussed in Section 9.2.2.2. Some idea of the need for an expert appraisal of the X-ray data can be inferred from the scatter in values shown in Figure 9.2.5.

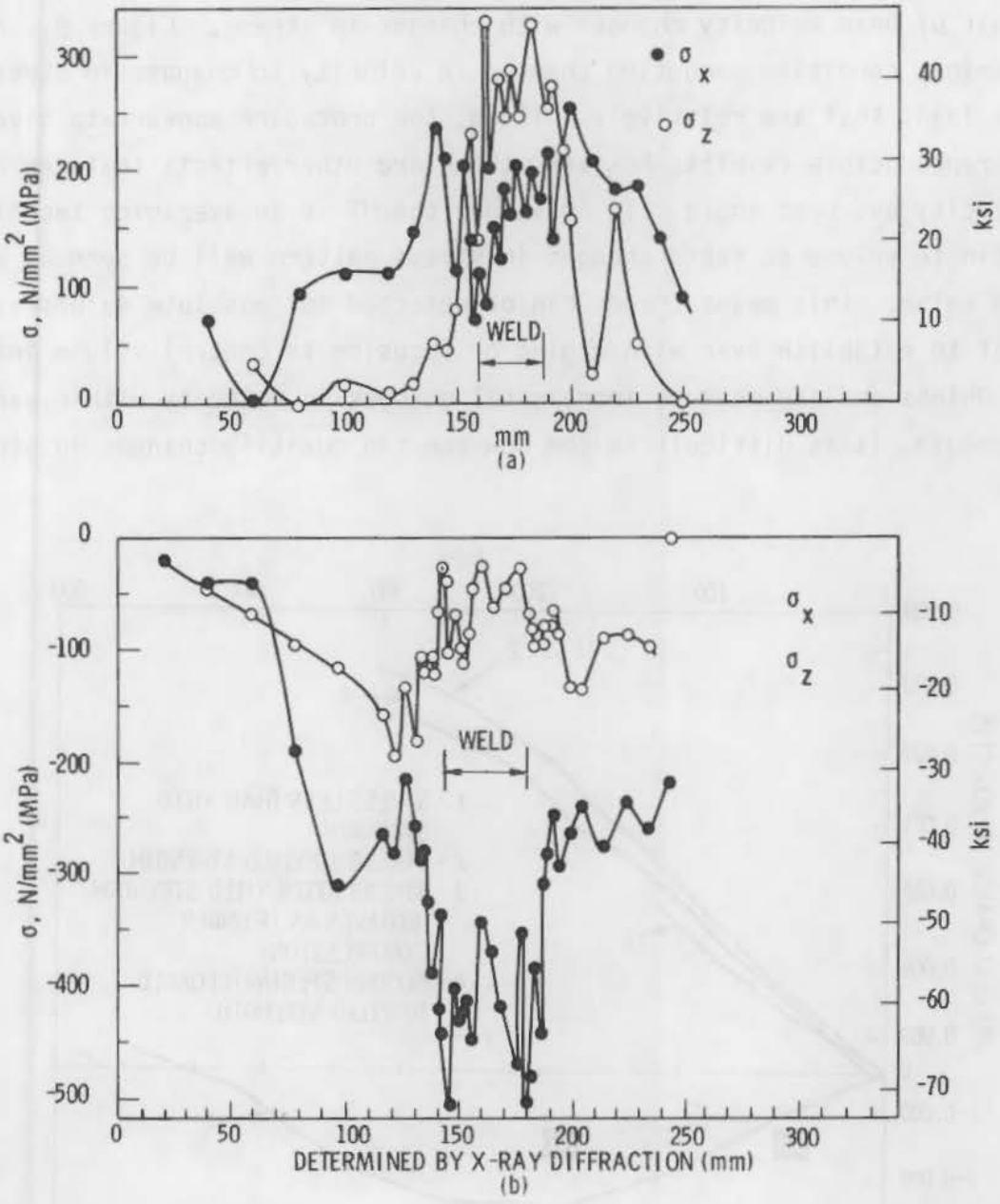

FIGURE 9.2.5. Corrected Values of σ_x and σ_z: (a) 28.3 mm Under Surface (for clarity some measurements have been excluded); and (b) Near Center of Specimen 77.9 mm Under Surface

9.2.1.7 Ultrasonics

Ultrasonics have been used to detect and measure residual stresses. A late study summarizes previous work and is cited here.(9.2.8) In essence, the technique is developed from the theory presented in Chapter 9A. It is

known that UT beam velocity changes with changes in stress. Figure 9.2.6 presents various conditions equating changes in velocity to changes in stress. For bulk loads that are relatively uniform, the procedure appears to give relatively reproducible results; however, there are other effects that can change both velocity and beam angle. In addition, the UT is an averaging technique over a finite volume so rapid changes in stress pattern will be seen as an averaged value. This means trends can be detected but absolute values will be difficult to establish even with gaging or focusing to control volume increments. Unless one can measure incremental changes in velocity within every volume module, it is difficult to see how one can quantify changes in stress patterns.

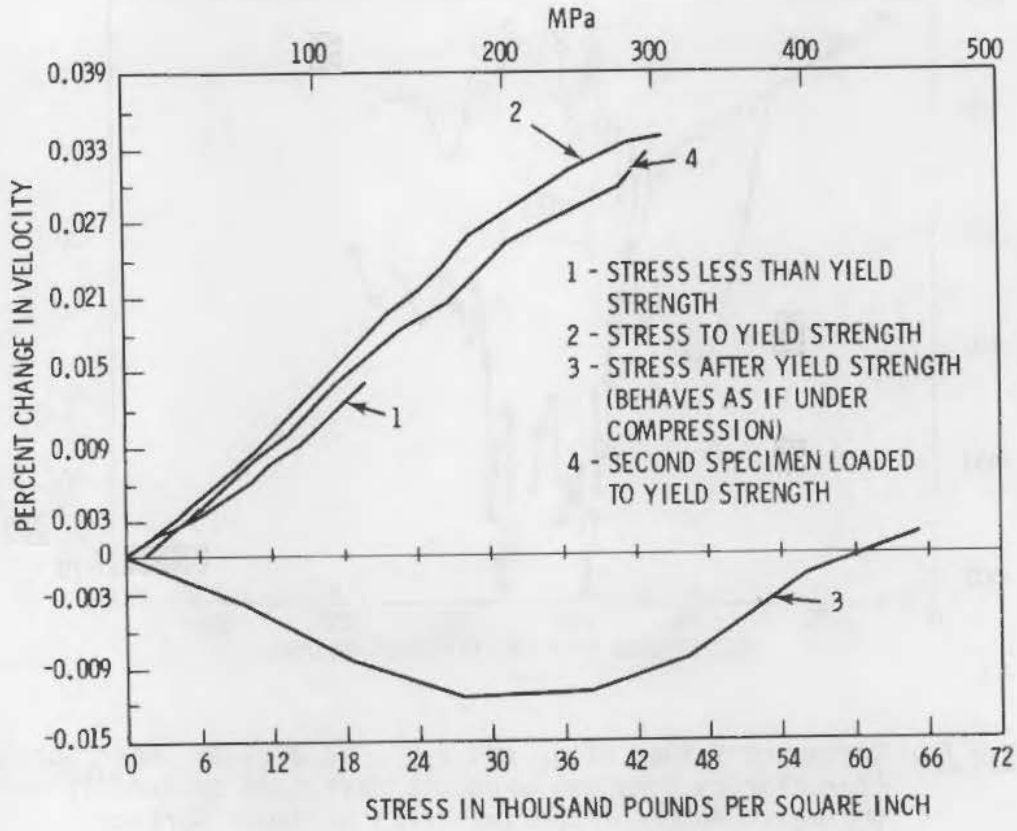

FIGURE 9.2.6. Ultrasonic Velocity Change as a Function of Tensile Strength

9.2.2 Austenitic Stainless Steels

The measurement of residual stresses in austenitic stainless steel piping weldments became important when the incidence of IGSCC in BWRs was attributed in a substantial degree to the high levels of residual stress. Several of the techniques discussed in Section 9.2.1 for ferritic steels are not applicable because they are limited to ferromagnetic materials, limiting the choice to strain gaging, X-ray diffraction and ultrasonics. An additional technique is to use analytic procedures coupled with available experimental information to "benchmark" the curves. The hole drilling technique is not applicable to austenitic steels because of their propensity to work harden.

9.2.2.1 Strain Gaging

Strain gaging has been used on the austenitic stainless steels to measure residual stress;[9.2.9,9.2.10,9.2.11] however, the reservations concerning the accuracy of strain gage measurements expressed by Rybicki[9.2.2] are equally applicable to this class of materials. In fact, they will tend to be more sensitive to relaxation of stresses.

The Japanese study[9.2.9] is quite extensive covering 9-, 10-, and 12-in.-dia piping; however, it does not include data generated by other techniques, and it was not possible to benchmark their strain gage data.

Gianuzzi et al. in EPRI NP-944[9.2.10] reported an extensive collection of residual stress data (for austenitic stainless steels). Included was a review of the relevant literature. Sizes of piping examined were 10- and 26-in. schedule 80 containing either gas tungsten arc or shielded metal arc weldments. Residual stress measurements were made by the strain gage technique, both gage removal and slitting the pipe, and by X-ray diffraction. Some interesting effects reported were 1) longitudinal residual stresses increase as pipe size decreases; there is about 20- to 25-ksi difference from 10- to 26-in.; 2) there was no measurable difference in residual stress in the 26-in. pipe for low heat input versus high heat input welds; and 3) surface grinding of 304 SS produces a brittle cold-worked layer that cracked under a modest tensile strain (~1%). This may have been a major contributor to the initiation of IGSCC in as-welded and ground 304 SS piping.

An example of the effects of grinding or machining can be seen in Figure 9.2.7.

Strain gages were used to measure surface and through-wall stresses. Profiles taken across weldments in both 10-in. and 26-in. piping are shown in

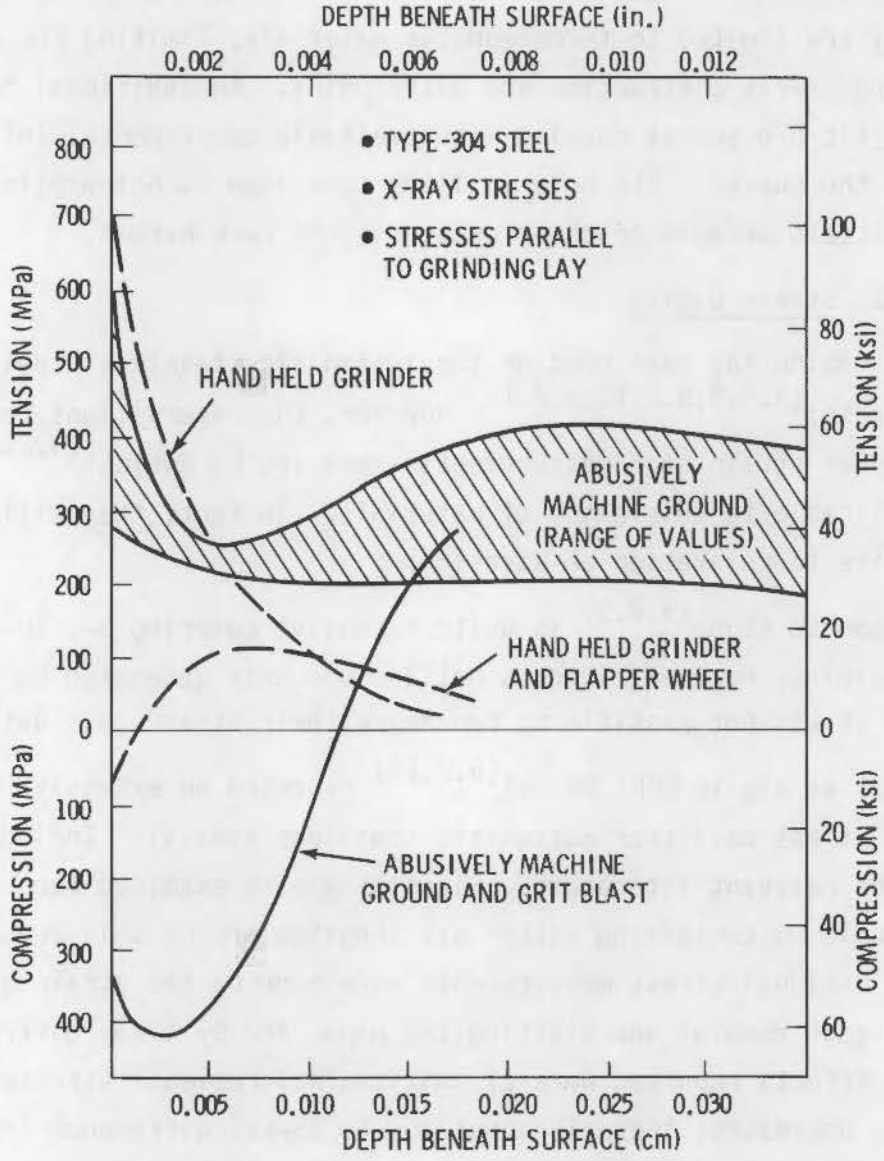

FIGURE 9.2.7. Comparison of Various Grinding and Post-Grinding Procedures for Type 304 SS Coupons; X-ray surface and subsurface stresses parallel to lay.

Figure 9.2.8. Recognizing the validity of Rybicki's[9.2.2] comments regarding sources of error in residual stresses, we should examine trends rather than considering the values as absolute.

Rybicki[9.2.11] used strain gages to determine residual stresses on 12-in. schedule 80 304 SS pipe containing either a 2-pass TIG weld or a 6-pass MIG

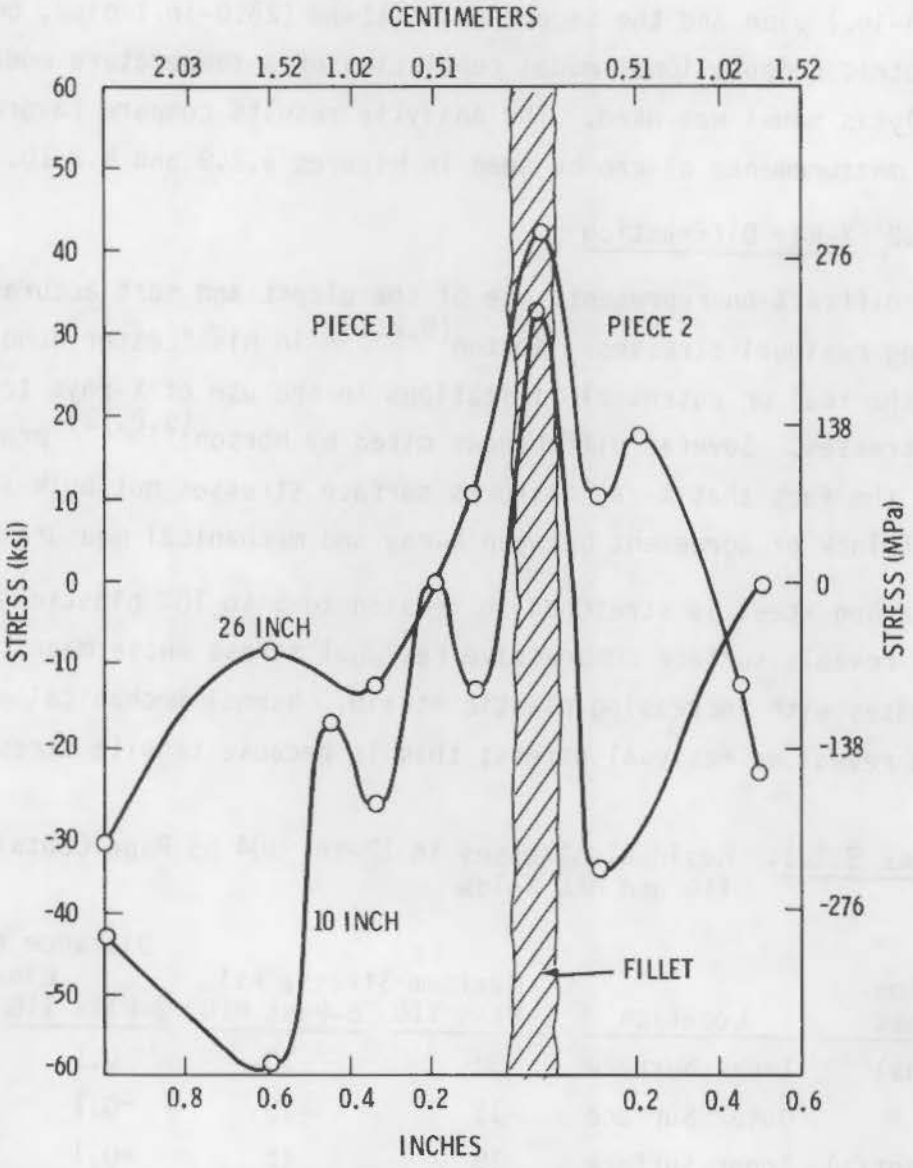

FIGURE 9.2.8. Maximum Surface Residuals for 25.2-cm (10 in.) and 66-cm (26 in.) Pipe; Inside Surface Versus Distance from Fillet at the 45° (10 in.) and 0° (26 in.) Azimuth

weld; a trepanning procedure was used to measure stresses by difference. The trepanning error was considered to be +0 -6000 psi.

Table 9.2.1 contains data obtained from the strain gage measurements. The trends cited follow those obtained by X-ray and other techniques.

Rybicki and Stonesifer[9.2.12] extended the earlier work of Rybicki[9.2.11] to 7-pass and 30-pass girth butt welds. The first was on a 114-mm (4.5-in.) pipe and the second on a 711-mm (28.0-in.) pipe, both 304 SS. An axisymmetric computational model consisting of a temperature model plus a stress analysis model was used. The analytic results compare favorably to the laboratory measurements as can be seen in Figures 9.2.9 and 9.2.10.

9.2.2.2 X-Ray Diffraction

X-ray diffraction represents one of the oldest and most accurate methods of measuring residual stresses. Norton[9.2.13] in his "Lester Honor Lecture" discussed the real or potential limitations in the use of X-rays to measure residual stresses. Several differences cited by Norton[9.2.13] probably are related to the fact that X-ray measures surface stresses not bulk stresses. Examples of lack of agreement between X-ray and mechanical measurements follow:

- Low carbon steel is stretched in tension to 5 to 10% plastic strain. X-ray reveals surface compressive residual stress whose magnitude increases with increasing plastic strain. Normal mechanical measurements reveal no residual stress; this is because tensile stresses

TABLE 9.2.1. Residual Stresses in 12-in. 304 SS Pipe Containing TIG and MIG Welds

Direction of Stress	Location	Maximum Stress, ksi		Distance from Fusion Line (in.)	
		2-Pass TIG	6-Pass MIG	2-Pass TIG	6-Pass MIG
Longitudinal	Inner Surface	30	30	0.1	-0.3
	Outer Surface	-15	-25	~0.1	-0.3
Circumferential	Inner Surface	~35	45	~0.1	-0.3
	Outer Surface	60 to 75	10	0.2, 0.30	-0.1

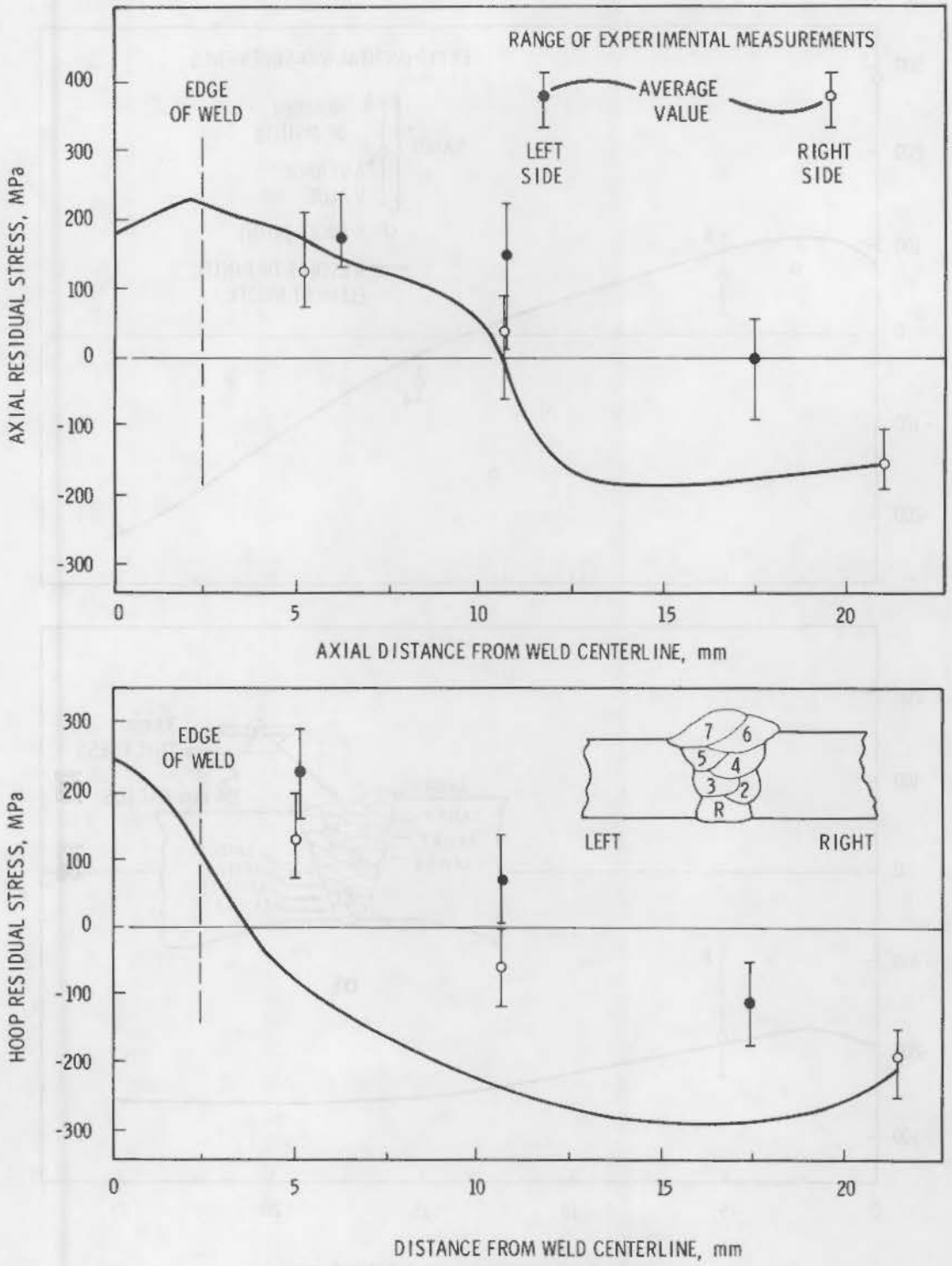

FIGURE 9.2.9. Comparison of Calculated and Experimentally Determined Residual Stresses for the Inner Surface of the 7-Pass Weld. Conversion factors: (in.) = (0.0394)(mm); (psi) = (145)(MPa)

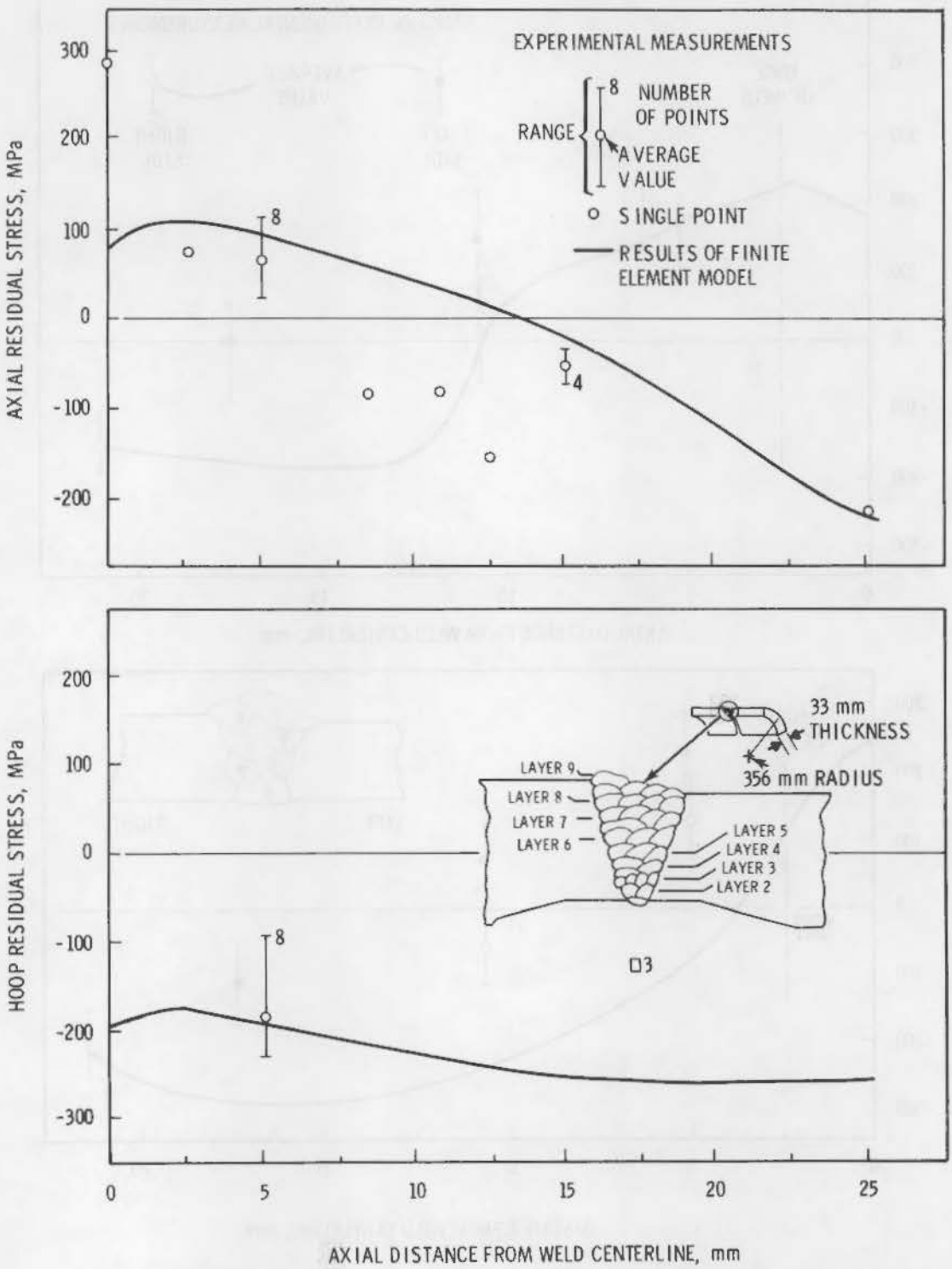

FIGURE 9.2.10. Comparison of Calculated and Experimentally Determined Residual Stresses for the Inner Surface of the 32-Pass Weld. Converions factors: (in.) = (0.0394)(mm); (psi) = (145)(MPa)

exist in center of bar balancing compressive stress due to a lower yield stress on surface than at center (often occurs in single phase alloys).

- Alloys with relatively soft matrix containing hard second phase may show superimposed compressive residual stress throughout specimens which cannot be true on basis of stress compatibility. This suggests answer is microstresses set up between hard and soft grains which balance locally.

The following are examples of real or potential limitations relevant to austenitic stainless steels:

- X-ray does not work well with large grained material because not enough crystals of correct orientation for diffraction occult beam. Typical of castings in welds, sometimes in well-annealed material.
- Metals which, because of their structure, do not give strong diffraction peaks at the desired angular range with any of the X-ray wavelengths; austenitic stainless steels and titanium base alloys are examples. Peaks exist but they occur at such low values of a theta angle that the stress constant is too large to give the desired sensitivity.

Chrenko[9.2.14] described X-ray diffraction equipment developed to resolve the limitations cited by Norton.[9.2.13] The system used parallel beam optics which permitted larger sizes of samples as well as reducing sample placement errors. An oscillating motion was incorporated to permit examination of larger grained specimens. The system was developed specifically to measure residual stresses, particularly weldments in 304 SS piping. Figure 9.2.11 illustrates the variations as a function of azimuthal position. These variations were cited by Tomlinson et al.[4.5.29] in Chapter 4. These azimuthal differences are seen much more clearly in Figure 9.2.12 where surface longitudinal inner surface residual stresses are measured at 0.1 in. from the fusion line. The total stresses cited in Figure 9.2.12 were obtained by adding the X-ray stresses to the stresses relieved when the pieces used for the X-ray measurements were cut out.

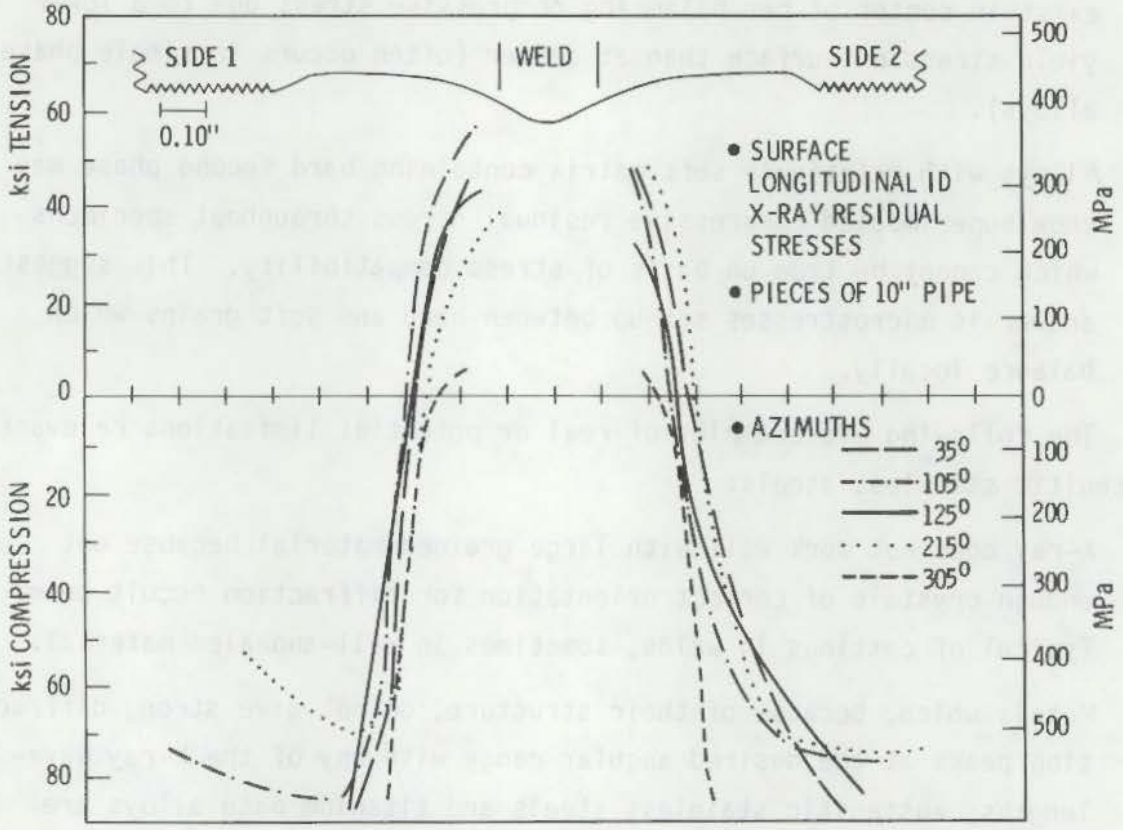

FIGURE 9.2.11. X-Ray Surface Longitudinal Residual Stresses as a Function of Distance from Weld. For ID of 10-in. Pipe. Data are shown for various azimuths.

A majority of the residual stress measurements discussed by Gianuzzi et al.[9.2.10] were obtained using X-ray diffraction. In fact, Chrenko[9.2.14] participated in the studies. Over 75 HAZs were measured to determine the level and distribution of residual stresses, both circumferentially and longitudinally. Measurements were made on inner and outer surfaces before and after stress relaxation. Generally, measurements were made parallel to the grinding direction (the lay). Several parameters were examined including the effects of surface treatments on residual stresses, variations from laboratory to laboratory in measurement by X-ray diffraction, azimuthal distribution of stresses, and variations of residual stress in the longitudinal direction. Figure 9.2.13 illustrates the degree of reproducibility of X-ray diffraction measurements of residual stresses with three laboratories.

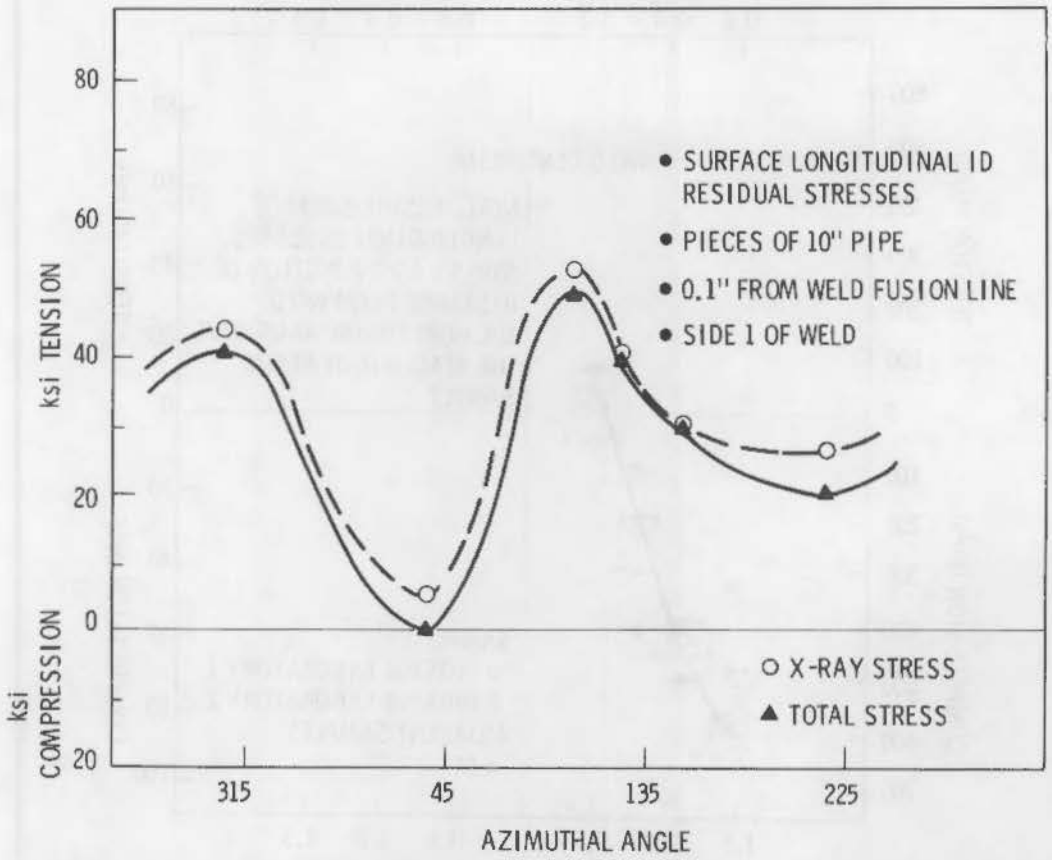

FIGURE 9.2.12. Azimuthal Variation of Surface Longitudinal ID Residual Stresses at 0.1 in. from Weld Fusion Line. Data are shown for a 10-in. dia pipe.

A tabular presentation of data comparable to that in Figure 9.2.12 by Chrenko[9.2.14] is given in Table 9.2.2. While the trends are similar, it is apparent that the absolute values vary markedly from pipe size to pipe size, and probably from one set of welding conditions to another set of welding conditions.

Several significant trends were cited by Gianuzzo et al.[9.2.10] and are quoted directly in the following paragraphs.

A number of general comments can be made about the X-ray longitudinal inside surface stresses measured on pieces of butt-welded Type-304 SS pipe. These pipes had been machined in the counter bore area prior to welding and had received no post-weld surface treatments:

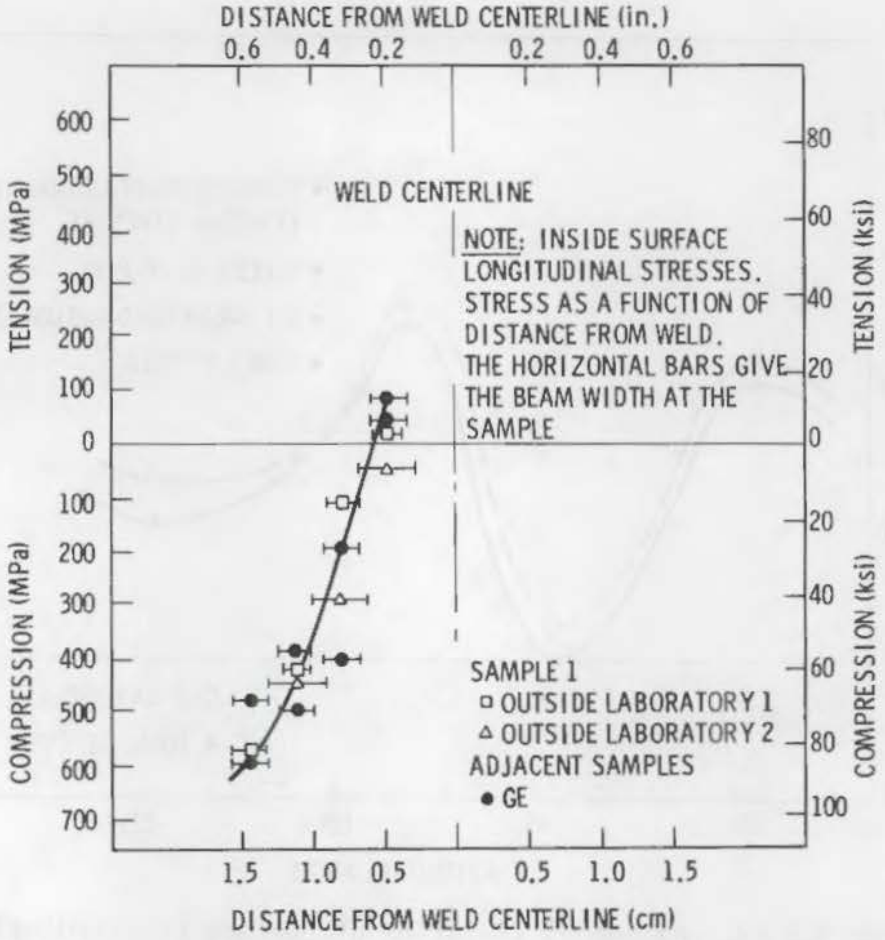

FIGURE 9.2.13. X-Ray Residual Stress Measurements from Several Laboratories on Pieces of 10.16-cm (4-in.) Dia Welded Type-304 SS Pipe

- Bell-shaped residual stress distributions centered at the weld have been found for all azimuths for pieces of 10.16-cm (4-in.) and 66-cm (26-in.) dia welded Type-304 SS pipe.
- This bell-shaped stress distribution with distance from the weld is similar for the three different diameter pipes, with variations occurring vertical displacement (stress axis) of the curves.
- The stresses are usually tensile in the heat-affected zone ~0.5 cm (0.2 in.) from the weld centerline.
- The stresses are highly compressive ~1.2 cm (0.5 in.) from the weld centerline.

TABLE 9.2.2. Inside Surface Residual Stresses, 0.50 cm (0.2 in.) from Weld Centerline,[a] Longitudinal Direction (high heat input weld, 66-cm (26-in.) dia Type 304 SS pipes)

		Residual Stress, MPa (ksi)[b]											
		Heat 834264 Side						Heat 17192 Side					
		X-Ray		Stress Relief Correction		Total		X-Ray		Stress Relief Correction		Total	
Panel°	Azimuth°												
30	9	+214	(+31)	+27	(+4)	+241	(+35)	+131	(+19)	+14	(+2)	+145	(+21)
	34	-41	(-6)	-7	(-1)	-48	(-7)	+28	(+4)	-7	(-1)	+21	(+3)
	48	+41	(+6)	+21	(+3)	+62	(+9)	+159	(+23)	+14	(+2)	+172	(+25)
90	70	+200	(+29)	+7	(+1)	+207	(+30)	+159	(+23)	+7	(+1)	+165	(+24)
	93	+234	(+34)	-21	(-3)	+214	(+31)	+172	(+25)	-28	(-4)	+145	(+21)
150	129	+172	(+25)	-48	(-7)	+124	(+18)	+55	(+8)	-48	(-7)	+7	(+1)
	154	+172	(+25)	-34	(-5)	+138	(+20)	+41	(+6)	-14	(-2)	+28	(+4)
	164	+200	(+29)	-28	(-4)	+172	(+25)	+186	(+27)	-14	(-2)	+172	(+25)
210	190	+138	(+20)	-14	(-2)	+124	(+18)	+131	(+19)	-28	(-4)	+103	(+15)
	215	+103	(+15)	-21	(-3)	+82	(+12)	+186	(+27)	-48	(-7)	+138	(+20)
270	247	+172	(+25)	-55	(-8)	+117	(+17)	+131	(+19)	-69	(-10)	+62	(+9)
	272	+103	(+15)	-34	(-5)	+69	(+10)	+172	(+25)	-21	(-3)	+152	(+22)
330	310	+172	(+25)	+34	(+5)	+207	(+30)	+159	(+23)	+14	(+2)	+72	(+25)
	334	+200	(+29)	-7	(-1)	+193	(+28)	+241	(+35)	+14	(+2)	+255	(+37)

(a) 0.25 cm (0.1 in.) from weld fusion line.
(b) The MPa readings were derived from ksi readings. Hence, because of rounding error, the MPa data in the Total column may not equal the sum of the two contributions.
NOTE: + = tension, - = compression.

- The widths (full width at half maximum intensity) of all the bell-shaped surface stress distributions were approximately the same, ~1.5 cm (~0.6 in.) wide, centered at the weld.
- A steep stress gradient occurs ~0.5 to 1.0 cm (0.2 in. to 0.4 in) from the weld centerline.
- At a constant distance from the weld centerline in the heat-affected zone, e.g., 0.5 cm (0.2 in.) the X-ray stresses can vary appreciably around the azimuth. The variations are less the larger the pipe diameter.
- In the heat-affected zone 0.5 cm (0.2 in.) from the weld centerline most tensile stresses are in the order of σ-10.16 cm > σ-25.4 cm < σ-66 cm, in agreement with analytical calculations.

The subsurface residual stresses obtained by electropolishing in from the inside surface are similar for the three different diameter welded pipes. In the HAZ 0.5 cm (0.2 in.) from the weld centerline, the stresses are usually tensile on the inside surface and remain tensile at least for the first 0.0025 cm to 0.050 cm (0.0010 in. to 0.020 in.) beneath the surface. The stresses further from the weld, ~1.2 cm (0.5 in.) from the weld centerline, change from being highly compressive at the surface to being much less compressive or even tensile at this same depth beneath the surface.

Some preliminary X-ray subsurface residual stress data have been obtained by having the X-ray beam incident on the side surface near the weld instead of the inside surface. For the 66-cm (26-in.) pipe, longitudinal stresses in the base metal are still tensile ~0.3 cm beneath the surface but become compressive at a depth of ~0.6 to 0.8 cm (0.25 to 0.3 in.) beneath the surface.

Deep subsurface X-ray residual stresses obtained by having the X-ray beam incident on the side edge near welds are consistent with those obtained by electropolishing in from the inside surface and having the X-ray beam incident on the inside surface. These side-view stresses are also consistent with the findings from tests in boiling $MgCl_2$. Based on these data it appears that measuring deep or through-wall residual stresses by having the beam incident on the side surface is a viable method.

A few X-ray inside surface data as a function of distance from the weld show that stresses in the circumferential (hoop) direction have bell-shaped distributions similar to those seen for the longitudinal direction. The circumferential stress data is sufficient to adequately compare the circumferential stresses in the various sized pipes.

An attempt was made to correlate several welding and weld appearance parameters and the residual stresses present at 0.50 cm (0.20 in.) from the weld centerline around the azimuth of the high heat input welded 66-cm (26-in.) dia Type-304 SS pipe. No convincing correlations were found to exist, although several of the parameters should be examined in future welds for their relationship to the stresses present.

An analytical study[9.2.15] discussing mechanisms for preventing IGSCC by limiting applied static loads uses data that undoubtedly were generated in the preceding study.[9.2.10] Figure 9.2.14 permits a comparison of general

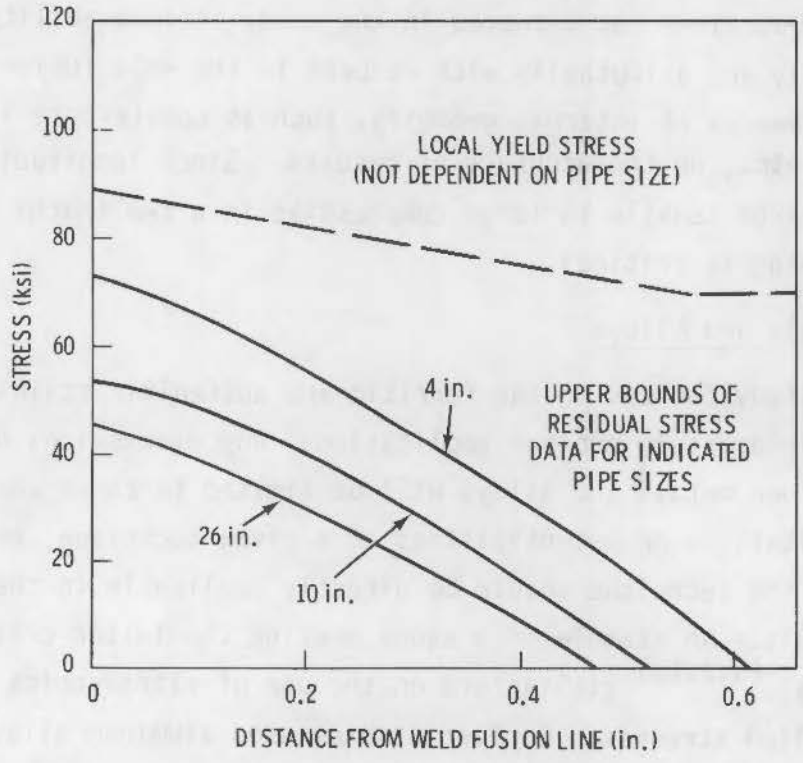

FIGURE 9.2.14. Residual Stress and Yield Stress Versus Distance from Welds

trends of residual stress as functions of pipe size and distance from the weld fusion line. Presumably, these represent longitudinal stresses.

Machining and grinding cause high tensile residual stresses at and below the surface, confirming the data of Gianuzzi et al.[9.2.10] Figures 9.2.15a and 9.2.15b contain the data. Obviously, grinding introduces deep tensile residual stresses.

The beneficial effects of sand or grit blasting and shot peening insofar as generating compressive residual stress is concerned can be seen in Figures 9.2.16a, 9.2.16b, 9.2.16c, and 9.2.16d. The sand blasting data in Figure 9.2.16a for rougher (40 μ) surfaces appears anomalous; however, the trends generally are as anticipated. Figure 9.2.16d permits a comparison of 304L to 304 (Figure 9.2.16c). Again values were as expected.

A portable X-ray unit capable of measuring residual stresses on the inner surface of piping has been developed and tested on 10-in. pipe.[9.2.17] The final unit is to be capable of fitting into a 4-in. pipe. Table 9.2.3 presents available data. Questions not answered in the study include ability to position longitudinally and azimuthally with respect to the weld fusion line interface and the influences of internal geometry, such as counterbore length and angle, mismatch, etc., on the accuracy of results. Since longitudinal stresses may change from large tensile to large compressive in a few tenths of an inch, accurate positioning is critical.

9.2.3 Other Metals and Alloys

Since this study focuses on the ferritic and austenitic stainless steels as materials of interest in nuclear applications, any discussions of NDE techniques used on other metals and alloys will be limited to cases where the data reveal basic limitations or potentialities of a given technique, or where it is apparent that the technique should be directly applicable to the austenitic and ferritic steels. An example of a study meeting the latter criterion is the work of Kino et al.[9.2.18] at Stanford on the use of ultra-sonics to measure residual and applied stresses. Earlier studies used aluminum alloys and pure metals to explore the feasibility of ultrasonics to measure and characterize residual stresses. These early studies are neither discussed nor cited here

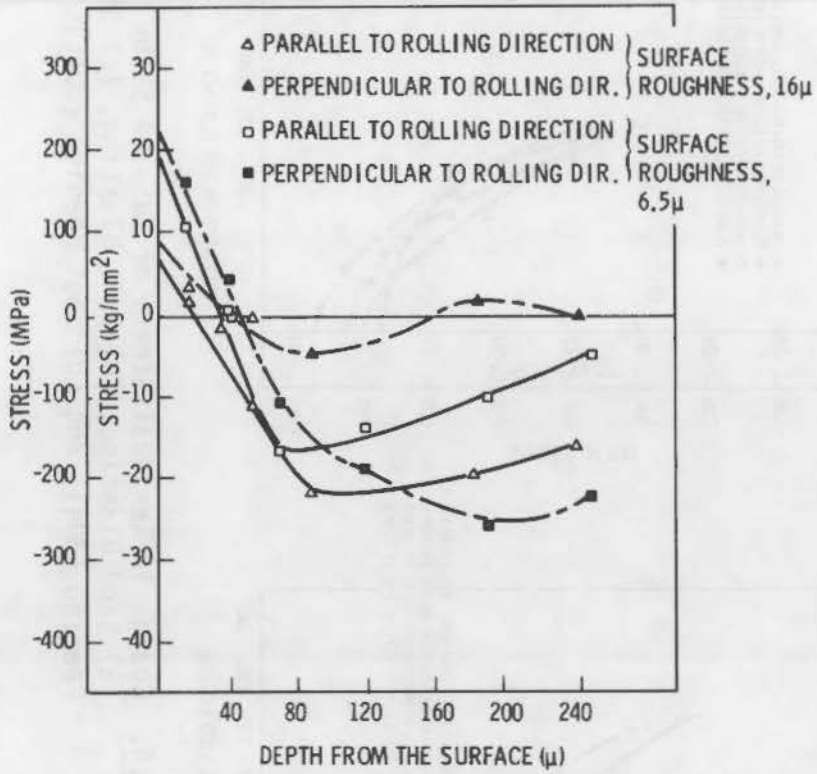

FIGURE 9.2.15a. Change in Residual Stress by Shaper Treatment of SUS-304 SS. (Shaper machining treatment direction is perpendicular to rolling direction.)

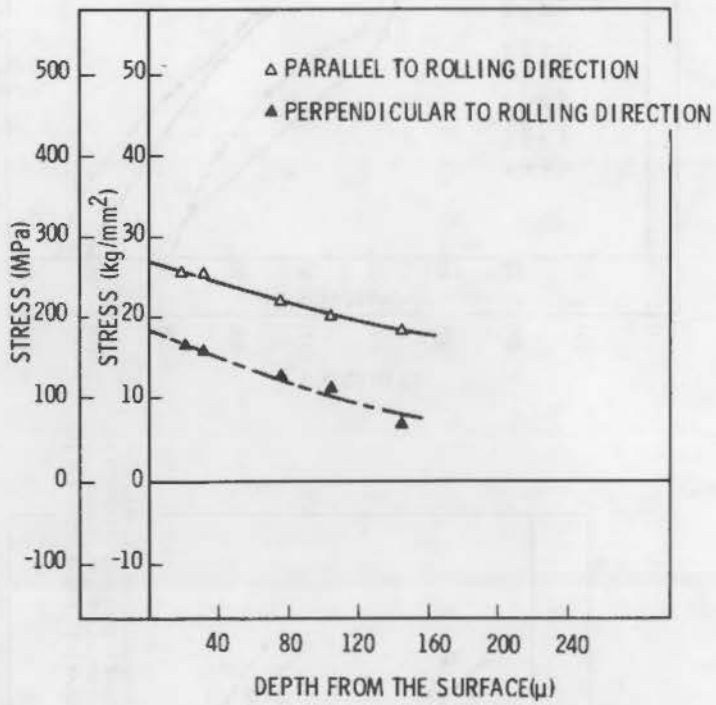

FIGURE 9.2.15b. Change in Residual Stress by Grinding of SUS-304 SS (surface roughness 14 μ)

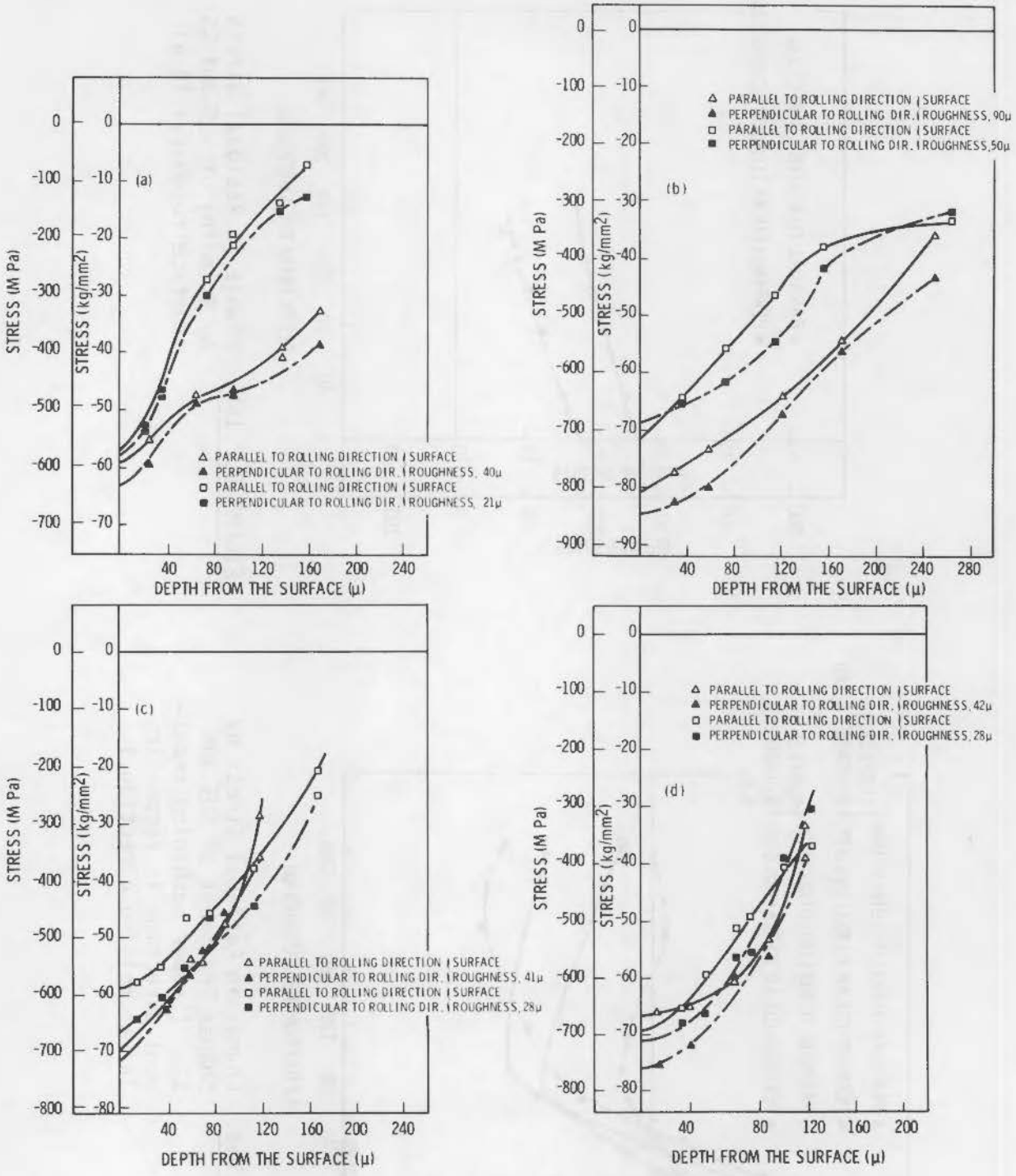

FIGURE 9.2.16. Change in Residual Stress of SUS-304 SS by (a) Sand Blasting, (b) Grit Blasting, (c) Shot Peening (304), and (d) Shot Peening (304L)

TABLE 9.2.3. Stress Exposure Technique (SET) Used to Measure Inner Surface Stresses in Welded Austenitic Piping

Location	Hoop Stress In Situ			Longitudinal Stress	
	SET (b = 25°) psi	82% of SET, psi	$\sin^2\psi$ psi	SET (b = 25°) psi	$\sin^2\psi$ psi
HAZ, 5 mm from Weld, 180° from Seam	-74,871	-61,374	-63,219		
HAZ, 1 mm from weld, 180° from Seam				-34,700	
HAZ, 5 mm from Weld, 90° from Seam	-91,848	-75,315			
HAZ, 6 mm from Weld, 180° from Seam				-77,900	
HAZ, 10 mm from Weld, 180° from Seam				-110,700	
HAZ 20 mm from Weld, 180° from Seam				-59,100	-84,100
Counter-Bored Area 100 mm from Weld, 90° from Seam	-42,898	-35,176			
As-Rolled Parent Material, 130° from Seam	+10,099	8,281			
As-Rolled Parent Material, 130° from Seam	+44,534(a)	36,518(a)			

(a) Data questionable due to larger variance in parabolic curve fit.

because they generally suffered from the faults cited in Section 9.2.1.7 with regard to UT being an averaging technique capable of detecting trends, but difficult or impossible to measure absolute values. While the studies of Kino et al.(9.2.18) represent a step toward answering the above reservations, the ultimate proof will be the examination of austenitic stainless steel weldments in situ.

The basic unit consists of a computer-controlled system which produces quantitative two-dimensional images of stress contours in planar metal samples resulting from both residual and externally applied stresses. The basis is the dependence of velocity of propagation of longitudinal sound waves on the state of stress in the interrogated material.

It was found that theory compared favorably with experimental results in cases of stress distribution around a hole in a large uniformly stressed plane sample, including the detection of regions where plastic yielding had occurred. Figure 9.2.17a illustrates the specimen geometry and Figure 9.2.17b is a comparison of experimental and theoretical stress contour about the circular hold.

Similar stress mapping has been done of the inhomogeneous regions typical of edge cracks. Again there was excellent agreement between theoretical calculations and experimental results. An example of the double edge-notched specimen is given in Figure 9.2.18a and a comparison of constant stress contours obtained acoustically and with photo-elasticity is given in Figure 9.2.18b.

In essence, the preceding results represent an extension of Murnaghan's third-order elastic constant theory described in Chapter 9A. Relative accuracies are 2 to 5 parts per million and stresses as small as 5 MPa can be determined. Measurements are taken on a uniformly stressed specimen serving as a control, then the inhomogeneous stress fields in the same type of material are scanned. Presumably, this is the first time quantitative stress maps have been made using ultrasonics. The system is capable of a 500 point scan in about 20 minutes.

The procedure is very sensitive to differences in microstructure which can mask the changes in velocity due to stress; therefore, considerable care must be exercised in interpretation unless the fabrication histories and final microstructures are thoroughly categorized. The significance of these factors is discussed in Chapter 9A.

An example of the double-pulse technique applied to the measurement of stressed regions is given in Figure 9.2.19. An aluminum disk containing a hole was stressed by forcing a steel rod into the hole generating pressure around the center of the disk of about 300 psi. After removal of the rod the two

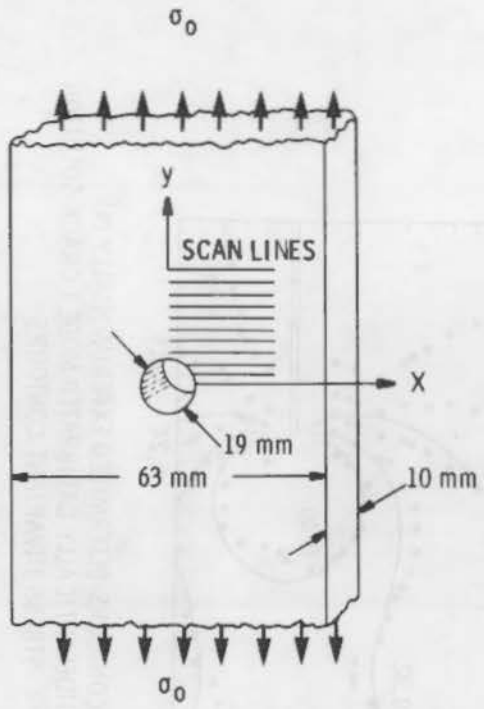

FIGURE 9.2.17a. Specimen Geometry for 6061-T6 Aluminum Panel with a Central Circular Hole

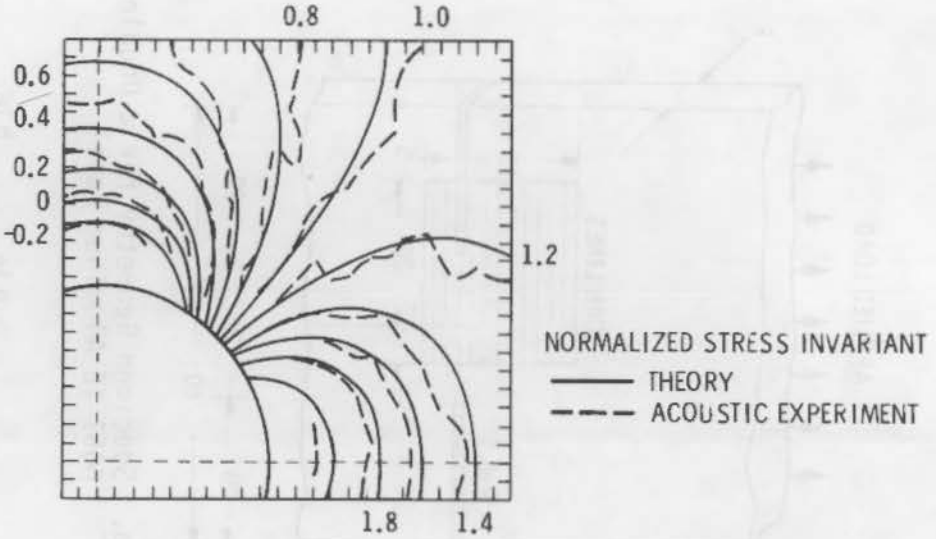

FIGURE 9.2.17b. Experimental and Theoretical Stress Contour Plots for 6061-T6 Aluminum Panel with a Central Circular Hole

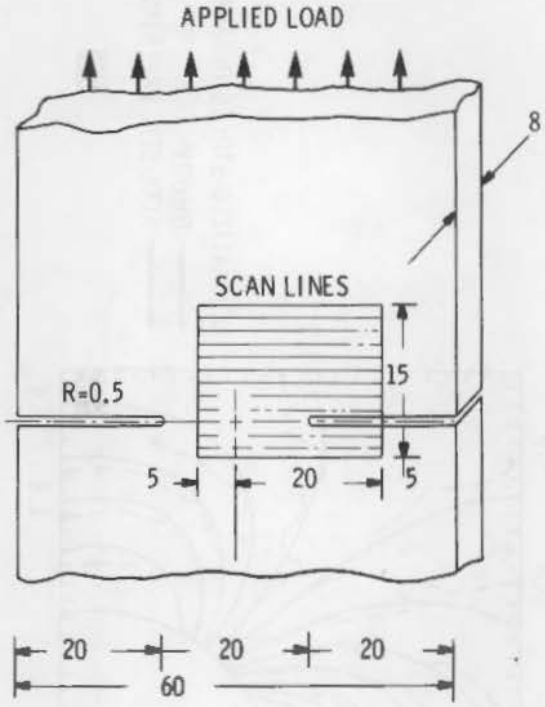

FIGURE 9.2.18a. Specimen Geometry for a Double Edge-Notched 6061-T6 Aluminum Panel

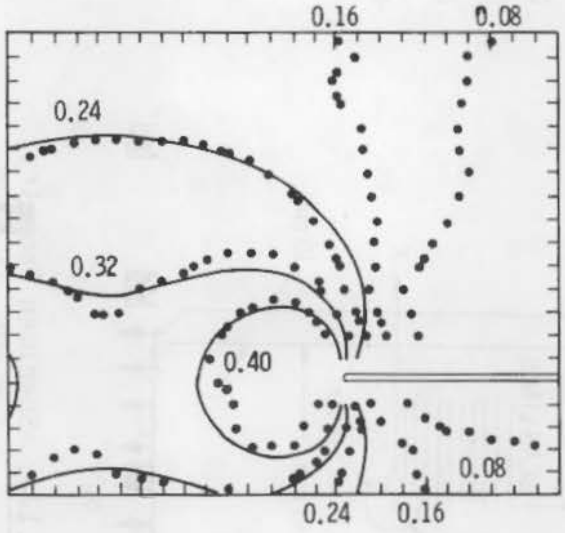

• Δf/f CONTOURS DETERMINED EXPERIMENTALLY (%)
—— PHOTOELASTICALLY CALIBRATED MODE I CRACK SOLUTION STRESS INVARIANT CONTOURS

FIGURE 9.2.18b. Constant Stress Contours Determined Acoustically and Photo-Elastically for a Double Edge-Notched Panel

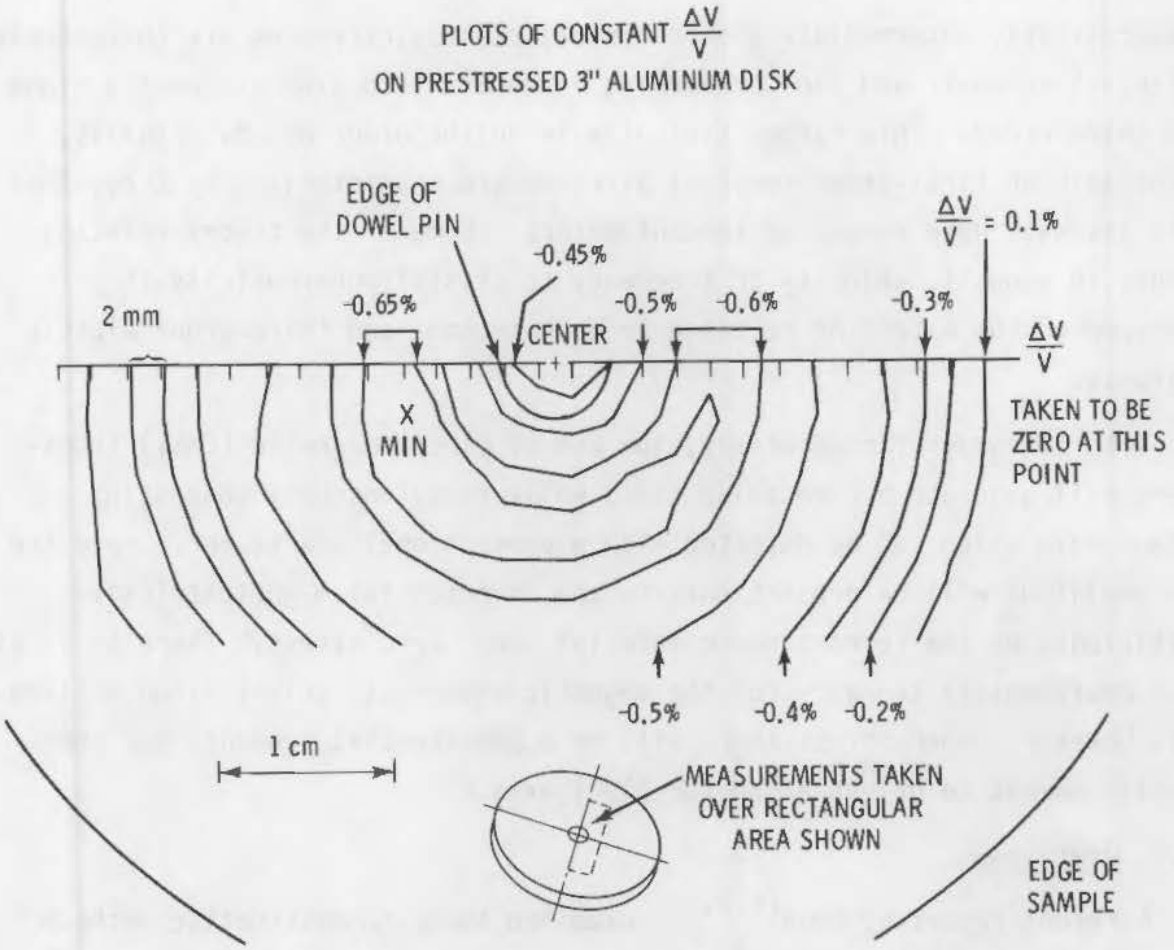

FIGURE 9.2.19. Contour Plot of Changes in Acoustic Velocity of Prestressed 3-in. Aluminum Disk. The acoustic velocity at a point 25 mm away from the center is chosen as the reference.

surfaces of the disk were machined flat and parallel. The initial deformation resulted in retained residual stress at a maximum nearest the hole decreasing to a baseline value at about 1 in. The maximum decrease in velocity due to the stress was $\Delta V/V = 0.65\%$.

The preceding approach appears to have considerable promise; however, it will be necessary to examine results from a three-dimensional residual stress distribution before a final assessment of the system can be made.

A combined theoretical/experimental study of Buck and Thompson[9.2.19] examined acoustic and magnetic techniques to detect and measure microscopic residual stresses (third order) typically having ranges of 100 to 1000Å

(dislocations); intermediate (second order) residual stresses are characterized by X-ray line shift and line broadening in contrast to line broadening alone with third order. This ranges typically is on the order of μm. Finally, macroscopic or first-order residual stresses are characterized by X-ray line shift and will have ranges up to centimeters. Some of the theory relating changes in acoustic velocity or frequency to crystal anharmonicity is developed to the extent of relating to both second- and third-order elastic constants.

With ferromagnetic materials, the use of electromagnetic (EMAT) transducers will generate a Lorentzian field while simultaneously generating a UT surface wave which can be detected with a conventional transducer. Here the peak amplitude will be proportional to the differential magnetostrictive coefficients of the ferromagnetic material under zero stress. There is little or no preferential tendency for the magnetic moments to orient along a given axis; however, under stress there will be a preferential tendency for the magnetic moment to orient along the [100] axis.

9.2.4 Overview

A recent report by Ruud[9.2.20] examined those nondestructive methods deemed to be applicable to nuclear reactor pressure vessels and piping. The author reviewed hole drilling x-ray diffraction, ultrasonics, BNA, magnetorestriction, Mossbauer and indentation methods. He considers x-ray diffraction to be the only proven technique at this time. In the long term, ultrasonic is considered to have the most potential for defining bulk residual stresses. Coverage is quite extensive in this report and is suggested as an excellent reference document. In excess of 150 references are cited in the report.

9.3 BULK TENSILE AND COMPRESSIVE STRESSES

A 1968 paper by Crecraft[9.3.1] describes a "sing-around" technique for measuring tensile and compressive stresses in materials with UT. In essence, his "sing-around" technique corresponds to the ultrasonic birefringence technique cited by later authors. Figure 9.3.1 from Crecraft[9.3.1] develops the analog of ultrasonic waves in stress analysis to light waves in photoelasticity. The polarized wave (either UT or light) enters the material and resolves into two components, each polarized along a principal stress axis. These two waves travel with different velocities, depending on stress and other characteristics of the solid. The waves may or may not have the same phase, depending on the number of wavelengths of "relative retardation" experienced; hence, the familiar fringes (birefringence). Velocity difference is measured because the change in total velocity is too small to measure with sufficient accuracy.

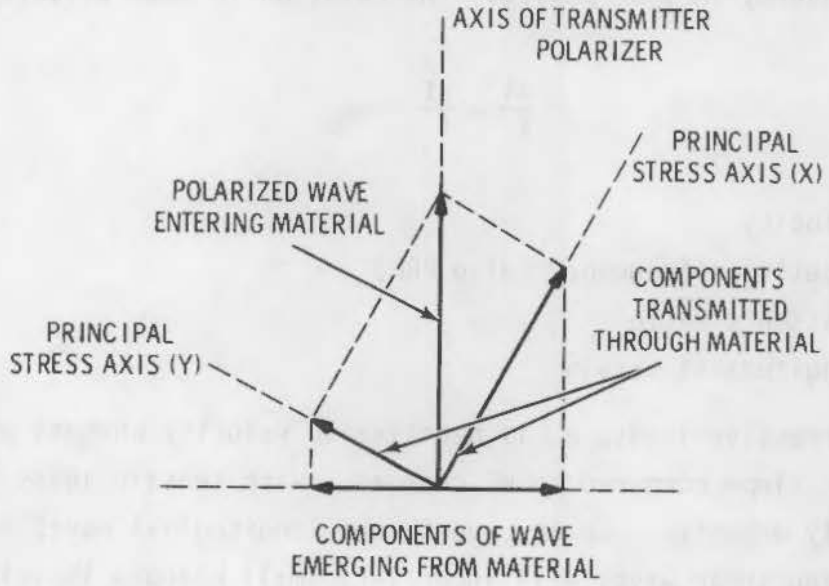

FIGURE 9.3.1. Section Through XY Plane of Material Under Stress Showing the Space Intensities of Light Waves in Photoelasticity and Ultrasonic Shear Waves in Sonoelasticity, with "Crossed" Polarizers

The bases for measurement are the transmittal of a shear wave through a specimen, an attempt to find the two principal stress axes in the plane normal to the direction of wave propagation, and a measurement of the phase shift between the two emerging waves.

The "sing-around" technique derives its name from the procedure which consists of selecting an echo from the transmitted pulse; this echo is used to trigger the transmitter so that the system recycles or "sings around" with a period of repetition which equals the time for the selected echo to arrive at the receiving transducer.

An example of data collected with the "sing-around" technique is given in Figure 9.3.2 for longitudinal waves and shear waves measured parallel and perpendicular to applied tensile and compressive stresses. As noted, the changes in longitudinal waves and in shear waves polarized perpendicular to the axis of stress are very small. The vertical axis on Figure 9.3.2 is in terms of repetition frequency (RF) or period. The relation to beam velocity is

$$\frac{\Delta V}{V} = \frac{\Delta f}{f} - \nu e_L \qquad (9.3.1)$$

where V = velocity
f = repetition frequency (also PRF)
ν = Poisson's ratio
e_L = longitudinal strain

Under compressive loads, e_L is negative so velocity changes will have a slight positive slope compared to RF changes. With tensile loads this slope will be slightly negative. In any event, the longitudinal waves and perpendicularly polarized shear waves will incur very small changes in velocity, confirming the futility of using longitudinal waves for stress measurements (including residual stress) since the very small changes are swamped out by variations in composition, inaccuracies in measurement of beam path lengths, etc.

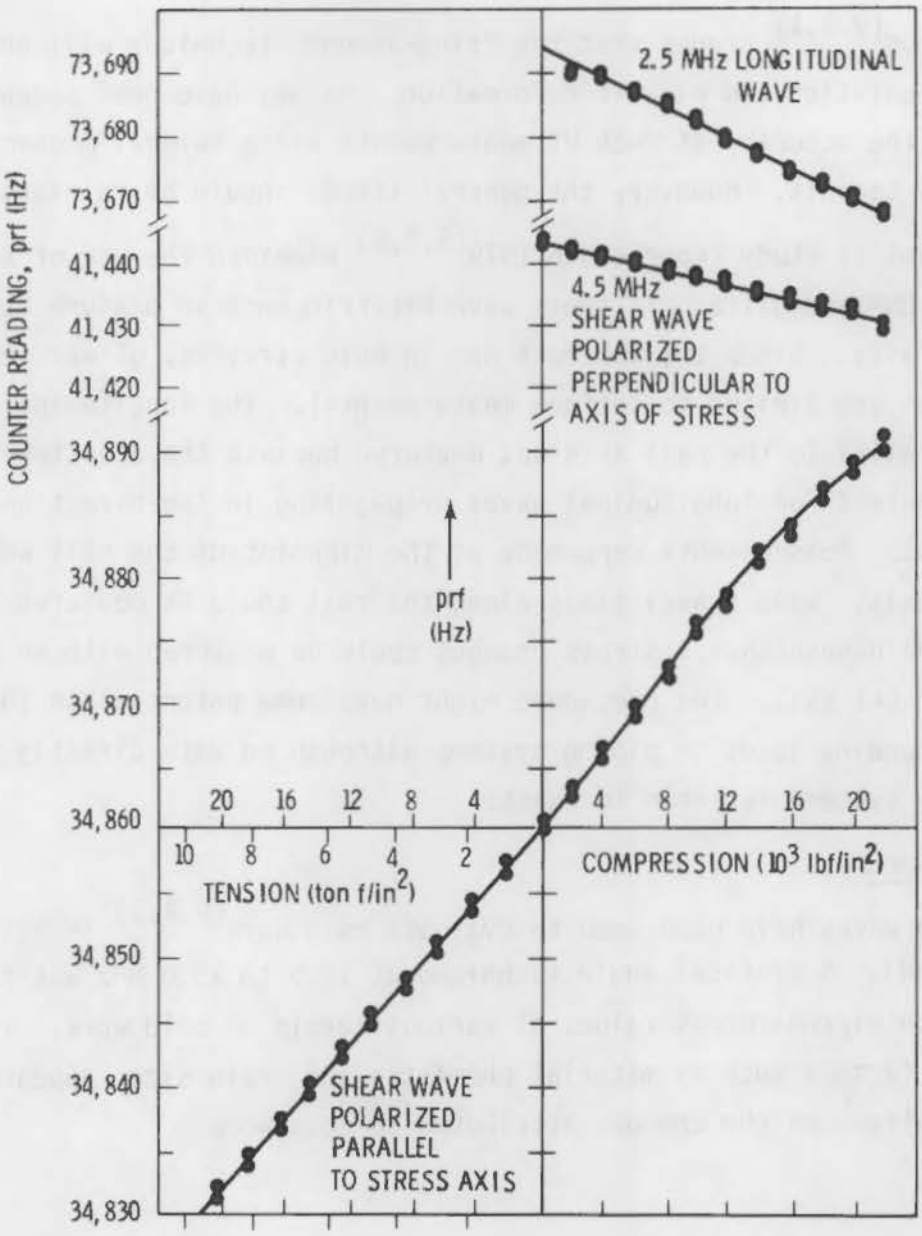

FIGURE 9.3.2. Variation of "Sing-Around" PRF with Compressive and Tensile Stress in Nickel Steel

The relatively large change in values for the shear wave polarized parallel to the axis of stress is believed due to changes in the effective shear, or rigidity modulus due to changes in the applied stress. The parallel polarized shear wave shears in these same planes, explaining the comparatively large variation. The perpendicularly polarized wave shears in the plane of the bar cross section where no shear strain occurs under axial loading.

The author[9.3.1] argues that the "sing-around" technique will detect preferred orientation and plastic deformation. He may have been somewhat optimistic as to the accuracy of such UT measurements since several mechanisms can lead to false signals. However, the general trends should be relevant.

A substantial study reported in 1979[9.3.2] examined the use of X-ray diffraction, BNA and ultrasonic shear wave birefringence to measure stresses in railroad rails. Since the interest was in bulk stresses, UT was selected (X-ray and BNA are limited to surface measurements). The longitudinal wave traveling parallel to the rail axis was measured because the acousto-elastic effect is greatest for longitudinal waves propagating in the direction of applied stress. Measurements were made at the midpoint of the rail web near the neutral axis. Wave travel times along the rail could be measured to an accuracy of ±3 nanoseconds. Stress changes could be measured with an accuracy of ±6.9 MN/m^2 (±1 ksi). The procedure might have some potential in the measurement of bending loads in piping systems although no data directly applicable to piping systems is known to exist.

9.3.1 Cold Work

Rayleigh waves have been used to evaluate cold work[9.3.3] in austenitic stainless steel. A critical angle technique at 12.5 to 15.0 MHz was found to correlate with microhardness values at various levels of cold work. At these frequencies, factors such as material chemistry and grain size, appeared to have little effect on the changes attributed to cold work.

9.4 SURFACE HARDNESS

Rayleigh waves were used to evaluate the surface and near-surface properties of a case-hardened steel.[9.4.1] A frequency range of 0.5 to 6.0 MHz was used. The basic assumption was that all hardness changes were due to changes in the shear constant, C_{55}. The mathematical development for C_{55} is given in Chapter 9A. In essence, a curve-fitting technique was used where the C_{55} limiting value was measured deep within the rod. Curves were benchmarked using the unperturbed elastic constants. Figure 9.4.1 relates Rayleigh wave frequency to penetration depth in a solid such as steel, together with pictorially representing the displacements in a solid accompanying exposure to

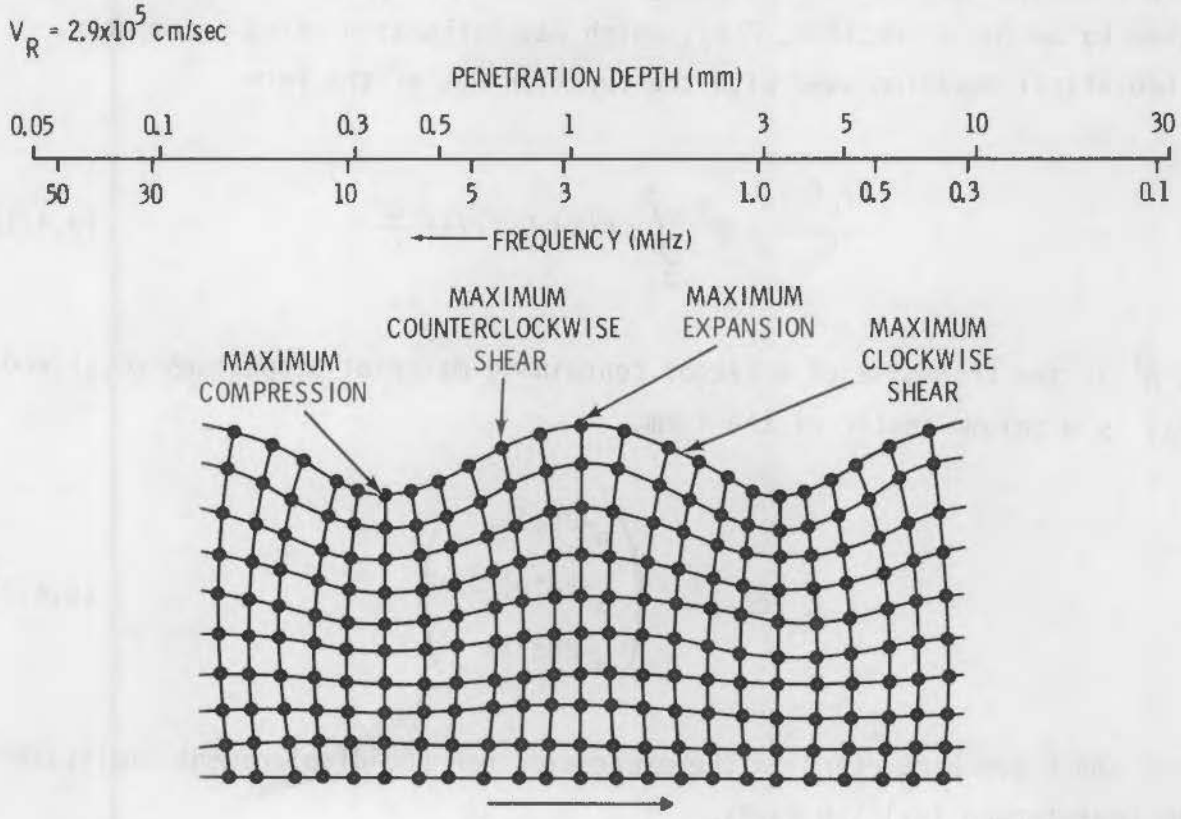

FIGURE 9.4.1. Pictorial Representation of Displacements Which Accompany a Rayleigh Wave. The line drawing in the upper figure is a logarithmic plot showing the penetration depths for various frequencies for a typical Rayleigh wave velocity of $V_R = 2.9 \times 10^5$ cm/sec.

Rayleigh waves. A 3-in.-dia bar of steel was oil quenched from above the austenitizing temperature to develop a hardened and stressed cylinder varying in properties from surface to center. Both hardness and Rayleigh wave velocity (6 MHz) gradients were measured by successively removing 0.030-in. layers and measuring hardness and wave velocity. Figure 9.4.2 presents these data as well as velocity changes measured on the hardened but unmachined bar. The curve shapes for Figures 9.4.2a and 9.4.2b are quite comparable as is Figure 9.4.2c; however, one might postulate that the similarity in curve shapes was fortuitous. The authors[9.4.1] attempted (apparently successfully) to establish that the measurements of velocity versus frequency contain the same information as the destructively determined Rayleigh wave velocity versus depth (Figure 9.4.2b). The measured Rayleigh wave veloc- ity as a function of depth was used to define a function, F(z), which was integrated using a computer. The theoretical equation used with the function was of the form

$$\frac{\Delta V_R(\lambda)}{V_R} = \underline{M}^T \int_0^\infty F(z)\, \underline{E}\,(Z/\lambda)\, \frac{dz}{\lambda} \qquad (9.4.1)$$

where $\underline{M}^T$ is the transpose of a vector containing material properties (C,ρ) and $\underline{E}\,(z/\lambda)$ is a column vector of the form.

$$\underline{E}\,(z/\lambda) = \begin{pmatrix} e^{-2az/\lambda} \\ e^{-(a+b)\, z/\lambda} \\ e^{-2bz/\lambda} \end{pmatrix} \qquad (9.4.2)$$

where a and b are parameters in the expression for the displacement amplitude of the unperturbed Rayleigh waves.

The basic assumption in the integration was that a change in shear constant, ΔC_{55}, was responsible for the entire variation in the surface wave velocity. The solid line in Figure 9.4.3 represents the integration of the

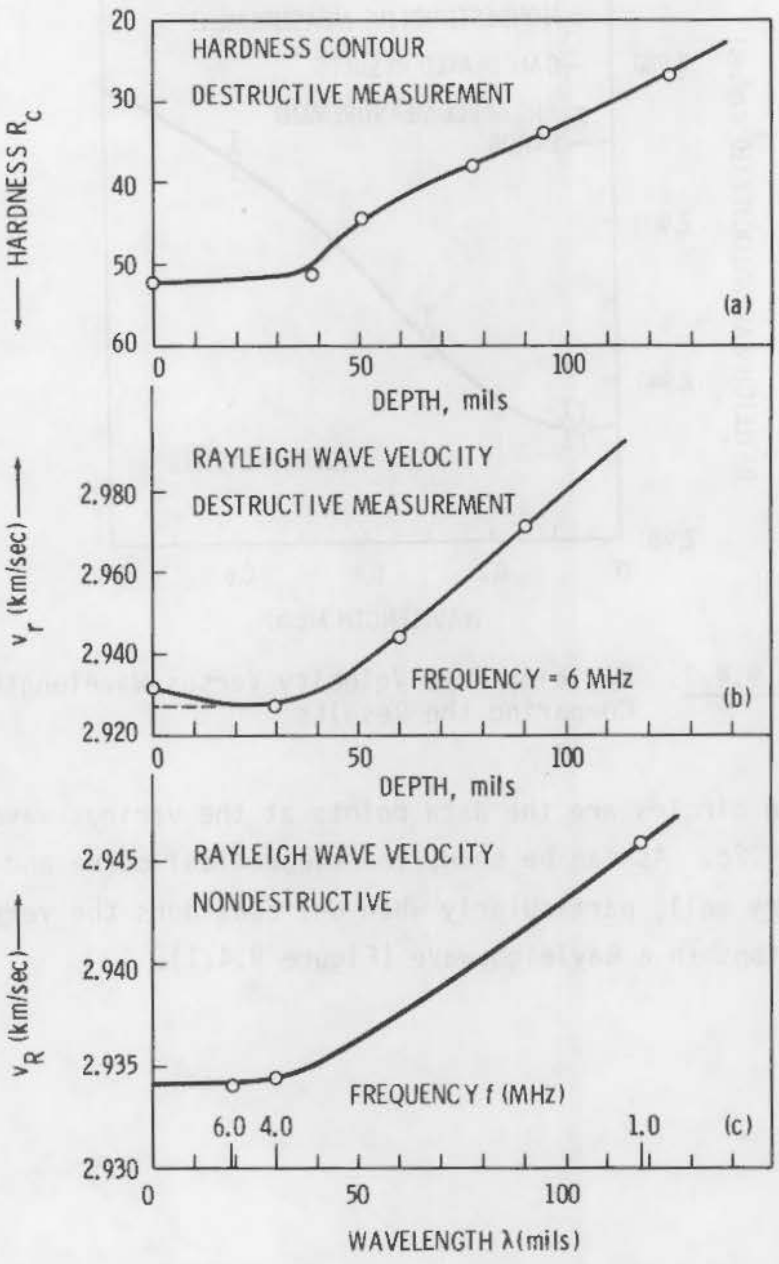

FIGURE 9.4.2. Respectively, (a) and (b), Plots of Hardness R_C and Rayleigh Wave Velocity V_R Versus Depth (measured from the surface) Obtained in Destructive Measurements, and (c), a Plot of V_R Versus Frequency and Wavelength Obtained in a Nondestructive Measurement.

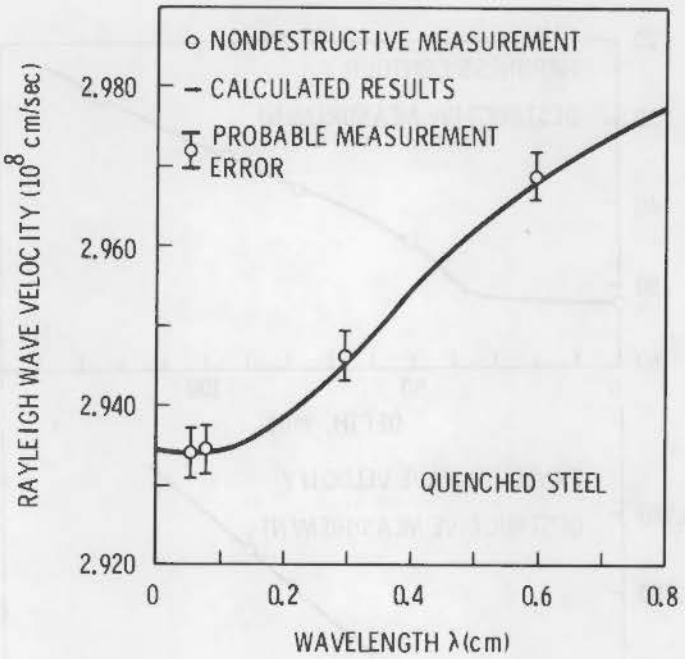

FIGURE 9.4.3. Rayleigh Wave Velocity Versus Wavelength, Comparing the Results

equation. The open circles are the data points at the various wavelengths shown in Figure 9.4.2c. As can be seen, the theoretical curve and the observed data points fit very well, particularly when one considers the very complicated displacement functions in a Rayleigh wave (Figure 9.4.1).

9.5 FATIGUE DAMAGE

Extensive work has been done relevant to the detection and characterization of fatigue damage. Green[9.5.1] critically reviewed the information relevant to detection of fatigue damage in a 1973 paper, citing some 44 references relevant to detection. He concentrated on four techniques used to measure fatigue damage:

- bulk wave reflection
- surface wave reflection
- ultrasonic attenuation
- acoustic emission.

On a rating basis, Green[9.5.1] dismissed both body and surface wave reflection techniques as being markedly inferior because both require a substantial fatigue crack prior to reliable detection. While acoustic emission was considered much better than the preceding two, it cannot detect static flaws, nor can it operate too satisfactorily in a high background noise field. This leaves ultrasonic attenuation as the preferred technique because it can detect motion of dislocations as well as the vibrations of dislocation loops. Again, it should be recognized that other factors contribute to attenuation and these need to be considered.

A study[9.5.2] of the early stages of fatigue in rotating beam specimens of aluminum and steel used Rayleigh waves and longitudinal waves as well as measurements of attenuation as methods of prediction of fatigue, either low cycle or medium cycle. A majority of the work was with Rayleigh waves so one should recall the reservations cited by Green.[9.5.1] Figure 9.5.1 permits a comparison of changes in UT signal during both early and late stages of fatigue crack growth. The influence of grain size can be observed in the lower figure.

ALN has been used to predict fatigue damage in low-cycle, reverse-bending, fatigue loading of 2024-T4 aluminum.[9.5.3] In this instance, 10-MHz, 45° UT was used to interrogate the fatigue specimens. Signatures used to detect and evaluate fatigue damage included signal-amplitude-time spectrum and cepstrum. They were able to detect fatigue damage after 10% of fatigue life with 92% success and estimates of damage could be made within ±20% of actual fatigue

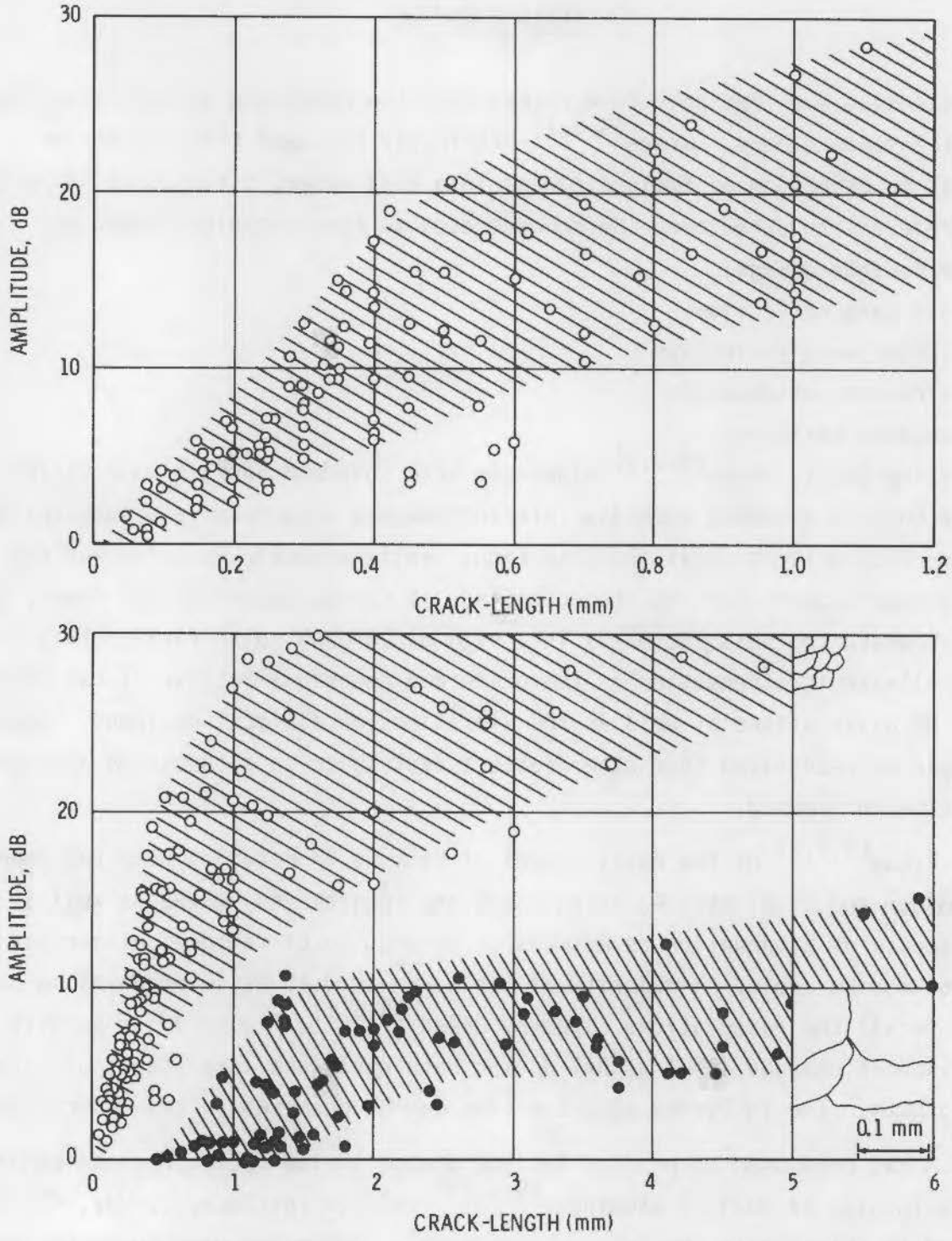

FIGURE 9.5.1. Comparison Between Rayleigh Wave Amplitude (dB) and Crack-Length (Steel CK 15)

life for about 76% of the data. Basically, the ALN detected very small cracks on the order of ~0.020-in. long by about 0.0030-in. deep. Definite differences in amplitude time signals occurred with increased fatigue.

High temperature creep-fatigue is less amenable to detection. A 2-1/4 Cr-1 Mo steel was examined after extensive creep-fatigue damage at 1100°F (595°C).[9.5.4] Ultrasonics and magnetic field analysis were used; however, neither yielded meaningful results.

9.6 GRAIN SIZE

A substantial paper[9.6.1] examined the relation between grain size and ultrasonic attenuation coefficients for both austenitic stainless steel and iron of various grain sizes. A comparison technique was used against a standard test block. Several parameters were investigated such as

Grain size--ASTM 7.5, 6, 5, 3.5, 3, 2.5, 1.5
Diameters 10^{-3} cm 3, 5, 7, 12, 14, 17, 23
Surface finish--~0.1 μ

Frequency MHz--2.25, 3, 5, 10, 15 (longitudinal)
Transducer size (mm-30ϕ, 25ϕ, 20ϕ, 20ϕ (X-cut), 10ϕ

Frequency MHz--3, 5, 10 (shear)
Transducer size (mm)--20 x 15, 20 x 13, 10 x 9 (Y-cut)
Couplants--spindle oil, vaseline, salol oil

The authors review the various theories for attenuation of ultrasound in polycrystalline metals (ignoring elastic anisotropy). The interested reader is referred to the report.[9.6.1] Table 9.6.1 contains the various theoretical derivations, together with an explanation of terminology.

If the scattering factor establishes the scattering attenuation, the ratio of the scattering factors of two materials such as stainless steel and iron will yield a similar ratio for scattering attenuation coefficients, providing the values of $\pi D/\lambda$ (grain size and wavelength) are the same for both materials. Available information would yield the following values as scattering factors:

Mode of Wave	Scattering Factor		R = Scattering Factor 18/8 / Scattering Factor Iron
	Iron	18/8 SS[a]	
Longitudinal	6.7×10^{-3}	$11 \text{ to } 14 \times 10^{-3}$	1.6 to 2.1
Shear	4.0×10^{-3}	$60 \text{ to } 90 \times 10^{-3}$	1.5 to 2.3

(a) Estimated from elastic moduli of 18/19, 18/14, 19/12 stainless steels determined experimentally.

TABLE 9.6.1. Comparison of Formulations Based on Various Theories for Attenuation of Ultrasound in Polycrystalline Metals (elastic anistropy ignored)

Theory		
Mason Longitudinal Wave	$\alpha_{sl}D = \frac{H}{3}\frac{(\pi D)^4}{\lambda}; \frac{D}{\lambda} < 1/3$	
Shear Wave	$\alpha_{ss}D = \frac{4H}{9}\frac{(\pi D)^4}{\lambda}; \frac{D}{\lambda} < 1/3$	
Bhatia Longitudinal Wave	$\alpha_{sl}D = \frac{H}{15}\left[1 + \frac{3}{2}\left(\frac{V_l}{V_s}\right)^5\right]\left(\frac{\pi D}{\lambda}\right)^4; \frac{D}{\lambda} < 1$	Velocity effects of Waves
Shear Wave	$\alpha_{ss}D = \frac{2H}{15}\left[1 + \frac{2}{3}\left(\frac{V_s}{V_l}\right)^5\right]\left(\frac{\pi D}{\lambda}\right)^4; \frac{D}{\lambda} < 1$	
Krainer Longitudinal Wave	$\alpha_{sl}D = \frac{H}{3}\left(\frac{\pi D}{\lambda}\right)^2; \frac{D}{\lambda} < 1$	
Morse as deduced by Richter and by Hikata	$\alpha D = 2H\left(\frac{\lambda}{\pi D}\right)^2 \sum_{m=0}^{\infty}(2m+1)\sin^2 d, \; 0 < \frac{D}{\lambda} < \infty$	Scattering by a sphere

NOTE: All above consider αD as product of $\pi D/\lambda$ and scattering factor, H.
α_s = scattering attenuation coefficient
H = scattering factor
D = grain diameter
f = frequency = $1/\lambda$
λ = wavelength
n = positive integer.

The R ratio did not bring the two sets of measurements into coincidence. This was due to the effective grain size of stainless steel being smaller than the apparent grain size because of the large number of twin boundaries having the same effect as grain boundaries on ultrasonic waves. An empirical procedure led to estimation of the effective size to be 0.62 to 0.65 D_A where D_A is apparent grain size. Measurement of effective grain size using photomacrographs and counting both twin and grain boundaries gave a range of 0.6 to

0.8, which was considered a reasonable check of 0.62 to 0.65. Figure 9.6.1a,b compares the experimental values and theories for both longitudinal and shear waves. As noted, only the theoretical approach proposed by Morse compared favorably to the data insofar as curve shape was concerned. A relatively minor correction would bring the curves into agreement.

Kinman et al.[9.6.2] investigated the relationship of ultrasonic attenuation to grain size, strength and toughness of plain carbon steel. Nine ingots varying in carbon, manganese and silicon contents were hot-rolled into 46 plates, each 0.75-in. thick. Emphasis was given to five heats denoted as A, F, G, H, and I, where the major variable was carbon content which ranged from 0.05 to 0.38%; the plates were annealed over a range of temperatures to produce grain sizes ranging from a low of ~12 μm to a high of 238 μm. Grain sizes, volume-percentage pearlite, tensile and impact properties were determined using ASTM procedures. In addition, the attenuation for each condition was determined at 5 MHz in terms of dB/in.

As will be seen from the figures and tables discussed in this section, as well as in 9.10 and 9.11, excellent correlations were obtained. Extrapolation to other materials, including low alloy steels, would be unjustified because the changes observed are due to the well-known relationships between grain size and yield strength or impact properties for pearlitic steels. The same relationships cannot be applied to bainitic or martensitic steels where hardenability, not grain size, controls. Even so, the grain size relationship might apply to thick-sectioned A-533 Gr B steels subjected to the same heat treatments or to materials such as SA-106 used in piping. Until substantial testing has been done it would be unwise to assume valid relationships between attenuation and mechanical properties for the alloy steels.

The authors[9.6.2] built on the extensive literature of plain carbon steels and the Hall-Petch relationships:

$$YS = Y_o + K_y d^{-1/2} \qquad (9.6.1)$$

$$TT = T_o + K_T d^{-1/2} \qquad (9.6.2)$$

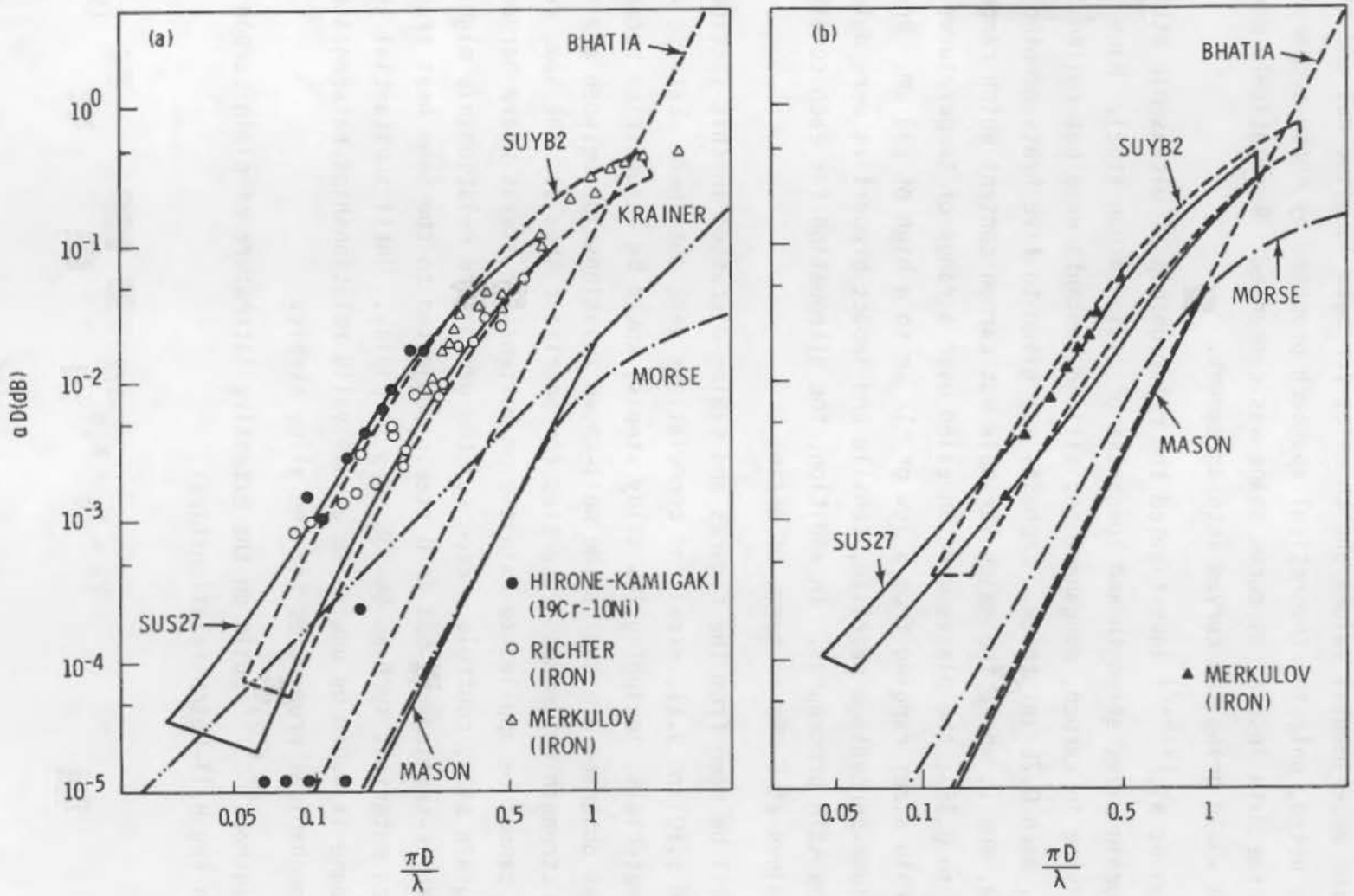

FIGURE 9.6.1. Comparison of Experimental Results and Theories in (a) Longitudinal Wave, and (b) Shear Wave

Y_o and T_o depend on alloy composition and percentage of pearlite; K_Y and K_T are constants, and d is the mean ferrite intercept, a measure of average grain diameter with tensile strength. Grain size has less influence while composition and pearlite are important.

Earlier work cited developed relationships with regard to UT such as

- Ultrasonic attenuation can be used to measure the mean ferrite grain diameter in a given type of steel.
- The application of UT attenuation should be in the Rayleigh region given by $\lambda > 2\pi d$, where λ is the wavelength.

The attenuation relationship in the Rayleigh region due to grain-boundary scattering is

$$\alpha_s = \alpha_o + Kd^3f^4 \qquad (9.6.3)$$

where α_o is approximately constant for a given material and f is the ultrasonic frequency.

Definitive relationships existed for attenuation versus grain size or reciprocal grain size as can be seen in Figures 9.6.2a and 9.6.2b. Figure 9.6.2a illustrates that too small a grain size or too low a frequency cannot be interpreted because of the flattening of the curve. At the other extreme, a grain size cutoff is suggested well below $d_c \leq \frac{\lambda}{2\pi}$, so $\frac{dc}{2}$ was selected. A reasonable range of grain size was deemed to be 35 μm to 115 μm. Figure 9.6.2b explores the relationship of $d^{-1/2}$ to attenuation over the range of 35 to 115 μm. The curve is a rough approximation of a straight line.

Based on work of Serabian[9.6.3] it appears possible that ultrasonic attenuation measurements can be used beyond the Rayleigh range. A wide spectrum of materials were examined having a spectrum of grain sizes. Values came from both the literature and work of the author.

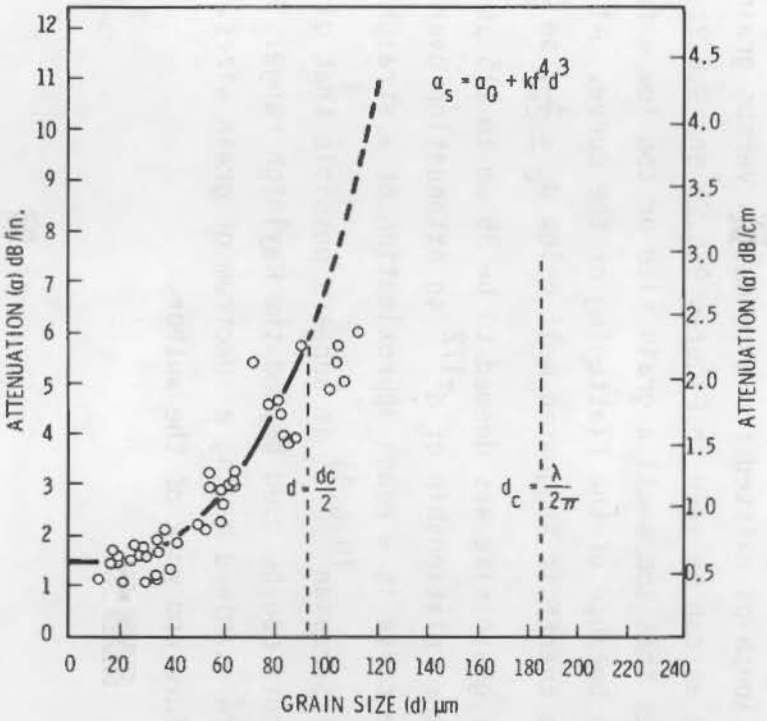

FIGURE 9.6.2a. Metallographically Measured Mean Ferrite Intercept (grain size) Versus the Ultrasonic Attenuation at 5 MHz

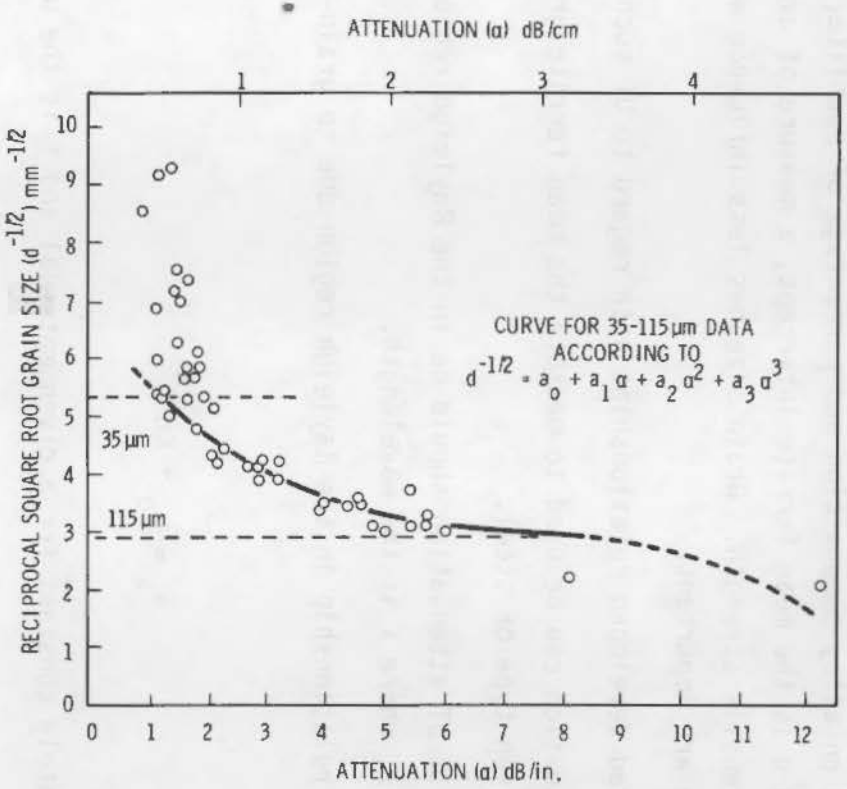

FIGURE 9.6.2b. Reciprocal Square Root Grain Size ($d^{-1/2}$) Versus Ultrasonic Attenuation (α) at 5 MHz

Reviewing the basic loss mechanisms involved in the scattering of ultrasound in polycrystalline materials the following summarizes these relationships:

Wavelength to Grain Diameter Range	Mechanism	Attenuation
$\lambda >> \overline{D}$	Rayleigh	$\left(\frac{\overline{\Delta K}}{K}\right)^2 \overline{D}^3 f^4$
$\lambda \cong \overline{D}$	Phase	$\left(\frac{\overline{\Delta K}}{K}\right)^2 \overline{D} f^2$
$\lambda << \overline{D}$	Diffusion	$\left(\frac{\overline{\Delta K}}{K}\right)^2 \frac{1}{\overline{D}}$

Typically, a $\overline{D}^m f^m$ type relationship.

Since most structures, even those with a highly uniform grain size, will have some mix of grains, one would not expect to see integers as exponents. Rather, there will be a mix of values. A plot such as Figure 9.6.3 provides values of m for the grain size dependency of attenuation. Plots of attenuation versus frequency, when measured over a wide range of MHz, yield values of the exponent n as slopes for a given specimen having a specific grain size. For each material and each grain size, a value of n can be obtained. Figure 9.6.4 from Serabian[9.6.3] illustrates a frequency dependency (n) versus grain diameter. The small grains are in the Rayleigh range; n is 3 to 4. However, at larger grain sizes, n is 1.5 to 2.5 typical of phase scattering. These results indicate that the grain size as such can be related to attenuation. Whether these relationships can be extended to predicting mechanical properties is another matter.

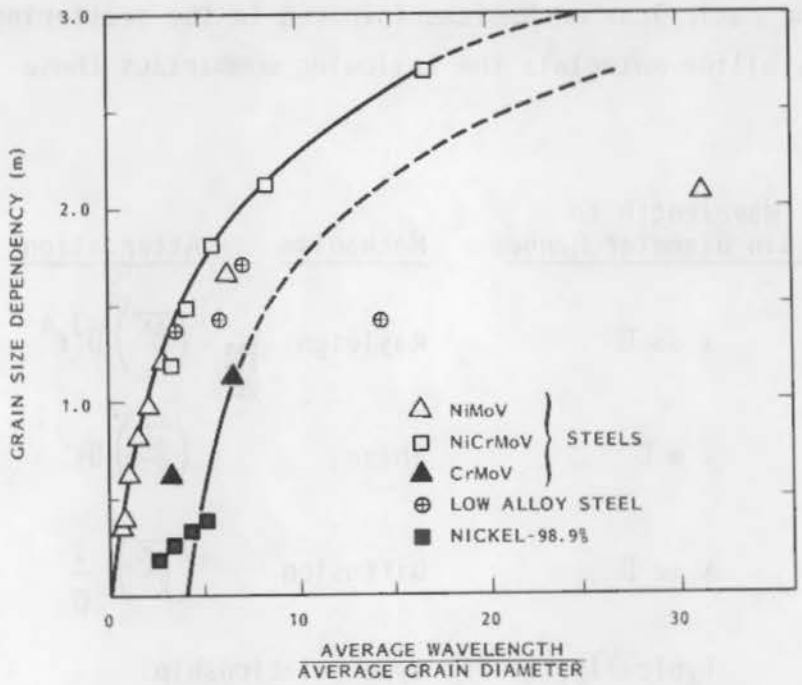

FIGURE 9.6.3. Grain Size Dependency (m) of Longitudinal Wave Attenuation as a Function of the Ratio of the Average Wavelength to the Average Grain Diameter

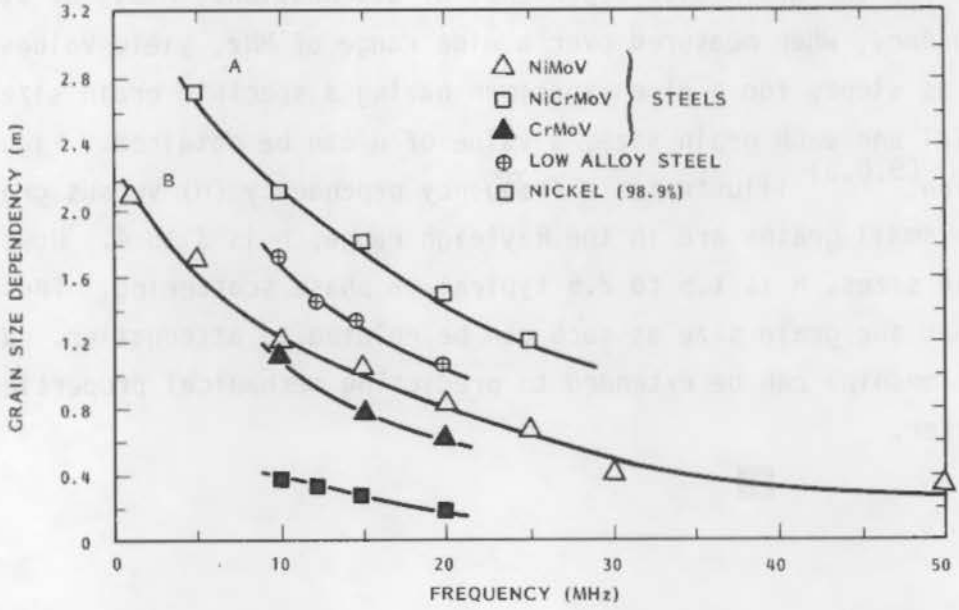

FIGURE 9.6.4. Grain Size Dependency (m) of Longitudinal Wave Attenuation as a Function of Frequency

9.7 RADIATION DAMAGE

A few studies[9.7.1,9.7.2,9.7.3] have examined the changes in ultrasonic velocities resulting from neutron irradiation of ferritic and austenitic steels. An initial study[9.7.1] with A-302 B and A-542 B steels which had been irradiated at relatively low temperatures (140° to 350°F) (60° to 180°C), did yield substantial velocity changes; however, a later study with A-533 B irradiated at 550°F (285°C) gave velocity changes of less than ±0.15%; these changes were considered too small to permit reasonable predictions.

A later study[9.7.3] measured changes in acoustic velocities as a mechanism for determining post-irradiation elastic moduli. Changes in shear, bulk and Young's moduli ranged from 1% to 1.7%, which was much better than earlier studies. However, high attenuation in the irradiated specimens, together with swelling, prevented the acoustic evaluation of all specimens.

9.8 LAMELLAR TEARING

One study[9.8.1] examined UT as a method for assessing the susceptibility to lamellar tearing. Earlier work at 5 to 20 MHz yielded very poor correlations using attenuation measurements as the bases. The modified procedure utilized high gain probes and correlated the data with percentage reduction of area values from short transverse tensile specimens. The correlations obtained were found to depend on the type(s) of inclusion present. A good correlation was obtained between the mean integrated echo signal-per-unit thickness ($\Sigma I/mm$) and short transverse reduction-in-area values. Total "echo count" values yielded a poor correlation. The integrated echo values give different correlations for aluminum-killed steels and for steels not aluminum killed. Work is continuing, particularly to better understand some predictions which were not accurately matched by the tensile data.

9.9 ELASTIC CONSTANTS

The development of mathematical derivations relevant to the spectrum of elastic constants has been given in Chapter 9A. The reader is referred to it since these derivations will not be repeated again. With regard to the specifics of second-order and third-order elastic constants, they will be addressed in subsection 9.9.1. Substantial work has been reported for elastic constants. The data presented herein will be limited to materials used in the reactor pressure boundary.

9.9.1 Second- and Third-Order Elastic Constants

Two cast (centrifugally) grades of austenitic stainless steel piping, CPF 8 and CPF 8M, were examined.[9.9.1] A closely parallel study by the same authors[9.9.2] was made using a 304 SS plate containing an electroslag 308 SS weld.[9.9.2] Both studies assumed orthotropic symmetry with a cylindrical coordinate system, [radial (r), circumferential (t), longitudinal (z)]. It was assumed that (r, t, z) were axes of symmetry. Both high and low ferrite alloys were examined. The t-z plane was considered to be a plane of isotropy whereas t-r and z-r planes were orthotropic. Microstructures confirmed the assumptions of isotropic and orthotropic symmetry. Table 9.9.1[9.9.1] confirms the validity of the isotropic symmetry in the t-z plane. It was not possible to obtain values for the CPF 8M high ferrite case due to very large grain size alignment away from r direction. The significance of different elastic constants in the various r, t, z directions is apparent in Table 9.9.2 where the radial strains are much greater for the anistropic case than for the generally accepted (by ASME) isotropic case. These larger strains will influence fatigue life predictions as one example.

The changes in elastic constants with direction are even more pronounced in the electroslag weld, Table 9.9.3.[9.9.2] Tensile tests further confirmed the orthotropic symmetry with isotropic symmetry in one plane. Figure 9.9.1 illustrates the changes in yield strength with orientation. In the isotropic plane values remain constant.

TABLE 9.9.1. Engineering Elastic Constants Measured by Ultrasonic Method

Constant	Value for Each Material: CPF 8 Low Ferrite	CPF 8 High Ferrite	CPF 8M Low Ferrite
Elastic Modulus, GPa			
E_t	133	158	145
E_z	135	153	147
E_r	123	127	125
Shear Modulus, GPa			
G_{rz}	95	93	91
G_{rt}	93	91	92
G_{zt}	62	63	58
Poisson's Ratio			
ν_{rz}	0.43	0.28	0.38
ν_{rt}	0.37	0.39	0.37
ν_{zt}	0.34	0.30	0.37

TABLE 9.9.2. Solutions Using Anisotropic Elastic Constants for Centrifugally Cast Stainless Steel Pipe (with outer-to-inner dia ratio of 1.21). Pipe is loaded by internal pressure p and restrained axially (plane strain).

Material	Dimensionless Stresses at Inner Surface: Hoop, $\sigma_{t/P}$	Axial, $\sigma_{z/P}$	Dimensionless Displacement at Inner Surface, Radial, $\mu E/pr_i$
CPF 8 Low Ferrite	5.3	2.02	7.11
CPF 8 High Ferrite	5.3	1.06	6.71
CPF 8M Low Ferrite	5.3	1.68	6.79
Austenitic Steel,[(a)] Isotropic Elastic Solution	5.3	1.25	5.61

(a) Value using room temperature E = 195 GPa and Poisson's Ratio = 0.29.

TABLE 9.9.3. Room Temperature Engineering Constants for Spatially Orthotropic Model of Electroslag Weld Metal and Reference Values

Constant	Measured Value
$E_{11} = E_{22}$	142 GPa
E_{33}	104 GPa
$G_{44} = G_{55}$	82 GPa
G_{66}	57 GPa
$\nu_{12} = 21$	0.24
$\nu_{13} = 23$	0.53
$\nu_{31} = 32$	0.39
E_{poly} (a)	195 GPa
E_{33} (b)	101 GPa

NOTE: E denotes Young's modulus, G shear modulus, and ν Poisson's ratio.
(a) Reference value for isotropic material.
(b) Reference value for single crystal.

Smith et al.(9.9.3) measured both second-order and third-order elastic moduli in several polycrystalline metals, steels, iron, aluminum alloys, magnesium, molybdenum, and tungsten. Only the steels are presented here. Only uniaxial stresses were used. Wave propagation directions were perpendicular to the stress direction (longitudinal); shear waves were polarized either normally or parallel to the stress direction. Table 9.9.4 contains both second- and third-order moduli. Table 9.9.5 contains pressure derivatives of the second-order moduli. The latter values check well with values from nonlinear elasticity tests.

The data in Table 9.9.4 are calculated using data such as are presented in Figure 9.9.2 which relate stress in the material to changes in ultrasonic

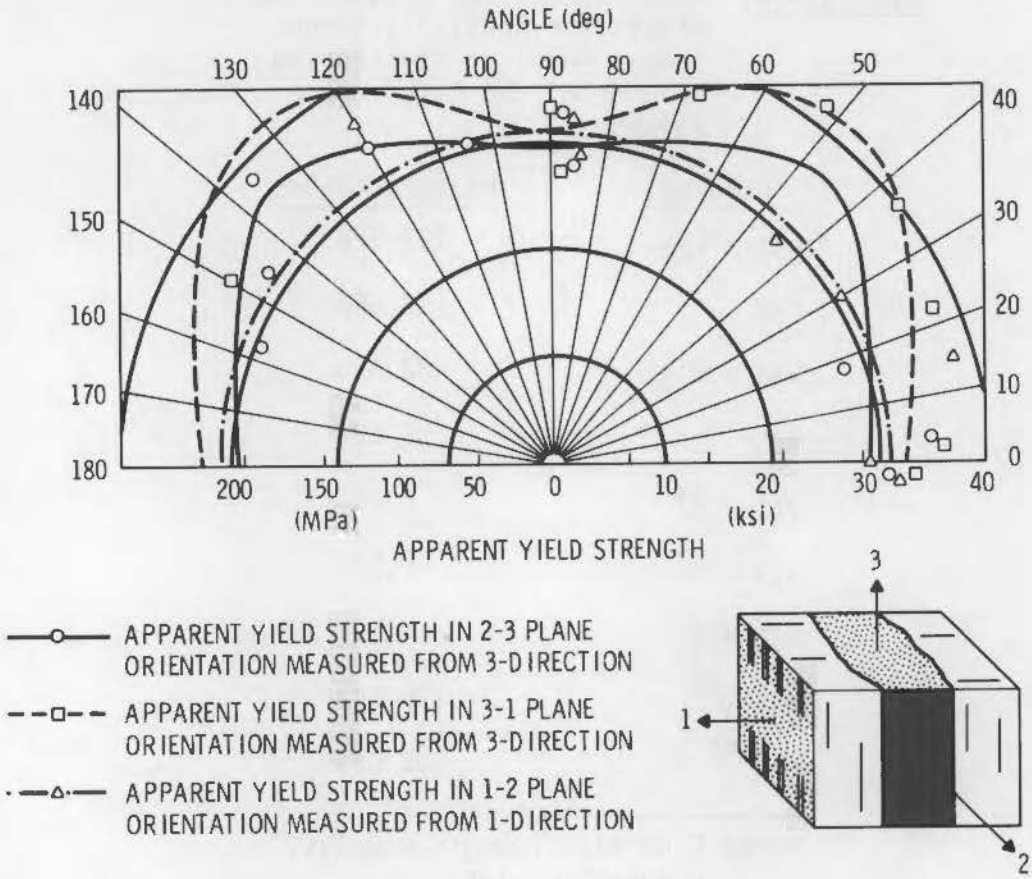

FIGURE 9.9.1. Directional Variation of Yield Strength at 0.1% Offset

TABLE 9.9.4. Elastic Data for Polycrystalline Specimens(9.9.3)

	Second-Order Moduli LAME' Constants		Third-Order Moduli		
Materials Steels	λ	μ	ν_1	ν_2	ν_3
Hecla 37 (0.4% C)	111 ± 1.0	82.1 ± 0.5	-358 ± 70	-282 ± 30	-177 ± 8
Hecla 17 (0.6% C)	110.5 ± 1.0	82.0 ± 0.5	-134 ± 20	-261 ± 30	-177 ± 6
Hecla 138A	109 ± 1.0	81.9 ± 0.5	-323 ± 50	-265 ± 30	-177 ± 10
Rex 535 Ni Steel	109 ± 1.0	81.8 ± 0.5	-175 ± 50	-240 ± 50	-169 ± 15
Hecla ATV (Aust.)	87 ± 2.0	71.6 ± 3.0	+34 ± 20	-552 ± 80	-100 ± 10

Note: Units Giga-Pascals.

TABLE 9.9.5. Pressure Derivatives of Second-Order Moduli

Material Steels	Stress MPa	Type Stress	Modulus (B_o), GPa	$\frac{\partial B}{\partial P_o}$	LAME' Constant (μ_o), GPa	$\frac{\partial \mu}{\partial P_o}$	Ref.
Hecla 37 (0.4%)	150	Uniaxial	166	6.5	82.1	1.96	9.9.3
Hecla 17 (0.6%)	150	Uniaxial	165	4.87	82.0	1.77	9.9.3
Hecla 138A (Ni-Cr-Mo Steel)	150	Uniaxial	164	6.17	81.9	1.89	9.9.3
Rex 535 (Ni Steel)	150	Uniaxial	164	4.92	81.8	1.68	9.9.3
Drill Rod	400	Hydrostatic	165	--	81.1	--	--
Hecla ATV (Aust.)	150	Uniaxial	135	8.6	71.6	3.9	9.9.3

NOTE: 1 MPa = 145.04 psi.

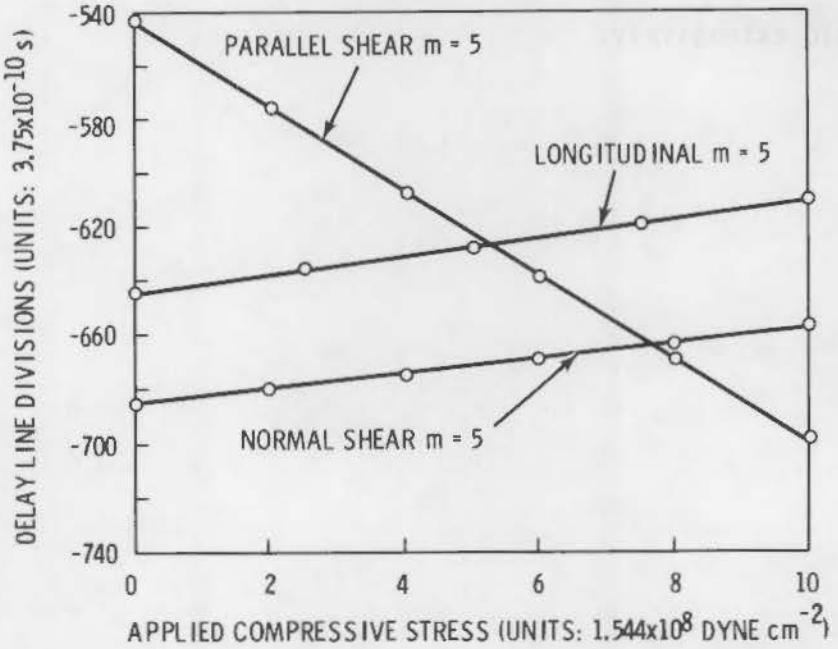

FIGURE 9.9.2. Typical Variation of ulse Transit Time Versus Applied Stress

wave velocity. The formulae in Chapter 9A are related to wave velocity, permitting calculation of relevant moduli of Tables 9.9.4 and 9.9.5. One can calculate the bulk and rigidity moduli as functions of pressure, using the third-order moduli data such as are given in Table 9.9.4 and the following equations:

$$\left(\frac{\partial \beta}{\partial P_o}\right) = -\left(\frac{1}{\beta_o}\right)\left[\nu_1 + 2\,\nu_2 + \frac{8}{9}\,\nu_3\right] \qquad (9.9.1)$$

$$\left(\frac{\partial \mu}{\partial P_o}\right) = -\left(\frac{1}{\beta_o}\right)\left[\nu_2 + \frac{4}{3}\,\nu_3 + \lambda + \mu\right] \qquad (9.9.2)$$

The preceding information, together with Chapter 9A, attempt to give the reader some idea of the theory underlying measurement of elastic constants, moduli, etc., as well as citing a few examples of results. No attempt was made to cover the field extensively.

9.10 FRACTURE TOUGHNESS

The published reports on the use of ultrasonics to "measure" fracture toughness properties are quite limited. Vary[9.9.1] cites his own work on the feasibility of ultrasonic measurement of K_{Ic} for two maraging steels and a titanium alloy. Empirical correlations were developeo relating ultrasonic attenuation factors to K_{Ic} and σ_y (0.2% yield strength) as noted in Figure 9.10.1. The equation for the line in Figure 9.10.1 is

$$\frac{K_{Ic}^2}{\sigma_y} = \Psi(V_e\ \beta_\delta)^e \qquad (9.10.1)$$

where v is ultrasonic velocity, β_δ is an ultrasonic attenuation factor, and Ψ and e are experimental constants.

Figure 9.10.2 relates yield strength to an ultrasonic "factor." The relationship appears to fit a linear equation of the form

$$\sigma_y + AK_{Ic} + B - \beta_1 = C \qquad (9.10.2)$$

where β_1 is an ultrasonic attenuation factor, and A, B and C are experimental constants that depend on the material involved. The author[9.1.1] states that seemingly essential measurements for deducing fracture toughness and yield strength can be made by purely ultrasonic techniques once calibration curves have been established for a given polycrystalline material. While the preceding section relevant to fracture toughness-yield strength is quite appealing, there are several reservations concerning its universal applicability. Ultrasonic attenuation results are due to many characteristics of a given material such as cold work, grain size, etc. Since this is the case, correlations such as appear in Figures 9.10.1 and 9.10.2 may be specific not only to a given material, but to each fabrication history. Obviously, such specificity will grossly limit the use of UT to measure such properties. It will require a substantial data base in order to permit a realistic evaluation of the validity of UT for measuring such properties.

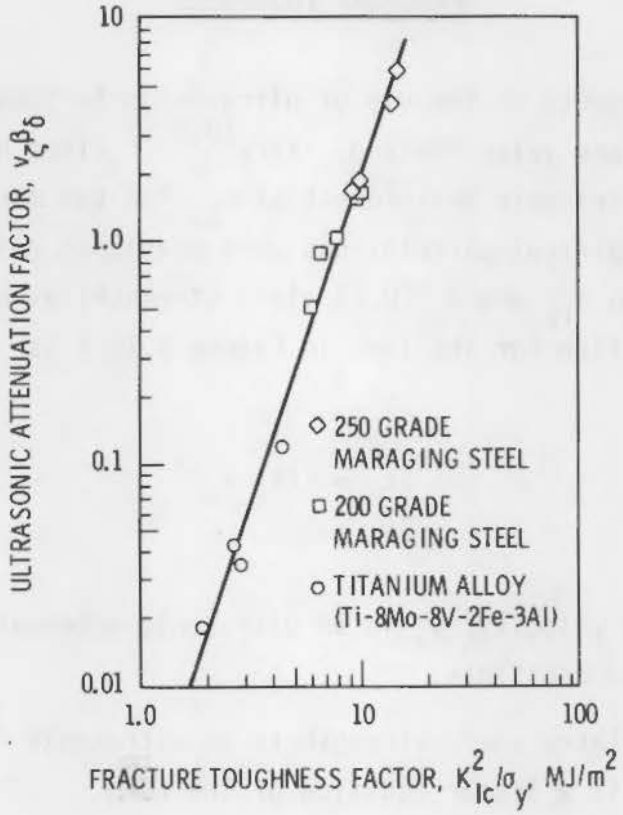

FIGURE 9.10.1. Correlation of Ultrasonic and Fracture Toughness Factors. The ultrasonic attenuation factor $v_\xi \beta_\delta$ is based on measurements of longitudinal velocity, V_ξ, and the slope of the attenuation versus frequency curve; $\beta_\xi \cdot K_{Ic}$ and σ_y are the plane strain fracture toughness and 0.2% yield strength respectively, as measured by destructive test methods.

Budiansky and Rice[9.10.1] developed a mathematical model for estimating the fracture mechanics parameter $K_\cdot = (K_1)\ max/\epsilon$ for a flat crack of initially unknown dimensions and orientation by using long wavelength NDE measurements. To date, the information published is limited to a model using previous long wavelength studies. It will be interesting to see how well the mathematical model is confirmed with specific UT data.

Kinman et al.[9.6.2] developed a grain-size toughness relationship for plain carbon steels. The same caveats apply with regard to attenuation cited

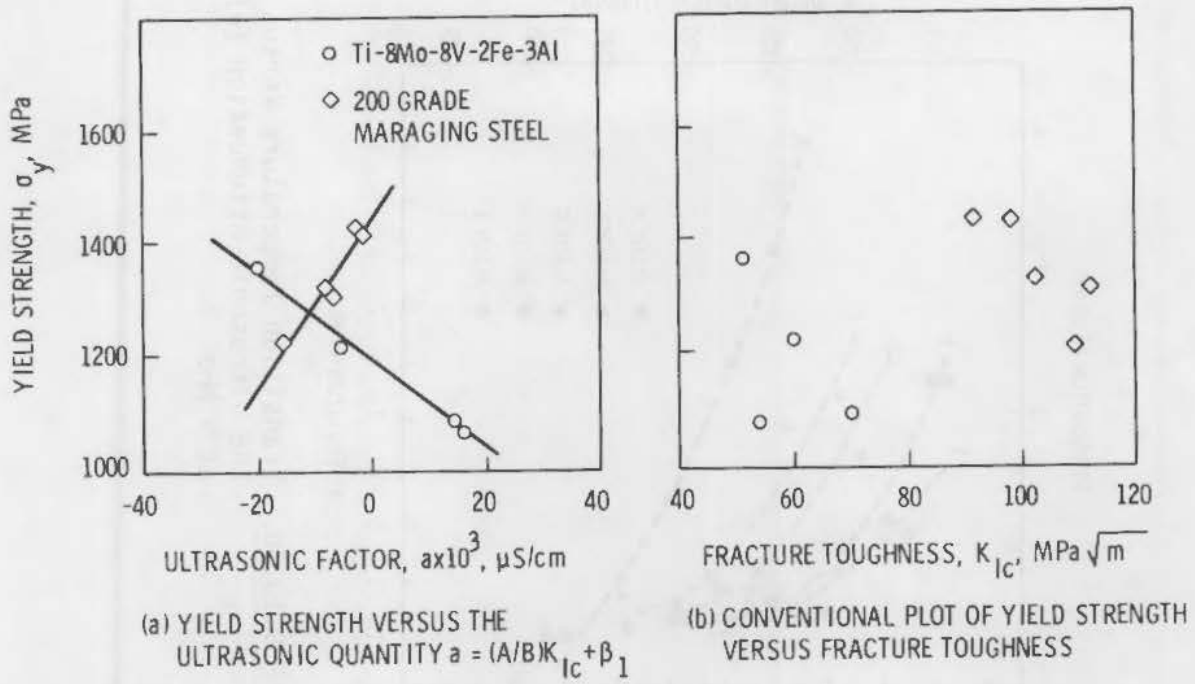

(a) YIELD STRENGTH VERSUS THE ULTRASONIC QUANTITY $a = (A/B)K_{Ic}+\beta_1$

(b) CONVENTIONAL PLOT OF YIELD STRENGTH VERSUS FRACTURE TOUGHNESS

FIGURE 9.10.2. Correlation of Yield Strength with Fracture Toughness via an Ultrasonic Factor. The ultrasonic quantity β_1 is determined by the slope of the attenuation versus frequency curve evaluated at unit attenuation. The quantities A and B are experimentally measured ultrasonic constants for a given material. K_{Ic} and σ_y are plane fracture toughness and 0.2% yield strength, respectively, as measured by destructive tests.

in section 9.6. While the relations given in Figures 9.10.3a and 9.10.3b and in Table 9.10.1 are good, similar relationships should not be assumed for low alloy steels. It can be seen that the curves generally are the same shape. More significantly, the confidence intervals over the 35- to 115-μm grain size range are very tight.

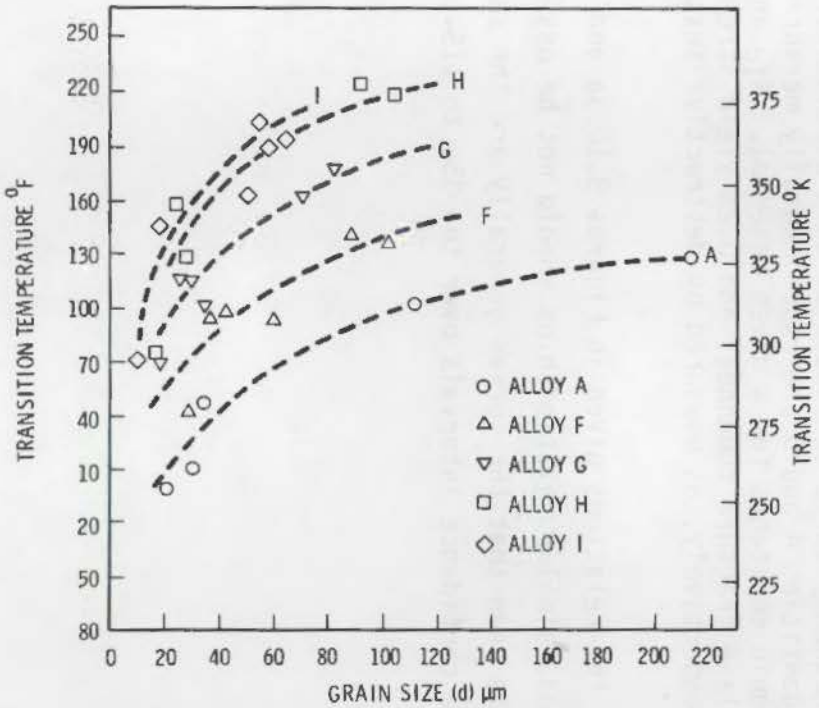

FIGURE 9.10.3a. Transition Temperature Versus Grain Size

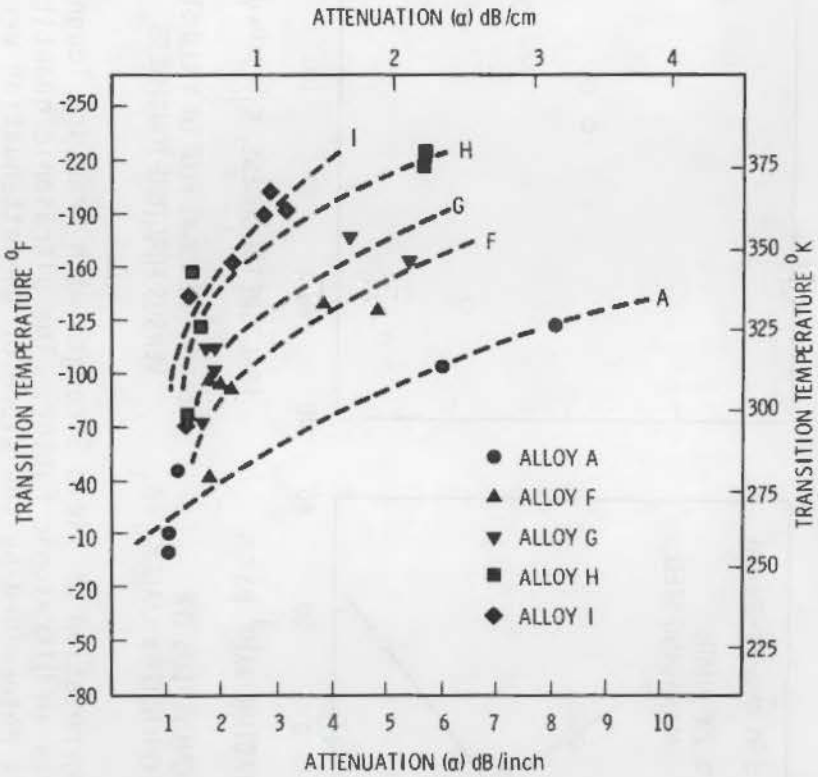

FIGURE 9.10.3b. Transition Temperature Versus the Ultrasonic Attenuation (α) at 5 MHz

TABLE 9.10.1. Regression-Equation Statistics for 15 ft-lb Transition Temperatures

Form of Equation	Statistics[a] For All Data: Variance Explained	For All Data: 95% Confidence Interval	For 35 μm<d<115 μm: Variance Explained	For 35 μm<d<115 μm: 95% Confidence Interval
1. $TT = b_0$ (Alloys)	0.666	±91°F (±51°K)	0.949	±36°F (±20°K)
2. $TT = b_0$ (Alloys) + $k_1 d^{-1/2}$	0.948	±37°F (±21°K)	0.973	±27°F (±15°K)
3. $TT = b_0$ (Alloys) + $b_1\alpha + b_2\alpha^2 + b_3\alpha^3$	--	--	0.985	±23°F (±13°K)

(a) Only five, rather than all twelve, specimens of Alloy A were Charpy tested.

9.11 TENSILE PROPERTIES

Specific approaches to predicting yield strength are cited in Section 9.10. The same reservations cited in that section for fracture toughness properties apply to tensile properties. Vary[9.1.1] discusses aspects such as bond strength, composite strength, etc. Generally, these have been developed for plastics and ceramics. The reader is referred to that report if interested. The absence of data on nuclear materials of construction served as a justification for not expanding here.

Tittman[9.11.1] discussed an indirect UT technique for predicting tensile properties, specifically tensile ductility. A correlation between dB drop in the frequency range 5 to 15 MHz in terms of known cross-sectional areas of voids was related to measured changes in tensile ductility. The theory of Nagumo, which relates voids in inclusion areas to ductility, was found to correlate with the measured values as can be seen in Figure 9.11.1.

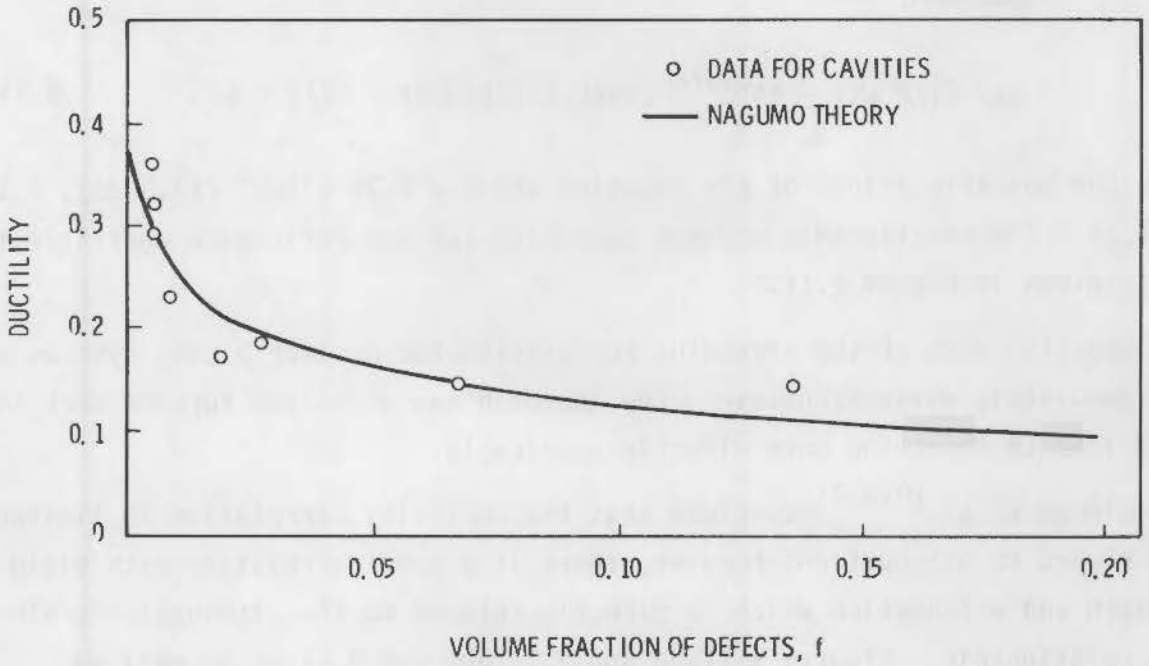

FIGURE 9.11.1. Comparison of Ductility Data for Cavities in Ti-6Al-4V Alloy with Theoretical Model by Nagumo with k = 12

The relevant relationships in terms of equations were

$$\rho = B \ln ca^2 \qquad (9.11.1)$$

where ρ = UT reflection coefficient

B = a constant equal to 10 $\log_{10} e$

c = a constant determined in fitting scattering theory to the data

a = void radius assuming spherical geometry.

$$\exp(1/2\ \epsilon K) - t\ (\ell/a)^3 \exp\ [-\epsilon\ (1/2 + K)] = 1 \qquad (9.11.2)$$

where $K \simeq \gamma/\epsilon_f$; the ratio of shear strain on the crack surface γ to the mean nominal fracture strain ϵ_f

ϵ = tensile ductility

t = a numerical constant

ℓ = a normalization factor equal to the radius of the tensile specimen.

$$\exp\ (1/2\ \epsilon K) - t\ell^3 c^{3/2}\ [\exp(-3\rho/2B)][\exp(-\epsilon 1/2 + K)] \qquad (9.11.3)$$

where the specific values of the equation are $C = 4.39 \times 10^{-2}$ (13.8 dB), K 12, $t = 1.24$. The relationship between ductility (ϵ) and reflection coefficient (ρ) is given in Figure 9.11.2.

Specific uses of the preceding correlation for nuclear piping systems are not immediately obvious; however, the approach may stimulate further work that could lead to something more directly applicable.

Kinman et al.[9.6.2] conclude that the ductility correlation is limited with regard to attenuation; however, there is a good correlation with yield strength and attenuation which is directly related to the attenuation grain-size relationship. Figures 9.11.3a and 9.11.3b, and 9.11.3c as well as Tables 9.11.1 and 9.11.2 show these relationships. Figure 9.11.3a presents

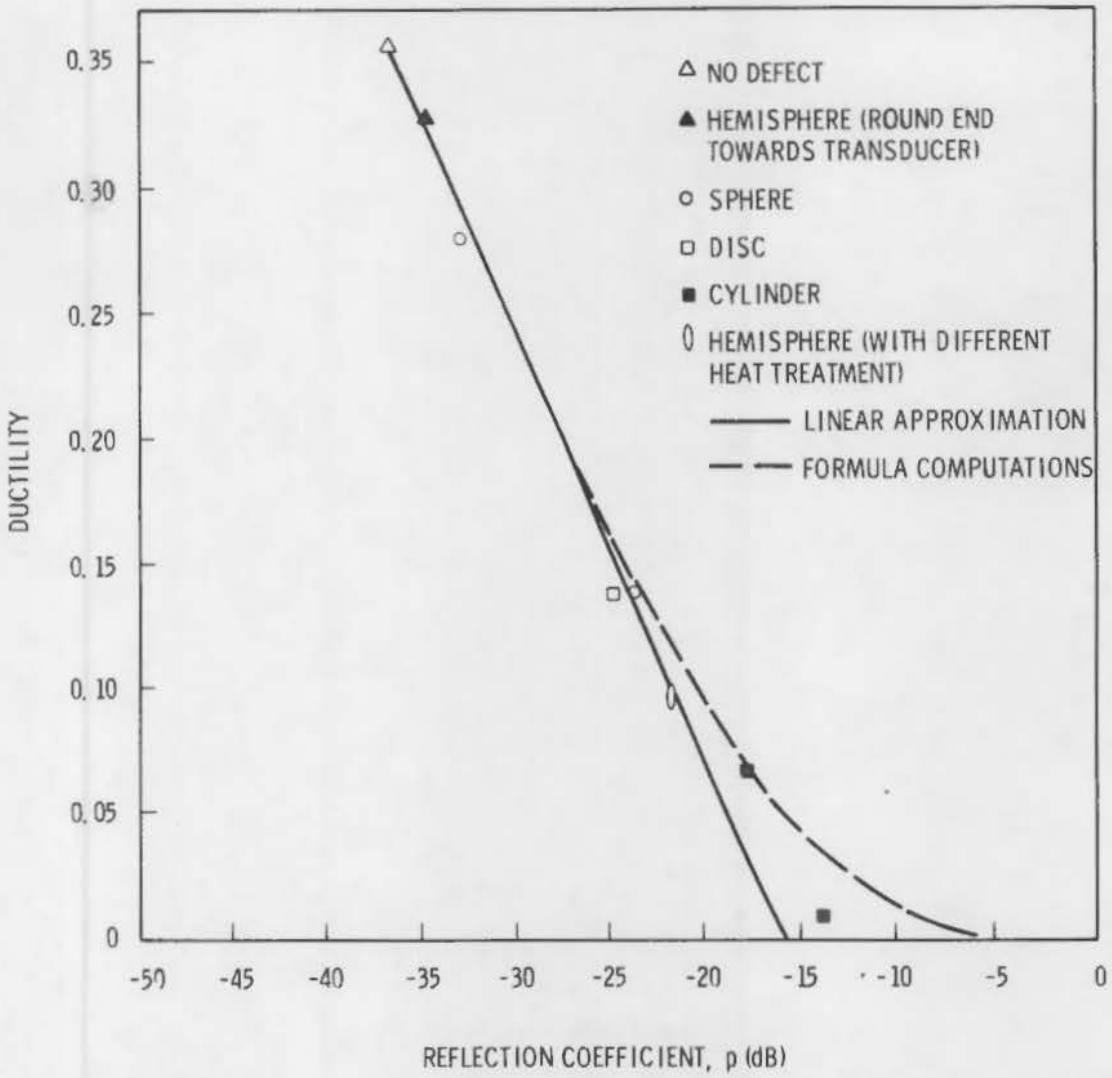

FIGURE 9.11.2. Plot of Ductility as a Function of the Reflection Coefficient Compared to Calculations from Equation 9.11.3 for the Best Fit to the Data

the transitional yield strength reciprocal square root grain size relationship of the Hall-Petch equation:

$$YS = X\ Y_o + K_Y\ d^{-1/2} \qquad (9.11.4)$$

Figure 9.11.3b is an attempt to present the attenuation reciprocal square-root, grain-size relationship with a similar orientation of axes. Finally, Figures 9.11.3c plots yield strength versus attenuation to show similar slopes.

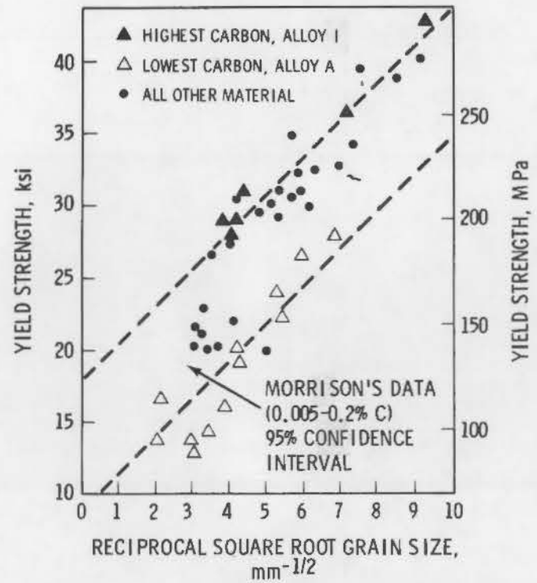

FIGURE 9.11.3a. Lower Yield Strength Versus the Reciprocal Square Root of the Metallographically Measured Grain Size

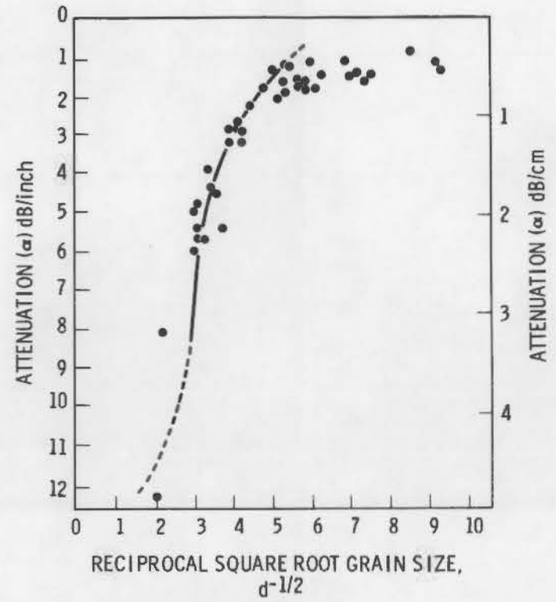

FIGURE 9.11.3b. Ultrasonic Attenuation (α) at 5 MHz Versus Reciprocal Square Root Grain Size ($d^{-1/2}$)

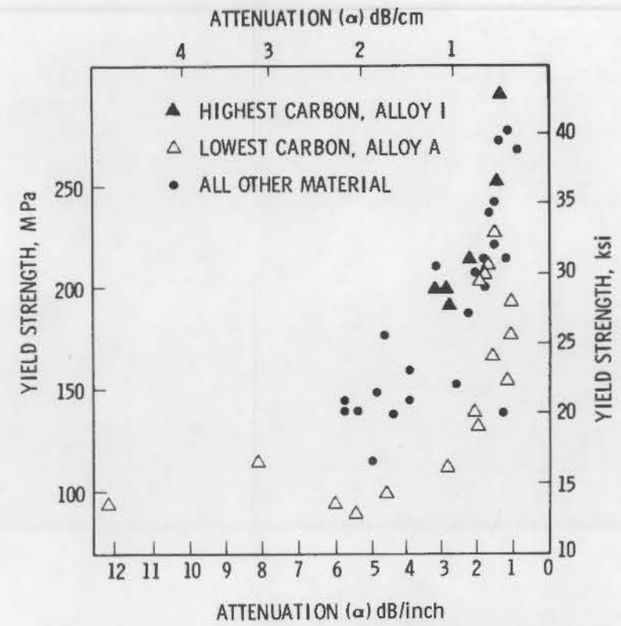

FIGURE 9.11.3c. Lower Yield Strength Versus the Ultrasonic Attenuation (α) at 5 MHz

Table 9.11.1 displays a high variance and tight 95% confidence interval. Table 9.11.2 is shown for tensile strength.

TABLE 9.11.1. Regression-Equation Statistics of Lower Yield Point

Form of Equation	Statistics: For All Data — Variance Explained	For All Data — 95% Confidence Interval	For 35 μm<d<115 μm — Variance Explained	For 35 μm<d<115 μm — 95% Confidence Interval
1. $LYP = b_0$ (Alloys)	0.521	±11.7 ksi (±80.7 MPa)	0.775	±6.3 ksi (±43.4 MPa)
2. $LYP = b_0$ (Alloys) + $k_1 d^{-1/2}$	0.945	±4.0 ksi (±27.6 MPa)	0.966	±2.5 ksi (±17.2 MPa)
3. $LYP = b_0$ (Alloys) + $b_1\alpha + b_2\alpha^2 + b_3\alpha^3$	--	--	0.954	±3.2 ksi (±22.1 MPa)

TABLE 9.11.2. Regression-Equation Statistics for Tensile Strength

Form of Equation	Statistics: For All Data — Variance Explained	For All Data — 95% Confidence Interval	For 35 μm<d<115 μm — Variance Explained	For 35 μm<d<115 μm — 95% Confidence Interval
1. $TS = b_0$ (Alloys)	0.965	±4.2 ksi (±30.0 MPa)	0.994	±1.8 ksi (±12.4 MPa)
2. $TS = b_0$ (Alloys) + $k_1 d^{-1/2}$	0.988	±2.5 ksi (±27.6 MPa)	0.998	±1.2 ksi (±8.3 MPa)
3. $TS = b_0$ (Alloys) + $b_1\alpha + b_2\alpha^2 + b_3\alpha^3$	--	--	0.997	±1.5 ksi (±10.3 MPa)

9.12 REFERENCES

9.1.1 Vary, A., "Quantitative Ultrasonic Evaluation of Mechanical Properties of Engineering Materials," Ultrasonic Materials Characterization. NBS SP-591, H. Berger and M. Linzer, eds., Proceedings of 1st International Symposium on Ultrasonic Materials Characterization, National Bureau of Standards, U.S. Government Printing Office, Washington, D.C., pp. 41-54, 1978.

9.2.1 Smith, G. C. and Holz, P. P., "Repair Weld Induced Residual Stresses in Thick-Walled Steel Pressure Vessels." NUREG/CR-0093, ORNL/NUREG/TM-153, U.S. Nuclear Regulatory Commission, Washington, D.C., June 1978.

9.2.2 Rybicki, E. F., "Residual Stress Due to Weld Repairs, Cladding and Electron Beam Welds and Effect of Residual Stresses on Fracture Behavior." NUREG/CR-0559 (BMI-2012), Annual Report, January 1, 1977 to November 30, 1978, U.S. Nuclear Regulatory Commission, Washington, D.C., 1978.

9.2.3 Suzuki, M., Komura, I. and Takahashi, H., "Non-Destructive Estimation of Residual Stress in Welded Pressure Vessel Steel by Means of Remanent Magnetization Measurement." Int. J. Pressure Vessels Piping 6:87-112, 1978.

9.2.4 Iwayanagi, J., Abuku, S. and Takizawa, C., "A Magnetic Method of Measurement of Residual Stress in Steel." Report G-4, 6th Conference on Nondestructive Testing, Deutsche Gesellschaft für Zerstörungsfreie Prüfung e.V., Berlin, Germany, 1970.

9.2.5 Sundström, O. and Torrönen, K., "The Use of Barkhausen Noise Analysis in Non-Destructive Testing." Mater. Eval. 37(3):51-56, February 1979.

9.2.6 Baer, W. H., et al., "Residual Weld Stress Measurement with the Mossbauer Effect." Proceedings of 9th Symposium on NDE, Southwest Research Institute, San Antonio, Texas, pp. 36-38, 1973.

9.2.7 Gott, K. E., "Residual Stresses in a Weldment of Pressure Vessel Steel." Paper 34, Conference Proceedings on Residual Stresses in Welded Construction and Their Effects, Welding Institute, Cambridge, England, pp. 259-265, November 1977.

9.2.8 Hildebrand, B. P. and Hufferd, D. E., "Utilization of Ultrasonic Tomography for the Mapping of Residual Stress Fields in Thick Metal Sections." EPRI NP-338, Electric Power Research Institute, Palo Alto, California, January 1977.

9.2.9 Umemoto, T. and Tanaka, S., "Residual Stress Improvement by Means of Induction Heating." IHI Eng. Rev. 11(4):1-10, October 1978.

9.2.10 Giannuzzi, A. J., et al., "Studies on AISI Type 304 Stainless Steel Piping Weldments for Use in BWR Application." EPRI NP-944, Electric Power Research Institute, Palo Alto, California, December 1978.

9.2.11 Rybicki, E. F., et al., "Residual Stresses at Girth Butt Welds in Pipes and Pressure Vessels." NUREG-0376, Final Report, April 1, 1976 to April 3, 1977, U.S. Nuclear Regulatory Commission, Washington, D.C., November 1977.

9.2.12 Rybicki, E. F. and Stonesifer, R. B., "Computation of Residual Stresses Due to Multipass Welds in Piping Systems." J. Pressure Vessel Technol. 101:149-154, May 1979.

9.2.13 Norton, J. T., "X-ray Determination of Residual Stress." Mater. Eval. 31(3):21A-41A, February 1973.

9.2.14 Chrenko, R. M., "X-ray Residual Stress Measurements Using Parallel Beam Optics," Advances in X-ray Analysis. H. F. McMurdie et al., eds., pp. 393-402, 1976.

9.2.15 Lemaire, J. C. and Ranganath, S., "Prevention of Stress Corrosion by Limitation of Applied Static Loads in BWR Piping and Components." NEDO-23684, General Electric Corporation, Nuclear Energy Division, San Jose, California, September 1978.

9.2.16 Takaku, H. and Tokiwai, M., "Basic Study on Some Metallurgical Factors and Surface Treatment Effects of Stainless Steels for BWR Cooling Pipes." NUREG/TR-0045, U.S. Nuclear Regulatory Commission, Washington, D.C., May 1977.

9.2.17 Ruud, C. O., et al., "Feasibility of Determining Stress in BWR Pipes with the DRI X-ray Stress Analyzer." EPRI NP-914, Electric Power Research Institute, Palo Alto, California, 1978.

9.2.18 Kino, G. S. and Shaw, J. H., "Acoustic Techniques for Measuring Stress Regions in Materials." EPRI NP-1043, Electric Power Research Institute, Palo Alto, California, April 1979.

9.2.19 Buck, O. and Thompson, R. B., "Acoustic Interactions with Internal Stresses in Metals." Proceedings of ARPA/AFML Review of Progress in Quantitative NDE, AFML-TR-77-44, USAF Technical Report, pp. 84-92, September 1977.

9.2.20 Ruud, C. O., "Review and Evaluation of Non-Destructive Methods for Residual Stress Measurements." EPRI NP-1971, Electric Power Research Institute, Palo Alto, California, September 1981.

9.3.1 Crecraft, D. I., "Ultrasonic Measurement of Stresses." Ultrasonics 6:117-121, 1968.

9.3.2 Egle, D. M. and Bray, D. E., "Application of the Acousto-Elastic Effect to Rail Stress Measurement." Mater. Eval. 37(4):41-46, March 1979.

9.3.3 Trantow, R. L., "Acoustic Evaluation of Cold Work in 316 Stainless Steel Tubing and Plate." HEDL-TME-73-37, Hanford Engineering Development Laboratory, Richland, Washington, June 1973.

9.4.1 Tittman, B. R. and Thompson, R. B., "Measurement of Physical Property Gradients with Elastic Surface Wave Dispersion." Proceedings of 9th Symposium on NDE, Southwest Research Institute, San Antonio, Texas, pp. 20-28, 1973.

9.5.1 Green, R. E., Jr., "Ultrasonic Attenuation Detection of Fatigue Damage." Proceedings of Ultrasonics International Conference, IPC Science and Technology Press, London, England, pp. 187-193, 1973.

9.5.2 Wellinger, K. and Betz, U., "Ultrasonic Crack Detection on Bending Fatigue Specimens." Paper E-3, 6th International Conference Nondestructive Testing, Hanover, pp. 25-35, 1970 (in German).

9.5.3 Carson, J. M. and Rose, J. L., "An Ultrasonic Test Procedure for the Early Detection of Fatigue Damage and the Prediction of Remaining Life." Paper Summaries, ASNT National Fall Conference, American Society for Nondestructive Testing, Columbus, Ohio, pp. 206-214, 1978.

9.5.4 Van DenAvyle, J. A., Jones, W. B. and Gieske, J. H., "Microstructural Evaluation and Non-Destructive Examination of 2.25 Cr-1Mo Steel Subjected to Elevated Temperature Creep and Fatigue Damage." NUREG/CR-0351, U.S. Nuclear Regulatory Commission, Washington, D.C., 1978.

9.6.1 Matsumoto, S. and Kimura, K., "The Relation Between Grain Size and Ultrasonic Attenuation Coefficient in Austenitic Stainless Steel and Iron." Trans. Nat. Res. Inst. Met. 14:(4):21-30 or 155-164, 1972.

9.6.2 Klinman, R., et al., "Ultrasonic Prediction of Grain Size, Strength, and Toughness in Plain Carbon Steel." Mater. Eval. 38(10):26-32, October 1960.

9.6.3 Serabian, S., "Frequency and Grain Size Dependency of Ultrasonic Attenuation in Polycrystalline Materials." Br. J. Nondestr. Test. 2:22, March 1980.

9.7.1 Hunter, D. O., "Ultrasonic Velocities and Critical-Angle Method Changes in Irradiated A-302-B and A-542-B Steels." BNWL-988, Pacific Northwest Laboratory, April 1969.

9.7.2 Hunter, D. O., "Effects of Neutron Irradiation at Thermal Reactor Temperatures on the Propagation Velocity of Ultrasonic Waves in A-543-B Steel." WHAN-FR-38, Westinghouse Hanford, Richland, Washington, December 1970.

9.7.3 Trantow, R. L., "Ultrasonic Measurement of Elastic Properties in Irradiated 304 Stainless Steel." HEOL-TME 73-92, Hanford Engineering Development Laboratory, Richland, Washington, December 1973.

9.8.1 Dolby, R. E., et al., "An Ultrasonic Method for Assessing Susceptibility to Lamellar Tearing--Development of General Techniques," Recent Developments in Non-Destructive Testing. Welding Institute, Cambridge, England, pp. 28-39, 1978.

9.9.1 Dewey, B. R., et al., "Application of Anisotropic Elasticity to Centrifugally Cast Piping." ORNL/TM-5994, Oak Ridge National Laboratory, Oak Ridge, Tennessee, October 1977.

9.9.2 Dewey, B. R., et al., "Measurement of Anisotropic Elastic Constants of Type 308 Stainless Steel Electroslag Welds." Exp. Mech. 17(11):420-426, November 1977.

9.9.3 Smith, R. T., Stern, R. and Stephens, R. W. B., "Third Order Elastic Moduli of Polycrystalline Metals from Ultrasonic Velocity Measurements." J. Acoust. Soc. Am. 40(4):1002-1008, 1966.

9.10.1 Budiansky, B. and Rice, J. R., "On the Estimation of a Crack Fracture Parameter by Long-Wavelength Scattering." J. Appl. Mech. 45(1):453-454, June 1978.

9.11.1 Tittman, R. B., "Ultrasonic Measurements for the Prediction of Mechanical Strength." NOT Int. 11(1):17-22, February 1978.

CHAPTER 9A

MATHEMATICAL DERIVATIONS OF EQUATIONS FOR SECOND- AND THIRD-ORDER ELASTIC CONSTANTS

CONTENTS

FIGURES

TABLES

CHAPTER 9A

MATHEMATICAL DERIVATIONS OF EQUATIONS FOR SECOND- AND THIRD-ORDER ELASTIC CONSTANTS

9A.1 INTRODUCTION

In considering the application of various NDE techniques to the determination of physical and mechanical properties of solids, the theory can be developed either in terms of wave behavior in a solid where wave speeds and particle displacements serve as the basis for the model, or in terms of elastic and/or inelastic behavior of a solid in terms of elasticity theory. The first (wave) approach is covered elegantly by Green[9A.1.1] in his text, Ultrasonic Investigation of Mechanical Properties. The second is available in many texts of articles such as Markham.[9A.1.2] An excellent development is given in the text Elastic Constants and Their Measurement by Schreiber et al.[9A.1.3]

The approach here will be to introduce the topic through measurement of engineering properties, develop the general elasticity theory, simplify to the case of major interest, cubic metals such as steel, handle the preceding in terms of dynamic effects, and expand to the nonlinear case. While the preceding uses solid mechanics rather than wave mechanics, I must emphasize that both approaches converge to yield precisely the same equations.

ENGINEERING PROPERTIES

Three types of engineering tests conducted on solids are tensile, shear and hydrostatic compression. These are illustrated three-dimensionally in Figures 9A.2.1, 9A.2.2, 9A.2.3.

The stress-strain relationships illustrate the proportionalities in the elastic range for uniaxial, shear and hydrostatic loads. The four constants derived from the proportionality relationships are Young's modulus, the Shear modulus, the Bulk modulus, and Poisson's ratio. If one assumes isotropic behavior, the moduli values check fairly well with the values obtained from cubic single crystals. In fact early values of elastic constants such as the moduli were determined by mechanical testing.

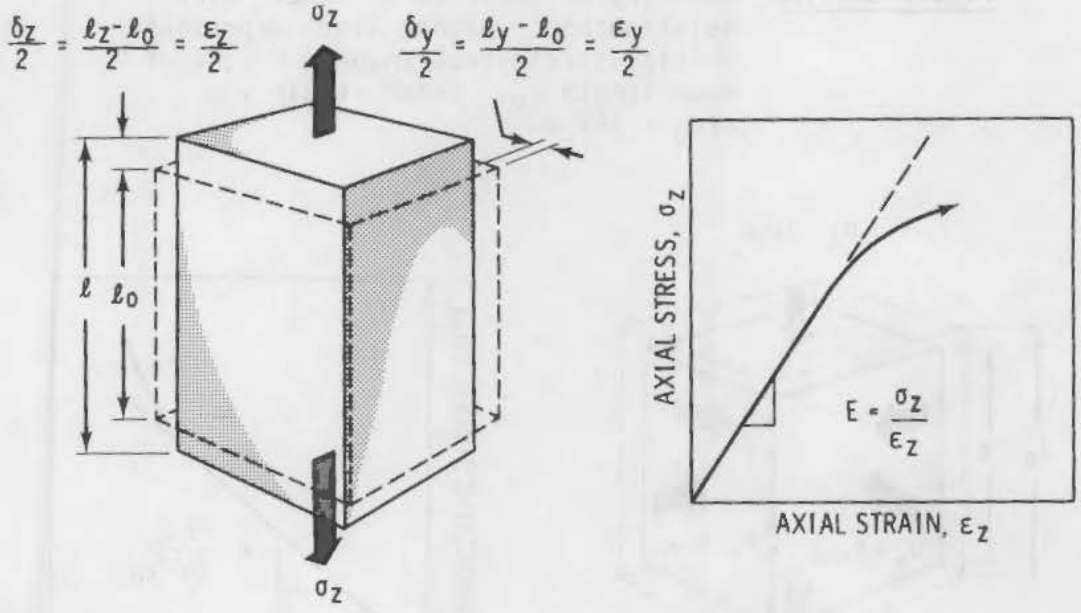

FIGURE 9A.2.1. Uniaxial Tensile (or compressive) Stress. Poisson's ratio, ν, is the ratio of transverse to axial strain. Dashed lines represent initial stress-free shape: a cube of edge length ℓ_0.

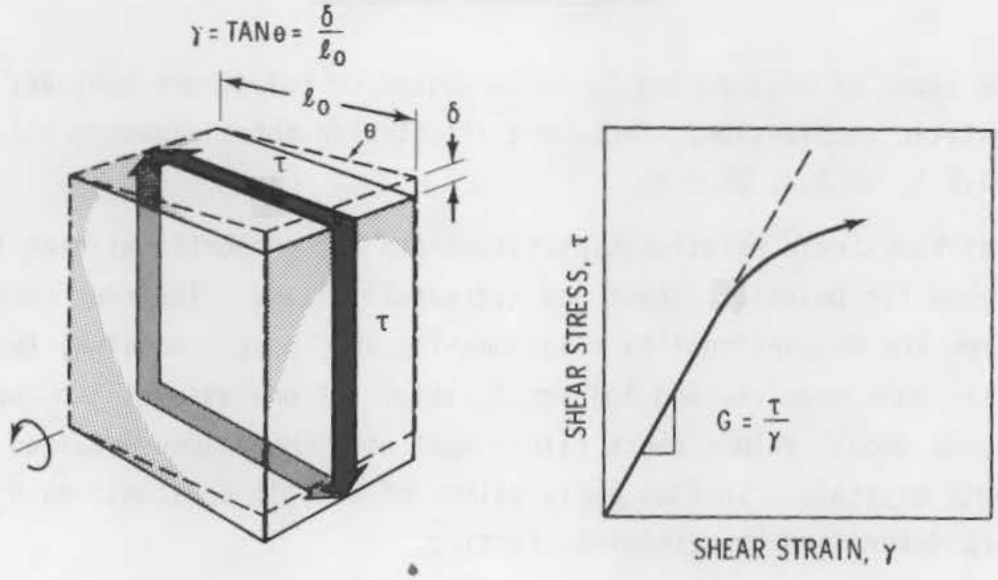

FIGURE 9A.2.2. Geometry of Shear Stress/Shear Strain Relationship. Dashed lines represent initial stress-free shape. A cube of edge length ℓ_0. Shear strain $\gamma = \delta/\ell_0 = \text{TAN}\ \theta$.

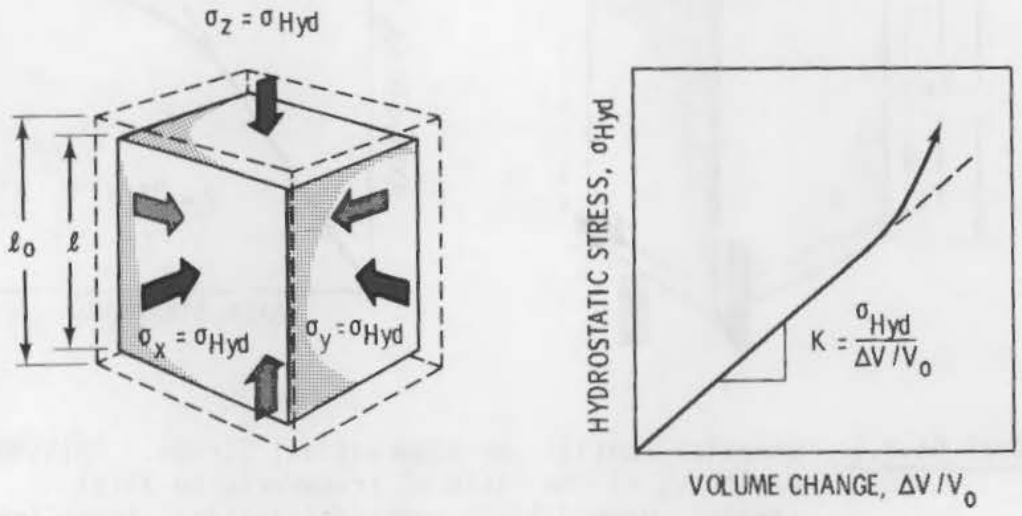

FIGURE 9A.2.3. Hydrostatic Stress Versus Volume Change. Dashed lines surrounding cube represent initial stress-free size.

9A.3 ELASTIC BEHAVIOR

A generalized presentation of stress in an elastic medium in terms of x, y, z axes is given in Figure 9A.3.1. This figure can be considered to represent the spectrum from the most general case where 21 elastic constants are required to define the stress-strain relations to the simplest isotropic case where only two contants are required. Figure 9A.3.2a,b illustrate the most general and the most reduced cases.

Figure 9A.3.1 presents the case for the various stress values in the x, y, z planes required to solve the generalized form of Hooke's law. The six stresses are designated as follows:

$$\sigma_{xx},\ \sigma_{yy},\ \sigma_{zz} \text{ normal stresses} \qquad (9A.3.1a)$$

$$\tau_{xy},\ \tau_{yz},\ \tau_{xz} \text{ shear stresses} \qquad (9A.3.1b)$$

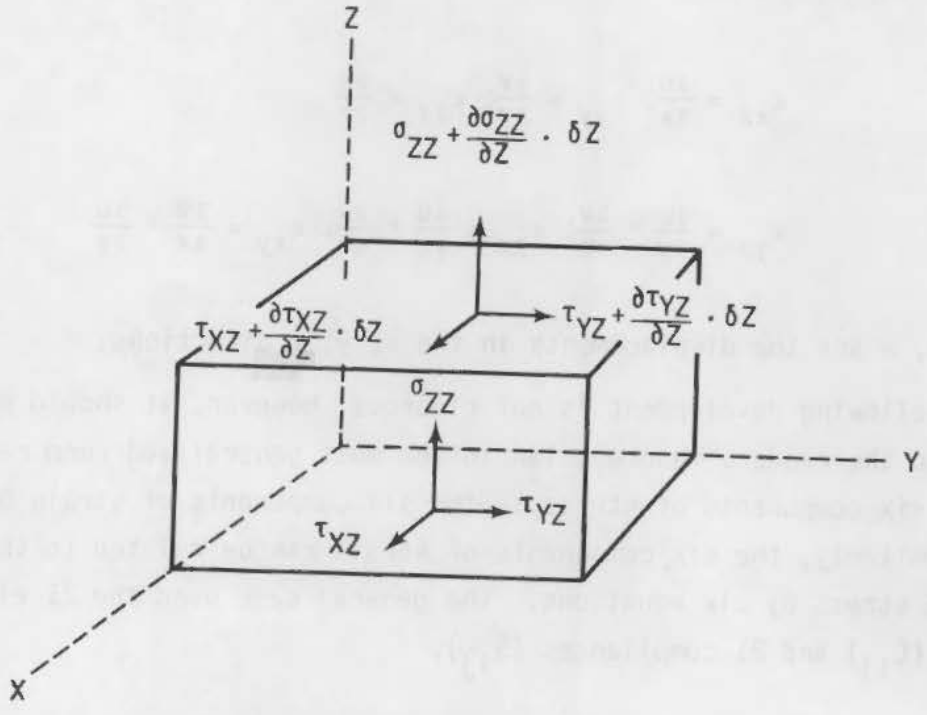

FIGURE 9A.3.1. Specification of Stress in an Elastic Medium

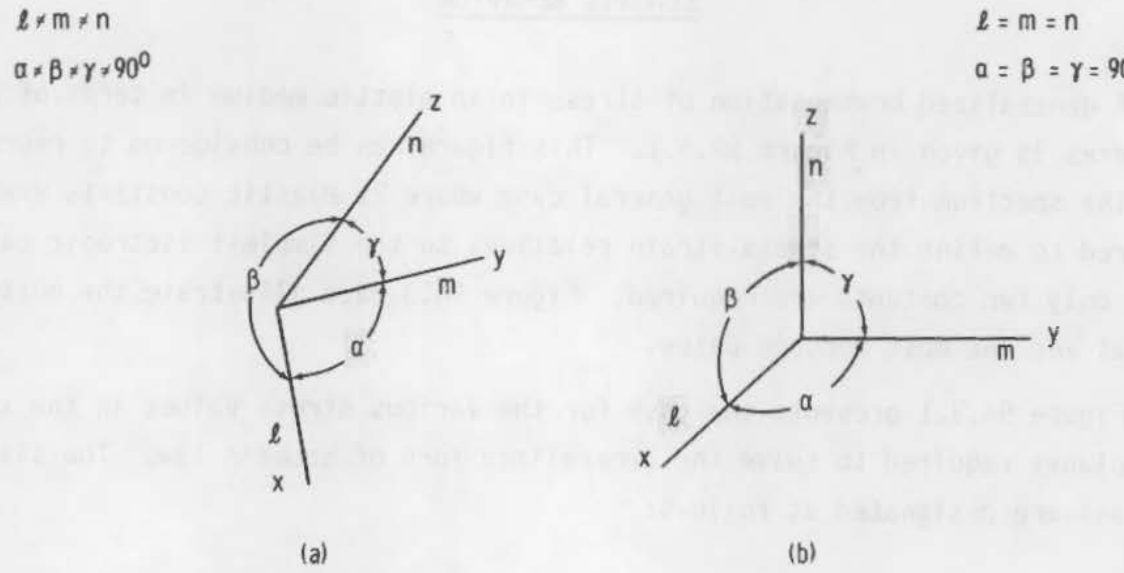

FIGURE 9A.3.2. The Most General (triclinic) and Most Reduced (isotropic) Case of Asymmetry

The comparable longitudinal and shear strains together with a differential for describing them follow:

$$\epsilon_{xx} = \frac{\partial u}{\partial x};\ \epsilon_{yy} = \frac{\partial v}{\partial y};\ \epsilon_{zz} = \frac{\partial w}{\partial z} \qquad (9A.3.2a)$$

$$\epsilon_{yz} = \frac{\partial w}{\partial y} + \frac{\partial v}{\partial z};\ \epsilon_{zx} = \frac{\partial u}{\partial z} + \frac{\partial w}{\partial x};\ \epsilon_{xy} = \frac{\partial v}{\partial x} + \frac{\partial u}{\partial y} \qquad (9A.3.2b)$$

where u, v, w are the displacements in the x, y, z directions.

The following development is not rigorous; however, it should present the approach to the reader. Hooke's law in the most generalized form related the preceding six components of stress to the six components of strain by six equations. Similarly, the six components of strain can be related to the six components of stress by six equations. The general case used the 21 elastic constants (C_{ij}) and 21 compliances (S_{ij}).

In matrix notation these can be designated

$$\sigma_i \text{ (or } \gamma_i) = \sum_{j=1}^{6} C_{ij}\epsilon_j \qquad (9A.3.3)$$

$$\epsilon_i = \sum_{j=1}^{6} S_{ij}\sigma_j \text{ (or } \gamma_i) \qquad (9A.3.4)$$

The 21 elastic constants (or compliances) fall into definite groups shown in Figure 9A.3.3 which can be written as follows:

1. C_{11}, C_{22}, and C_{33} relate the longitudinal strains to the longitudinal stresses.

2. C_{44}, C_{55}, and C_{66} relate the shear strains to the shear stresses.

3. C_{23}, C_{13}, and C_{12} relate the lateral contractions to the longitudinal extensions when the material is under uniaxial (Poisson's ratio) tension. This case can be further expanded, as will be noted later, in recognition of the fact that the uniaxial tension case is composed of a hydrostatic stress equal to one-third the tension value and to two shear stresses, each equal to one-third the tension value. For the case of cubic symmetry, which will be developed, the total strain will be made up of a bulk strain inversely proportional to $(C_{11} + C_{12})$ and to two shear strains inversely proportional to $(C_{11} - C_{12})$. This difference may be regarded as a shear constant equivalent to C_{44}.

4. The constants C_{56}, C_{46}, and C_{45} relate shear strains in one direction to shear strains in another.

5. The group of nine elastic constants C_{14}, C_{15}, C_{16}, C_{24}, C_{25}, C_{26}, C_{34}, C_{35}, C_{36} are basically similar to C_{56}, C_{46}, and C_{45}; however, in low orders of symmetry such as triclinic (21 constants) hydrostatic stress may cause shear strain and the corresponding factors of proportionality are also comprised in this group.

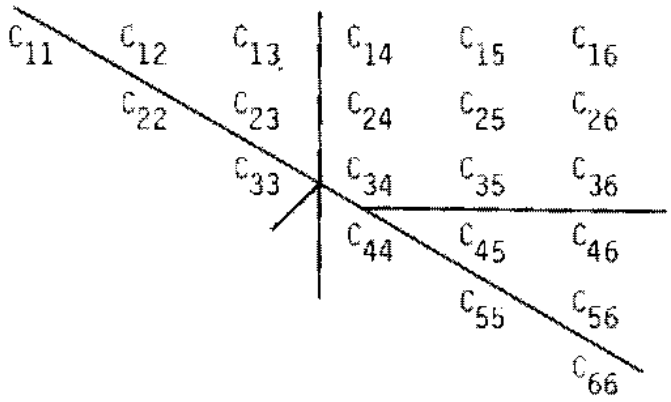

FIGURE 9A.3.3. Grouping of Elastic Constants

Any crystal, even one with cubic symmetry, when referred to axes other than axes of symmetry, will have all 21 effective constants different from zero. When referred to the principal axis of symmetry, interaction between shears and direct strains, and between shears in different planes occurs only when the symmetry is low.

The compliances S_{ij} may be written in the same format as the elastic constants C_{ij} and the preceding items 1 to 5 apply with the proviso that stress is substituted for strain in the statements.

Expanding the matrix denoted by $\sigma_i \ (\gamma_i) = \sum_{J=1}^{6} C_{ij}\epsilon_j$ will give the matrix on the following page.

$$\sigma_{xx} = C_{11}\epsilon_{xx} + C_{12}\epsilon_{yy} + C_{13}\epsilon_{zz} + C_{14}\epsilon_{yz} + C_{15}\epsilon_{zx} + C_{16}\epsilon_{xy} \quad (9A.3.5a)$$

$$\sigma_{yy} = C_{21}\epsilon_{xx} + C_{22}\epsilon_{yy} + C_{23}\epsilon_{zz} + C_{24}\epsilon_{yz} + C_{25}\epsilon_{zx} + C_{26}\epsilon_{xy} \quad (9A.3.5b)$$

$$\sigma_{zz} = C_{31}\epsilon_{xx} + C_{32}\epsilon_{yy} + C_{33}\epsilon_{zz} + C_{34}\epsilon_{yz} + C_{35}\epsilon_{zx} + C_{36}\epsilon_{xy} \quad (9A.3.5c)$$

$$\gamma_{yz} = C_{41}\epsilon_{xx} + C_{42}\epsilon_{yy} + C_{43}\epsilon_{zz} + C_{44}\epsilon_{yz} + C_{45}\epsilon_{zx} + C_{46}\epsilon_{xy} \quad (9A.3.5d)$$

$$\gamma_{zx} = C_{51}\epsilon_{xx} + C_{52}\epsilon_{yy} + C_{53}\epsilon_{zz} + C_{54}\epsilon_{yz} + C_{55}\epsilon_{zx} + C_{56}\epsilon_{xy} \quad (9A.3.5e)$$

$$\gamma_{xy} = C_{61}\epsilon_{xx} + C_{62}\epsilon_{yy} + C_{63}\epsilon_{zz} + C_{64}\epsilon_{yz} + C_{65}\epsilon_{zx} + C_{66}\epsilon_{xy} \quad (9A.3.5f)$$

The matrix denoted by $\epsilon_i = \sum_{j=1}^{6} S_{ij}\sigma_j \ (\gamma_j)$ will give

$$\epsilon_{xx} = S_{11}\sigma_{xx} + S_{12}\sigma_{yy} + S_{13}\sigma_{zz} + S_{14}\gamma_{yz} + S_{15}\gamma_{zx} + S_{16}\gamma_{xy} \quad (9A.3.6a)$$

$$\epsilon_{yy} = S_{21}\sigma_{xx} + S_{22}\sigma_{yy} + S_{23}\sigma_{zz} + S_{24}\gamma_{yz} + S_{25}\gamma_{zx} + S_{26}\gamma_{xy} \quad (9A.3.6b)$$

$$\epsilon_{zz} = S_{31}\sigma_{xx} + S_{32}\sigma_{yy} + S_{33}\sigma_{zz} + S_{34}\gamma_{yz} + S_{35}\gamma_{zx} + S_{36}\gamma_{xy} \quad (9A.3.6c)$$

$$\epsilon_{yz} = S_{41}\sigma_{xx} + S_{42}\sigma_{yy} + S_{43}\sigma_{zz} + S_{44}\gamma_{yz} + S_{45}\gamma_{zx} + S_{46}\gamma_{xy} \quad (9A.3.6d)$$

$$\epsilon_{zx} = S_{51}\sigma_{xx} + S_{52}\sigma_{yy} + S_{53}\sigma_{zz} + S_{54}\gamma_{yz} + S_{55}\gamma_{zx} + S_{56}\gamma_{xy} \quad (9A.3.6e)$$

$$\epsilon_{xy} = S_{61}\sigma_{xx} + S_{62}\sigma_{yy} + S_{63}\sigma_{zz} + S_{64}\gamma_{yz} + S_{65}\gamma_{zx} + S_{66}\gamma_{xy} \quad (9A.3.6f)$$

The above compromise 6 x 6 matrices of elastic and compliance constants. Since C_{ij} and S_{ij} are the inverse of one another, to go from C_{ij} to the S_{ij}

matrix or vice versa requires inversion of the matrix which is best handled with a computer. In matrix notation we will have

$$(\varepsilon) = [C]^{-1} (\sigma) = [S] (\sigma) \tag{9A.3.7}$$

for the first group, and

$$(\sigma) = [S]^{-1} (\varepsilon) = [C] (\varepsilon) \tag{9A.3.8}$$

for the second group.

9A.4 EFFECTS OF CRYSTAL SYMMETRY

The least symmetric crystal, a triclinic, requires all 21 elastic constants to define the stress-strain relationships. As crystals increase in symmetry, fewer elastic constants are required to define the relationships. The most symmetric is an isotropic crystal which may be applied to polycrystalline materials in some instances. The next most symmetric, and the one of interest in an engineering sense, is the cubic which encompasses simple, body-centered and face-centered cubics. The class of ferritic steels is body-centered cubic and the austenitics face-centered cubic.

The elastic constants reduce to

$$C_{11} = C_{22} = C_{33} \tag{9A.4.1a}$$

$$C_{12} = C_{23} = C_{13} \tag{9A.4.1b}$$

$$C_{44} = C_{55} = C_{66} \tag{9A.4.1c}$$

and all other constants are zero. Returning to our diagram of the elastic constants we can rewrite it for the cubic case as given in Figure 9A.4.1. This

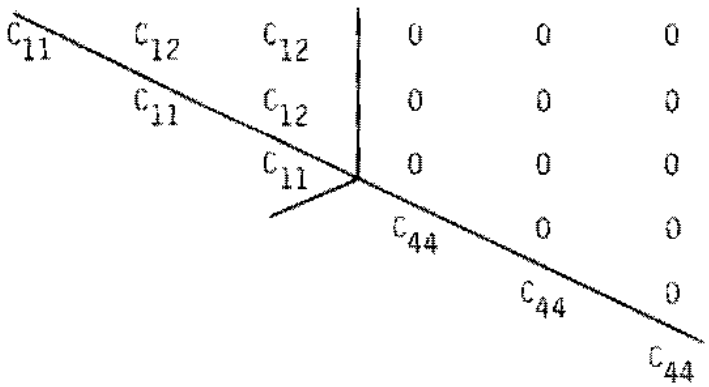

FIGURE 9A.4.1. Elastic Constants--Cubic Case

case means that only three constants are required to describe the elastic properties of cubic materials.

The preceding sets of equations will reduce to the following matrices for the cubic case:

$$\begin{Bmatrix} \sigma_{xx} \\ \sigma_{yy} \\ \sigma_{zz} \\ \tau_{yz} \\ \tau_{zx} \\ \tau_{xy} \end{Bmatrix} = \begin{bmatrix} C_{11} & C_{12} & C_{12} & 0 & 0 & 0 \\ C_{12} & C_{11} & C_{12} & 0 & 0 & 0 \\ C_{12} & C_{12} & C_{11} & 0 & 0 & 0 \\ 0 & 0 & 0 & C_{44} & 0 & 0 \\ 0 & 0 & 0 & 0 & C_{44} & 0 \\ 0 & 0 & 0 & 0 & 0 & C_{44} \end{bmatrix} \begin{Bmatrix} \epsilon_{xx} \\ \epsilon_{yy} \\ \epsilon_{zz} \\ \epsilon_{yz} \\ \epsilon_{zx} \\ \epsilon_{xy} \end{Bmatrix} \qquad (9A.4.2)$$

or

$$\begin{Bmatrix} \epsilon_{xx} \\ \epsilon_{yy} \\ \epsilon_{zz} \\ \epsilon_{yz} \\ \epsilon_{zx} \\ \epsilon_{xy} \end{Bmatrix} = \begin{bmatrix} S_{11} & S_{12} & S_{12} & 0 & 0 & 0 \\ S_{12} & S_{11} & S_{12} & 0 & 0 & 0 \\ S_{12} & S_{12} & S_{11} & 0 & 0 & 0 \\ 0 & 0 & 0 & S_{44} & 0 & 0 \\ 0 & 0 & 0 & 0 & S_{44} & 0 \\ 0 & 0 & 0 & 0 & 0 & S_{44} \end{bmatrix} \begin{Bmatrix} \sigma_{xx} \\ \sigma_{yy} \\ \sigma_{zz} \\ \tau_{yz} \\ \tau_{zx} \\ \tau_{xy} \end{Bmatrix} \qquad (9A.4.3)$$

with inversion possible by

$$\sigma = [S]^{-1}(\epsilon) = [C]\ (\epsilon) \qquad (9A.3.8)$$

or

$$\epsilon = [C]^{-1}(\sigma) = [S]\ (\sigma) \qquad (9A.3.7)$$

We can rewrite the first group in terms of the partials of displacement as follows:

$$\sigma_{xx} = C_{11}\frac{\partial u}{\partial x} + C_{12}\frac{\partial v}{\partial y} + C_{13}\frac{\partial w}{\partial z} + C_{14}\left(\frac{\partial v}{\partial z} + \frac{\partial w}{\partial y}\right) + C_{15}\left(\frac{\partial w}{\partial x} + \frac{\partial u}{\partial z}\right) + C_{16}\left(\frac{\partial u}{\partial y} + \frac{\partial v}{\partial x}\right) \quad (9A.4.4a)$$

$$\sigma_{yy} = C_{21}\frac{\partial u}{\partial x} + C_{22}\frac{\partial v}{\partial y} + C_{23}\frac{\partial w}{\partial z} + C_{24}\left(\frac{\partial v}{\partial z} + \frac{\partial w}{\partial y}\right) + C_{25}\left(\frac{\partial w}{\partial x} + \frac{\partial u}{\partial z}\right) + C_{26}\left(\frac{\partial u}{\partial y} + \frac{\partial v}{\partial x}\right) \quad (9A.4.4b)$$

$$\sigma_{zz} = C_{31}\frac{\partial u}{\partial x} + C_{32}\frac{\partial v}{\partial y} + C_{33}\frac{\partial w}{\partial z} + C_{34}\left(\frac{\partial v}{\partial z} + \frac{\partial w}{\partial y}\right) + C_{35}\left(\frac{\partial w}{\partial x} + \frac{\partial u}{\partial z}\right) + C_{36}\left(\frac{\partial u}{\partial y} + \frac{\partial v}{\partial x}\right) \quad (9A.4.4c)$$

$$\gamma_{yz} = C_{41}\frac{\partial u}{\partial x} + C_{42}\frac{\partial v}{\partial y} + C_{43}\frac{\partial w}{\partial z} + C_{44}\left(\frac{\partial v}{\partial z} + \frac{\partial w}{\partial y}\right) + C_{45}\left(\frac{\partial w}{\partial x} + \frac{\partial u}{\partial z}\right) + C_{46}\left(\frac{\partial u}{\partial y} + \frac{\partial v}{\partial x}\right) \quad (9A.4.4d)$$

$$\gamma_{zx} = C_{51}\frac{\partial u}{\partial x} + C_{52}\frac{\partial v}{\partial y} + C_{53}\frac{\partial w}{\partial z} + C_{54}\left(\frac{\partial v}{\partial z} + \frac{\partial w}{\partial y}\right) + C_{55}\left(\frac{\partial w}{\partial x} + \frac{\partial u}{\partial z}\right) + C_{56}\left(\frac{\partial u}{\partial y} + \frac{\partial v}{\partial x}\right) \quad (9A.4.4.e)$$

$$\gamma_{xy} = C_{61}\frac{\partial u}{\partial x} + C_{62}\frac{\partial v}{\partial y} + C_{63}\frac{\partial w}{\partial z} + C_{64}\left(\frac{\partial v}{\partial z} + \frac{\partial w}{\partial y}\right) + C_{65}\left(\frac{\partial w}{\partial x} + \frac{\partial u}{\partial z}\right) + C_{66}\left(\frac{\partial u}{\partial y} + \frac{\partial v}{\partial x}\right) \quad (9A.4.4f)$$

We can use the preceding equations after suitable differentiation to determine the values of the elastic constants. This can be done by measuring the velocities of ultrasound at which the three types of plane waves travel in

known directions. These velocities are dependent on the elastic constants, the direction at which the wavefront travels with respect to the crystallographic axes, and the density. Assuming we know the latter two, we can calculate the elastic constants from measurements of the wave velocities.

The dynamic equations of equilibrium of a small element of the solid can be written as

$$\frac{\partial}{\partial x}\sigma_{xx} + \frac{\partial}{\partial y}\tau_{xy} + \frac{\partial}{\partial z}\tau_{xz} = \rho\frac{\partial^2 u}{\partial t^2} \qquad (9A.4.5a)$$

$$\frac{\partial}{\partial x}\tau_{yx} + \frac{\partial}{\partial y}\sigma_{yy} + \frac{\partial}{\partial z}\tau_{yz} = \rho\frac{\partial^2 v}{\partial t^2} \qquad (9A.4.5b)$$

$$\frac{\partial}{\partial x}\tau_{zx} + \frac{\partial}{\partial y}\tau_{xy} + \frac{\partial}{\partial z}\sigma_{zz} = \rho\frac{\partial^2 w}{\partial t^2} \qquad (9A.4.5c)$$

where ρ is the density of the solid.

The preceding equations for a small element of the solid can be generalized for the case of a periodic infinite plane wave. We can define the plane wave as a vector according to Figure 9A.4.2

An infinite plane wave, periodic in time, which is travelling in any direction (ℓ, m, n) can be defined by the following equations:

$$u = A_x \sin(\ell_x + m_y + n_z - vt) \qquad (9A.4.6a)$$

$$v = A_y \sin(\ell_x + m_y + n_z - vt) \qquad (9A.4.6b)$$

$$w = A_z \sin(\ell_x + m_y + n_z - vt) \qquad (9A.4.6c)$$

A_x, A_y, and A_z are constants which determine the amplitude of the wave; v is the phase velocity.

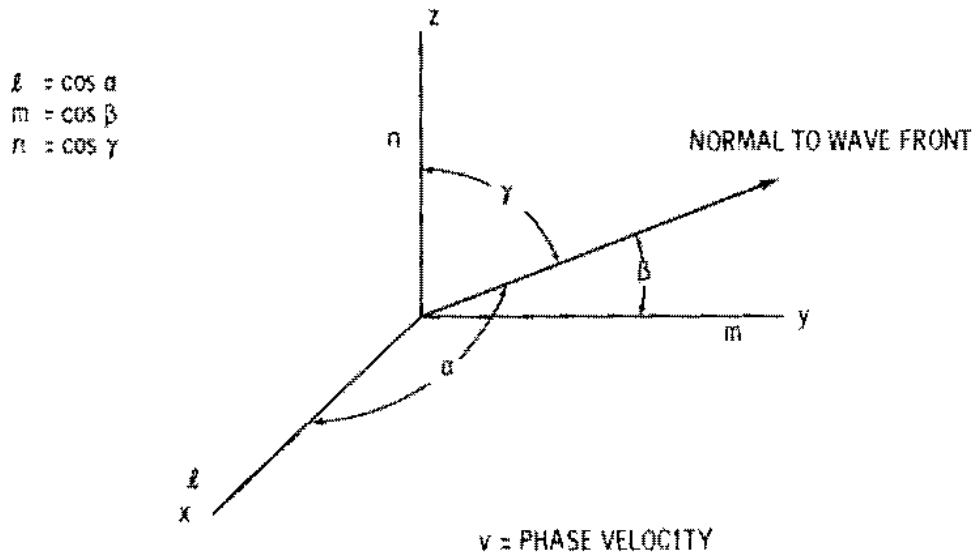

FIGURE 9A.4.2. Direction Numbers and Direction Cosines Referred to Reference Axes x, y, z

We have shown in Equation 9A.3.5 that the various stresses are functions of the second-order elastic constants and strains. The same is true in Equation 9A.4.4 for stress as functions of second-order elastic constants and displacements in terms of $\partial u/\partial x, \partial y, \partial z$, $\partial v/\partial x, \partial y, \partial z$.

It follows that the partial of stress will equal the partial of strain after differentiating. This means Equation 9A.4.5 in terms of $\partial^2 u, v, w/\partial t^2$ will relate equally to partials of stress and strain.

Differentiating the above equations and substituting into the equations of motion will give equations in the tensor form:

$$(C_{ijkl}\ell_i\ell_j - \rho v^2 S_{ik})\, e_k = 0 \qquad (9A.4.7)$$

We are interested in six equations either parallel to each of the direction cosines ℓ, m, n or a combination of them; e.g.,

x Direction L $\qquad L_{xx} = \lambda_{11}$ $\qquad (9A.4.8a)$

y Direction M $\qquad M_{yy} = \lambda_{22}$ $\qquad (9A.4.8b)$

z Direction N $\qquad N_{zz} = \lambda_{33}$ (9A.4.8c)

yz Direction $\overline{MN}$ $\qquad \overline{MN}_{yz} = \lambda_{23}$ (9A.4.8d)

zx Direction $\overline{LN}$ $\qquad \overline{LN}_{zx} = \lambda_{31}$ (9A.4.8e)

xy Direction $\overline{LM}$ $\qquad \overline{LM}_{xy} = \lambda_{12}$ (9A.4.8f)

The λ terminology is used in many reports and will be used here in the context of L, M, N, $\overline{MN}$, $\overline{LN}$, $\overline{LM}$:

$$\lambda_{ik} = C_{ijkl}\ell_i\ell_j \quad \text{in tensor notation}$$
$$\ell_1 = \ell \quad \ell_2 = m \quad \ell_3 = n \quad \text{in matrix notation} \qquad (9A.4.9)$$
$$11 \rightarrow 1; \quad 23 \rightarrow 4$$
$$22 \rightarrow 2; \quad 31 \rightarrow 5$$
$$33 \rightarrow 3; \quad 12 \rightarrow 6$$

$$L = \lambda_{11} = C_{1111}\ell_1\ell_1 + C_{1112}\ell_2\ell_1 + C_{1113}\ell_3\ell_1 + C_{1211}\ell_1\ell_2 + C_{1212}\ell_2\ell_2 + C_{1213}\ell_3\ell_2 + C_{1311}\ell_1\ell_3 + C_{1312}\ell_2\ell_3 + C_{1313}\ell_3\ell_3 \qquad (9A.4.10a)$$

which when converted to matrix terms become

$$L = \lambda_{11} = \ell^2 C_{11} + m^2 C_{66} + n^2 C_{55} + 2mn C_{56} + 2n\ell C_{15} + 2\ell m C_{16} \qquad (9A.4.10b)$$

$$M = \lambda_{22} = C_{1212}\ell_i\ell_1 + C_{2212}\ell_1\ell_2 + C_{2312}\ell_1\ell_3 + C_{1222}\ell_1\ell_2 + C_{2222}\ell_2\ell_2 + C_{2322}\ell_2\ell_3 + C_{1223}\ell_1\ell_2 + C_{2223}\ell_2\ell_3 + C_{2323}\ell_3\ell_3 \qquad (9A.4.11a)$$

$$\lambda_{22} = C_{66}\,\ell^2 + C_{22}\,m^2 + C_{44}\,n^2 + 2\,\ell m\,C_{26} + 2\,\ell n\,C_{46} + 2\,mn\,C_{24} \quad (9A.4.11b)$$

In similar fashion the other equations can be derived:

$$L = \lambda_{11} = \ell^2\,C_{11} + m^2\,C_{66} + n^2\,C_{55} + 2\,mn\,C_{56} + 2\,n\,\ell C_{15} + 2\,\ell m\,C_{16} \quad (9A.4.10b)$$

$$M = \lambda_{22} = \ell^2\,C_{66} + m^2\,C_{22} + n^2\,C_{44} + 2\,mn\,C_{24} + 2\,n\,\ell C_{46} + 2\,\ell m\,C_{26} \quad (9A.4.11)$$

$$N = \lambda_{33} = \ell^2\,C_{55} + m^2\,C_{44} + n^2\,C_{33} + 2\,mn\,C_{34} + 2\,n\,\ell C_{35} + 2\,\ell m\,C_{45} \quad (9A.4.12)$$

$$\overline{MN} = \lambda_{23} = \ell^2\,C_{56} + m^2\,C_{24} + n^2\,C_{34} + mn\,(C_{44} + C_{23}) + n\,\ell\,(C_{36} + C_{45}) + \ell m\,(C_{25} + C_{46}) \quad (9A.4.13)$$

$$\overline{LN} = \lambda_{13} = \ell^2\,C_{15} + m^2\,C_{46} + n^2\,C_{35} + mn\,(C_{45} + C_{36}) + n\,\ell\,(C_{13} + C_{55}) + \ell m\,(C_{14} + C_{56}) \quad (9A.4.14)$$

$$\overline{LM} = \lambda_{12} = \ell^2\,C_{16} + m^2\,C_{26} + n^2\,C_{45} + mn\,(C_{46} + C_{25}) + n\ell\,(C_{14} + C_{56}) + \ell m\,(C_{12} + C_{66}) \quad (9A.4.15)$$

The differentiation of the wave equations will give

$$(L - \rho V^2)\,A_x + \overline{LM}\,A_y + \overline{LN}\,A_z = 0 \quad (9A.4.16)$$

$$\overline{LM}\,A_x + (M - \rho V^2)\,A_y + \overline{MN}\,A_z = 0 \quad (9A.4.17)$$

$$\overline{LN}\,A_x + \overline{MN}\,A_y + (N - \rho V^2)\,A_z = 0 \qquad (9A.4.18)$$

This equation can be written into the following matrix notation:

$$\begin{bmatrix} L - \rho V^2 & \overline{LM} & \overline{LN} \\ \overline{LM} & M - \rho V^2 & \overline{MN} \\ \overline{LN} & \overline{MN} & N - \rho V^2 \end{bmatrix} = 0 \qquad (9A.4.19)$$

Solution of this matrix will give the wave speeds for the three plane waves propagating in a linear elastic homogeneous anisotropic medium.

If we wish to solve for the direction cosines of the particle displacements, we can write the following matrix:

$$\begin{bmatrix} L & \overline{LM} & \overline{LN} \\ \overline{LM} & M & \overline{MN} \\ \overline{LN} & \overline{MN} & N \end{bmatrix} \begin{vmatrix} \alpha \\ \beta \\ \gamma \end{vmatrix} = \rho V^2 \begin{bmatrix} 1 & 0 & 0 \\ 0 & 1 & 0 \\ 0 & 0 & 1 \end{bmatrix} \begin{vmatrix} \alpha \\ \beta \\ \gamma \end{vmatrix} \qquad (9A.4.20)$$

or

$$\alpha L + \beta \overline{LM} + \gamma \overline{LN} = \alpha \rho V^2 \qquad (9A.4.21a)$$

$$\alpha \overline{LM} + \beta M + \gamma \overline{MN} = \beta \rho V^2 \qquad (9A.4.21b)$$

$$\alpha \overline{LN} + \beta \overline{MN} + \gamma N = \gamma \rho V^2 \qquad (9A.4.21c)$$

The preceding represent the most generalized forms of the equations. The method of solution for a given crystalline material is known density ρ and second-order elastic constants C, is to solve Equations 9A.4.10 to 9A.4.15 for L, M, N, etc., components for the wave normal (crystallographic direction

cosines ℓ, m, n) of interest. These values are substituted into the velocity matrix together with the density ρ and solved for the three plane-wave speeds V_1, V_2, V_3. Each of these wave speeds is substituted along with relevant values of L, M, N, etc., and ρ into the three equations above (9A.4.21) to solve for the particle displacement direction cosines appropriate to the particular wave speed (using $\alpha^2_2 + \beta^2_2 + \gamma^2_2 = 1$). Generally, the three particle displacements will have components both normal and parallel to the surface of the medium so the waves are neither purely compressional nor purely transverse.

The situation is greatly simplified in isotropic or cubic solids where in certain special directions of the crystal one of the waves will be purely longitudinal and the other two purely transverse.

The generalized equations become greatly simplified when specific wave propagation directions are selected. For example, in the [100] direction,

$$\begin{matrix} (a) & (b) & (c) & (d) & (e) & (f) \\ L = C_{11}; & M = C_{66}; & N = C_{55}; & \overline{MN} = C_{56}; & \overline{LN} = C_{15}; & \overline{LM} = C_{16} \end{matrix} \qquad (9A.4.22)$$

In the [110] direction,

$$L = C_{11} + C_{66}\ 2C_{16};\ \overline{MN} = C_{56} + C_{24} + C_{25} + C_{46} \qquad (9A.4.23a)$$

$$M = C_{66} + C_{22} + 2C_{26};\ \overline{LN} = C_{15} + C_{46} + C_{14} + C_{65} \qquad (9A.4.23b)$$

$$N = C_{55} + C_{44}\ 2C_{45};\ \overline{LM} = C_{16} + C_{26} + C_{12} + C_{66} \qquad (9A.4.23c)$$

In the [111] direction,

$$L = C_{11} + C_{66} + C_{55} + 2(C_{15} + C_{16} + C_{56}) \qquad (9A.4.24a)$$

$$M = C_{66} + C_{22} + 3C_{44} + 2(C_{26} + C_{46}) \qquad (9A.4.24b)$$

$$N = C_{55} + C_{44} + C_{33} + 2(C_{45} + C_{35} + C_{34}) \qquad (9A.4.24c)$$

$$\overline{MN} = C_{56} + C_{24} + C_{34} + C_{25} + C_{46} + C_{36} + C_{45} + C_{34} + C_{44} \qquad (9A.4.24d)$$

$$\overline{LN} = C_{15} + C_{46} + C_{35} + C_{14} + C_{65} + C_{13} + C_{55} + C_{36} + C_{45} \qquad (9A.4.24e)$$

$$\overline{LM} = C_{16} + C_{26} + C_{45} + C_{12} + C_{66} + C_{14} + C_{56} + C_{25} + C_{46} \qquad (9A.4.24f)$$

9A.5 CUBIC CRYSTALS

The preceding equations are greatly simplified in cubic materials such as iron, steel, stainless steel, the high alloys, etc.

Recalling that

$$C_{11} = C_{22} = C_{33} \tag{9A.4.1a}$$

$$C_{12} = C_{21} = C_{13} = C_{31} = C_{23} = C_{32} \tag{9A.4.1b}$$

$$C_{44} = C_{55} = C_{66} \tag{9A.4.1c}$$

All other C values are zero; we can substitute into the equations for elastic constants:

$$L = \ell^2 C_{11} + (m^2 + n^2) C_{44} \tag{9A.5.1a}$$

$$M = \ell^2 C_{44} + m^2 C_{11} + n^2 C_{44} = m^2 C_{11} + (\ell_2 + n^2) C_{44} \tag{9A.5.1b}$$

$$N = (\ell^2 + m^2) C_{44} + n^2 C_{11} \tag{9A.5.1c}$$

$$\overline{LM} = \ell m (C_{12} + C_{44}) \tag{9A.5.1d}$$

$$\overline{LN} = n\ell (C_{12} + C_{44}) \tag{9A.5.1e}$$

$$\overline{MN} = mn (C_{12} + C_{44}) \tag{9A.5.1f}$$

For cubics where the principal axes coincide with three crystallographic axes, the solutions are

[100] direction

$$\rho_1 V_1^{2\,(a)} = C_{11} \text{ (long.)}; \quad \rho_2 V_2^{2\,(b)} = C_{44}; \quad \rho_3 V_3^{2\,(c)} = C_{44} \text{ (shear)} \tag{9A.5.2}$$

[110] direction $\ell = 1/\sqrt{2}$; $m = 1/\sqrt{2}$; $n = 0$

$$\rho V_2^{2\,(a)} = C_{44} \text{ (shear)}; \quad \rho V^{2\,(b)} = \frac{1}{2}(C_{11} - C_{12}) \text{ shear};$$
$$\rho V^{2\,(c)} = \frac{1}{2}(C_{11} + C_{12} + 2C_{44}) \text{ long.} \tag{9A.5.3}$$

[111] direction $\ell = m = n = 1/\sqrt{3}$

$$\rho V^2 = 1/3\,(C_{11} - C_{12} + C_{44}) \text{ shear} \tag{9A.5.4a}$$

$$\rho V^2 = 1/3\,(C_{11} - C_{12} + C_{44}) \text{ shear} \tag{9A.5.4b}$$

$$\rho V^2 = 1/3\,(C_{11} + 2C_{12} + 4C_{44}) \text{ long.} \tag{9A.5.4c}$$

9A.6 ISOTROPIC SOLIDS

The simplest case in the context of number of independent elastic constants is that of isotropic solids. This case is more applicable than might appear at first glance because most polycrystalline materials, where the grain size is not excessively large and where heat treatment has reduced greatly or removed preferred orientation due to hot or cold working, can be considered to be isotropic solids. One must be careful in applying this criterion since many so-called isotropic materials have some degree of anisotropy.

Before developing the isotropic case we need to introduce another set of constants, the Lamé constants.

9A.6.1. LAMÉ CONSTANTS

At the beginning of the chapter we discussed the various moduli--elastic, shear, and bulk--together with Poisson's ratio. While the bulk and shear moduli represent fundamental elastic constants arising from basic considerations, they do not necessarily coincide with those elastic constants easiest to measure.

In the case of isotropic solids such as we are discussing, the geometric considerations lead to two simple equations covering wave propagation. The first is the longitudinal wave equation where displacements perpendicular to the wave front direction are zero; the second equation covering shear is controlled by the displacement along the direction of the wavefront being zero. These reduce (in the one-dimensional case) to

$$\frac{d^2u}{dt^2} = \frac{Kd^2u}{\rho dx^2} \text{ longitudinal} \qquad (9A.6.1a)$$

$$\frac{d^2u}{dt^2} = \frac{\mu d^2u}{\rho dx^2} \text{ shear} \qquad (9A.6.2a)$$

where u is displacement, μ in the shear case is one Lamé constant and is the same as G, the shear modulus. The K value is equal to

$$\rho V_\ell^2 = K = \lambda + 2\mu \qquad (9A.6.1b)$$

where λ is the second Lamé constant and

$$\rho V_S^2 = \mu \qquad (9A.6.2b)$$

This can be seen from the following relationships for isotropic solids:

$$C_{11} = C_{22} = C_{33} = \lambda + 2\mu \text{ (long.)} \qquad (9A.6.3a)$$

$$C_{12} = C_{21} = C_{13} = C_{31} = C_{23} = C_{32} = \lambda \qquad (9A.6.3b)$$

$$C_{44} = C_{55} = C_{66} = \mu \text{ (shear)} \qquad (9A.6.3c)$$

all other values of C = 0.

The Lame constants are related to the other moduli as follows:

Young's (elastic)	$E = \mu (3\lambda + 2\mu)/(\lambda + \mu)$	(9A.6.4a)
Shear	$G = \mu$	(9A.6.4b)
Bulk	$B = \lambda + \frac{2\mu}{3}$	(9A.6.4c)
Poisson's Ratio	$\nu = \lambda/2\ (\lambda + \mu)$	(9A.6.4d)

The various relationships are given in Table 9A.6.1(9A.1.1) somewhat modified from those in Reference 9A.1.3.

TABLE 9A.6.1. The Connection Between Elastic Constants of Isotropic Bodies: v_l = Longitudinal wave velocity; v_s = Shear wave velocity; λ, μ = Lamé constants

B Bulk Modulus	E Young's Modulus	λ Lamé Constant	ν Poisson's Ratio	$K = \rho v_l^2$ Longitudinal Modulus	$G = \rho v_s^2 = \mu$ Shear Modulus	How Obtained
$\lambda + \frac{2G}{3}$	$G\frac{3\lambda + 2G}{\lambda + G}$	--	$\frac{\lambda}{2(\lambda + G)}$	$\lambda + 2G$	--	λ (Lamé constant) is always calculated
--	$9B\frac{B - \lambda}{3B - \lambda}$	--	$\frac{\lambda}{3B - \lambda}$	$3B - 2\lambda$	$\frac{3(B - \lambda)}{2}$	
--	$\frac{9BG}{3B + G}$	$B - \frac{2G}{3}$	$\frac{3B - 2G}{2(3B + G)}$	$B + \frac{4G}{3}$	--	Static measurement of B and G
$\frac{EG}{3(3G - E)}$	--	$G\frac{E - 2G}{3G - E}$	$\frac{E}{2G} - 1$	$G\frac{4G - E}{3G - E}$	--	Static measurement of E and G; dynamic (resonance) measurement of E and G
--	--	$3B\frac{3B - E}{9B - E}$	$\frac{3B - E}{6B}$	$3B\frac{3B + E}{9B - E}$	$\frac{3BE}{9B - E}$	Static measurement of B; dynamic (resonance) measurement of E
$\lambda\frac{(1 + \nu)}{3\nu}$	$\lambda\frac{(1 + \nu)(1 - 2\nu)}{\nu}$	--	--	$\lambda\frac{(1 - \nu)}{\nu}$	$\lambda\frac{1 - 2\nu}{\nu}$	
--	$3B(\ - 2\nu)$	$3B\frac{\nu}{1 + \nu}$	--	$3B\frac{1 - \nu}{1 + \nu}$	$3B\frac{1 - 2\nu}{2 + 2\nu}$	Static measurement of B and ν
$\frac{E}{3(1 - 2\nu)}$	--	$\frac{E}{(1 + \nu)(1 - 2\nu)}$	--	$\frac{E(1 - \nu)}{(1 + \nu)(1 - 2\nu)}$	$\frac{E}{2 + 2\nu}$	Static or dynamic measurement of E and ν
$\rho(v_l^2 - \frac{4}{3}v_s^2)$	$\frac{3v_s^2v_l^2 - 4v_s^4}{(v_l^2 - v_s^2)}$	$\rho(v_l^2 - 2v_s^2)$	$\frac{v_l^2 - 2v_s^2}{2(v_l^2 - v_s^2)}$	--	--	Dynamic (velocity) measurement of v_l and v_s

We can evaluate the elastic constants for an isotropic solid in the same fashion used for the cubic system:

$$L = \ell^2 C_{11} + C_{44} (1 - \ell^2) = \ell^2 (\lambda + \mu) + \mu \qquad (9A.6.5a)$$

$$M = m^2 C_{22} + C_{44} (1 - m^2) = m^2 (\lambda + \mu) + \mu \qquad (9A.6.5b)$$

$$N = n^2 C_{33} + C_{44} (1 - n^2) = n^2 (\lambda + \mu) + \mu \qquad (9A.6.5c)$$

$$\overline{MN} = mn (C_{44} + C_{12}) = mn (\lambda + \mu) \qquad (9A.6.5d)$$

$$\overline{LN} = n\ell (C_{44} + C_{12}) = n\ell (\lambda + \mu) \qquad (9A.6.5e)$$

$$\overline{LM} = \ell m (C_{44} + C_{12}) = \ell m (\lambda + \mu) \qquad (9A.6.5f)$$

The determinant is

$$0 = \begin{vmatrix} \ell_2^2 (\lambda + \mu) + \mu - \rho V^2 & \ell m (\lambda + \mu) & n\ell (\lambda + \mu) \\ \ell m (\lambda + \mu) & m^2 (\lambda + \mu) + \mu - \rho V^2 & mn (\lambda + \mu) \\ n\ell (\lambda + \mu) & mn (\lambda + \mu) & n^2 (\lambda + \mu) + \mu - \rho V^2 \end{vmatrix} \qquad (9A.6.6)$$

or

$$(\mu - \rho V^2)^2 (\lambda + 2\mu - \rho V^2) = 0 \text{ (long.) } V_1 = \frac{\lambda + 2\mu}{\rho}^{1/2}; \; V_2 = V_3 = (\mu/\rho)^{1/2} \text{ trans.} \qquad (9A.6.7)$$

Another approach is to consider the coefficients with respect to the various crystallographic directions:

[100] (a) (b) (c) (d) (e) (f)

$$L = C_{11};\ M = C_{44};\ N = C_{44};\ \overline{MN} = 0;\ \overline{LN} = 0;\ \overline{LM} = 0 \qquad (9A.6.8)$$

[110] (a) (b) (c) (d) (e)

$$L = \tfrac{1}{2}(C_{11} + C_{44});\ M = \tfrac{1}{2}(C_{11} + C_{44});\ N = C_{44};\ \overline{MN} = 0;\ \overline{LN} = 0; \qquad (9A.6.9)$$

(f)

$$\overline{LM} = \tfrac{1}{2}(C_{44} + C_{12})$$

[111] (a) (b) (c)

$$L = \tfrac{1}{3}C_{11} + \tfrac{2}{3}C_{44};\ M = \tfrac{1}{3}C_{22} + \tfrac{2}{3}C_{44};\ N = \tfrac{1}{3}C_{11} + \tfrac{2}{3}C_{44} \qquad (9A.6.10)$$

(d) (e) (f)

$$\overline{MN} = \tfrac{1}{3}(C_{44} + C_{12});\ \overline{LN} = \tfrac{1}{3}(C_{44} + C_{12});\ \overline{LM} = \tfrac{1}{3}(C_{44} + C_{12})$$

The determinants will be

General

$$\begin{vmatrix} L - \rho V^2 & \overline{LM} & \overline{LN} \\ \overline{LM} & M - \rho V^2 & \overline{MN} \\ \overline{LN} & \overline{MN} & N - \rho V^2 \end{vmatrix} = 0 \qquad (9A.4.19)$$

[100]

$$\begin{vmatrix} C_{11} - \rho V^2 & 0 & 0 \\ 0 & C_{44} - \rho V^2 & 0 \\ 0 & 0 & C_{44} - \rho V^2 \end{vmatrix} \qquad (9A.6.11)$$

[110]
$$\begin{vmatrix} \frac{1}{2}(C_{11}+C_{44})-\rho V^2 & \frac{1}{2}(C_{44}+C_{12}) & 0 \\ \frac{1}{2}(C_{44}+C_{12}) & \frac{1}{2}(C_{11}+C_{44})-\rho V^2 & 0 \\ 0 & 0 & C_{44}-\rho V^2 \end{vmatrix} \qquad (9A.6.12)$$

[100]
$$(C_{11}-\rho V^2)(C_{44}-\rho V^2)^2 = 0$$

$$V = \left(\frac{C_{11}}{\rho}\right)^{1/2} \qquad V_2 = V_3 \left(\frac{C_{44}}{\rho}\right)^{1/2} \qquad (9A.6.13)$$

Recalling that the two Lamé constants completely describe an isotropic solid, it follows that if

$$C_{11} = C_{22} = C_{33} = \lambda + 2\mu \qquad (9A.6.3a)$$

$$C_{12} = C_{21} = C_{13} = C_{31} = C_{23} = C_{32} = \lambda \qquad (9A.6.3b)$$

$$C_{44} = C_{55} = C_{66} = \mu \qquad (9A.6.3c)$$

then

$$\frac{\lambda + 2\mu - \lambda}{2} = \mu \qquad (9A.6.14)$$

and

$$\frac{C_{11} - C_{12}}{2} = C_{44} \qquad (9A.6.15)$$

Therefore, an isotropic solid will be described by

$$\begin{matrix} C_{11} & C_{12} & C_{12} & 0 & 0 & 0 \\ & C_{11} & C_{12} & 0 & 0 & 0 \\ & & C_{11} & 0 & 0 & 0 \\ & & & \frac{1}{2}(C_{11} - C_{12}) & & \\ & & & & \frac{1}{2}(C_{11} - C_{12}) & \\ & & & & & \frac{1}{2}(C_{11} - C_{12}) \end{matrix} \qquad (9A.6.16)$$

$$(C_{11} - \rho V^2)\left[\frac{1}{2}(C_{11} - C_{12})\,\rho V^2\right]^2 = 0 \qquad (9A.6.17)$$

$$V_1 = \left(\frac{C_{11}}{\rho}\right)^{1/2};\ V_2 = \frac{C_{11} - C_{12}}{2\rho};\ V_3 = \frac{C_{11} - C_{12}}{2\rho} \qquad (9A.6.18)$$

Long(a) Snear(b) (c)

Since $V_2 = V_3$, only one is required to define the crystal.

9A.7 THIRD-ORDER ELASTIC CONSTANTS (inelastic deformation)

A solid may be elastically isotropic under stress-free conditions, or at very low elastic strains; however, the same solid may or will have anisotropic characteristics when stress is applied, particularly when there is any inelastic deformation. This situation is of considerable scientific interest in initially isotropic materials such as stress-free polycrystalline solids with random grain orientations.

A more general and more correct approach is to consider the behavior of nonlinear elastic waves as they propagate in solid materials. Such nonlinear effects results from various causes. In some instances, higher amplitudes of the initially elastic wave may generate finite strains; in other cases, the application of external static stresses cause nonlinear behavior; many solids may contain a variety of energy absorbing mechanisms which result in locally nonlinear or even nonelastic behavior; one possible cause of the latter is the existence of microscopic stresses. This third form is usually handled as a form of attenuation.

A linear elastic wave behaves in a fairly predictable fashion; this is not true for nonlinear elastic waves. For example, the initial wave such as a sinusoidal longitudinal stress wave at a given frequency will distort as it propagates, and energy will be transferred from the fundamental to the harmonics that appear. This behavior will be a function of wave amplitude. Nonlinear transverse curves may propagate without distortion in ideal (defect free) solids; they can interact with other waves, and such interactions may generate additional waves.

We discussed second-order elastic constants earlier. In stressed conditions third-order elastic constants exist. These constants permit the evaluation of first-order anharmonic terms of interatomic potential or generalized Grüneisen parameters, both of which are basic to all theories related to anharmonic phenomena such as the interaction of acoustic and thermal phonons and the equation of state. The same approach to measuring constants occur. The difference in velocity measurements permits the evaluation of third-order elastic constants. These elastic constants are also known as third-order Murnaghan

constants from the man who initially developed the relationship for elastic strain energy for an isotropic solid, including third-order terms but omitting terms independent of strain. The following is the equation:

$$\phi = \frac{2\mu + \lambda}{2} I_1^2 - 2\mu I_2 + \frac{\ell + 2m}{3} I_1^3 - 2mI_1I_2 + nI_3 \qquad (9A.7.1)$$

where ϕ is the elastic strain energy; μ and λ are the Lamé constants; ℓ, m and n are the third-order Murnaghan constants; and I_1, I_2 and I_3 are the three invariants of the Lagrangian strain tensor.

The equations developed in the preceding section of this chapter provide the basis for the development that follows. Principal sources used were Ratcliffe,[9A.7.1] Smith,[9A.7.2] Hughes and Kelly,[9A.7.3] Thurston and Brugger[9A.7.4] and Green.[9A.1.1]

The equations pertinent to isotropic solids in the form desired for development of third-order constants follow:

$$L = \ell^2 (\lambda + \mu) + \mu \qquad (9A.6.5a)$$

$$M = m^2 (\lambda + \mu) + \mu \qquad (9A.6.5b)$$

$$N = n^2 (\lambda + \mu) + \mu \qquad (9A.6.5c)$$

$$\overline{MN} = mn (\lambda + \mu) \qquad (9A.6.5d)$$

$$\overline{LN} = n\ell (\lambda + \mu) \qquad (9A.6.5e)$$

$$\overline{LM} = \ell m (\lambda + \mu) \qquad (9A.6.5f)$$

In fact, even fewer are used because of the complexity of the development. Only the one-dimensional case was used in most of the theoretical developments. The basic equation used by Hughes and Kelly[9A.7.3] is

$$\frac{d^2u}{dt^2} = \frac{Kd^2u}{\rho dx^2} \qquad (9A.6.1a)$$

which becomes, for isotropic solids,

$$\rho V_{\ell}^{\ 2} = K = \lambda + 2\mu \qquad (9A.6.1b)$$

The analogous equation for shear is

$$\frac{d^2u}{dt^2} = \frac{\mu d^2u}{\rho dx^2} \qquad (9A.6.2a)$$

or

$$\rho V_S^{\ 2} = \mu \qquad (9A.6.2b)$$

As will be noted later, when the equations are expanded to cover the cases of tensile or hydrostatic stress, they reduce to 9A.6.1b and 9A.6.2b as the applied stress approaches zero.

The initial set of equations relating wave velocity and second- and third-order elastic constants were derived by Hughes and Kelly[9A.7.3] using Murnaghan's Equation (9A.7.1). The authors[9A.7.3] limited their strain equations to no more than square terms and their stress equations to no more than first- and second-power terms. Furthermore, cases of wave propagation were limited to the x-axis for the longitudinal and shear-wave (2) cases. The seven equations derived by Hughes and Kelly[9A.7.3] are given below as presented by Ratcliffe:[9A.7.1]

$$\rho_o V_{lp}^{\ 2} = \lambda + 2\mu - \frac{P}{3K_o}(7\lambda + 10\mu + 6l + 4m) \qquad (9A.7.2)$$

$$\rho_o V_{sp}^2 = \mu - \frac{P}{3K_o}(3\lambda + 6\mu + 3m - n/2) \qquad (9A.7.3)$$

$$\rho_o V_{1x}^2 = \lambda + 2\mu + \frac{T}{3K_o}\left(\frac{\lambda + \mu}{\mu}[4\lambda + 10\mu + 4m] + \lambda + 2l\right) \qquad (9A.7.4)$$

$$\rho_o V_{iy}^2 = \lambda + 2\mu + \frac{T}{3K_o}(2\lambda/\mu\,[\lambda + 2\mu = m] - 2l) \qquad (9A.7.5)$$

$$\rho_o V_{sx}^2 = \mu + \frac{T}{3K_o}(4\lambda + 4\mu + m + \lambda n/4\mu) \qquad (9A.7.6)$$

$$\rho_o V_{sy}^2 = \mu + \frac{T}{3K_o}(\lambda + 2\mu + m + \lambda n/4\mu) \qquad (9A.7.7)$$

$$\rho_o V_{sz}^2 = \mu - \frac{T}{3K_o}(2\lambda - m + n/2 + \lambda n/2\mu) \qquad (9A.7.8)$$

where ρ_o = density of the material in the unstrained state

V = ultrasonic wave velocity

λ and μ = 2nd-order Lamé elastic constants for an isotropic material

l,m and n = 3rd-order Murnaghan elastic constants for an isotropic material

P = hydrostatic pressure

T = uniaxial tension

$B = K_o$ = bulk modulus = $\frac{1}{3}(3\lambda + 2\mu)$

and,

1st subscript l refers to longitudinal wave

1st subscript s refers to shear wave

2nd subscript p refers to hydrostatic pressure

2nd subscript x, y or z refer to uniaxial tension in the x, y or z directions respectively.

Other authors have developed similar equations, using somewhat different approaches. Table 9A.7.1[9A.1.1] presents the relations between third-order elastic constants for isotropic solids as used by different authors. Smith[9A.7.2] rationalized the differences among the various third-order constants. The author[9A.7.2] also illustrated the procedure for measuring the third-order elastic constants. The velocities in Equation 9A.7.2 to 9A.7.8 are difficult to measure accurately in absolute terms; however, differences in velocity, even though relatively small, can be measured quite accurately. The velocity-difference approach permits substantial simplification of the equations. One such example follows. The velocity difference between two principal shear waves propagated normal to a uniaxial stress and with polarization parallel and normal to the stress is shown in an example using Equations 9A.7.2 and 9A.7.8:

$$\rho_o V_{sy}^2 = \mu + \frac{T}{3K_o}(\lambda + 2\mu + m + \lambda n/4\mu) \qquad (9A.7.7)$$

$$\rho_o V_{sz}^2 = \mu - \frac{T}{3K_o}(2\lambda - m + n/2 + \lambda n/2\mu) \qquad (9A.7.8)$$

$$\rho_o \left(V_{sy}^2 - S_z^2\right) = \frac{T}{3K_o}\left(3\lambda + 2\mu + n/2 + \frac{3\lambda n}{4\mu}\right) \qquad (9A.7.9a)$$

$$\rho_o \left(V_{sy}^2 - S_z^2\right) = \frac{T}{3\frac{1}{3}(3\lambda + 2\mu)}\left[(3\lambda + 2\mu) + \frac{4\mu n + 3\lambda n}{2 + 4\mu}\right] \qquad (9A.7.9b)$$

$$\rho_o \left(V_{sy}^2 - S_z^2\right) = \frac{T}{3\lambda + 2\mu}\left[(3\lambda + 3\mu) + n\,\frac{(3\lambda + 2\mu)}{4\mu}\right] \qquad (9A.7.9c)$$

$$\rho_o \left(V_{sy}^2 - S_z^2\right) = \frac{T}{4\mu}(4\mu + n) \qquad (9A.7.9d)$$

TABLE 9A.7.1. Relations Between Third-Order Elastic Constants for Isotropic Solids as Used by Various Authors

Brugger	Truesdell, Hyperelastic $\alpha_4+\alpha_5 = 2[(\lambda/\mu)-1]$	Toupin and Bernstein	Landau and Lifshitz, Goldberg, Jones and Kobett	Murnaghan, Hughes and Kelly
c_{111}	$2\lambda-8\mu+2\mu(\alpha_3-\alpha_4+\alpha_6)$	$v_1+6v_2+8v_3$	$2A+6B+2C$	$2\ell+4m$
c_{112}	$2\lambda+2\mu\alpha_3$	v_1+2v_2	$2B+2C$	2ℓ
c_{123}	$2\lambda+2\mu\alpha_3+\mu\alpha_4$	v_1	$2C$	$2\ell-2m+n$
c_{144}	$-(\mu/2)\alpha_4$	v_2	B	$m-\frac{1}{2}n$
c_{155}	$-2\mu-(\mu/2)(\alpha_4-\alpha_6)$	v_2+2v_3	$B+\frac{1}{2}A$	m
c_{456}	$-\mu+(\mu/3)\alpha_6$	v_3	$\frac{1}{4}A$	$\frac{1}{4}n$
$(1/\mu)(-\lambda+c_{144}+\frac{1}{2}c_{123})$	α_3	$(1/\mu)(-\lambda+v_2+\frac{1}{2}v_1)$	$(1/\mu)(-\lambda+B+C)$	$(1/\mu)(-\lambda+\ell)$
$-(2/\mu)c_{144}$	α_4	$-(2/\mu)v_2$	$-(2/\mu)B$	$-(2/\mu)(m-\frac{1}{2}n)$
$(2/\mu)(\lambda-\mu+c_{144})$	α_5	$(2/\mu)(\lambda-\mu+v_2)$	$(2/\mu)(\lambda-\mu+B)$	$(2/\mu)(\lambda-\mu+m-\frac{1}{2}n)$
$(4/\mu)(\mu+c_{456})$	α_6	$(4/\mu)(\mu+v_3)$	$(4/\mu)(\mu+\frac{1}{4}A)$	$(4/\mu)(\mu+\frac{1}{4}n)$
c_{123}	$2\lambda+2\mu\alpha_3+\mu\alpha_4$	v_1	$2C$	$2\ell-2m+n$
c_{144}	$-(\mu/2)\alpha_4$	v_2	B	$m-\frac{1}{2}n$
c_{456}	$-\mu+(\mu/4)\alpha_6$	v_3	$\frac{1}{4}A$	$\frac{1}{4}n$
$4c_{456}$	$-4\mu+\mu\alpha_6$	$4v_3$	A	n
c_{144}	$-(\mu/2)\alpha_4$	v_2	B	$m-\frac{1}{2}n$
$\frac{1}{2}c_{123}$	$\lambda+\mu\alpha_3+(\mu/2)\alpha_4$	$\frac{1}{2}v_1$	C	$\ell-m+\frac{1}{2}n$
$\frac{1}{2}c_{112}$	$\lambda+\mu\alpha_3$	$\frac{1}{2}v_1+v_2$	$B+C$	ℓ
c_{155}	$-2\mu-(\mu/2)(\alpha_4-\alpha_6)$	v_2+2v_3	$\frac{1}{2}A+B$	m
$4c_{456}$	$-4\mu+\mu\alpha_6$	$4v_3$	A	n

The velocity differences, when stressed, are in the range of 10^{-4} even when high stresses are used. This means that

$$V_{sy} \approx V_{sz} \approx V_{so}$$

where V_{So} represents the unstressed state.

Therefore,

$$V_{sy} + V_{sz} \approx 2V_{so}$$

and

$$V_{sy} - V_{sz} = \frac{T}{8\mu V_{so} \rho_o} (4\mu + n) \qquad (9A.7.9e)$$

since

$$\rho_o V_s^2 = \rho_o V_{so}^2 = \mu \qquad (9A.4.20b)$$

We can divide both sides by this equation:

$$\frac{\Delta V}{V_{so}} = \frac{T}{8\mu^2} (4\mu + n) \qquad (9A.7.9f)$$

which permits us to evaluate one of the Murnaghan constants, n.

A similar approach can be used to determine the other third-order constants.

The problem rapidly becomes more complicated and difficult as one shifts to less symmetric crystals or away from the simple [100] directions. An

example of the elastic strain energy Equation 9A.7.1 converted to a working equation follows:

$$\phi = \frac{2\mu + \lambda}{2} I_1^2 - 2\mu I_2 + \frac{\ell + 2m}{3} I_1^3 - 2m I_1 I_2 + n I_3$$

$$\begin{aligned}\phi = {} & [(2\mu + \lambda)/2](\gamma_{11} + \gamma_{22} + \gamma_{33})^2 \\ & - 2\mu (\gamma_{22}\gamma_{33} - \gamma_{23}\gamma_{32} + \gamma_{33}\gamma_{11} - \gamma_{13}\gamma_{31} + \gamma_{11}\gamma_{22} - \gamma_{12}\gamma_{21}) \\ & + [(1 + 2m)/3] (\gamma_{11} + \gamma_{22} + \gamma_{33})^3 - 2m (\gamma_{11} + \gamma_{22}\gamma_{33}) \\ & (\gamma_{22}\gamma_{33} - \gamma_{23}\gamma_{32} + \gamma_{33}\gamma_{11} - \gamma_{13}\gamma_{31} + \gamma_{11}\gamma_{22} - \gamma_{12}\gamma_{21}) \\ & + n (\gamma_{11}\gamma_{22}\gamma_{33} - \gamma_{11}\gamma_{23}\gamma_{32} - \gamma_{21}\gamma_{12}\gamma_{33} + \gamma_{21}\gamma_{13}\gamma_{32} + \gamma_{31}\gamma_{12}\gamma_{23} \\ & + \gamma_{31}\gamma_{13}\gamma_{22})\end{aligned} \qquad (9A.7.10)$$

The similar equation for a cubic crystal is

$$\begin{aligned}\phi = {} & \frac{1}{2} C_{11} (\gamma_{11}^2 + \gamma_{22}^2 + \gamma_{33}^2) + C_{12} (\gamma_{11}\gamma_{22} + \gamma_{22}\gamma_{33} + \gamma_{33}\gamma_{11}) \\ & + C_{44} (\gamma_{12}^2 + \gamma_{21}^2 + \gamma_{23}^2 + \gamma_{32}^2 + \gamma_{31}^2 + \gamma_{13}^2) + C_{111} (\gamma_{11}^3 + \gamma_{22}^3 + \gamma_{33}^3) \\ & + C_{112} [\gamma_{11}^2 (\gamma_{22} + \gamma_{33}) + \gamma_{22}^2 (\gamma_{33} + \gamma_{11}) + \gamma_{33}^2 (\gamma_{11} + \gamma_{22})] \\ & + \frac{1}{2} C_{144} [\gamma_{11} (\gamma_{23}^2 + \gamma_{32}^2) + \gamma_{22} (\gamma_{31}^2 + \gamma_{13}^2) + \gamma_{33} (\gamma_{12}^2 + \gamma_{21}^2)] \\ & + \frac{1}{2} C_{166} [(\gamma_{12}^2 + \gamma_{21}^2)(\gamma_{11} + \gamma_{22}) + (\gamma_{23}^2 + \gamma_{32}^2)(\gamma_{22} + \gamma_{33}) \\ & + (\gamma_{31}^2 + \gamma_{13}^2)(\gamma_{33} + \gamma_{11})] + C_{123}\gamma_{11}\gamma_{22}\gamma_{33} \\ & + C_{456} (\gamma_{12}\gamma_{23}\gamma_{31} + \gamma_{21}\gamma_{32}\gamma_{13})\end{aligned} \qquad (9A.7.11)$$

which utilizes C_{ij} for second-order and C_{ijk} for third-order constants. The preceding equations can be converted to other terminology with the relationships of Table 9A.7.1

The following two relationships using Equation 9A.7.10 illustrate the enhanced complexity of shifting from [100] to [110] to [111]:

$$[100]\quad \phi = \tfrac{1}{2} C_{11}\gamma_{11}^2 + C_{44}\left(\gamma_{12}^2 + \gamma_{21}^2 + \gamma_{31}^2 + \gamma_{13}^2\right) + C_{111}\gamma_{11} + \tfrac{1}{2} C_{166}\left[\gamma_{11}\left(\gamma_{12}^2 + \gamma_{21}^2 + \gamma_{31}^2 + \gamma_{13}^2\right)\right] \tag{9A.7.12}$$

$$\begin{aligned}[110]\quad \phi = {} & \tfrac{1}{4} C_{11}\left[\gamma_{11}'^2 + \left(\gamma_{12}' + \gamma_{21}'\right)^2\right] + \tfrac{1}{4} C_{12}\left[\gamma_{11}'^2 - \left(\gamma_{12}' + \gamma_{21}'\right)^2\right] \\ & + \tfrac{1}{2} C_{44}\left[\gamma_{11}'^2 + \left(\gamma_{12}'^2 - \gamma_{21}\right)^2 + 2\left(\gamma_{13}'^2 + \gamma_{31}'^2\right)\right] \\ & + \tfrac{1}{4} C_{111}\left[\gamma_{11}'^2 + 3\gamma_{11}'\left(\gamma_{12}' + \gamma_{21}'\right)^2\right] \\ & + \tfrac{1}{4} C_{112}\left[\gamma_{11}'^3 - \gamma_{11}'\left(\gamma_{12}' + \gamma_{21}'\right)^2\right] + \tfrac{1}{4} C_{144}\,\gamma_{11}'\left(\gamma_{13}'^2 + \gamma_{31}'^2\right) \\ & + \tfrac{1}{4} C_{166}\left[\gamma_{11}'^3 + \gamma_{11}'\left(\gamma_{12}' - \gamma_{21}'\right)^2 + \gamma_{11}'\left(\gamma_{13}'^2 + \gamma_{31}'^2\right)\right] \\ & + \tfrac{1}{2} C_{456}\,\gamma_{11}'\gamma_{13}'\gamma_{31}'\end{aligned} \tag{9A.7.13}$$

$$\begin{aligned}[111]\quad \phi = {} & \tfrac{1}{6} C_{11}\left[\gamma_{11}'^2 + \left(\gamma_{21}' + \gamma_{12}'\right)^2 + \left(\gamma_{31}' + \gamma_{13}'\right)^2\right] \\ & + C_{12}\left[\tfrac{1}{3}\gamma_{11}'^2 - \tfrac{1}{6}\left(\gamma_{21}' + \gamma_{12}'\right)^2 - \tfrac{1}{6}\left(\gamma_{31}' + \gamma_{13}'\right)^2\right] \\ & + \tfrac{2}{3} C_{44}\left[\gamma_{11}'^2 + \gamma_{31}'^2 + \gamma_{13}'^2 - \gamma_{31}'\gamma_{13}' + \gamma_{21}'^2 + \gamma_{12}'^2 - \gamma_{21}'\gamma_{12}'\right] \\ & + C_{111}\left[\tfrac{1}{9}\gamma_{11}'^3 + \tfrac{1}{3}\gamma_{11}'\left(\gamma_{21}' + \gamma_{12}'\right)^2 + \tfrac{1}{3}\gamma_{11}'\left(\gamma_{31}' + \gamma_{13}'\right)^2\right. \\ & \left. - \left(\sqrt{2}/18\right)\left(\gamma_{21}' + \gamma_{12}'\right)^3 + \left(\sqrt{2}/6\right)\left(\gamma_{21}' + \gamma_{12}'\right)\left(\gamma_{31}' + \gamma_{13}'\right)^2\right]\end{aligned} \tag{9A.7.14}$$

$$+ C_{112}\left[\frac{2}{9}\gamma'^{3}_{11} + (\sqrt{2}/18)\left(\gamma'_{21} + \gamma'_{12}\right)^{3}\right. \qquad \text{(9A.7.14 contd)}$$

$$\left. - (\sqrt{2}/6)\left(\gamma'_{21} + \gamma'_{12}\right)\left(\gamma'_{31} + \gamma'_{13}\right)^{2}\right]$$

$$+ C_{144}\left\{\frac{1}{9}\gamma'^{3}_{11} - \frac{1}{3}\gamma'_{11}\left(\gamma'_{21}\gamma'_{12} + \gamma'_{31}\gamma'_{13}\right)\right.$$

$$+ (\sqrt{2}/36)\left(\gamma'^{3}_{21} + \gamma'^{3}_{12} - 3\gamma'^{2}_{21}\gamma'_{12} - 3\gamma'^{2}_{12}\gamma'_{21}\right)$$

$$\left. + (\sqrt{2}/12)\left[\gamma'_{21}\left(\gamma'^{2}_{13} + 2\gamma'^{2}_{31}\gamma'_{13} - \gamma'^{2}_{31}\right) + \gamma'_{12}\left(\gamma'^{2}_{31} + 2\gamma'_{31}\gamma'_{13} - \gamma'^{2}_{13}\right)\right]\right\}$$

$$+ C_{166}\left\{\frac{2}{9}\gamma'^{3}_{11} + \frac{1}{3}\gamma'_{11}\left(\gamma'^{2}_{21} + \gamma'^{2}_{12} + \gamma'^{2}_{31} + \gamma'^{2}_{13}\right)\right.$$

$$+ (\sqrt{2}/36)\left(-\gamma'^{3}_{21} - \gamma'^{3}_{12} + 3\gamma'^{2}_{21}\gamma'_{12} + 3\gamma'^{2}_{12}\gamma'_{21}\right)$$

$$\left. + (\sqrt{2}/12)\left[\gamma'_{21}\left(\gamma'^{2}_{31} - 2\gamma'_{31}\gamma'_{13} - \gamma'^{2}_{13}\right) + \gamma'_{12}\left(-\gamma'^{2}_{31} - 2\gamma'_{31}\gamma'_{13} + \gamma'^{2}_{13}\right)\right]\right\}$$

$$+ C_{123}\left[\frac{1}{27}\gamma'^{3}_{11} - \frac{1}{18}\gamma'_{11}\left(\gamma'_{21} + \gamma'_{12}\right)^{2} - \frac{1}{18}\gamma'_{11}\left(\gamma'_{31} + \gamma'_{13}\right)^{2}\right.$$

$$\left. - (\sqrt{2}/54)\left(\gamma'_{21} + \gamma'_{12}\right)^{3} + (\sqrt{2}/18)\left(\gamma'_{21} + \gamma'_{12}\right)\left(\gamma'_{31} + \gamma'_{13}\right)^{2}\right]$$

$$+ C_{456}\left\{\frac{2}{27}\gamma'^{3}_{11} + \frac{1}{9}\gamma'_{11}\left(-\gamma'^{2}_{31} - \gamma'^{2}_{13} + \gamma'_{31}\gamma'_{13}\right)\right.$$

$$+ \frac{1}{9}\gamma'_{11}\left(-\gamma'^{2}_{21} - \gamma'^{2}_{12} + \gamma'_{21}\gamma'_{12}\right)$$

$$+ (\sqrt{2}/54)\left(-2\gamma'^{3}_{21} - 2\gamma'^{3}_{12} + 3\gamma'_{21}\gamma'^{2}_{12} + 3\gamma'_{12}\gamma'^{2}_{21}\right)$$

$$\left. - (\sqrt{2}/18)\left[\gamma'_{21}\left(\gamma'^{2}_{13} - 2\gamma'^{2}_{31} + 2\gamma'_{31}\gamma'_{13}\right) + \gamma'_{12}\left(\gamma'^{2}_{31} - 2\gamma'^{2}_{13} + 2\gamma'_{31}\gamma'_{13}\right)\right]\right\}$$

The preceding equations are in the simplest state prior to differentiation and substitution. The reader is referred to Green[9A.7.1] for further derivations.

Thurston and Brugger[9A.7.4] developed the relationships for cubic crystals in [100] and [110] directions as influenced by uniaxial compressive

stresses in those directions. These authors[9A.7.4] used W, the wave speed, and N, a unit vector, rather than the more conventional V and n.

The preceding has touched briefly on the mathematical developments derived from solid state theory and the implications of the equations in terms of acoustic wave behavior. The actual data obtained through experiment are presented in the body of Chapter 9.

9A.8 REFERENCES

9A.1.1 Green, R. E., Jr., Ultrasonic Investigation of Mechanical Properties, Vol. 3 of Treatise on Materials Science Technology. Academic Press, New York, New York, 1973.

9A.1.2 Markham, M. F., "Measurement of Elastic Constants by the Ultrasonic Pulse Method." Br. J. Appl. Phys. Supp. 6:S56-S64, 1957.

9A.1.3 Schreiber, E., Anderson, O. L. and Soga, N., Elastic Constants and Their Measurement. McGraw-Hill, New York, New York, 1973.

9A.7.1 Ratcliffe, B. J., "A Review of the Techniques Using Ultrasonic Waves for the Measurement of Stress Within Materials." Br. J. Nondestr. Test. 9:48-58, 1969.

9A.7.2 Smith, R. T., "Stress-Induced Anistropy in Solids--The Acoustic-Elastic Effect." Ultrasonics 1:135-147, July/September 1963.

9A.7.3 Hughes, D. S. and Kelly, J. L., "Second Order Elastic Deformation of Solids." Phys. Rev. 95(5):1145-1149, 1953.

9A.7.4 Thurston, R. N. and Brugger, K., "Third-Order Elastic Constants and the Velocity of Small Amplitude Elastic Waves in Homogeneously Stressed Media." Phys. Rev. 133(6A):A1604-A1610, 1964.

CHAPTER 10

FAILURE STATISTICS AND FLAW SIGNIFICANCE

CONTENTS

FIGURES

TABLES

CHAPTER 10

FAILURE STATISTICS AND FLAW SIGNIFICANCE

10.1 INTRODUCTION

This chapter will assess the probability of failure of piping systems on the basis of available statistics. Where sufficient data on nuclear piping exist, they will be used. In the case of large pipes, such as are used in the recirculation system and as steam lines, their failure probability will be inferred from failure statistics of non-nuclear pressure vessels.

An attempt will be made to predict failure in terms of both piping size and piping systems. Where possible, PWR and BWR piping systems will be assessed separately to determine whether differences exist in failure probabilities and in failure modes.

The data will be presented in a variety of formats to aid in quantification of the probabilistic fracture mechanics tasks in Chapter 12.

Failure is defined in terms of substantial cracking or leaking of the pipe with an upper bound, a major split or guillotine break. Lesser cracking has the potential for converting to upper bound failure if subjected to dynamic loads such as water hammer, water slugging, or possibly, major seismic loads.

Failure modes or mechanisms are very sensitive to both materials and piping sizes and, to a greater or lesser degree, to the environment.

The value of NDE depends to a major degree on the safety significance of a given failure, the failure mechanism which often defines the failure location, and the mean-time-to-failure. Table 10.1.1 is a subjective judgment concerning a reasonable breakdown in terms of pipe size, failure mechanisms and safety implications of failure. The chapter will follow the breakdowns of Table 10.1.1 in terms of piping size and failure significance.

A class of failure mechanisms of major safety significance in many systems embraces the functional unreliability of valves. In many systems such

TABLE 10.1.1. Suggested Divisions by Pipe Size, Failure Significance, Failure Probability and Value of NDE

Pipe Size	Safety Implications	Probable Failure Mechanisms	Failure Data	Value of NDE	Remarks
Small <4 in. (usually <2 in.)	Usually minimal	Predominantly vibrational fatigue	Substantial	Little or none	---
Intermediate >4, <14	May be minor because of system	Generic: IGSCC, thermal fatigue	Moderate to substantial	Marginal	IGSCC has more safety significance in BWRs than PWRs
	Substantial in some systems	Several other failure mechanisms on random basis		Substantial	
Large >14	Major in recirculation boundary; may be significant in feedwater, etc.	Very low failure probabilities	Little or none	Substantial as a form of insurance	Water hammer, water slugging and seismic loads require quantification for both intermediate and large safety-related systems.
	Some systems have limited safety implications				

functional unreliability poses a much greater potential safety hazard than the spectrum of piping failures. While the significance of valve failure is noted, further discussion is outside the scope of this "white paper."

The further sections of this chapter will concentrate on failure probabilities by component size, system, and type of reactor. Failure mechanisms will be classified and discussed in detail when generic. Obvious examples of generic failure mechanisms include stress corrosion, erosion and cavitation, fatigue--both thermal and vibrational, and water hammer or water slugging. Other mechanisms tend to be more random.

The Licensing Event Reports (LERs) or their precursor, the Abnormal Occurrence Reports (AORs) have been the source of most of the data used in this chapter. There have been general overviews such as those of Bush[10.1.1,10.1.2,10.1.3] or Basin and Burns.[10.1.4] Incidents specific to intergranular stress corrosion cracking (IGSCC) in BWRs have been covered in General Electric[10.1.5] and NUREG[10.1.6,10.1.7] reports. The probability of cracking of large pipes is based on pressure vessel failure statistics. Bush[10.1.8] has given a broad overview, and Smith and Warwick[10.1.9] have updated earlier information as well as examining failures from a different point of view.

10.2 AN OVERVIEW OF PIPING FAILURES

The purpose of this section is to give a semi-quantitative overview of pipe cracking. The dearth of information in many Licensing Event Reports (LERs) does not permit quantification other than in certain systems, or where failure occurred by specific mechanisms. Usually, in these cases the manufacturer provided the information.

Pipe cracking incidents in pipe sizes below 4 in. have been limited to brief comparisons as have most data from foreign reactors. The information from other countries appears somewhat inconsistent when compared to the United States data. Since there was no procedure for assuring that all of the foreign data was available, the decision was made to limit foreign input to the IGSCC case.

Four methods of presenting the data are used; namely, failures by reactor type (Table 10.2.1), failures by mechanism (Table 10.2.2), failures by pipe size (Table 10.2.3), and failures by system (Table 10.2.4).

Data from smaller reactors such as VBWR and ERR have been omitted since these reactors have been decommissioned.

Incidents in Table 10.2.1 tend to be equal in BWRs and PWRs, if one removes IGSCC incidents.

Table 10.2.2 covers causal mechanisms. Again the numbers should be examined in terms of trends, not absolutes. Obviously, IGSCC is a prime contributor. The incidents of thermal fatigue are also quite high. Most other failures tend to be random with the possible exception of erosion-cavitation.

Table 10.2.3 presents failures in terms of pipe size. The large number of incidents in BWRs in the range of 4 to 10 in. are caused by IGSCC. The peak in PWRs at 16 to 18 in. occurs because of feedwater line thermal fatigue.

Table 10.2.4 presents a relatively incomplete picture of failures by systems. The size trends cited earlier appear again by system because of IGSCC in BWRs and thermal fatigue in PWRs.

TABLE 10.2.1. Number of Failures by Reactor Type (U.S. reactors--pipe > 4 in.)

BWR	IGSCC	Other	Total
1	25	10	35
2	12	7	19
3	37	26	63
4	62	12	74
	136	55	191

PWR	
Early W	6
2-Loop	4
3-Loop	24
4-Loop	10
CE	12
B W	0
	68(a)

(a) 19 of 68 IGSCC.

TABLE 10.2.2. Incidence of Major Cracking or Leaking in Nuclear Components[a] (may be multiple events in same component)

Cause of Defect	Type of Plant	1964	1965	1966	1967	1968	1969	1970	1971	1972	1973	1974	1975	1976	1977	1978	1979	1980	1981	
Thermal fatigue	BWR									1	4	6	18	20	7		2			58
	PWR							1			1					1	24			27
Design-dynamic load	BWR	1											1					2		4
	PWR							1	1									1	1	4
Construction defects/errors	BWR									2		2		5		4	2	4	1	20
	PWR												1					8	2	11
Water hammer (line failure)	BWR																	1		1
	PWR										1				2					3
Fatigue-vibrational	BWR																1	1		2
	PWR												2				3	10	5	20
Erosion/corrosion	BWR										1	2	2		4	2	1	1		13
	PWR															2				2
Corrosion/fatigue	BWR																		4	4
	PWR																	1	3	4
Unknown cause	BWR															2		5	3	10
	PWR															1	1	1	1	4
		1	0	0	0	0	0	2	1	3	7	10	24	25	13	13	34	35	20	187

(a) Piping >4-in. dia. unless otherwise noted as to component.

TABLE 10.2.3. Number of Failures by Pipe Size Through 1979 (U.S. reactors only)

Pipe Size (inches)	BWR			PWR
	IGSCC	Other		
4	50	13	63	8
6	35	12	47	5
8	20	2	22	4
10	51	6	57	12
12	8		8	
14	1	2	3	
16		1	1	18
18		1	1	7
20				
22				1
24				1
26				
>26				

TABLE 10.2.4. Number of Failures by System > 4 in. Except CRD (U.S. reactors only)

	Reactor Type		Typical Material
	BWR	PWR	
Feedwater	15	28	Ferritic (A-106)
Recirculation	2	2	Austenitic (BWR) Ferritic (PWR)
Charging	--	9	Ferritic
Steam	--	5	Ferritic (PWR)
Decay heat	14	4	
Service water	--	--	Austenitic (BWR)
Core spray	4	5	
CRD	6	5	Austenitic (BWR)
Other	2	5	--
Recirculation bypass	4	--	Austenitic (BWR)
RWCU	2	1	Austenitic (BWR)
Isolation condenser	--	--	
Reactivity	--	9	
	49	73	

10.3 FAILURES IN SMALL PIPING

The majority of pipe leaks and breaks occur in smaller sizes of piping typical of instrument, vent and drain lines. Many such lines are 1 in. or less in diameter. In addition, many breaks occur in the "less than 4 in." range. The Licensing Event Reports (LERs) classify piping into several size ranges, one of which is less than 4 inches. Often it becomes necessary to examine the original LER rather than the computer readout to establish the actual sizes of the failed piping. Even this may be insufficient, and one must examine the SARs for information as to specific piping sizes.

Many small pipe breaks are due to vibrational fatigue. As the sizes increase above 1 to 4 in., the failure mechanisms shift somewhat to thermal fatigue and IGSCC. It is difficult to establish definitive statistics because of the probability that many of the failures in small lines are not reported, particularly in instrument lines and in secondary or tertiary systems. A recent report[10.3.1] listed failures in small 4-in. lines. These data are reported as Tables 10.3.1 and 10.3.2 (limited to PWRs).

This author considers pipe breaks in the sizes below a diameter of 2 in. to have little or no safety significance in many instances. In the range 2 to 4 in., one must examine specific systems to establish the safety significance, if any, of breaks. Factors such as makeup capability set by charging pumps and safety function of lines such as control-rod drive tubes need to be examined. Usually, this is difficult to do because of the limited information available in LERs. For example, in PWRs, leaks or breaks are cited in systems such as coolant recirculation, reactor heat removal, reactor coolant cleanup, main steam condensate, feedwater and chemical and volume control. Obviously, such systems have substantial safety significance. It is less obvious whether failure of instrument or drain lines teed off these systems become a safety problem. The same applies to BWR lines. A NUREG report of the Third Pipe Crack Study Group[10.3.1] highlighted possible problems caused by failures in smaller pipes in conjunction with various design basis accidents.

TABLE 10.3.1. Summary of Pressurized Water Reactor Cracking in Pipes Smaller than 4 in.(10.3.1)

System	Plants	License Event Report Citations	Crack Location	Probable Cause
Chemical and Volume Control	Arkansas #2	1	Most cracks in welds located near pumps	Fatigue caused by vibration
	Calvert Cliffs #1	4		
	Calvert Cliffs #2	5		
	Haddam Neck	2		
	Fort Calhoun #1	2		
	Indian Point #2	3		
	Indian Point #3	1		
	Kewaunee #1	2		
	North Anna #1	1		
	Palisades #1	1		
	Point Beach #2	1		
	R.E. Ginna #1	3		
	Salem #1	1		
	Surry #1	1		
	Turkey Point #3	1		
	Turkey Point #4	3		
	Yankee Rowe	4		
	Zion #1	1		
	Zion #2	1		
Coolant Recirculation	Arkansas #2	1	In welds at small T's, and nipples, etc.	Vibration
	Calvert Cliffs #2	3		
	Fort Calhoun #1	1		
	Palisades #1	2		
	Point Beach #2	1		
	Salem #1	1		
	Three Mile Island #1	1		
	Indian Point #1	1		
	San Onufre	1		
Residual Heat Removal	Arkansas #1	3	Most cracks in welds near pumps or valves	Vibration
	D.C. Cook	2		
	Indian Point #2	3		
	Prairie Island #1	1		
	Three Mile Island #2	1		
	Three Mile Island #1	1		
Reactor Coolant Cleanup	Calvert Cliffs #1	3	Most cracks in welds in lines located near pumps	Fatigue caused by vibration
	Calvert Cliffs #2	3		
	Kewaunee #1	1		
	Trojan #1	1		
	Yankee Rowe	1		
Emergency Core Cooling	Arkansas #2	1	Most cracks in welds of vent or drain lines	Vibration
	Beaver Valley #1	1		
	Calvert Cliffs #2	1		
	Farley #1	1		
	Millstone #2	1		
	Oconee #2	1		
Main Steam Supply	North Anna #1	1	Cracks in weld in instrument lines	Not determined
Condensate Feedwater	Three Mile Island #1	1	Crack in socket weld	Vibration
Other Engineered Safety Features	Turkey Point #3	1	Crack in drain line weld	Vibration
Reactor Core Isolation Cooling	Oconee #3	1	Crack in weld in sample line	Vibration
Spent Fuel Pool	Arkansas #1	2	In weld HAZ	Not determined IGSCC
	Three Mile Island #1	1		
Containment Heat Removal	Indian Point #2	1	Vent to pump weld	Vibration

TABLE 10.3.2. Summary of Miscellaneous Small-Line Cracking[a] in 2-in dia.(and over) PWR Pipes[10.3.1]

Plant	System	Event Date	Nominal Pipe Diameter[b]	Material (tentative)	Location of Crack	Suspected Cause of Crack	Corrective Action	Comment[c]
Arkansas #2	Chemical and volume control	04/18/79	2 in.	304 SS	Weldolet, suction piping, "A" charging pump	Fatigue	Replace	
Calvert Cliffs #1	Service water	12/02/74 03/31/76 07/21/76 12/12/76	?	Carbon steel	Salt water return heat exchanger outlet piping	Erosion	Replace, repair, modify	
Calvert Cliffs #1	Steam	12/12/75	?	Carbon steel	Elbow, downstream of orifice	Erosion	Replace	Two-phase flow suspected as cause
Calvert Cliffs #2	Reactor coolant cleanup	04/27/77	2 in.	304 SS	Discharge pipe, volume control tank	Fatigue	Replace, redesign restraints	Possible resonance with pump
Ginna	Reactor cleanup	12/16/76	2 in.	304 SS	Socket weld, letdown diversion line	?	Replace	
Haddam Neck	Chemical and volume control	03/10/79	2 in.	304 SS	"T" primary drain cooler	Thermal and/or IGSCC	Replace	
Indian Point #2	Chemical and volume control	03/11/77	2 in.	304 SS	Seal injection line 23 charging pump	Fatigue	Repair	
Palisades #1	Chemical and volume control	06/04/78	2 to 4 in.	304 SS	Suction line P-55A	Fatigue		Hydraulic damage failed on discharge line
Point Beach #1	Reactor coolant	03/12/79	3 in.	304 SS	Nipple, downstream of bellows on pressurizer spray valve	?	Replace	Changed from pipe schedule 80 to 160
Surry #1	Chemical and volume control	04/10/75	2 in.	304 SS	Pump recirculation line	Fatigue		
Three Mile Island #1	Reactor coolant	05/31/74	?	304 SS	Recirculation orifice "B" pump	Erosion	Replace	
Trojan #1	Reactor coolant	03/01/77	2 in.	304 SS	"CVCS" letdown "T" support	Fatigue	Replace	
Trojan #1	Chemical and volume control	09/23/77	4 in.	304 SS	Charging pump suction line	Fatigue	Replace	
Turkey Point #4	Chemical and volume control	03/15/79	4 in.	304 SS	Crack at drain/ suction line weld, ¾in. long	Fatigue	Replace	

(a) Does not include IGSCC and feedwater piping cracking.
(b) For S.I. multiply by 2.5 to convert to centimeters.
(c) In all cases, the method of discovery was a leak.

10.4 FAILURES IN INTERMEDIATE SIZES OF PIPING

The preponderance of pipe failures of safety significance occur in pipes 4 to 14 in. in diameter. In BWRs most of the failures are due to IGSCC. In PWRs, there are fewer incidents of IGSCC; however, IGSCC represents a substantial percentage in some classes of lines. This size range of lines is amenable to NDE in most reactors and the early detection of cracking represents a net gain in safety. Furthermore, there are sufficient data to permit the prediction of trends. Three major categories will be considered; namely,

1. IGSCC in BWRs
2. cracking from all cases other than IGSCC in BWRs
3. cracking in PWRs.

10.4.1 IGSCC in BWRs

The predominant cracking mechanism in BWR piping has been IGSCC. Nearly 200 incidents had been reported by the end of 1979. In some pipe sizes, nearly 3% of the welds had suffered IGSCC. Some idea of the number of IGSCC incidents by type of BWR (Table 10.4.1), specific systems (Table 10.4.2) and pipe size (Tables 10.4.3a and 10.4.3b) is given in the following tables. In Table 10.4.1, the high ratio noted in domestic BWR Mark-I's is due to the high

TABLE 10.4.1. IGSCC Incidents by BWR Type Through 1979

Type Reactor	Number of Operating Reactors		Number of Incidents		Ratio Incidents/Reactors	
	U.S.	Foreign	U.S.	Foreign	U.S.	Foreign
BWR-1	3	7	26	13	9⁻	2⁻
BWR-2	2	1	14	4	7	4
BWR-3	7	9	37	16	5+	1+
BWR-4	13	1	67	9	5+	9
	25	18	144	42		

NOTE: No guarantee concerning accuracy of number of incidents.

TABLE 10.4.2. IGSCC Incidents in BWRs by System[a]

System	Inches	Incidents
Control Rod	3	3
Core Spray	6, 8, 10, 12	66
Isolation Condenser	10	4
Recirculation Bypass	4, 6	42
Recirculation--Large	10, 12, 14	8
RHR	12, 14	1
RWCU (Decay/Cleanup)	3, 4, 6, 8, 10	43
Steam Lines	26	6
Other		13
		186

(a) Sizes of typical BWR piping systems experiencing IGSCC given.

welding heat input used in Dresden-1. Otherwise the ratios in domestic BWRs are reasonably consistent. The apparently lower ratios in foreign BWRs probably is due to lack of complete data.

Certain systems appear to be more susceptible to IGSCC; notably, the core spray, recirculation bypass and decay/cleanup (RWCU) systems. It is suspected that these trends may be more related to pipe size than to system.

The relation between pipe size and IGSCC can be seen in Tables 10.4.3a and 10.4.3b. The majority of incidents occur in pipes 4 to 10 inches in diameter. The lower incidence below 4 in. is probably caused by difficulties in recognizing IGSCC versus other failure mechanisms. There is no reason to believe that the incidence should be less than that in the 4- to 10-in. range. Above 10 in. the decreasing incidence probably is caused by the distribution of residual stresses through the wall. While cracks may initiate in the thicker walled pipes of larger diameter, the evidence appears to support the conclusion that they do not continue to propagate through the wall.

Incidents of IGSCC are important for a variety of reasons. Such cracks initiate at the inner surface so volumetric NDE is required to detect them.

TABLE 10.4.3a. Incidents of IGSCC BWRs in (1965-1979)

Size of Pipe (in.)	Pre-July 1975	Pre-July 1978	Pre-1979 Number Reported Cracks and Leaks	Pre-1979 Number of Leaks
<4	2	10	14	9
4	30	45	50	19
6	17	27	36	11
8	7	19	22	2
10	8	17	49	8
12		8	8	0
14		1	1	0
24		6	6	
	64	133	186	49

TABLE 10.4.3b. Effect of Pipe Size on the Incidence of IGSCC as of July 1979

Pipe Size, (inches)	Number of Welds	Number of IGSCC Incidents	Frequency (percent)
<3	6774	14 (9)	0.21 (0.13)
4	1766	50 (19)	2.83 (1.07)
6	1226	35 (11)	2.93 (0.90)
8	1061	22 (2)	2.08 (0.20)
10	994	49 (8)	5.00 (0.80)
12	2065	8 (0)	0.38 (--)
14	194	1 (0)	0.52 (--)
16	535	0	0
18	296	0	0
20	182	0	0
22	397	0	0
24	403	6 (0)	1.50 (--)
26	141	0	0
28	812	0	0

NOTE: ( )--Numbers in parentheses denote cases of leaking for total number reported.

Further, they may propagate around the inner surface and then proceed at a relatively uniform rate through the wall. This occurred in Duane Arnold [10.4.1] where eight pipes suffered IGSCC and all propagated more than 60% through the wall relatively uniformly with only one developing into a through-wall crack.

10.4.2 BWR Pipe Cracking Other Than IGSCC

Various failure mechanisms other than IGSCC have been observed in BWR piping in the intermediate size range. Fatigue, usually vibrational, has occurred in 4- to 6-in. pipes. Thermal fatigue has cracked 10-in. lines. Erosion and cavitation have occurred in the size range of 6 to 18 inches. Other failures have been due to construction defects, design errors and impact damage. In a few instances, pipes have suffered guillotine failures or major splits due to events such as seizure of a pump or poor quality welds. Table 10.4.4 contains incidents of pipe cracking by system. The data in Table 10.4.2 are reproduced to permit a comparison of IGSCC incidents versus those from all other causes.

TABLE 10.4.4. Incidents of Pipe Cracking in BWR Systems from Causes Other Than IGSCC (IGSCC incidents from Table 10.4.2 are repeated to permit comparison)

System	Significant to Safety	Cracking All Others	Incidents IGSCC
Feedwater	Yes	14	--
Recirculation	Yes	1	8
Recirculation Bypass	Yes	4	42
Steam Lines	Marginal	--	6
Reactor Water Cleanup	Partial	2	43
Decay Heat Removal (RHR)	Yes	4	1
CRD's	Yes	6	3
HPCI	Yes	4	--
Core Spray	Yes	2	66
Isolation Condenser	Yes	--	4

10.4.3 PWR Pipe Cracking (>4 to <14 in.)

The total number of incidents of cracking in intermediate sizes of PWR piping is substantially less than reported in BWRs. If the instances of IGSCC are removed from both data sets, the total numbers of events from causes other than IGSCC are roughly 2 to 1, BWR versus PWR. This can be seen in Table 10.2.2 by cause, in Table 10.2.3 by pipe size, and in Table 10.2.4 by system. The preponderance of incidents in PWRs have occurred in feedwater systems with most of the incidents of cracking occurring in 1979 by thermal fatigue (Table 10.4.5).

Several cases of cracking due to IGSCC have been reported in PWRs, usually in secondary or tertiary lines of marginal safety significance. Most incidents have occurred in relatively thin-walled piping carrying borated solutions (Table 10.4.6).

One category of failures in PWR piping (and in BWRs also) is that where failure is caused by dynamic loads with or without contributions from design errors, construction defects, etc. The predominant dynamic load has been water hammer; however, there are instances of jet or slugging loads that can be classed only loosely as water hammer. Table 10.8.1 in Section 10.8 contains a limited number of the cases of water hammer where major damage or cracking occurred in the piping.

Several random failures have occurred in the intermediate pipe diameters (>4 to <14 in.). These are reported in Table 10.4.7.

At H. B. Robinson reactor, the safety relief valves were blown off because of a combination of jet loads and a severe stress concentration, and because of weld joint design, plus a lack in the ASME Section III Code with regard to consideration of dynamic loads. A similar event occurred at Turkey Point where jet loads blew off valves and split a header. A water hammer at Indian Point-2 caused a 180° circumferential crack in feedwater pipe at a discontinuity where the pipe penetrated a wall.

TABLE 10.4.5. Summary of PWR Feedwater Piping Cracks

Plant	Extent of Cracking (nozzle vicinity) Maximum Depth (in.)	Location Maximum Depth Crack	No. of Lines Cracked	Piping Component	Probable Cause	Comments
Westinghouse						
D. C. Cook 1 & 2	Thru wall	TOP	8 of 8	Elbow	Thermal fatigue	2 cracks thru wall
Beaver Valley	0.400	9 O'clock	3 of 3	Elbow	Thermal fatigue	13 additional fab. related indications repaired
Kawaunee	0.050	7 O'clock	2 of 2	Pipe	Thermal fatigue	3 in. dia. aux. feed near SG inlet
Pt. Beach 1 & 2	0.047	3 O'clock	2 of 2	Reducer	Thermal fatigue	3 in. dia. aux. feed near SG inlet
H. B. Robinson 2	0.0750	9 O'clock	3 of 3	Reducer	Thermal fatigue	Shallow cracking in nozzle under thermal sleeve
Salem 1	0.235		4 of 4	Elbow reducer	Thermal fatigue	
San Onofre 1	0.100	Lower half of reducer	3 of 3	Reducer	Thermal fatigue	Multiple branched cracks evidence of some fatigue
Surry 1 & 2	0.080	2 and 5 O'clock	6 of 6	Reducer	Thermal fatigue	
Ginna	0.107	8:30 O'clock	2 of 2	Elbow	Thermal fatigue	Cracks also at deep machining marks
Zion 1 & 2	0.088	4 O'clock	8 of 8	Elbow pipe	Thermal fatigue	
Combustion Engineering						
Millstone 2	0.250	12 O'clock	2 of 2	Pipe	Thermal fatigue	
Palisades	0.170	3 and 9 O'clock	2 of 2	Pipe	Thermal fatigue	Cracks found also at weld vicinity of horizontal piping

TABLE 10.4.6. Pressurized Water Reactor Facilities Reporting Pipe Cracks and Leaks Caused by IGSCC

Facility	System	Pipe Size
Arkansas #1	Building (containment spray)	10-in. and 8-in. Sch. 10
	Decay heat removal	10-in. Sch. 10
	Spent fuel pool cooling	3-in. 2-in. reducer
Crystal River #3	Containment spray	8-in. Sch. 40
Ginna	Safety injection	8-in. Sch. 10
H. B. Robinson #2	Boron injection	4-in
San Onofre #1	Containment spray	10-in. Sch. 10
	Refueling water storage tank Discharge pipe	8-in. Sch. 10
Surry #1	Containment spray	10-in. Sch. 40
Surry #2	Containment spray	10-in. Sch. 40
Three Mile Island #1	Spent fuel pool cooling Borated water storage tank to RHR suction	8-in. Sch. 40 10-in. Sch. 40

TABLE 10.4.7. Examples of Failures in PWR Piping in the Intermediate Size Range

Palisades	Fire main break	
Connecticut Yankee	Service water steam generator blowdown	
Robinson	Auxiliary feedwater line PWR weld	
Calvert Cliffs #2	Chemical volume control 4-c	June 1978
Indian Point #1	Main steam line	September 1970
Indian Point #1	Desuperheater line	January 1973
Surry	Surge line	August 1972
Fort Calhoun	16-in. Expansion joint	September 1973
Connecticut Yankee	Expansion joint	July 1971
North Anna #1	6-in Suction line	January 1978
St. Lucie	Charging pump cavitation	July 1978
Turkey Point #4	Chemical control--4-in.	March 1979
Indian Point #2	RHR discharger 6 to 11	August 1978
Fort Calhoun	Charging pump--crack	February 1978
Trojan	Suction line--4-in.	September 1977

10.5 LARGE (>20-IN.) PIPING

There have been a few cases of IGSCC in a BWR-1 steam line (26-in.). Also, the PWR feedwater lines where cracking has been reported are 16 to 18 in. in diameter. Otherwise most of the incidents have been in smaller lines.

If one wishes to predict failures in the larger sizes of thick-walled piping, it becomes necessary to revert to failure statistics for non-nuclear pressure vessels. Failure statistics have been inferred for large piping and are repeated here[10.1.8] as Table 10.5.1. A later study of Smith and Warwick[10.1.9] developed failure statistics similar to those in Table 10.5.1. These were incorporated in the conclusions to their report which are included here. While this report deals with pressure vessels, the conclusions are generally relevant to large pipes. Their statements concerning variability in statistics, contribution of weldments to failure, thickness effects, and necessity for improved NDE are particularly appropriate.

- Data compiled from U.K. experience from unfired pressurized plants indicates the following values for failure rates based on failures as defined in the text:
  - Potential (99% upper bound confidence level)--7.6×10^{-4} per vessel year
  - Catastrophic (99% upper bound confidence level)--7.9×10^{-5} per vessel year.
- Before any comparisons between different data sources are attempted agreement must be reached on definitions, terminology, and type of plant considered in the data collection process. There is also a need to be more precise in the use of the terms employed.
- It is suggested that there should be only two definitions of failure for the purpose of surveys into plant behavior. The two categories are

TABLE 10.5.1. Use of Pressure Vessel Statistics to Predict Large Pipe Failures; Comparison of Failure Statistics per Vessel-Year

Data Source	Vessel-Years Operation	Number of Failures, If Known, by Classes			Failure Rates			99% Confidence Upper Bound		
					Nondisruptive		Disruptive	Nondisruptive		Disruptive
					Noncritical	Potentially Disruptive		Noncritical	Potentially Disruptive	
		Noncritical	Potentially Disruptive	Disruptive						
EEI TVA	67,000	0 to 10		0	0 to 1.0×10^{-3}		--	4.6×10^{-4} to 2.0×10^{-3}		4.6×10^{-4}
EEI	22,700	1	0	0	4.6×10^{-5}	--		2.9×10^{-4}	< 2.1×10^{-4}	----------→
ABMS	725,200		Not known	0						5.3×10^{-6}
Phillips & Warwick	100,300	33	←	4	3.3×10^{-4}	----------→	4.0×10^{-5}	1.1×10^{-3}		1.2×10^{-4}
Smith & Warwick	310,100	215		13	6.9×10^{-4}	----------→	4.2×10^{-5}	7.4×10^{-4}		7.0×10^{-5}
Kellermann				--	2.1×10^{-4}	----------				
						9×10^{-5} ----------	--	9×10^{-5} ----------		
Kellermann & Seipel	1,700,000	< 547	----------→		1.5×10^{-4}	----------	3×10^{-6}			2.7×10^{-6} to 4.0×10^{-5}
		49	----------→			----------				
Kellermann et al.	67,000			0						6.9×10^{-5}

- Potential--Local degradation of the pressure boundary which would be extended by continued operation. This type of defect will require remedial action before being returned to service conditions.

- Disruptive--Failures of pressure boundary necessitating major repair, replacement, or withdrawal from service because of the dangerous conditions of the component. If bolted closures are included in the plant under consideration then failure of a significant fraction of closure bolting comes within this category.

- Weld metal and weld affected material are the most likely sites for failure initiation. Experience shows that this type of event is more likely to occur in areas of complex geometry such as nozzles where volumetric inspection is at best difficult and often impossible.

- Research into the effects of thickness either by experiment or by a further breakdown of data should be undertaken by organizations processing relevant data.

- Evidence seems to suggest that all industrialized countries encounter similar service experience from conventional plants but process their experience differently for the purposes of deriving failure statistics.

- Inservice inspection tends to restore probability figures to those assessed at the beginning of the inspection interval.

- Efforts must be made to improve volumetric NDE techniques. The results of the Plate Inspection Steering Committee Programs, an international exercise involving the U.S. inspection of a flawed thick plate specimen which would indicate the areas most in need of development and refinement--detection, positioning, sizing, recording.

- Data gathered by the various reporters are always retrospective. Caution should be exercised when applying the results or conclusions to new plant as there is always difficulty assessing the effects of

introducing changes in design, allowable stress levels, materials of construction, new fabrication techniques and requirements. As examples of this there were numerous problems following the introduction of Ni and Cu into boiler drum material in Germany and the introduction of low alloy steel into the British experience led to a rash of problems.

- There should be an international body to which all failures from an agreed type of plant could be reported. Alternatively some independent national body could be made responsible for collecting data from plants within agreed selective guidelines. Either type of organization should pool or report data periodically at a suitable forum.
- Treatment of data should reflect the nature of the use to which it is to be put and the accuracy with which it is collected.

An excellent study by Salter and Gethin[10.5.1] presented the frequency of occurrence of defects in pressure vessels. Such a study is an acceptable analog for the larger sizes of piping. A total of 599 pressure vessel main seams, 2,330 meters in length, served as the data base. The vessels ranged in thickness from 0.5 to 5.0 inches and were produced by three manufacturers, all in the United Kingdom.

Defects were classified as non-critical, consisting of porosity (110) and inclusions (543) or 81% of total defects, and critical, either cracks (114) or lack-of-fusion (39) or 19% of total. Table 10.5.2 presents the defect distribution as functions of type of weld and welding process.

TABLE 10.5.2. Analysis of Defects by Joint Type and Process

Joint Type and Process	Cracks		Lack of Fusion		Porosity		Inclusions		Total		Total Seam Length, m
	No. of Defects	Defect Length[a] / Seam Length	No. of Defects	Defect Length[a] / Seam Length	No. of Defects	Defect Length[a] / Seam Length	No. of Defects	Defect Length[a] / Seam Length	No. of Defects	Defect Length[a] / Seam Length	
Circumferential[b] subarc	69	0.25	15	0.11	50	0.11	448	1.89	582	2.36	1550
Circumferential	16	0.44	6	0.5	47	0.69	47	1.36	116	2.99	192
Longitudinal subarc	28	0.69	9	0.22	6	0.04	27	0.60	70	1.56	198
Longitudinal manual metal-arc	0	0	0	0	3	0.08	5	0.11	8	0.19	65
Longitudinal	1	0.04	9	0.21	4	0.04	14	0.07	28	0.36	330

(a) Expressed as $\frac{\text{Total defect length}}{\text{Total seam length}} \times 100$

(b) Including welds with manual root or sealing runs.

10.6 SIGNIFICANCE OF PIPING DEFECTS

The great majority of the incidents of pipe cracking or failure have had relatively little safety significance either because of the small sizes of the pipes or the nature of the cracks. Many have been cracks detected prior to leaking, or when the leaks were small with little or no probability of catastrophic failure. Most cases of erosion and cavitation can be included in this category. Many instances of IGSCC probably had little potential for progressing to catastrophic failure. While this can be said for many instances, because of crack geometry, toughness and ductility of the piping material, or generally low load levels, it is hazardous to generalize about IGSCC because instances have been reported of uniform crack progression around the circumference and then through the wall so that there was no early warning. This occurred at Duane Arnold.[10.4.1] While analyses indicated that the remaining 30% to 40% ligament was sufficient to sustain anticipated faulted loads, one wonders whether the same would be true at 10% ligament.

A potential concern is the failure of pipes under dynamic loads. As noted in the preceding sections such failures have occurred. Generally, due to system redundancy such major failures can be accommodated. Some of those cited occurred during non-nuclear testing so that the systems have not been tested under the ultimate conditions.

Another concern has to do with multiple concurrent failures. There is no real answer to this other than that probability of such concurrent events is very low.

Two articles of faith in reactor licensing have been that one must accommodate the large loss of coolant accident (LOCA) and all piping critical to safety must be suitably supported to prevent failure during an earthquake.

The author considers himself an iconoclast with both of the preceding items as graven images. To his knowledge, based on an extensive review of the literature as well as discussions with experts in the design and seismic fields, no unburied pipe of substantial size has failed during a severe earthquake (he is not considering buried cast iron piping). In fact, most

non-nuclear industries do not consider seismic loads in their design and prefer flexible systems. None of those contacted recalled pipe failures during seismic events. Certainly, piping can be grossly overstressed. Damage to piping during the Alaska and San Fernando quakes led to grossly bent and distorted lines.

In larger piping, the dearth of failure data forces one to revert to pressure vessel failure statistics such as given in Table 10.5.1. The concern with the large LOCA, which was developed originally to size containments, has grossly distorted legitimate concerns relevant to failures in smaller piping. The small LOCA, which is much more probable, has not received the attention it merits. In fact, this conclusion was evolved during the Three Mile Island-2 post-accident analyses. Systems designed primarily for the large LOCA may not be optimum for the small LOCA, and operator response may be more critical for this class of accidents than for the large LOCA because the latter depends primarily upon automatic response of equipment.

10.6.1 Influence of Defects on Static Failure Properties

Kato and Morita[10.6.1] examined the influence of defects on the static strength and deformability of welded joints. Three types of welding procedures were used; namely, manual arc (M), CO_2 shielded semiautomatic arc welding (C), and self-shielded semiautomatic arc welding (S), with the latter alternating current (S(AC)), or direct current (S(DC)). Six types of defects were inserted:

1. internal cracks (C_i)
2. root cracks (C_r)
3. internal lack-of-penetration (LP_i)
4. lack-of-penetration at root (LP_r)
5. internal slag inclusions (SI_i)
6. slag inclusions at root (SI_r).

Weld sample thicknesses were 25, 32, and 40 mm.

One can plot the relation between the mechanical properties such as maximum stress (σ_B) or elongation (El) versus the actual defect ratio (α) which is defined as the ratio of the actual defect area to the gross cross-sectional area of the test specimen at the weldment.

Another method of plotting is the ratio of σ_B over the actual tensile strength of an undefected weld (σ_w), or $\sigma_B/\sigma w$ versus α_S. Data are given for σ_B versus α_S covering various welding procedures. Figures 10.6.1 through 10.6.9 cover tensile strength, σ_B/α_W, and the percentage of elongation versus defect ratio, (α_S).

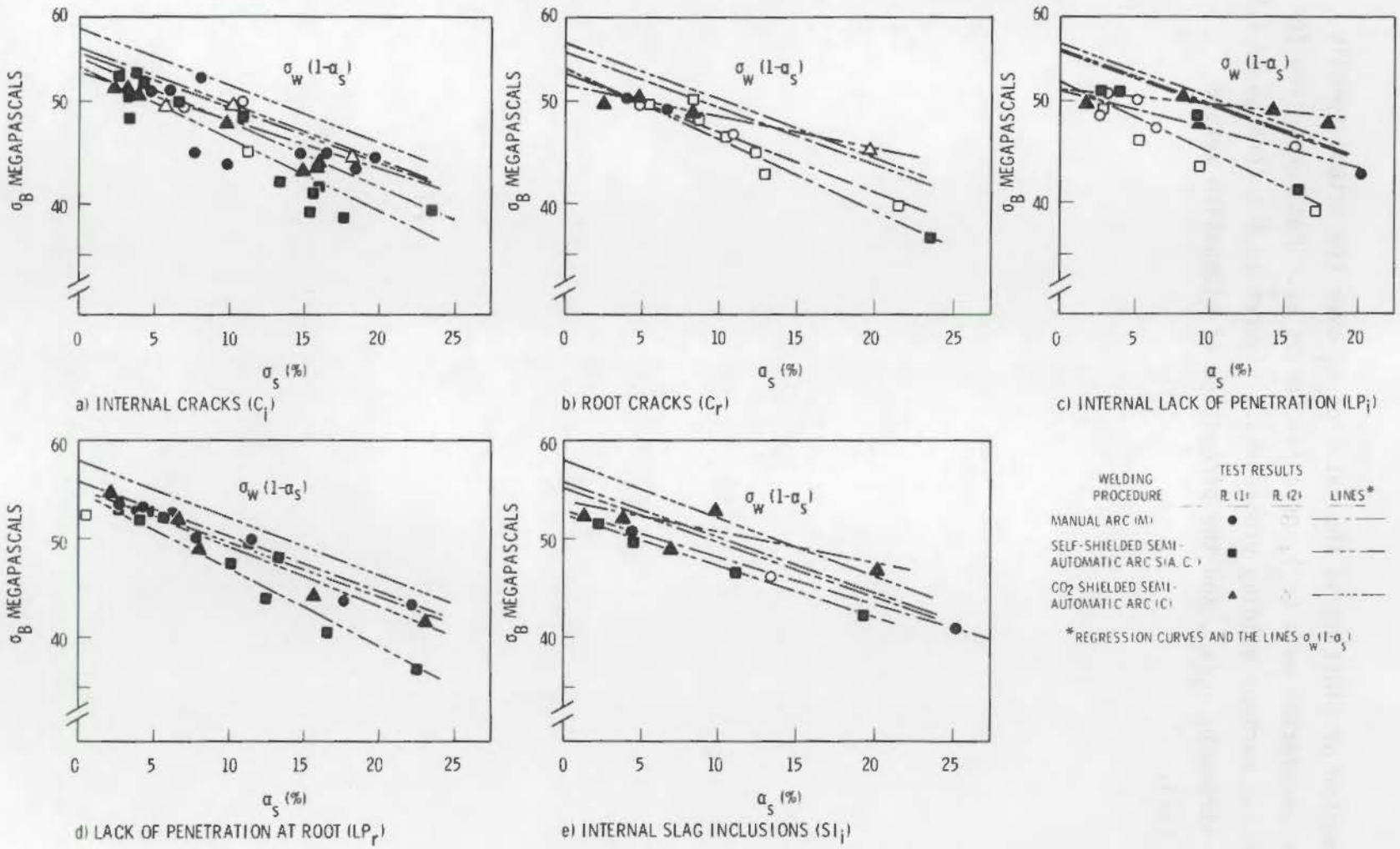

FIGURE 10.6.1. The Relation Between Nominal Maximum Stress (σ_B) and Actual Defect Ratio (α_S) - Plate Thickness 40 mm

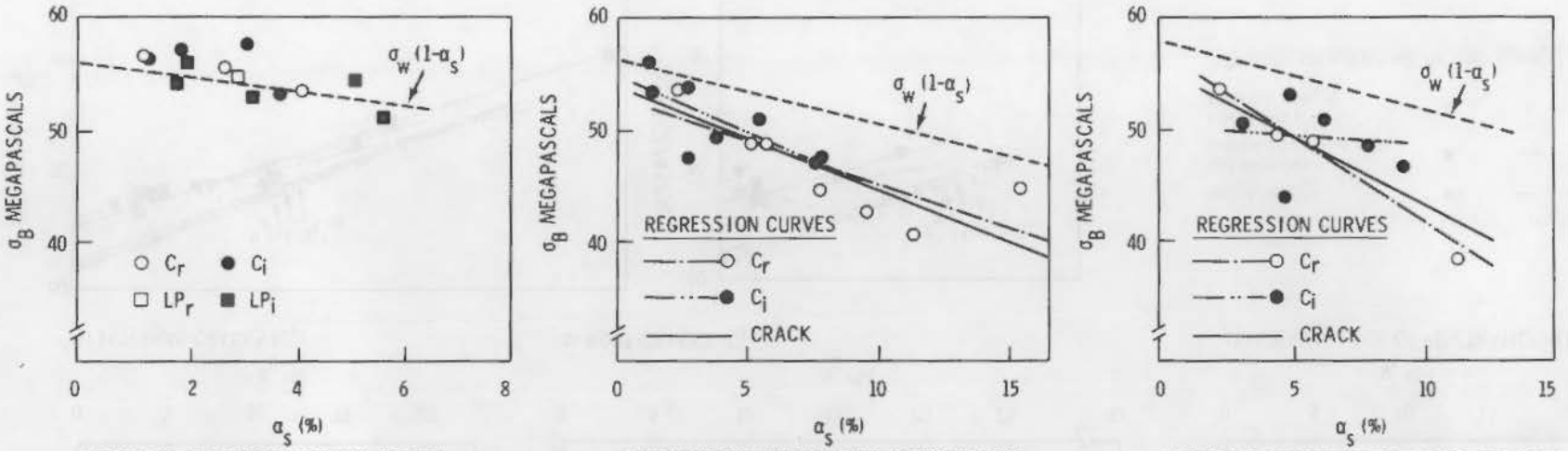

a) WELDING PROCEDURE MANUAL ARC (M)

b) WELDING PROCEDURE SELF-SHIELDED SEMI-AUTOMATIC ARC, AC [S(A. C.)]

c) WELDING PROCEDURE SELF-SHIELDED SEMI-AUTOMATIC ARC, DC [S(D. C.)]

FIGURE 10.6.2. The Relation Between Nominal Maximum Stress (σ_B) and Actual Defect Ratio (α_S) - Plate Thickness 32 mm

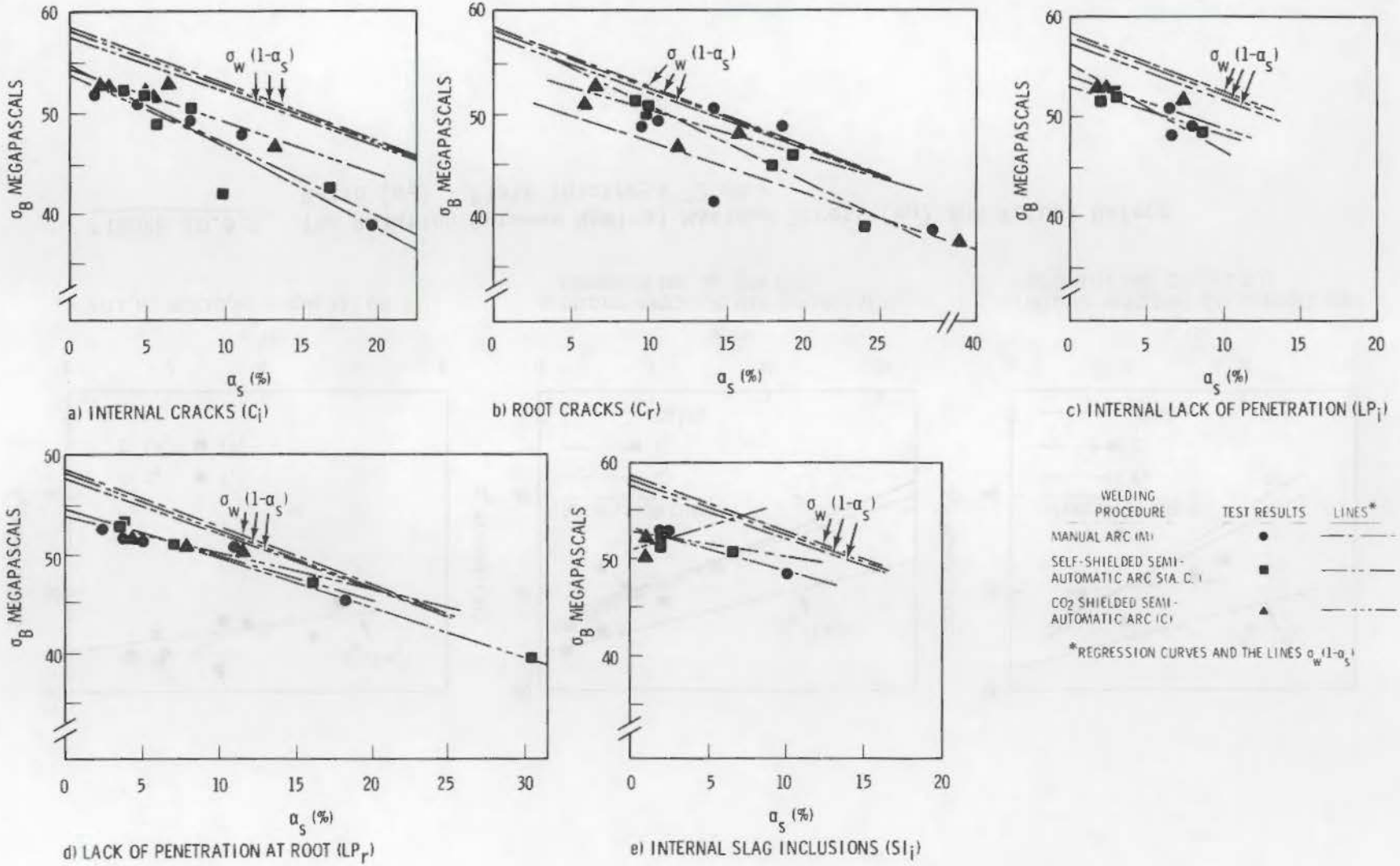

FIGURE 10.6.3. The Relation Between Nominal Maximum Stress (σ_B) and Actual Defect Ratio (α_s) - Plate Thickness 25 mm

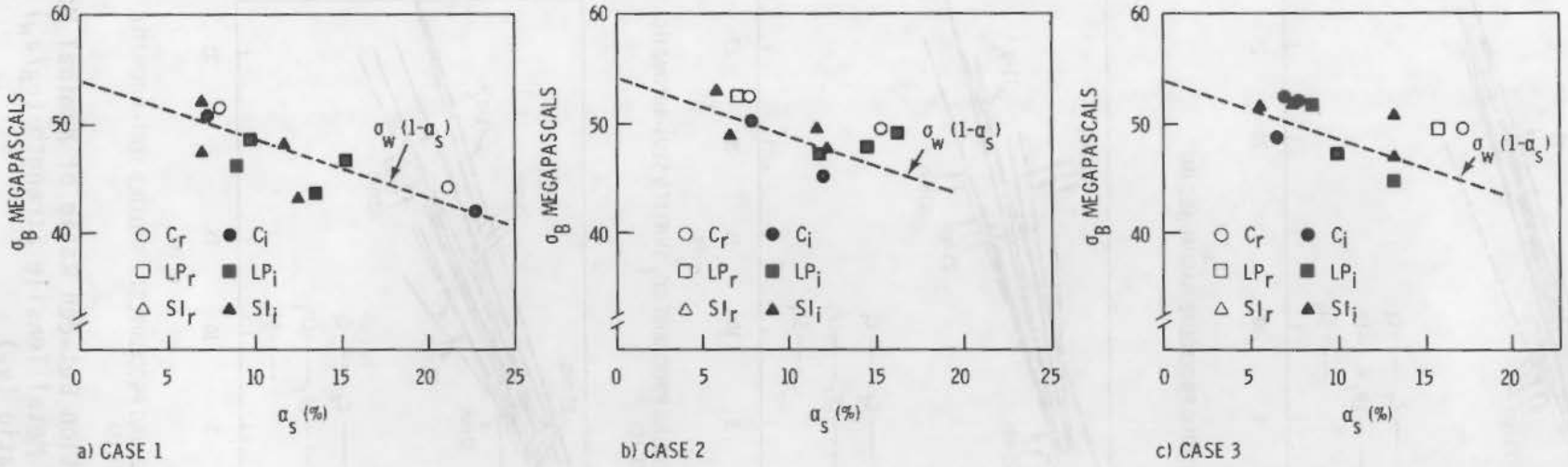

FIGURE 10.6.4. The Relation Between Nominal Maximum Stress (σ_B) and Actual Defect Ratio (α_S) - Plate Thickness 25 mm, Welding Procedure Manual Arc-Low Amperage (M*)

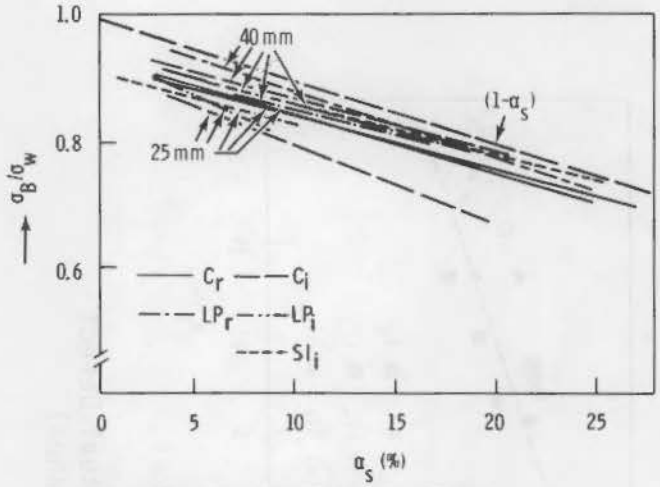

a) WELDING PROCEDURE MANUAL ARC (M)

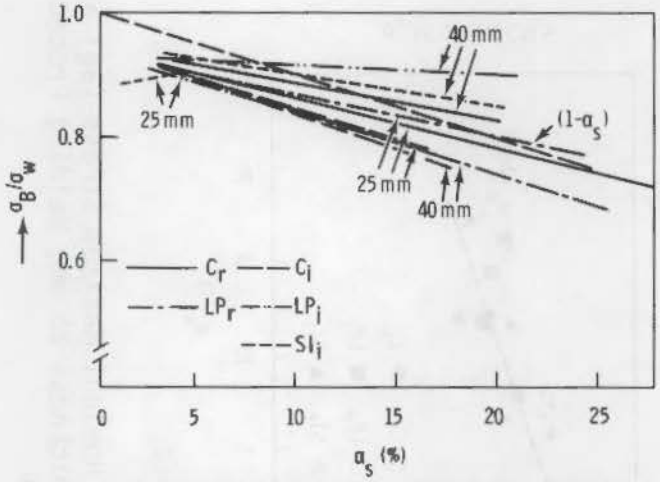

b) WELDING PROCEDURE CO_2 SHIELDED SEMI-AUTOMATIC ARC (C)

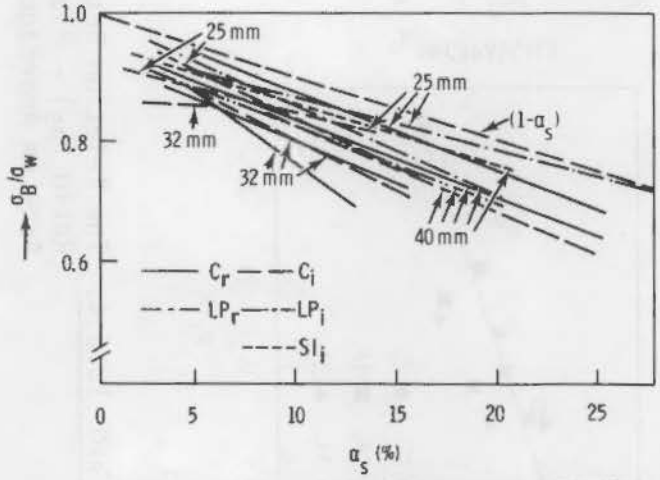

c) WELDING PROCEDURE SELF SHIELDED SEMI-AUTOMATIC ARC (S)

FIGURE 10.6.5. The Relation Between Ratio of Nominal Maximum Stress and Weld Metal Tensile Strength (σ_B/σ_w) and Actual Defect Ratio (α_s)

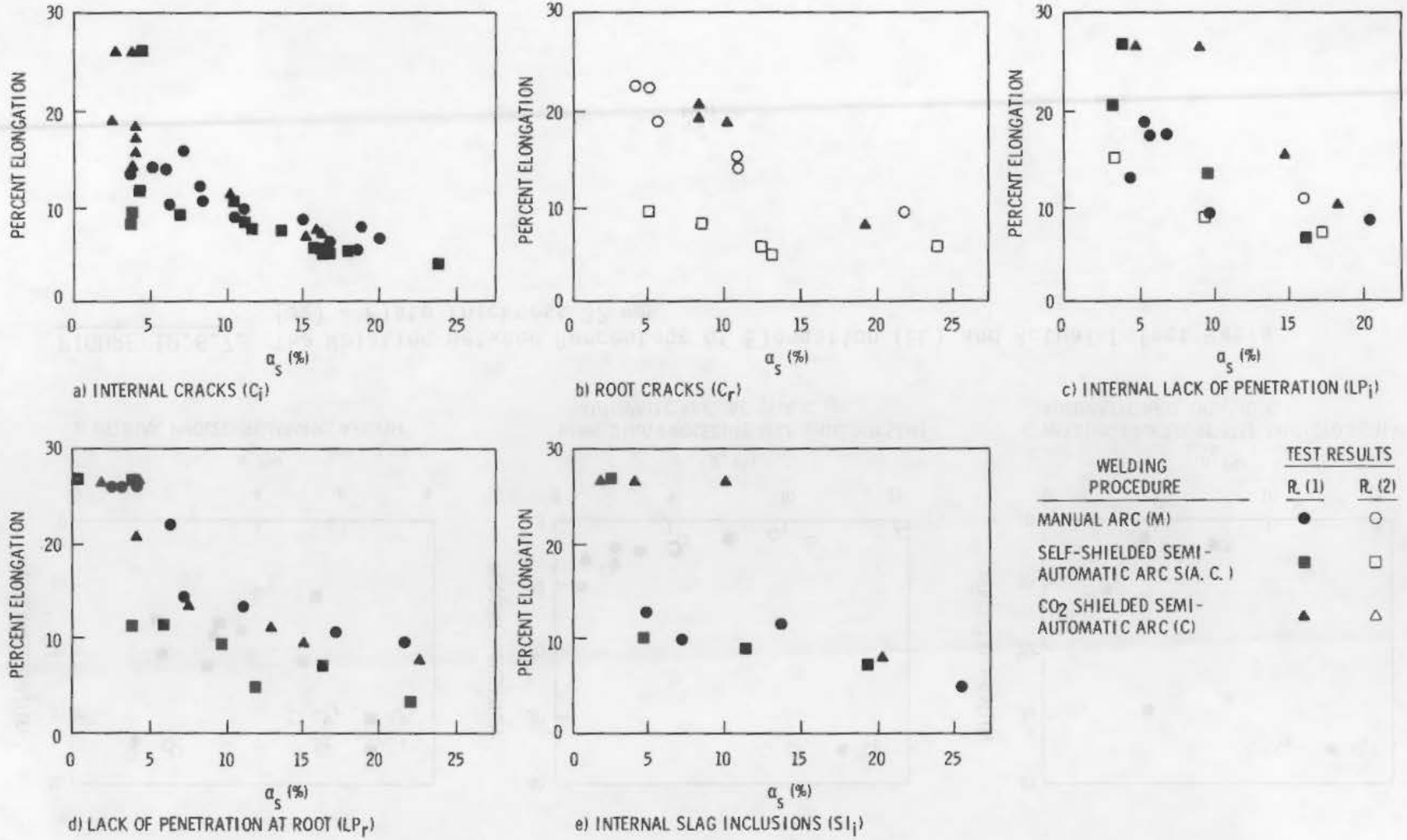

FIGURE 10.6.6. The Relation Between Percentage of Elongation (EL) and Actual Defect Ratio (α_S) - Plate Thickness 40 mm

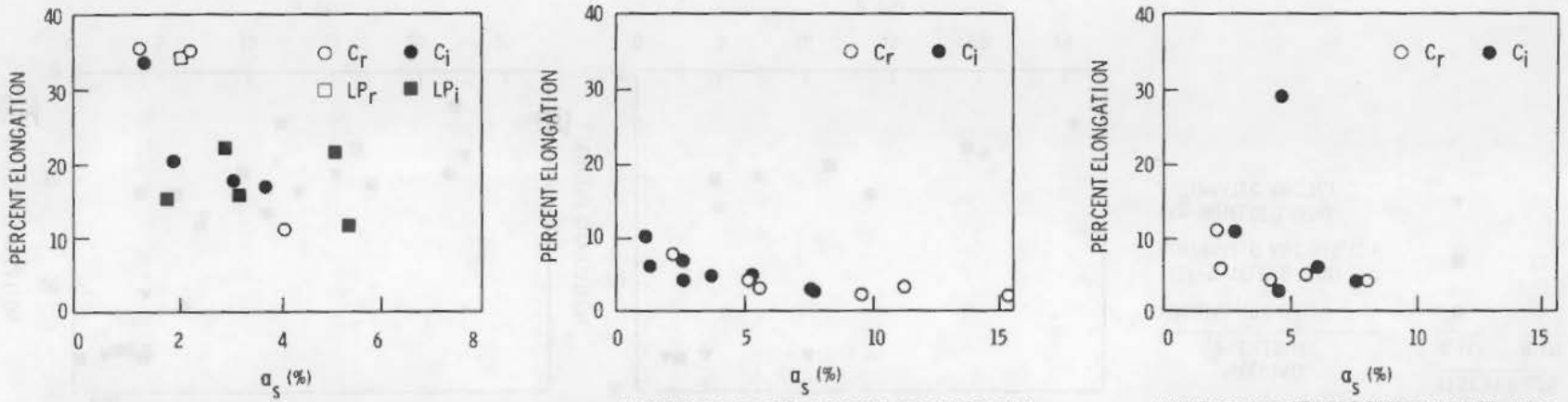

FIGURE 10.6.7. The Relation Between Percentage of Elongation (EL) and Actual Defect Ratio (α_S) - Plate Thickness 32 mm

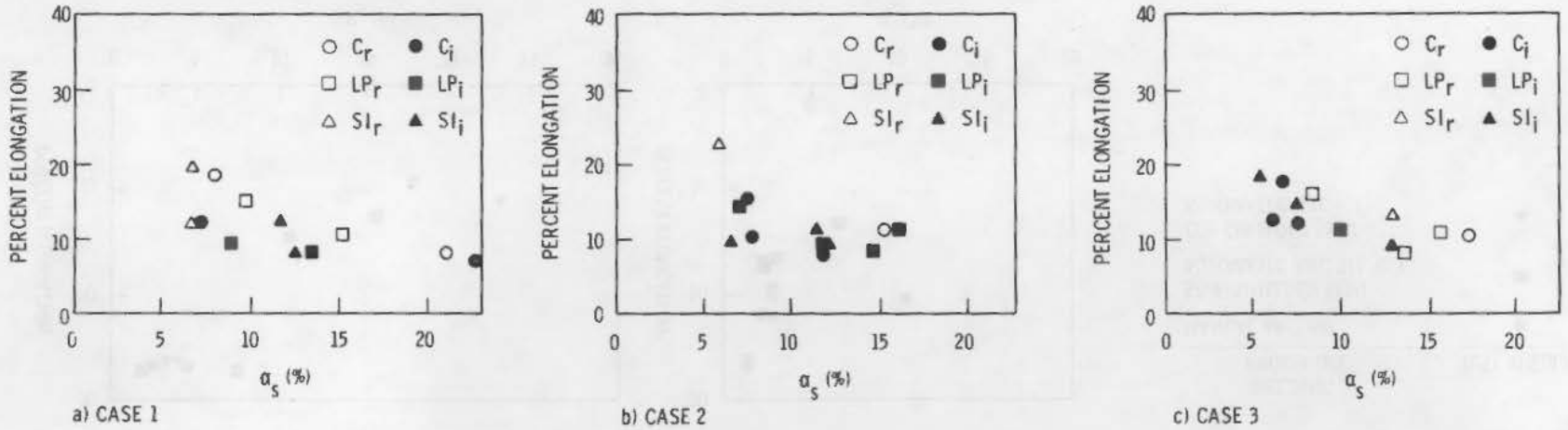

FIGURE 10.6.8. The Relation Between Percentage of Elongation (EL) and Actual Defect Ratio (α_S) - Plate Thickness 25 mm, Welding Procedure Manual Arc-Low Amperage (M*)

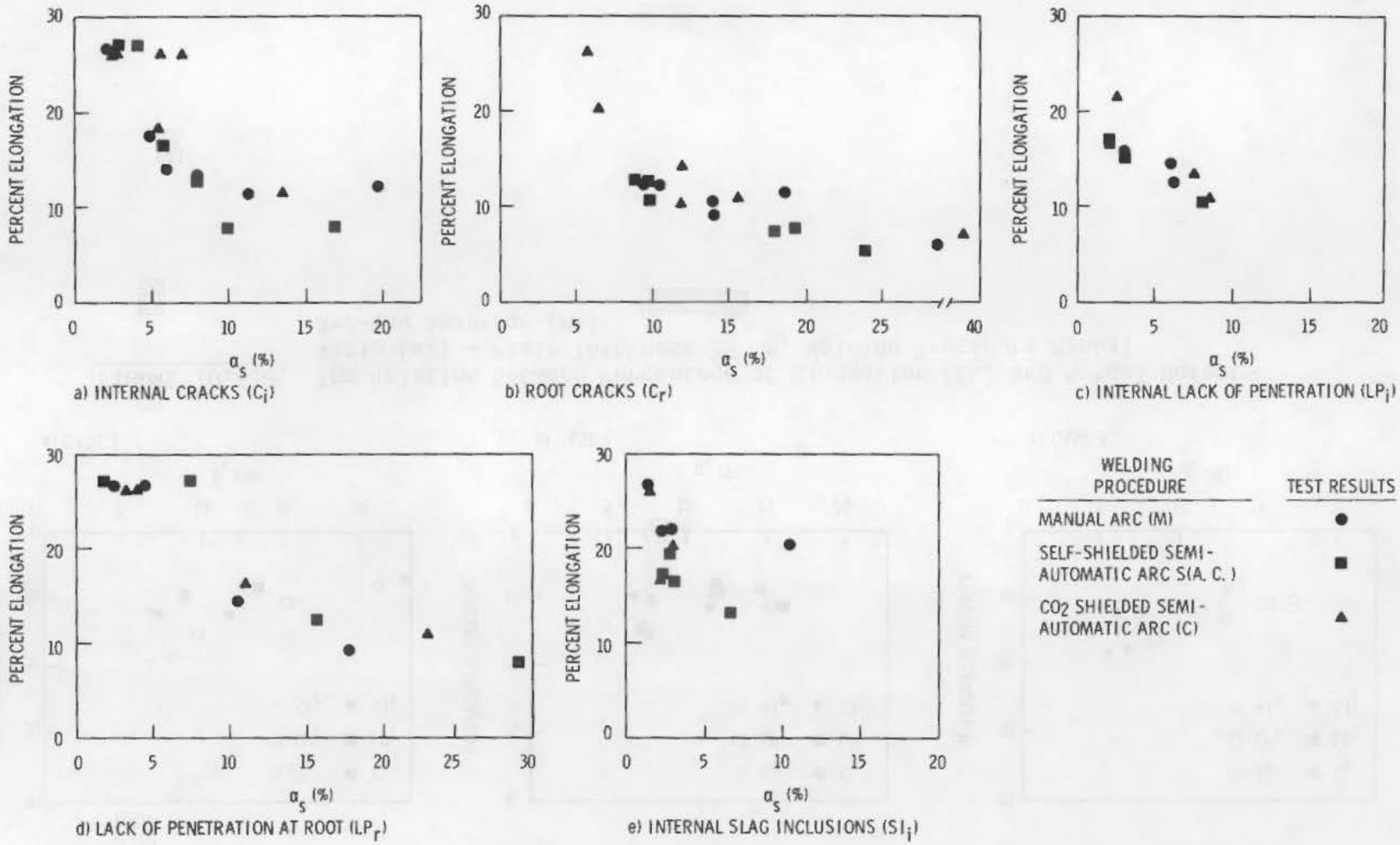

FIGURE 10.6.9. The Relation Between Percentage of Elongation (EL) and Actual Defect Ratio (α_S) - Plate Thickness 25 mm

10.7 IMPLICATIONS OF FATIGUE

Many fatigue failures have occurred in nuclear piping; however, almost all such failures have occurred in lines 10 inches or less in diameter, mostly in those 2 inches or less in diameter. In the author's estimation, this will be a continuing problem not particularly amenable to correction at least not on the bases of cost-benefit.

Relatively few vibrationally induced failures have occurred in larger nuclear piping; however, as cited in an earlier section, thermal fatigue has caused several incidents of cracking in both BWRs and PWRs. Many of the thermal fatigue failures have not been anticipated, simply because the actual mechanism was not recognized before the fact.

Several studies have addressed the probability of vibrational fatigue (variable-amplitude loading) in piping, tees, elbows, etc. These data are contained in a 1978 NUREG report.(10.7.1) It provides a good summary of the code procedures for analyzing piping. These are presented with minimal deletion in the following paragraphs.(10.7.1)

10.7.1 Background of the ASME Code Fatigue Evaluation Method

Piping in nuclear power plants is designed in accordance with the Code. Piping which constitutes portions of the primary coolant pressure boundary are designed by Class 1 rules of the Code; specifically, under NB-3600 of the Code. Because of the complexity of piping products, it has been found useful to establish "stress indices" and "flexibility factors" to describe, in a simple manner, the characteristics of such complex products as elbows or branch connections. These stress indices are contained in Table NB-3682.2-1 of the Code.(a)

A piping system analysis starts with an analysis of the system modeled as a one-dimensional assembly of straight and curved beams with appropriate restraints to represent anchors, guides, hangers, snubbers, etc. The behavior of complex piping products such as elbows is represented by flexibility

---

(a) Code in this report, refers to the ASME Boiler and Pressure Vessel Code, Section III, Div. 1, "Nuclear Power Plant Components", Subsection NB.

factors incorporated into the system analysis model. Flexibility factors are given in NB-3687 of the Code. The piping system model is then loaded by the weight of the piping, contents and insulation; by displacements representing the relative motion between restraints; and by dynamic loadings induced by such effects as relief valve and earthquake-induced motions. The piping system analysis is accomplished using computer programs that have been developed for that purpose. General purpose finite element computer programs can be used for a piping system analysis but usually it is more economical to use a special purpose program. The analysis is ordinarily an elastic analysis even though the loadings may induce a limited amount of plastic response in portions of the piping.

From the piping system analysis, one obtains loads at each restraint (e.g., the load on a pressure vessel nozzle or pump nozzle) and, of particular significance in this report, the moments[(a)] acting on the piping products. The loads on the piping system will have some (postulated in the design stage) time-dependent history; hence, the moments will also have a time-dependent history, and from this we can obtain the number of cycles of moments and the magnitude of these moments. The cycles of moments are translated into cycles of stress by use of the Code stress indices; specifically, those indices identified with a subscript "2" are for moment loading.

Two other loadings can product significant cycles of stress in the piping: 1) internal pressure, and 2) thermal gradients.

The history of pressure is normally postulated in the design stage, and by using the Code stress indices for pressure loading, identified by a subscript "1," the pressure history can be translated into cycles of stress due to cycles of pressure.

Evaluation of stresses due to thermal gradients follows from a "Heat Transfer" analysis in which the postulated cycles of fluid temperatures are translated into cycles of metal temperatures in the pressure boundary of the piping products. This analysis involves fluid temperature change rates, fluid

---

(a) A piping system analysis also gives axial forces acting on the piping and piping products, but the effect of these on stresses in the piping and piping products are usually negligible.

velocities, film coefficients, etc. The cycles of metal temperatures are then characterized as certain types of gradients according to Code specified procedures as indicated in NB-3653 of the Code. These gradients, when multiplied by the thermal gradient stress indices (identified by a subscript "3"), give the cycles of stresses due to thermal gradients.

The Code gives criteria to determine the acceptability of the combinations of cyclic stresses due to cycles of moments, pressure, and thermal gradients. In the evaluation of the fatigue characteristics of piping components, several variables are of interest. These variables are calculated based on the moment, pressure, and thermal stresses determined in the stress analysis as noted earlier. The Code presents relevant equations covering 1) primary plus secondary stress intensity range, 2) peak stress intensity range, and 3) alternating stress intensity. The values of the stress indices are determined from Table NB-3682.2-1 of the Code.

The values of S_{alt} determined in this fashion represent an extrapolated elastic stress that should provide conservative estimates of the fatigue life of the component.

This Code evaluation procedure is an elastic type analysis. Combinations of loads that exceed the proportional limit of the component are treated as fictitious elastic loads. Care must be taken in the evaluation of experimental results. Values of extrapolated elastic loads must be used to obtain evaluations compatible with elastic analysis.

The use of an elastic analysis and extrapolated elastic loads has been justified in the "Criteria of the ASME Boiler and Pressure Vessel Code for Design by Analysis" in Sections III and VIII, Division 2 which states

- Allowable stresses higher than yield appear in the values for primary-plus-secondary stress and in the fatigue curves. In the case of the former, the justification for allowing calculated stresses higher than yield is that the limits are such as to assure shake-down to elastic action after repeated loading has established a favorable pattern of residual stresses. Therefore the assumption of elastic behavior is justified because it really exists in all load cycles--subsequent to shake-down.

- In the case of fatigue analysis, plastic action can actually persist throughout the life of the vessel, and the justification for the specified procedure is somewhat different. Repetitive plastic action occurs only as the result of peak stresses in relatively localized regions and these regions are intimately connected to larger regions of the vessel which behave elastically. A typical example is the peak stress at the root of a notch, in a fillet, or at the edge of a small hole. The material in these small regions is strain-cycled rather than stress-cycled and the elastic calculations give numbers which have the dimensions of stress but are really proportional to the strain. The factor of proportionality for uniaxial stress is, of course, the modulus of elasticity. The fatigue design curves have been specially designed to give numbers comparable to these fictitious calculated stresses. The curves are based on strain-cycling data and the strain values have been multiplied by the modulus of elasticity. Therefore stress intensities calculated from the familiar formulas of strength-of-materials texts are directly comparable to the allowable stress values in the fatigue curves.

Once an appropriate value of S_{alt} is determined, the evaluation of the code allowable number of load cycles (N_c) can be made through the use of the S-N curves (Figures 1.9.1 and 1.9.2 of the Code).

The fatigue data are presented in terms of cycles to failure and compared to design cycles at similar loads so that the ratio of cycle to failure (N_f) versus design cycles (N_c) represents a safety margin. Failure usually was defined as a through-wall crack.

10.7.2 Effect of Defects on Fatigue Life

Once one has examined the cycles to failure of components ostensibly free from defects, it should be possible to qualitatively or semi-quantitatively predict the effect of various defects on the reductions in cycles to failure by a study such as that of Iida.[10.7.2] The data are presented in terms of net stress range versus cycles to failure for defects such as porosity, slag inclusions, incomplete penetration, internal cracks, surface cracks and undercut. Figures 10.7.1 through 10.7.7 contain the results of this study. The author develops proposed S-N curves for the various defects. To permit interpolation of dimensions and flaw sizes, curves were developed using a weld defect severity parameter α_s. No obvious method exists for ratioing the decrease in failure cycles for a given defect. Furthermore, we are comparing high cycle fatigue[10.7.2] to low or intermediate cycle fatigue which can be difficult.

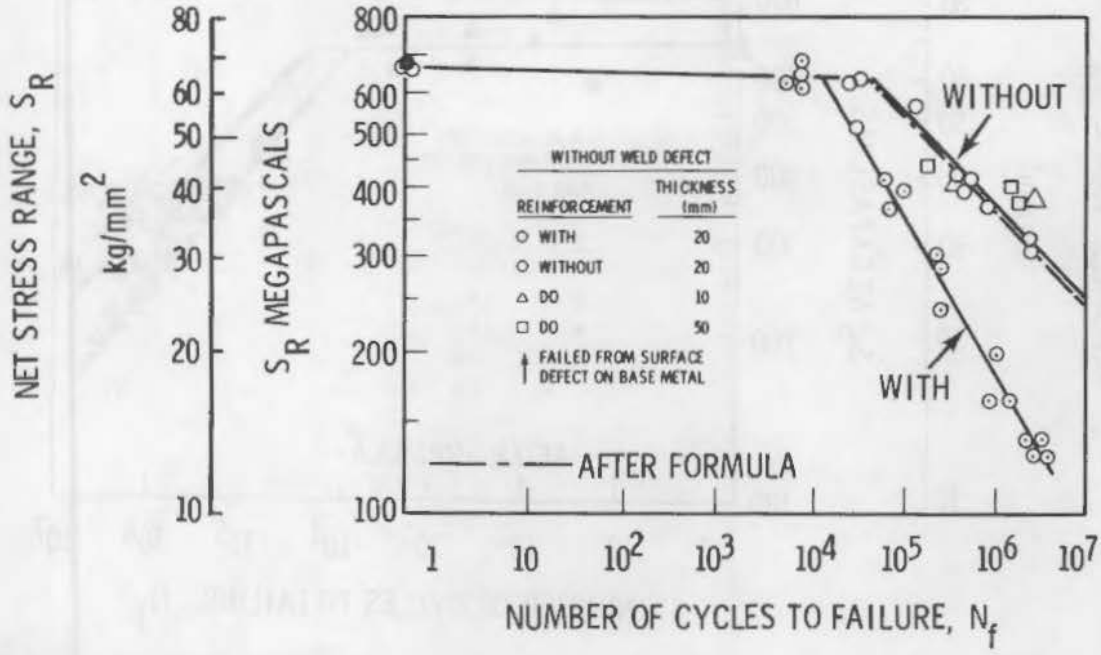

FIGURE 10.7.1. Results of Load-Controlled, Repeated Stress Fatigue Tests on Butt Welds Without Weld Defect

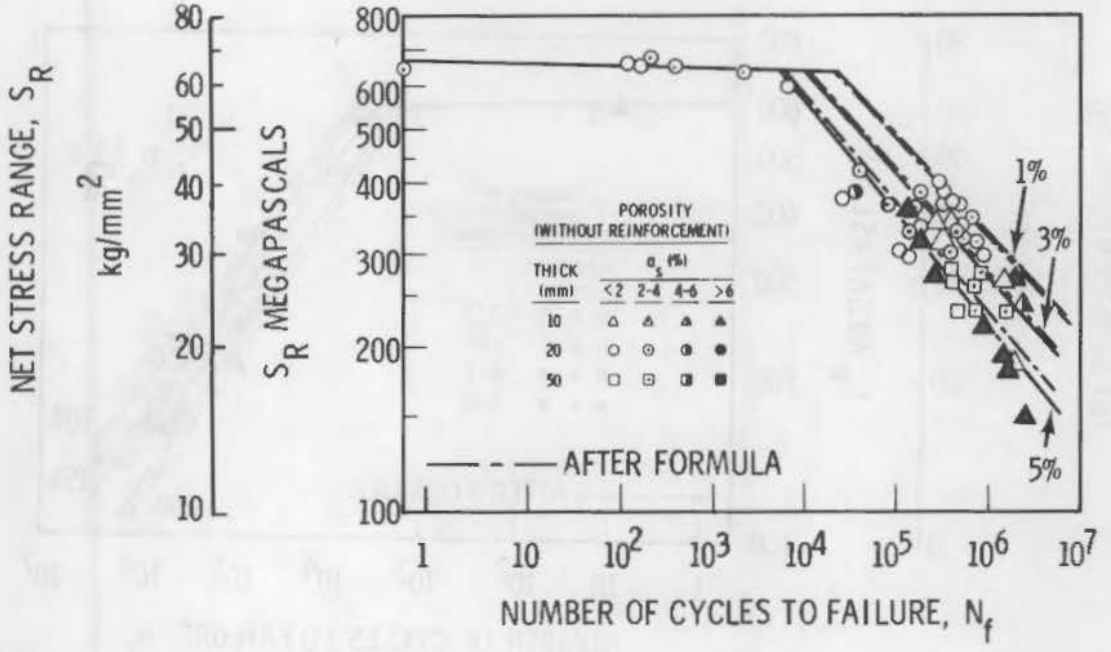

FIGURE 10.7.2. Results of Load-Controlled, Repeated Stress Fatigue Tests on Butt Welds Containing Porosity (Parameter: α_s)

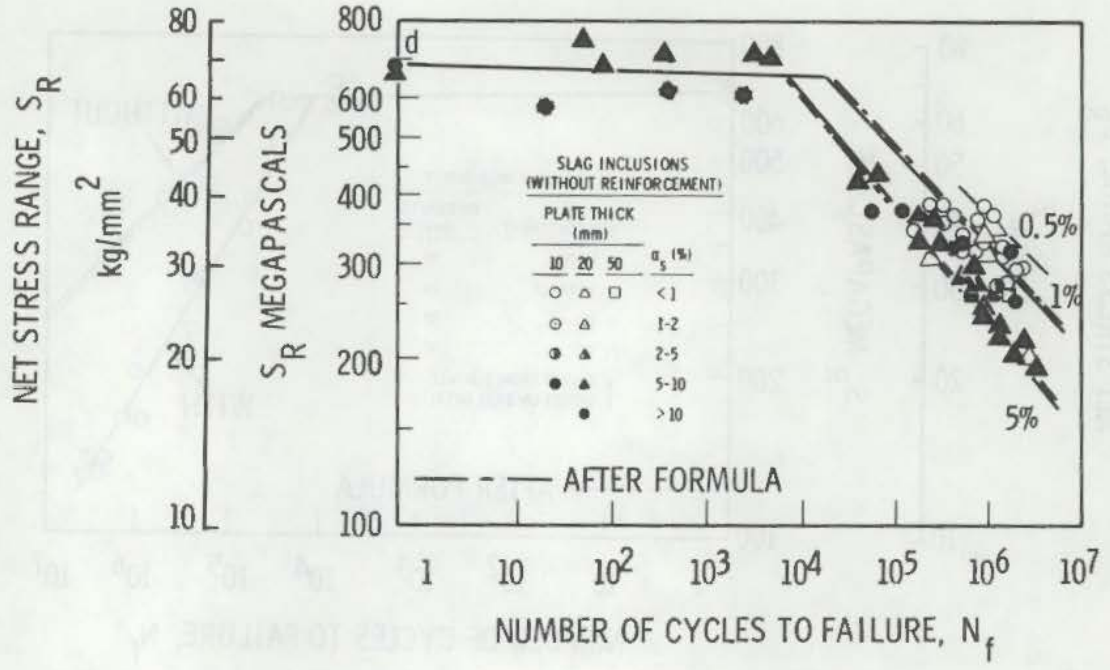

FIGURE 10.7.3. Results of Load-Controlled, Repeated Stress Fatigue Tests on Butt Welds Containing Slag Inclusions (Parameter: α_s)

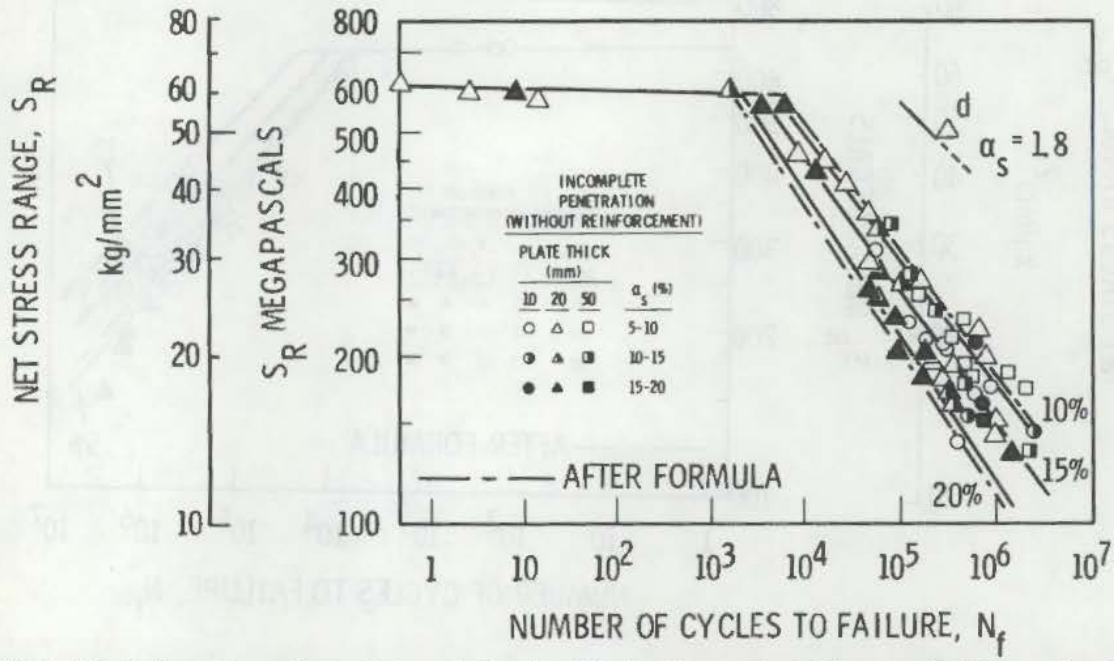

FIGURE 10.7.4. Results of Load-Controlled, Repeated Stress Fatigue Tests on Butt Welds Containing Incomplete Penetration (Parameter: α_s)

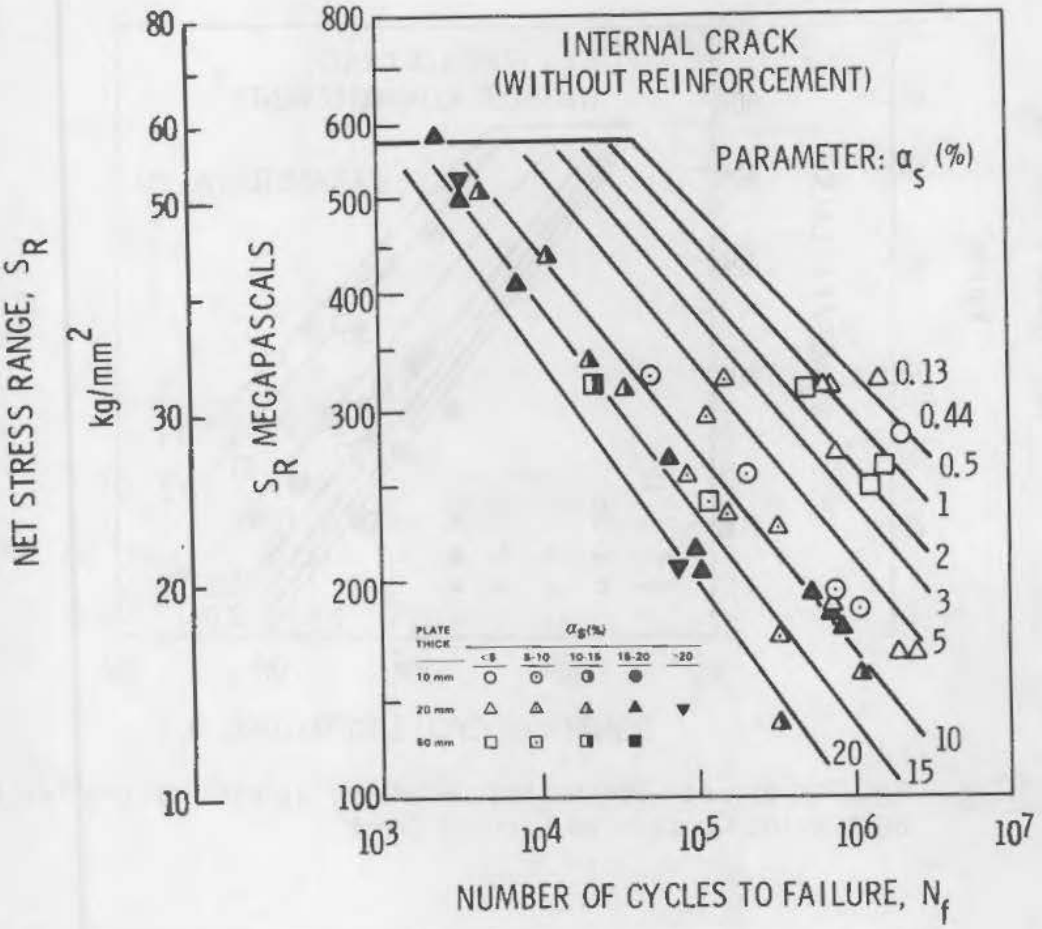

FIGURE 10.7.5. Results of Load-Controlled, Repeated Stress Fatigue Tests on Butt Welds Containing Internal Crack

10.7.3 Influence of Dissimilar Metal Welds

One further parameter of interest pertains to the effect of dissimilar metal welds on the fatigue cycles to failure. This effect is discussed in Reference 10.7.3. A comparison is made with free-run piping of the same dimensions and same flaw sizes for similar loads. In the free-run piping, the time to generate through-wall cracks was given in terms of several (from 2 to 20) 40-yr plant lives. For dissimilar metal welds, similar calculations predicted through-wall cracking in less than one plant life (which has not been supported by available data).

Specific conservatisms in the analyses prevented a "realistic assessment of time-to-failure." For example, the assumed stress consisted of maxima for membrane, plus thermally-induced differential displacement, plus the absolute

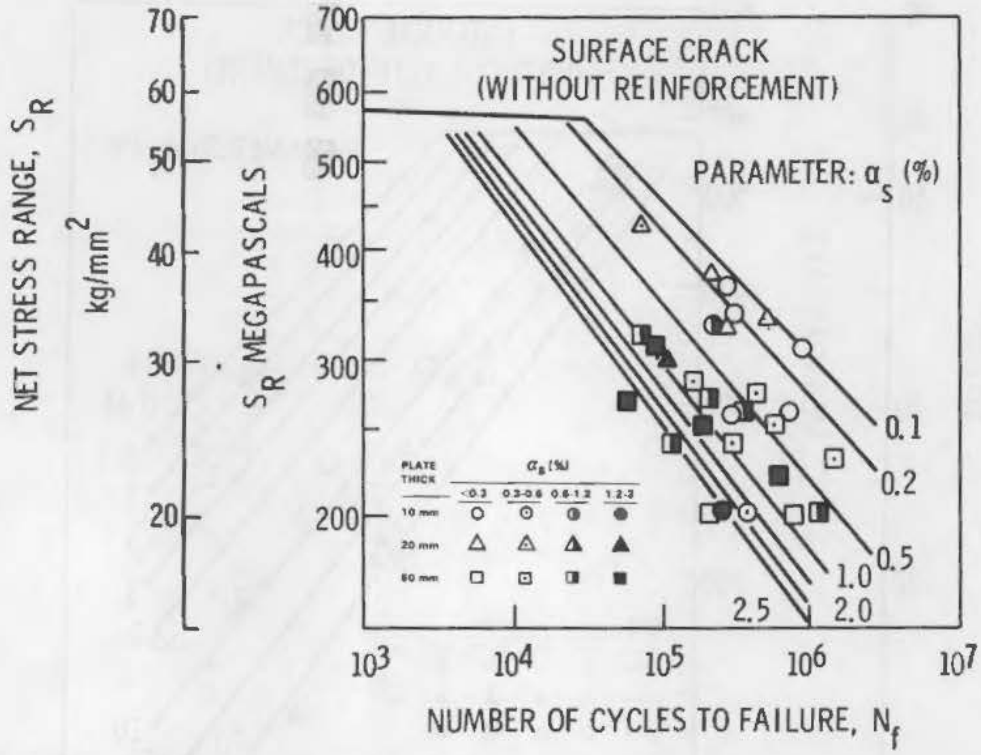

FIGURE 10.7.6. Results of Load-Controlled, Repeated Stress Fatigue Tests on Butt Welds Containing Surface Crack

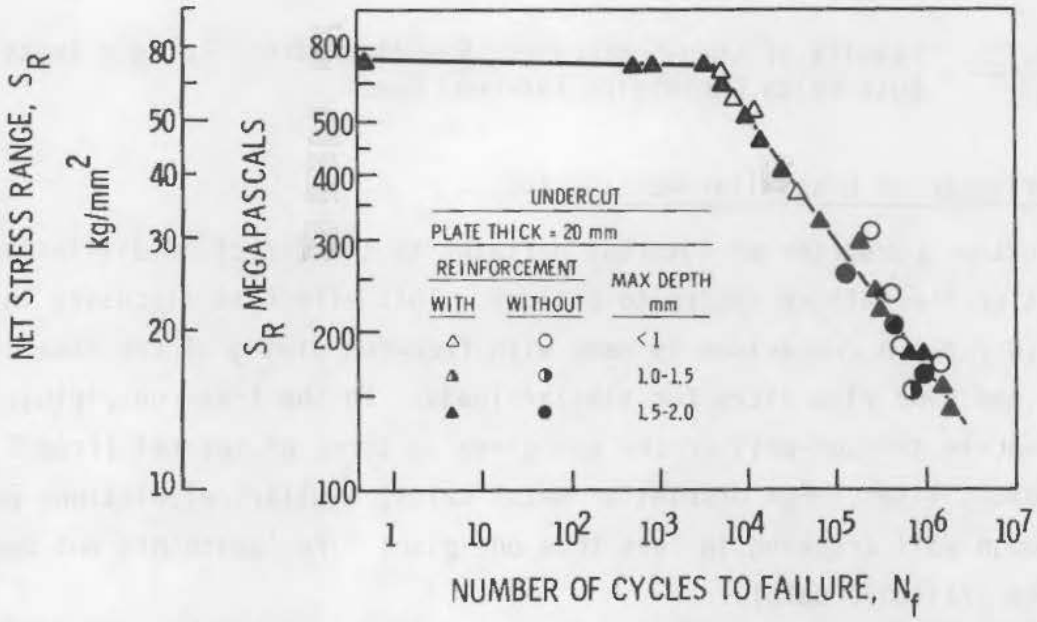

FIGURE 10.7.7. Results of Load-Controlled, Repeated Stress Fatigue Tests on Butt Welds Containing Undercut (Parameter: maximum depth of undercut)

sum of stresses from all other loadings. This does not consider such factors as decrease in membrane, stress with through-thickness crack growth and relaxation of thermally induced differential displacements with crack growth, both of which should extend time-to-failure.

10.8 WATER HAMMER AND WATER SLUGGING

Water hammer and water slugging represent very severe loading conditions usually representing an upper limit on ASME faulted conditions loads. In fact, such loads substantially exceed most seismic faulted loads. Water hammer is defined as a repetitive or multi-cyclic load initiated by a resonance or pulsation induced in the coolant. Water slugging is a single load induced by accelerating a "slug" of water trapped in a location such as between two valves.

Water hammer and water slugging represent unpredictable events that may fail a piping system. While the existence of a prior flaw may contribute to the failure probability, there is no assurance that the pipe would not fail if defect free, when subjected to the more severe loads.

A large number of water hammer events have occurred. In BWRs, the number is substantially more than 100 and, in PWRs, it should be approaching 100. The incidents vary from the trivial to the few causing breakage of piping and major damage to a given system. A selected list of water hammer incidents is given in Table 10.8.1. The incidents cited are representative and no emphasis should be given to the listing or to specific cases cited. But a few specific cases of failure cited in Table 10.8.1 are worthy of further mention. The Indian Point 2 failure in 1973[10.8.1] nearly severed an 18-in. feedwater line.

Water slugging caused failure of safety valve systems during hot functional testing at H. B. Robinson[10.8.2] and Turkey Point.[10.8.3] The valves were blown off the headers when opened. In these instances, the dynamic loads of water slugging had not been considered in the system's design.

The preceding discussion gives no more than a flavor to the problem. The interested reader is referred to a USNRC report, "Water Hammer in Nuclear Power Plants"—NUREG-0582[10.8.4] and to a report to the USNRC.[10.8.5] A 1981 study at BMI-PNL examined incidents of water hammer and evaluated the effects of upper limit loads on piping response and probability of failure.[10.8.6]

TABLE 10.8.1. Some Examples of Water Hammer and Water Slugging Resulting in Substantial Damage To Systems

Plant	Type of Plant	Year	Type of Damage
Dresden-2	BWR	1970	Water behind valve in HPCI line accelerated and dented 10-ft of pipe, breaking or bending several restraints and snubbers.
Quad Cities-1	BWR	1972	RHR's seismic restraints and pipe hangers were damaged due to water hammer resulting from improper venting and air accumulation. Three seismic restraints were damaged, a spring hanger bottomed, grout chipped on another; and four hangers were damaged.
Millstone-1	BWR	1973	Hangers on Torus ring header for 18-in. LPCI system were damaged due to sudden injection of 260 psi water into line while empty.
Fitzpatrick	BWR	1974	RHR pipe moved up to 10 in.; seismic supports were damaged.
Browns Ferry-1	BWR	1974	Operator error-moved HPCI pipe, broke 3 pipe restraints, bent and damaged others, and fractured journal.
H. B. Robinson	PWR	1970	During hot functional testing, a 6-in. pipe nozzle between main steam line and safety valve failed completely due to crack initiated at excessively machined taper. Failure was initiated by dynamic forces when safety valve opened.

TABLE 10.8.1. (continued)

Plant	Type of Plant	Year	Type of Damage
Turkey Point-3	PWR	1972	Three of four safety valves on main steam line header blew off and split a header due to system not designed for reaction forces under dynamic loads.
Surry	PWR	1972	Water hammer occurred while steam generators were being fed by auxiliary feedwater system and damaged main steam line and check valve, and local displacement of feedwater piping.
Indian Point-2	PWR	1973	A turbine trip due to a high water level in a steam generator (at 7% power) interrupted normal feedwater flow causing the level in another steam generator to drop to where the reactor tripped on low-low level. After reactor trip, a continued decrease in level was observed accompanied by a rise in containment temperature and humidity. Investigation showed that the A-106 Grade C 18-in. main feedwater pipe to one steam generator had cracked 180° circumferentially at the weld attaching the pipe to the penetration inside containment. Shaking was accompanied by a loud noise at about the time of reactor trip. A water-steam reaction in the horizontal feedwater line adjacent to the steam generator was considered to be responsible for the (water slug) leaks. After pipe failure, steam water impinging on the containment caused

TABLE 10.8.1. (continued)

Plant	Type of Plant	Year	Type of Damage
Indian Point-2 (Continued)	PWR	1973	localized bulging of the liner. Corrective actions included shortening of the feedwater line, installing feedring jets, and J-tube modifications of the feedring. Subsequent to the initial failure and prior to the complete "fix," other water hammers occurred at Indian Point-2 under conditions of low feedwater flow when the water level fell below the spargers; simultaneous with the recovery of the sparger with water (covering and sealing holes in the bottom of the sparger).
Beaver Valley-1	PWR	1976-77	A series of events occurred during ascension-to-power tests. These included severe feedwater line vibration, probably due to valve behavior, and severe hydraulic pulses, possibly due to steam-water slugging. The vibrations broke a 0.75 in. drain line, a bypass valve air line, hydraulic snubber shaft, locked another snubber, and broke off the motor operator on a 3-in. valve as well as shaking off insulation.

10.9 SUMMARY

A spectrum of failure data on piping has been presented. Failure mechanisms include IGSCC, thermal and vibrational fatigue, erosion and cavitation, and water hammer. The first three have some possibility of detection with NDE assuming one recognizes the probable failure sites. Leak detection represents the ultimate detection mechanism for all failure classes. Water hammer is presented not because it is amenable to prior detection by NDE; but, rather because such loads may represent the maximum load conditions and need to be examined in that context when applying fracture mechanics either deterministic or probabilistic.

Failure probabilities range from about 10^{-5} for large piping to 10^{-2} to 10^{-3} for small and intermediate sizes of piping. In the smaller sizes break may occur with little or no advance warning. Usually cracks are detected by leakage in IGSCC well before they fail (catastrophically). Thermal fatigue has resulted in several instances of cracking without failure. However, failure cannot be ruled out even though the probability is believed to be low.

10.10 REFERENCES

10.1.1 Bush, S. H., "Reliability of Piping in Light Water Reactors." Nucl. Saf. 17(5):568-579, 1976.

10.1.2 Bush, S. H., "Reliability of Piping in Light Water Reactors." Proceedings of Symposium on Reliability Problems of Reactor Pressure Components, Vol. I, International Atomic Energy Agency, Vienna, Austria, pp. 199-232, 1977.

10.1.3 Bush, S. H., "Non-Destructive Examination and Component Reliability--What Should We Be Looking For?" Paper presented at the International Conference on Non-Destructive Evaluation in the Nuclear Industry, American Society for Metals, Metals Park, Ohio, February 11-13, 1980.

10.1.4 Basin, S. L. and Burns, E. J., Characteristics of Pipe System Failures in Light Water Reactors. EPRI NP-438, Electric Power Research Institute, Palo Alto, California, 1977.

10.1.5 Klepfer, H. H., et al., Vols. 1 and 2 of Investigation of Cause of Cracking in Austenitic Stainless Steel Piping. NEDO-21000, General Electric Corporation, Nuclear Energy Division, San Jose, California, 1975.

10.1.6 Pipe Crack Study Group, Investigation and Evaluation of Stress-Corrosion Cracking in Piping of Light Water Reactor Plants. NUREG-0531, U.S. Nuclear Regulatory Commission, Washington, D.C., 1979.

10.1.7 Pipe Crack Study Group, Technical Report-Investigation and Evaluation of Cracking in Austenitic Stainless Steel Piping of Boiling Water Reactor Plants. NUREG-75-067, U.S. Nuclear Regulatory Commission, Washington, D.C., 1975.

10.1.8 Bush, S. H., "Pressure Vessel Reliability." J. Pressure Vessel Technol. 97(1):54-70, 1975.

10.1.9 Smith, T. A. and Warwick, W. A., "Survey of Defects in Pressure Vessels Built to High Standards of Construction," Inservice Data Reporting and Analysis for Pressure Vessels, Piping, Pumps and Valves. PVP-PB-032, J. T. Fong, ed., American Society of Mechanical Engineers, New York, New York, pp. 21-53, 1978.

10.3.1 PWR Pipe Crack Study Group, Investigation and Evaluation of Cracking Incidents in Piping in Pressurized Water Reactors. NUREG-0691, U.S. Nuclear Regulatory Commission, Washington, D.C., 1980.

10.4.1 Pasupathi, V., et al., Examination of Inconel Safe End from Duane Arnold. BCL-585-9, Prepared for Parameter, Inc. by Battelle's Columbus Laboratories, Columbus, Ohio, 1979.

10.5.1 Salter, G. R. and Gethin, J. W., "An Analysis of Defects in Pressure Vessel Main Seams." Conference Proceedings on Welding Research Related to Power Plants, Central Electricity Generating Board, London, England, 1972.

10.6.1 Kato, B. and Morita, K., The Influence of Defects on the Static Strength and Deformability of Welded Joints. Doc. XV-34, XV-343-73, International Institute of Welding, Paris, France, 1973.

10.7.1 Mayfield, M. E., Rodabaugh, E. C. and Eiber, R. J., Relevance of Fatigue Tests to Cold Leg Piping. NUREG/CR-0325, Prepared for U.S. Nuclear Regulatory Commission by Battelle's Columbus Laboratories, Columbus, Ohio, 1978.

10.7.2 Iida, K., "Fatigue Strength of Defective Butt Welded Joints." Proceedings of the Japan-U.S. Seminar, Significance of Defects in Welded Structures, T. Kanazawa and A. S. Kobayshi, eds., University of Tokyo Press, Tokyo, Japan, pp. 224-234, 1973.

10.7.3 Mayfield, M. E., et al., Cold Leg Integrity Evaluation. Prepared for U.S. Nuclear Regulatory Commission by Battelle's Columbus Laboratories, Columbus, Ohio. Final report, 1979.

10.8.1 Feedwater Line Incident Report--Indian Point Station Unit 2. Docket 50247-197, Consolidated Edison, New York, New York, January 1974.

10.8.2 Incident Report--H. B. Robinson No. 2 Steam Pipe Break. Docket 50-261, Carolina Power and Light, Raleigh, North Carolina, June 1970.

10.8.3 Incident Report Safety Valve Headers--Turkey Point Unit No. 3. Docket 50-250, Florida Power and Light, Miami, Florida, December 1971.

10.8.4 U.S. Nuclear Regulatory Commission, Water Hammer in Nuclear Power Plants. NUREG-0582, Washington, D.C., 1979.

10.8.5 Chapman, R. L., Hanner, O. M., Jr. and Wells, M. E., Review and Evaluation of Actual and Potential Water Hammer Events in Nuclear Plants. CAAP-TR-042, Prepared for U.S. Nuclear Regulatory Commission by EG&G Idaho, Inc., Idaho Falls, Idaho, 1979.

CHAPTER 11

RELEVANT STATISTICAL AND PROBABILISTIC MODELS

CONTENTS

FIGURES

TABLES

CHAPTER 11

RELEVANT STATISTICAL AND PROBABILISTIC MODELS

11.1 INTRODUCTION

Our concern in Chapters 12 and 13 of this report is to predict with reasonable accuracy the probability of a given event or events. Relevant examples might be the cracking or failure of piping in a specific system or subsystem, or the reliability of detection of a flaw in a component using various NDE techniques. In this chapter we will review the tools available to us for predicting probabilities, their strengths and their weaknesses. Such tools include continuous and discrete statistical distributions, inferential statistics and probabilistic modelling using techniques such as Bayesian and Monte Carlo.

Most of the failure or detection processes of interest to us tend to be stochastic (random). We are faced with situations in which observations are made over a period of time and are influenced by chance or random effects, not just at a single instant but throughout the entire interval of time or sequence of times being considered. In a rough sense, a stochastic process is a phenomenon that varies to some degree unpredictably as time goes on. This implies that, if one observed an entire time-sequence of a process on several different occasions under presumably identical conditions, the resulting observation sequences generally would be different. Probability enters, but not in the sense that each result of a random experiments determines only a single number. Instead, the random experiment determines the behavior of some systems for an entire sequence or interval of time. For example, an experiment is a sequence or series of values; i.e., a function, not just a single number.

In both component failure and NDE reliability, there may be a spectrum of conditions and data. This spectrum can be arbitrarily divided into discrete packages such as given in the following diagram.(11.1.1)

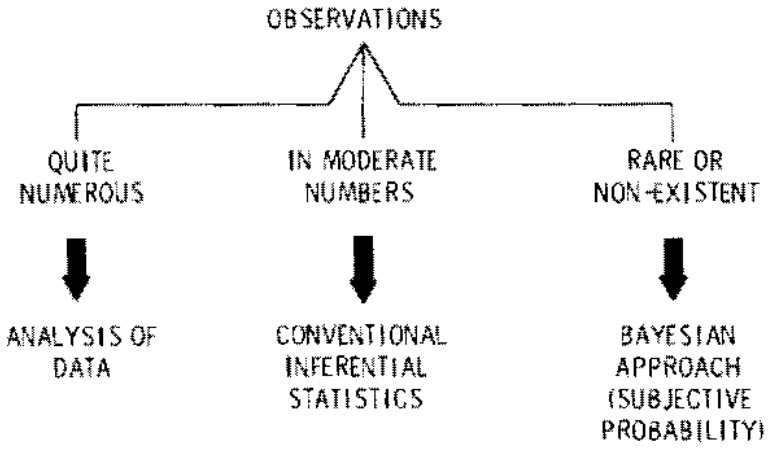

In nuclear components our observations range from rare to moderate.

This chapter will contain sections dealing with terminology, hazard functions and hazard plotting, discrete statistical distributions, continuous statistical distributions, statistical and probabilistic tools for testing assumptions, probability and random variables, and strengths and weaknesses of various statistical distributions.

Several sources were investigated with regard to coverage of statistical and probability functions. One of the most extensive coverages was in the book by Hahn and Shapiro[11.1.2] and their terminology has been partially adopted in this chapter. Specifically, exceptions are taken in the section on hazard functions where x is used as the time variable rather than t to permit consistency within tables, particularly in Section 11.3 - "Hazard Functions," and in Section 11.5 - "Continuous Statistical Distributions."

11.2 TERMINOLOGY

This section is limited to the definition of terms used in this and the following two chapters insofar as statistical and probabilistic processes are concerned. The definitions given are those commonly found in statistical and probability texts. The treatment given here is very brief and serves only to establish a reference point for illustration. For more extensive review of any particular point see Hahn and Shapiro[11.1.2] or other specifically listed references.

11.2.1 Random Variables and Probability Functions

1. Random Variable – a function often denoted by X, which relates a real number to the potential outcome of a random experiment. For example, in tossing a coin the outcome is either a head or a tail. A random variable might assign a "1" to the outcome of a head and a "0" to the outcome of a tail. Another random variable might assign a "6" to a tail and a "-2" to a head, etc.

   A random variable may be discrete in which case the possible values are countable, represented often by the positive integers 1,2,...etc.

   A random variable may be continuous in which case the possible values are uncountable and are usually represented by an interval; e.g., from 0 to 1 or $-\infty$ to ∞ etc.

Example: In metallurgy studies, the dynamic stresses, both physical and corrosive, are often modeled as random inputs to stressing a piece of metal. (Theoretically, if we knew all the physical and chemical conditions, we would be able to describe the stress exactly. However, in the face of much ignorance we are forced to make up the lack of information by hypothesizing a probabilistic model). The crack growth (in mm) in the metal is a random variable relating the outcome of these random inputs to a real number. Usually, we would call such a random variable continuous although the limitation of measurement devices will

assuredly induce a discretization. A discrete random variable would be, say, one which assigns a value of 0 if no observed cracking, "1" if mild cracking, "2" if moderate, etc.

2. Cumulative Distribution Function (cdf) - A function, usually denoted F(x), which gives the probability that the random variable X will take values no greater than x:

$$F(x) = Pr\{X \leq x\}$$

3. Probability Mass Function (pmf) - A function, p(x), which gives the probability that a discrete random variable X will have an outcome x:

$$p(x) = Pr\{X = x\}$$

Some common probability mass functions (also referred to as discrete distributions) are given in Table 11.2.1.

4. Probability Density Function (pdf) - A function, f(x), such that for a continuous random variable X with cdF F,

$$F(x) = \int_{-\infty}^{x} f(x)dx$$

Although f(x) does not exist for every form of F(x), the most common forms of F(x) admit the definition of a function f(x). This function is often thought of as the derivative of F(x). Table 11.2.2 lists names of commonly used continuous pdfs. Tables 11.3.2(a) and (b) gives their mathematical formulation.

TABLE 11.2.1. Summary: Applications of Discrete Statistical Distributions

Distribution	Application	Example	Comments
Binomial	Gives probability of exactly x successes in n independent trials, when probability of success p on single trial is a constant. Used frequently in quality control, reliability, survey sampling, and other industrial problems.	What is the probability of 2 or more "heads" in 10 tosses of a fair coin?	Can sometimes be approximated by normal or by Poisson distribution.
Multinomial	Gives probability of exactly x outcomes of event i, for $i = 1,2,\ldots, k$, in n independent trials when the probability p of event i in a single trial is a constant. Used frequently in quality control and other industrial problems.	Four companies are bidding for each of three contracts, with specified success probabilities. What is the probability that a single company will receive all the orders?	Generalization of binomial distribution for more than 2 outcomes.
Hypergeometric	Gives probability of picking x good units in a sample of n units from a population of N units when there are k bad units in the population. Used in quality control and related applications.	Given a lot with 21 good units and four defectives. What is the probability that a sample of five will yield not more than one defective?	May be approximated by binomial distribution when n is small relative to N.
Geometric	Gives probability of requiring exactly x binomial trials before the first success is achieved. Used in quality control, reliability, and other industrial situations.	Determination of probability of requiring exactly five test firings before first success is achieved.	
Pascal	Gives probability of exactly x failures preceding the sth success.	What is the probability that the third success takes place on the 10th trial?	
Negative Binomial	Gives probability similar to Poisson distribution (see below) when events do not occur at a constant rate and occurrence rate is a random variable that follows a gamma distribution.	Distribution of number of cavities for a group of dental patients.	Generalization of Pascal distribution when s is not an integer. Many authors do not distinguish between Pascal and negative binomial distributions.
Poisson	Gives probability of exactly x independent occurrences during a given period of time if events take place independently and at a constant rate. May also represent number of occurrences over constant areas or volumes. Used frequently in quality control, reliability, queueing theory, and so on.	Used to represent distribution of number of defects in a piece of material, customer arrivals, insurance claims, incoming telephone calls, alpha particles emitted, and so on.	Frequently used as approximation to binomial distribution.

TABLE 11.2.2. Summary: Aplications of Continuous Statistical Distributions(11.1.2)

Distribution	Application	Example	Comments
Normal	A basic distribution of statistics. Many applications arise from central limit theorem [average of values of n observations approaches normal distribution, irrespective of form of original distribution under quite general conditions]. Consequently, appropriate model for many--but not all--physical phenomena.	Distribution of physical measurements on living organisms, intelligence test scores, product dimensions average temperatures, and so on.	Tabulations of cumulative values of standardized normal distribution readily available. Many methods of statistical analysis presume normal distribution.
Gamma	A basic distribution of statistics for variables bounded at one side--for example, $0 < x < \infty$. Gives distribution of time required for exactly k independent events to occur, assuming events take place at a constant rate. Used frequently in queueing theory, reliability, and other industrial applications.	Distribution of time between recalibrations of instrument that needs recalibration after k uses; time between inventory restocking, time to failure for a system with standby components.	Cumulative distribution values have been tabulated. Erlangian, exponential, and chi-square distributions are special cases.
Exponential	Gives distribution of time between independent events occurring at a constant rate. Equivalently, probability distribution of life, presuming constant conditional failure (or hazard) rate. Consequently, applicable in many--but not all--reliability situations.	Distribution of time between arrival of particles at a counter. Also life distribution of complex nonredundant systems, and usage life of some components--in particular, when these are exposed to initial burn-in, and preventive maintenance eliminates parts before wear-out.	Special case of both Weibull and gamma distributions.
Beta	A basic distribution of statistics for variables bounded at both sides--for example $0 \leq x \leq 1$. Useful for both theoretical and applied problems in many areas.	Distribution of proportion of population located between lowest and highest value in sample; distribution of daily percent yield in a manufacturing process; description of elapsed times to task completion (PERT).	Cumulative distribution values have been tabulated. Uniform, right triangular, and parabolic distributions are special cases.
Uniform	Gives probability that observation will occur within a particular interval when probability of occurrence within that interval is directly proportional to interval length.	Used to generate random values.	Special case of beta distribution.
Log-normal	Permits representation of random variable whose logarithm follows normal distribution. Model for a process arising from many small multiplicative errors. Appropriate when the value of an observed variable is a random proportion of the previously observed value.	Distribution of sizes from a breakage process; distribution of income size, inheritances and bank deposits; distribution of various biological phenomena; life distribution of some transistor types.	"Error function" terminology often used for both normal, analog - normal distribution.
Rayleigh	Gives distribution of radial error, when the errors in two mutually perpendicular axes are independent and normally distributed around zero with equal variances.	Bomb-sighting problems; amplitude of noise envelope when a linear detector is used.	Special case of Weibull distribution.
Cauchy	Gives distribution of ratio of two independent standardized normal variates.	Distribution of ratio of standardized noise readings; distribution of $\tan \theta$ when θ is uniformly distributed.	Has no moments.
Weibull	General time-to-failure distribution due to wide diversity of hazard-rate curves, and extreme-value distribution for minimum of N values from distribution bounded at left.	Life distribution for some capacitors, ball bearings, relays, and so on.	Rayleigh and exponential distributions are special cases.
Extreme Value	Limiting model for the distribution of the maximum or minimum of N values selected from an "exponential-type" distribution, such as the normal, gamma, or exponential.	Distribution of breaking strength of some materials, capacitor breakdown voltage, gust velocities encountered by airplanes, bacteria extinction times.	Cumulative distribution has been tabulated.

11.2.2 Moments

1. Mean (μ) - the center of gravity of a pmf or pdf:

$$\mu = \sum_{\text{all } x} x\, p(x) \qquad \text{Discrete Case}$$

$$\mu = \int x\, f(x)dx \qquad \text{continuous case with existing pdf.}$$

The mean, μ, is usually estimated by the sample average. If n values of X are observed, i.e., if we have the n data points $x_1, x_2, \ldots, x_n$, the estimate $\hat{\mu}$ of μ is

$$\hat{\mu} = \bar{x} = \frac{1}{n} \sum_{i=1}^{n} x_i$$

2. Median - the smallest number Z such that

$$\sum_{\text{All } X \leq Z} p(x) = 0.5 \qquad \text{Discrete}$$

or

$$\int_{-\infty}^{Z} f(x)dx = 0.5 \qquad \text{Continuous}$$

The median is referred to as the "middle" of the distribution. The median is estimated from X_1 and X_n as the the middle value (or average of two middle values for n even) when the data is in ascending order.

3. Variance (σ^2) - the second moment about the mean, μ:

$$\sigma^2 = \sum_x (x-\mu)^2 \, p(x)$$

or

$$\sigma^2 = \int_{-\infty}^{\infty} (x-\mu)^2 \, f(x)dx$$

Two estimates of σ^2 are common:

$$\hat{\sigma}^2 = \frac{1}{n} \sum (x_i - \bar{x})^2 = \frac{\sum x_i^2 - \frac{\left(\sum x_i\right)^2}{n}}{n}$$

$$s^2 = \frac{n}{n-1} \hat{\sigma}^2 = \frac{\sum x_i^2 - \frac{\left(\sum x_i\right)^2}{n}}{n-1}$$

The first of these is the maximum likelihood estimate for the normal or Gaussian distribution while the second is the unbiased estimate in this case. The square root of σ^2 is called the standard deviation.

4. Coefficient of Variation – Ratio of standard deviation to mean, σ/μ. This coefficient is used as an index of relative variability.

5. k-th Order Moments about the mean, $k \geq 2$:

$$\mu_k = \sum_x (x - \mu)^k \, p(x)$$

$$\mu_k = \int_{-\infty}^{\infty} (x - \mu)^k \, f(x)dx$$

These moments are usually estimated from the data $x_1, x_2, \ldots, x_n$ by

$$\hat{\mu}_k = \frac{1}{n} \sum_{i=1}^{n} (x_i - \bar{x})^k$$

In most practical situations, one does not estimate moments greater than k=4 due to the potential instability of higher order moments.

6. Skewness (α_3 or $\sqrt{\beta_1}$) - an index measuring lack of symmetry about the mean

$$\sqrt{\beta_1} = \mu_3 / (\mu_2)^{3/2}$$

If the distribution is symmetrical, $\sqrt{\beta_1} = 0$. If $\sqrt{\beta_1}$ is negative, the distribution is skewed to the left. A positive value of $\sqrt{\beta_1}$ indicates skewed to the right.

7. Kurtosis (α_4 or β_2) - an index of peakedness is given by

$$\beta_2 = \frac{\mu_4}{\mu_2^2}$$

The larger the value of β_2 the more peaked the distribution. As a standard, the normal distribution, which has a value of β_2 of 3, is often used.

11.2.3 Inequalities on Random Variables

1. Tchebychev Inequality. If X is a random variable with mean μ and variance σ^2,

$$\Pr \{ |X - \mu| \geq \epsilon \} \leq \frac{\sigma^2}{\epsilon^2}$$

for any positive ε. If $\bar{X}_N$ represents the average of N independent realizations of X, then

$$\Pr\left\{|\bar{X}_N - \mu| \geq \varepsilon\right\} \leq \frac{\sigma^2}{n\varepsilon^2}$$

Although the Chebychev inequality has virtually no requirements on X other than the existence of a finite mean and variance, the inequality may prove too weak for many situations.

2. Markov Inequality - If the expected value of $|X|^r$, i.e., the r^{th} absolute moment about zero exists,

$$\Pr\left\{X \geq \varepsilon\right\} \leq \frac{E|X|^r}{\varepsilon^r}$$

$$\text{where } E|X|^r = \int_{-\infty}^{\infty} |X|^r f(x)dx$$

3. Camp-Meidell Inequality - If X has a unimodal distribution (one bump) and the tails are "close to" the x-axis,

$$\Pr\left\{|X - \mu| \geq \varepsilon\right\} \leq \frac{\sigma^2}{2.25\,\varepsilon^2}$$

11.2.4 Parameter Estimation

One major purpose of gathering data is to get a feel for the distributional characteristics of the random variable of interest. To do this, the form of the distribution (or pdf) is assumed known with a set of unknown parameters to estimate. This case is referred to as parametric statistics since the function form is assumed. An alternative is to assume less about the distribution of the random variable. This second case is often referred

to as nonparametric although in most situations some constraining assumptions on distributional characteristics are still made.

In this section we note a very brief list of common parametric estimation procedures. In all of these, the parameter θ (possibly a vector of parameters) is to be estimated from the N data points, $x_1, x_2, \ldots, x_N$. The probability density function is denoted $f_\theta(x)$.

1. Maximum Likelihood - The parameter $\hat{\theta}_m$ is the maximum likelihood estimate of θ if $\hat{\theta}$ is the "most likely" based upon the data. Explicitly, $\hat{\theta}$ maximizes the likelihood $L(\theta) = \prod_{i=1}^{N} f_\theta(x_i)$.

   Certain problems with $\hat{\theta}_m$ are

   A. $\hat{\theta}_m$ need not be unique

   B. $\hat{\theta}_m$ is not necessarily unbiased

   C. It is often hard to computationally implement a procedure to solve for $\hat{\theta}_m$.

   Conversely, $\hat{\theta}_m$ is optimal in that, under mild constraints on $f_\theta(x)$, $\hat{\theta}_m$ is asymptotically normal with mean θ and variance smaller than any other asymptotically unbiased normal estimator.

2. Least Squares - This procedure originally proposed by Gauss, minimizes the squared difference between the data and the predicted value of the data based upon the parameter-values. If $P_i(\theta)$ is the predicted value of the i^{th} realization of X, then $\hat{\theta}_L$, the least squares estimate of θ, minimizes $\sum_{i=1}^{N} (x_i - P_i(\theta))^2$. Although the $\hat{\theta}_L$ is usually unique, it is less efficient than $\hat{\theta}_\mu$. When $f_\theta(x)$ is the normal or Gaussian distribution, then $\hat{\theta}_L = \hat{\theta}_m$ whenever θ is parameterized as an additive mean.

3. Method of Moments - The moments about the mean or about zero can usually easily be expressed as functions of the parameter θ. The method of moments estimate of θ, say $\hat{\theta}_p$, is that value of θ which

gives the same moments as observed in the data. The number of moments matched depends upon the number of parameters θ represents. For example, suppose $\theta = (\alpha,\beta)$. Since we need to estimate only two parameters, we need only the relationship of the mean and variance of a random variable associated with $f_\theta(x)$. Let these two functions be denoted $g_1(\alpha,\beta)$ and $g_2(\alpha,\beta)$, respectively. Then α and β are those values which satisfy

$$\bar{x} = g_1(\hat{\alpha},\hat{\beta})$$

$$S^2 = g_2(\hat{\alpha},\hat{\beta})$$

where x and S^2 are, respectively, the mean and variance estimates based on the sampled data.

For an in-depth discussion of the method of moments the reader is referred to Elderton and Johnson (1969), "Systems of Frequency Curves," Cambridge Press (England).

Other, less common, procedures of estimating parameters from data appear in more advanced engineering statistics tests (See, for example, Mendel, J. M., Discrete Techniques of Parameter Estimation, Marcel Dekker, 1973.).

4. W_E Test - A test used to evaluate the assumption of an exponential distribution when origin is unknown:

$$W_E = \frac{(\bar{X} - X_i)^2}{\sum(x_i - \bar{X})^2}$$

11.3 THE HAZARD FUNCTION

An important application of probability distribution is as time-to-failure models for components or systems. The number of hours or years, or cycles of satisfactory operation is a random variable whose exact value depends on many factors. Once an appropriate probabilistic model for time-to-failure has been constructed and its parameters estimated, this information may be used to predict life, plan future reliability test programs, etc. In this section we are concerned with distributions for time-to-failure.

It is frequently meaningful to consider a function that gives the probability of failure during a very small time increment, assuming that no failure occurred before that time. This function, known as the hazard function (and also as the conditional failure function, or intensity function, or force of mortality), is

$$h(x) = \frac{f(x)}{1 - F(x)} \tag{11.3.1}$$

where $f(x)$ and $F(x)$ are the probability density and cumulative distribution functions for time-to-failure. Consequently, $[1 - F(x)]$ is the probability of survival to time x, and $h(x)\,dx$ represents the proportion of the items surviving at time x that fail during the interval $(x + dx)$.

A hazard function appropriate for many phenomena, including human life, is the so-called "bathtub curve" shown in Figure 11.3.1. For an initial period up to time x_0, $h(x)$ is relatively large, but decreasing in value, because of "infant mortality"--that is, early failures often attributable to manufacturing defects. Subsequently, $h(x)$ remains approximately constant until time x_1 after which it increases because of wear-out failures. We can optimize "in usage" reliability for products with this hazard function by a) initial burn-in until time x_0 to weed out early failures, and b) replacement at time x_1 to avoid wear-out failures.

The hazard function corresponding to a specified probability density function can be found directly from Equation 11.3.1.

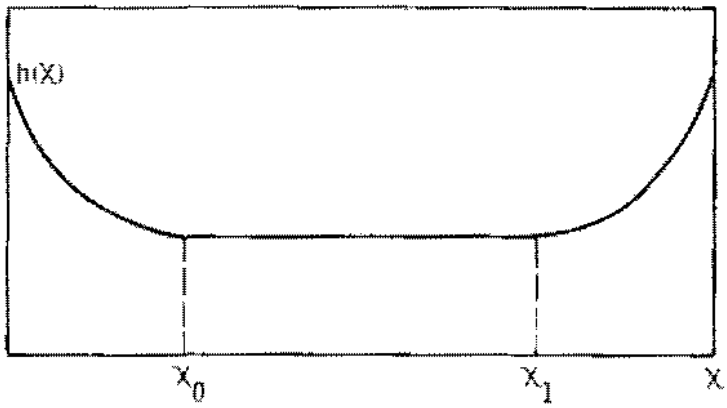

FIGURE 11.3.1. Typical Hazard Function (Bathtub Curve)

The cumulative hazard function, H(x), can be evaluated for any distribution for $x \geq 0$ by

$$H(x) = \int_0^x h(x)\, dx \qquad (11.3.2(a))$$

$$H(x) = -\ln [1 - F(x)] \qquad (11.3.2(b))$$

and

$$F(x) = 1 - \exp [-H(x)] \qquad (11.3.2(c))$$

This latter form permits the conversion of probability paper for a given distribution into hazard paper.

Table 11.3.1 contains the various general equations relevant to hazards analyses.

Some idea of the pronounced differences in hazard functions is given in Figure 11.3.2 for a) normal distribution with $\mu = 5$ and $\sigma = 1$; b) uniform distribution over interval (0,10); and c) exponential distribution with $\lambda = 0.2$. The normal distribution may not be applicable as a time-to-failure model, because a normally distributed variate can take on negative values; whereas, time-to-failure, which may be close to zero due to infant mortality, cannot be negative. The uniform distribution is limited as a time-to-failure model,

TABLE 11.3.1. General Equations in Hazards Analyses

$F(x)$ = Cumulative distribution function
= Probability of failure by time x

$F(x)$ for $x \geq 0$ $\quad F(x) > 0 \rightarrow 1$
as $(x) \rightarrow 0 \rightarrow \infty$

$f(x)$ = Probability density function
= Derivative of cumulative distribution function

$$= \frac{d}{dx} F(x)$$

or $$F(x) = \int_0^x f(x)\, dx$$

$h(x)$ = The hazard function of a distribution
= Conditional probability of failure at time x, given failure has not occurred

= Instantaneous failure rate at time x

$$h(x) = \frac{f(x)}{1 - F(x)}$$

$H(x)$ = Cumulative hazard function of the hazard function distribution for $x \geq 0$

$$H(x) = \int_0^x h(x)\, dx$$

$$H(x) = \int_0^x \frac{f(x)dx}{1 - F(x)}$$

$$H(x) = \int_0^x \frac{dF(x)}{1 - F(x)} = -\ln [1 - F(x)] = \ln \left[\frac{1}{1 - F(x)}\right]$$

$$-H(x) = \ln [1 - F(x)]$$

$$\exp [-H(x)] = 1 - F(x)$$

$R(x)$ = Reliability Function

$$R(x) = 1 - F(x) = \exp [-H(x)]$$

$$F(x) = 1 - \exp [-H(x)]$$

$$P_D = 1 - \exp \left(-PN_0\right)$$

$F(x) = 1 - \exp [-H(x)]$; $F(x) \approx H(x)$ if $P(x) < 1$ to 2%

$H(x)$ = PN = Cumulative hazard function

$F(x)$ = P_D = Cumulative distribution function

$P(x)$ = Probability of a given failure

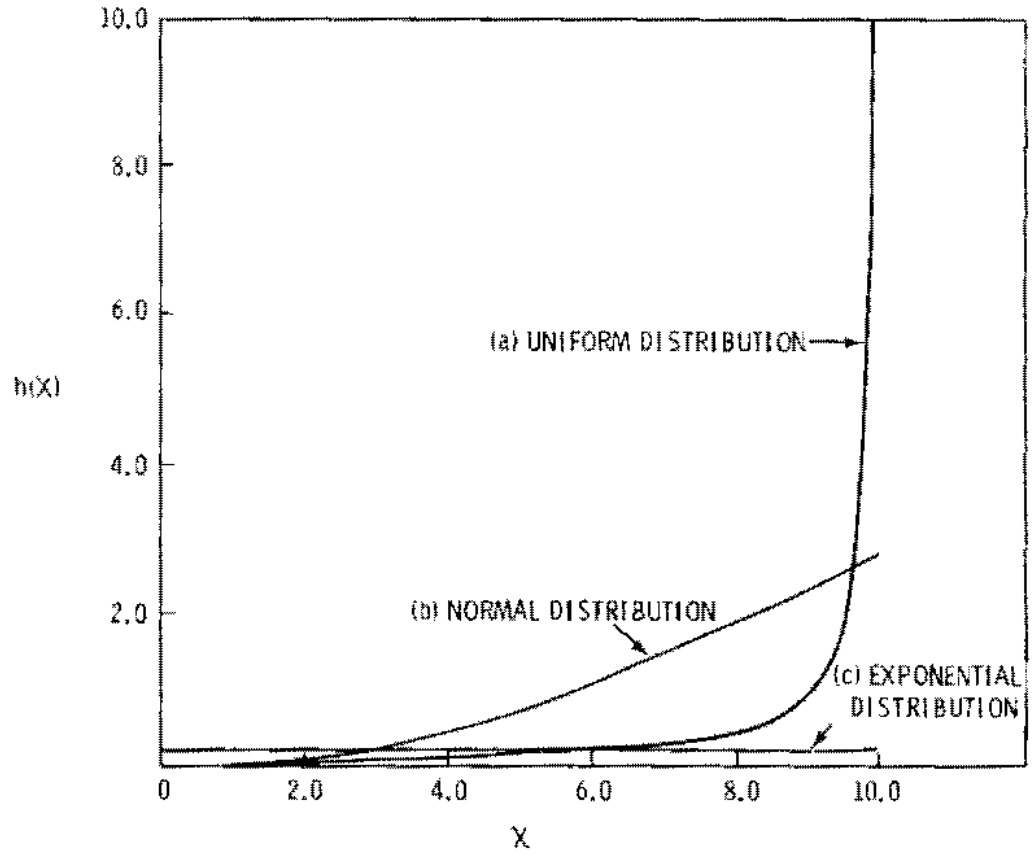

FIGURE 11.3.2. Hazard Functions for Normal, Uniform, and Exponential Distributions

because there is a specified upper limit before which the failure must occur. Therefore, its hazard rate approaches infinity as x approaches the upper limit, since all units that have not yet failed must fail in a smaller and smaller time interval.

The hazard function for an exponentially distributed variate is a constant. This result and its implications are discussed below using Hahn and Shapiro as a source.(11.1.2)

11.3.1 The Exponential Distribution as a Time-To-Failure Model

The exponential probability density function,

$$f(x) = \lambda \exp - (\lambda x) \qquad (11.3.3(a))$$

is the most commonly used time-to-failure distribution. It plays a central role in reliability, comparable to that of the normal distribution in other applications.

The hazard function for an exponentially distributed variate is

$$h(x) = \frac{\lambda \exp(-\lambda x)}{1 - \int_0^x \lambda \exp-(\lambda x)dx} = \frac{\lambda \exp^{-\lambda x}}{\exp^{-\lambda x}} = \lambda \qquad (11.3.3(b))$$

Thus, the probability of failure during a specified time interval is a constant depending only on the length of the interval and is the same irrespective of whether the unit in question is in its first hour of operation or has previously survived 100 hours, 1000 hours, or 10^6 hours. The parameter λ is referred to as the failure rate.

From the previous discussion, it follows that time-to-failure for a unit is exponentially distributed if the unit fails as soon as some single event, such as the disintegration of a particle, occurs, assuming such events happen independently at a constant rate. Frequently, although the time-to-failure distribution for a component is not exponential over its entire life, the in-usage portion is; for example, a component whose hazard function can be represented by a bathtub curve is installed in a system only after it has been successfully "burned in" until time x. Also, the component is replaced after $(x_1 - x_0)$ hours by another component from the same population, which had been previously exposed to the same burn in. This process is continued indefinitely. The time-to-failure for the components in system usage is then exponentially distributed, because the applicable hazard function is constant. This is so, even if the time-to-failure distribution over the total life of the component is far from exponential.

The exponential distribution is more appropriate as a time-to-failure model for complex systems than it is for components. This distribution is the "in-the-limit" model for time-to-failure for a system with a large number of in-series components, none of which individually contributes very heavily to

the total failure probability, even if the distributions for the individual components are not exponential. This result corresponds to the central limit theorem which establishes the normal distribution as the appropriate model in many nonlife-test situations. It also applies to the distribution of the time between failures for such systems if each failed component is replaced immediately by another component of the same type.

The use of the exponential distribution has also been justified in reliability problems on strictly empirical grounds. However, the simplicity of the theory and of the required calculations should not delude the engineer into believing that the time-to-failure distribution for all elements is exponential. For many components there is no physical reason to expect a constant hazard rate. Such an assumption could be as erroneous as the assumption of normality for all nonlife-test data, or even more so, since the exponential distribution in many instances does not enjoy the robust properties of the normal distribution. Procedures for evaluating the validity of the exponential distribution assumption are discussed later.

Cumulative probabilities for an exponential variate are discussed in Section 11.5. For example, if the time-to-failure for a piece of equipment follows an exponential distribution with $\lambda = 0.1$ per year, the probability of failure during the first year is

$$F(1;0.1) = 1 - \exp(-0.1) = 0.095$$

Note that $F(x) = 1 - \exp(-\lambda x) \simeq \lambda x$

if λx is small, as is the case in most reliability problems.

In some situations, the parameter λ is known from physical considerations, but more frequently its value must be estimated from the test data by the following expression (obtained by the method of maximum likelihood):

$$\hat{\lambda} = \frac{\text{total number of failures } (F)}{\text{total test time of failed and unfailed units } (x)} \qquad (11.3.4)$$

The expected value of time-to-failure x, known as mean time-to-failure and denoted by $1/\lambda$, is also frequently of interest.

As noted in Equation 11.3.2(b) the cumulative hazard function H(x) is

$$H(x) = - \ln [1 - F(x)] \qquad (11.3.2(b))$$

For an exponential distribution,

$$H(x) = \ln [1 - 1 + \exp (-\lambda x)] \qquad (11.3.5(a))$$

$$H(x) = -\ln [\exp (-\lambda x)] \qquad (11.3.5(b))$$

$$H(x) = \lambda x \qquad (11.3.5(c))$$

This can be used to obtain the time-to-failure by

$$x(H) = H/\lambda \qquad (11.3.5(d))$$

where $1/\lambda$ will be the slope of the function; or, alternately, the value where $H = 1$.

Note that it does not matter how many test units are involved in accumulating the total time x. For example, if three failures occurred during a total test time of 100 hours, $\hat{\lambda} = 3/100$, irrespective of whether the 100 hours were obtained on 100 units tested an average of one hour each or 10 units tested for an average of 10 hours each. This is a direct consequence of assuming an exponential distribution for time-to-failure, with the resulting implication that probability of future failure for an unfailed unit is independent of its history.

The simplicity of these expressions has been a contributing factor to the popular use (and misuse) of the exponential distribution. Thus, it is possible to obtain the same information about reliability for a single mission of 100 hours duration by testing 100 units each for a single hour or by testing one unit for 100 hours, assuming failed units are immediately replaced by good

ones. This procedure is valid if the exponential model for time-to-failure is correct, but can lead to erroneous results otherwise.

Some more general models for life testing are frequently more realistic, though more complex, than the exponential distribution.

A special form of the exponential equation is the Laplace or double exponential. In terms of the constants used previously, the double exponential will be, in the most general form,

$$f(x) = \frac{\lambda}{2} \exp - \lambda (x - \mu) \qquad (11.3.6)$$

The other forms can be easily derived from this equation.

11.3.2 The Weibull Distribution

In many cases, the inadequacy of the exponential distribution as a model for time-to-failure is due to the restrictive assumption of a constant hazard function. Consequently, more general distributions are needed for cases where the failure probability varies with time.

The Weibull distribution results from the hazard function,

$$h(x) = \frac{n}{\sigma} \left(\frac{x}{\sigma}\right)^{n-1} \qquad (11.3.7(a))$$

Its probability density function is

$$f(x) = \frac{n}{\sigma} \left(\frac{x}{\sigma}\right)^{n-1} \exp \left[- \left(\frac{x}{\sigma}\right)^{n} \right] \qquad (11.3.7(b))$$

where σ is the scale parameter and n is the shape parameter. The hazard function, failure time, cumulative distribution function and the probability density function for the Weibull distribution have a wide variety of shapes, as can be seen from the plots for differing values of n in Figure 11.3.3(a, b, c, d). In particular, when $n > 1$, the Weibull probability density function is

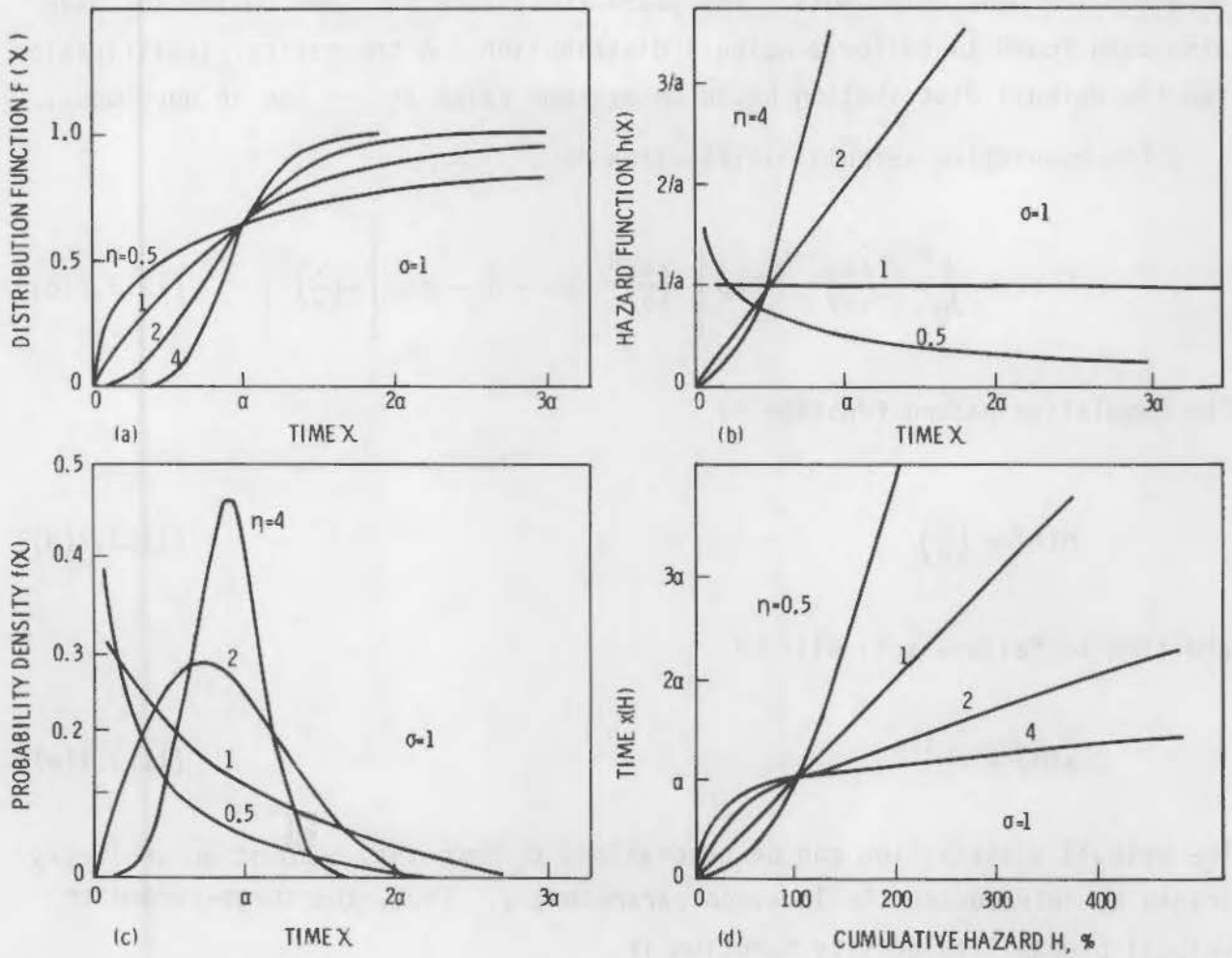

FIGURE 11.3.3. Weibull Distribution; $\eta = 1$ is Exponential Distribution

single-peaked and the hazard function increases with x; for $\eta < 1$ the probability density function is reverse J shaped and the hazard function decreases with x. When $\eta = 1$, the hazard function is a constant and the Weibull distribution is equivalent to the exponential distribution; in this case, the Weibull scale parameter σ equals the reciprocal of the exponential distribution parameter λ. The Rayleigh distribution is a Weibull distribution with $\eta = 2$. It is apparent that the corresponding hazard function is a linear increasing function of x.

The Weibull distribution has been frequently suggested as a time-to-failure model on empirical grounds, and satisfactory representations have been

obtained for many components. The years-to-failure for some businesses have also been found to follow a Weibull distribution. A theoretical justification for the Weibull distribution based on extreme value theory can be developed.

The cumulative Weibull distribution is

$$F(x) = \int_0^x \frac{\eta}{\sigma}\left(\frac{x}{\sigma}\right)^{\eta-1} \exp\left[-\left(\frac{x}{\sigma}\right)^{\eta}\right] dx = 1 - \exp\left[-\left(\frac{x}{\sigma}\right)^{\eta}\right] \qquad (11.3.7(c))$$

The cumulative hazard function is

$$H(x) = \left(\frac{x}{\sigma}\right)^{\eta} \qquad (11.3.7(d))$$

and time to failure x(H) will be

$$x(H) = \sigma H^{1/\eta} \qquad (11.3.7(e))$$

The Weibull distribution can be generalized to take into account an arbitrary origin by introducing the location parameter, μ. Thus, the three-parameter Weibull probability density function is

$$f(x) = \frac{\eta}{\sigma}\left(\frac{x-\mu}{\sigma}\right)^{\eta-1} \exp\left[-\left(\frac{x-\mu}{\sigma}\right)^{\eta}\right] \qquad (11.3.8)$$

In life testing, μ represents an initial period during which no failures can take place. Estimation of the Weibull distribution parameters from test data generally involves solution of nonlinear equations.

11.3.3 The Type I and Other Extreme Value Distributions

Failure of a component or system may frequently be linked to extremal phenomena dependent directly on either the smallest or largest value in a sample from a particular distribution.

In these cases, we are interested in the distribution of the smallest element (minimum value) or largest element (maximum value) in a sample from some initial distribution. Frequently, this initial distribution is not known and cannot be sampled directly, such as in fatigue, where only minimum or maximum values are observed. The distribution of the smallest or largest element will in general depend on the sample size n and on the nature of the initial distribution. However, if n is large, we can use certain general asymptotic results that depend on some limited assumptions concerning the initial distribution.

Three types of asymptotic distributions have been developed for both minimum and maximum values based on different (but not all possible) initial distributions. The following cases are of special interest:

1. Type I - asymptotic distribution for maximum values
2. Type I - asymptotic distribution for minimum values
3. Type III - asymptotic distribution for minimum values

The Type I asymptotic distribution has been referred to as the "Type I extreme value distribution," "Gumbel's extreme value distribution," or simply "the extreme value distribution." The Type III asymptotic distribution for minimum values is the Weibull distribution. These three cases are now discussed.

A Type I asymptotic distribution for maximum values is the limiting model as n approaches infinity for the distribution of the maximum of n independent values from an initial distribution whose right tail is unbounded and which is "exponential type"; that is, the initial cumulative distribution approaches unity with increasing values at least as rapidly as an exponential distribution function. Because the gamma (exponential, special case), normal, and log-normal distributions are all unbounded to the right and exponential type, this leads to a wide choice of possible initial distributions.

The Type I asymptotic distribution for maximum values may be used to represent time to failure for a circuit with n elements in parallel; assuming that n is a large number, the component failure times come from the same exponential-type distribution and failures occur independently. This model, however, is not limited to life test and reliability situations.

Phenomena which have been represented by the Type I asymptotic distribution for maximum values include gust velocities encountered by airplanes, extinction times for bacteria, the maxima of stock market indices over a given year, and depths of corrosion pits.

The Type I asymptotic distribution for minimum values is the limiting model as n approaches infinity for the distribution of the minimum of n independent values from an initial distribution whose left tail is unbounded and which is exponential type for decreasing values. The normal distribution is exponential type unbounded to the right and is clearly the same to the left. Thus, the Type I asymptotic distribution for minimum values is applicable as a time-to-failure model given a large number of components in series, assuming the times-to-failure for the individual components are independently and identically normally distributed.

The hazard functions and probability density functions for the Type I asymptotic distributions for the largest and smallest elements, respectively, are

$$h(x) = \frac{\exp\left[-(1/\sigma)(x-\mu)\right]}{\sigma\left\{\exp\left[e^{-(1/\sigma)(x-\mu)}\right] - 1\right\}} \qquad (11.3.9(a))$$

$$h(x) = \frac{1}{\sigma}\exp\left(\frac{x-\mu}{\sigma}\right) \qquad (11.3.10(a))$$

$$f(x) = \frac{1}{\sigma}\exp\left[-\frac{1}{\sigma}(x-\mu) - e^{-(1/\sigma)(x-\mu)}\right] \qquad (11.3.9(b))$$

$$f(x) = \frac{1}{\sigma}\exp\left[\frac{1}{\sigma}(x-\mu) - e^{(1/\sigma)(x-\mu)}\right] \qquad (11.3.10(b))$$

Plots are given in Figures 11.3.4(a, b, c, d).

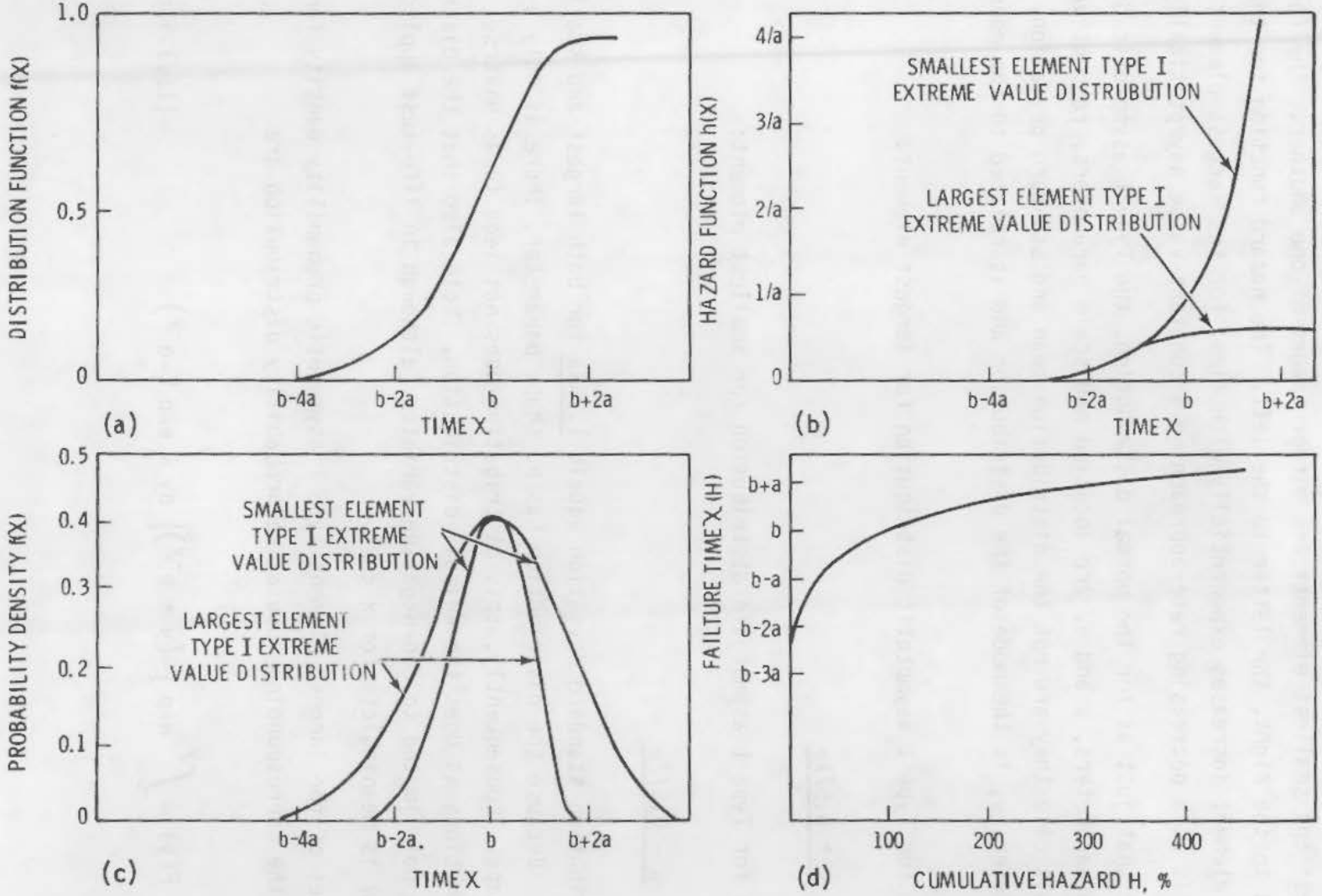

FIGURE 11.3.4. Smallest and Largest Extreme Value Distribution

It is clear that the Type I asymptotic probability density functions for the largest and smallest elements are mirror images of one another. The former is skewed to the right, the latter to the left. The hazard function for the smallest element increases exponentially with time; for the largest element the increase is at a decreasing rate approaching a constant value asymptotically.

Note that just as for the normal distribution, the Type I asymptotic distribution parameters, μ and σ, are location and scale parameters, respectively, but in this case they are not the distribution mean and standard deviation. The parameter, μ, is the mode of the distribution and is related to the mean as follows:

Mean for Type I asymptotic distribution for largest element:

$$\mu + 0.577\sigma$$

Mean for Type I asymptotic distribution for smallest element:

$$\mu - 0.577\sigma$$

The distribution standard deviation equals 1.283σ for both largest and smallest elements. Because the distribution has no shape parameter, there is only a single shape. Consequently, this distribution does not lead to as diverse hazard functions as does the Weibull distribution. Note also that the distribution is not limited to non-negative variates (although in life-test applications $h(x)$ is meaningless for $x < 0$).

Values of the largest element Type I asymptotic probability density function and the corresponding cumulative probability distribution are

$$F(y) = \int_{-\infty}^{y} \exp\left[-\left(y + e^{-y}\right)\right] dy = \exp\left(-e^{-y}\right) \qquad (11.3.9(c))$$

for the standardized or "reduced" variate

$$y = \frac{x - \mu}{\sigma}$$

or

$$F(x) = \exp\left[-\exp -\left(\frac{x - \mu}{\sigma}\right)\right] \qquad (11.3.9(c))$$

Distribution percentiles, that is, values of

$$y(\alpha) = -\ln\left[\ln\left(\frac{1}{\alpha}\right)\right]$$

for various α can be determined. These tabulations can be used for the Type I asymptotic distribution for smallest elements using $-y$ in place of y in the probability density function and $1-F(-y)$ in place of $F(y)$ in the cumulative probability distribution. The latter substitution follows from the fact that the cumulative distribution function for the Type I asymptotic reduced variate for the smallest element is

$$F(y) = 1 - \exp\left(-e^{-y}\right) \qquad (11.3.10(c))$$

or

$$F(x) = 1 - \exp\left[-\exp\left(\frac{x - \mu}{\sigma}\right)\right] \qquad (11.3.10(c))$$

The cumulative hazard function, $H(x)$, for the largest element will be

$$H(x) = \exp\left[\exp -\left(\frac{x - \mu}{\sigma}\right)\right]$$

For the smallest element, it will be

$$H(x) = \exp\left(\frac{x - \mu}{\sigma}\right) \qquad (11.3.10(d))$$

The time-to-failure x is a function of the cumulative hazard H given by the following equations for smallest extreme values.

$$x(H) = \mu + \sigma \ln H \qquad (11.3.10(e))$$

Estimates of the parameters of the extreme-value distribution from given data may be obtained graphically by probability plotting. Alternately, the previously stated relationships between the mean and standard deviation of the distribution and its parameters may be used by matching moments.

The Type III asymptotic distribution for the smallest element is equivalent to the Weibull distribution. This is the limiting model as n approaches infinity for the distribution of the minimum of n values from various initial distributions bounded at the left. The gamma is one such initial distribution. Thus, if in a circuit identical components are connected in series and if their time-to-failure distribution is gamma, the circuit time to failure follows a Type III asymptotic or Weibull distribution rather than a Type I asymptotic distribution, as would have been the case if the initial distribution were normal. The use of the Weibull distribution to represent the distribution of the breaking strength of materials has been justified by using extreme value theory. This model has also been used in drought analyses in a manner similar to flood studies. However, in droughts minimum rather than maximum values are of interest.

The following general observations apply to extreme value distributions:

1. The gamma distribution illustrates the fact that the asymptotic distribution for minimum and maximum values from the same initial distribution are not necessarily of the same type. Thus, as stated above, the asymptotic distribution for minimum values from a gamma distribution is Type III and that for the maximum values is Type I.

2. Selection of the minimum value in a sample from a Type I or Type III asymptotic distribution for minimum values leads to an asymptotic distribution of the same type, and a similar result holds in taking the maximum value in a sample from an asymptotic distribution for

maximum values. However, the asymptotic distribution of the minimum value from a maximum value asymptotic distribution and the distribution of the maximum value from a minimum value asymptotic distribution are Type I (minimum and maximum value, respectively), regardless of whether the initial distribution is Type I or Type III.

3. The various type extreme value distributions are themselves closely related. For example, it can be easily shown that the logarithm of a Weibull variate is distributed as minimum value Type I. This result has been used in developing procedures for estimating the parameters of the Weibull distribution.

4. The preceding discussion has dealt with the asymptotic distribution of the minimum and maximum values. The asymptotic distribution for the mth largest and mth smallest values have also been considered in the literature.

5. The preceding results are asymptotic; that is, they are derived for the case in which n approaches infinity. The rate of convergence to this asymptotic result, that is, the extent to which it is applicable for moderate size n, depends on the initial distribution. For example, fewer observations are required for the distribution of the largest value to approach the Type I asymptotic distribution if the initial distribution is exponential than if it is normal. Plots indicate that good convergence to the asymptotic distribution is obtained for as few as 10 samples from an initial exponential distribution, whereas the agreement at the tails of the asymptotic distribution is questionable for the extreme of as many as 100 observations from a normal distribution. On the other hand, if the initial distribution is already extreme value and of the same type as the asymptotic distribution, the asymptotic result is applicable for all n.

The theory underlying the exact (as opposed to the asymptotic) distribution of the largest or smallest or mth largest observation from a sample of size n is well known and useful tabulations have been obtained for some distributions. Most notable of these are the

tables of percentiles of the distribution for maximum values from a normal distribution for samples of size n = 3, 5, 10, 20, 30, 50, 100, (100), 1000, and the tabulations of percentiles of the distribution of the mth value in samples of size 1 to 10 from gamma distributions with η = 1(1)5. Thus, when n is relatively small and the nature of the underlying distribution is known, it is preferable to use exact results, whenever possible. This would, for example, be the case in evaluating time-to-failure in the circuit problem if there were a total of five components whose time-to-failure is known to follow the same normal or gamma distribution with specified values of the parameters.

However, in many cases the initial distribution is neither known nor can be observed, and we must frequently resort to the asymptotic theory.

6. In addition to the Type I asymptotic distributions and the Type III asymptotic distribution for minimum values discussed in this section, there are also Type II asymptotic distributions and a Type III asymptotic distribution for maximum values. The latter is related to the Type III asymptotic distribution for minimum values in a manner similar to the relationship between the minimum value and maximum value Type I asymptotic distributions. Thus, it is the limiting model for the distribution of maximum values from many initial distributions bounded to the right. The Type II asymptotic distributions for minimum and maximum values arise from initial distributions, such as the Cauchy distribution, for which all moments do not exist. Because the required initial distributions do not arise frequently in practice, the applications of the Type III asymptotic distribution for maximum values and the Type II asymptotic distributions are limited.

One must be careful in using extreme value distributions, particularly in predicting maximum events. Unless one applies reality to a prediction, one may be faced with improbable results. For example, the available data, if used in a Type I extreme value equation, would predict the temperature of Boston to be

200°F within 100 years. This same caution must be applied to ongoing studies on reactor components using extreme value theory.

Table 11.3.2 presents the various continuous distributions used as hazard functions. Included are probability density functions, cumulative distributions, hazard functions, cumulative hazard functions, and time-to-failure.

11.3.4 Normal (Gaussian) Distribution

The normal distribution finds extensive use in failure analysis. The hazard function will be an increasing function of time which makes the distribution appropriate to wear-out types of failure. Nelson[11.3.1] gives the hazard function as:

$$h(x) = \frac{\frac{1}{\sigma(2\pi)^{1/2}} \exp - \frac{1}{2}\left(\frac{x-\mu}{\sigma}\right)^2}{1 - \frac{1}{\sigma(2\pi)^{1/2}} \int_{-\infty}^{x} \exp - \frac{1}{2}\left(\frac{x-\mu}{\sigma}\right)^2 dx} \qquad (11.3.11(a))$$

The probability density function is

$$f(x) = \frac{1}{\sigma(2\pi)^{1/2}} \exp - \frac{1}{2}\left(\frac{x-\mu}{\sigma}\right)^2 dx \qquad (11.3.11(b))$$

The cumulative distribution is

$$F(x) = \frac{1}{\sigma(2\pi)^{1/2}} \int_{-\infty}^{x} \exp - \frac{1}{2}\left(\frac{x-\mu}{\sigma}\right)^2 dx \qquad (11.3.11(c))$$

The probability density function is symmetric about the mean value μ as can be seen in Figure 11.3.5(c) and this symmetry should be considered in deciding on the appropriateness of the distribution for a given set of data.

A method of analyzing both functions 11.3.11(b) and 11.3.11(c), and then 11.3.11(a) is through the use of the functions 11.3.12(a) and 11.3.12(b), both widely tabulated:

TABLE 11.3.2(b). Less Common Functions Used in Probability Modeling

DISTRIBUTION	CUMULATIVE DISTRIBUTION FUNCTION F(x)	PROBABILITY DENSITY FUNCTION f(x)	EXPECTED VALUE (MEAN)	MOMENTS OF DISTRIBUTION (FIRST = 0)		
				SECOND (VARIANCE)	THIRD (SKEWNESS) $B_1^{1/2}$	FOURTH (KURTOSIS) B_2
1* GAMMA $\lambda > 0$, $\eta > 0$	$F(x) = \frac{\lambda^\eta}{\Gamma(\eta)} \int_0^x x^{\eta-1} \exp(-\lambda x) dx$	$f(x) = \begin{cases} \frac{\lambda^\eta}{\Gamma(\eta)} x^{\eta-1} \exp(-\lambda x) ; x \geq 0 \\ 0 \text{ ELSEWHERE} \end{cases}$	η/λ	η/λ^2	$2/\eta^{1/2}$	$\frac{3(\eta+2)}{\eta}$
2* RAYLEIGH $\sigma > 0$	$F(x) = 1 - \exp\left[-\frac{x^2}{2\sigma^2}\right]$	$f(x) = \begin{cases} \left(\frac{x}{\sigma^2}\right) \exp -\left(\frac{x^2}{2\sigma^2}\right) ; x \geq 0 \\ 0 \text{ ELSEWHERE} \end{cases}$	$\left(\frac{\sigma^2 \pi}{2}\right)^{1/2}$	$0.429\sigma^2$	0.63	3.26
3* CAUCHY $-\infty < \mu < \infty$ $\sigma > 0$	$F(x) = \frac{1}{2} + \frac{1}{\pi} \arctan \frac{(x-\mu)}{\sigma}$	$f(x) = \frac{1}{\sigma\pi} \left[1 + \frac{(x-\mu)^2}{\sigma^2}\right]^{-1}$	NO FINITE VALUES			
4* BETA $\eta > 0$ $\gamma > 0$	$F(x) = \frac{\Gamma(\eta+\gamma)}{\Gamma(\gamma)\Gamma(\eta)} \int_0^x x^{\gamma-1}(1-x)^{\eta-1} dx$	$f(x) = \begin{cases} \frac{\Gamma(\eta+\gamma)}{\Gamma(\eta)\Gamma(\gamma)} x^{\gamma-1}(1-x)^{\eta-1} ; 0 \leq x \leq 1 \\ 0 \text{ ELSEWHERE} \end{cases}$	$\frac{\gamma}{\eta+\gamma}$	$\frac{\eta\gamma}{(\eta+\gamma)^2(\eta+\gamma+1)}$	**	***
5* UNIFORM (SPECIAL CASE OF β) μ_0, μ_1 WHERE $\mu_0 < \mu_1$	$F(x) = \frac{x}{\mu_1 - \mu_0}$	$f(x) = \begin{cases} \frac{1}{\mu_1 - \mu_0} ; \mu_0 \leq x \leq \mu_1 \\ 0 \text{ ELSEWHERE} \end{cases}$	$\frac{\mu_0 + \mu_1}{2}$	$\frac{(\mu_1 - \mu_0)^2}{12}$	0	1.8

NOTES:

*SEE FIGURES AT BOTTOM OF PAGE

**$B_1^{1/2} = \frac{2(\eta-\gamma)(\gamma+\eta+1)^{1/2}}{(\eta\gamma)^{1/2}(\gamma+\eta+2)}$

***$B_2 = \frac{3(\eta+\gamma+1)[2(\gamma+\eta)^2 + \eta\gamma(\eta+\gamma-6)]}{\eta\gamma(\eta+\gamma+2)(\eta+\gamma+3)}$

1. GAMMA DISTRIBUTION

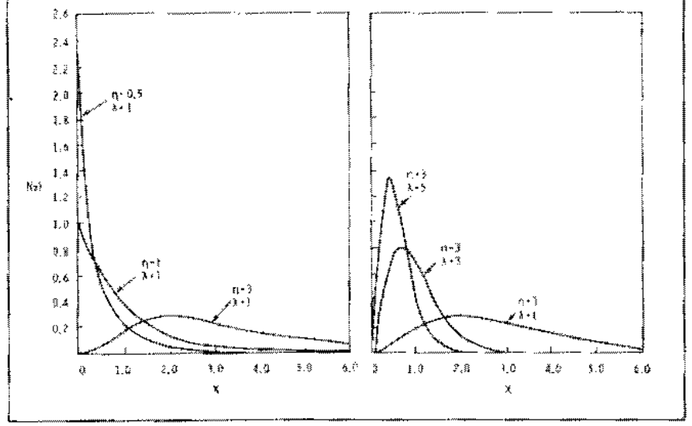

2. RAYLEIGH DISTRIBUTION

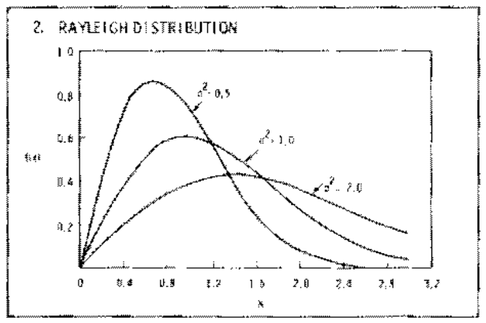

3. CAUCHY DISTRIBUTION

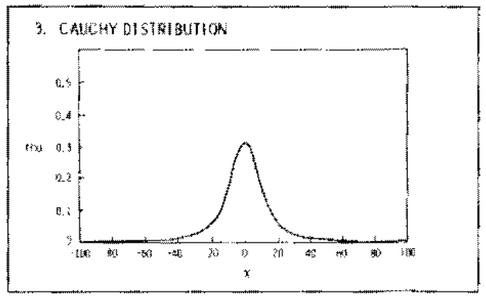

4. BETA DISTRIBUTION

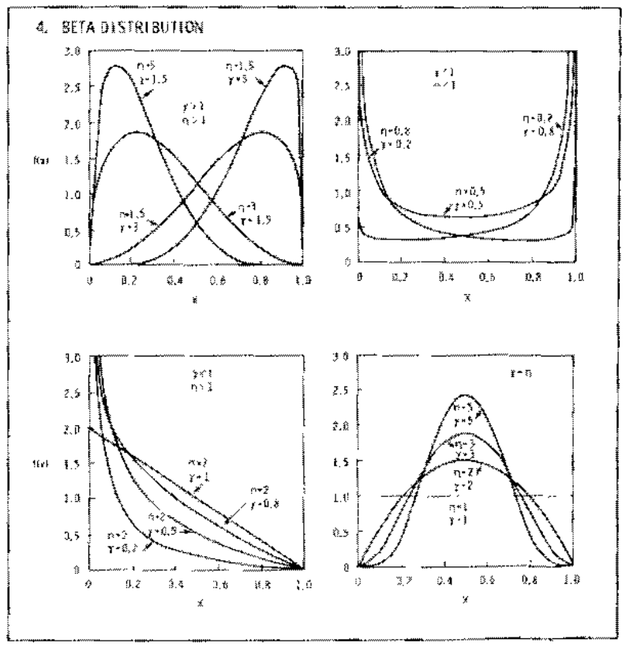

5. UNIFORM DISTRIBUTION

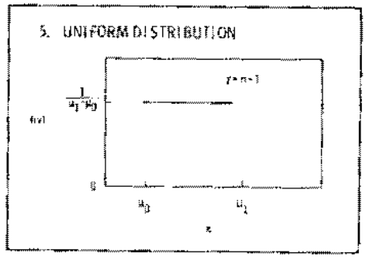

TABLE 11.3.2(a). Common Functions Used in Probability Modeling

FACTOR	CUMULATIVE DISTRIBUTION FUNCTION F(x)	PROBABILITY DENSITY FUNCTION f(x)	HAZARD FUNCTION h(x)	CUMULATIVE HAZARD FUNCTION H(x)	TIME TO FAILURE x(H)	EXPECTED VALUE (MEAN)	VARIANCE
TYPICAL TERMINOLOGY	PROBABILITY OF FAILURE BY TIME x						
LIMITS	F(x) IS 0 TO 1 AS x IS 0 TO ∞						
MOST COMMON INTERRELATIONS	$F(x) = \int_0^x f(x)dx$ $F(x) = 1 - \exp[-H(x)]$	$f(x) = \frac{d}{dx} F(x)$	$h(x) = \frac{f(x)}{1-F(x)}$	$H(x) = \int h(x)dx$ $H(x) = -\ln[1-F(x)]$			
DISTRIBUTION*							
1** EXPONENTIAL ($\lambda > 0$)	$F(x) = 1 - \exp(-x/\theta) = \frac{x}{\theta} = \lambda x$	$f(x) = \begin{cases} \frac{1}{\theta} \exp(-x/\theta) = \lambda \exp(-\lambda x) ; x \geq 0 \\ 0 \text{ ELSEWHERE} \end{cases}$	$h(x) = 1/\theta = \lambda$	$H(x) = x/\theta = x\lambda$	$x(H) = \theta H = \frac{H}{\lambda}$	$1/\lambda$	$1/\lambda^2$
2** WEIBULL ($\alpha > 0$) (ALSO TYPE III ASYMPTOTIC FOR MINIMUM VALUES) $\eta > 0$; $\sigma > 0$	$F(x) = 1 - \exp\left[-\left(\frac{x}{\sigma}\right)^{\eta}\right]$	$f(x) = \begin{cases} \frac{\eta}{\sigma}\left(\frac{x}{\sigma}\right)^{\eta-1} \exp\left[-\left(\frac{x}{\sigma}\right)^{\eta}\right] ; x \geq 0 \\ 0 \text{ ELSEWHERE} \end{cases}$	$h(x) = \frac{\eta}{\sigma}\left(\frac{x}{\sigma}\right)^{\eta-1}$	$H(x) = \left(\frac{x}{\sigma}\right)^{\eta}$	$x(H) = \sigma H^{1/\eta}$	$\sigma\,\Gamma(1/\eta + 1)$	$\sigma^2[\Gamma(2/\eta) - \Gamma^2(1/\eta + 1)]$
3** NORMAL* $-\infty < x < \infty$ $\sigma > 0$	$F(x) = \frac{1}{\sigma(2\pi)^{1/2}} \int_{-\infty}^{t} \exp -(x-\mu)^2 dx = \Phi\frac{(x-\mu)}{\sigma}$	$f(x) = \frac{1}{\sigma(2\pi)^{1/2}} \exp -\frac{1}{2}\frac{(x-\mu)^2}{\sigma^2} = \frac{1}{\sigma}\,\Phi\frac{(x-\mu)}{\sigma}$	$h(x) = \frac{1}{\sigma}\frac{(x-\mu)}{\sigma} / 1 - \Phi\frac{(x-\mu)}{\sigma}$	$H(x) = -\ln\left[1 - \Phi\frac{(x-\mu)}{\sigma}\right]$	$x(H) = \mu + \sigma\,\Phi^{-1}\,(1-\exp-(H)$	μ	σ^2
4** LOG-NORMAL* $(x \geq 0)$ $-\infty < \mu < \infty$ $\sigma > 0$	$F(x) = \Phi\left(\frac{\log x - \mu}{\sigma}\right)$	$f(x) = \frac{1}{\sigma x (2\pi)^{1/2}} \exp\left[\frac{-1}{2\sigma^2}(\log x - \mu)^2\right] = \frac{0.4343}{x\sigma}\,\Phi\left(\frac{\log x - \mu}{\sigma}\right)$	$h(x) = \frac{\frac{0.4343}{x\sigma}\,\Phi\frac{\log x - \mu}{\sigma}}{1 - \Phi\frac{\log x - \mu}{\sigma}}$	$H(x) = -\ln\left[1 - \Phi\frac{(\log x - \mu)}{\sigma}\right]$	$\log x(H) = \mu + \sigma\,\Phi^{-1}\,1-\exp-(H)$	$\exp(\mu + \sigma^2/2)$	$\exp(2\mu + \sigma^2)[\exp(\sigma^2) - 1]$
5** SMALLEST EXTREME VALUE $-\infty < x < \infty$ OR TYPE I ASYMPTOTIC FROM MINIMUM VALUE $\sigma > 0$	$F(x) = 1 - \exp\left[-\exp\left(\frac{x-\mu}{\sigma}\right)\right]$	$f(x) = \frac{1}{\sigma}\exp\left[\frac{1}{\sigma}(x-\mu) - \exp\frac{(x-\mu)}{\sigma}\right]$	$h(x) = \frac{1}{\sigma}\exp\frac{(x-\mu)}{\sigma}$	$H(x) = \exp\left(\frac{x-\mu}{\sigma}\right)$	$x(H) = \mu + \sigma \ln H$	$\mu - 0.577\sigma$	$1.645\sigma^2$
LARGEST EXTREME VALUE $-\infty < x < \infty$ OR TYPE I $\sigma > 0$	$F(x) = \exp\left[-\exp -\left(\frac{x-\mu}{\sigma}\right)\right]$	$f(x) = \frac{1}{\sigma}\exp\left[\frac{1}{\sigma}(x-\mu) - \exp\frac{1}{\sigma}(x-\mu)\right]$	$h(x) = \frac{\exp -[1/\sigma](x-\mu)}{\sigma \exp \exp -[1/\sigma](x-\mu) - 1}$	$H(x) = \exp \exp -\frac{(x-\mu)}{\sigma}$	$\mu + 0.577\sigma$		$1.645\sigma^2$

NOTES:

*FOLLOWING FUNCTIONS USED WITH NORMAL $\quad \Phi(u) = \frac{1}{(2\pi)^{1/2}} \int_{-\infty}^{\mu} \exp -\frac{(u^2)}{2}\, du$; $\quad \Phi(u) = \frac{1}{(2\pi)^{1/2}} \exp -\frac{u^2}{2}$

**SEE FIGURES AT BOTTOM OF PAGE

***$B_1 = \dfrac{\Gamma(1+3/\eta) - 3\Gamma(1+2/\eta)\Gamma(1+1/\eta) + 2[\Gamma(1+1/\eta)]^3}{[\Gamma(1+2/\eta) - [\Gamma(1+1/\eta)]^2]^{3/2}}$

****$B_2 = \dfrac{\Gamma(1+4/\eta) - 4\Gamma(1+3/\eta)\Gamma(1+1/\eta) + 6\Gamma(1+2/\eta)[\Gamma(1+1/\eta)]^2 - 3[\Gamma(1+1/\eta)]^4}{[\Gamma(1+2/\eta) - [\Gamma(1+1/\eta)]^2]^2}$

*****$B_2 = 3 + (W^4 + 2W^3 + 3W^2 + 6W + 6)(W + \exp\sigma^2$

1. EXPONENTIAL DISTRIBUTION

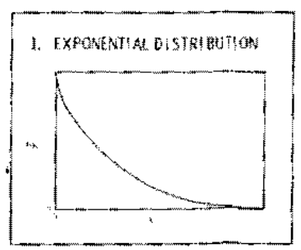

2. WEIBULL DISTRIBUTION

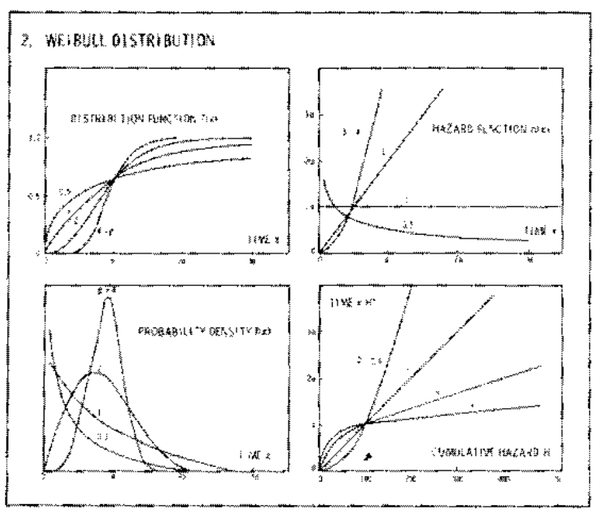

3. NORMAL DISTRIBUTION

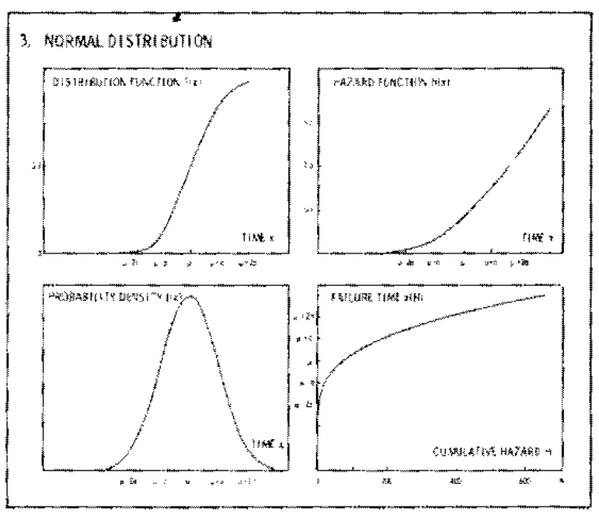

4. LOG-NORMAL DISTRIBUTION

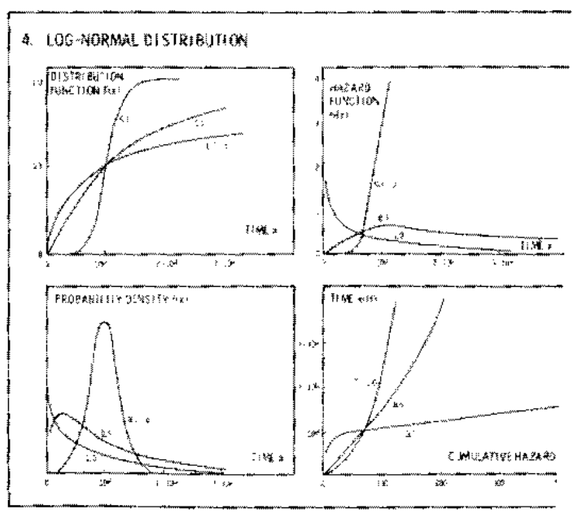

TABLE 11.3.2(a). Common Functions Used in Probability Modeling

DISTRIBUTION FUNCTION F(x)	PROBABILITY DENSITY FUNCTION f(x)	HAZARD FUNCTION h(x)	CUMULATIVE HAZARD FUNCTION H(x)	TIME TO FAILURE x(H)	EXPECTED VALUE (MEAN)	MOMENTS OF DISTRIBUTION FIRST (ALWAYS ZERO)	SECOND (VARIANCE)	THIRD (SKEWNESS) $B_1^{1/2}$	FOURTH (KURTOSIS) B_2
E BY TIME x									
TO ∞	$f(x) = \frac{d}{dx} F(x)$	$h(x) = \frac{f(x)}{1-F(x)}$	$H(x) \int h(x)dx$ $H(x) = -\ln[1-F(x)]$						
x	$f(x) = \begin{cases} \frac{1}{\theta} \exp(-x/\theta) = \lambda \exp(-\lambda x) ; x \geq 0 \\ 0 \text{ ELSEWHERE} \end{cases}$	$h(x) = 1/\theta = \lambda$	$H(x) = x/\theta = x\lambda$	$x(H) = \theta H = \frac{H}{\lambda}$	$1/\lambda$	$1/\lambda^2$	2.0	9.0
	$f(x) = \begin{cases} \frac{\eta}{\sigma}\left(\frac{x}{\sigma}\right)^{\eta-1} \exp\left[-\left(\frac{x}{\sigma}\right)^{\eta}\right]; x \geq 0 \\ 0 \text{ ELSEWHERE} \end{cases}$	$h(x) = \frac{\eta}{\sigma}\left(\frac{x}{\sigma}\right)^{\eta-1}$	$H(x) = \left(\frac{x}{\sigma}\right)^{\eta}$	$x(H) = \sigma H^{1/\eta}$	$\sigma\Gamma(1/\eta + 1)$	$\sigma^2 \{\Gamma(2/\eta + 1) - [\Gamma(1/\eta + 1)]^2\}$	***	****
$\exp-(x-\mu)^2 dx = \Phi\frac{(x-\mu)}{\sigma}$	$f(x) = \frac{1}{\sigma(2\pi)^{1/2}} \exp-\frac{1}{2}\frac{(x-\mu)^2}{\sigma^2} = \frac{1}{\sigma}\Phi\frac{(x-\mu)}{\sigma}$	$h(x) = \frac{1}{\sigma}\frac{(x-\mu)}{\sigma} / 1-\Phi\frac{(x-\mu)}{\sigma}$	$H(x) = -\ln\left[1-\Phi\frac{(x-\mu)}{\sigma}\right]$	$x(H) = \mu + \sigma\ \Phi^{-1}\ (1-\exp-(H)$	μ	σ^2	0	3
	$f(x) = \frac{1}{\sigma x (2\pi)^{1/2}} \exp\left[\frac{-1}{2\sigma^2}(\log x-\mu)^2\right] = \frac{0.4343}{x\sigma}\Phi\left(\frac{\log x-\mu}{\sigma}\right)$	$h(x) = \frac{\frac{0.4343}{x\sigma}\Phi\frac{\log x-\mu}{\sigma}}{1-\Phi\frac{\log x-\mu}{\sigma}}$	$H(x) = -\ln\left[1-\Phi\frac{(\log x-\mu)}{\sigma}\right]$	$\log x(H) = \mu + \sigma\Phi^{-1}\ 1-\exp-(H)$	$\exp(\mu + \sigma^2/2)$	$\exp(2\mu + \sigma^2)\left[(\exp\sigma^2)-1\right]$	$\left[(\exp\sigma^2)-1\right]^{1/2}\left[(\exp\sigma^2)+2\right]$	*****
$\left.\frac{\mu}{\sigma}\right)\Big]$	$f(x) = \frac{1}{\sigma}\exp\left[\frac{1}{\sigma}(x-\mu) - \exp\frac{(x-\mu)}{\sigma}\right]$	$h(x) = \frac{1}{\sigma}\exp\frac{(x-\mu)}{\sigma}$	$H(x) = \exp\left(\frac{x-\mu}{\sigma}\right)$	$x(H) = \mu + \sigma \ln H$	$\mu - 0.577\sigma$	–	-1.14	–
]	$f(x) = \frac{1}{\sigma}\exp\left[\frac{-1}{\sigma}(x-\mu) - \exp\frac{-1}{\sigma}(x-\mu)\right]$	$h(x) = \frac{\exp -(1/\sigma)(x-\mu)}{\sigma \exp \exp-(1/\sigma)(x-\mu)^{-1}}$	$H(x) = \exp \exp-\frac{(x-\mu)}{\sigma}$		$\mu + 0.577\sigma$	$1.645\sigma^2$	1.14	5.4

$\exp-\frac{(u^2)}{2}\ du;$ $\quad \Phi(u) = \frac{1}{(2\pi)^{1/2}} \exp -\frac{u^2}{2}$

$(\eta)]^4$

RIBUTION

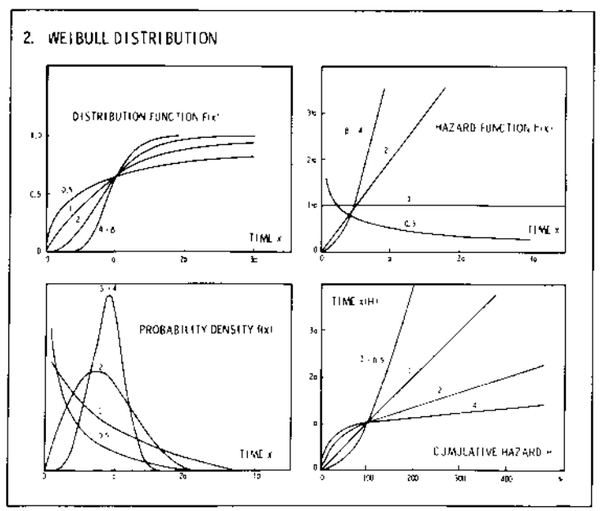

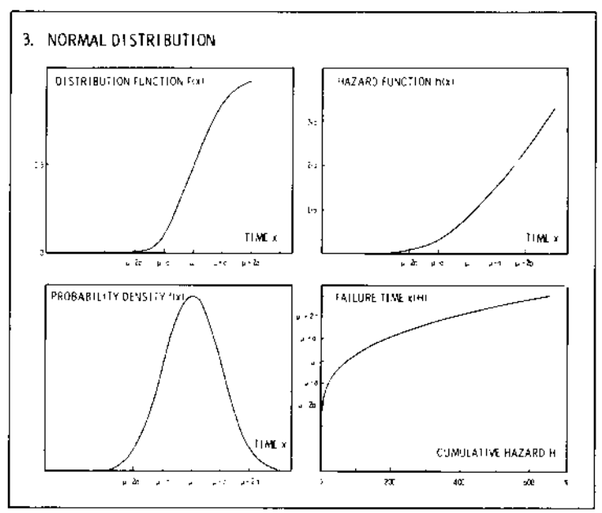

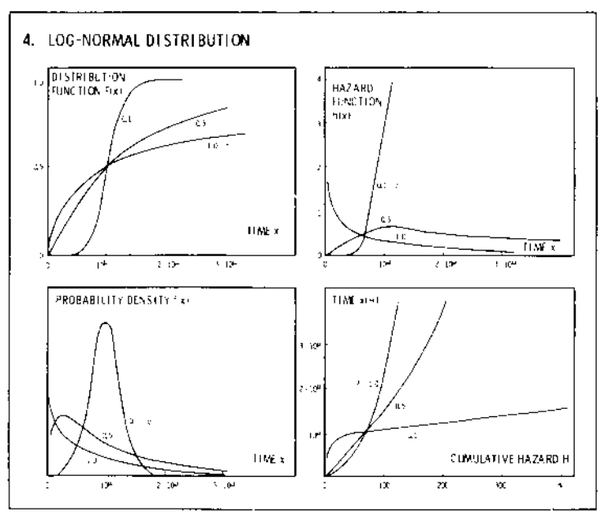

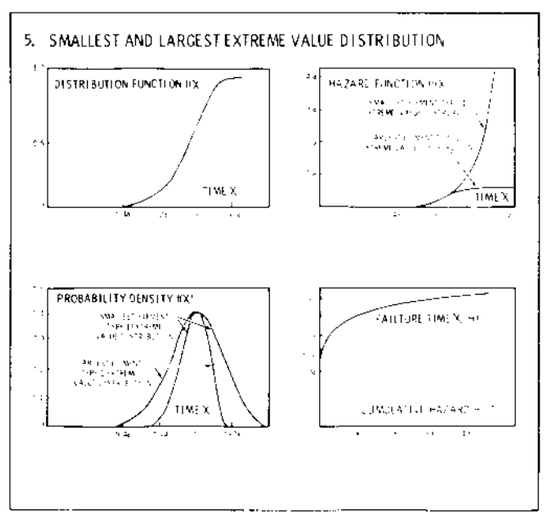

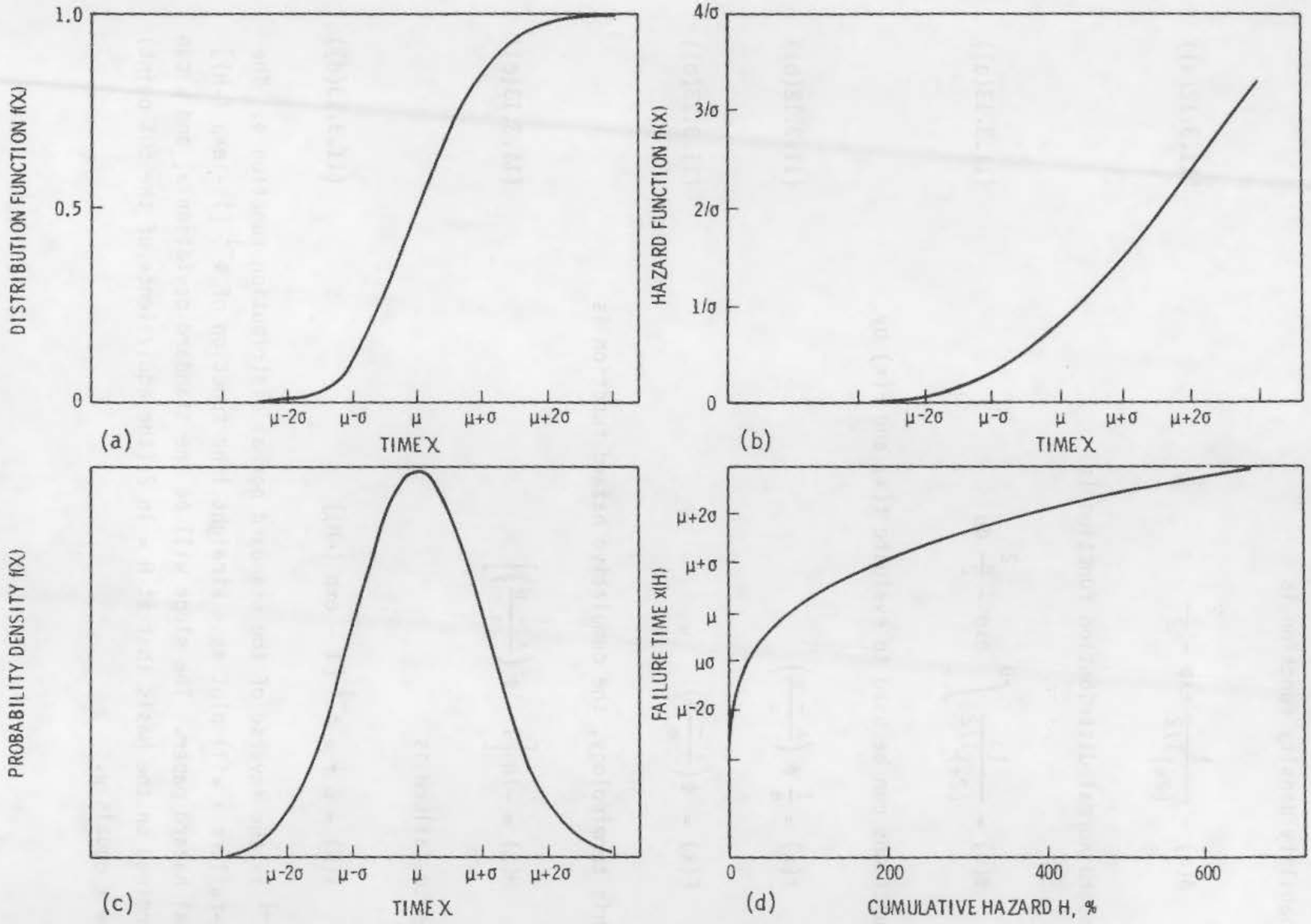

FIGURE 11.3.5. Normal Distribution

The probability density function is

$$\phi(u) = \frac{1}{(2\pi)^{1/2}} \exp - \frac{u^2}{2} \qquad (11.3.12(a))$$

The standard normal distribution function is

$$\Phi(u) = \frac{1}{(2\pi)^{1/2}} \int_{-\infty}^{u} \exp - \frac{u^2}{2}\, du \qquad (11.3.13(a))$$

These functions can be used to evaluate f(x) and F(x) by

$$f(x) = \frac{1}{\sigma} \phi \left(\frac{x - \mu}{\sigma}\right) \qquad (11.3.12(b))$$

$$F(x) = \Phi\left(\frac{x - \mu}{\sigma}\right) \qquad (11.3.13(b))$$

Using this terminology, the cumulative hazard function is

$$H(x) = -\ln \left[1 - \Phi \left(\frac{x - \mu}{\sigma}\right)\right] \qquad (11.3.13(c))$$

and time-to-failure is

$$x(H) = \mu + \sigma\, \Phi^{-1} [1 - \exp (-H)] \qquad (11.3.13(d))$$

where Φ^{-1} is the inverse of the standard normal distribution function Φ. The time-to-failure x will plot as a straight line function of $\Phi^{-1} [1 - \exp (-H)]$ on normal hazard paper. The slope will be the standard deviation σ, and μ can be determined on the basis that at $H = \ln 2$ (the equivalence of the 50% point) the time x equals μ.

11.3.5 The Log-Normal Distribution

The same functions $\phi(u)$ 11.3.12(a) and $\phi(u)$ 11.3.13(a) may be used to develop the equations for the log-normal distributions:

Hazard function -

$$h(x) = \frac{\frac{0.4343}{x\sigma}\,\phi\left(\frac{\log x - \mu}{\sigma}\right)}{1 - \Phi\left(\frac{\log x - \mu}{\sigma}\right)} \qquad (11.3.14(a))$$

Probability density function -

$$f(x) = \frac{0.4343}{x\sigma}\,\phi\left(\frac{\log x - \mu}{\sigma}\right) \qquad (11.3.14(b))$$

Cumulative distribution -

$$F(x) = \Phi\left(\frac{\log x - \mu}{\sigma}\right) \qquad (11.3.14(c))$$

Cumulative hazard function -

$$H(x) = -\ln\left[1 - \Phi\left(\log\frac{x - \mu}{\sigma}\right)\right] \qquad (11.3.14(d))$$

Time-to-failure -

$$\log x(H) = \mu + \sigma\,\Phi^{-1}\,[1 - \exp(-H)] \qquad (11.3.14(e))$$

Note that base 10 logarithms are used since this facilitates plotting. For these functions the alternative approach is to use the functions in the fully developed form. These will be for the probability density function and cumulative probability function.

$$f(x) = \frac{1}{\sigma x (2\pi)^{1/2}} \exp\left[-\frac{1}{2\sigma^2}(\ln x - \mu)^2\right] \qquad (11.3.14(f))$$

$$F(x) = \frac{1}{\sigma (2\pi)^{1/2}} \int_{-\infty}^{x} \exp -\left[\frac{1}{2\sigma^2}(\ln x - \mu)^2\right] \qquad (11.3.14(g))$$

The failure rate is zero at time zero, and increases with time to a maximum, then decreases back to zero with increasing time (see Figure 11.3.6). Obviously, this characteristics of decreasing to zero after some time may make it unsuitable for wearout failure. A Weibull cumulative distribution function with a shape parameter value of less than 2 will be close to certain log-normal functions on the lower tail. Therefore, it may be difficult to choose between Weibull and log normal for a given set of data, leading to problems because different conclusions as to failure rate in the upper tail will result. This will be discussed further in a later section.

The log-normal distribution is related to the gamma distribution as a time-to-failure distribution. The gamma distribution may be considered as a generalization of the exponential distribution where failure occurs as soon as exactly k events have taken place, assuming such events occur independently at a constant rate. Therefore, the gamma distribution is an appropriate time-to-failure model for a system with one operating unit and k-1 standby units where a new unit goes into operation as soon as the preceding unit has failed and where each of the units has an exponential time-to-failure distribution during operation. System failure occurs when the last unit fails. As k increases, the gamma distribution approaches a normal distribution. In this case, the system time-to-failure would not be peaked near zero so the earlier objection to the normal distribution versus a time-to-failure model is not applicable.

The justification of the log-normal distribution to represent time-to-failure is based on the multiplicative-effect properties of that distribution. However, this property leads more directly to a log-normal distribution for the degree of deterioration by a specified time than for the time-to-failure.

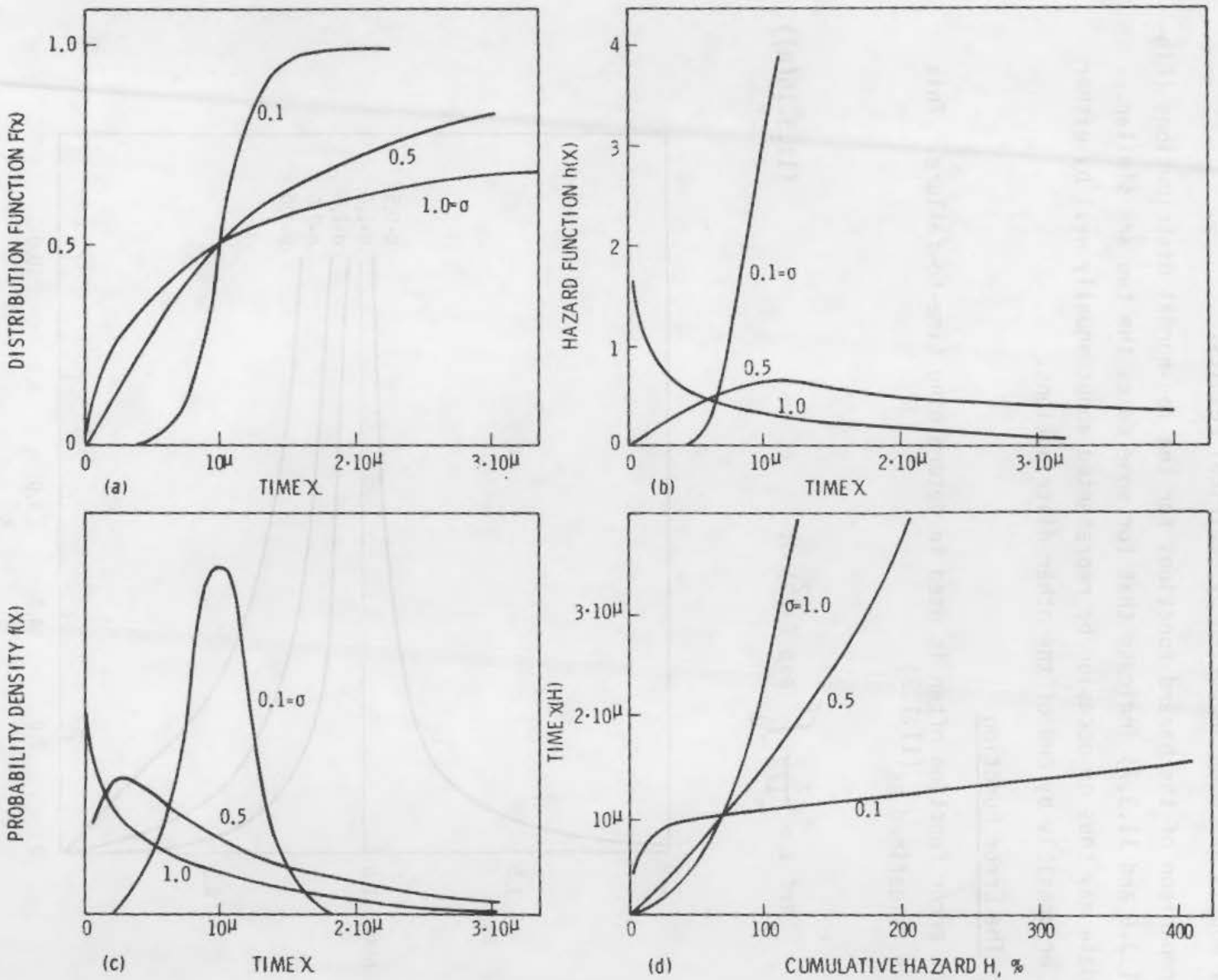

FIGURE 11.3.6. Log-Normal Distributions

The theory supporting the gamma and log-normal distributions as time to failure models has been supported by empirical results.

Comparison of the hazard functions for the log-normal distributions (Figures 11.3.6 and 11.3.7) indicate that for some cases the two are similar. Given data may thus on occasion be represented about equally well by either model, or possibly by one of the other distributions.

11.3.6 The Error Function

The error function often is used in determining time-to-failure. This function is defined as(11.1.3)

$$\text{erf } z = \frac{2}{\pi^{1/2}} \int_0^z \exp(-t^2)\, dt \qquad (11.3.15(a))$$

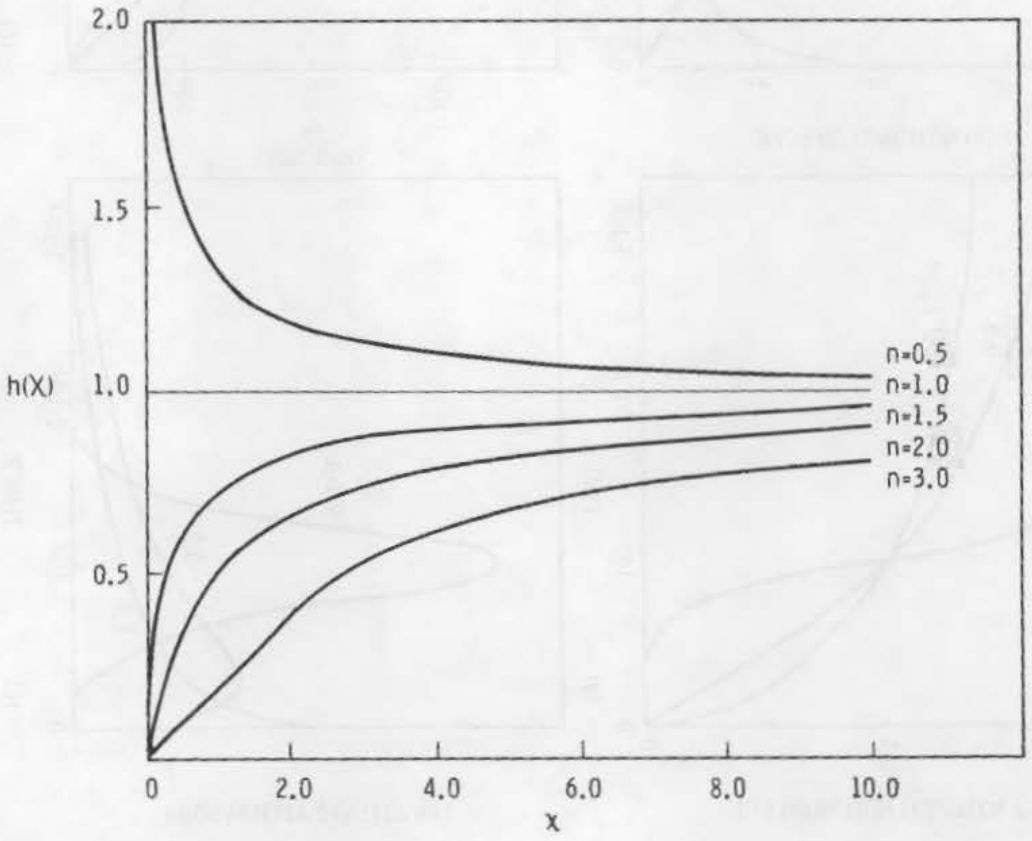

FIGURE 11.3.7. Hazard Functions for Gamma Distributions with $\lambda = 1$

The complementary error function is

$$\text{erfc } z = \frac{2}{\pi^{1/2}} \int_z^\infty \exp(-t^2)\, dt \qquad (11.3.15(b))$$

$$\text{erfc } z = 1 - \text{erf } z$$

In terms of a normal (Gaussian) distribution,

$$F(x) = \frac{1}{\sigma(2\pi)^{1/2}} \int_{-\infty}^{x} \exp - \frac{1}{2}\left[\frac{(x-\mu)}{\sigma}\right]^2 dx \qquad (11.3.11(a))$$

In terms of the error function, Equation 11.3.11(a) becomes

$$F(x) = \frac{1}{2}\left[1 + \text{erf}\left(\frac{x-\mu}{\sigma 2^{1/2}}\right)\right] \qquad (11.3.15(c))$$

In like fashion, the log-normal distribution becomes

$$F(x) = \frac{1}{2}\left[1 + \text{erf } \ln\left(\frac{x-\mu}{\sigma 2^{1/2}}\right)\right] \qquad (11.3.15(d))$$

These substitutions simplify the evaluation of the equations.

11.3.7 Examples of Hazard Function Calculations

Solutions of problems in terms of hazard functions are relatively uncommon in the literature compared to other probability functions. The following problem pertaining to turbine-generator failure probabilities has been modified in terminology to agree with that used in this chapter. Two continuous functions are used in the solution. The first is the Weibull, and the second a Duane model, which is derived to indicate that probably it is a hybrid exponential-Weibull (and somewhat suspect); however, the Duane model is one of the few methods of expressing failure rates in terms of cumulative operating time in a chronological sequence.

The Weibull Function is believed to yield the most meaningful values of reliability, cumulative failure rate, and instantaneous failure rate for problems such as turbine failure. This technique has been used extensively in the evaluation of both large and small populations of pressure vessels. Other time-to-failure models such as exponential, gamma and log-normal have serious limitations. For example, unlike the exponential model the Weibull has the flexibility to handle hazard functions which vary with time. It was necessary to place the equation in linear form to permit a regression analysis. The procedure used is presented here, combining approaches cited elsewhere.(11.3.1)

Tables 11.3.3(a) and 11.3.3(b) contain all data necessary to conduct a linear regression analysis for any specific combination of failures; e.g., all failures, all missiles, relevant failures, relevant missiles (Figure 11.3.8). Table 11.3.3(b) summarizes the data from all regression analyses and includes the Weibull functions for reliability R(x) and failure rate h(x). The reliability represents the effect of cumulative failures.

The failure rate equation permits one to determine the time-dependent failure rate, h(x), for any time during operation, and to extrapolate to end-of-life. Figure 11.3.9 covers the two cases of failures and failures with missiles. Based on these curves, there is no indication of wear-out near end-of-life. The instantaneous (time-dependent) failure rate, h(x), for the missile case varies from about 7×10^{-3} to 4×10^{-2}. Since these are expressed in percentage, a conversion to rates yields 7×10^{-5} to 4×10^{-4} which compares favorably to the Duane Model λ_t. These comparisons are given in Table 11.3.4.

Table 11.3.4 also includes values for Weibull distributions covering "relevant" failures and "relevant" missiles in the context of relevance to nuclear reactors. This relevance, as cited earlier, is a highly subjective judgment. Even if the selection is accepted, a valid question can be raised concerning the number of turbines used as a denominator in calculating the hazard function in Table 11.3.3(a). If one is selective in the numerator values, it follows that one may need to be selective in the denominator. This approach was explored for the "relevant" missiles case and data are presented in Table 11.3.5. The population after retirement was considered as a base line then expanded by 1.33 to cover those failures outside the known population.

TABLE 11.3.3(a). Data Arranged for Regression Analysis in Calculating Weibull Distribution (Maximum Population Assumed Without Retirement x 1.33)[a]

	Failure (Year)	Turbine Population Greater Than Failure Time	Operating Years Prior To Failure	Failures (1) All	(2) Missiles	(3) Relevant Failure	(4) Relevant Missiles	Hazard (1)	(2)	(3)	(4)	H(x) Cumulative Hazard (1)	(2)	(3)	(4)
1	Ariz. Pub. Ser (54)	6675	0.08	1				0.015				0.015			
2	Calder Hall (58)	6675	0.08	1	1	1	1	0.015	0.015	0.015	0.015	0.030	0.015	0.015	0.015
3	Siemens (51)	6650	0.17	1	1			0.015	0.015			0.045	0.030		
4	Cromby-1 (51)	6625	0.25	1				0.015				0.060			
5	Ridgeland (54)	6575	0.42	1	1			0.015	0.015			0.075	0.045		
6	Uskmouth (56)	6525	0.58	1	1	1	1	0.015	0.015	0.015	0.015	0.090	0.060	0.030	0.030
7	Kainan (72)[a]	6500	0.67	1				0.015				0.115			
8	unknown (58)[a]	6475	0.75	1	1	1	1	0.015	0.015	0.015	0.015	0.120	0.075	0.045	0.045
9	ENESA (70)[a]	6450	0.83	1	1			0.016	0.016			0.136	0.091		
10	BBC-Denmark (75)	6375	1.30	1				0.016				0.152			
11	Utah Power (76)	6350	1.50	1				0.016				0.168			
12	Tanners Creek (53)	6325	1.70	1				0.016				0.184			
13	Nanticoke (74)[a]	6325	1.70	1				0.016				0.200			
14	Pittsburg-1 (56)	6315	1.80	1				0.016				0.216			
15	Hearn-1 (54)[b]	6225	2.30	1	1			0.016	0.016			0.232	0.107		
16	Hearn-2 (54)[b]	6150	2.70	1	1			0.016	0.016			0.248	0.123		
17	Alstrom-Rateau (77)[b]	6125	2.80	1				0.017				0.265			
18	Hinkley Point (69)	6000	3.40	1	1	1	1	0.017	0.017	0.017	0.017	0.282	0.140	0.062	0.062
19	Hinkley Point (70)	6000	3.40	1	1			0.017	0.017			0.299	0.157		
20	Hinkley Point (69)	5925	3.80	1	1			0.017	0.017			0.316	0.174		
21	Unknown (58)[a]	5800	4.50	1	1	1		0.017	0.017	0.017		0.333	0.191	0.079	
22	Bold (60)	5725	5.90	1	1	1	1	0.017	0.017	0.017	0.017	0.350	0.208	0.096	0.079
23	Cutler-6 (69)	5250	9.50	1				0.019				0.369			
24	Sendai (72)	4500	13.5	1				0.022				0.391			
25	Northern States (71)	4350	14.5	1				0.023				0.414			
26	Shippingport (74)	4150	15.5	1		1		0.024		0.024		0.438		0.120	
27	Gallatin (74)	3850	17.5	1	1			0.026	0.026			0.464	0.234		
28	Morenci-3 (59)	3820	17.8	1	1			0.026	0.026			0.490	0.260		
29	Oak Creek (77)	2875	22.0	1	1	1	1	0.035	0.035	0.035	0.035	0.525	0.295	0.155	0.114
30	Essex-1 (72)	2075	25.5	1				0.048				0.573			

(a) 1.33 is correction factor to accommodate manufacturers outside known population.
(b) Not in known population.

TABLE 11.3.3(b). Regression Analysis Parameters for Weibull Distributions Covering All Known Turbine Failures, Failures Generating Missiles, "Relevant" Failures and Relevant Failures Generating Missiles; Pertinent Equations Given

Parameter	All Failures	All Missiles	Relevant Failures	Relevant Missiles
σ	41.9	151	2076	5900
$1/n$	1.77	1.92	2.41	2.70
n	0.57	0.52	0.41	0.37
r^2	0.94	0.95	0.98	0.97
γ (1 yr)	3.39	4.1	5.73	0.47
γ (10 yr)	19.3	21.4	27.4	30.7
γ (30 yr)	54.6	59.8	75.6	84.7
Sy X	0.17	0.16	0.12	0.16
S_o	0.07	0.12	0.17	0.30
S_1	0.08	0.11	0.13	0.22
$R(x) = \exp\left[-\left(\frac{x}{\sigma}\right)^n\right]$	$\exp\left(-1.2.10^{-3}x^{0.57}\right)$	$\exp\left(-7.36.10^{-4}x^{0.52}\right)$	$\exp\left(-4.36.10^{-4}x^{0.41}\right)$	$\exp\left(-4.02.10^{-4}x^{0.37}\right)$
$h(x) = \frac{\beta}{\alpha^\beta} x^{\beta-1} = \frac{n}{\sigma^n} x^{n-1}$	$6.78.10^{-2}x^{-0.43}$	$3.83.10^{-2}x^{-0.48}$	$1.79.10^{-2}x^{-0.59}$	$1.49.10^{-2}x^{-0.63}$
$H(x) = \frac{x^\beta}{\alpha} = \left(\frac{x}{\sigma}\right)^n$	$0.119\ x^{0.57}$	$7.36.10^{-2}x^{0.52}$	$4.36.10^{-2}x^{0.41}$	$4.02.10^{-2}x^{0.37}$
$x(H) = \sigma H^{1/n}$	$41.9\ H^{1.77}$	$151\ H^{1.92}$	$2076\ H^{2.41}$	$5900\ H^{2.70}$

R(x) multiplied exponent by 10^{-2} to get value.

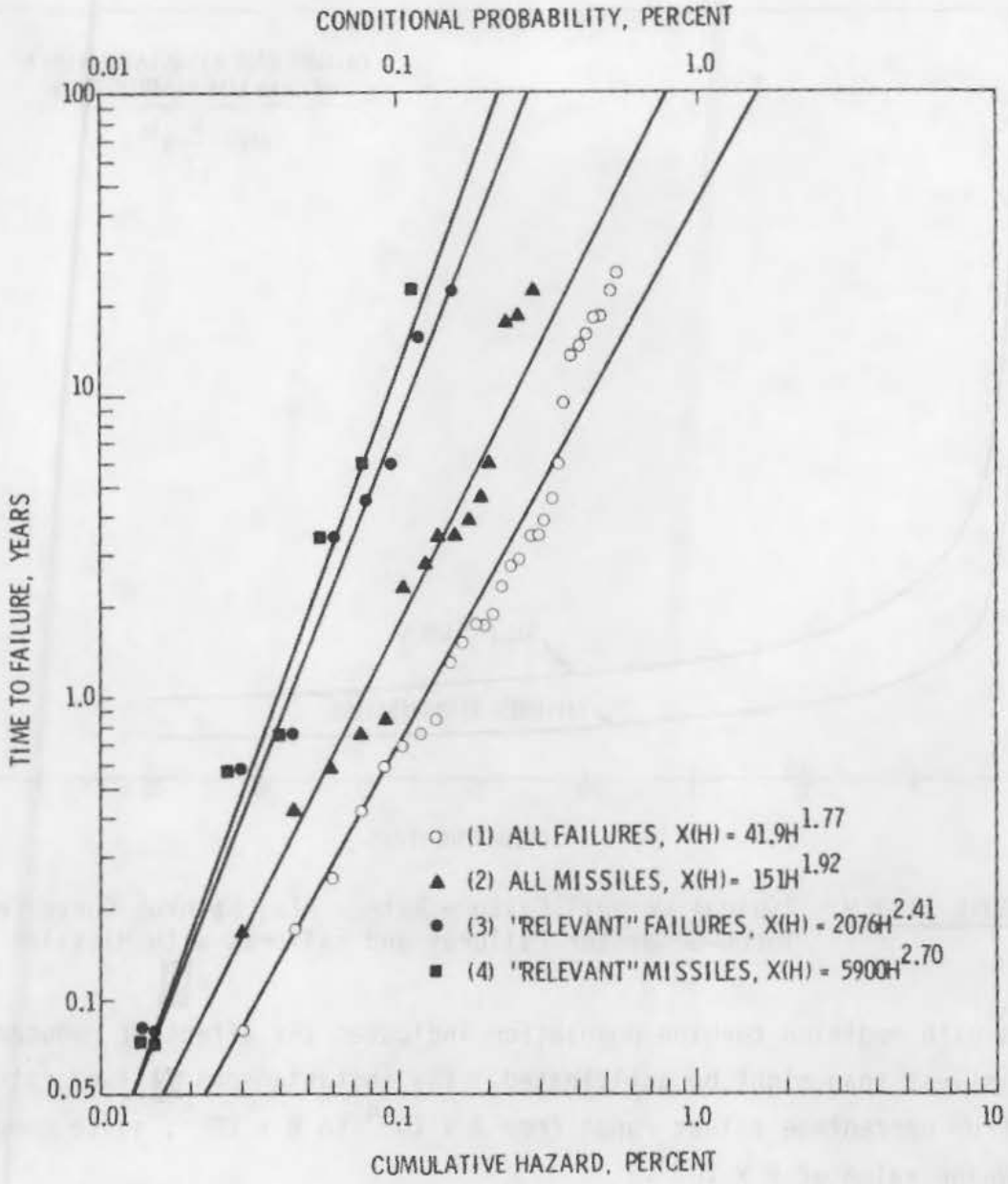

FIGURE 11.3.8. Regression Analyses, Weibull Hazard Plots of Turbo-Generator Failure Data

This population was reduced by two-thirds for failures early in life and approximately one-half for failures later in life to eliminate smaller units and those with different operating conditions than experienced by nuclear turbines. Again, this approach is quite arbitrary, but it does have the effect of shifting the regression line to higher values of H and changing the slope $1/n$. A comparison of $h(x)$ values for all missiles, relevant missiles and relevant

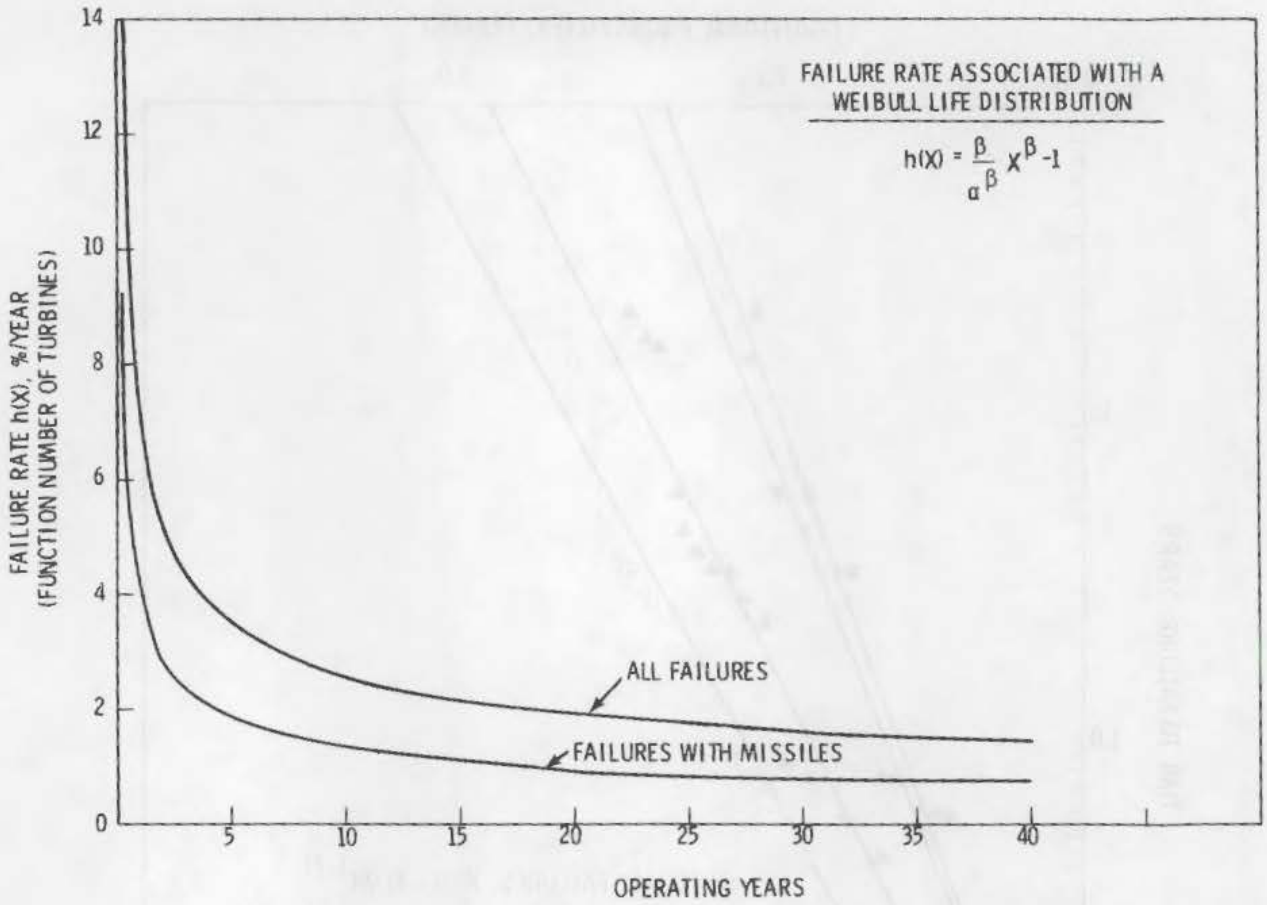

FIGURE 11.3.9. Typical Weibull Failure Rate = h(x) Bathtub Curve for Turbo-Generator Failures and Failures with Missiles

missiles with modified turbine population indicates the effect of reduced population is less than might be anticipated. The instantaneous failure rates converted from percentage values range from 3×10^{-4} to 8×10^{-5}, quite comparable to the Duane value of 5×10^{-5}.

Table 11.3.1 contains the terminology used in this section. Note that the reliability, R(x), is equal to 1 - F(x) on exp [-H(x)]. Also $F(x) \cong H(x)$ when the probability of failure is low. The justification for the preceding follows:

TABLE 11.3.4. Typical Values Obtained from Duane Equation and Weibull Distributions for Turbine Failures

DUANE EQUATION

TURBINE-YEARS

Parameter	All Missiles	Missiles Known Turbine Population
Cumulative Failure Rate (λ_Σ)		
1977	$1.26.10^{-4}$	$8.86.10^{-5}$
1987	$1.06.10^{-4}$	$7.59.10^{-5}$
Instantaneous Failure Rate (λ_X)		
1977	$7.28.10^{-5}$	$5.49.10^{-5}$
1987	$6.11.10^{-5}$	$4.71.10^{-5}$
Cumulative Mean Time Between Failures (MTBF)		
1977	$7.95.10^{3}$	$1.13.10^{4}$
1987	$9.47.10^{3}$	$1.32.10^{4}$
Instantaneous Mean Time Between Failures (MTBF)		
1977	$1.37.10^{4}$	$1.82.10^{4}$
1987	$1.64.10^{4}$	$2.13.10^{4}$

GLOBAL ESTIMATES

1977	$1.2.10^{-4}$	$9.1.10^{-5}$	$2.4.10^{-3}$	$1.8.10^{-3}$

WEIBULL DISTRIBUTION (ALL IN PERCENT)

Parameter	All Failures			All Missiles		
	1 Yr	10 Yr	30 Yr	1 Yr	10 Yr	30 Yr
Reliability [R(x)]	99.88	99.56	99.27	99.93	99.76	99.57
Instantaneous Failure Rate [(h(x)]	$6.78.10^{-2}$	$2.52.10^{-2}$	$1.57.10^{-2}$	$3.83.10^{-2}$	$1.27.10^{-2}$	$7.48.10^{-3}$
Cumulative Failure Rate [H(x)]	0.119	0.442	0.827	$7.36.10^{-2}$	0.244	0.432
	"Relevant" Failures			"Relevant Missiles"		
	1 Yr	10 Yr	30 Yr	1 Yr	10 Yr	30 Yr
Reliability [R(x)]	99.6	99.89	99.82	99.96	99.91	99.86
Instantaneous Failure Rate h(x)	$1.79.10^{-2}$	$4.6.10^{-3}$	$2.41.10^{-3}$	$1.49.10^{-2}$	$3.49.10^{-3}$	$1.75.10^{-3}$
Cumulative Failure Rate H(x)	$4.36.10^{-2}$	0.112	0.176	$4.02.10^{-2}$	$9.42.10^{-2}$	0.141

TABLE 11.3.5. Sensitivity Study Varying Turbine Population to Determine Effect on Weibull Distribution for "Relevant" Missiles

Failure Cause	Time-to-Failure Years	Turbine Population Table 11.3.3	Cumulative Hazard Table 11.3.3	Revised[a] Turbine Population	Hazard Value (%)	Cumulative Hazard (%)
Overspeed	0.08	6675	0.015	3400	0.036	0.030
Overspeed	0.58	6525	0.030	3200	0.030	0.060
Overspeed	0.75	6475	0.045	3100	0.031	0.091
SCC/Brittle	3.4	6000	0.062	2700	0.037	0.128
Overspeed	5.9	5725	0.079	2500	0.040	0.168
Brittle ?	22.0	2875	0.114	1250	0.080	0.248

(a) Revision based on using population with retirement. Time 1.33, which removes many smaller units, then taking 2/3 to 1/2 of this population as being "relevant" to nuclear.

VALUES FROM REGRESSION ANALYSIS

$\sigma = 651$ $\quad 1/\eta = 2.59$ $\quad \eta = 0.386$ $\quad r^2 = 0.98$

$$R(x) = \exp\left(-8 \times 10^{-4} x^{0.39}\right)$$

$$h(x) = 3.1 \times 10^{-2} x^{-0.61}$$

$$H(x) = 8 \times 10^{-2} x^{0.39}$$

$$x(H) = 651\ H^{2.59}$$

From Table 11.3.1,

$$R(x) = 1 - F(x)$$

$$H(x) = \ln\left[\frac{1}{1 - F(x)}\right]$$

$$\therefore\ H(x) = \ln \frac{1}{R(x)}$$

Let $R(x) = Z$:

By series expansion,

$$\ln Z = (Z - 1) - \frac{1}{2}(Z - 1)^2 + \frac{1}{3}(Z - 1)^3 \ldots \qquad (11.3.16)$$

If $|z - 1| \leq 1$ $z \neq 0$

Substituting

$$\ln \frac{1}{R(x)} = \frac{1}{R(x)} - 1 - \frac{1}{2}\left[\frac{1}{R(x)} - 1\right]^2 + \frac{1}{3}\left[\frac{1}{R(x)} - 1\right]^3 \ldots \qquad (11.3.17)$$

For high reliabilities, where $R(x) > 0.99$, only the first two terms in the expansion are significant, or

$$\ln \frac{1}{R(x)} \cong \frac{1}{R(x)} - 1 \qquad (11.3.18(a))$$

or

$$\ln \left[\frac{1}{1 - F(x)}\right] = \frac{1}{1 - F(x)} - 1 \qquad (11.3.18(b))$$

$$= \frac{1 - 1 + F(x)}{1 - F(x)} \qquad (11.3.18(c))$$

$$= \frac{F(x)}{1 - F(x)} \qquad (11.3.18(d))$$

If $R(x) \gtrsim 0.99$, $F(x) \lesssim 0.01$

or

$$\frac{F(x)}{1 - F(x)} \cong F(x) \qquad (11.3.18(e))$$

Recalling that

$$H(x) = - \ln [1 - F(x)]$$

For $F(x) \lesssim 0.01$

$$H(x) \cong F(x) \qquad (11.3.18(f))$$

The preceding approach can be applied to exponential functions or to Weibull functions using the series expansion to minimize terms in cases of high reliability.

For instance, using the preceding logic, the exponential equation given in Table 11.3.2 reduce to

$$H(x) = F(x) \cong \frac{x}{\sigma} \qquad (11.3.19)$$

for $R(x) > 0.99$

In the case of Weibull equations,

for $F(x) \lesssim 0.01$

$$F(x) \cong H(x) = \left(\frac{x}{\sigma}\right)^n \qquad (11.3.20)$$

Taking logarithms of $x(H) = \sigma H^{1/n}$,

$$\log x(H) = \left(\frac{1}{n}\right) \log H + \log \sigma$$

As Logs to Base 10, this will plot as a straight line function of H on Log-Log graph paper since Log x is a linear function of Log H. Thus, Weibull Hazard

paper is merely Log-Log Graph paper. The slope of the straight line equals $1/\eta$; this fact is used to estimate η from data plotted on Weibull Hazard paper. Also for $H = 1$ the corresponding time x equals σ; this fact is used to estimate σ from data plotted on Weibull Hazard paper.

Note that

$\eta > 0$ is the shape parameter

$\sigma > 0$ is the scale parameter

A linear regression will quantify σ and η. Since most statistical routines include the Weibull Function, the equation can be quantified covering time-to-failure, cumulative hazard values, and average failure probability per service year.

Duane model equations have been used to determine cumulative and current failure rates for low probability events. While reservations have been expressed concerning the validity of the Duane equations, they appear to parallel Weibull results as noted in the following:

The Duane Model equation is

$$\lambda_{\Sigma} = \frac{F}{H} = KH^{-\alpha} \qquad (11.3.21)$$

where λ_{Σ} = cumulative failure rate
H = total test time (years or hours)
F = failures during H
K = constant
α = growth rate (normally 0.3 to 0.5)

Note that a modification of the Weibull Function,

$$H(x) = \sigma x^{\eta} \qquad (11.3.22)$$

to a rate function,

$$\frac{H(T)}{T} = \alpha T^{\beta-1} \text{ cumulative hazard } \underline{\text{rate}} \qquad (11.3.23)$$

$$\frac{H(x)}{x} = \sigma x^{n-1}$$

is similar to the Duane Model

where	Weibull	Duane
	σ	K
	$n - 1$	$-\alpha$
	x	H
	$H(x)/x$	λ_Σ

This would indicate the Duane Model is a hybrid Exponential/Weibull.

A regression analysis was made using the equation

$$\ln \lambda_\Sigma = \ln K - \alpha \ln H \qquad (11.3.24)$$

In addition to the regression coefficients (K,α), values of r^2, $s_y \cdot X$, S_o, and S_1 were obtained

where r^2 = coefficient of determination, a measurement of the "goodness of fit" of the regression line; $0 \leq r^2 \leq 1$ $r^2 = 1$ is a perfect fit

$S_y \cdot X$ = standard error of estimate of y on X

S_o = standard error of the regression coefficient a_o

S_1 = standard error of the regression coefficient, a_1

The preceding are evaluated in Tables 11.3.6(a) and 11.3.6(b). Table 11.3.4 permits a comparison of Weibull and Duane Model results. Figure 11.3.10 contains cumulative and instantaneous failure rates. As can be seen, the two approaches agree relatively well.

11.3.8 Other Continuous Distributions

The distributions cited previously in 11.3 are those most commonly used; however, there are other distributions used under certain circumstances. These distributions will be discussed more extensively in Section 11.5. At this time, only the distributions of interest will be noted. They, together with those covered previously in this section, are given in Table 11.3.2.

TABLE 11.3.6(a). Data Necessary for Duane Equation Regression Analysis (Turbine Years Only)

Year	H Turbine Years x 1.33	F Cumulative Missiles	$\frac{F}{H}$	$H(a)$ Turbine Years	$F(a)$ Cumulative Missiles	$\frac{F(a)}{H(a)}$
1954	21 100	5	$2.4.10^{-4}$	15 860	3	$1.8.10^{-4}$
1956	25 600	6	$2.3.10^{-4}$			
1958	33 700	8	$2.4.10^{-4}$			
1959	37 400	9	$2.4.10^{-4}$			
1960	41 300	10	$2.4.10^{-4}$	31 050	4	$1.3.10^{-4}$
1969	85 200	12	$1.4.10^{-4}$	64 060	6	$9.4.10^{-5}$
1970	90 800	14	$1.5.10^{-4}$	68 250	7	$1.0.10^{-4}$
1974	115 000	15	$1.3.10^{-4}$	86 100	8	$9.3.10^{-5}$
1977	133 000	16	$1.2.10^{-4}$	99 030	9	$9.1.10^{-5}$

(a) Denotes failures and data within known population.

TABLE 11.3.6(b). Regression Analyses for Duane Equation Limited to Missiles Only

Parameter	All Missiles	Missiles Known Population
Factor (F)	16	9
a_0 (Log K)	-1.7487	-2.1532
K	$1.78.10^{-2}$	$7.03.10^{-3}$
a_1 (α)	-0.42	-0.38
r^2	0.894	0.960
Years		
$\hat{\lambda}$ ($H = 10^4$)	$3.74.10^{-4}$	$3.68.10^{-4}$
$\hat{\lambda}$ ($H = 5.10^4$)	$1.90.10^{-4}$	$1.12.10^{-4}$
$\hat{\lambda}$ ($H = 10^5$)	$1.42.10^{-4}$	$8.0.10^{-5}$
$S_{y \cdot X}$	0.046	0.027
S_0	0.259	0.184
S_1	0.055	0.004

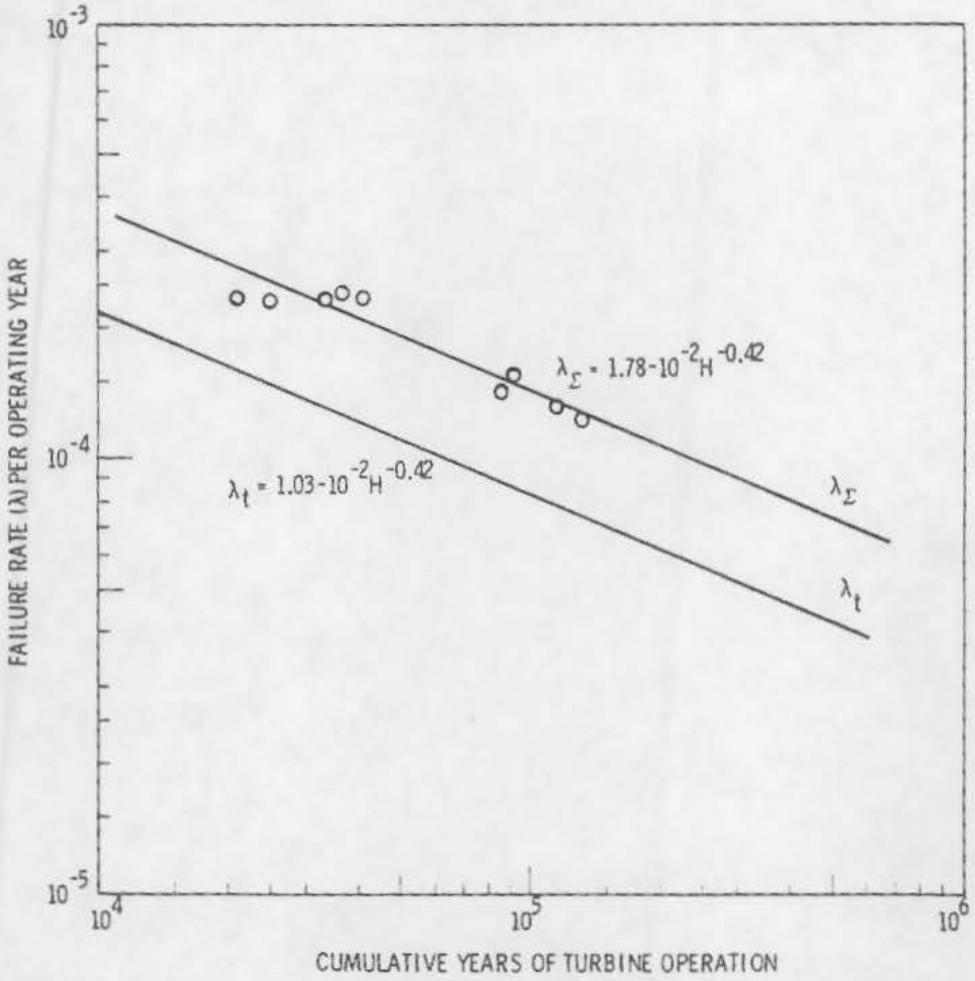

FIGURE 11.3.10. Duane Equation Plot of Cumulative and Current Failure Rates for Turbines (External Missiles Only) as a function of cumulative years of turbine operation (x1.33).

11.4 DISCRETE DISTRIBUTIONS

The various discrete distributions have specific albeit limited applications. They find less use than is the case for the continuous distributions discussed in Sections 11.3 and 11.5. There are interrelationships among these functions as is the case with continuous distributions. Table 11.4.1 permits a comparison of these interrelationships. Table 11.4.2 contains these discrete distributions and their means, variances, $B_1^{1/2}$, B_2 values.

Packman[11.4.1] cites some of the major uses of the binomial and Poisson distributions in components; namely, for nondestructive examination. Since NDE basically is a yes-no situation, it is described by discrete distributions such as the binomial where p will indicate the true probability of detection and q the true probability of a miss. If the number of examinations is large and the flaw detection probability high (>0.90) or low (<0.10), the Poisson distribution can be used. Table 11.4.2 contains the mathematical formulation for the discrete distributions.[11.1.2]

TABLE 11.4.1. Relative Relationships Among Various Oiscrete Oistributions

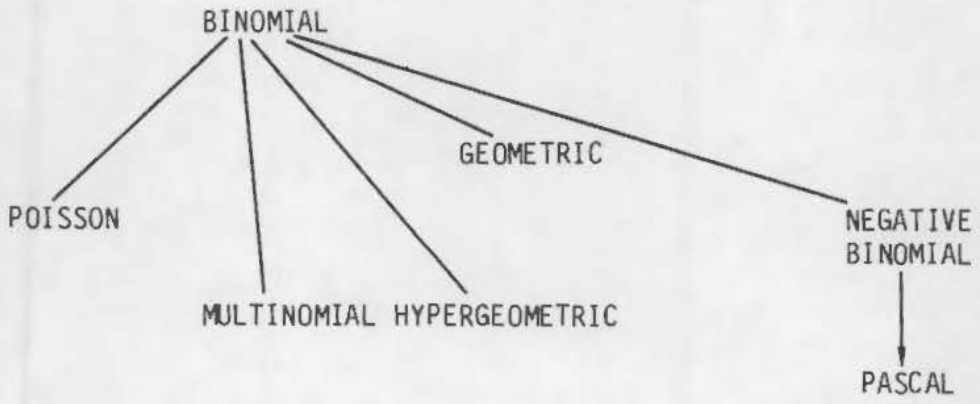

TABLE 11.4.2. Summary of Important Discrete Distributions

DISTRIBUTION NAME	PARAMETERS	PROBABILITY FUNCTION	EXPECTED VALUE	VARIANCE	$\sqrt{\beta_1}$	β_2
1.** GEOMETRIC	$0 \le p \le 1$	$(1-p)^{x-1}p,\ x = 1,2,\ldots$	$\frac{1}{p}$	$\frac{1-p}{p^2}$	$\frac{2-p}{(1-p)^{1/2}}$	$\frac{p^2-9p+9}{1-p}$
2.** NEGATIVE BINOMIAL AND PASCAL	$0 \le p \le 1$; NEGATIVE BINOMIAL IF $s \ge 0$, PASCAL IF s IS A POSITIVE INTEGER.	$\binom{x+s-1}{x} p^s(1-p)^x,\quad x = 0,1,2,\ldots$	$\frac{s(1-p)}{p}$	$\frac{s(1-p)}{p^2}$	$\frac{2-p}{[s(1-p)]^{1/2}}$	$\frac{p^2-6p+6}{s(1-p)}+3$
3.** POISSON	$\lambda > 0$	$\frac{\lambda^x e^{-\lambda}}{x!},\quad x = 0,1,2,\ldots$	λ	λ	$\frac{1}{\sqrt{\lambda}}$	$\frac{1+3\lambda}{\lambda}$
4.** BINOMIAL	POSITIVE INTEGER n, $0 \le p \le 1$	$\binom{n}{x} p^x(1-p)^{n-x},\quad x = 0,1,2,\ldots,n$	np	$np(1-p)$	$\frac{1-2p}{[np(1-p)]^{1/2}}$	$3+\frac{1-6p(1-p)}{np(1-p)}$
MULTINOMIAL	POSITIVE INTEGER n, $p_1 \ge 0, p_2 \ge 0, \ldots, p_k \ge 0$, WHERE $\sum_{i=1}^{k} p_i = 1$	$\frac{n!}{x_1!\,x_2!\cdots x_k!} p_1^{x_1}p_2^{x_2}\cdots p_k^{x_k},\quad x_1 = 0,1,2,\ldots;$ $x_2 = 0,1,2,\ldots;\ldots x_k = 0,1,2,\ldots;\quad \sum_{i=1}^{k} x_i = n$	np_i FOR $i = 1,2,\ldots,k$	$np_i(1-p_i)$ FOR $i = 1,2,\ldots,k$	$\frac{1-2p_i}{[np_i(1-p_i)]^{1/2}}$ FOR $i = 1,2,\ldots,k$	$3+\frac{1-6p_i(1-p_i)}{np_i(1-p_i)}$ FOR $i = 1,2,\ldots,k$
5.** HYPERGEOMETRIC	POSITIVE INTEGERS N, n AND k	$\frac{\binom{k}{x}\binom{N-k}{n-x}}{\binom{N}{n}},\quad x = 0,1,2,\ldots,n,\ x \le k,\ n-x \le N-k$	$\frac{nk}{N}$	$\frac{nk(N-k)(N-n)}{N^2(N-1)}$	$\frac{(N-2k)(N-2n)(N-1)^{1/2}}{(N-2)[nk(N-k)(N-n)]^{1/2}}$	*

NOTES:

* $\frac{N^2(N-1)}{(N-2)(N-3)nk(N-k)(N-n)}\left\{N(N+1)-6n(N-n)+3\frac{k}{N^2}(N-k)[N^2(N-2)-Nn^2+6n(N-n)]\right\}$

** SEE FIGURES AT BOTTOM OF PAGE

1. GEOMETRIC DISTRIBUTION

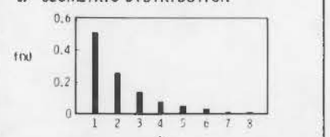

2. NEGATIVE BINOMIAL AND PASCAL

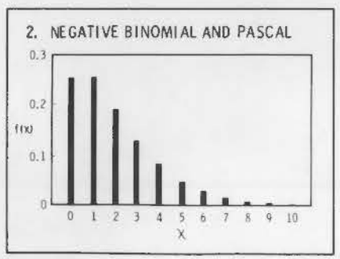

3. POISSON DISTRIBUTION

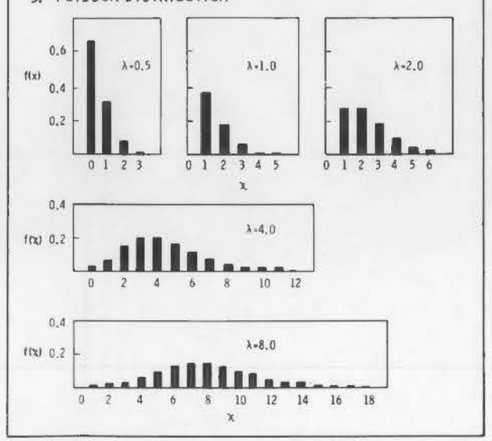

4. BINOMIAL DISTRIBUTION

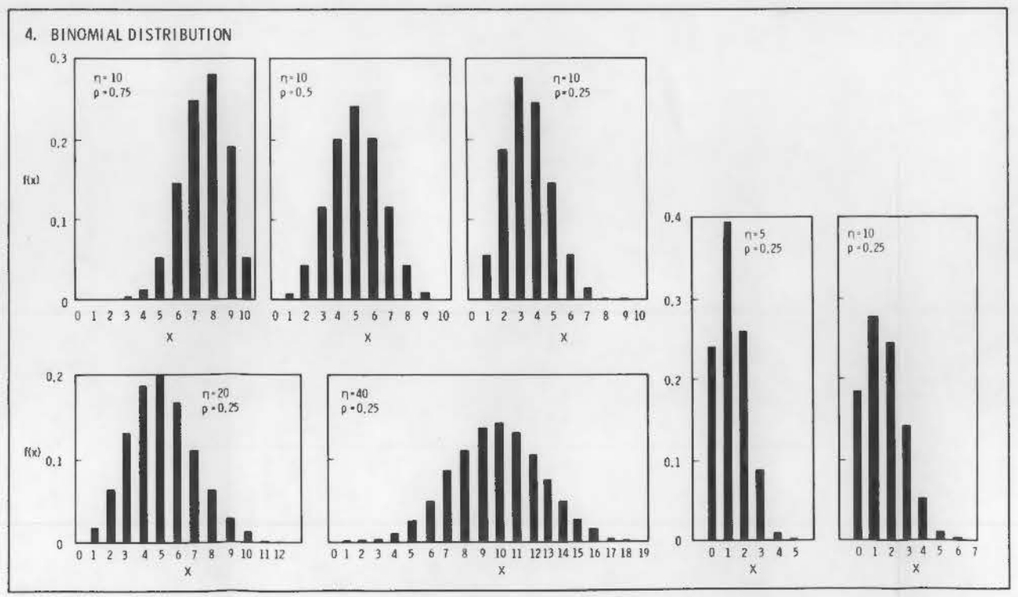

5. HYPERGEOMETRIC DISTRIBUTION

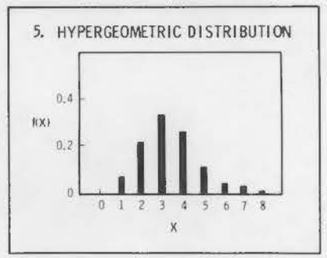

11.5 CONTINUOUS DISTRIBUTIONS

Continuous distributions such as the normal, log-normal, gamma, exponential, Weibull, etc., were discussed extensively in Section 11.3. Table 11.3.2 presented the equations for probability density functions, cumulative density functions, the hazard function, the cumulative hazard function and time-to-failure functions. This section will present other properties of these functions of interest to the analyst.

Some idea of the interrelationships among the various functions is given in Table 11.5.1. As noted, many functions are simplified forms of more general functions. An obvious example is the exponential which is a simple case of the gamma or Weibull. Hahn and Shapiro[11.1.2] present excellent tables illustrating the general form of the probability density function. The function itself, the bounding parameters, the mean, the variance, the $(B_1)^{1/2}$ and the B_2 functions have been incorporated into Table 11.3.2. As noted in Section 11.2 on definitions, B_1 is the skewness and B_2 is the excess or kurtosis. It must be recognized that there are two definitions of these two terms:

$$\text{Skewness} = \alpha_3 = (B_1)^{1/2} = \frac{\mu_3}{\sigma^3} = \frac{\mu_3}{(\mu_2)^{3/2}} \qquad (11.5.1(a))$$

$$= B_1 = \alpha_3{}^2 = \left(\frac{\mu_3}{\sigma^3}\right)^2 = \left(\frac{\mu_3}{\mu_2{}^3}\right)^2 \qquad (11.5.1(b))$$

Excess or kurtosis

$$\alpha_4 = \frac{\mu_4}{\sigma^4} - 3 \qquad (11.5.2(a))$$

$$B_2 = \alpha_4 + 3 = \frac{\mu_4}{\sigma^4} \qquad (11.5.2(b))$$

TABLE 11.5.1. Relative Relationships Among Various Continuous Distributions

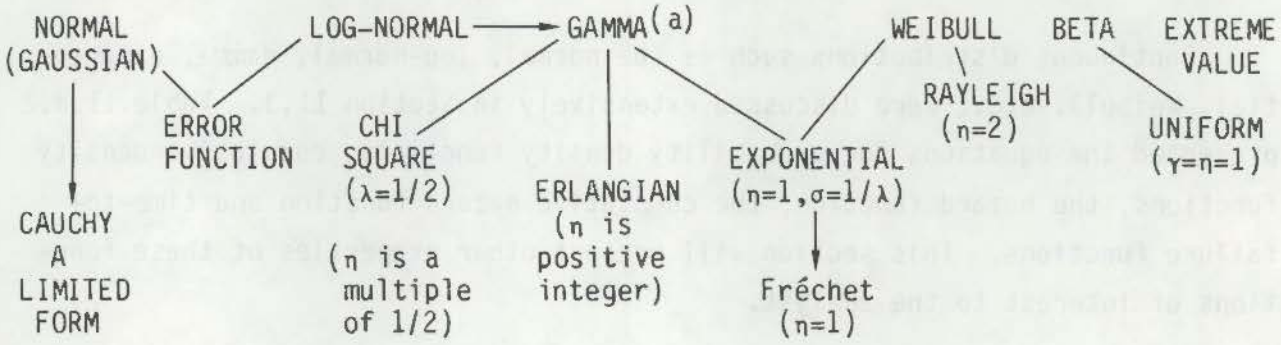

(a) Gamma distribution approaches normal distribution for large values of n.

Tables 11.3.2(a), 11.3.2(b), and 11.4.1 compare the various distributions as contained in Hahn and Shapiro.(11.1.2) In addition, a limited number of other continuous distributions are contained. The mean is an obvious value having some use. The variance is much more significant.

11.5.1 Variance

An important datum of use in calculating probability density functions is the variance of a given function. While it is possible to carry out sensitivity studies using Monte Carlo or Importance Sampling simulation, ensuring a sufficiently large population, the analysis of trends from a limited population of incidents is more difficult and subject to considerable error. If a general function,

$$Z = f(x_1, x_2 \ldots x_n) \tag{11.5.3}$$

is examined where $x_1, x_2 \ldots x_n$ represent independent random variables, the results will be sensitive to n. Typically, used are either a partial derivative method using an equation of the form

$$\sigma_Z^2 = \sum_{i=1}^{n} \left(\frac{\partial Z}{\partial \alpha_1}\right)^2 \sigma_{x_i}^2 \tag{11.5.4(a)}$$

or a numerical equation

$$\sigma_Z^2 = \sum_{i=1}^{n} \left(\frac{Z_{iu} - Z_{iL}}{2} \right)^2 \qquad (11.5.4(b))$$

Both have built-in limitations with small values of n. The variance in the partial derivative equation will be accurate (with small n) only if the following conditions are met: 1) the design parameters must be normally distributed (unlikely); 2) The function must be linear with each design parameter; and 3) the coefficients of variation must be less than 0.1. The numerical method suffers from the same limitations with its principal advantage being that it avoids having to obtain partial derivatives of complex functions.

The transform method can be used to make reliability estimates of two interacting variables each with its own pdf:

$$\text{If } R = \int_0^1 G\,dg \qquad (11.5.5(a))$$

$$\text{where} \quad G = \int_S^0 f(S)\,dS \qquad (11.5.5(b))$$

$$dF = f(s)\,ds \qquad (11.5.5(c))$$

with S representing strength and s representing stress.

If both strength and stress are assumed to be normal, the coupling equation can be used to obtain an estimate of reliability; e.g.,

$$Z = \frac{\bar{S} - \bar{s}}{\sqrt{\sigma_S^2 + \sigma_s^2}} \qquad (11.5.6)$$

and the appropriate probability value (reliability estimate) can be determined with the standard normal variate, z, using standard normal tables. If s>S, failure can occur. As z increases, the probability of failure will decrease exponentially. The inherent unreliability is the lowest unreliability possible and is defined in terms of

$$z = \frac{\bar{S}}{\sigma_s} \tag{11.5.7}$$

Generally, low probability failure events will be characterized by values of z close to those given by the preceding equation.

Another way of expressing the above is

$$\frac{\bar{S}}{\sigma_s} - \frac{(\bar{S} - \bar{s})}{\left(\sigma_S^2 + \sigma_s^2\right)^{1/2}} \simeq 0 \tag{11.5.8}$$

A value of calculated unreliability implies a loading representing virtually no threat to component integrity, even with the statistical uncertainties inherent in materials and loads.

On the other hand, if the inherent unreliability is close to the maximum acceptable unreliability, there is a need to improve the mean strength, $\bar{S}$, or to reduce the strength uncertainty, σ_s.

11.5.2 Estimation of Parameters

Statistical parameters such as shape (σ) and scale (n) parameters often are estimated both to establish the validity of the assumed statistical distributions and to quantify that distribution. At least three techniques have been proposed for estimating the values of these parameters: 1) linear estimation, 2) method of moments, and 3) maximum likelihood.

Linear estimates can be made graphically from a probability plot such as suggested by Nelson[11.3.1] and Wirsching and Jones[11.5.1] where the scale parameter will be given by the slope, and the shape parameter is given by extrapolating to x = 0. A least square fit is suggested to remove subjectivity in the estimate. While results can be obtained by the linear estimate technique, it is not considered to be the most efficient.

An alternate technique discussed more extensively under moment matching is the method of moments which involves a computation of the mean and variance as well as higher order moments. Again, the method of moments is not considered to be the most efficient in that it does not most accurately represent the true values of the statistical parameters.

The method of maximum likelihood estimates is suggested as the most accurate. Values of the shape and scale parameters can be obtained by solution of appropriate simultaneous equations which depend on the continuous distribution being used. A digital computer usually is used for such solutions. One justification for the use of maximum likelihood is that it tends to yield the least bias and the smallest variance. A Monte Carlo analysis by Wirsching and Jones[11.5.1] for the maximum extreme value distribution confirmed that the maximum likelihood technique was better than the method of moments; however, the differences were not large and the maximum likelihood estimate is more complicated. Therefore, either may be used with little loss in accuracy.

11.5.2.1 Moment Matching

The moment matching method can approximate a probability density function (pdf) when its first few moments are available.[11.1.2, 11.5.2] If the first few moments of a random variable are known, its pdf can be approximated by fitting an appropriate distribution to the existing information (expressed collectively in the form of the first few moments). Usually, the first four moments are adequate for fitting two-parameter pdf's. The third and fourth moments determine the "shape" or the form of the distribution while the first two moments define its parameters. This procedure is called the moment-matching method and it has been widely used in uncertainty analysis, in nuclear and

non-nuclear applications. In the Reactor Safety Study (1975), for example, the pdf of the top-event of a fault-tree was approximated by a log-normal distribution.

The pdf of a bounded random variable is uniquely determined by its moments; therefore, pdf's of bounded random variables with a finite number of the lower moments in common exhibit similarities. For example, if all moments were the same they would coincide in a unique pdf. If only the first few moments of a bounded random variable are known, a pdf may be developed in such a way that it has as its first few moments these known moments. This would constitute an approximation to the pdf of the random variable. This method of approximating a pdf is called the moment-matching method.

The reliability of a system, being a probability, is bounded since it can take values only in the interval (0,1), and the moment-matching method can be applied if its n first moments are known. Obviously, the more moments available, the more exact the approximation would be. In most instances, however, the first four moments are adequate. This is the case when a two-parameter pdf, such as a member of the Johnson or Pearson families, is chosen as an approximation. The third and fourth moments determine the shape or the "type" of the distribution and the first two its parameters. More precisely, the shape of a distribution is partly characterized by 1) its third central moment or skewness which is a measure of the asymmetry of the distribution, and 2) its fourth central moment or kurtosis which is related to its peakedness. To make these two "measures" of the shape of a pdf independent from its scale, they are calculated using Equations 11.5.1(b) and 11.5.2(b).

Thus, if the coefficients β_1 and β_2 can be obtained, the shape of the distribution is approximately defined. Figure 11.5.1 gives numerical values of the coefficients, β_1 and β_2, of the various "theoretical"[11.1.2] types of densities presented in Table 11.5.2. Hahn and Shapiro[11.1.2] developed similar equations in their Chapter 7. From this figure, the type of density that has the same β_1 and β_2 with the sought pdf can be obtained. The remaining two parameters (defining the location and the scale of the pdf) are then determined by the first two moments.

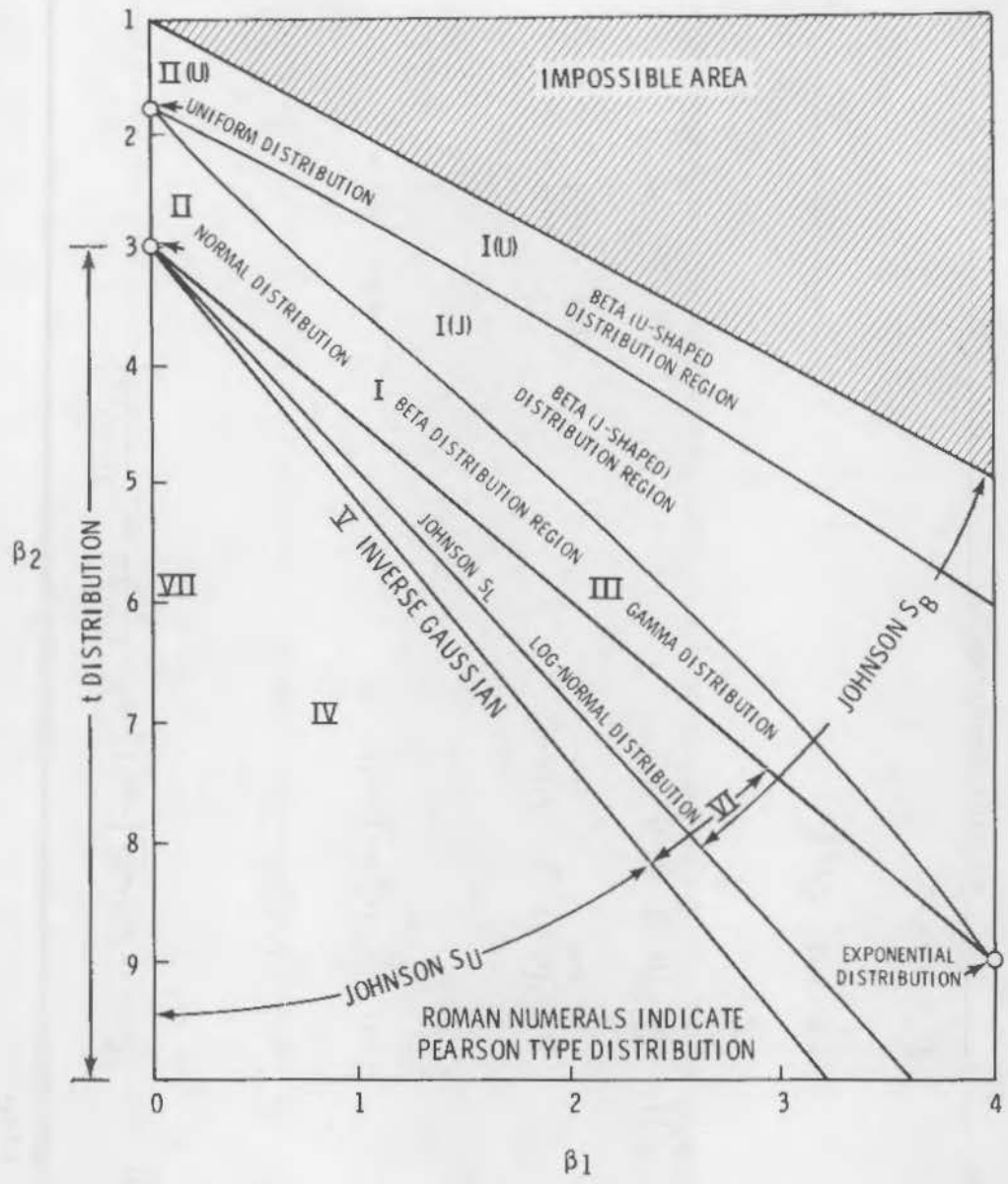

FIGURE 11.5.1. Regions in (β_1,β_2) Plane for Various Distributions

11.5.3 Empirical Distributions

In many instances, there are insufficient theoretical bases for selecting a given statistical distribution. Under these circumstances, one of the empirical distributions is an excellent alternate. These distributions tend to eliminate some of the variability common to free hand fitting of data as well as assisting in the automation of data analysis with a digital computer.

TABLE 11.5.2. The Pearson Distribution Functions

Type	Differential Equation	Probability Density Function	Compares To
General	$\frac{1}{p}\frac{dp}{dx} = -\frac{a+x}{c_0+c_1x+c_2x^2}$	$\int_{-\infty}^{\infty} p(x)\,dx = 1$	
0	$\frac{d\ln p(x)}{dx} = -\frac{a+x}{c_0}$ $C_1 = C_2 = 0$	$p(x) = K\exp\left[\frac{-(x+a)^2}{2c_0}\right]$	= Normal Distribution
I	$\frac{d\ln p(x)}{dx} = \frac{1}{c_2(a_2-a_1)}\left(\frac{a+a_1}{x-a_1} + \frac{a+a_2}{a_2-x}\right)$ $a_1 < 0 < a_2$	$p(x) = K(x-a_1)^{m_1}(a_2-x)^{m_2}$ $m_1 = \frac{a+a_1}{c_2(a_2-a_1)}$; $m_2 = -\frac{a+a_2}{c_2(a_2-a_1)}$	Type I(U) $\begin{cases} m_1 < 0 \\ m_2 < 0 \end{cases}$ Type I(J) if $m_1 < 0$ and $m_2 > 0$ or $m_1 > 0$ and $m_2 < 0$
II	Symmetric form of I; $m_1 = m_2$; if negative is Type II(U)		
III	$\frac{d\ln p(x)}{dx} = -\frac{x+a}{c_0+c_1x}$ $c_2 = 0\ (c_1 \neq 0)$	$p(x) = K(c_0+c_1x)^m \exp(-x/c_1)$ $m = c_1^{-1}(c_0c_1^{-1}-a)$ $c_1 > 0,\ x > -c_0/c_1$ $c_1 < 0,\ x < -c_0/c_1$	Gamma Distribution
IV	$\frac{d\ln p(x)}{dx} = -\frac{(x-C_1)-(a-C_1)}{C_0+c_2(x+C_1)^2}$	$p(x) = K\left[C_0+c_2(x+C_1)^2\right]^{-(2c_2)^{-1}} \exp\left[-\frac{a-C_1}{(c_2C_0)^{1/2}}\tan^{-1}\frac{x+C_1}{(C_0/c_2)^{1/2}}\right]$	

$C_0 = c_0 - 1/4\ c_1^2\ c_2^{-1}$; $C_1 = 1/2\ c_1c_2^{-1}$

No common statistical distribution corresponds to Type IV; in essence, it is rarely used because of intractable math.

TABLE 11.5.2. (contd)

Type	Differential Equation	Probability Density Function	Compares To
V	$\frac{d\ln p(x)}{dx} = -\frac{x+a}{c_2(x+c_1)^2}$	$p(x) = K(x+c_1)^{1/c_2} \exp\left[\frac{a-c_1}{c_2(x+c_1)}\right]$	Inverse Gaussian
VI	$\frac{d\ln p(x)}{dx} = -\frac{x+a}{c_2(x-a_1)(a_2-x)}$	$p(x) = K(x-a_1)^{m_1}(x-a_2)^{m_2}$	
Roots real, same sign		$x > a_2$; $m_2 < -1$; $m_1 + m_2 < 0$	
If $a_1 < a_2 < 0$		$m_2 < -1$; $m_1 + m_2 < 0$	
VII	$\frac{d\ln p(x)}{dx} = -\frac{x}{c_0+c_2x^2}$	$p(x) = K(c_0+c_2x^2)\left[-(2c_2)^{-1}\right]$	Central t - Distribution Similar
	$c_1 = a = 0$; $c_0 > 0$; $c_2 > 0$		
VIII	$\frac{d\ln p(x)}{dx} = -\frac{x+c_1}{c_2(x+c_1)^2}$	$p(x) = K(x+c_1)^{-1/c_2}$ $0 < c_2 < 1$	
	$a = c_1$		
IX	$\frac{d\ln p(x)}{dx} = -\frac{x+c_1}{c_2(x+c_1)^2}$	$p(x) = K(x+c_1)^{-1/c_2}$	
	$a = c_1$	$c_2 < 0$	

The various continuous distributions are discussed in Section 11.3, specifically, in Table 11.3.2. Such models as the log-normal, beta and gamma lead to a wide diversity of distribution shapes; however, they do not provide the degree of generality that may be desired. This is illustrated in Figure 11.5.1 where β_1 and β_2 are skewness and kurtosis, respectively, as defined in Section 11.2 and Equations 11.5.1(b) and 11.5.2(b). As can be seen, distributions such as the uniform, normal, and exponential are points on the diagram. Distributions defined by a shape parameter such as beta, gamma, and log-normal appear as lines in Figure 11.5.1. In the case of two distributions having two shape parameters such as the beta, there will be a region of the diagram occupied. While the beta distribution occupies a substantial portion of Figure 11.5.1, there are extensive regions not covered. This section will identify distribution families such as the Johnson and Pearson permitting representation over the entire possible area of Figure 11.5.1. Other distributions include Cornish-Fisher, Charlier, Edgeworth, and Kopteyn. The latter find less use than the Johnson and Pearson, and discussion will be limited to these.

If sufficient data exist to permit estimation of b_1 (β_1) and b_2 (β_2), the values can be plotted on Figure 11.5.1 to establish the logical distribution function(s) to represent the data. Caution must be exercised because estimation of b_1 and b_2 is very sensitive to variability in the data.

11.5.3.1 Johnson Distribution

Hahn and Shapiro[11.1.2] discuss both Johnson and Pearson distributions. In the Johnson distribution, there is a transformation of a standard normal variate where tables covering areas under standard normal distributions can be used. The form of the transformation is

$$z = \gamma + \eta\, T(x,\varepsilon,\lambda);\ \eta > 0,\ -\infty < \lambda\gamma < \infty,\ \lambda > 0,\ -\infty < \varepsilon < \infty$$

Here x is the variable, T is an arbitrary function, γ, η, ε and λ are four parameters and z is a standard normal variate.

Three families are considered for T, each taking different shapes as noted in Figure 11.5.1. These families are:

$$1)\ T_1(x,\varepsilon,\lambda) = \ln\left[\frac{(x-\varepsilon)}{\lambda}\right];\ x \geq \varepsilon \qquad (11.5.9(a))$$

$$2)\ T_2(x,\varepsilon,\lambda) = \ln\left[\frac{(x-\varepsilon)}{\lambda+\varepsilon-x}\right];\ \varepsilon \leq x \leq \varepsilon + \lambda \qquad (11.5.9(b))$$

$$3)\ T_3(x,\varepsilon,\lambda) = \sinh^{-1}\left[\frac{x-\varepsilon}{\lambda}\right],\ -\infty < x < \infty \qquad (11.5.9(c))$$

The first yields a log-normal distribution $f_1(x)$

$$f_1(x) = \frac{\eta}{(2\pi)^{1/2}\,(x-\varepsilon)} \exp\left\{\frac{-1\eta^2}{2}\left[\frac{\gamma^*}{\eta} + \ln(x-\varepsilon)\right]^2\right\} \qquad (11.5.10)$$

where

$$\gamma^* = \gamma - \eta \ln \lambda$$

The usual form of a three-parameter log-normal can be obtained by substituting

$$\eta = \frac{1}{\sigma} \text{ and } \gamma^* = \frac{-\mu}{\sigma}$$

The log-normal form in the preceding context is known as the Johnson S_L family fitting the log-normal line on Figure 11.5.1.

The function in Equation 11.5.9(b) leads to

$$f_2(x) = \frac{\eta}{(2\pi)^{1/2}} \frac{\lambda}{(x-\varepsilon)\,(\lambda-x+\varepsilon)} \exp\left\{\frac{-1}{2}\left[\gamma + \eta \ln\left(\frac{x-\varepsilon}{\lambda-x+\varepsilon}\right)\right]^2\right\} \qquad (11.5.11)$$

This four parameter equation represents the Johnson S_B family of distribution.

The third function (11.5.9(c)) is

$$f_3(x) = \frac{\eta}{(2\pi)^{1/2}} \frac{1}{\left[(x-\varepsilon)^2 + \lambda^2\right]^{1/2}} \exp\left\{ \frac{-1}{2} (\gamma + \eta) \ln\left[\left(\frac{x-\varepsilon}{\lambda}\right) + \left(\frac{x-\varepsilon}{\lambda}\right)^2 + 1 \right]^{1/2} \right\}^2 \tag{11.5.12}$$

This equation represents the Johnson S_U family of distributions.

Some idea of the flexibility of the three and four parameter approaches can be seen from the curves of the distributions with various values of the parameters. Figure 11.5.2(a, b, c, d) illustrate this diversity for the Johnson S_B, distribution and Figures 11.5.3(a, b, c, d) does the same for the Johnson S_U distribution.

11.5.3.2 Pearson Distribution

The Pearson distributions are generated as a solution to the differential equation

$$\frac{df(x)}{dx} = \frac{(x-\phi_3)\, f(x)}{\phi_0 + \phi_1 x + \phi_2 x^2} \tag{11.5.13}$$

where x is the random variable and ϕ_0, ϕ_1, ϕ_2, ϕ_3 are parameters in the probability density function f(x). There are twelve types of distributions derived from the Pearson equation; several of which are no longer used. Those most commonly used are the Pearson type I (normal beta) which may be U-shaped or J-shaped distribution as noted in Figure 11.5.1; and the Pearson type III (gamma). Pearson V is close to a log-normal, and Pearson IV encompassed the same region as the Johnson S_U distribution. The relevant Pearson equations appear in Table 11.5.2.

Fitting the Pearson distributions may be lengthy and complex since each family requires the solution of a different set of equations. Computer programs exist both for estimating the first four moments, and β_1 and β_2, and for the various forms of the Pearson distribution. This permits the estimated fit to be compared to the actual data.

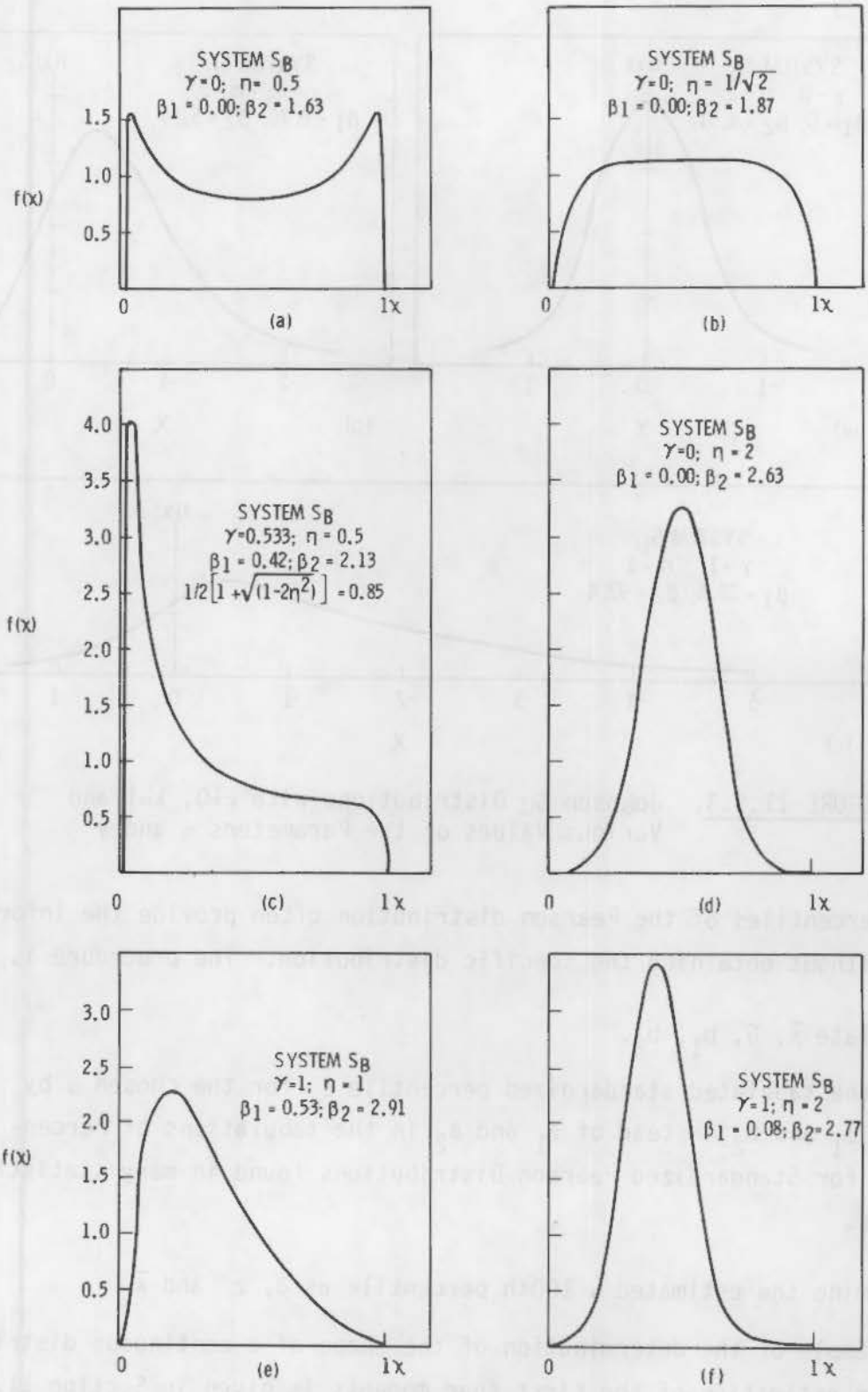

FIGURE 11.5.2. Johnson S_B Distributions with $\varepsilon=0$, $\lambda=1$ and Various Values of the Parameters η and γ

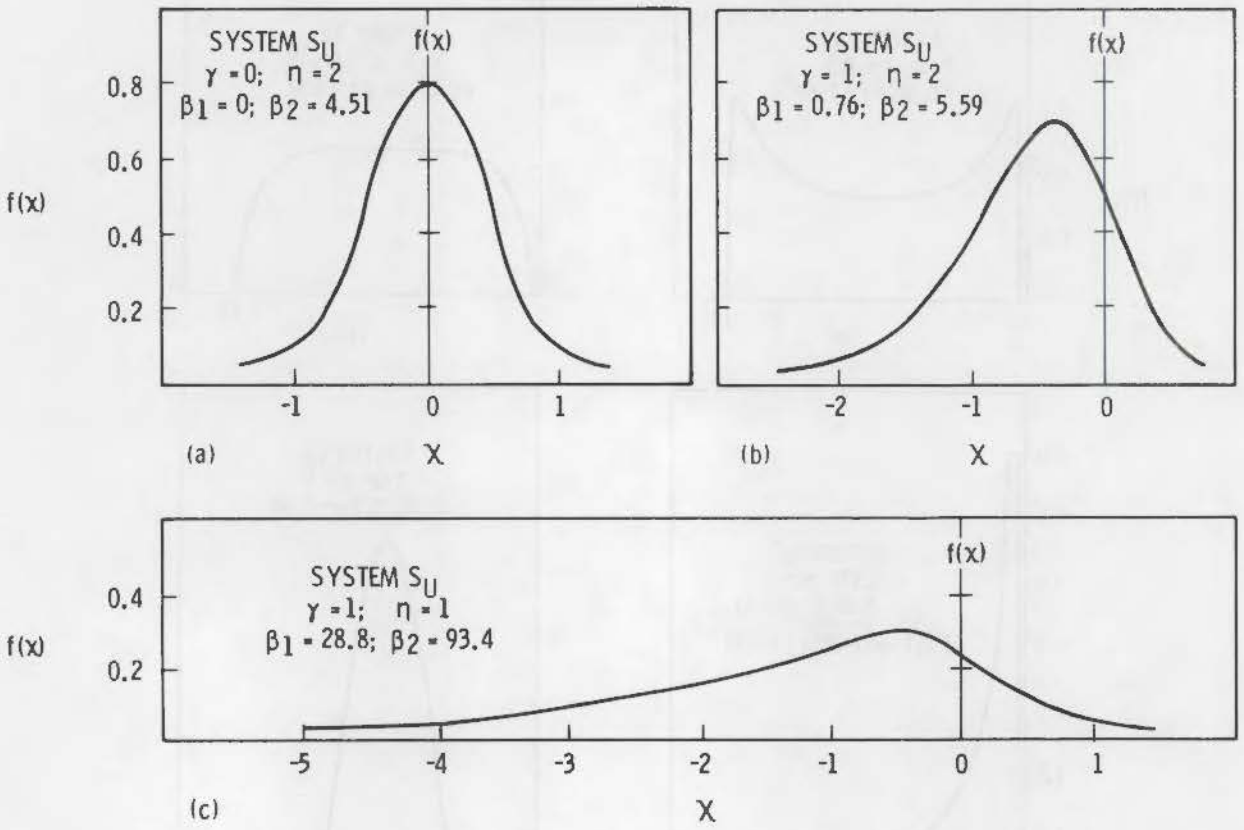

FIGURE 11.5.3. Johnson S_U Distributions with ϵ=0, λ=1 and Various Values of the Parameters η and γ

The percentiles of the Pearson distribution often provide the information required without obtaining the specific distribution. The procedure is

1. Calculate $\bar{x}$, $\hat{\sigma}$, b_1, b_2.
2. Find the tabulated standardized percentile Z_α for the chosen α by using b_1 and b_2 instead of β_1 and β_2 in the tabulations of Percentiles for Standardized Pearson Distributions found in many statistics tables.
3. Determine the estimated α 100th percentile as $\hat{\sigma}$, z and $\bar{x}$.

An example of the determination of the shape of a continuous distribution based on an estimation of the first four moments is given in Section 11.5.4 to illustrate the procedures used.

11.5.4 Estimation of Moments and Prediction of Distribution

In many instances, the performance of individual components can be modeled by relatively simple continuous or discrete probability density functions; however, when these components are combined into a system, the situation becomes much more complex with performance fluctuating due to variations from component to component.

An example cited by Hahn and Shapiro[11.1.2] provides an excellent illustration of the procedures followed in estimating the first four moments and predicting the approximate distribution. Such problems often are too complex to permit solution by direct analytic methods such as transformation of variables. Therefore, approximate methods such as application of the central limit theorem or Monte Carlo simulation will be used; the first two in this section and the Monte Carlo in Section 11.8.

11.5.4.1 Central Limit Theorem

The central limit theorem may be applied to linear systems. In this instance, the example taken from Hahn and Shapiro[11.1.2] consists of a test and repair facility consisting of six stations used to check out various systems. Each system must pass through each station with the time spent at any station a random variable whose distribution has been estimated from available data and is independent of the times at other stations. The maximum time to check a randomly chosen system is to be determined.

This theorem states that the distribution of the average-and, therefore, the sum-of independent observations from distributions with finite mean and variance approaches a normal distribution as the number of observations becomes large. Consequently, this theorem is applicable for linear systems such as the test-and-repair facility where total checkout time is the sum of the times at each of the n stations, for the case in which n is large. The normal distribution is completely specified once its mean, μ, and standard deviation, σ, are known. These can be obtained from the random variables x_1, x_2 ... x_n:

$$E(x_1 + x_2 + \ldots + x_n) = E(x_1) + E(x_2) + \ldots + E(x_n) = \mu \qquad (11.5.14)$$

and, if the variables are uncorrelated,

$$\text{Var}\,(x_1 + x_2 + \ldots + x_n) = \text{Var}(x_1) + \text{Var}(x_2) + \ldots + \text{Var}(x_n) = \sigma^2 \qquad (11.5.15)$$

In the problem of the test-and-repair facility assume, for example, that the distribution for the time in hours spent at the ith station (i = 1,2...6) is as given in Table 11.5.3. The normal, gamma, exponential, and chi-square distributions have been used as models for the checkout time at individual stations, and the parameter values have been specified in each case. (For plots of the distributions, see Figure 11.8.2.)

TABLE 11.5.3. Assumed Distributions for Test and Repair Time in Hours at Each of Six Stations

Station No. 1	$f_1(x_1) = \frac{1}{\sqrt{2\pi}} e^{-1/2(x_1-10)^2}$	Normal distribution with $\mu = 10$ and $\sigma = 1$
Station No. 2	$f_2(x_2) \frac{1}{\sqrt{2}\sqrt{2\pi}} e^{-1/2\left[(x_2-20)^2/2\right]}$	Normal distribution with $\mu = 20$ and $\sigma = \sqrt{2}$
Station No. 3	$f_3(x_3) = \frac{(6)^9}{\Gamma(9)} (x_3)^8 e^{-6x_3}$	Gamma distribution with $\eta = 9$ and $\lambda = 6$
Station No. 4	$f_4(x_4) = \frac{1}{\Gamma(10)} (x_4)^9 e^{-x_4}$	Gamma distribution with $\eta = 10$ and $\lambda = 1$
Station No. 5	$f_5(x_5) = 5e^{-5x_5}$	Exponential distribution with $\lambda = 5$
Station No. 6	$f_6(x_6) = \frac{1}{2^5\Gamma(5)} (x_6)^4 e^{-x_6/2}$	Chi-square distribution with $\nu = 10$

We are interested in the distribution of total time $T = x_1 + x_2 + x_3 + x_4 + x_5 + x_6$ spent by system at a facility. The means and variances shown in the tabulation were obtained for hours at each station:

	Station No. 1	Station No. 2	Station No. 3	Station No. 4	Station No. 5	Station No. 6
Mean	10	20	1.5	10	0.2	10
Variance	1	2	0.25	10	0.04	20

Substitution of the station means and variances into 11.5.14 and 11.5.15 yields a system mean of (10 + 20 + 1.5 + 10 + 0.2 + 10) = 51.7 hours and a variance of 1 + 2 + 0.25 + 10 + 0.04 + 20 = 33.29. From the central limit theorem, the total test and repair time can thus be approximated by a normal distribution with a mean, μ, of 51.7 hours and a standard deviation, σ, of $\sqrt{33.29} = 5.8$ hours. From the properties of the normal distribution, we can now say that the chances are nine out of ten that the checkout time for a random system will not exceed $\mu + 1.28\sigma$ hours, 95 out of 100 that it will not exceed $\mu + 1.65\sigma$ hours, and 99 out of 100 that it will not exceed $\mu + 2.33\sigma$ hours. Hence, the approximate 90, 95, and 99 percent upper limits are 59.1, 61.2, and 65.2 hours, respectively.

This problem involved a six-element system, rather than one with "very many elements." More important, the variances of the individual elements are far from equal, and the total variance is highly dominated by the variances of the times at stations 4 and 6. Therefore, the applicability of the central limit theorem in this problem is questionable. The adequacy of the normal distribution approximation will be compared with those obtained by the method of moments and Monte Carlo.

Exact knowledge of the distribution for each of the component variables is not essential, since all that is needed to use 11.5.14 and 11.5.15 are the means and variances.

11.5.4.2 Generation of System Moments

The method for the generation of system moments, sometimes referred to as statistical error propagation or the delta method, will now be described.

Let the relationship between system performance z and the component variables $x_1, x_2 \ldots x_n$ be given by the function $z = h(x_1, x_2 \ldots x_n)$. For example, in the case of the six-station test-and-repair facility $z = x_1 + x_2 + x_3 + x_4 + x_5 + x_6$--that is, total checkout time is the sum of the times at each of the times at each of the stations.

Let $E(x_i)$ be the mean or expected value for the ith component variable and let $\mu_k(x_i)$ denote its kth central moment (or moment about the mean). Similarly, $E(z)$ and $\mu_k(z)$ denote the expected value and the kth moment about the mean for system performance, respectively. The problem is to obtain an estimate of $E(z)$ and $\mu_k(z)$ for $k = 2, 3$, and 4, based on a) data on the component variables from which estimates of $E(x_i)$ and $\mu_k(x_i)$ for $i = 1,2...n$ can be obtained and b) knowledge of the system structure $h(x_1, x_2 \ldots x_n)$.

The method consists of expanding $h(x_1, x_2 \ldots x_n)$ about $E(x_1), E(x_2) \ldots E(x_n)$, the point at which each component variables takes on its expected value, by a multivariable Taylor series. Assuming that the component variables are uncorrelated, the final expression for mean system performance, retaining terms up to second order, is

$$E(z) = h\left[E(x_1), E(x_2) \ldots E(x_n)\right] + \frac{1}{2} \sum_{i=1}^{n} \frac{\partial^2 \bar{h}}{\partial x_i^2} \mathrm{Var}(x_i) \qquad (11.5.16)$$

where $\partial^2 \bar{h}/\partial x_i^2$ denotes $\partial^2 h/\partial x_1^2$ evaluated at $E(x_r)$--that is, with the $E(x_r)$ substituted for x_r for $r = 1,2...n$. For example, if $h(z) = x_1 x_2^2 x_3^3$

$$\frac{\partial^2 h}{\partial x_3^2} = \left[E(x_1)\right] \left[E(x_2)\right]^2 \left[6E(x_3)\right]^3 \qquad (11.5.17)$$

Henceforth, $\partial^2 \bar{h}/\partial x_i^2$ is written without the bar on h--that is, as $\partial^2 h/\partial x_i^2$.

Equation 11.5.16 requires knowledge or estimates of the means and variances for each of the component variables.

Note that estimating mean performance by substituting the component means into the system equation--that is, setting

$$E(z) = h\left[E(x_1),\ E(x_2)\ \ldots\ E(x_n)\right]$$

--provides an exact result when all second- and higher-order partial derivatives are zero; for example, when system performance is a linear function of the component variables, as in the test-and-repair facility problem. However, the expression is only approximate in the general case.

The Taylor-series expansion for the variance of system performance, assuming the component variables to be uncorrelated, and retaining terms up to third order, reduces to

$$\mathrm{Var}(z) = \sum_{i=1}^{n} \left(\frac{\partial h}{\partial x_i}\right) \mathrm{Var}\ (x_i) + \sum_{i=1}^{n} \left(\frac{\partial h}{\partial x_i}\right)\left(\frac{\partial h}{\partial x_1^2}\right) \mu_3(x_i) \qquad (11.5.18(a))$$

where $\mu_3\ (x_i)$ is the third central moment for the ith variate and all derivatives are evaluated at their mean values. Often, the last term is omitted and only the following expression is used:

$$\mathrm{Var}(z) = \sum_{i=1}^{n} \left(\frac{\partial h}{\partial x_i}\right)^2 \mathrm{Var}(x_i) \qquad (11.5.18(b))$$

which is frequently a satisfactory approximation.

Expressions for the third and fourth central moments for system performance--that is, $\mu_3(z)$ and $\mu_4(z)$--may be derived in a manner analogous to that for the variance. The resulting expressions, retaining only the lowest-order non-zero terms, are

$$\mu_3(z) = \sum_{i=1}^{n} \left(\frac{\partial h}{\partial x_i}\right)^3 \mu_3(x_i) \qquad (11.5.19)$$

$$\mu_4(z) = \sum_{i=1}^{n} \left(\frac{\partial h}{\partial x_i}\right)^4 \mu_4(x_i) + 6 \sum_{\substack{i \\ i > l}} \sum_{l} \left(\frac{\partial h}{\partial x_i}\right)^2 \left(\frac{\partial h}{\partial x_l}\right)^2 \text{Var}(x_i)\ \text{Var}(x_j) \quad (11.5.20)$$

The preceding methods are now applied to the test-and-repair facility problem in Table 11.5.3. Total checkout time z is represented by the linear function $z = x_1 + x_2 + x_3 + x_4 + x_5 + x_6$, where x_i is the time at the ith station (i=1,2...6) with assumed statistical distributions given in Table 11.5.3. Then,

$$\frac{\partial z}{\partial x_i} = 1, \qquad i = 1,2...6$$

and

$$\frac{\partial^2 z}{\partial x_i^2} = 0 \qquad i = 1,2...6$$

Thus, 11.5.16, 11.5.18(a), 11.5.19 and 11.5.20 reduce to

$$E(z) = \sum_{i=1}^{6} (x_i)$$

$$\text{Var}(z) = \sum_{i=1}^{6} \text{Var}(x_i)$$

$$\mu_3(z) = \sum_{i=1}^{6} \mu_3(x_i)$$

and

$$\mu_4(z) = \sum_{i=1}^{6} \mu_4(x_i) + 6 \sum_{\substack{i \\ i > j}} \sum_{j} \text{Var}\ (x_i)\ \text{Var}\ (x_j)$$

The third and fourth central moments for the distributions of time at each station can be obtained from Table 11.5.3 by the methods of Section 11.5.3.1. The resulting values, together with the means and variances are

	Station No. 1	Station No. 2	Station No. 3	Station No. 4	Station No. 5	Station No. 6
Mean	10	20	1.5	10	0.2	10
Variance	1	2	0.25	10	0.04	20
$\mu_3(x_i)$	0	0	0.08	20	0.02	80
$\mu_4(x_i)$	3	12	0.23	360	0.01	1680

Thus,

$$E(z) = 10 + 20 + 1.5 + 10 + 0.2 + 10 = 51.7$$

$$Var(z) = 1 + 2 + 0.25 + 10 + 0.04 + 20 = 33.3$$

$$\mu_3(z) = 0 + 0\ 0.08 + 20 + 0.02 + 80 = 100.1$$

$$\mu_4(z) = (3 + 12 + 0.23 + 360 + 0.01 + 1680)$$

$$+ 6\,[1(2 + 0.25 + 10 + 0.04 + 20) + 2(0.25 + 10 + 0.04 + 20)$$

$$+ 0.25(10 + 0.04 + 20) + 10(0.04 + 20) + 0.04(20)]$$

$$= 3864.7$$

and $$\sqrt{\beta_1} = \frac{100.1}{(33.3)^{3/2}} = 0.52$$

$$\beta_2 = \frac{3864.7}{(33.3)^2} = 3.49$$

Using only the upper tail in a Pearson distribution approximation, we find that total checkout and repair time will exceed a) 59.4 hours 10 percent of the time, b) 62.0 hours 5 percent of the time, c) 67.4 hours 1 percent of the time. These results compare with the corresponding values of 59.1 hours, 61.2 hours, and 65.2 hours that were obtained by invoking the central limit theorem; total time had been assumed to be normally distributed. It is noted that although there is a close correspondence for the 90th and 95th percentiles, the divergence increases for the 99th percentile, thus illustrating the fact that the normal distribution approximation is frequently least adequate at the extreme tails of a distribution.

By locating values of $\beta_1 = 0.27$ and $\beta_2 = 3.49$ in Figure 11.5.1, it can be seen that the checkout problem may be approximated by a Johnson S_U distribution and the methods discussed in Section 11.5.4 for estimating the parameters for this distribution based on the calculated moments can be used. Alternately, the Pearson IV distribution can be used. The third possibility cited previously is to use the percentile values for the upper tail in a Pearson distribution approximation.

In the case of a Johnson S_U distribution, where μ, σ, β_1, and β_2 are known, the following procedure is used. Generally, the four parameters γ, η, λ, and ε are unknown. However, they can be estimated using information such as found in Table V of Hahn and Shapiro.[11.1.2] This procedure is based on the method of moments.

1. Obtain $\bar{x}$, $\hat{\sigma}$, $\sqrt{b_1}$ and b_2 from available data. The last two values were obtained previously and used in determining that S_U was the appropriate Johnson distribution family.
2. Values of estimates $\hat{\gamma}$ and η can be obtained from $\sqrt{b_1}$ and b_2 using Table V cited above.[11.1.2] The tables permit interpolation. For greater accuracy an iterative method is available.

3. Calculate

$$\hat{\lambda} = \frac{\hat{\sigma}}{\left\{\frac{1}{2}(\omega - 1)\left[\omega\cosh\left(2\frac{\hat{\gamma}}{\hat{\eta}}\right) + 1\right]\right\}^{1/2}} \qquad (11.5.21)$$

and

$$\hat{\varepsilon} = \bar{x} + \hat{\lambda}\,\omega^{1/2}\sinh\left(\frac{\hat{\gamma}}{\hat{\eta}}\right) \qquad (11.5.22)$$

where

$$\omega = \exp\left(\frac{1}{\hat{\eta}^2}\right) \qquad (11.5.23)$$

Recalling that

$$\text{Mean } E(z) = 51.7$$

$$\text{Var}(z) = 33.3 \qquad \sigma = 5.77$$

$$\mu_3(z) = 100.1$$

$$\mu_4(z) = 3864.7$$

$$b_1^{1/2} \simeq \beta_1^{1/2} = 0.52; \quad \beta_1 = 0.27$$

$$b_2 \simeq \beta_2 = 3.49$$

Interpolating in tables of Johnson functions will yield

$$\left.\begin{aligned}\hat{\eta} &= 4.7\\ -\hat{\gamma} &= 4.2\end{aligned}\right) \text{ by extrapolation}$$

$$\omega = \exp \frac{1}{\hat{\eta}^2} = \exp \frac{1}{4.7^2} = 1.05$$

$$\hat{\lambda} = \frac{5.77}{\left[\frac{1}{2}\,(1.05 - 1)\,1.05\,\cosh 2\left(\frac{-4.2}{4.7}\right) + 1\right]^{1/2}}$$

$$\hat{\lambda} = \frac{5.77}{0.186} = 30.94$$

$$\hat{\varepsilon} = \bar{x} + \hat{\lambda}\,\omega^{1/2}\,\sinh\left(\frac{\hat{x}}{\hat{\eta}}\right)$$

$$\hat{\varepsilon} = 51.7 + 30.94\left[1.05^{1/2}\,\sinh\left(\frac{-4.2}{4.7}\right)\right]$$

$$\hat{\varepsilon} = 19.46$$

Therefore,

$$f_3(x) = \frac{\eta}{(2^{\pi})^{1/2}} \frac{1}{\left[(x - \varepsilon)^2 + \lambda^2\right]^{1/2}} \exp\left[-\frac{1}{2}\left(\gamma + \eta \ln\left\{\left(\frac{x - \varepsilon}{\lambda}\right) + \left[\left(\frac{x - \varepsilon}{\lambda}\right)^2 + 1\right]^{1/2}\right\}\right)^2\right] \tag{11.5.12}$$

$$f_3(x) = \frac{4.7}{(2^{\pi})^{1/2}} \frac{1}{\left[(x - 19.46)^2 + 30.94^2\right]^{1/2}} \exp\left[-\frac{1}{2}\left(-4.2 + 4.7 \ln \left\{\left(\frac{x - 19.46}{30.94}\right) + \left[\left(\frac{x - 19.46}{30.94}\right)^2 + 1\right]^{1/2}\right\}\right)^2\right]$$

$$f_3(x) = 1.87 \frac{1}{\left[(x-19.46)^2 + 957.3\right]^{1/2}} \exp\left[\left(+ 2.1 - 2.35 \ln\left\{\left(\frac{x - 19.46}{30.94}\right) + \left[\left(\frac{x - 19.46}{30.94}\right)^2 + 1\right]^{1/2}\right\}\right)^2\right]$$

The preceding equation could be solved for the distribution. Up to this point, variables have been assumed to be uncorrelated. Correlation between components occurs when the random value taken by one or more components in a system is related to the random value of one or more other components in the same system. For example, in the test-and-repair problem the times are correlated if a defect that causes above-average checkout time at one station also leads to above-average times at other stations.

Expressions for system performance when component variables are correlated can be obtained in a fashion analogous to the uncorrelated case. The results are given in Appendix 7B of Hahn and Shapiro.(11.1.2)

11.6 STRENGTHS AND WEAKNESSES OF VARIOUS CONTINUOUS DISTRIBUTIONS

Wirsching and Jones[11.5.1] examined the influence specific probability density functions can have on the values of probability estimates in the tails (2σ–4σ) regions. Both the upper tail and the lower tail were examined. As will be seen, the values are very sensitive to the statistical distribution selected. Since we are concerned with the possible overlap of the upper tail of one function with the lower tail of another--for example, stress versus strength--this sensitivity to the pdf selected can be very important.

Wirsching and Jones[11.5.1] examined normal, log normal, Gamma, Weibull, Type I Extreme Value distributions of Maxima, Fréchet, a modified exponential and a power function. In addition, the values for a Camp-Meidell inequality were used.

The parameter used in the comparisons was the coefficient of variation, C, defined as σ/μ where σ is the standard deviation and μ is the mean. The specific value of σ used is defined in terms of a parameter K, which is calculated as follows:

$$P_o = \text{probability of some low probability event}$$

$$P_o = P\ (D > V_o)$$

where D = specific statistical distribution

V_o = in essence, the area under the pdf curve

μ_D = mean

σ_D = standard deviation

$$P_o = P\ (D > \mu_D + K\ \sigma_D)$$

or

$$K = \frac{V_o - \mu_D}{\sigma_D}$$

and K is used as the multiplier of the standard deviation. Figures 11.6.1(a) and (b) compare upper and lower tails at a fixed value of the coefficient of variation of 0.25 at the same values of mean and standard deviation.

The relative order for the various cases ranging from the largest to the smallest values are as follows:

C = 0.10

Lower tail - Cm > P > W > N > G > LN > EVD

Upper tail - Cm > EXP > F > EVD > LN > G > N > W

C = 0.25

Lower tail - CM > P > N > W > G > LN > EVD

Upper tail - CM > F > EXP > EVD > LN > G > N > W

The Camp Meidell (C-M) inequality is defined as

$$P/X - \mu / \geq K\sigma / < \frac{1}{2.25\ K^2} \quad ; \quad K > 0 \qquad (11.6.1)$$

With regard to the various relationships, the Camp-Meidell is considered too weak for design purposes. The Fréchet distribution is considered to lack physical significance in the context of engineering practice. The exponential distribution gives essentially the same values as the Fréchet and is suggested for use in the upper tail because of its ease of use. The power distribution is suggested as a quasi-upper bound for the lower tail.

Nelson[11.3.1] suggests specific procedures for hazard plotting from incomplete failure data. He proposes specific rules to follow to develop appropriate probability paper. He notes sources of error either due to the form of probability paper used or to the continuous functions used. Deviation from a straight line may be due to either source of error. Curves that are not straight regardless of paper may indicate two or more failure modes with different distributions of times to failure.

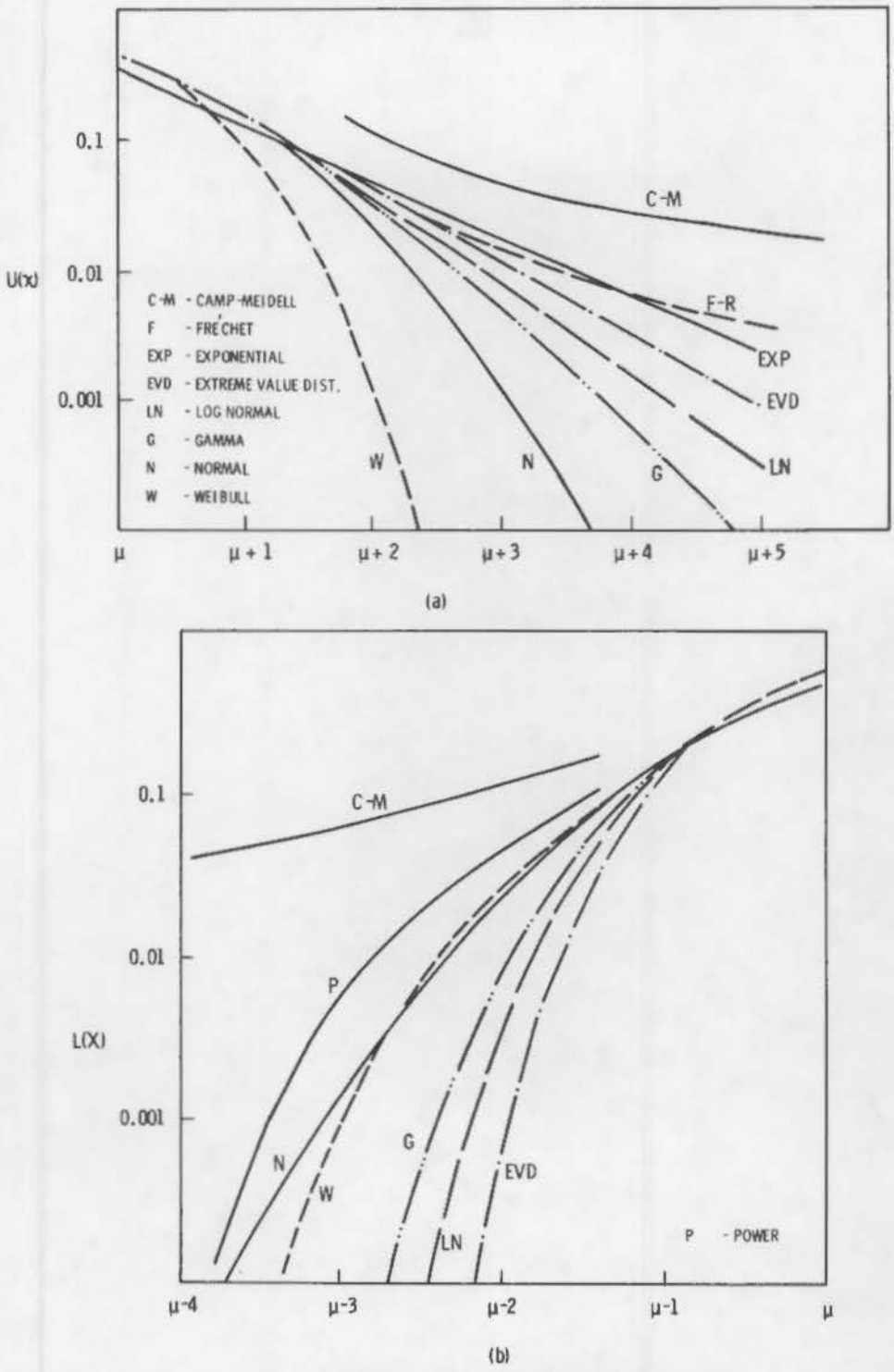

FIGURE 11.6.1. Tail Probabilities for Common Statistical Models Having the Same Mean and Standard Deviation (Coefficient of Variation $\left(\frac{\sigma}{\mu}\right) = 0.25$); (a) Upper Tail, (b) Lower Tail

11.7 FUNCTIONS FOR TESTING SIGNIFICANCE

A statistical test of a distributional assumption provides an objective technique for assessing whether an assumed model provides an adequate description of observed data. The following basic steps are usually involved:

Step 1. A number known as a test statistic is calculated from the observed data.

Step 2. The probability of obtaining the calculated test statistic, assuming the selected model is correct, is determined. This is frequently done by referring to a table of percentiles of the distribution of the test statistic.

Step 3. If the probability of obtaining the calculated test statistic is "low," we conclude that the assumed model does not provide an adequate representation. The definition of "low" depends on the user's preferences and the consequences of rejecting the model. A probability of 0.10 or 0.05 or less is frequently said to be "low." If the probability associated with the test statistic is not "low," then the data provide no evidence that the assumed model is inadequate.

It should be clearly understood that, although this procedure permits us to reject a model as inadequate, it never allows us to prove that the model is correct. In fact, the outcome of a statistical test depends highly upon the amount of available data--the more data there are, the better are the chances of rejecting an inadequate model. If too few data points are available, even a model that deviates grossly from the assumed model frequently cannot be established as inadequate.

A myriad of statistical tests to evaluate distributional assumptions have been evolved. Some are valid for specific models; others are applicable for a wide range of distributions. Many of the procedures require exact knowledge of the values of each of the parameters in the model. Because in most engineering problems the parameters are not known, but must be estimated, such tests will not be considered here.

Once the distribution function of a stochastic variable is known, the mean and standard deviation can be determined. For a normal distribution 68.3 percent of the probability is within $\pm 1\sigma$ around the mean and 99.5 and 99.7 percent of the probability are within $\mu \pm 2\sigma$ and $\mu \pm 3\sigma$, respectively.

Chebycheff's theorem gives some information about an inverse problem. To what extent do the mean and the standard deviation characterize the distribution when we do not know the mathematical form of the distribution function? Chebycheff's theorem (or inequality) permits the determination of very conservative bounds if the distribution is unknown. Basically, it says, "The probability of determining a value of the standardized variable which is numerically less than or equal to a specified number a is larger than $1 - 1/k^2$." Another way of expressing the theorem is for any distribution with finite mean and variance, at least $(1 - 1/k^2)$ times 100 percent of the probability is in the range $\pm k\sigma$ around the mean. For most distributions at least 75 percent of the area under the distribution curve is within $\mu \pm 2\sigma$ and at least 88.9 percent is within $\mu \pm 3\sigma$.

Another inequality test is the Camp-Meidell discussed in Section 11.6. If the distributions of two stochastic variables are not known, an upper bound value can be estimated. The Camp-Meidell theorem provides a stronger probability statement than Chebycheff's theorem. However, it is subject to the restriction that the distribution(s) be unimodal and have a high order of contact with the abscissa at $\pm\infty$. The Camp-Meidell inequality for X is

$$P//X - \mu / \geq K\sigma \leq \frac{1}{2.25K^2} ; \quad K > 0$$

11.7.1 Distribution of Variance Ratio

An exact test for the hypothesis that one variance is equal to another, or $\sigma_1^2 = \sigma_2^2$, was developed by R. A. Fisher. This test is known as the variance ratio, V^2 or F distribution.

If S_1^2 and S_2^2 are two stochastically independent variables, both having S^2 distributions with parameters (σ^2, f_1) and (σ^2, f_2), respectively (f is degree of freedom), so that

$$S_1^2 = \sigma^2 \frac{\chi_1^2}{f_1}$$

$$S_2^2 = \sigma^2 \frac{\chi_2^2}{f_2}$$

the variance ratio will be

$$F = V^2 = \frac{S_1^2}{S_2^2} = \frac{\chi_1^2/f_1}{\chi_2^2/f_2} \qquad 0 < V^2 < \infty$$

F-distribution tables are available to test linear regressions, the significance of correlation ratios, linearity of regressions, etc. The F-distribution is related to the incomplete beta function, which in turn is related to the χ^2 function.

11.7.2 Students' t Test

If X is a random variable following a normal distribution with mean zero and variance unity and χ^2 is a random variable following an independent χ^2 distribution with ν degrees of freedom, then the distribution of the ratio $X/(\alpha^2/\nu)^{1/2}$ is called Student's t distribution with ν degrees of freedom. The probability that $X/\alpha^2/\nu)^{1/2}$ will be less in an absolute value than a fixed constant t is

$$A(t/\nu) = \Pr\left\{ / \frac{X}{(\alpha^2/\nu)^{1/2}} / < t \right\}$$

Students t or the t distribution is a specific probability density function and tables of t-distribution percentiles commonly are included in statistical tables.

In the t-test, t is defined as

$$t = \frac{\bar{X} - \mu}{\frac{S}{n^{1/2}}}$$

where $\bar{X}$ is the mean of a sample, μ is the population mean, and $\frac{S}{n^{1/2}}$ is the estimated standard deviation of the mean. The Student t-test may be used for testing the significance of the difference between two means, the significance of a regression coefficient, the significance of the difference between two regression coefficients, etc.

The precision of $\bar{X}$ as an estimate of the normal distribution mean μ when is unknown can be obtained from a confidence interval usually expressed in terms of 0.90, 0.95 and 0.99 confidence levels where these are derived from the t-distribution.

The precision of the estimate of the normal distribution parameter μ is done through a confidence interval for μ calculated as

$$\bar{X} \pm \left(t_{CL,\ n-1}\right) \frac{S}{n^{1/2}}$$

where $\bar{X}$ and S are estimates of mean and standard deviation and $t_{CL;\ n-1}$ is given in most statistical tables for confidence levels CL = $1-\alpha$ = 0.90, 0.95, 0.99.

11.7.3 The W Tests

The W tests to evaluate the assumption of a normal (or log-normal) and an exponential distribution will be presented. The chi-squared test can be used for any distributional model, including the normal and exponential. However, for these two cases the W tests are generally more powerful--that is, they provide a better chance of rejecting an incorrect model. Thus, when the data are limited, it is generally advisable to use the appropriate W test, rather than the Chi-squared test, to evaluate the assumption of normality or of exponentiality.

11.7.3.1 Test to Evaluate the Assumption of a Normal or Log-Normal Distribution

The W test is shown in Reference[11.1.2] to be an effective procedure for evaluating the assumption of normality against a wide spectrum of non-normal alternatives, even if only a relatively small number of observations are given. For example, if 20 samples are taken from a process that is actually exponentially distributed, the chances are about 80 out of 100 that by applying the W test we shall correctly conclude that the normal distribution does not give a reasonable representation.[a]

To use the test for a random sample of size n, when $n \leq 50$, we proceed as follows:

Step 1. Rearrange the observations to obtain the ordered sample from smallest to largest.

Step 2. Compute

$$S^2 = \sum_{i=1}^{n} \left(x_1 - \bar{x}\right)^2$$

where $\bar{x}$ is the data mean.

Step 3. If n is even, set k = n/2; if n is odd, set K = (n - 1)2. Then compute

$$b = \sum_{i=1}^{k} a_{n-i+1} \left(x_{n-i+1} - x_1\right)$$

where the values of a_{n-i+1} for i = 1...k, are given in various statistical texts for n = 3...50. When n is odd, x_{k+1} does not enter into this computation.

(a) This result is for a 5 percent test--that is, we are ready to take a one-in-twenty chance of wrongly claiming the model inadequate when the underlying distribution is in fact normal.

Step 4. Compute the test statistic

$$W = \frac{b^2}{S^2}$$

Step 5. Compare the calculated value of W with the percentiles of the distribution of this test statistic. This gives the minimum values of W that we would obtain with k, 2, 5, 10, and 50 percent probability as a function of n, if the data actually came from a normal distribution. Thus, small values of W indicate non-normally. For example, if the value of W is less than the 5 percent tabulated value, there is less than one chance in 20 that the sample could have drawn from a normal distribution. We might then conclude that the assumption of a normal distribution does not appear to be reasonable.

11.7.3.2 Test to Evaluate the Assumption of an Exponential Distribution--Origin Known (WE_o Test)

The exponential probability density function can be generalized into a two-parameter model where one parameter, λ, scales the distribution and the second parameter, μ, defines the distribution origin--that is, the point above which all observations lie. The resulting probability density function is

$$f(x;\ \lambda,\ \mu) = \lambda e^{-\lambda\ (x\ -\ \mu)},\ \mu \leq x < \infty,\ -\infty < \mu < \infty;\quad \lambda > 0$$

In the following discussion it will be assumed that μ is known to equal zero. This leads to no loss of generality. If $\mu = 0$, but is known, we subtract μ from each observation. The resulting variable will have an origin of zero.

The procedure for assessing whether a random sample could reasonably have been drawn from an exponential distribution with an origin of zero is known as the WE_o test.

11.7.3.3 Test to Evaluate the Assumption of an Exponential Distribution--Origin Unknown (WE Test)

The procedure, known as the WE test, can be used to test the assumption that a given sample of 7 to 35^{+} observations came from the exponential distribution, when the values of both parameters, μ and λ, are unknown.

11.7.4 The Chi-Squared Goodness-of-Fit Test

The oldest, most commonly used, and perhaps most versatile procedure for evaluating distributional assumptions is the chi-squared goodness-of-fit test. To use this test, the given data are grouped into frequency cells and compared to the expected number of observations based on the proposed distribution. From this comparison a test statistic that approximately follows a chi-square distribution only if the assumed model is correct is calculated. The test statistic will tend to exceed a chi-square variate if the assumed model is not correct. Thus tables which give percentiles for the chi-square distribution, may be used to determine whether the data provide evidence contrary to the assumed model. The specific calculational procedure is described below.

The major advantage of the chi-squared test is its versatility. It can be applied simply to test any distributional assumption, without our having to know the values of the distribution parameters. Its major drawbacks are its lack of sensitivity in detecting inadequate models when few observations are available, and the frequent need to arrange the data into arbitrary cells, which can affect the outcome of the test.

Operational Instructions. The chi-squared test is used as follows:(11.1.2)

Step 1. Estimate each of the unknown parameters of the assumed distribution. To be theoretically correct, the method of maximum likelihood should be used after the data have been arranged in frequency cells. For practical convenience, however, the various techniques indicated in this book for estimating parameters may be applied to the original data.

Step 2. Divide the data into k classes or cells and determine the probability of a random value from the assumed model falling within

each class. We shall consider two methods for doing this: the first is applicable if the data are initially arranged in frequency classes or can be naturally assigned to such classes. This would be the case when the observations are from a discrete distribution, such as the Poisson. The second method applies when the data are not initially tabulated in classes.

Method a The number of cells, k, will be the number of classes of the tabulated data subject to the restriction that the expected number of observations in each cell under the assumed model (see below) is at least five. If this number turns out to be less than five for any cell, the cell should be combined with an adjoining cell or cells so that the expected number in the combined cell is at least five.

Let CL, and CU, denote the lower and upper bounds of the ith frequency cell. The distribution of the assumed model (using the estimated parameters) is then used to estimate.

$$Pr\ (CL_i < x < CU_i)\ i = 1, 2 \ldots k$$

--that is, the probability of a random observation falling within each class is estimated.

Method b In this case the choice of k is more arbitrary. When the number of observations, n, is large (say, over 200) one possible rule is to take k as the integer closest to

$$k' = 4\ [0.75(n-1)^2]\ 1/5$$

For moderate values of n a good rule is to make k as large as possible, subject to the restriction that it must not exceed n/5. The cell boundaries $x_1, x_2 \ldots x_k$ are determined from the cumulative distribution for the assumed model (using the estimated parameters) as the values such that

$$Pr(x \leq x_1) = 1/k,\ Pr(x < x_2) = \frac{2}{k} \ldots Pr(x < x_{k-1}) = \frac{(k-1)}{k}$$

The lower bound of the first cell and the upper bound of the last cell are the smallest and largest values that the random variable may take on. We have thus set up the cell boundaries in such a way that the probability of a random value falling within a given class is estimated to be 1/k for each class.

Step 3. Multiply each of the cell probabilities by the sample n. This yields the expected number E of observations for each cell under the assumed model. For Method 2a, we obtain E, by multiplying the probabilities by n. For Method 2b

$$E_i = \frac{n}{k},\ i = 1, 2 \ldots k$$

Step 4. If the data are not initially tabulated, count the number of observed values in each cell. Denote this number as M_i, where $i = 1, 2 \ldots k$. Otherwise, determine the M, directly.

Step 5. Compute the test statistic

$$\chi^2 = \sum_{i=1}^{k} \frac{(M_i - E_i)^2}{E_i}$$

Note that for Method 2b this expression simplifies to

$$\chi^2 = \frac{k}{n}\left(\sum_{i=1}^{k} M_i\right)^2 - n$$

Step 6. Compare the computed value χ^2 with the tabulated percentiles for a chi-square variate using $k - r - 1$ degrees of freedom, where r is the number of parameters that were estimated in

Step 1. High values of χ^2 signify that the observed data contradicts the assumed model. For example, if the above calculated value χ^2 exceeds the 0.95 tabulated value of chi square, the chances are less than one in twenty that the data could have emanated from the assumed distribution and the model is frequently rejected as inadequate. In this case it is instructive to compare the actual with the expected frequencies to see which classes contributed most heavily to the value of χ^2. This provides an indication of the nature of the deviations from the assumed model.

The chi-squared test will be used to evaluate the reasonableness of an exponential model for time-to-failure. In this example the data are not naturally grouped and thus the second method of setting up frequency classes is applicable.

11.8 MONTE CARLO SIMULATION

Monte Carlo simulation is another method for obtaining information about system performance from component data. This method has also been referred to as synthetic sampling or empirical sampling. It consists of "building" many systems by computer calculations and evaluating the performance of such synthesized systems.(11.1.2)

If the relationship between the component variables and system performance is known, system performance can be calculated from the component measurements without actually building the systems. It is possible to obtain synthetic measurements on components by drawing random values from each distribution. These random values can then be used to calculate the performance of synthetic system. This procedure, the so-called Monte Carlo method, is shown graphically in Figure 11.8.1. T'e availability of high-speed computers that can economically and rapidly synthesize the performance of complex systems has led to the popularization of Monte Carlo procedures.

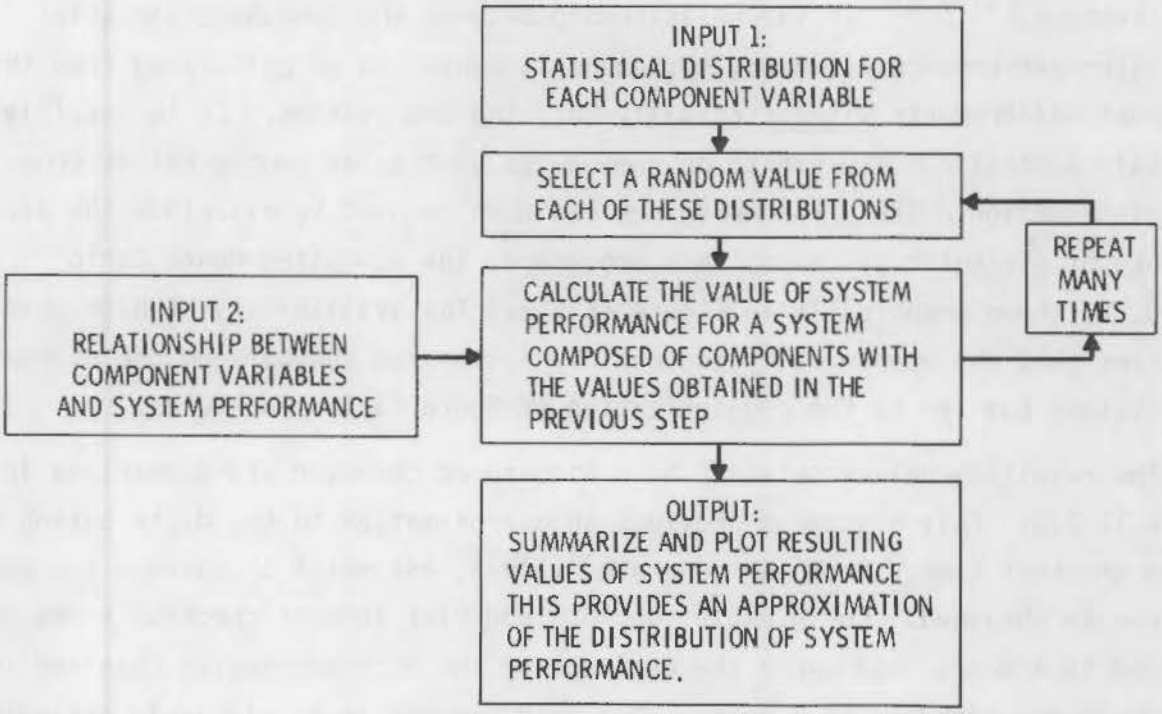

FIGURE 11.8.1. Flow Chart of Monte Carlo Simulation Method

Before we discuss the details for obtaining random values from designated distributions, we apply the method to the six-station test-and-repair facility problem in Section 11.5.4. The distribution of checkout time at the first station was assumed to be normal, with a mean of 10 hours and a standard deviation of one hour. A random value is selected from this distribution--say, 11.3 hours. This represents the checkout time for the first synthetic system at station 1. Random values are similarly obtained to represent checkout times at each of the remaining stations, as follows: station 2, 17.5 hours; station 3, 1.9 hours; station 4, 6.3 hours; station 5, 0.3 hours; and station 6, 9.2 hours.

Thus, the total checkout time for the first simulated system is 46.5 hours. The process is illustrated in Figure 11.8.2. This procedure is followed a total of 100 times, each time drawing new random values.

Monte Carlo simulation is another method for obtaining information about system performance from component data. This method has also been referred to as synthetic sampling or empirical sampling. It consists of "building" many systems by computer calculations and evaluating the performance of such synthesized systems.(11.1.2) If the relationship between the component variables and system performance is known, system performance can be calculated from the component measurements without actually building the systems. It is possible to obtain synthetic measurements on components by drawing random values from each distribution. These random values can then be used to calculate the performance of synthetic systems. This procedure, the so-called Monte Carlo method, is shown graphically in Figure 11.8.2. The availability of high-speed computers that can economically and rapidly synthesize the performance of complex systems has led to the popularization of Monte Carlo procedures.

The resulting values obtained by a high-speed computer are summarized in Figure 11.8.3. This histogram provides an approximation to the distribution of system checkout time. From the generated values, estimates of maximum checkout time can be obtained. For example the 90th and 91st longest checkout times are 58.8 and 59.4 hours, and hence the estimate of the 90th percentile obtained in the manner described is 59.3 hours. The 95th percentile is similarly estimated as 61.0 hours. These values compare closely with the corresponding values calculated in Section 11.5.4.

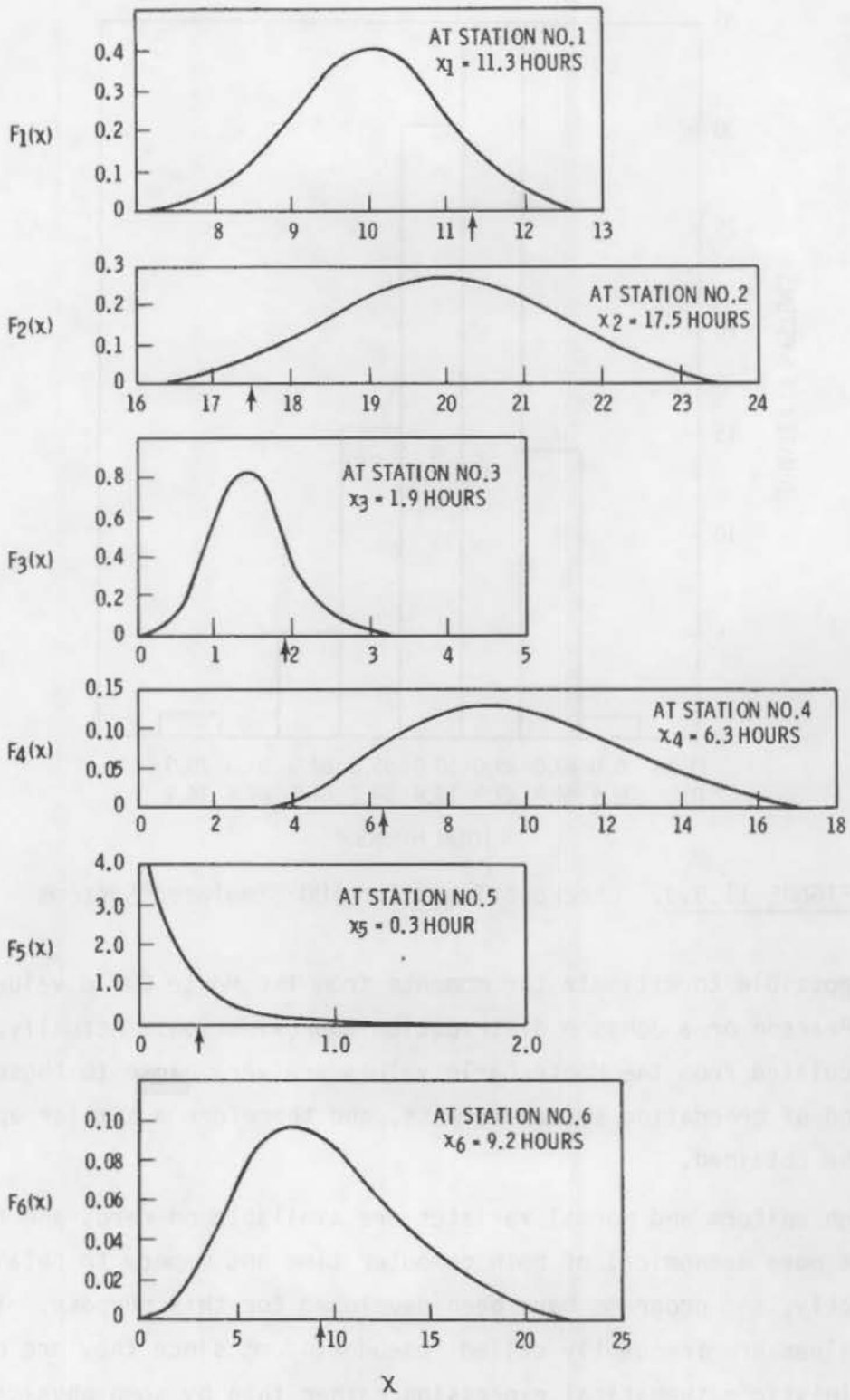

FIGURE 11.8.2. Steps in System Simulation for Checkout Problem

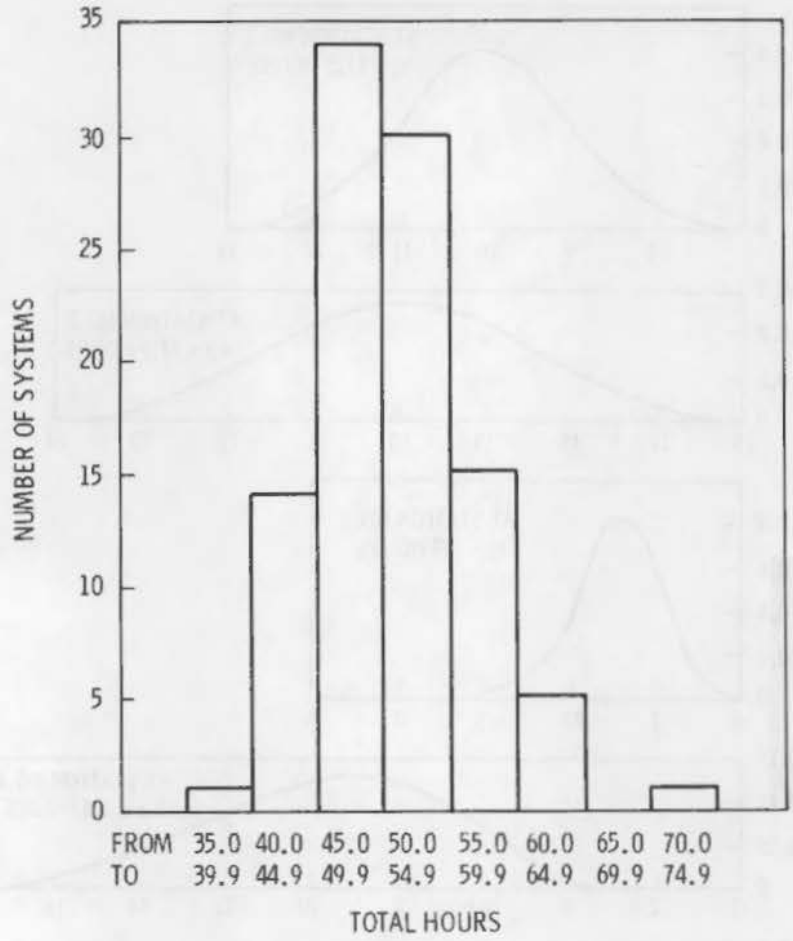

FIGURE 11.8.3. Checkout Times for 100 Simulated Systems

It is possible to estimate the moments from the Monte Carlo values and use these in a Pearson or a Johnson distribution approximation. Actually, the moments calculated from the Monte Carlo values are very close to those obtained by the method of generating system moments, and therefore a similar approximation would be obtained.

Although uniform and normal variates are available on cards and tape, it is sometimes more economical of both computer time and memory to obtain such values directly, and programs have been developed for this purpose. The resulting values are frequently called "pseudorandom" since they are obtained by a deterministic mathematical expression rather than by some physical mechanism.

Statistical tests can be applied to the generated values to determine whether they represent the desired distribution adequately.

Because Monte Carlo simulation involves random values, the results are subject to statistical fluctuations. Thus, any estimate will not be exact but will have an associated error band. The larger the number of trials in simulation, the more precise will be the final answer, and we can obtain as small an error as desired by conducting sufficient trials. In practice, the allowable error is generally specified, and this information is used to determine the required trials. A typical Monte Carlo problem is the estimate of the proportion of the population between two limits or above or below some specified value, based on the results of n trials. This problem is the same as estimating the parameter p of a binomial distribution.

It is possible to determine the approximate sample size for a Monte Carlo study. In doing so we must initially specify E, the maximum allowable error in estimating p; $1 - \alpha$, the desired probability or confidence level that the estimated proportion p does not differ from p by more than $\pm E$; and p', an initial estimate of p.

For example, we might want to conduct sufficient Monte Carlo trials to be 95 percent sure that the proportion p of the population between two specified values (or above or below some specified value) does not differ by more than $E = 0.05$ from the final estimated value, assuming an initial estimate $p' = 0.80$. A trial-and-error procedure for determining n would then be as follows.

If 1000 Monte Carlo trials had been conducted and 800 of these, or 80 percent, fell within the initially specified range, the resulting 95 percent confidence interval for p is 0.775 to 0.825. Similar intervals for 400 trials and 200 trials, each with 80 percent of the resulting observations within the specified range, are 0.755 to 0.84 and 0.74 to 0.85, respectively. Because we wish to estimate p within ± 0.05 with 95 percent confidence, somewhat more than 200 trials are required. Note that the length of the error range is smaller if the sample percentage is above 80 percent and larger if it is between 50 and 80 percent. Thus, the chosen sample size might be found to be either slightly too conservative or slightly too liberal after the trials have actually been conducted (see later discussion).

The following expression, based on the normal distribution approximation to the binomial distribution may also be used to estimate the number of trials;

$$n = p' \frac{(1 - p')}{E^2} z^2_{1-\alpha/2} \qquad (11.8.1)$$

where E and p' have been previously defined and $z_{1-\alpha/2}$ designates the $(1-\alpha/2)$ 100 percent point of a standard normal distribution. For example, if the desired confidence level is $1 - \alpha = 0.95$, then $\alpha = 0.05$ and $z_{1-\alpha/2} = 1.96$; and if $1 - \alpha = 0.99$, then $\alpha = 0.01$ and $z_{1-\alpha/2} = 2.58$. This approximation is generally adequate, except when np or n(1-p) is less than 5.

The use of Equation 11.8.1 to determine n requires an initial estimate of p, the very quantity to be determined by the Monte Carlo study. The largest sample size is required when $p = 0.5$. Thus, when nothing is known initially about the magnitude of p, the estimate $p' = 0.5$ leads to the most conservative sample size. Sometimes it might be advantageous to conduct some preliminary Monte Carlo trials to obtain an estimate p', which would then be used to determine the additional required number of trials.

To determine initially the required number of trials we must specify

E = the maximum allowable error in estimating

$1-\alpha$ = the desired probability or confidence level that does not differ from μ by more than $\pm E$,

σ = an initial estimate of the process standard deviation.

The approximate number of Monte Carlo trials is then found as

$$n = \left(\frac{z_{1-\alpha/2}\sigma'}{E} \right)^2 \qquad (11.8.2)$$

where $z_{1-\alpha/2}$ is the $(1-\alpha/2)$ 100 percent point of a standard normal distribution.

The adequacy of this expression depends on how close the estimate σ' is to the true standard deviation σ.

From the preceding, it is evident that the usual statistical methods for obtaining confidence bands on estimates or parameters and determining the required number of observations to obtain a desired degree or precision are directly applicable in a Monte Carlo analyses.

The assumption of normality of system performance, based on the central limit theorem, is strictly applicable only when system performance is the sum of the effects of many component variables, with no single one having a dominant variance. Even for the nonadditive systems the method of moments often is used to calculate the average and variance for system performance, which is then assumed to be normally distributed. This assumption is sometimes reasonable when performance is affected by a number of variables whose effect on system performance are of similar magnitude and the functional relationship is not "too nonlinear." However, indiscriminate assumptions of normality could lead to erroneous conclusions. In a particular case it is not always clear whether a normal distribution will yield a reasonable approximation without generating higher system moments.

Monte Carlo simulation has more intuitive appeal than does the generation of system moments and consequently is easier to understand. The desired precision can be obtained by conducting sufficient trials. Also, the Monte Carlo method is very flexible and can be applied to many highly complex situations for which the method of generation of system moments becomes too difficult. This is especially true when there are interrelationships between the component variables.

A major drawback of the Monte Carlo method is that there is frequently no way of determining whether any of the variables are dominant or more important than others. Furthermore, if a change is made in one variable, the entire simulation must be redone. Also, the method generally requires developing a complex computer program; and if a large number of trials are required, a great deal of computer time may be needed to obtain the necessary answers.

Consequently, the generation of system moments in conjunction with a Pearson or Johnson distribution approximation is sometimes the most economical approach. Although the precision of the answers usually cannot be easily

assessed for this method, this approach often does provide an adequate approximation. In addition, the generation of system moments allows us to analyze the relative importance of each component variable by examining the magnitude of its partial derivative. As a result, it might be desirable to set more stringent tolerances on those components that contribute most heavily to the system variance.

Also, unlike Monte Carlo, the generation of system moments does not necessarily require any assumptions concerning the form of the component distributions. For example, in the circuit problem only the estimates of the moments of the component variables were required, rather than the complete component performance distributions.

For these reasons the practicality of the procedure of systems moment should be examined before resorting to Monte Carlo methods in evaluating system performance from component data. Perhaps a given situation is so complex that Monte Carlo simulation provides the only workable tool. On the other hand, when the method of generation of system moments can be applied, it provides a cheaper and more refined approach.

One important application of Monte Carlo simulation has been in the estimation of the reliability of complex systems by Monte Carlo simulation, using a computer to "build" a large number of synthetic systems. For each system, the performance of each component is evaluated by picking a uniform variate over the interval (0,1) and comparing it with the required reliability. For example, a reliability of 0.9 is synthesized by denoting a failure every time a random value of 0.9 or above is obtained and otherwise denoting a success. The procedure is repeated many times, and the estimated reliability is the proportion of successful systems to the total number simulated.

Reliability problems can be programmed simply on a high-speed computer. There are many other application of Monte Carlo simulation in analyzing complex operational situations, such as in the evaluation of inventory-management rules and the operation of transportation facilities.

Such methods are also used in theoretical statistics when it is not possible to find the distributions of some variable directly. For example, the distribution of the W statistics can be approximated by Monte Carlo methods.

Monte Carlo simulation can be a powerful tool. As in any other method, the validity of the answers depends on the adequacy of the input data. Therefore, careful attention must be given to the development of a realistic description of the underlying physical situation to serve as input to the Monte Carlo analysis.

11.9 BAYESIAN RELIABILITY ESTIMATION

Many of the tools used in reliability estimation have been developed in previous sections of Chapter 11. For example, the discrete (Section 11.4) and continuous distributions, (Section 11.5) hazard functions, (Section 11.3) estimation by both maximum likelihood and method of moments (Section 11.5.3) have been covered previously.

Since reliability is the inverse of failure, it can be defined as

$$R(x) = 1 - F(x) \tag{11.9.1}$$

The various tools cited in the first paragraph are used in Bayesian estimates. Recalling the figure in Section 11.1, if sufficient data exist, we can determine reliability by nonparametric analysis of data. The more common case of moderate to limited data can be handled with classical inferential statistics. Finally, when little or no data exist, we can use Bayes and empirical Bayes. These latter two will be discussed in this section.

11.9.1 Bayes' Theorem

Kaplan and Garrick[11.9.1] quote Jaynes' as best defining probability, "Probability theory is an extension of logic which describes the inductive reasoning of an idealized being who represents degrees of plausibility by real numbers." The numerical value of any probability (A/B) will in general depend not only on A and B, but also on the entire background of other propositions that this being is taking into account. A probability assignment is "subjective" in the sense that it describes a state of knowledge rather than any property of the "real world"; but it is completely objective in the sense that it is independent of the personality of the user; two beings faced with the same total background of knowledge must assign the same probabilities.

In essence, probability is a numerical expression of a state of confidence, a state of knowledge--which may be influenced by statistical measurements, if available. If not, then it is the lack of data that influences our state of knowledge and that is reflected in the numerical values we assign.

We can define terms commonly used in probability theory. Some of these are

P(A)--the probability of the occurrence of event A

P(B)--the probability of the occurrence of event B

$s \in S$--s is an element of S

$s \notin S$--s is not an element of S

A U B--The union of A and B, or the set whose elements belong to either A or B or both

$$A \cup B = \{s : s \in A \text{ or } s \in B\}$$

$A \cap B$--the intersection of A and B, or the set whose elements belong to both A and B

$$A \cap B = \{s : s' \in A \text{ and } s \in B\}$$

P(A/B)--conditional probability of an event A given that the event B occurs, or the conditional probability of A given B.

From a basic axiom of probability theory, the probability of two simultaneous propositions A and B is

$$P(A \cap B) = P(A)\, P(B/A) \qquad (11.9.2)$$

and

$$P(A \cap B) = P(B)\, P(A/B) \qquad (11.9.3)$$

If the right sides of these two equations are equated

$$P(A)\, P(B/A) = P(B)\, P(A/B) \qquad (11.9.4)$$

Dividing by P(B) yields

$$P(A/B) = \frac{P(A)\ P(B/A)}{P(B)} \qquad (11.9.5(a))$$

or

$$P(A/B) = P(A)\left[\frac{P(B/A)}{P(B)}\right] \qquad (11.9.5(b))$$

The final form is Bayes' Theorem.

Bayes' Theorem says that P(A/B), the probability of A given information B is equal to P(A), the probability of A prior to having information B, times the correction factor appearing in brackets (11.9.5(b)).

This theorem is both powerful and simple. It shows us how the state of confidence with respect to A changes upon getting new information.

Basically, the philosophy behind Bayes' Theorem is that two sources of information exist regarding the parameters of the data model. First, in assuming a prior model for the parameter or parameters of interest, we suppose that the assumed prior model summarizes and represents the totality of knowledge available concerning the parameter prior to the observation of data. Second, any observed experimental data contains information about the parameters of the data model. Bayes' Theorem is a technique for combining the information about the parameters from both the prior model and the data model into a single model.

The combined model provided by Bayes' Theorem is called a posterior model because it represents the state of knowledge about the parameters after (posterior) sample data information is combined with the prior data information.

11.9.2 Prior Models

The assumed probability prior models for parameters may take the form of the discrete or the continuous distributions of Section 11.4 and 11.5. The specific selection of a prior model is based on a subjective decision by the experimenter. Because of this subjectivity, two different experimenters will not necessarily choose the same prior model because of different assumptions.

Obviously, the choice of the prior model will influence both analysis and results. This lack of uniqueness is a criticism of Bayesian methods. However, in cases where either engineering judgments or previous empirical data are available and can be expressed in the form of prior models, the Bayesian approach allows the researcher to incorporate the information into the decision process.

No rigid rules exist for selecting prior models; however, intuitive guidelines have been suggested.[11.9.2, 11.9.3]

It should be understood that the Bayesian estimation philosophy treats statistical parameters as variables rather than constants.

MacFarland[11.9.3(a)] expands upon the various options influencing the validity of results derived from applying Bayes' Theorem:

- If the prior probabilities are known, Bayes' Theorem becomes a simple, error-free truism.
- If the prior probabilities are not completely known but are carefully and cautiously selected, estimated and employed (in terms of the guidelines discussed later), then Bayes' Theorem can be successfully utilized to extend the power of reliability inference.
- If the prior probabilities, being in fact unknown, are capriciously and arbitrarily adopted for use in Bayes' Theorem, the end results of Bayesian manipulation may be inaccurate and misleading.
- It is apparent that the key to successful use of the Bayesian method resides in the appropriate choice of the prior probability distributions. A well considered engineering judgment such as is suggested by MacFarland[11.9.3.(a)] should answer several of the reservations cited by Easterling.[11.9.3(g)]

An examination of several of problems to which Bayes' Theorem was applied indicates that most of those where the reader has some belief in the conclusions are based on a partial knowledge of the probable shape of the probability density function. In some instances, one wonders why an inferential statistic approach was not selected rather than the Bayesian approach.

11.9.3 Bayesian Inference

MacFarland[11.9.3(a)] discusses the three basic types of Bayesian inference; soft, hard and mixed.

The soft Bayesian estimate usually is limited to a subjective development of the prior distribution to aid in a decision theory approach. Rarely, if ever, are objective data generated to quantify P (A/B).

The hard Bayesian estimate generally will have a large amount of test data available--so large that it swamps out the prior even if the prior were largely incorrect. Basically, one has used an inferential statistic approach without designating it as such.

The mixed case lies between the soft and the hard. Usually, the data are insufficient to point to errors in the prior distribution. Here the careful selection of the prior distribution is very important. Such a prior distribution should meet the criteria suggested by MacFarland:[11.9.3(a)]

- Relative simplicity of use--all things being equal, simplicity of mathematical manipulation is desirable.
- Simplicity and completeness of interpretation--in general, if the Bayesian process can be made to yield as an output the resultant posterior distributions in their entirety, this is superior to an output limited merely to a measure of central tendency (such as the mean of the posterior distribution) and one or two probability bounds.
- Richness of distributional form--all things being equal, it is better to be able to depict prior belief in a reasonably full manner, rather than in a constrained and artificial manner. It is also desirable that, whenever test results differ widely from prior belief, that this difference be directly signaled in the posterior distribution rather than merely merged and blended into a smooth artificial composite of data and prior belief.
- Possession of common sense properties--the Bayesian distribution should change in a sensible manner under the impact of limited data

running counter to its initial formulation. Conversely, if the data essentially confirm the prior distribution (no failures in limited testing; high reliability initially predicted), then the Bayesian posterior should essentially resemble the initial prior. Bayesian probability-bound properties should also be reasonable; both in the prior, and under the impact of subsequent test data (see below, on preposterior analysis).

11.9.4 Preposterior Analysis

MacFarland[11.9.3(a)] discusses the iterative process followed in a preposterior analysis aimed at validating the prior:

- Set up a prior distribution initially considered satisfactory.
- Using the amount of test information ultimately expected to be available as a base, assume an ensemble of both extremal and anticipated test results (possibly 0 successes in ten trials, 5 successes in ten trials (extremals), and 9 or 10 successes in ten trials (anticipated).
- Put these hypothetical test results through Bayesian analysis, using the selected prior.
- Study the resulting posterior distributions to see whether or not they seem reasonable under the impact of the postulated data.
- If they are reasonable, the prior may be employed; if they are not, readjust the prior and begin again the sequence of preposterior analysis until the price is satisfactory.

This preposterior analysis (so-called because it examines possible test results in a Bayesian context before they have actually occurred, and while it is therefore still possible to suitably adjust and "fine tune" the prior) should definitely be employed with Bayesian reliability formulations.

11.9.5 Conjugate Priors

MacFarland discusses the possible use of conjugate priors. These are discussed further by Raiffa and Schlaifer.[11.9.4]

A desirable additional property for the pdf's to have is ease of mathematical manipulation of the prior and subsequently obtained test data within the framework of Bayes' Equation to yield a posterior distribution. No "free hand" distribution meets this requirement, and in general many well known mathematical distributions potentially selectable as priors do not "go together" well with test data of various types. Normally, such cases require extensive computer use to yield approximate conjugations of the prior with the data.

These difficulties have led to the concept of conjugate distributions, primarily by Raiffa and Schlaifer[11.9.4] who were the major developers of conjugate prior distributions to meet the needs for probability density functions relatively easy to manipulate mathematically as a prior and also with test data obtained within the framework of the Bayes' Equation to yield a posterior distribution. Many of the well known continuous or discrete distributions having potentiality as priors are difficult to handle with test data; in many cases they require extensive computer time to yield a posterior distribution.

Their[11.9.4] family of conjugate distributions should meet these criteria:

1. Be rich enough so that the decision makers' prior beliefs can be represented quite closely by at least one of the members of the family.
2. Go together with test data readily, yielding a posterior distribution of the same family as the prior. For example, with binomial data, the Beta family of distributions is the appropriate prior choice according to the conjugate theory.

Examples of conjugate distributions are given in Table 11.9.1.[11.9.4] While the conjugate distributions simplify some aspects of the handling of test data, there may be other problems as noted in comments by MacFarland.[11.9.3(a)]

MacFarland[11.9.3(a)] examined a typical conjugate prior, the Beta Function for both strong and weak formulations. He argues that such continuous

TABLE 11.9.1. Distributions of Statistics and Posterior Parameters

Process	Conjugate Prior Distribution	Distribution of Statistic		Distribution of Posterior Parameter
		Conditional	Marginal	
Bernoulli	beta	binomial	beta-binomial	--
		Pascal	beta-Pascal	--
		Poisson	negative-binomial	--
Poisson	gamma-1	gamma-1	inverted-beta-2	--
Normal	σ known $\tilde{\mu}$ normal	normal	normal	normal
	μ known σ gamma-2	gamma-2	inverted-beta-2	inverted-beta-1
	normal-gamma			
Multinormal	σ known $\tilde{\mu}$ normal	normal	normal	normal
	normal-gamma	--	--	--
Regression	σ known $\tilde{\beta}$ normal	normal	normal	normal
	normal-gamma	--	--	--

functions suffer serious limitations for both strong and weak formulations. For example, a strong prior may lead to overly optimistic conclusions even after several successive failures. The weak prior suffers from an excess of strengths if a short test sequence contains no failures. For these and other reasons, MacFarland[11.9.3(a)] prefers discrete distributions such as the binomial and his article develops this concept extensively. His conclusions concerning the key advantages of the discrete binomial distribution are

- Its simplicity and understandability.
- Its flexibility in terms of number and breadth of probability cells.

- Its freedom from constraint to unimodality. This is of value to the engineer who would like to quantize his belief that his recently designed component will "either work or it won't"; and also in subsequent analysis where the early appearance of subsidiary peaks often foreshadows coming events and permits early program attention and investigation. Neither of these features exists in the continuous conjugate Beta formulation.
- High visibility--the posterior distribution is totally available for examination at all times. Most uses of continuous conjugate formulations, on the other hand, often deal at best with one or two distributional points or average values (e.g., possibly a mean or probability bound) and nothing else.

There is nothing that restricts the general method to the reliability realm or to binomial or exponential inference. It can be applied (after suitable initial tailoring to the intended purpose) to other distributional forms and other realms of inference. All that is needed is a defined finite parameter space (or what amounts to the same thing, an infinite parameter space of which some finite subset can be defined as containing all cases of real interest) and the ability to obtain likelihoods on the subsequently observed data, given the hypotheses considered.

11.9.6 Illustrative Problems

11.9.6.1 Bionominal Estimation of Reliability

MacFarland[11.9.3(a)] utilized an excellent (and simple) illustrative example within the framework of the binomial estimation of reliability to demonstrate the use of Bayes' Equation.

In essence a go, no-go test of a pyrotechnic device was used where go (success) occurred if it fires and no-go (failure) when it does not fire. Two lots were available, one with a reliability of R = 0.9, the other R = 0.50; however, their identities have been lost.

If one lot is randomly selected so that the probability for each lot is 0.50, a single item is selected which fails in test.

Recalling the Bayes' Equation

$$P(A/B) = \frac{P(A)\ P(B/A)}{P(B)} \qquad (11.9.5(a))$$

with the following definitions:

A A hypothesis or statement of belief. ("The reliability of this component is 0.90.")

B A piece of evidence, such as a reliability test result that has bearing upon the truth or credibility of the hypothesis. ("The component failed on a single trial.")

Pr(A) The prior probability; the probability we assign to the hypothesis A before evidence B becomes available. ("We believe, based on engineering experience, that there is a 50/50 chance that the reliability of this component is about 0.90, as opposed to something drastically lower, e.g., Pr A = 0.5.")

Pr(B/A) The likelihood: the probability of the evidence assuming the truth of the hypothesis. ("The probability of the observed failure, given that the true component reliability is indeed 0.90, is obviously 0.10.")

Pr(B) The probability of the evidence B, evaluated over the entire weighted ensemble of hypotheses A_i.

Pr(A/B) The posterior probability of A given the evidence of B.

Defining terms for the example problem,

$A_1 \equiv$ Lot chosen has R = 0.50

$A_2 \equiv$ Lot chosen has R = 0.90

Then based on selection process,

$$P(A_1) = 0.5$$

$$P(A_2) = 0.5$$

Note that the probabilities in both cases sum to unity a requirement that must be met in all Bayesian procedures. Figure 11.9.1(a) portrays the prior distribution.

The test results were

B ≡ one unit was tested and it failed

Then

$$P(B/A_1) = P(\text{single test failure}/R = 0.5) = (1 - 0.5) = 0.5$$

$$P(B/A_2) = P(\text{single test failure}/R = 0.9) = (1 - 0.9) = 0.1$$

Then, if A is partitioned into a set of states $(A_1, A_2 \ldots A_n)$ and if $P(A_i)$ and $P(B/A_i)$ are known for each i, the Bayes' Equation becomes

$$P(A_i/B) = P(A_i) \frac{P(B/A_i)}{\Sigma P(B/A_i)\ P(A_i)} \qquad (11.9.5(c))$$

$$P(B) = P(B/A_i)\ P(A_i) + P(B/A_2)\ P(A_2) \qquad (11.9.6)$$

$$= 0.5(0.5) + 0.1(0.5)$$

$$= 0.30$$

Finally,

$$P(A_1/B) = \frac{P(A_1)\ P(B/A_1)}{P(B)} = \frac{0.5(0.5)}{0.30} = 0.833$$

$$P(A_2/B) = \frac{P(A_2)\ P(B/A_2)}{P(B)} = \frac{0.5(0.1)}{0.30} = 0.167$$

The prior distribution in Figure 11.9.1(a) has been transformed in this single test resulting in failure, to the posterior distribution depicted in Figure 11.9.1(b). While the single test is not absolute, it does lead one to suspect that the lot with R = 0.9 was not picked.

11.9.6.2 Discrete Distributions

Another example of a Bayesian approach used with discrete distributions is that of Kaplan and Garrick[11.9.1] for the transport of spent fuel. A Bayesian approach was used to establish the relative frequency and probability of an accident resulting in the release of radioactivity. The format used in the previous example is repeated here:

Let:

A_1 stand for the statement, "The frequency rate is 10^{-3}"
A_2 stand for the statement, "The frequency rate is 10^{-4}"
A_3 stand for the statement, "The frequency rate is 10^{-5}"
A_4 stand for the statement, "The frequency rate is 10^{-6}"
A_5 stand for the statement, "The frequency rate is 10^{-7}"
A_6 stand for the statement, "The frequency rate is 10^{-8}"

Let B stand for the statement, "There have been 4000 shipments with no releases of radioactivity."

Let:

$P(A_i)$ (where i = 1-6) have the values given in Table 11.9.2 where these are the prior probabilities assigned to the hypothesis A before the evidence B becomes available (see Figure 11.9.2).

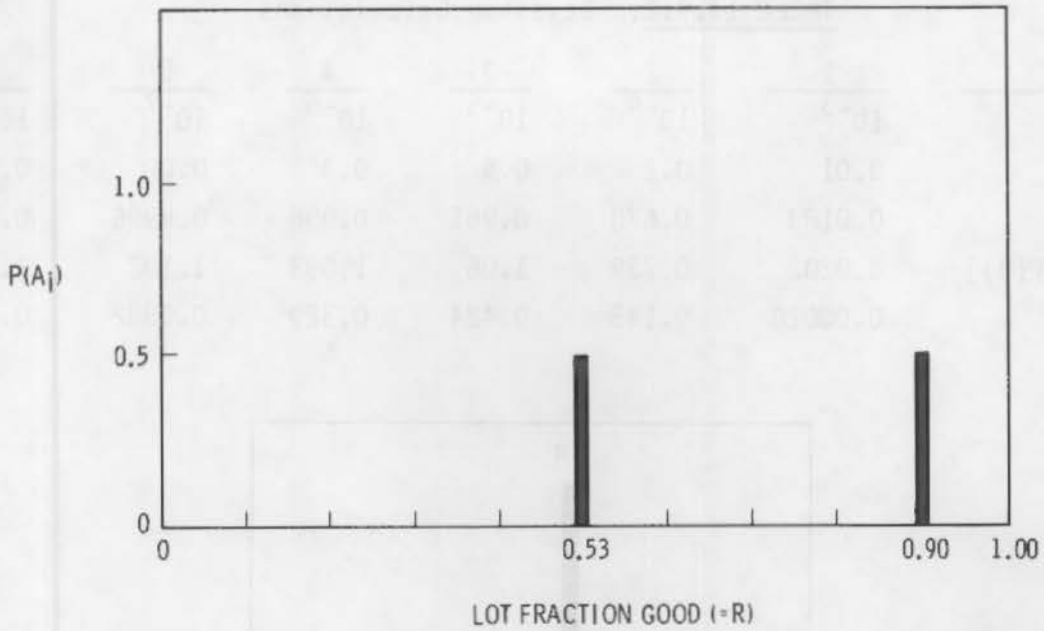

FIGURE 11.9.1(a). Simple Prior Distribution

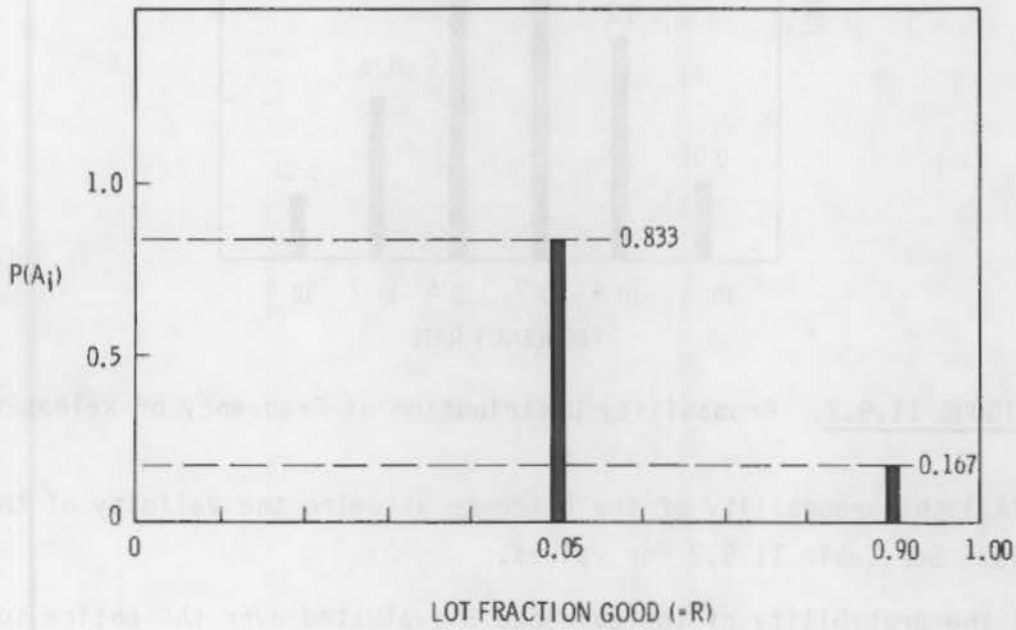

FIGURE 11.9.1(b). Simple Posterior Distribution

TABLE 11.9.2. Bayesian Calculations

i	1	2	3	4	5	6
A_i	10^{-3}	10^{-4}	10^{-5}	10^{-6}	10^{-7}	10^{-8}
$P(A_i)$	0.01	0.2	0.4	0.3	0.08	0.01
$P(B/A_i)$	0.0183	0.670	0.961	0.996	0.9996	0.99996
$[P(B/A_i)/P(B)]$	0.0202	0.739	1.06	1.098	1.102	1.102
$P(A_i/B)$	0.00020	0.148	0.424	0.329	0.0882	0.01102

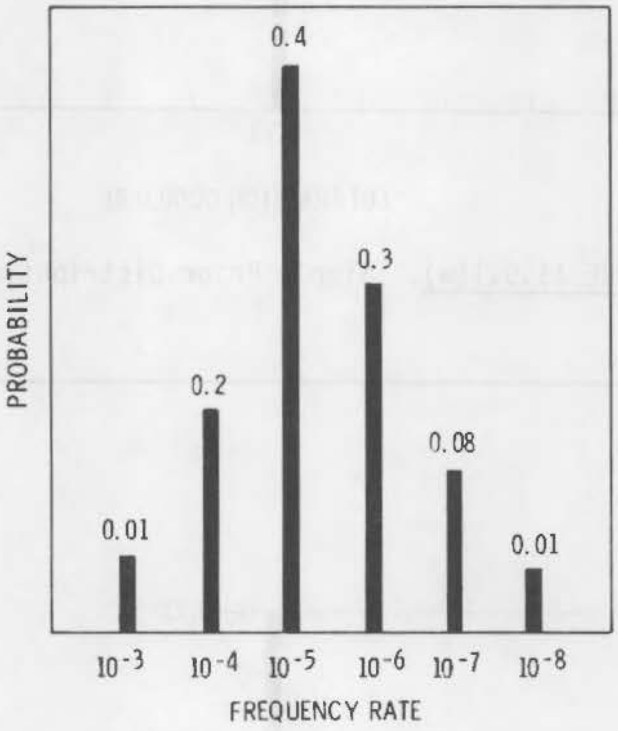

FIGURE 11.9.2. Probability Distribution of Frequency of Releases

$P(B/A_i)$ the probability of the evidence assuming the validity of the hypothesis. See Table 11.9.2 for values.

$P(B)$ the probability of the evidence B evaluated over the entire spectrum of hypotheses A_i.

$P(A_i/B)$ the posterior probability of A given the evidence B.

Determination of $P(B/A_i)$ represents a special case of the binomial distribution where all trials are successful; e.g.,

$$P(B/A_i) = \left|\begin{matrix} n \\ x \end{matrix}\right| p^x (1 - P)^{n-x} \qquad (11.9.7)$$

For $A_1 = 10^{-3}$ $P(B/A_1) = (1 - 10^{-3})^{4000}$

$= 1(0.999)^{4000}$

$= 0.0183$

The probability B or P(B) is determined by

$$P(B) = \sum_{i-1}^{6} P(A_i)\, P(B/A_i) = 0.907$$

The 0.907 can be obtained by plugging the appropriate numbers from Table 11.9.2 into the equation. The values for $P(B/A_i)/P(B)$ are obtained by simple division and $P(A_i/B)$ by multiplication.

One can conclude from the evidence of the 4000 shipments without release that the probability cited at 10^{-3} is much too high. To a degree this is true for A_2. For the smaller frequencies $<10^{-4}$ the model provides little information.

Considering the quantity of data available, the authors[11.9.1] could have used inferential statistics rather than Bayesian with the same end results.

11.9.6.3 Probability Density Function

An example more relevant to this report is that discussed by Tang[11.9.5] who used ultrasonic results on the detection of surface fatigue cracks to generate the crack size probability density function. The author[11.9.5] attempted to answer the three questions:

1. How would previous experience, engineering judgment and NDE data be utilized to estimate the probability distribution of flaw sizes and density?
2. How would these distributions relate to the detectability and accuracy of a particular NDE model?
3. How would these distributions be updated relative to the degree of repair of flaws subsequent to NDE?

We will examine the answers to the first two questions. Tang[11.9.5] used data of DeYoung on detection and measurement of fatigue cracks to construct his model. The original terminology is considered somewhat confusing; however, it will be retained to permit comparison with the reference. Figure 11.9.3 represents the actual versus measured crack depths. This fit the equation

$$C_a = \alpha + \beta C_m + \varepsilon \tag{11.9.8}$$

where C_a and C_m are actual and measured flaw depths; α, β, are coefficients determined from the linear regression analysis and ε represents calibration error which is a normal random variable with zero mean and standard deviation σ^*. These values will depend on the UT equipment, calibration and specimens.

The mean $E(C_a)$ and variance $V(C_a)$ of the equation are

$$E(C_a) = \alpha + \beta E(C_m) \tag{11.9.9}$$

$$V(C_a) = \beta^2 V(C_m) + (\sigma^*)^2 \tag{11.9.10}$$

As noted in the definitions of the Bayes' Equation,

$$P(A/B) = P(E_1/E_2) = P(A) \cdot \frac{P(B/A)}{P(B)} = P(E_1) \cdot \frac{P(E_2/E_1)}{P(E_2)} \tag{11.9.11}$$

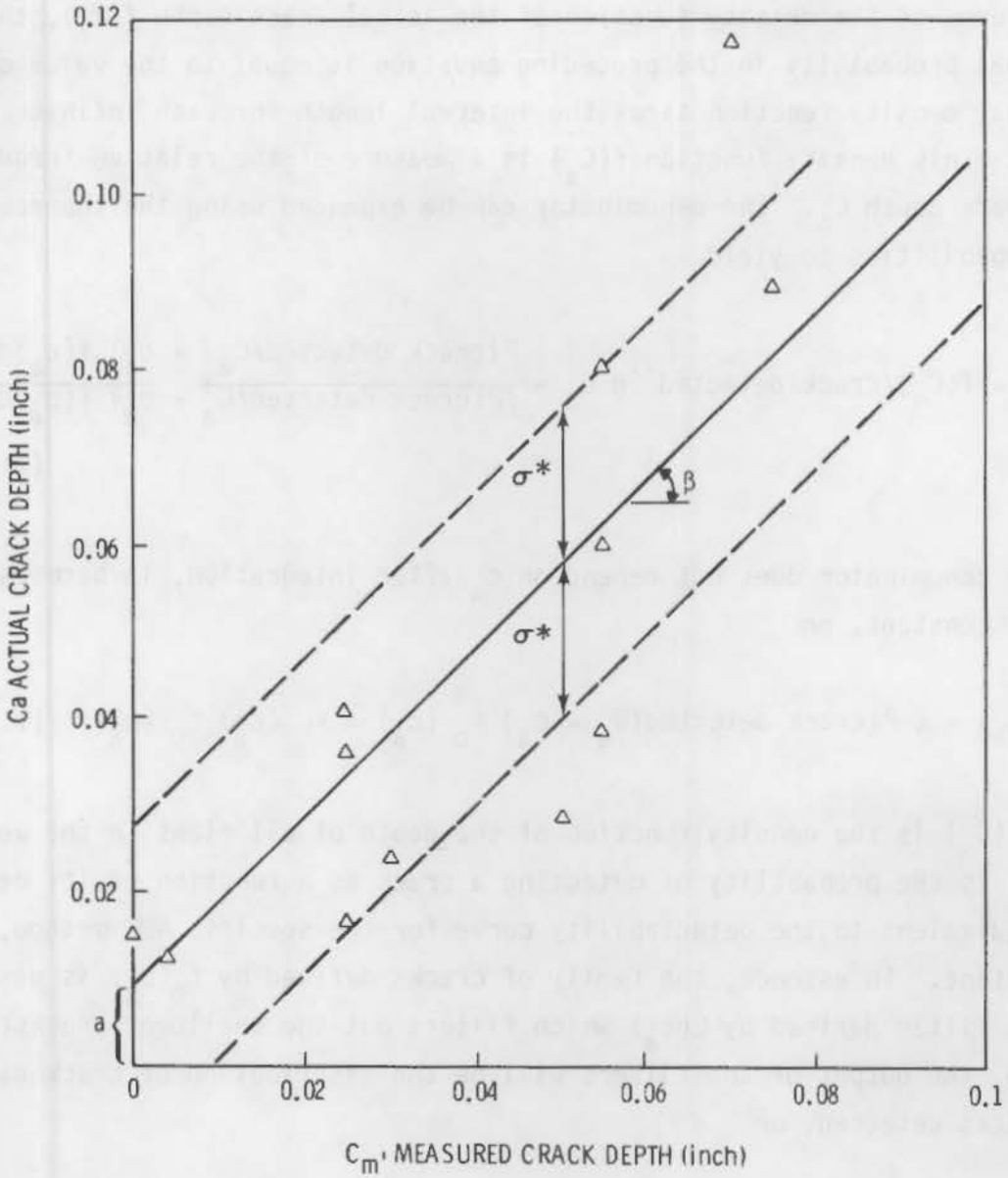

FIGURE 11.9.3. Actual Versus Measured Crack Depth

or, substituting from the definition,

$$P(E_1/E_2) = \frac{P(\text{crack detected}/\ c_a \le C_a \le c_a + d\,c_a)\ P\ (C_a \le C_a \le c_a + d\,c_a)}{P(\text{crack detected})} \qquad (11.9.12)$$

In terms of the density function of the actual crack depth $f(c_a)$, the conditional probability in the preceding equation is equal to the value of the conditional density function times the interval length for each infinitesimal interval. This density function $f(C_a)$ is a measure of the relative frequency of the crack depth C_a. The denominator can be expanded using the theorem of total probabilities to yield.

$$P(E_1/E_2) = f(C_a)/\text{crack detected} \quad d\,c_a = \frac{P(\text{crack detected}/C_a = c_a)\, f(c_a)dc_a}{\int P(\text{crack detected}/C_a = c_a)\, f(c_a)dc_a} \tag{11.9.13}$$

Since the denominator does not depend on c_a after integration, it becomes a numerical constant, or

$$f_1(C_a) = k\, P(\text{crack detected}/C_a = c_a)\, f_o(c_a) = kL(c_a)\, f_o(c_a) \tag{11.9.14}$$

where $f_o(C_a)$ is the density function of the depth of all flaws in the weld, and $L(C_a)$ is the probability of detecting a crack as a function of its depth c_a, or equivalent to the detectability curve for the specific NDE method, and k is a constant. In essence, the family of cracks defined by $f_o(c_a)$ is passed through a filter defined by $L(c_a)$ which filters out the shallower cracks; therefore, the output of the filters will be the distribution of crack depths for those cracks detected, or

$$f_o(c_a) = \frac{f_1(c_a)}{kL(c_a)} = k' \frac{f_1(c_a)}{L(c_a)} \tag{11.9.14}$$

Here k' is a normalizing constant such that $f_o(c_a)$ will be a correct probability density function, or the integral of $f_o(c_a)$ over the entire range of C_a will be unity. Note that $f_1(c_a)$ is a measure of the relative frequency of actual depths of detected cracks.

An example of the solution of the problem follows. Based on available data, the calibration curve comparing actual to measured crack depth is $E(C_a/C_m) = 0.0592 + 0.839\ C_m$ for $0 < C_m < 0.2$.

The detectability of the UT as a function of actual crack depth is given by

$$L(c_a) = \begin{cases} 0 & c_a \leq 0 \\ 5c_a & 0 \leq c_a \leq 0.02 \\ 9c_a - 0.08 & \text{for } 0.02 \leq c_a \leq 0.12 \\ 1.0 & c_a \geq 0.12 \end{cases}$$

This distribution is given in Figure 11.9.4. Prior to determining the distribution of flaw depth, the measured data on detected cracks must be adjusted to actual crack depths using the equation for mean and variance, or

$$E(C_a) = 0.0592 + 0.839 \times 0.05 = 0.10115$$

$$V(C_a) = (0.839)^2\ (0.0004) + (0.0342)^2 = 0.00145$$

The distribution of detected crack depth $f_1(c_a)$ is assumed to be log-normal. The actual crack depths for all cracks is back figured using the concept of a reverse filter given in Equation 11.9.14. The normalized crack depth distribution for the total crack population is determined and plotted in Figure 11.9.5 where it is compared to the plot for detected cracks $[f_1(c_a)]$. As noted $f_1(c_a)$ tends to bias towards deeper cracks because such cracks are more likely to be detected.

This example provides a basis for back calculating to the original pdf for flaws in a component. However, caution must be exercised in cases such as embedded cracks where a simplistic model for crack detection such as given in Figure 11.9.4 will not apply for larger flaws.

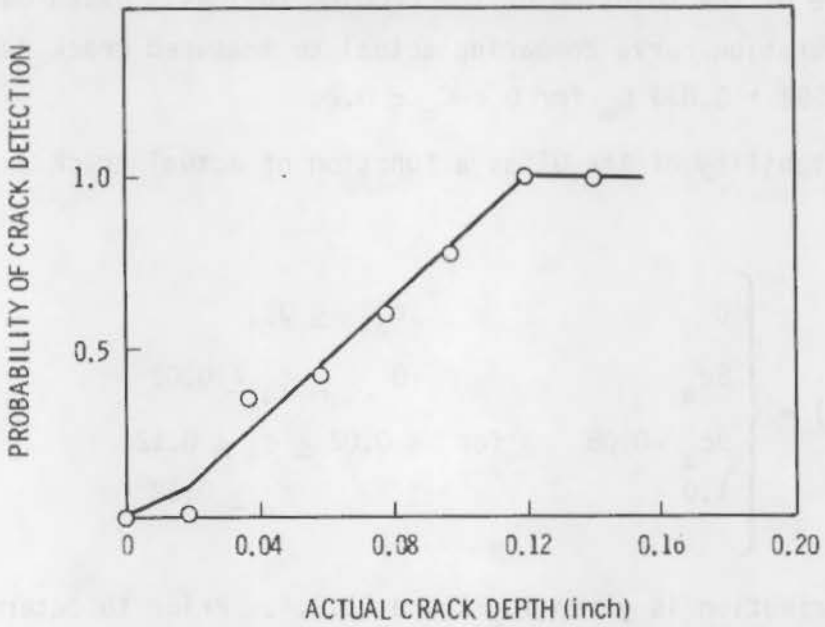

FIGURE 11.9.4. Detectability Versus Actual Crack Depth

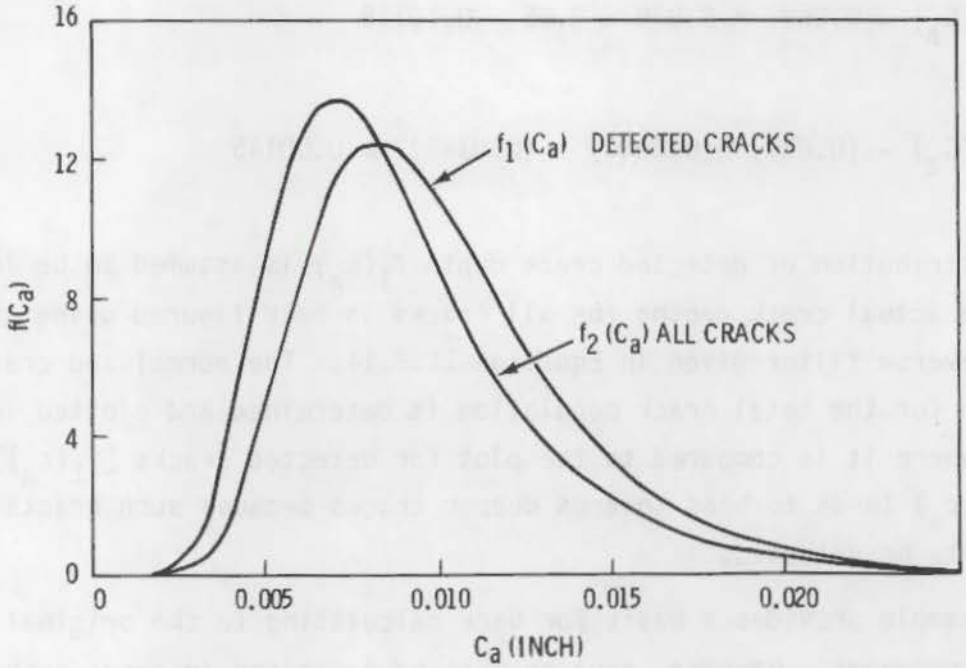

FIGURE 11.9.5. Comparison of Crack Depth Distribution for the Entire and the Detected Crack Sample

11.9.7 Continuous Distributions

Other authors[11.9.3] in the reliability seminar made arguments similar to those of MacFarland.[11.9.3(a)] Schafer and Feduccia[11.9.3(b)] describe use of the X^2 goodness-of-fit test to validate prior distribution using eight sets of field data and inverted gamma prior distributions. Bury[11.9.3(d)] determined the hazard function h(x) using a Weibull model suitably modifying the Weibull parameters by preposterior analyses. A similar approach in determining hazard rate is described by Stewart and Johnson.[11.9.3(e)]

Wilson[11.9.3(f)] examines various continuous strong and weak prior for various failure rate histories. The coefficient of variation μ/σ^2 is defined as T where weak priors will have small values of T. These priors were selected for each component of the system. Values of T ranged from 4 to several thousand, but with the average for the system near 4-a weak overall prior. The calculated system failure rates (best estimate and 80 percent upper confidence limit) for both the classical and Bayesian methods over the duration of the program are plotted as Figure 11.9.6.

It can be seen that the Bayesian and classical estimates converged rapidly, as would be expected in view of the weak prior. The merit of a weak prior is apparent in this case, since the system did not achieve its predicted failure rate, i.e., the prior was poorly positioned on the ordinate. Figure 11.9.7 shows the extent to which the Bayesian measurements would have proved misleading throughout the entire program had a strong prior (r=41), similarly located, been employed.

If however, the system had exhibited its predicted failure rate throughout the test program, then the prior would have been positioned accurately on the failure rate axis ($\lambda = \lambda_{predicted}$). In this case, and with a weak prior as in Figure 11.9.8, the Bayesian technique would have conferred little benefit over objective measurement. With a strong prior an appreciable narrowing of the uncertainty interval would have resulted, as seen in Figure 11.9.9.

The study did help to justify both the technique and criteria used for establishing priors.

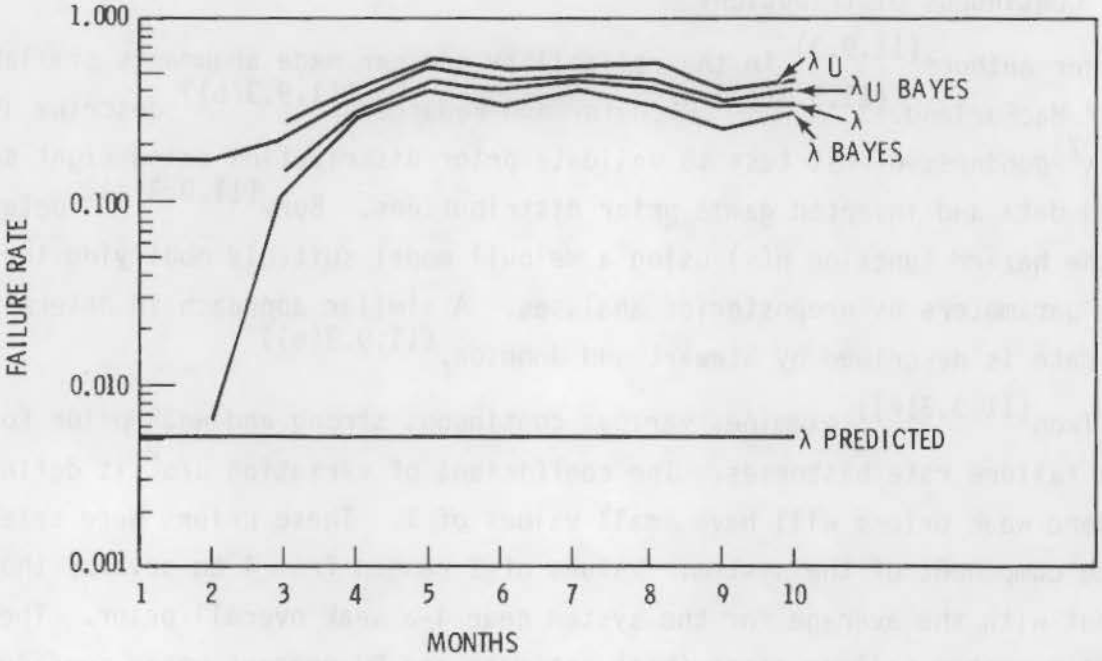

FIGURE 11.9.6. System Failure Rate History: Weak Prior, Inaccurately Placed

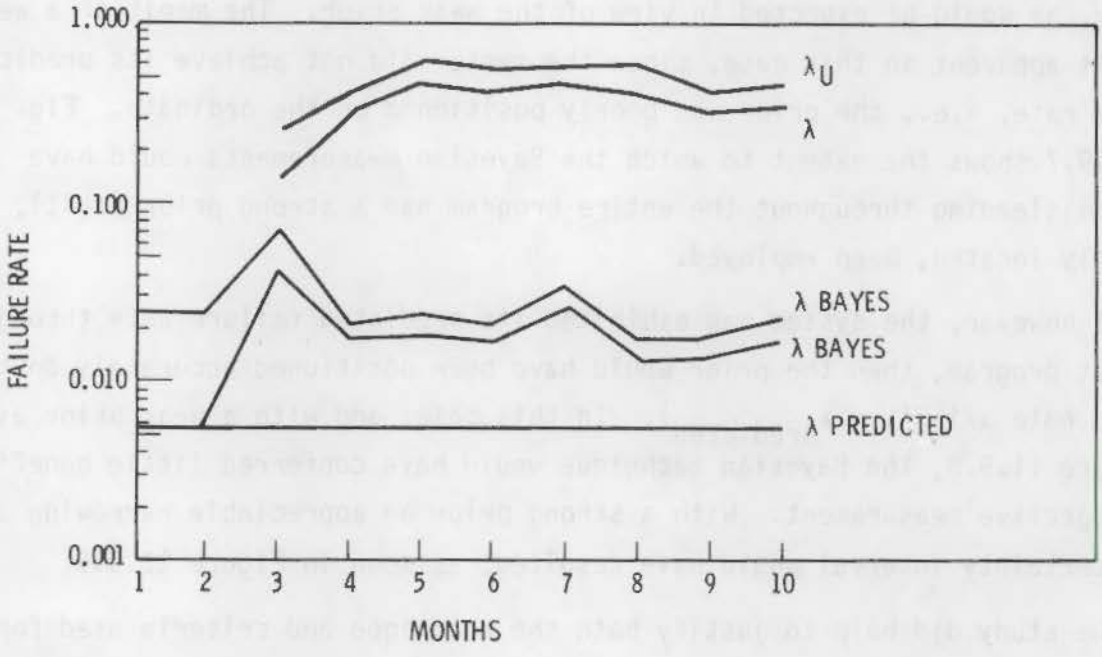

FIGURE 11.9.7. Hypothesized Failure Rate History: Strong Prior, Inaccurately Placed

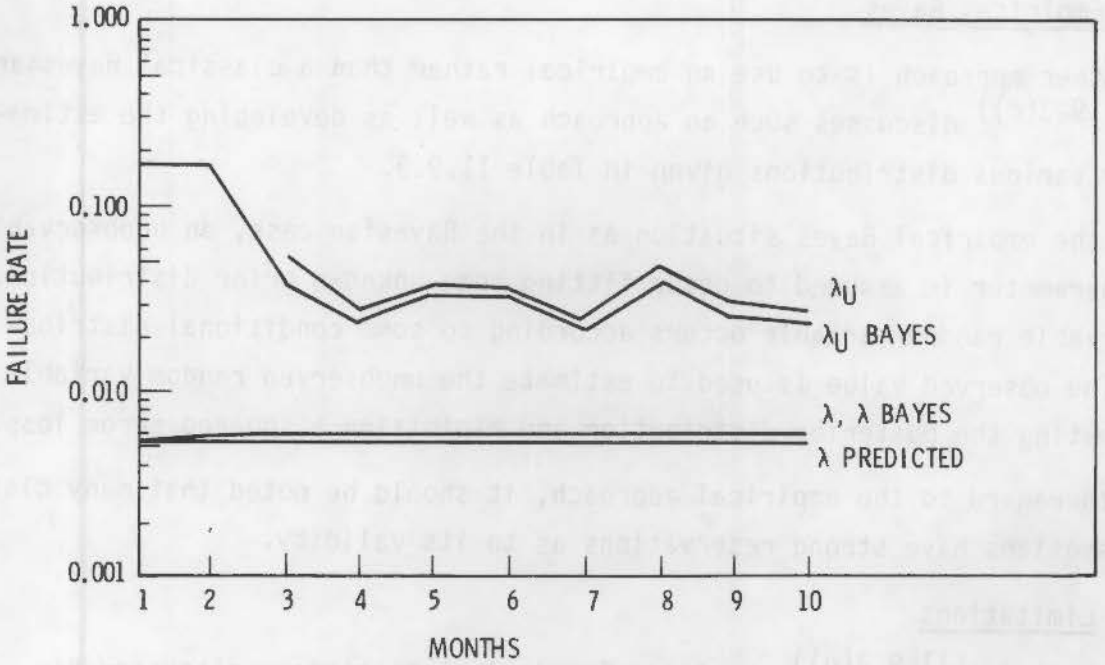

FIGURE 11.9.8. Hypothesized Failure Rate History: Weak Prior, Accurately Placed

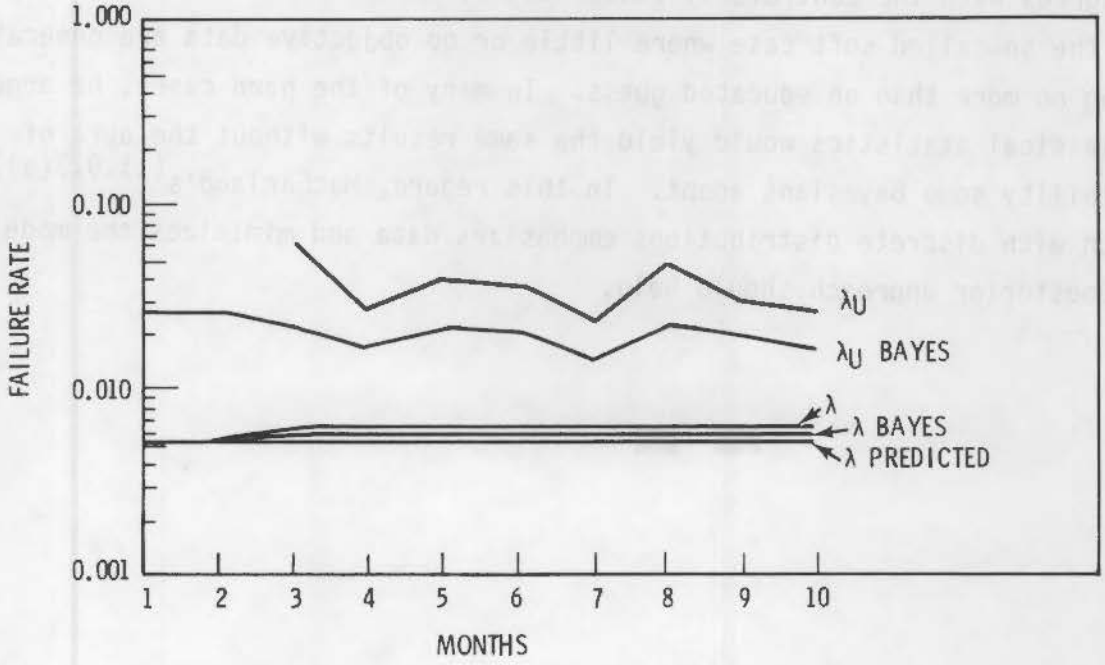

FIGURE 11.9.9. Hypothesized Failure Rate History: Strong Prior, Accurately Placed

11.9.8 Empirical Bayes

Another approach is to use an empirical rather than a classical Bayesian. Lemon[11.9.3(c)] discusses such an approach as well as developing the estimators for various distributions given in Table 11.9.3.

In the empirical Bayes situation as in the Bayesian case, an unobservable random parameter is assumed to occur fitting some unknown prior distribution. An observable random variable occurs according to some conditional distribution. The observed value is used to estimate the unobserved random variable by estimating the posterior distribution and minimizing a squared error loss.

With regard to the empirical approach, it should be noted that many classical Bayesians have strong reservations as to its validity.

11.9.9 Limitations

Easterling,[11.9.3(g)] who is a classical statistician, discussed his reservations concerning the Bayesian approach. He argues that statisticians are tending to ignore the Bayesian approach for real-world problems. His major point agrees with the controversy concerning selection of the prior. He denigrates the so-called soft case where little or no objective data are generated as being no more than an educated guess. In many of the hard cases, he argues that classical statistics would yield the same results without the aura of infallibility some Bayesians adopt. In this regard, MacFarland's[11.9.3(a)] approach with discrete distributions emphasizes data and mimimizes the model. The preposterior approach should help.

TABLE 11.9.3. Empirical Bayes Estimators

Distribution Name	Conditional Distribution Form	Parameter Name	Classical Estimator	Empirical Bayes Estimator $E_n(\theta/x)$*
Binomial	$\binom{N}{X}\theta^X(1-\theta)^{N-X}$	Reliability	X/N	$\dfrac{\sum\binom{N}{X}\left(\frac{X_i}{N}\right)^{X+1}\left(1-\frac{X_i}{N}\right)^{N-X}}{\sum\binom{N}{X}\left(\frac{X_i}{N}\right)^{X}\left(1-\frac{X_i}{N}\right)^{N-X}}$
Normal	$\frac{1}{\sqrt{2\pi\sigma}}\exp\left(-\frac{(x-\theta)^2}{2\sigma^2}\right)$	Mean	X	$\dfrac{\sum X_i\frac{1}{\sqrt{2\pi\sigma}}\exp\left(-\frac{(X-X_i)^2}{2\sigma^2}\right)}{\sum\frac{1}{\sqrt{2\pi\sigma}}\exp\left(-\frac{(X-X_i)^2}{2\sigma^2}\right)}$
Exponential	$\theta e^{-\theta X}$	Failure Rate	1/X	$\dfrac{\sum e^{-X_i X}}{\sum X_i e^{-X_i X}}$
Poisson	$\dfrac{e^{-\theta}\theta^X}{X!}$	Mean	X	$\dfrac{\sum e^{-X_i}X_i^{X+1}}{\sum e^{-X_i}X_i^{X}}$

11.10 REFERENCES

11.1.1 Morlat, G., "On Decision Theory Applied to Rare Events." NR-TR-003, Presented at meeting of the Committee on the Safety of Nuclear Installations of OECD Nuclear Energy Agency, Ispra, Italy, June 1976.

11.1.2 Hahn, G. J. and Shapiro, S. S., Statistical Models in Engineering. John Wiley and Sons, New York, New York, 1967.

11.1.3 Abramowitz, M. and Stegun, L. A., Handbook of Mathematical Functions. Applied Mathematics Series 55, National Bureau of Standards, U.S. Government Printing Office, Washington, D.C., 1964.

11.3.1 Nelson, W., "Hazard Plotting for Incomplete Failure Data." J. Qual. Technol. 1(1):27-52, January 1969.

11.3.2 Bush, S. H., "A Reassessment of Turbine-Generator Failure Probabilty." Nucl. Saf. 19(6):681-698, November-December 1978.

11.4.1 Packman, P. F., et al., "Reliability of Flaw Detection by Nondestructive Inspection," Metals Handbook. Vol. 11, 8th ed., American Society for Metals, Metals Park, Dhio, pp. 414-424, 1976.

11.5.1 Wirsching, P. H. and Jones, L. H., "On the Use of the Extreme Value Distribution in Reliability Analysis and Design." Paper 75-WA/DE-123, J. Eng. Ind. 98(3):1080-1085, August 1976.

11.5.2 Papazoglou, I. A. and Gyftopoulos, E. P., Markovian Reliability Analysis Under Uncertainty with an Application on the Shutdown System of the Clinch River Breeder Reactor. NUREG/CR-0405, U.S. Nuclear Regulatory Commission, Washington, D.C., August 1978.

11.6.1 Wirsching, P. H., "On the Behavior of Statistical Models Used in Design." J. Eng. Ind. 98(2):601-606, 1976. Also Paper 75-WA/DE-28, Transactions of the American Society of Mechanical Engineers, New York, New York, 1976..

11.9.1 Kaplan, S. and Garrick, B. J., "On the Use of a Bayesian Reasoning in Safety and Reliability Decisions - Three Examples." Nucl. Technol. 44:231-245, July 1979.

11.9.2 Martz, H. F., Jr. and Waller, R. A., Bayesian Reliability Analysis. John Wiley and Sons, New York, New York, 1982.

11.9.3 Crellin, G. L., ed., "Special Issue on Bayesian Reliability Techniques." IEEE Trans. Reliab. R-21(3):127-194, August 1972.

11.9.3a MacFarland, W. J., "Bayes Equation Reliability and Multiple Hypothesis Testing." IEEE Trans. Reliab. R-21(3):136-147, August 1972.

11.9.3b Shaffer, R. E. and Feduccia, A. J., "Prior Distributions Fitted to Observed Reliability Data." IEEE Trans. Reliab. R-21(3):148-154, August 1972.

11.9.3c Lemon, G. H., "An Empirical Bayes Approach to Reliability." IEEE Trans. Reliab. R-21(3):155-158, August 1972.

11.9.3d Bury, K. V., "Bayesian Decision Analysis of the Hazard Rate for a Two-Parameter Weibull Process." IEEE Trans. Reliab. R-21(3):159-169, August 1972.

11.9.3e Stewart, L. T. and Johnson, J. D., "Determining Optimum Burn-in and Replacement Times Using Bayesian Decision Theory." IEEE Trans. Reliab. R-21(3):170-175, August 1972.

11.9.3f Wilson, M. A., "Experience with Bayesian Reliability Measurement of Large Systems." IEEE Trans. Reliab. R-21(3):181-185, August 1972.

11.9.3g Easterling, R. G., "A Personal View of the Bayesian Cointroversy in Reliability and Statistics." IEEE Trans. Reliab. R-21(3):186-194, August 1972.

11.9.4 Tang, W. H., "Probabilistic Updating of Flaw Information." J. Test. Eval. 1(6):459-467, November 1973.

DISTRIBUTION

No. of Copies

OFFSITE

Division of Technical Information
and Document Control
U.S. Nuclear Regulatory
Commission
7920 Norfolk Avenue
Bethesda, MD 20014

Division of Engineering
Technology
Office of Nuclear Regulatory
Research
U.S. Nuclear Regulatory
Commission
Washington, DC 20555

W. F. Anderson
U.S. Nuclear Regulatory
Commission
Mail Stop NL-5650
Washington, DC 20555

C. Y. Cheng
U. S. Nuclear Regulatory
Commission
Office of Nuclear Reactor
Regulation
Engineering Branch
Mail Stop P-1030
Washington, DC 20555

Mr. Robert Hermann
U.S. Nuclear Regulatory
Commission
Mail Stop 516
Washington, DC 20555

Martin Hum
U.S. Nuclear Regulatory
Commission
Mail Stop P-1000
Washington, DC 20555

No. of Copies

E. L. Jordan
U.S. Nuclear Regulatory
Commission
Inspection and Enforcement
Main Stop EW-359
Washington, DC 20555

Dr. Thomas G. McCreless
Asst. Exec. Director of
Technical Activity
1717-H USNRC-ACRS
Washington, DC 20555

12 Joseph Muscara
U.S. Nuclear Regulatory
Commission
Division of Reactor Safety
Research
Mail Stop SS-1130
Washington, DC 20555

S. S. Pawlicki
U.S. Nuclear Regulatory
Commission
Mail Stop TS-1000
Washington, DC 20555

G. A. Walton
U.S. Nuclear Regulatory
Commission
Office Inspection & Licensing
631 Park Avenue
King of Prussia, PA 19406

C. W. Allison
Dept. of Labor
Boiler Inspection & Codes
Division
501 Union Bldg./Suite 200B
Nashville, TN 37219

No. of
Copies

W. H. Bamford
Westinghouse Electric Corp.
Nuclear Energy Systems
P.O. Box 355
Pittsburgh, PA 15230

F. L. Becker
EPRI NDE Center
J. A. Jones Applied Research
1300 Harrison
Charlotte, NC 28221

Carl Bennett
Battelle-Human Affairs Research
Center
4000 N.E. 41st Street
Seattle, WA 98105

F. C. Berry
Chicago Bridge & Iron Co.
P.O. Box 277
Birmingham, AL 35201

M. Buckley
Science Center
Rockwell International
1049 Camina Des Rios
P.O. Box 1085
Thousand Oaks, CA 91360

H. Burger
National Bureau of Standards
Materials Building
Washington, DC 20234

Hans Burte, Chief
Metals and Ceramics Division
Airforce Materials Laboratory
(APSC)
Wright Patterson
Air Force Base, OH 45433

L. J. Chockie
General Electric Company
Nuclear Energy Division
175 Curtner Avenue M/C 827
San Jose, CA 95125

No. of
Copies

R. C. Cipolla
Aptech Eng. Services
795 San Antonio Road
Los Altos, CA 94303

W. E. Cooper
Teledyne Engineering Services
303 Bear Hill Road
Waltham, MA 02154

A. E. Curtis
Rochester Gas & Electric Co.
89 E. Avenue
Rochester, NY 14649

J. Danko
Electric Power Research Institute
3412 Hillview Avenue
P.O. Box 10412
Palo Altro, CA 94303

G. J. Dau/K. Stahlkopf
Electric Power Research Institute
3412 Hillview Avenue
P.O. Box 10412
Palo Alto, CA 94303

F. J. Dodd/W. C. Ham
Pacific Gas & Electric Co.
3400 Crow Canyon Road
San Ramon, CA 94583

F. T. Duba
Hartford Steam Boiler
Inspection & Insurance Co.
56 Prospect Street
Hartford, CT 06102

J. H. Gieske/D. Ballard
Sandia Laboratories
P.O. Box 5800
Albuquerque, NM 87115

K. Hannah
Washington Public Power Supply
System
3000 George Washington Way
Richland, WA 99352

No. of Copies

O. F. Hedden/D. J. Ayres
Combustion Engineering, Inc.
1000 Prospect Hill Road
Dept. 9004-2226
Windsor, CT 06095

A. E. Holt
Babcock and Wilcox Co.
P.O. Box 1260
Lynchburg, VA 24505

L. R. Katz/J. S. Caplan
Westinghouse Electric Corp.
PWR Systems/Forest Hill Site
P.O. Box 355
Pittsburgh, PA 15230

J. R. Knoke
Power Production Engineering
P.O. Box 1325
San Clemente, CA 92672

Dave Kupperman
Argonne National Laboratories
9700 South Cass Avenue
Argonne, IL 60439

J. J. Lance
Yankee Atomic Electric Co.
20 Turnpike Road
Westboro, MA 01581

W. Lawrie
Babcock and Wilcox Co.
Alliance Research Center
1562 Beeson Street
Alliance, OH 44601

N. R. MacDearman
Combustion Engineering, Inc.
911 W. Main Street
Chattanooga, TN 37401

R. W. McClung
Oak Ridge National Laboratory
Post Office Box X
Oak Ridge, TN 37830

No. of Copies

J. G. Merkle
Oak Ridge National Laboratory
P.O. Box X
Oak Ridge, TN 37830

Thomas A. Nemzek, Vice President
Special Projects Services Division
J. A. Jones Construction Co.
One South Executive Park
Charlotte, NC 28231

P. F. Packman
Southern Methodist University
Department of Mechanical Engineering
Dallas, TX 75275

Prof. Steven Serabian
University of Lowell
Mechanical Engineering Dept.
North Campus
Lowell, MA 01854

Jack C. Spanner, P.E.
Spanner Engineering, Inc.
2042 George Washington Way
Richland, WA 99352

R. M. Stone
J. A. Jones Construction Co.
One South Executive Park
Charlotte, NC 28231

D. O. Thompson
Ames Lab., U.S. DOE
Iowa State University
Ames, IA 50011

W. A. Van Der Sluys
Babcock and Wilcox Company
Alliance Research Center
1562 Beeson Street
Alliance, OH 44601

No. of Copies

A. R. Whiting/A. Greer
Southwest Research Institute
6220 Culebra Road
Post Office Drawer 28510
San Antonio, TX 78284

Howard Woo
Lawrence Livermore Laboratories
P.O. Box 808
Mail Stop L-90
Livermore, CA 94550

Edward Wright
Department of Energy
Clinch River Project
P.O. Box U
Oak Ridge, TN 37830

Sumio Yukawa
General Electric Company
Large Steam Generator Division
Building 55/Rm 111
One River Road
Schenectady, NY 12345

R. Zong
Philadelphia Electric Company
2301 Market Street
Philadelphia, PA 19101

I. P. Bell
Risley Nuclear Power Development Laboratories
United Kingdom Atomic Energy Authority
Risley, Warrington WA3 6AT
England

John Darlaston/R. P. Harrison
Central Electricity Generating Board
Research Department
Berkeley Nuclear Laboratories
Berkeley Gloucestershire GL13 9PB
England

No. of Copies

N. F. Haines
Central Electricity Generating Board
Research Department
Berkeley Nuclear Laboratories
Berkeley Gloucestershire GL13 9PB
England

J. D. Harrison/T. J. Jessop
The Welding Institute
Research Laboratory
Abington Hall
Abington Cambridge CBI 6 AL
England

R. W. Nichols
Risley Nuclear Power Development Laboratories
United Kingdom Atomic Energy Authority
(Northern Division)
Risley Warrington WA3 6AT
England

Mr. R. O'Neil
Safety and Reliability Directrate
United Kingdom Atomic Energy Authority
Wigshaw Lane
Culcheth, Warrington WA3 4NE
England

R. Sharpe/G. Silk
Nondestructive Testing Centre
Atomic Energy Research Establishment
Harwell Oxfordshire OX11 ORG
England

B. Watkins
Risley Nuclear Power Development Laboratories
United Kingdom Atomic Energy Authority
(Northern Division)
Wigshaw Lane
Culcheth, Warrington WA3 6AT
England

No. of Copies

Jacques Pierre Dufresne
Commissariat a l'Energie Atomique
CEN SAR BNO6
92260 Fontenay-aux-Roses
France

P. Oliver
Nuclear Safety Division
OECD Nuclear Energy Agency
38 bld Suchet
75016 Paris
France

Andre C. Prot/Robert Saglio
Centre D'Etudes Superieure de
Mecanique et D'Aerotechnique
B.P. N 91190 Gif-sur-Yvette
France

J. Eisenblatter
Battelle Institut e.V.
Am Romerhof 35
6000 Frankfurt am Main 90
West Germany

Guenter Engl
K.W.U.
Hammerbackerstr
P.O. Box 3220
D-852 Erlangen
Dept. R214
Germany

P. Höller
Institut für Zerstörungsfreie
Prüfverfahren
Saarbrucken
West Germany

Otto Kellerman, Dipl-Ing.
Direktor des Institut fur
Reaktorsicherheit
5 Köln 1
Glockengasse 2
West Germany

No. of Copies

H. J. Meyer
Machinenfabrik Augsburg-Nürnberg AG
Katzwangstr. 101
85 Nürnberg 2
West Germany

E. Mundry/Ing. H. Wüstenberg
Bundevsanstalt für
Materialprüfung
Unter den Eichen 87
D-1000 Berlin 45
West Germany

Professor D. Munz
Universitat Karlsruhe (TH)
7500 Karlsruhe 1, den
Postfach 3640
West Germany

A. J. Tietze
Technischen Uberwachungs-Verein
Rheinland e.V.
5000 Köln 1
Postfach 101750
West Germany

R. Trumpfheller
Deputy Director
Rheinisch-Westfalischer
Technischen Uberwachungs-Verein
E. V. 43 Essen 1
Steubenstr. 53
West Germany

Serge Crutzen
Commission of the European
Communities
Joint Research Centre
Ispra Establishment
21020 Ispra (VA)
Italy

A. deSterke
Röntgen Technische Dienst, B.V.
Delftweg 144
NL 3046 Rotterdam
The Netherlands

No. of Copies

Prof. Ir. D.G.H. Latzko
Dept. of Mechanical Engineering
University of Technology
Delft
The Netherlands

A. Nielsen/P. Becher
RISO Research Establishment
DK-4000 Roskilde
Denmark

Lars-Ake Kornvik
Section Manager
Nuclear Department
Kemistvagen 21
Box 51
S-183 21 TABY
Sweden

Dr. Gustaf Ostberg
Engineering Materials
Lund Institute of Technology
Box 725
S-220 07 - Lund 7
Sweden

Xaver Edelmann
Sulzer Brothers Limited
GH-8401
Winterthur, Switzerland

Dr. Yoshio Ando
Professor, Nuclear Engineering
Dept. of Nuclear Engineering
Faculty of Engineering
University of Tokyo
7-3-1 Hongo
Bunkyo-Ku
Japan

K. Iida
Professor, Naval Architecture
Faculty of Engineering
University of Tokyo
7-3-1 Hongo
Bunkyo-Ku
Japan

No. of Copies

T. Matsubara
Mitsubishi Heavy Industries, LTD
Takasago Technical Institute
2-1-1 Shinhama, Arai-Cho
Takasago 676
Japan

Dr. Shinsaku Onodera
Associate Director Engineering
The Japan Steel Works, Ltd
Hibiya-Mitsui Bldg
1-1-2 Yurakucho, Chiyoda-Ku
Tokyo, Japan

Y. Saiga
Ishikawajima-Harima Heavy
Industries Co., Ltd
1-15, Toyosu 3
Koto-Ku
Tokyo, 135-91
Japan

S. Sasaki
Hitachi Research Lab
4026 Kuji-Machi
Hitachi-Shi
Baraki-Ken
Japan

J. Watanabe
Japan Steel Works, Ltd
4 Chatsu-Machi
Muroran, Hokkaido
Japan

T. Yamaguchi
Mitsubishi Heavy Industries, Ltd
Takasago Technical Institute
2-1-1 Shinhama, Arai-Cho
Takasago 676
Japan

No. of
Copies

ONSITE

50 Pacific Northwest Laboratory

S. H. Bush (39)
S. R. Doctor
P. G. Heasler
G. J. Posakony
F. C. Simonen
Publishing Coordination (2)
Technical Information (5)

HEDL

T. E. Michaels

NRC FORM 335 (11-81)

U.S. NUCLEAR REGULATORY COMMISSION

BIBLIOGRAPHIC DATA SHEET

1. REPORT NUMBER *(Assigned by DDC)*
NUREG/CR-3110, Vol. 2
PNL-4584

4. TITLE AND SUBTITLE *(Add Volume No., if appropriate)*
Reliability of Nondestructive Examination
Chapters 7 - 11

2. *(Leave blank)*

3. RECIPIENT'S ACCESSION NO.

7. AUTHOR(S)
Spencer H. Bush, Senior Staff Consultant

5. DATE REPORT COMPLETED
MONTH: August YEAR: 1983

9. PERFORMING ORGANIZATION NAME AND MAILING ADDRESS *(Include Zip Code)*
Pacific Northwest Laboratory
Operated by Battelle Memorial Institute
P.O. Box 999
Richland, WA 99352

DATE REPORT ISSUED
MONTH: October YEAR: 1983

6. *(Leave blank)*

8. *(Leave blank)*

12. SPONSORING ORGANIZATION NAME AND MAILING ADDRESS *(Include Zip Code)*
Division of Engineering Technology
Office of Nuclear Regulatory Research
U.S. Nuclear Regulatory Commission
Washington, D.C. 20555

10. PROJECT/TASK/WORK UNIT NO.

11. FIN NO.
B-2289

13. TYPE OF REPORT
Technical

PERIOD COVERED *(Inclusive dates)*
October 1979 to August 1983

15. SUPPLEMENTARY NOTES

14. *(Leave blank)*

16. ABSTRACT *(200 words or less)*

This eighteen-chapter, three-volume study evaluates the various nondestructive examination (NDE) techniques now used to detect flaws in components of nuclear systems so that the reliability of the techniques may be increased. The significance of flaws at various locations in pressure boundary components are assessed along with ways to optimize the NDE procedures needed to detect, locate and size them. Emphasis is placed on an integrated program which also considers design, fabrication procedures, and materials. The data available on the reliability of detecting, locating and sizing flaws by NDE are used to construct a probabilistic fracture mechanics model. The model highlights the significance of the failure to detect flaws, and to accurately locate or size them in the context of component failure probability.

This study was conducted under the U.S. Nuclear Regulatory Commission program on the "Integration of NDE Reliability and Fracture Mechanics." Its objectives include 1) improving examination procedures for incorporation into the American Society for Mechanical Engineers (ASME), Boiler and Pressure Vessel Codes, Section III, V, XI; and 2) gaining a better insight into the influence of improved reliability of NDE in detecting, locating and sizing flaws on component failure probabilities.

17. KEY WORDS AND DOCUMENT ANALYSIS

17a. DESCRIPTORS

Ultrasonics
Reliability
Nondestructive Examination
Austenitic Metals
Flaws
Flaw Detection
Flaw Sizing

17b. IDENTIFIERS/OPEN-ENDED TERMS

18. AVAILABILITY STATEMENT
Unlimited

19. SECURITY CLASS *(This report)*
Unclassified

21. NO. OF PAGES

20. SECURITY CLASS *(This page)*
Unclassified

22. PRICE
S